



Observational probes of cosmic acceleration



David H. Weinberg^{a,b,*}, Michael J. Mortonson^b, Daniel J. Eisenstein^{c,d},
Christopher Hirata^e, Adam G. Riess^f, Eduardo Rozo^g

^a Department of Astronomy, Ohio State University, Columbus, OH, United States

^b Center for Cosmology and Astro-Particle Physics, Ohio State University, Columbus, OH, United States

^c Steward Observatory, University of Arizona, Tucson, AZ, United States

^d Harvard College Observatory, Cambridge, MA, United States

^e California Institute of Technology, Pasadena, CA, United States

^f Department of Physics and Astronomy, Johns Hopkins University, Baltimore, MD, United States

^g Kavli Institute for Cosmological Physics, University of Chicago, Chicago, IL, United States

ARTICLE INFO

Article history:

Accepted 6 May 2013

Available online 13 May 2013

editor: M.P. Kamionkowski

ABSTRACT

The accelerating expansion of the universe is the most surprising cosmological discovery in many decades, implying that the universe is dominated by some form of “dark energy” with exotic physical properties, or that Einstein’s theory of gravity breaks down on cosmological scales. The profound implications of cosmic acceleration have inspired ambitious efforts to understand its origin, with experiments that aim to measure the history of expansion and growth of structure with percent-level precision or higher. We review in detail the four most well established methods for making such measurements: Type Ia supernovae, baryon acoustic oscillations (BAO), weak gravitational lensing, and the abundance of galaxy clusters. We pay particular attention to the systematic uncertainties in these techniques and to strategies for controlling them at the level needed to exploit “Stage IV” dark energy facilities such as BigBOSS, LSST, *Euclid*, and *WFIRST*. We briefly review a number of other approaches including redshift-space distortions, the Alcock–Paczynski effect, and direct measurements of the Hubble constant H_0 . We present extensive forecasts for constraints on the dark energy equation of state and parameterized deviations from General Relativity, achievable with Stage III and Stage IV experimental programs that incorporate supernovae, BAO, weak lensing, and cosmic microwave background data. We also show the level of precision required for clusters or other methods to provide constraints competitive with those of these fiducial programs. We emphasize the value of a balanced program that employs several of the most powerful methods in combination, both to cross-check systematic uncertainties and to take advantage of complementary information. Surveys to probe cosmic acceleration produce data sets that support a wide range of scientific investigations, and they continue the longstanding astronomical tradition of mapping the universe in ever greater detail over ever larger scales.

© 2013 Elsevier B.V. All rights reserved.

Contents

1. Introduction.....	89
1.1. History.....	90
1.2. Theories of cosmic acceleration.....	91
1.3. Looking forward.....	93

* Corresponding author at: Department of Astronomy, Ohio State University, Columbus, OH, United States. Tel.: +1 6142926543; fax: +1 6142922928.
E-mail address: dhw@astronomy.ohio-state.edu (D.H. Weinberg).

2.	Observables, parameterizations, and methods	95
2.1.	Basic equations	96
2.2.	Model parameterizations	98
2.3.	CMB anisotropies and large scale structure	99
2.4.	Parameter dependences and CMB constraints	102
2.5.	Overview of methods	108
3.	Type Ia supernovae	109
3.1.	General principles.....	109
3.2.	The current state of play.....	109
3.3.	Observational considerations.....	112
3.4.	Systematic uncertainties and strategies for amelioration	113
3.5.	Space vs. ground	114
3.6.	Prospects	115
4.	Baryon acoustic oscillations	115
4.1.	General principles.....	115
4.2.	The current state of play.....	116
4.3.	Theory of BAO	119
4.3.1.	Linear theory.....	119
4.3.2.	Non-linear evolution and galaxy clustering bias.....	120
4.3.3.	Reconstruction.....	122
4.3.4.	Fitting to data.....	124
4.4.	Observational considerations.....	125
4.4.1.	Statistical errors.....	125
4.4.2.	From BAO to dark energy	126
4.4.3.	Sampling density	127
4.4.4.	Spectroscopic vs. photometric redshifts	128
4.4.5.	Tracers of structure.....	128
4.5.	Systematic uncertainties and strategies for amelioration	129
4.5.1.	Measurement systematics	129
4.5.2.	Astrophysical systematics.....	130
4.5.3.	Cosmological systematics	131
4.6.	Space vs. ground	131
4.7.	Prospects	132
5.	Weak lensing.....	133
5.1.	General principles: overview.....	134
5.2.	Weak lensing principles: mathematical discussion	135
5.2.1.	Deflection of light in cosmology.....	135
5.2.2.	Cosmic shear, magnification, and flexion	136
5.2.3.	Power spectra and correlation functions*.....	137
5.2.4.	Method I: cosmic shear power spectrum*.....	139
5.2.5.	Method II: power spectrum tomography*.....	139
5.2.6.	Method III: galaxy–galaxy lensing*.....	140
5.2.7.	Method IV: cosmography*.....	141
5.2.8.	Method V: non-Gaussian statistics*.....	142
5.3.	The current state of play.....	143
5.3.1.	Cosmic shear	143
5.3.2.	Galaxy–galaxy lensing as a cosmological probe.....	144
5.3.3.	Lensing outside the optical bands	146
5.4.	Observational considerations and survey design	146
5.4.1.	Statistical errors.....	146
5.4.2.	The galaxy population for optical surveys	148
5.4.3.	Photometric redshifts and their calibration.....	148
5.4.4.	Lensing in the radio.....	150
5.4.5.	Lensing of the CMB.....	151
5.5.	Measuring shears.....	151
5.5.1.	The idealized problem.....	152
5.5.2.	Shape measurement algorithms*.....	153
5.5.3.	Shape measurement errors*.....	156
5.5.4.	Noise rectification and selection biases*.....	156
5.5.5.	Determining the PSF and instrument properties.....	157
5.6.	Astrophysical systematics	158
5.6.1.	Intrinsic alignments*.....	158
5.6.2.	Theoretical uncertainties in the matter power spectrum*.....	161
5.7.	Systematic errors and their amelioration: summary	162
5.8.	Advantages of a space mission.....	163
5.9.	Prospects	163

6.	Clusters of galaxies.....	166
6.1.	General principles.....	166
6.2.	The current state of play.....	168
6.3.	Observational considerations.....	170
6.3.1.	Expected numbers and cosmological sensitivity.....	170
6.3.2.	Cluster finding.....	174
6.3.3.	Calibrating the observable–mass relation.....	176
6.4.	Systematic uncertainties and strategies for amelioration.....	179
6.4.1.	Redshift uncertainties.....	179
6.4.2.	Contamination and incompleteness: the tails of $P(X M, z)$	179
6.4.3.	Calibrating the core of $P(X M, z)$	180
6.4.4.	Theoretical systematics.....	183
6.5.	Space vs. ground.....	184
6.6.	Prospects.....	184
7.	Alternative methods.....	186
7.1.	Measurement of the Hubble constant at $z \approx 0$	186
7.2.	Redshift-space distortions.....	188
7.3.	The Alcock–Paczynski test.....	191
7.4.	Alternative distance indicators.....	192
7.5.	Standard sirens.....	193
7.6.	The Ly α forest as a probe of structure growth.....	194
7.7.	Other tests of modified gravity.....	195
7.8.	The integrated Sachs–Wolfe effect.....	196
7.9.	Cross-correlation of weak lensing and spectroscopic surveys.....	197
7.10.	Strong gravitational lenses.....	198
7.11.	Galaxy ages.....	198
7.12.	Redshift drift.....	199
7.13.	Alternative methods: summary.....	199
8.	A balanced program on cosmic acceleration.....	200
8.1.	A fiducial program.....	200
8.2.	Forecasting constraints.....	202
8.3.	Results: forecasts for the fiducial program and variations.....	206
8.3.1.	Constraints in simple $w(z)$ models.....	206
8.3.2.	Constraints on structure growth parameters.....	210
8.3.3.	Dependence on the $w(z)$ model and binning of data.....	212
8.3.4.	Constraints on $w(z)$ in the general model.....	214
8.4.	Forecasts for clusters.....	220
8.5.	Forecasts for alternative methods.....	223
8.5.1.	The Hubble constant.....	223
8.5.2.	The Alcock–Paczynski test.....	223
8.5.3.	Redshift-space distortions.....	225
8.5.4.	Distances.....	226
8.6.	Observables and aggregate precision.....	226
8.7.	Prospects with many probes.....	230
9.	Conclusions.....	232
	Appendix. Glossary of acronyms and facilities.....	236
	References.....	238

1. Introduction

Gravity pulls. Newton's *Principia* generalized this longstanding fact of human experience into a universal attractive force, providing compelling explanations of an extraordinary range of terrestrial and celestial phenomena. Newtonian attraction weakens with distance, but it never vanishes, and it never changes sign. Einstein's theory of General Relativity (GR) reproduces Newtonian gravity in the limit of weak spacetime curvature and low velocities. For a homogeneous universe filled with matter or radiation, GR predicts that the cosmic expansion will slow down over time, in accord with Newtonian intuition. In the late 1990s, however, two independent studies of distant supernovae found that the expansion of the universe has accelerated over the last five billion years (Riess et al., 1998; Perlmutter et al., 1999), a remarkable discovery that is now buttressed by multiple lines of independent evidence. On the scale of the cosmos, gravity repels.

Cosmic acceleration is the most profound puzzle in contemporary physics. Even the least exotic explanations demand the existence of a pervasive new component of the universe with unusual physical properties that lead to repulsive gravity. Alternatively, acceleration could be a sign that GR itself breaks down on cosmological scales. Cosmic acceleration may be the crucial empirical clue that leads to understanding the interaction between gravity and the quantum vacuum, or reveals the existence of extra spatial dimensions, or sheds light on the nature of quantum gravity itself.

Because of these profound implications, cosmic acceleration has inspired a wide range of ambitious experimental efforts, which aim to measure the expansion history and growth of structure in the cosmos with percent-level precision or better. In this article, we review the observational methods that underlie these efforts, with particular attention to techniques that are likely to see major advances over the next decade. We will emphasize the value of a balanced program that pursues several of these methods in combination, both to cross-check systematic uncertainties and to take advantage of complementary information.

The remainder of this introduction briefly recaps the history of cosmic acceleration and current theories for its origin, then sets this article in the context of future experimental efforts and other reviews of the field. Section 2 describes the basic observables that can be used to probe cosmic acceleration, relates them to the underlying equations that govern the expansion history and the growth of structure, and introduces some of the parameters commonly used to define “generic” cosmic acceleration models. It concludes with an overview of the leading methods for measuring these observables. In Sections 3–6 we go through the four most well developed methods in detail: Type Ia supernovae, baryon acoustic oscillations (BAO), weak gravitational lensing, and clusters of galaxies. Section 7 summarizes several other potential probes, whose prospects are currently more difficult to assess but in some cases appear quite promising. Informed by the discussions in these sections, Section 8 presents our principal new results: forecasts of the constraints on cosmic acceleration models that could be achieved by combining results from these methods, based on ambitious but feasible experiments like the ones endorsed by the Astro2010 Decadal Survey report, *New Worlds, New Horizons in Astronomy and Astrophysics*. We summarize the implications of our analyses in Section 9.

1.1. History

Just two years after the completion of General Relativity, Einstein (1917) introduced the first modern cosmological model. With little observational guidance, Einstein assumed (correctly) that the universe is homogeneous on large scales, and he proposed a matter-filled space with finite, positively curved, 3-sphere geometry. He also assumed (incorrectly) that the universe is static. Finding these two assumptions to be incompatible, Einstein modified the GR field equation to include the infamous “cosmological term”, now usually known as the “cosmological constant” and denoted Λ . In effect, he added a new component whose repulsive gravity could balance the attractive gravity of the matter (though he did not describe his modification in these terms). In the 1920s, Friedmann (1922, 1924) and Lemaître (1927) introduced GR-based cosmological models with an expanding or contracting universe, some of them including a cosmological constant, others not. In 1929, Hubble discovered direct evidence for the expansion of the universe (Hubble, 1929), thus removing the original motivation for the Λ term.¹ In 1965, the discovery and interpretation of the cosmic microwave background (CMB; Penzias and Wilson, 1965; Dicke et al., 1965) provided the pivotal evidence for a hot big bang origin of the cosmos.

From the 1930s through the 1980s, a cosmological constant seemed unnecessary to explaining cosmological observations. The “cosmological constant problem” as it was defined in the 1980s was a theoretical one: why was the gravitational impact of the quantum vacuum vanishingly small compared to the “naturally” expected value (see Section 1.2)? In the late 1980s and early 1990s, however, a variety of indirect evidence began to accumulate in favor of a cosmological constant. Studies of large scale galaxy clustering, interpreted in the framework of cold dark matter (CDM) models with inflationary initial conditions, implied a low matter density parameter $\Omega_m = \rho_m / \rho_{\text{crit}} \approx 0.15\text{--}0.4$ (e.g., Maddox et al., 1990; Efstathiou et al., 1990), in agreement with direct dynamical estimates that assumed galaxies to be fair tracers of the mass distribution. Reconciling this result with the standard inflationary cosmology prediction of a spatially flat universe (Guth, 1981) required a new energy component with density parameter $1 - \Omega_m$. Open-universe inflation models were also considered, but explaining the observed homogeneity of the CMB (Smoot et al., 1992) in such models required speculative appeals to quantum gravity effects (e.g., Bucher et al., 1995) rather than the semi-classical explanation of traditional inflation.

By the mid-1990s, many cosmological simulation studies included both open-CDM models and Λ -CDM models, along with $\Omega_m = 1$ models incorporating tilted inflationary spectra, non-standard radiation components, or massive neutrino components (e.g., Ostriker and Cen, 1996; Cole et al., 1997; Gross et al., 1998; Jenkins et al., 1998). Once normalized to the observed level of CMB anisotropies, the large-scale structure predictions of open and flat- Λ models differed at the tens-of-percent level, with flat models generally yielding a more natural fit to the observations (e.g., Cole et al., 1997). Conflict between high values of the Hubble constant and the ages of globular clusters also favored a cosmological constant (e.g., Pierce et al., 1994; Freedman et al., 1994; Chaboyer et al., 1996), though the frequency of gravitational lenses pointed in the opposite direction (Kochanek, 1996). Thus, the combination of CMB data, large-scale structure data, age of the universe, and inflationary theory led many cosmologists to consider models with a cosmological constant, and some to declare it as the preferred solution (e.g., Efstathiou et al., 1990; Krauss and Turner, 1995; Ostriker and Steinhardt, 1995).

Enter the supernovae. In the mid-1990s, two teams set out to measure the cosmic deceleration rate, and thereby determine the matter density parameter Ω_m , by discovering and monitoring high-redshift, Type Ia supernovae. The recognition that the peak luminosity of supernovae was tightly correlated with the shape of the light curve (Phillips, 1993; Riess et al., 1996) played a critical role in this strategy, reducing the intrinsic distance error per supernova to $\sim 10\%$. While the first

¹ Several recent papers have addressed the contributions of Lemaître, Friedmann, and Slipher to this discovery; the story is interestingly tangled (see, e.g., Block, 2011; van den Bergh, 2011; Livio, 2011; Belenkiy, 2012; Peacock, 2013).

analysis of a small sample indicated deceleration (Perlmutter et al., 1997), by 1998 the two teams had converged on a remarkable result: when compared to local Type Ia supernovae (Hamuy et al., 1996), the supernovae at $z \approx 0.5$ were fainter than expected in a matter-dominated universe with $\Omega_m \approx 0.2$ by about 0.2 mag, or 20% (Riess et al., 1998; Perlmutter et al., 1999). Even an empty, freely expanding universe was inconsistent with the observations. Both teams interpreted their measurements as evidence for an accelerating universe with a cosmological constant, consistent with a flat universe ($\Omega_{\text{tot}} = 1$) having $\Omega_\Lambda \approx 0.7$.

Why was the supernova evidence for cosmic acceleration accepted so quickly by the community at large? First, the internal checks carried out by the two teams, and the agreement of their conclusions despite independent observations and many differences of methodology, seemed to rule out many forms of observational systematics, even relatively subtle effects of photometric calibration or selection bias. Second, the ground had been well prepared by the CMB and large scale structure data, which already provided substantial indirect evidence for a cosmological constant. This confluence of arguments favored the cosmological interpretation of the results over astrophysical explanations such as evolution of the supernova population or gray dust extinction that increased toward higher redshifts. Third, the supernova results were followed within a year by the results of balloon-borne CMB experiments that mapped the first acoustic peak and measured its angular location, providing strong evidence for spatial flatness (de Bernardis et al., 2000; Hanany et al., 2000; see Netterfield et al., 1997 for earlier ground-based measurements hinting at the same result). On its own, the acoustic peak only implied $\Omega_{\text{tot}} \approx 1$, not a non-zero Ω_Λ , but it dovetailed perfectly with the estimates of Ω_m and Ω_Λ from large scale structure and supernovae. Furthermore, the acoustic peak measurement implied that the alternative to Λ was not an open universe but a strongly decelerating, $\Omega_m = 1$ universe that disagreed with the supernova data by 0.5 magnitudes, a level much harder to explain with observational or astrophysical effects. Finally, the combination of spatial flatness and improving measurements of the Hubble constant (e.g., $H_0 = 71 \pm 6 \text{ km s}^{-1} \text{ Mpc}^{-1}$; Mould et al., 2000) provided an entirely independent argument for an energetically dominant accelerating component: a matter-dominated universe with $\Omega_{\text{tot}} = 1$ would have age $t_0 = (2/3)H_0^{-1} \approx 9.5 \text{ Gyr}$, too young to accommodate the 12–14 Gyr ages estimated for globular clusters (e.g., Chaboyer, 1998).

A decade later, the web of observational evidence for cosmic acceleration is intricate and robust. A wide range of observations – including larger and better calibrated supernova samples over a broader redshift span, high-precision CMB data down to small angular scales, the baryon acoustic scale in galaxy clustering, weak lensing measurements of dark matter clustering, the abundance of massive clusters in X-ray and optical surveys, the level of structure in the Ly α forest, and precise measurements of H_0 – are all consistent with an inflationary cold dark matter model with a cosmological constant, commonly abbreviated as ΛCDM .² Explaining all of these data simultaneously *requires* an accelerating universe. Completely eliminating any one class of constraints (e.g., supernovae, or CMB, or H_0) would not change this conclusion, nor would doubling the estimated systematic errors on all of them. The question is no longer *whether* the universe is accelerating, but *why*.

1.2. Theories of cosmic acceleration

A cosmological constant is the mathematically simplest solution to the cosmic acceleration puzzle. While Einstein introduced his cosmological term as a modification to the curvature side of the field equation, it is now more common to interpret Λ as a new energy component, constant in space and time. For an ideal fluid with energy density u and pressure p , the effective gravitational source term in GR is $(u + 3p)/c^2$, reducing to the usual mass density $\rho = u/c^2$ if the fluid is non-relativistic. For a component whose energy density remains constant as the universe expands, the first law of thermodynamics implies that when a comoving volume element in the universe expands by a (physical) amount dV , the corresponding change in energy is related to the pressure via $-pdV = dU = u dV$. Thus, $p = -u$, making the gravitational source term $(u + 3p)/c^2 = -2u/c^2$. A form of energy that is constant in space and time must have a repulsive gravitational effect.

According to quantum field theory, “empty” space is filled with a sea of virtual particles. It would be reasonable to interpret the cosmological constant as the gravitational signature of this quantum vacuum energy, much as the Lamb shift is a signature of its electromagnetic effects.³ The problem is one of magnitude. Since virtual particles of any allowable mass can come into existence for short periods of time, the “natural” value for the quantum vacuum density is one Planck Mass per cubic Planck Length. This density is about 120 orders of magnitude larger than the cosmological constant suggested by observations: it would drive accelerated expansion with a timescale of $t_{\text{Planck}} \approx 10^{-43} \text{ s}$ instead of $t_{\text{Hubble}} \approx 10^{18} \text{ s}$. Since the only “natural” number close to 10^{-120} is zero, it was generally assumed (prior to 1990) that a correct calculation of the quantum vacuum energy would eventually show it to be zero, or at least suppressed by an extremely large exponential factor (see review by Weinberg, 1989). But the discovery of cosmic acceleration raises the possibility that the quantum vacuum really does act as a cosmological constant, and that its energy scale is 10^{-3} eV rather than 10^{28} eV for reasons that we do not yet understand. To date, there are no compelling theoretical arguments that explain either why the fundamental quantum vacuum energy might have this magnitude *or* why it might be zero.

² Many of the relevant observational references will appear in subsequent sections on specific topics.

³ This interpretation of the cosmological constant in the context of quantum field theory, originally due to Wolfgang Pauli, was revived in the late 1960s by Zel'dovich (1968). For further discussion of the history see Peebles and Ratra (2003). For a detailed discussion in the context of contemporary particle theory, see the review by Martin (2012).

The other basic puzzle concerning a cosmological constant is: Why now? The ratio of a constant vacuum energy density to the matter density scales as $a^3(t)$, so it has changed by a factor of $\sim 10^{27}$ since big bang nucleosynthesis and by a factor $\sim 10^{42}$ since the electroweak symmetry breaking epoch, which seems (based on our current understanding of physics) like the last opportunity for a major rebalancing of matter and energy components. It therefore seems remarkably coincidental for the vacuum energy density and the matter energy density to have the same order of magnitude today. In the late 1970s, Robert Dicke used a similar line of reasoning to argue for a spatially flat universe (see Dicke and Peebles, 1979), an argument that provided much of the initial motivation for inflationary theory (Guth, 1981). However, while the universe appears to be impressively close to spatial flatness, the existence of two energy components with different $a(t)$ scalings means that Dicke’s “coincidence problem” is still with us.

One possible solution to the coincidence problem is anthropic: if the vacuum energy assumes widely different values in different regions of the universe, then conscious observers will find themselves in regions of the universe where the vacuum energy is low enough to allow structure formation (Efstathiou, 1995; Martel et al., 1998). This type of explanation finds a natural home in “multiverse” models of eternal inflation, where different histories of spontaneous symmetry breaking lead to different values of physical constants in each non-inflating “bubble” (Linde, 1987), and it has gained new prominence in the context of string theory, which predicts a “landscape” of vacua arising from different compactifications of spatial dimensions (Susskind, 2003). One can attempt to derive an expectation value of the observed cosmological constant from such arguments (e.g., Martel et al., 1998), but the results are sensitive to the choice of parameters that are allowed to vary (Tegmark and Rees, 1998) and to the choice of measure on parameter space, so it is hard to take such “predictions” beyond a qualitative level. A variant on these ideas is that the effective value (and perhaps even the sign) of the cosmological constant varies in time, and that structure will form and observers arise during periods when its magnitude is anomalously low compared to its natural (presumably Planck-level) energy scale (Brandenberger, 2002; Griest, 2002).

A straightforward alternative to a cosmological constant is a field with negative pressure (and thus repulsive gravitational effect) whose energy density changes with time (Ratra and Peebles, 1988; Frieman et al., 1995; Ferreira and Joyce, 1997). In particular, a canonical scalar field ϕ with potential $V(\phi)$ has energy density and pressure

$$\begin{aligned} u_\phi &= \frac{1}{2} \frac{1}{\hbar c^3} \dot{\phi}^2 + V(\phi), \\ p_\phi &= \frac{1}{2} \frac{1}{\hbar c^3} \dot{\phi}^2 - V(\phi), \end{aligned} \quad (1)$$

so if the kinetic term is subdominant, then $p_\phi \approx -u_\phi$. A slowly rolling scalar field of this sort is analogous to the inflaton field hypothesized to drive inflation, but at an energy scale many, many orders of magnitude lower. In general, a scalar field has an equation-of-state parameter

$$w \equiv \frac{p}{u} \quad (2)$$

that is greater than -1 and varies in time, while a true cosmological constant has $w = -1$ at all times. Some forms of $V(\phi)$ allow attractor or “tracker” solutions in which the late-time evolution of ϕ is insensitive to the initial conditions (Ratra and Peebles, 1988; Steinhardt et al., 1999), and a subset of these allow u_ϕ to track the matter energy density at early times, ameliorating the coincidence problem (Skordis and Albrecht, 2002). Some choices give a nearly constant w that is different from -1 , while others have $w \approx -1$ as an asymptotic state at either early or late times, referred to respectively as “thawing” or “freezing” solutions (Caldwell and Linder, 2005).

Scalar field models in which the energy density is dominated by $V(\phi)$ are popularly known as “quintessence” (Zlatev et al., 1999). A number of variations have been proposed in which the energy density of the field is dominated by kinetic, spin, or oscillatory degrees of freedom (e.g., Armendariz-Picon et al., 2001; Boyle et al., 2002). Other models introduce non-canonical kinetic terms or couple the field to dark matter. Models differ in the evolution of $u_\phi(a)$ and $w(a)$, and some have other distinctive features such as large scale energy density fluctuations that can affect CMB anisotropies. Of course, none of these models addresses the original “cosmological constant problem” of why the true vacuum energy is unobservably small.

The alternative to introducing a new energy component is to modify General Relativity itself on cosmological scales, for example by replacing the Ricci scalar R in the gravitational action with some higher order function $f(R)$ (e.g., Capozziello and Fang, 2002; Carroll et al., 2004), or by allowing gravity to “leak” into an extra dimension in a way that reduces its attractive effect at large scales (Dvali et al., 2000). GR modifications can alter the relation between the expansion history and the growth of matter clustering, and, as discussed in subsequent sections, searching for mismatches between observational probes of expansion and observational probes of structure growth is one generic approach to seeking signatures of modified gravity. To be consistent with tight constraints from solar system tests, modifications of gravity must generally be “shielded” on small scales, by mechanisms such as the “chameleon” effect, the “symmetron” mechanism, or “Vainshtein screening” (see the review by Jain and Khoury, 2010). These mechanisms can have the effect of introducing intermediate scale forces. GR modifications can also alter the relation between non-relativistic matter clustering and gravitational lensing, which in standard GR is controlled by two different potentials that are equal to each other for fluids without anisotropic stress.

The distinction between a new energy component and a modification of gravity may be ambiguous. The most obvious ambiguous case is the cosmological constant itself, which can be placed on either the “curvature” side or the “stress–energy”

side of the Einstein field equation. More generally, many theories with $f(R)$ modifications of the gravitational action can be written in a mathematically equivalent form of GR plus a scalar field with specified properties (Chiba, 2003; Kunz and Sapone, 2007). Relative to expectations for a cosmological constant or a simple scalar field model, models in which dark matter decays into dark energy can produce a mismatch between the histories of expansion and structure growth while maintaining GR (e.g., Jain and Zhang, 2008; Wei and Zhang, 2008). Thus, even perfect measurements of all relevant observables may not uniquely locate the explanation of cosmic acceleration in the gravitational or stress–energy sector.

There is a minority opinion (see Buchert, 2011 for a recent review article) that the phenomena interpreted as evidence for dark energy could instead arise from the backreaction of small scale inhomogeneities on the large scale cosmic expansion. This line of argument contends that the expansion rate of a universe with small scale inhomogeneity can differ significantly from that of a homogeneous universe with the same average density. In our view, the papers on this theme present an incorrect interpretation of correct underlying equations, and we do not see these “inhomogeneous averaging” effects as a viable alternative to dark energy. Baumann et al. (2012) present a detailed counter-argument, treating inhomogeneous matter as a fluid with an effective viscosity and pressure and demonstrating that the backreaction on the evolution of background expansion and large scale perturbations is extremely small. (See Green and Wald (2011) for an alternative form of this counter-argument and Peebles (2010) for a less formal but still persuasive version.) In a somewhat related vein, the suggestion that acceleration could arise from superhorizon fluctuations generated by inflation (Barausse et al., 2005; Kolb et al., 2005) is ruled out by a complete perturbation analysis (Hirata and Seljak, 2005).

While the term “dark energy” seems to presuppose a stress–energy explanation, in practice it has become a generic term for referring to the cosmic acceleration phenomenon. In particular, the phrase “dark energy experiments” has come to mean observational studies aimed at measuring acceleration and uncovering its cause, regardless of whether that cause is a new energy field or a modification of gravity. We will generally adopt this common usage of “dark energy” in this review, though where the distinction matters we will try to use “cosmic acceleration” as our generic term. It is important to keep in mind that we presently have strong observational evidence for accelerated cosmic expansion but no compelling evidence that the cause of this acceleration is really a new energy component.

The magnitude and coincidence problems are challenges for any explanation of cosmic acceleration, whether a cosmological constant, a scalar field, or a modification of GR. The coincidence problem seems like an important clue for identifying a correct solution, and some models at least reduce its severity by coupling the matter and dark energy densities in some way. Multiverse models with anthropic selection arguably offer a solution to the coincidence problem, because if the probability distribution of vacuum energy densities rises swiftly toward high values, then structure may generically form at a time when the matter and vacuum energy density values are similar, in that small subset of universes where structure forms at all. But sometimes a coincidence is just a coincidence. Essentially all current theories of cosmic acceleration have one or more adjustable parameters whose value is tuned to give the observed level of acceleration, and none of them yield this level as a “natural” expectation unless they have built it in ahead of time. These theories are designed to explain acceleration itself rather than emerging from independent theoretical considerations or experimental constraints. Conversely, a theory that provided a compelling account of the observed magnitude of acceleration – like GR’s successful explanation of the precession of Mercury – would quickly jump to the top of the list of cosmic acceleration models.

1.3. Looking forward

The deep mystery and fundamental implications of cosmic acceleration have inspired numerous ambitious observational efforts to measure its history and, it is hoped, reveal its origin. The report of the Dark Energy Task Force (DETF; Albrecht et al., 2006) played a critical role in systematizing the field, by categorizing experimental approaches and providing a quantitative framework to compare their capabilities. The DETF categorized then-ongoing experiments as “Stage II” (following the “Stage I” discovery experiments) and the next generation as “Stage III”. It looked forward to a generation of more capable (and more expensive) “Stage IV” efforts that might begin observations around the second half of the coming decade. The DETF focused on the same four methods that will be the primary focus of this review: Type Ia supernovae, baryon acoustic oscillations (BAO), weak gravitational lensing, and clusters of galaxies.

Six years on, the main “Stage II” experiments have completed their observations though not necessarily their final analyses. Prominent examples include the supernova and weak lensing programs of the CFHT Legacy Survey (CFHTLS; Conley et al., 2011; Semboloni et al., 2006a; Heymans et al., 2012b), the ESSENCE supernova survey (Wood-Vasey et al., 2007), BAO measurements from the Sloan Digital Sky Survey (SDSS; Eisenstein et al., 2005; Percival et al., 2010; Padmanabhan et al., 2012), and the SDSS-II supernova survey (Frieman et al., 2008). These have been complemented by extensive multi-wavelength studies of local and high-redshift supernovae such as the Carnegie Supernova Project (Hamuy et al., 2006; Freedman et al., 2009), by systematic searches for $z > 1$ supernovae with *Hubble Space Telescope* (Riess et al., 2007; Suzuki et al., 2012), by dark energy constraints from the evolution of X-ray or optically selected clusters (Henry et al., 2009; Mantz et al., 2010; Vikhlinin et al., 2009; Rozo et al., 2010), by improved measurements of the Hubble constant (Riess et al., 2009, 2011; Freedman et al., 2012), and by CMB data from the *WMAP* satellite (Bennett et al., 2003; Larson et al., 2011) and from ground-based experiments that probe smaller angular scales.⁴ Most data remain consistent with a spatially flat universe

⁴ We follow the convention in the astronomical literature of italicizing the names and acronyms of space missions but not of ground-based facilities. For reference, note that the many acronyms that appear in the article are all defined in Appendix, the glossary of acronyms and facilities.

and a cosmological constant with $\Omega_\Lambda = 1 - \Omega_m \approx 0.75$, with an uncertainty in the equation-of-state parameter w that is roughly ± 0.1 at the $1-2\sigma$ level. Substantial further improvement will in many cases require reduction in systematic errors as well as increased statistical power from larger data sets.

The clearest examples of “Stage III” experiments, now in the late construction or early operations phase, are the Dark Energy Survey (DES), Pan-STARRS,⁵ the Baryon Oscillation Spectroscopic Survey (BOSS) of SDSS-III, and the Hobby–Eberly Telescope Dark Energy Experiment (HETDEX).⁶ All four projects are being carried out by international, multi-institutional collaborations. Pan-STARRS and DES will both carry out large area, multi-band imaging surveys that go a factor of ten or more deeper (in flux) than the SDSS imaging survey (Abazajian et al., 2009), using, respectively, a 1.4-Gigapixel camera on the 1.8-m PS1 telescope on Haleakala in Hawaii and a 0.5-Gigapixel camera on the 4-m Blanco telescope on Cerro Tololo in Chile. These imaging surveys will be used to measure structure growth via weak lensing, to identify galaxy clusters and calibrate their masses via weak lensing, and to measure BAO in galaxy angular clustering using photometric redshifts. Each project also plans to carry out monitoring surveys over smaller areas to discover and measure thousands of Type Ia supernovae. Fully exploiting BAO requires spectroscopic redshifts, and BOSS will carry out a nearly cosmic-variance limited survey (over 10^4 deg^2) out to $z \approx 0.7$ using a 1000-fiber spectrograph to measure redshifts of 1.5 million luminous galaxies, and a pioneering quasar survey that will measure BAO at $z \approx 2.5$ by using the Ly α forest along 150,000 quasar sightlines to trace the underlying matter distribution. HETDEX plans a BAO survey of 10^6 Ly α -emitting galaxies at $z \approx 3$.

There are many other ambitious observational efforts that do not fit so neatly into the definition of a “Stage III dark energy experiment” but will nonetheless play an important role in “Stage III” constraints. A predecessor to BOSS, the WiggleZ project on the Anglo-Australian 3.9-m telescope, recently completed a spectroscopic survey of 240,000 emission line galaxies out to $z = 1.0$ (Blake et al., 2011a). The Hyper Suprime-Cam (HSC) facility on the Subaru telescope will have wide-area imaging capabilities comparable to DES and Pan-STARRS, and it is likely to devote substantial fractions of its time to weak lensing surveys. Other examples include intensive spectroscopic and photometric monitoring of supernova samples aimed at calibration and understanding of systematics, new *HST* searches for $z > 1$ supernovae, further improvements in H_0 determination, deeper X-ray and weak lensing studies of samples of tens or hundreds of galaxy clusters, and new cluster searches via the Sunyaev–Zel’dovich (1970) effect using the South Pole Telescope (SPT), the Atacama Cosmology Telescope (ACT), or the *Planck* satellite. In addition, Stage III analyses will draw on primary CMB constraints from *Planck*.

The Astro2010 report identifies cosmic acceleration as one of the most pressing questions in contemporary astrophysics, and its highest priority recommendations for new ground-based and space-based facilities both have cosmic acceleration as a primary science theme.⁷ On the ground, the Large Synoptic Survey Telescope (LSST), a wide-field 8.4-m optical telescope equipped with a 3.2-Gigapixel camera, would enable deep weak lensing and optical cluster surveys over much of the sky, synoptic surveys that would detect and measure tens of thousands of supernovae, and photometric-redshift BAO surveys extending to $z \approx 3.5$. BigBOSS, highlighted as an initiative that could be supported by the proposed “mid-scale innovation program”, would use a highly multiplexed fiber spectrograph on the NOAO 4-m telescopes to carry out spectroscopic surveys of $\sim 10^7$ galaxies to $z \approx 1.6$ and Ly α forest BAO measurements at $z > 2.2$. Another potential ground-based method for large volume BAO surveys is radio “intensity mapping”, which seeks to trace the large scale distribution of neutral hydrogen without resolving the scale of individual galaxies. In the longer run, the Square Kilometer Array (SKA) could enable a BAO survey of $\sim 10^9$ HI-selected galaxies and weak lensing measurements of $\sim 10^{10}$ star-forming galaxies using radio continuum shapes.

Space observations offer two critical advantages for cosmic acceleration studies: stable high resolution imaging over large areas, and vastly higher sensitivity at near-IR wavelengths. (For cluster studies, space observations are also the only route to X-ray measurements.) These advantages inspired the Supernova Acceleration Probe (SNAP), initially designed with a concentration on supernova measurements at $0.1 < z < 1.7$, and later expanded to include a wide area weak lensing survey as a major component. Following the National Research Council’s Quarks to Cosmos report (Committee on the Physics of the Universe, 2003), NASA and the U.S. Department of Energy embarked on plans for a Joint Dark Energy Mission (JDEM), which has considered a variety of mission architectures for space-based supernova, weak lensing, and BAO surveys. The Astro2010 report endorsed as its highest priority space mission a Wide Field Infrared Survey Telescope (WFIRST), which would carry out imaging and dispersive prism spectroscopy in the near-IR to support all of these methods, and, in addition, a planetary microlensing program, a Galactic plane survey, and a guest observer program. The recently completed report of the WFIRST Science Definition Team (Green et al., 2012) presents detailed designs and operational concepts, with a primary design reference mission that includes three years of dark energy programs (out of a five year mission) on an unobstructed 1.3-meter telescope with a 0.375 deg^2 near-IR focal plane (150 million $0.18''$ pixels). The recent transfer of two 2.4-meter diameter telescopes from the U.S. National Reconnaissance Office (NRO) to NASA opens the door for a potential

⁵ Pan-STARRS, the Panoramic Survey Telescope and Rapid Response System, is the acronym of the facility rather than the project, but cosmological surveys are among its major goals. Pan-STARRS eventually hopes to use four coordinated telescopes, but the surveys currently underway (and now nearing completion) use the first of these telescopes, referred to as PS1.

⁶ As we enter the forest of acronyms, please note the glossary in the Appendix.

⁷ We will use the term “Astro2010 report” to refer collectively to *New Worlds*, *New Horizons* and to the panel reports that supported it. In particular, detailed discussion of these science themes and related facilities can be found in the individual reports of the Cosmology and Fundamental Physics (CFP) Science Frontiers Panel and the Electromagnetic Observations from Space (EOS), Optical and Infrared Astronomy from the Ground (OIR), and Radio, Millimeter, and Sub-Millimeter Astronomy from the Ground (RMS) Program Prioritization Panels. Information on all of these reports can be found at http://sites.nationalacademies.org/bpa/BPA_049810.

implementation of *WFIRST* on a larger platform; this possibility is now a subject of active, detailed study (see Dressler et al., 2012 for an initial assessment). *WFIRST* faces significant funding hurdles, despite its top billing in Astro2010, but a launch in the early 2020s still appears likely. On the European side, ESA recently selected the *Euclid*⁸ satellite as a medium-class mission for its Cosmic Vision 2015–2025 program, with launch planned for 2020. *Euclid* plans to carry out optical and near-IR imaging and near-IR slitless spectroscopy over roughly 14,000 deg², for weak lensing and BAO measurements. In its current design (Laureijs et al., 2011), *Euclid* utilizes a 1.2-meter telescope, a 0.56 deg² optical focal plane (604 million 0.10'' pixels), and a near-IR focal plane with similar area but larger pixels (67 million 0.30'' pixels). Well ahead of either *Euclid* or *WFIRST*, the European X-ray telescope *eROSITA* (on the Russian *Spectrum Roentgen Gamma* satellite) is expected to produce an all-sky catalog of $\sim 10^5$ X-ray selected clusters, with X-ray temperature measurements and resolved profiles for the brighter clusters (Merloni et al., 2012).⁹

The completion of the Astro2010 Decadal Survey and the *Euclid* selection by ESA make this an opportune time to review the techniques and prospects for probing cosmic acceleration with ambitious observational programs. Our goal is, in some sense, an update of the DETF report (Albrecht et al., 2006), incorporating the many developments in the field over the last few years and (the difference between a report and a review) emphasizing explanation rather than recommendation. We aim to complement other reviews of the field that differ in focus or in level of detail. To mention just a selection of these, we note that Frieman et al. (2008) and Blanchard (2010) provide excellent overviews of the field, covering theory, current observations, and future experiments, while Astier and Pain (2012) cover the observational approaches concisely; Peebles and Ratra (2003) and Copeland et al. (2006) are especially good on history of the subject and on theoretical aspects of scalar field models; Jain and Khoury (2010) review the observational and (especially) theoretical aspects of modified gravity models in much greater depth than we cover here; Carroll (2003) and Linder (2003b, 2007) provide accessible and informative introductions at the less forbidding length of conference proceedings; Linder (2010) provides a review aimed at a general scientific audience; and the conference proceedings by Peebles (2010) nicely situates the cosmic acceleration problem in the broader context of contemporary cosmology. The distinctive features of the present review are our in-depth discussion of individual observational methods and our new quantitative forecasts for how combinations of these methods can constrain parameters of cosmic acceleration theories.

To the extent that we have a consistent underlying theme, it is the importance of pursuing a balanced observational program. We do not believe that all methods or all implementations of methods are equal; some approaches have evident systematic limitations that will prevent them reaching the sub-percent accuracy level that is needed to make major contributions to the field over the next decade, while others would require prohibitively expensive investments to achieve the needed statistical precision. However, for a given level of community investment, we think there is more to be gained by doing a good job on the three or four most promising methods than by doing a perfect job on one at the expense of the others. A balanced approach offers crucial cross-checks against systematic errors, takes advantage of complementary information contained in different observables or complementary strengths in different redshift ranges, and holds the best chance of uncovering “surprises” that do not fit into the conventional categories of theoretical models. This philosophy will emerge most clearly in Section 8, where we present our quantitative forecasts. For understandable reasons, most articles and proposals (including some we have written ourselves) start from current knowledge and show the impact of adding a particular new experiment. We will instead start from a “fiducial program” that assumes ambitious but achievable advances in several different methods at once, then consider the impact of strengthening, weakening, or omitting its individual elements.

We expect that different readers will want to approach this lengthy article in different ways. For a reader who is new to the field and wants to learn it well, it makes sense to start at the beginning and read to the end. A reader interested in a specific method can skim Section 2 to get a sense of our notation, then jump to the section that describes that method (Type Ia supernovae in Section 3, BAO in Section 4, weak lensing in Section 5, and clusters in Section 6). We think that these sections will provide useful insights even to experts in the field. Section 7 provides a brief overview of emerging methods that could play an important role in future studies. Readers interested mainly in the ways that different methods contribute to constraints on cosmic acceleration models and the quantitative forecasts for Stage III and Stage IV programs can jump directly to Section 8. Finally, Section 9 provides a summary of our findings and their implications for experimental programs, and some readers may choose to start from the end (we recommend including Sections 8.6 and 8.7 as well as Section 9), then work backwards to the supporting details.

2. Observables, parameterizations, and methods

The two top-level questions about cosmic acceleration are:

1. Does acceleration arise from a breakdown of GR on cosmological scales or from a new energy component that exerts repulsive gravity within GR?
2. If acceleration is caused by a new energy component, is its energy density constant in space and time?

⁸ Not an acronym.

⁹ More detailed description of *Euclid* and *WFIRST* can be found in Section 5.9, and of *eROSITA* in Section 6.5.

As already discussed in Section 1.2, the distinction between “modified gravity” and “new energy component” solutions may not be unambiguous. However, the cosmological constant hypothesis makes specific, testable predictions, and the combination of GR with relatively simple scalar field models predicts testable consistency relations between expansion and structure growth.

The answer to these questions, or a major step toward an answer, could come from a surprising direction: a theoretical breakthrough, a revealing discovery in accelerator experiments, a time-variation of a fundamental “constant”, or an experimental failure of GR on terrestrial or solar system scales (see Section 7.7 for brief discussion). However, “wait for a breakthrough” is an unsatisfying recipe for scientific progress, and there is one clear path forward: measure the history of expansion and the growth of structure with increasing precision over an increasing range of redshift and lengthscale.

2.1. Basic equations

In GR, the expansion of a homogeneous and isotropic universe is governed by the Friedmann equation, which can be written in the form

$$\frac{H^2(z)}{H_0^2} = \Omega_m(1+z)^3 + \Omega_r(1+z)^4 + \Omega_k(1+z)^2 + \Omega_\phi \frac{u_\phi(z)}{u_\phi(z=0)}, \quad (3)$$

where $(1+z) \equiv a^{-1}$ is the cosmological redshift and $a(t)$ is the expansion factor relating physical separations to comoving separations. The Hubble parameter is $H(z) \equiv \dot{a}/a$, and Ω_m , Ω_r , and Ω_ϕ are the *present day* energy densities of matter, radiation, and a generic form of dark energy ϕ .¹⁰ These are expressed as ratios to the critical energy density required for flat space geometry

$$\Omega_x = \frac{u_x}{\rho_{\text{crit}} c^2}, \quad \rho_{\text{crit}} = \frac{3H_0^2}{8\pi G}. \quad (4)$$

At higher redshifts,

$$\Omega_m(z) \equiv \frac{\rho_m(z)}{\rho_{\text{crit}}(z)} = \Omega_m(1+z)^3 \frac{H_0^2}{H^2(z)}, \quad (5)$$

where the second equality follows from the scaling $\rho_m(z) = \rho_{m,0} \times (1+z)^3$ and from the definition of $\rho_{\text{crit}}(z)$. In the formulation (3), the impact of curvature on expansion is expressed like that of a “dynamical” component with scaled energy density

$$\Omega_k \equiv 1 - \Omega_m - \Omega_r - \Omega_\phi, \quad (6)$$

with $\Omega_k = 0$ for a spatially flat universe. In a standard cold dark matter scenario, the matter density is the sum of the densities of CDM, baryons, and non-relativistic neutrinos, $\Omega_m = \Omega_c + \Omega_b + \Omega_\nu$. In detail, one must beware that the neutrino energy density does not scale as $(1+z)^3$ at higher redshifts, when they are mildly relativistic, and that the clustering of neutrinos on small scales is suppressed by their residual thermal velocities.

There are some routes to direct measurement of $H(z)$, most notably via BAO (see Section 4). For the most part, however, observations constrain $H(z)$ indirectly by measuring the distance–redshift relation or the history of structure growth.

Hogg (1999) provides a compact and pedagogical summary of cosmological distance measures. The comoving line-of-sight distance to an object at redshift z is

$$D_C(z) = \frac{c}{H_0} \int_0^z dz' \frac{H_0}{H(z')}. \quad (7)$$

Defining a dimensional (length^{−2}) curvature parameter

$$K = -\Omega_k (c/H_0)^{-2} \quad (8)$$

allows us to write the comoving angular diameter distance,¹¹ relating an object’s comoving size l to its angular size $\theta = l/D_A$, as

$$D_A(z) = K^{-1/2} \sin(K^{1/2} D_C), \quad (9)$$

¹⁰ We will refer to values of these parameters at $z \neq 0$ as $\Omega_m(z)$, $\Omega_\phi(z)$, etc. For other quantities (e.g., H_0), we use subscripts 0 to denote values at $z = 0$. When we assume a cosmological constant, we will replace Ω_ϕ by Ω_Λ .

¹¹ Note that Hogg (1999) refers to this quantity as the comoving transverse distance and uses D_A to denote the quantity relating *physical* size to angular size.

which applies for either sign of Ω_k .¹² Noting that observations imply $|\Omega_k| \ll 1$, we can Taylor expand Eq. (9) to write

$$D_A(z) \approx D_C \left[1 + \frac{1}{6} \Omega_k \left(\frac{D_C}{c/H_0} \right)^2 \right], \quad (10)$$

which also yields the correct result $D_A = D_C$ for $\Omega_k = 0$. Note that positive space curvature ($\Omega_{\text{tot}} > 1, K > 0$) corresponds to negative Ω_k , hence a smaller D_A and larger angular size than in a flat universe. If $u_\phi(z) > u_{\phi,0}$ then the Hubble parameter at $z > 0$ is higher compared to a cosmological constant model with the same matter density and curvature (Eq. (3)), and distances to redshifts $z > 0$ are lower (Eq. (9)).

The luminosity distance relating an object's bolometric flux f_{bol} to its bolometric luminosity L_{bol} is

$$D_L = \sqrt{L_{\text{bol}}/4\pi f_{\text{bol}}} = D_A \times (1+z). \quad (11)$$

The relation between luminosity and angular diameter distance is independent of cosmology, so the two measures contain the same information about $H(z)$ and Ω_k . For this reason, we will sometimes use $D(z)$ to stand in generically for either of these transverse distance measures. Some methods (e.g., counts of galaxy clusters) effectively probe the comoving volume element that relates solid angle and redshift intervals to comoving volume V_C . We will denote this quantity

$$dV_C(z) \equiv cH^{-1}(z)D_A^2(z)d\Omega dz. \quad (12)$$

On large scales, the gravitational evolution of fluctuations in pressureless dark matter follows linear perturbation theory, according to which

$$\delta(\mathbf{x}, t) \equiv \frac{\rho_m(\mathbf{x}, t) - \bar{\rho}_m(t)}{\bar{\rho}_m(t)} = \delta(\mathbf{x}, t_i) \times \frac{G(t)}{G(t_i)}, \quad (13)$$

where t_i is an arbitrarily chosen initial time, the linear growth function $G(t)$ obeys the differential equation

$$\ddot{G}_{\text{GR}} + 2H(z)\dot{G}_{\text{GR}} - \frac{3}{2}\Omega_m H_0^2(1+z)^3 G_{\text{GR}} = 0, \quad (14)$$

and the GR subscript denotes the fact that this equation applies in standard GR.¹³ The solution to this equation can only be written in integral form for specific forms of $H(z)$, and thus for specific dark energy models specifying $u_\phi(z)$. However, to a very good approximation the logarithmic growth rate of linear perturbations in GR is

$$f_{\text{GR}}(z) \equiv \frac{d \ln G_{\text{GR}}}{d \ln a} \approx [\Omega_m(z)]^\gamma, \quad (15)$$

where $\gamma \approx 0.55\text{--}0.6$ depends only weakly on cosmological parameters (Peebles, 1980; Lightman and Schechter, 1990). Integrating this equation yields

$$\frac{G_{\text{GR}}(z)}{G_{\text{GR}}(z=0)} \approx \exp \left[- \int_0^z \frac{dz'}{1+z'} [\Omega_m(z')]^\gamma \right], \quad (16)$$

where $\Omega_m(z)$ is given by Eq. (5). Linder (2005) shows that Eq. (16) is accurate to better than 0.5% for a wide variety of dark energy models if one adopts

$$\gamma = 0.55 + 0.05[1 + w(z=1)] \quad (17)$$

(see also Wang and Steinhardt, 1998; Weinberg, 2005; Amendola et al., 2005). While the full solution of Eq. (14) should be used for high accuracy calculations, Eq. (16) is useful for intuition and for approximate calculations. Note in particular that if $u_\phi(z) > u_{\phi,0}$ then, relative to a cosmological constant model, $\Omega_m(z) \propto H^{-2}(z)$ is lower (Eq. (5)), so $G_{\text{GR}}(z)/G_{\text{GR}}(z=0)$ is higher — i.e., there has been *less* growth of structure between redshift z and the present day because matter has been a smaller fraction of the total density over that time. It is often useful to refer the growth factor not to its $z=0$ value but to the value at some high redshift when, in typical models, dark energy is dynamically negligible and $\Omega_m(z) \approx 1$. We will frequently use $z=9$ as a reference epoch, in which case Eq. (16) becomes

$$\frac{G_{\text{GR}}(z)}{G_{\text{GR}}(z=9)} \approx \exp \left[\int_z^9 \frac{dz'}{1+z'} [\Omega_m(z')]^\gamma \right]. \quad (18)$$

In the limit $\Omega_m(z) \rightarrow 1$, $G_{\text{GR}}(z) \propto (1+z)^{-1}$, i.e., the amplitude of linear fluctuations is proportional to $a(t)$.

¹² Recall that $\sin(ix) = i \sinh(x)$.

¹³ This equation applies on scales much smaller than the horizon. On scales close to the horizon one must pay careful attention to gauge definitions. Yoo (2009) and Yoo et al. (2009) provide a unified and comprehensive discussion of the multiple GR effects that influence observable large scale structure on scales approaching the horizon.

2.2. Model parameterizations

The properties of dark energy influence the observables – $H(z)$, $D(z)$, and $G(z)$ – through the history of $u_\phi(z)/u_{\phi,0}$ in the Friedmann equation (3). This history is usually framed in terms of the value and evolution of the equation-of-state parameter $w(z) = p_\phi(z)/u_\phi(z)$. Provided that the field ϕ is not transferring energy directly to or from other components (e.g., by decaying into dark matter), applying the first law of thermodynamics $dU = -p dV$ to a comoving volume implies

$$d(u_\phi a^3) = -p_\phi da^3 \quad (19)$$

$$\implies a^3 du_\phi + 3u_\phi a^2 da = -3w(z)u_\phi a^2 da \quad (20)$$

$$\implies d \ln u_\phi = -3[1 + w(z)]d \ln a = 3[1 + w(z)]d \ln(1 + z), \quad (21)$$

where the last equality uses the definition $a = (1 + z)^{-1}$. Integrating both sides implies

$$\frac{u_\phi(z)}{u_\phi(z=0)} = \exp \left[3 \int_0^z [1 + w(z')] \frac{dz'}{1 + z'} \right]. \quad (22)$$

For a constant w independent of z we find

$$\frac{u_\phi(z)}{u_\phi(z=0)} = (1 + z)^{3(1+w)}, \quad (23)$$

which yields the familiar results $u \propto (1 + z)^3$ for pressureless matter and $u \propto (1 + z)^4$ for radiation ($w = +\frac{1}{3}$), and which shows once again that a cosmological constant $u_\phi(z) = \text{constant}$ corresponds to $w = -1$.

The first obvious way to parameterize $w(z)$ is with a Taylor expansion $w(z) = w_0 + w'z + \dots$, but this expansion becomes ill-behaved at high z . A more useful two-parameter model (Chevallier and Polarski, 2001; Linder, 2003a) is

$$w(a) = w_0 + w_a(1 - a), \quad (24)$$

in which the value of w evolves linearly with scale factor from $w_0 + w_a$ at small a (high z) to w_0 at $z = 0$. Observations usually provide the best constraint on w at some intermediate redshift, not at $z = 0$, so statistical errors on w_0 and w_a are highly correlated. This problem can be circumvented by recasting Eq. (24) into the equivalent form

$$w(a) = w_p + w_a(a_p - a) \quad (25)$$

and choosing the “pivot” expansion factor a_p so that the observational errors on w_p and w_a are uncorrelated (or at least weakly so). The value of the pivot redshift depends on what data sets are being considered, but in practice it is usually close to $z_p \equiv a_p^{-1} - 1 \approx 0.4\text{--}0.5$ (see Table 8). The best-fit w_p is, approximately, the parameter of the constant- w model that would best reproduce the data. A cosmological constant would be statistically ruled out either if w_p were inconsistent with -1 or if w_a were inconsistent with zero. In practice, error bars on w_a are generally much larger than error bars on w_p , by a factor of 5–10. More generally, it is much more difficult to detect time dependence of w than to show $w \neq -1$, typically requiring sub-percent measurements of observables even if w changes by order unity in an interval $\Delta z < 1$ at low redshift (Kujat et al., 2002). The DETF proposed a figure of merit (FoM) for dark energy programs based on the expected error ellipse in the w_0 - w_a plane (similar to the approach described by Huterer and Turner (2001)). We will frequently refer to this DETF figure of merit, adopting the definition

$$\text{FoM} = [\sigma(w_p)\sigma(w_a)]^{-1}, \quad (26)$$

and we will refer to dark energy models defined by Eqs. (24) or (25) as “ w_0 - w_a models”.

An alternative parameterization approach is to approximate $w(z)$ as a stepwise-constant function defined by its values in a number of discrete bins, perhaps with priors or constraints on the allowed values (e.g., $-1 \leq w(z) \leq 1$). For a given set of observations, this function can then be decomposed into orthogonal principal components (PCs), with the first PC being the one that is best constrained by the data, the second PC the next best constrained, and so forth (Huterer and Starkman, 2003). Variants of this approach have been widely adopted in recent investigations (e.g., Albrecht and Bernstein, 2007; Sarkar et al., 2008b; Mortonson et al., 2009b), including the report of the JDEM Figure-of-Merit Science Working Group (Albrecht et al., 2009). The PCA approach has the advantage of allowing quite general $w(z)$ histories to be represented, though in practice only a few PCs can be constrained well; Linder and Huterer (2005) and de Putter and Linder (2008) have argued that the w_0 - w_a parameterization has equal power for practical purposes. We will use both characterizations for our forecasts in Section 8. For scalar field models, one can attempt to reconstruct the potential $V(\phi)$ instead of $w(z)$ (Starobinsky, 1998; Huterer and Turner, 1999; Nakamura and Chiba, 1999), an approach that we discuss briefly at the end of Section 8.3.4. Gott and Slepian (2011) emphasize that slowly rolling scalar field models generically predict $1 + w \approx (1 + w_0)H_0^2/H^2(z)$ for $|1 + w| \ll 1$, making the space of $w(z)$ models, to leading order, one-dimensional, rather than the two-dimensional parameterization of w_0 - w_a . As a complement to parameterized models, one can attempt to construct non-parametric “null tests” for a cosmological constant or scalar field models (Sahni et al., 2008).

If $w \neq -1$, then the dark energy density should display spatial inhomogeneities, but for simple scalar field models these inhomogeneities are strongly suppressed on scales below the horizon. More complicated models that have a sound speed ($c_s^2 = \delta p / \delta \rho$) much smaller than c allow fluctuations to grow on sub-horizon scales (e.g., Hu, 1998; Erickson et al., 2002; Weller and Lewis, 2003; DeDeo et al., 2003; Bean and Doré, 2004). de Putter et al. (2010) provide a clear discussion of the background physics and observable consequences of dark energy inhomogeneities. In general these inhomogeneities are very difficult to detect, because their growth is significant only when w is far from -1 and $c_s \ll c$, and because the fluctuations in dark energy density are much smaller than those in dark matter. We will mostly ignore dark energy inhomogeneities in this article, though we return to the subject briefly in Section 7.8.

Our equations so far have assumed that GR is correct. The alternative to dark energy is to modify GR in a way that produces accelerated expansion. One of the best-studied examples is DGP gravity (Dvali et al., 2000), which posits a five-dimensional gravitational field equation that leads to a Friedmann equation

$$H^2(z) = \frac{8\pi G}{3} \rho(z) \pm \frac{cH}{r_c} \quad (27)$$

for a spatially flat, homogeneous universe confined to a $(3 + 1)$ -dimensional brane. Above the “crossover scale” r_c , which relates the five-dimensional and four-dimensional gravitational constants, the gravitational force law scales as r^{-3} instead of the usual r^{-2} . Choosing the positive sign for the second term in Eq. (27) and setting $r_c \sim c/H_0$ leads to an initially decelerating universe that transitions to accelerating, and ultimately exponential, expansion. Other modifications to the gravitational action that replace the curvature scalar R by some function $f(R)$ will modify the Friedmann equation in different ways, some of which can produce late-time acceleration (e.g., Capozziello and Fang, 2002; Carroll et al., 2004). Alternatively, one can simply postulate a modified Friedmann equation without specifying a complete gravitational theory, e.g., by replacing ρ on the right hand side of $H^2 \propto \rho$ with a parameterized function $H^2 \propto g(\rho)$ (Freese and Lewis, 2002; Freese, 2005). Of course, there is no guarantee that such a function can in fact be derived from a self-consistent gravitational theory.

Using Eqs. (3) and (22), one can express a modified Friedmann equation in terms of an effective time-dependent dark energy equation of state. In this review, we will use $w(z)$ to parameterize the expansion histories of both dark energy and modified gravity theories. Given $w(z)$, $H(z)$ and $D(z)$ generally follow from the same set of equations for both types of theories, so observations that only probe the geometry of the universe are incapable of distinguishing between the two possible explanations of cosmic acceleration. In addition to changing the Friedmann equation, however, a modified gravity model may alter the Eq. (14) that relates the growth of structure to the expansion history $H(z)$. Therefore, one general approach to testing modified gravity explanations is to search for inconsistency between observables that probe $H(z)$ or $D(z)$ and observables that also probe the growth function $G(z)$. Some methods effectively measure $G(z)/G(z=0)$, others measure $G(z)$ relative to an amplitude anchored in the CMB, and others measure the logarithmic growth index γ of Eq. (15). For “generic” parameters that describe departures from GR-predicted growth, we will use a parameter G_9 that characterizes an overall multiplicative offset of the growth factor and a parameter $\Delta\gamma$ that characterizes a change in the fluctuation growth rate. We define these parameters in Section 2.4 below, following our review of CMB anisotropy and large scale structure. These parameters serve as useful diagnostics for deviations from GR, but they do not provide a complete description of the effects of modified gravity theories. In particular, it is also possible (see Section 7.7) that modified gravity will cause $G(z)$ to be scale-dependent, or that it will alter the relation between gravitational lensing and non-relativistic mass tracers, or that it will reveal its presence through a high-precision test on solar system or terrestrial scales.

The above considerations lead to the following general strategy for probing the physics of cosmic acceleration: use observations to constrain the functions $H(z)$, $D(z)$, and $G(z)$, and use these constraints in turn to constrain the history of $w(z)$ for dark energy models and to test for inconsistencies that could point to a modified gravity explanation. For pure $H(z)$ and $D(z)$ measurements, the “nuisance parameters” in such a strategy are the values of Ω_m and Ω_k , in addition to parameters related directly to the observational method itself (e.g., the absolute luminosity of supernovae). Assuming a standard radiation content, the value of $\Omega_\phi = 1 - \Omega_m - \Omega_r - \Omega_k$ is fixed once Ω_m and Ω_k are known. The effects of Ω_m and Ω_k are separable both from their different redshift dependence in the Friedmann equation (3) and from the influence of Ω_k on transverse distances (Eq. (9)) via space curvature.

2.3. CMB anisotropies and large scale structure

CMB anisotropies have little direct constraining power on dark energy, but they play a critical role in cosmic acceleration studies because they often provide the strongest constraints on nuisance parameters such as Ω_m , Ω_k , and the high-redshift normalization of matter fluctuations. In particular, the amplitudes of the acoustic peaks in the CMB angular power spectrum depend sensitively (and differently) on the matter and baryon densities, and the locations of the peaks depend sensitively on spatial curvature. Using CMB constraints necessarily brings in additional nuisance parameters such as the spectral index n_s and curvature $dn_s/d \ln k$ of the scalar fluctuation spectrum, the amplitude and slope of the tensor (gravitational wave) fluctuation spectrum, the post-recombination electron-scattering optical depth τ , and the Hubble constant

$$h \equiv H_0 / (100 \text{ km s}^{-1} \text{ Mpc}^{-1}). \quad (28)$$

However, some of these parameters are themselves relevant to cosmic acceleration studies, and current CMB measurements yield tight constraints even after marginalizing over many parameters (e.g., Komatsu et al., 2011). The strength of these

constraints depends significantly on the adopted parameter space – for example, current CMB data provide tight constraints on h if one assumes a flat universe with a cosmological constant, but these constraints are much weaker if Ω_k and w are free parameters.

CMB data are usually incorporated into dark energy constraints, or forecasts, by adding priors on parameters that are then marginalized over in the analysis. We will adopt this strategy in Section 8, using the level of precision forecast for the *Planck* satellite. However, it is worth noting some rules of thumb. For practical purposes, *Planck* data will give near-perfect determinations of $\Omega_m h^2$ and $\Omega_b h^2$ from the heights of the acoustic peaks, where the h^2 dependence arises because it is the physical density that affects the acoustic features, not the density relative to the critical density. “Near-perfect” means that marginalizing over the expected uncertainties in $\Omega_m h^2$ and $\Omega_b h^2$ adds little to the error bars on dark energy parameters even from ambitious “Stage IV” experiments, relative to assuming that they are known perfectly.¹⁴ *Planck* data will also give near-perfect determinations of the sound horizon at recombination $r_s(z_*)$, which determines the physical scale of the acoustic peaks in the CMB and the scale of BAO in large scale structure (see Section 4.1). Since the angular scale of the acoustic peaks is precisely measured, *Planck* data should also yield a near-perfect determination of the angular diameter distance to the redshift of recombination, $D_* \equiv D_A(z_*)$, where $z_* \approx 1091$. Finally, the amplitude of CMB anisotropies gives a near-perfect determination (after marginalizing over the optical depth τ , which is constrained by polarization data) of the amplitude of matter fluctuations at z_* , and thus throughout the era in which dark energy (or deviation from GR) is negligible. As emphasized by Hu (2005; an excellent source for more detailed discussion of CMB anisotropies in the context of dark energy constraints), these determinations all depend on the assumptions of a standard thermal and recombination history, but the CMB data themselves allow tests of these assumptions at the required level of accuracy. CMB data also allow tests of cosmic acceleration models via the integrated Sachs–Wolfe (ISW) effect, which we discuss briefly in Section 7.8.

If primordial matter fluctuations are Gaussian, as predicted by simple inflation models and supported by most observational investigations to date, then their statistical properties are fully specified by the power spectrum $P(k)$ or its Fourier transform, the two-point correlation function $\xi(r)$. Defining the Fourier transform of the density contrast¹⁵

$$\tilde{\delta}(\mathbf{k}) = \int d^3r e^{-i\mathbf{k}\cdot\mathbf{r}} \delta(\mathbf{r}), \quad \delta(\mathbf{r}) = (2\pi)^{-3} \int d^3k e^{i\mathbf{k}\cdot\mathbf{r}} \tilde{\delta}(\mathbf{k}), \quad (29)$$

the power spectrum is defined by

$$\langle \tilde{\delta}(\mathbf{k}) \tilde{\delta}(\mathbf{k}') \rangle = (2\pi)^3 P(k) \delta_D^3(\mathbf{k} - \mathbf{k}'), \quad (30)$$

where δ_D^3 is a 3-d Dirac-delta function and isotropy guarantees that $P(\mathbf{k})$ is a function of $k = |\mathbf{k}|$ alone. The power spectrum has units of volume, and it is often more intuitive to discuss the dimensionless quantity

$$\Delta^2(k) \equiv (2\pi)^{-3} \times 4\pi k^3 P(k) = \frac{d\sigma^2}{d \ln k}, \quad (31)$$

which is the contribution to the variance $\sigma^2 \equiv \langle \delta^2 \rangle$ of the density contrast per logarithmic interval of k . The variance of the density field smoothed with a window $W_R(r)$ of scale R is

$$\sigma^2(R) = \int_0^\infty \frac{dk}{k} \Delta^2(k) \tilde{W}_R^2(k), \quad (32)$$

where the Fourier transform of a top-hat window, $W_R(r) = (4\pi R^3/3)^{-1} \Theta(1 - r/R)$, is

$$\tilde{W}_R(k) = \frac{3}{k^3 R^3} [\sin(kR) - kR \cos(kR)], \quad (33)$$

and the Fourier transform of a Gaussian window, $W_R(r) = (2\pi)^{-3/2} R^{-3} e^{-r^2/2R^2}$, is

$$\tilde{W}_R(k) = e^{-k^2 R^2/2}. \quad (34)$$

The correlation function is

$$\xi(r) \equiv \langle \delta(\mathbf{x}) \delta(\mathbf{x} + \mathbf{r}) \rangle = \int_0^\infty \frac{dk}{k} \Delta^2(k) \frac{\sin(kr)}{kr}. \quad (35)$$

In linear perturbation theory, the power spectrum amplitude is proportional to $G^2(z)$, and we will take $P_{\text{lin}}(k)$ to refer to the $z = 0$ normalization when the redshift is not otherwise specified:

$$P_{\text{lin}}(k, z) = \frac{G^2(z)}{G^2(z=0)} P_{\text{lin}}(k). \quad (36)$$

¹⁴ However, the effects of *Planck*-level CMB uncertainties are not completely negligible. For the fiducial Stage IV program discussed in Section 8, fixing $\Omega_m h^2$ and $\Omega_b h^2$ instead of marginalizing increases the DETF FoM from 664 to 876.

¹⁵ A variety of Fourier conventions float around the cosmology literature. Here we adopt the same Fourier conventions and definitions as Dodelson (2003).

We discuss the normalization of $G(z)$ and $P_{\text{lin}}(k)$ more precisely in Section 2.4 below. The evolution of $P(k)$ remains close to linear theory for scales $k \ll k_{\text{nl}}$, where

$$\int_0^{k_{\text{nl}}} \frac{dk}{k} \Delta^2(k) = 1. \quad (37)$$

For realistic power spectra, non-linear evolution on small scales does not feed back to alter the linear evolution on large scales (Peebles, 1980; Shandarin and Melott, 1990; Little et al., 1991). However, the shape of the power spectrum does change on scales approaching k_{nl} , in ways that can be calculated using N -body simulations (Heitmann et al., 2010) or several variants of cosmological perturbation theory (Carlson et al., 2009 and references therein). Non-linear evolution is a significant effect for weak lensing predictions and for the evolution of BAO, as we discuss in the corresponding sections below.

While there are many ways of characterizing the matter distribution in the non-linear regime, the two measures that matter the most for our purposes are the mass function and clustering bias of dark matter halos. There are several different algorithms for identifying halos in N -body simulations, all of them designed to pick out collapsed, gravitationally bound dark matter structures in approximate virial equilibrium. It is convenient to express the halo mass function in the form

$$\frac{dn}{d \ln M} = f(\sigma) \bar{\rho}_m \left| \frac{d \ln \sigma}{dM} \right|, \quad (38)$$

where σ^2 is the variance of the linear density field smoothed with a top-hat filter of mass scale $M = \frac{4}{3}\pi R^3 \bar{\rho}_m$ (Eqs. (32) and (33)). To a first approximation, the function $f(\sigma)$ is universal, and the effects of power spectrum shape, redshift (and thus power spectrum amplitude), and background cosmological model (e.g., Ω_m and Ω_Λ) enter only through determining $|d \ln \sigma / dM|$ and $\bar{\rho}_m$. The state-of-the-art numerical investigation is that of Tinker et al. (2008), who fit a large number of N -body simulation results with the functional form

$$f(\sigma) = A \left[\left(\frac{\sigma}{b} \right)^{-a} + 1 \right] e^{-c/\sigma^2}, \quad (39)$$

finding best-fit values $A = 0.186$, $a = 1.47$, $b = 2.57$, $c = 1.19$ for $z = 0$ halos, defined to be spherical regions centered on density peaks enclosing a mean interior overdensity of 200 times the cosmic mean density $\bar{\rho}_m$. (Different halo mass definitions lead to different coefficients.) A similar functional form was justified on analytic grounds by Sheth and Tormen (1999), following a chain of argument that ultimately traces back to Press and Schechter (1974) and Bond et al. (1991). Discussions of the halo population frequently refer to the characteristic mass scale M^* , defined by

$$\sigma(M^*) = \delta_c = 1.686, \quad (40)$$

which sets the location of the exponential cutoff in the Press–Schechter mass function. Here δ_c is the linear theory overdensity at which a spherically symmetric perturbation would collapse.¹⁶

In detail, Tinker et al. (2008) find that $f(\sigma)$ depends on redshift at the 10%–20% level, probably because of the dependence of halo mass profiles on $\Omega_m(z)$. At overdensities of ~ 200 , the baryon fraction in group and cluster mass halos ($M > 10^{13} M_\odot$) is expected to be close to the cosmic mean ratio Ω_b / Ω_m , but gas pressure, dissipation, and feedback from star formation and AGN can alter this fraction and change baryon density profiles relative to dark matter profiles. We discuss these issues further in Section 6.

Massive halos are more strongly clustered than the underlying matter distribution because they form near high peaks of the initial density field, which arise more frequently in regions where the background density is high (Kaiser, 1984; Bardeen et al., 1986). On large scales, the correlation function of halos of mass M is a scale-independent multiple of the matter correlation function $\xi_{hh}(r) = b_h^2(M) \xi_{mm}(r)$. The halo-mass cross-correlation in this regime is $\xi_{hm}(r) = b_h(M) \xi_{mm}(r)$, and similar scalings (b_h^2 and b_h) hold for the halo power spectrum and halo-mass cross spectrum at low k . Analytic arguments suggest a bias factor (Cole and Kaiser, 1989; Mo and White, 1996)

$$b_h(M) = 1 + \frac{[\delta_c / \sigma(M)]^2 - 1}{\delta_c}. \quad (41)$$

There have been numerous refinements to this formula based on analytic models and numerical calibrations. The state-of-the-art numerical study is that of Tinker et al. (2010).

Galaxies reside in dark matter halos, and they, too, are biased tracers of the underlying matter distribution. Here one must allow for the fact that different kinds of galaxies reside in different mass halos and that massive halos host multiple galaxies. More massive or more luminous galaxies are more strongly clustered because they reside in more massive halos that have higher $b_h(M)$. At low redshift, the large scale bias factor is $b_g \leq 1$ for galaxies below the characteristic cutoff L^*

¹⁶ See Gunn and Gott (1972), but note that their argument must be corrected to growing mode initial conditions, as is done in standard textbook treatments. The value $\delta_c = 1.686$ is derived for $\Omega_m = 1$, but the cosmology dependence is weak.

of the Schechter (1976) luminosity function, but it rises sharply at higher luminosities (Norberg et al., 2001; Zehavi et al., 2005, 2011).

For a galaxy sample defined by a threshold L_{\min} in optical or near-IR luminosity (or stellar mass), theoretical models and empirical studies (too numerous to list comprehensively, but our summary here is especially influenced by Kravtsov et al., 2004; Conroy et al., 2006; Zehavi et al., 2011) suggest the following approximate model. The minimum host halo mass is the one for which the comoving space density $n(M_{\min})$ of halos above M_{\min} matches the space density $n(L_{\min})$ of galaxies above the luminosity threshold. Each halo above M_{\min} hosts one central galaxy, and in addition each such halo hosts a mean number of satellite galaxies $\langle N_{\text{sat}} \rangle = (M - M_{\min})/15M_{\min}$, with the actual number of satellites drawn from a Poisson distribution with this mean.¹⁷ The large scale galaxy bias factor b_g is the average bias factor $b_h(M)$ of halos above M_{\min} , with the average weighted by the product of the halo space density and the average number of galaxies per halo. In addition to increasing b_g by giving more weight to high mass halos, satellite galaxies contribute to clustering on small scales, where pairs or groups of galaxies reside in a single halo (Seljak, 2000; Scoccimarro et al., 2001; Berlind and Weinberg, 2002). In detail, at high luminosities one must allow for scatter between galaxy luminosity and halo mass, which reduces the bias below that of the sharp threshold model described above. Furthermore, selecting galaxies by color or spectral type alters the relative fractions of central and satellite galaxies; redder, more passive galaxies are more strongly clustered because a larger fraction of them are satellites, and the reverse holds for bluer galaxies with active star formation. Thus each class of galaxies has its own halo occupation distribution (HOD), which describes the probability $P(N|M)$ of finding N galaxies in a halo of mass M and specifies any relative bias of galaxies and dark matter within halos.

On large scales, where $b_g^2 \Delta_{\text{lin}}^2(k, z) \ll 1$, the galaxy power spectrum should have the same shape as the linear matter power spectrum, $P_{\text{gg}}(k, z) = b_g^2 P_{\text{lin}}(k, z)$. However, scale-dependence of bias at the 10%–20% level can persist to quite low k , especially for luminous, highly biased galaxy populations, and the effective “shot noise” contribution to $P_{\text{gg}}(k)$ can differ from the naive $1/\bar{n}_g$ term expected for Poisson statistics (Yoo et al., 2009). Combinations of CMB power spectrum measurements with galaxy power spectrum measurements can yield tighter cosmological parameter constraints than either one in isolation (e.g., Cole et al., 2005; Reid et al., 2010). In particular, this combination provides greater leverage on the Hubble constant h , since CMB-constrained models predict galaxy clustering in Mpc while galaxy redshift surveys measure distances in h^{-1} Mpc (or, equivalently, in km s^{-1}).

Another complicating factor in galaxy clustering measurements is redshift-space distortion (Kaiser, 1987; see Hamilton, 1998 for a comprehensive review), which arises because galaxy redshifts measure a combination of distance and peculiar velocity rather than true distance. On small scales, velocity dispersions in collapsed objects stretch structures along the line of sight. On large scales, coherent inflow to overdense regions compresses them in the line-of-sight direction, and coherent outflow from underdense regions stretches them along the line of sight. In linear perturbation theory, the divergence of the peculiar velocity field is related to the density contrast field by

$$\vec{\nabla} \cdot \mathbf{v}(\mathbf{x}, z) = -(1+z)^{-1} H(z) \frac{d \ln G}{d \ln a} \delta(\mathbf{x}, z) \approx -(1+z)^{-1} H(z) [\Omega_m(z)]^\gamma \delta(\mathbf{x}, z), \quad (42)$$

with γ defined by Eq. (15). The galaxy redshift-space power spectrum in linear theory is anisotropic, depending on the angle θ between the wavevector \mathbf{k} and the observer’s line of sight as

$$P_g(k, \mu) = b_g^2 (1 + \beta \mu^2)^2 P(k) = [b_g + \mu^2 f(z)]^2 P(k), \quad (43)$$

where $P(k)$ is the real-space matter power spectrum, $\mu \equiv \cos \theta$, and $f(z) \approx [\Omega_m(z)]^\gamma$ is the logarithmic growth rate (Eq. (15)). The strength of the anisotropy depends on the ratio $\beta \equiv f(z)/b_g$; because linear bias amplifies galaxy clustering isotropically, more strongly biased galaxies exhibit weaker redshift-space distortion. A variety of non-linear effects, most notably the small scale dispersion and its correlation with large scale density, mean that Eq. (43) is rarely an adequate approximation in practice, even on quite large scales (Cole et al., 1994; Scoccimarro, 2004). In the galaxy correlation function, one can remove the effects of redshift-space distortion straightforwardly by projection, counting galaxy pairs as a function of projected separation rather than 3-d redshift-space separation. For the power spectrum, one can correct for redshift-space distortion, but the analysis is more model-dependent (see, e.g., Tegmark et al., 2004). However, redshift-space distortion can be an asset as well as a nuisance, since it provides a route to measuring $d \ln G/d \ln a$. We will discuss this idea at some length in Section 7.2, as it is emerging as a powerful route to measuring the expansion history and testing GR growth predictions.

2.4. Parameter dependences and CMB constraints

Fig. 1 illustrates the four statistics discussed above: the CMB temperature angular power spectrum, the matter variance $\Delta_{\text{lin}}^2(k)$ computed from the linear theory power spectrum at $z = 0$, the $z = 0$ halo mass function computed from Eqs. (38) and (39), and the halo bias factor computed from Eq. (6) of Tinker et al. (2010) for overdensity 200 halos (relative to the mean matter density). Curves in the main panels show a fiducial model with the likelihood-weighted mean parameters for the

¹⁷ To make the model more accurate, one should adjust M_{\min} iteratively so that the total space density of galaxies, central+satellite, matches the observed $n(L_{\min})$, but this is usually a modest correction because the typical fraction of galaxies that are satellites is 5%–20%.

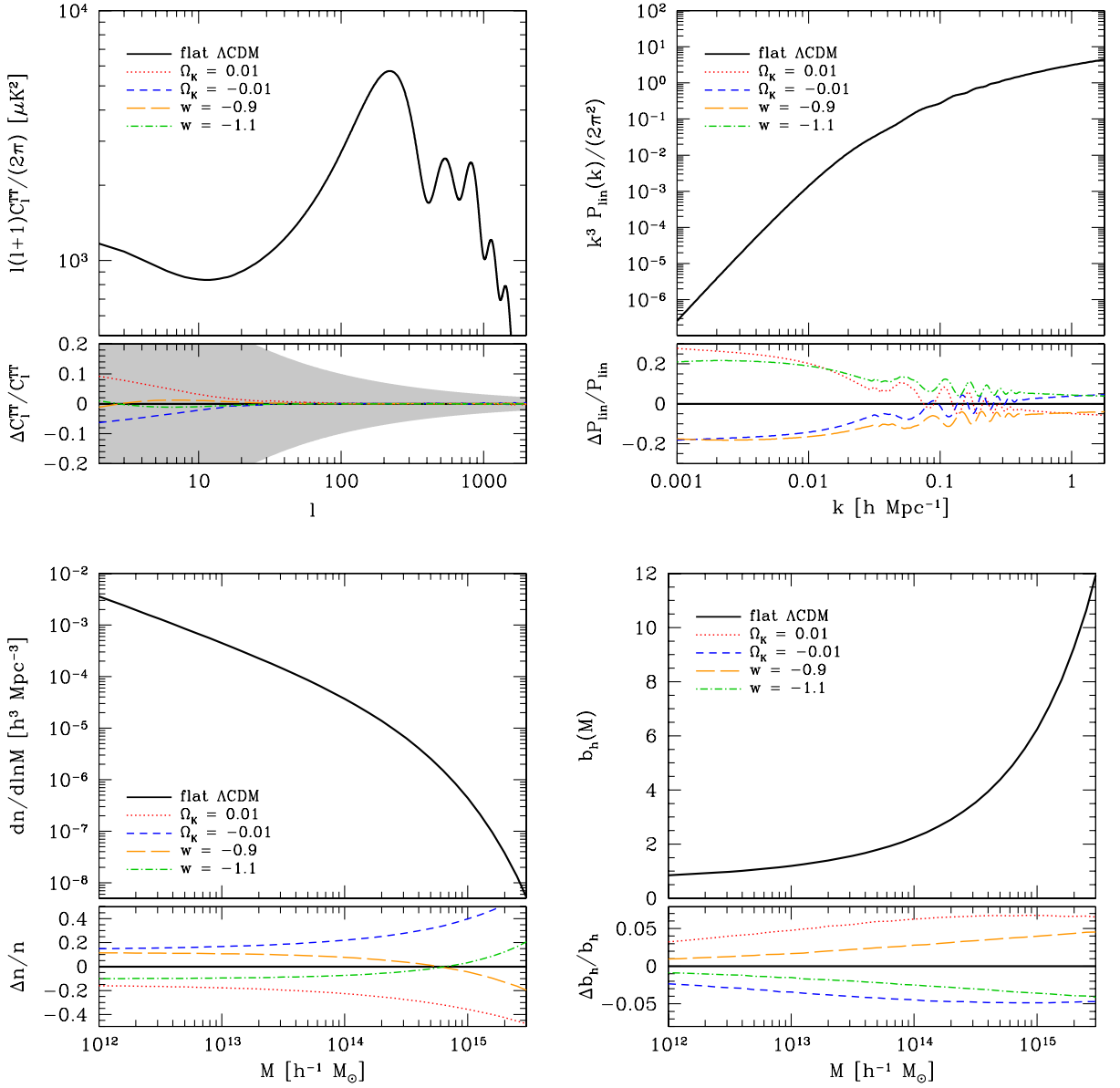


Fig. 1. CMB angular power spectrum (upper left), variance of matter fluctuations (upper right), halo mass function (lower left), and halo bias factor (lower right). Solid curves in the main panels show predictions of the fiducial Λ CDM panel listed in Table 1. Curves in the lower panels show the fractional changes in these statistics induced by changing $1 + w$ to ± 0.1 or Ω_k to ± 0.01 (see legend). For each parameter change, we keep $\Omega_m h^2$, $\Omega_b h^2$, and D_s fixed by adjusting Ω_m , Ω_b , and h (see Table 1). These compensating changes keep deviations in the CMB spectrum minimal, much smaller than the cosmic variance errors indicated by the shaded region.

seven-year WMAP CMB measurements (hereafter WMAP7; Larson et al., 2011) assuming a flat universe with a cosmological constant: $\Omega_c = 0.222$, $\Omega_b = 0.045$, $\Omega_\Lambda = 0.733$, $h = 0.71$, $n_s = 0.963$, $\tau = 0.088$, and primordial power spectrum amplitude $A_s(k = 0.002 \text{ Mpc}^{-1}) = 2.43 \times 10^{-9}$. (These parameters also assume no tensor fluctuations and $dn_s/d \ln k = 0$.) The CMB power spectrum shows the familiar pattern of acoustic peaks, with the angular scale of the first peak corresponding approximately to the sound horizon at recombination divided by the angular diameter distance to the last scattering surface. The matter variance $\Delta_{\text{lin}}^2(k)$ shows a slow change of slope starting at $k \approx 0.02 h \text{ Mpc}^{-1}$, corresponding to the horizon scale at matter–radiation equality, and low amplitude wiggles at smaller scales produced by BAO. The halo mass function has an approximate power-law form at low masses changing slowly to an exponential cutoff for $M \gg M^* = 3 \times 10^{12} h^{-1} M_\odot$. The $b_h(M)$ relation is roughly flat for $M \lesssim 5M^*$ before rising steeply at higher masses. The h -dependences used for k , $dn/d \ln M$, and M reflect the dependences that typically arise when distances are estimated from redshifts and thus scale as h^{-1} .

In the lower panels, we show the fractional change in these statistics that arises when changing $1 + w$ from 0 to ± 0.1 and when changing Ω_k from 0 to ± 0.01 . With any parameter variation, there is the crucial question of what one holds

Table 1
Fiducial model and simple variants.

w	Ω_k	Ω_c	Ω_b	Ω_ϕ	h	σ_8
-1.0	0.00	0.222	0.045	0.733	0.710	0.806
-0.9	0.00	0.246	0.050	0.704	0.675	0.774
-1.1	0.00	0.201	0.041	0.758	0.746	0.837
-1.0	0.01	0.186	0.038	0.766	0.776	0.809
-1.0	-0.01	0.256	0.052	0.702	0.661	0.802

All models have $n_s = 0.963$, $\tau = 0.088$, $A_s(k = 0.002 \text{ Mpc}^{-1}) = 2.43 \times 10^{-9}$. In addition, all models have the same values $\Omega_m h^2$, $\Omega_b h^2$, and distance to the last scattering surface D_* , so they produce nearly indistinguishable CMB power spectra.

fixed. For this figure, we have held fixed the parameter combinations that have the strongest impact on the CMB power spectrum: $\Omega_m h^2$ and $\Omega_b h^2$, which determine the heights of the acoustic peaks and the physical scale of the sound horizon, and $D_* = D_A(z_*)$, which maps the physical scale of the peaks into the angular scale. We satisfy these constraints by allowing h and Ω_m to vary, maintaining $\Omega_k = 0$ for the w -variations and $w = -1$ for the Ω_k -variations, with n_s , A_s , and τ fixed to the fiducial model values. The parameter values for these variant models appear in Table 1.

From the CMB panel, we can see that the changes in the angular power spectrum induced by these parameter variations are small compared to the cosmic variance error at every l , since we have fixed the parameter combinations that mostly determine the CMB spectrum.¹⁸ The changes are coherent, of course, but even considering model fits to the entire CMB spectrum the w changes would be undetectable at the level of errors forecast for *Planck*, while the $\Omega_k = \pm 0.01$ models would be distinguishable from the fiducial model at about 1.5σ . The impact of these parameter changes must instead be sought in other statistics at much lower redshifts. Changes to the matter variance are $\sim 5\%$ at small scales, growing to $\sim 20\%$ at large scales, with oscillations that reflect the shift in the BAO scale. Fractional changes to the halo space density at fixed mass can be much larger, especially at high masses where the halo mass function is steep. We caution, however, that the fractional change in mass at fixed abundance is significantly smaller, a point that we emphasize in Section 6. The impact of a change in w reverses sign at $M \approx 6 \times 10^{14} h^{-1} M_\odot \approx 200 M^*$, where the mass function begins to drop sharply. Changes in bias factor at fixed mass are $\sim 5\%$ at high masses and smaller at low masses.

Fig. 2 shows the redshift evolution and parameter sensitivity of the Hubble parameter (Eq. (3)) and the comoving angular diameter distance (Eq. (9)), for the same fiducial model and parameter variations used in Fig. 1. The upper panels show $H(z)$ and $D_A(z)$ in absolute units, while the lower panels plot them in h^{-1} Gpc units. BAO studies measure in absolute units, but supernova studies effectively measure $hD_A(z)$ because they are calibrated in the local Hubble flow. Equivalently, supernova distances are determined in h^{-1} Mpc rather than Mpc.¹⁹ Weak lensing predictions depend on distance ratios rather than absolute distances, so in practice they also constrain $hD_A(z)$ rather than absolute $D_A(z)$.

In absolute units, model predictions diverge most strongly at $z = 0$, and the impact of $\Omega_k = \pm 0.01$ is larger than the impact of $1 + w = \pm 0.1$. The impact of the w change on $H(z)$ reverses sign at $z \approx 0.6$, a consequence of our CMB normalization. Changing w to -0.9 would on its own reduce the distance to z_* , and H_0 must therefore be lowered to keep D_* fixed. However, with $\Omega_m h^2$ fixed, lower H_0 implies a higher Ω_m , which raises the ratio $H(z)/H_0$, and at high redshift this effect wins out over the lower H_0 . At $z > 2$, $D_A(z)$ remains sensitive to Ω_k but is insensitive to w , while the sensitivity of $H(z)$ to w is roughly flat for $1 < z < 3$. In h^{-1} Mpc units, models converge at $z = 0$ by definition, and the impact of $1 + w = \pm 0.1$ is generally larger than the impact of $\Omega_k = \pm 0.01$. The sensitivity of $hD_A(z)$ to parameter changes increases monotonically with increasing redshift, growing rapidly until $z = 0.5$ and flattening beyond $z = 1$.

For structure growth, the issues of normalization are more subtle. The normalization of the matter power spectrum is known better from CMB anisotropy at z_* than it is from local measurements at $z = 0$, and this will be still more true in the *Planck* era. It therefore makes sense to anchor the normalization in the CMB, even though the value at $z = 0$ then depends on cosmological parameters. Fig. 3 (left panel) plots $(1+z)G_{\text{GR}}(z)$, where $G_{\text{GR}}(z)$ obeys Eq. (14) and is normalized to unity at $z = 9$. In most models, dark energy is dynamically negligible at $z > 9$, making the growth from the CMB era up to that epoch independent of dark energy. In an $\Omega_m = 1$ universe, $G_{\text{GR}}(z) \propto (1+z)^{-1}$, so the plotted ratio falls below unity when $\Omega_m(z)$ starts to fall below one. For $\Omega_k = 0.01$, $\Omega_m(z)$ is below that in our fiducial model (see Eqs. (3) and (5)) both because of the Ω_k term in the Friedmann equation and because we lower $\Omega_m(z = 0)$ from 0.27 to 0.22 to keep D_* fixed, thus depressing $G_{\text{GR}}(z)$ increasingly toward lower z . For $w = -0.9$, however, the depression of $\Omega_m(z)/\Omega_m(z = 0)$ from the Friedmann equation is countered by the higher value of $\Omega_m(z = 0) = 0.30$ adopted to fix D_* , so the depression of $G_{\text{GR}}(z)$ is smaller, and it actually recovers toward the fiducial value as z approaches zero. The effects on the growth rate $f(z)$ (right panel) are similar but stronger, with our adopted parameter changes producing larger deviations from the fiducial model and the influence of w actually reversing sign at $z < 0.5$.

¹⁸ The CMB cosmic variance error is $\Delta \ln C_l^T = [(2l+1)/2]^{-1/2}$, determined simply by the number of modes on the sky at each angular scale l .

¹⁹ To be more precise, studies of supernovae at redshifts z_1 and z_2 yield the distance ratio $D(z_2)/D(z_1)$. When the z_1 population is local, in the sense that inferred distances have negligible cosmology dependence except for the H_0^{-1} scaling, then one gets the distance $D(z_2)$ in h^{-1} Mpc.

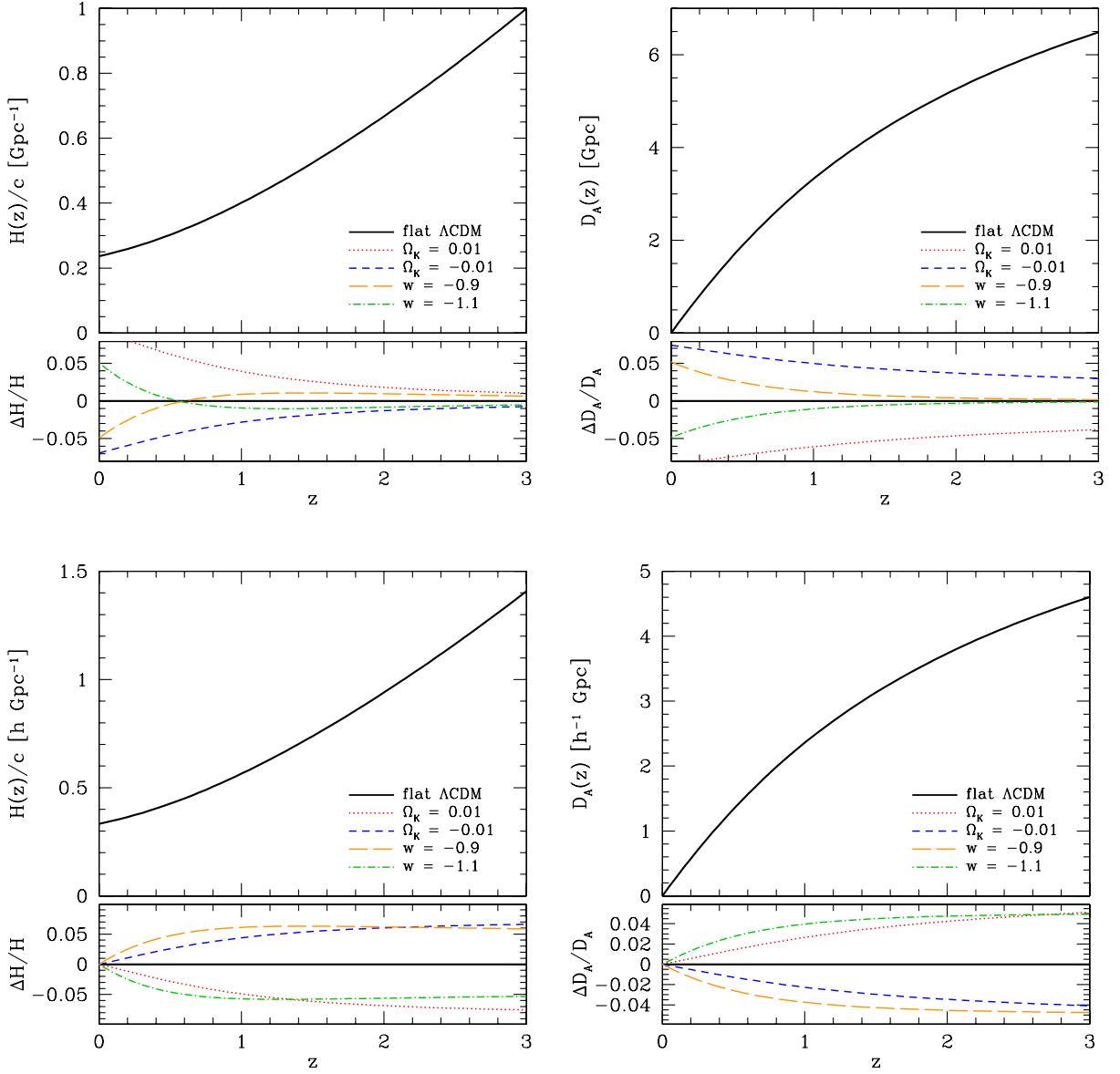


Fig. 2. Evolution of the Hubble parameter (left) and the comoving angular diameter distance (right) for the fiducial Λ CDM model and for the variant models shown in Fig. 1. Upper panels are in absolute units, relevant for BAO, while lower panels show distances in h^{-1} Gpc, relevant for supernovae or weak lensing.

In practice, observations do not probe the growth factor itself but the amplitude of matter clustering, and in this case we must also account for the changing relation between the CMB power spectrum and the matter clustering normalization. The left panel of Fig. 4 plots $\sigma_8(z) \times (1+z)$, where $\sigma_8(z)$ is the rms linear theory density contrast in a sphere of comoving radius $8h^{-1}$ Mpc (Eqs. (32) and (33)). The right panel instead plots $\sigma_{11,\text{abs}}(z) \times (1+z)$, where $\sigma_{11,\text{abs}}$ refers to a sphere of radius 11 Mpc (equivalent to σ_8 for $h = 0.727$). At high redshift these curves go flat as $\Omega_m(z)$ approaches one and the growth rate approaches $G_{\text{GR}}(z) \propto (1+z)^{-1}$. In the CMB-matched models considered here, the impact of w or Ω_k changes is complex, since changing these parameters alters the best-fit values of Ω_m and h as well as changing the growth factor directly through Eq. (16). The values of $\sigma_8(z)$ change by 4%–5% at all z for $1+w = \pm 0.1$, but these changes mostly track the changes in h . In absolute units, the changes to $\sigma_{11,\text{abs}}(z)$ are $\lesssim 1\%$, tracking (by definition) the changes in $G_{\text{GR}}(z)$ shown in Fig. 3. For $\Omega_k = \pm 0.01$, $\sigma_8(z)$ changes by 4%–5% at high z but converges nearly to the fiducial value at $z = 0$, while $\sigma_{11,\text{abs}}(z)$ shows only 1% differences at high z but diverges at low z .

All of these models have the WMAP7 (Larson et al., 2011) normalization of the power spectrum of inflationary fluctuations, $A_s = 2.43 \times 10^{-9}$ at comoving scale $k = 0.002 \text{ Mpc}^{-1}$ at $z = z_* = 1091$. The primary uncertainty in this normalization is the degeneracy with the electron optical depth τ , since late-time scattering suppresses the amplitude of the primary CMB

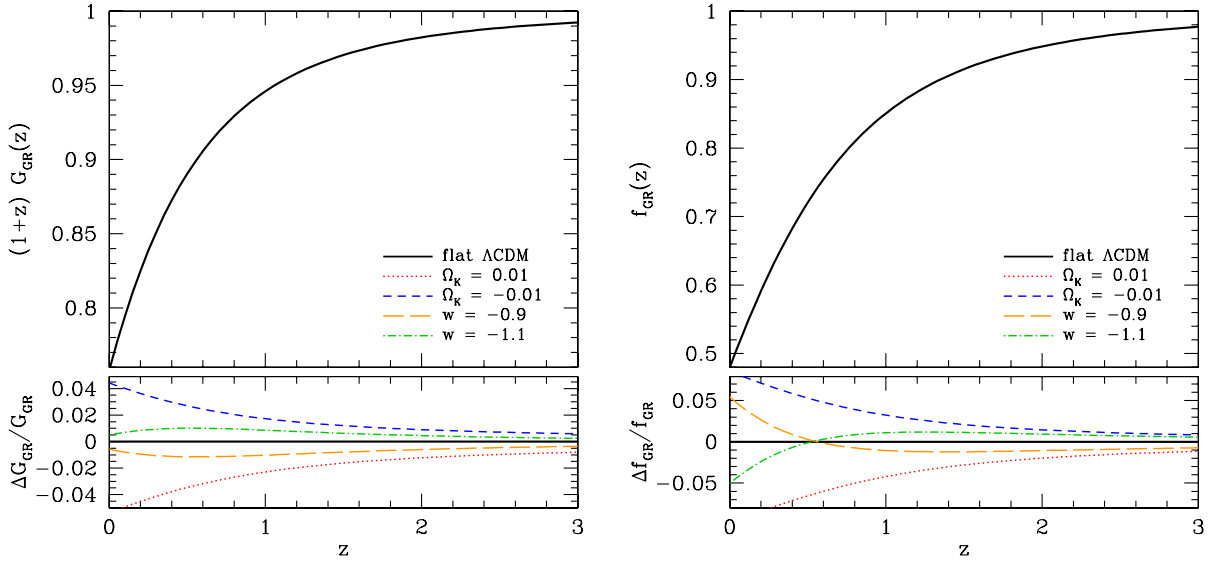


Fig. 3. Evolution of the linear growth factor $G(z)$ and growth rate $f(z)$ for the models shown in Fig. 2, assuming GR. The scaling in the left panel removes the $(1+z)$ evolution that would arise in an $\Omega_m = 1$ universe and normalizes $G_{\text{GR}}(z)$ to one at $z = 9$.

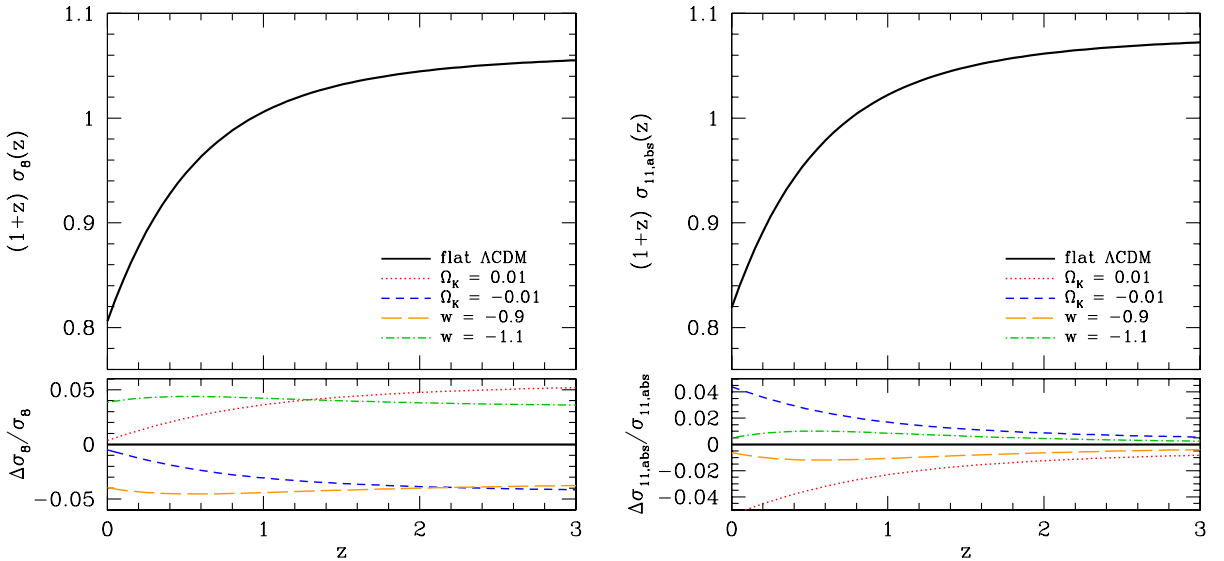


Fig. 4. Evolution of the matter fluctuation amplitude for the models shown in Fig. 3, characterized by the rms linear fluctuation in comoving spheres of radius $8h^{-1}$ Mpc (left) or 11 Mpc (right). All models are normalized to the WMAP7 CMB fluctuation amplitude.

anisotropies by a factor $e^{-\tau}$ on the scales that determine the normalization. The WMAP7 constraints are $\tau = 0.088 \pm 0.015$ (1σ), so the associated uncertainty in the matter fluctuation amplitude is 1.5%. (Recall that the power spectrum amplitude is $\propto \sigma_8^2$, so its fractional error is a factor of two larger.) For *Planck*, Holder et al. (2003) estimate uncertainty $\sigma_\tau = 0.01$ allowing for complex reionization history, and we use this value in our own forecasts. While there have been some changes in the situation since then (the polarized foregrounds at large scales are worse than anticipated, and τ is lower than the central value from the first-year WMAP results), this expectation seems broadly consistent with more recent studies (e.g., Mortonson and Hu, 2008; Colombo and Pierpaoli, 2009).²⁰ This will likely be the limiting factor for comparison of high-redshift (CMB) measurements with low-redshift (e.g., WL) measurements of the growth of structure (as opposed to measurements of evolution within the observed low- z range), unless other probes of reionization such as 21 cm provide constraints on the reionization history (see Section 5.9 for further discussion).

Following Albrecht et al. (2009), we parameterize departures from the GR growth rate by a change $\Delta\gamma$ of the growth index (Eq. (15)) and by an overall amplitude shift G_9 that is the ratio of the matter fluctuation amplitude at $z = 9$ to the

²⁰ For example, Colombo and Pierpaoli (2009) find $\sigma_\tau \sim 0.006$, albeit under somewhat optimistic assumptions regarding foregrounds and sky cuts.

value that would be predicted by GR given the same cosmological parameters and $w(z)$ history.²¹ Some caution is required in defining $\Delta\gamma$, since Eqs. (15)–(17) are not exact, and their inaccuracies should not be defined as failures of GR! For precise calculations, therefore, we adopt the Albrecht et al. (2009) expressions for growth factor evolution:

$$f(z) = f_{\text{GR}}(z) (1 + \Delta\gamma \ln \Omega_m(z)) \quad (44)$$

$$G(z) = G_9 \times G_{\text{GR}}(z) \times \exp \left[\Delta\gamma \int_z^9 \frac{dz'}{1+z'} f_{\text{GR}}(z') \ln \Omega_m(z') \right], \quad (45)$$

where $G_{\text{GR}}(z)$ and $f_{\text{GR}}(z)$ follow the (exact) solution to Eq. (14).

For practical purposes, one can use our definition of growth parameters to calculate the normalized linear theory matter power spectrum at redshift z , given an assumed set of cosmological parameter values and a $w(z)$ history, as follows. First, use CAMB (Lewis et al., 2000) or some similar program to compute the normalized linear matter power spectrum at $z = 9$. Then multiply the power spectrum by $G^2(z)/G_{\text{GR}}^2(z = 9)$, with $G(z)$ given by Eq. (45) and $G_{\text{GR}}(z)/G_{\text{GR}}(z = 9)$ given by the exact solution to Eq. (14), or by the approximate integral solution (18), computing $H(z)$ and $\Omega_m(z)$ from Eqs. (3) and (5) given the cosmological parameters and $w(z)$. For reference, we note that CAMB normalization with WMAP7 data yields, for a flat Λ CDM model,

$$\sigma_{11,\text{abs}}(z = 9) \times (1 + 9) = 1.134 \left[\frac{A_s}{2.43 \times 10^{-9}} \right]^{1/2} e^{2(n_s-1)} \left(\frac{\Omega_b h^2}{0.023} \right)^{-0.34} \left(\frac{\Omega_m h^2}{0.13} \right)^{0.57}, \quad (46)$$

$$\sigma_8(z = 9) = \sigma_{11,\text{abs}}(z = 9) \times 0.9859 \left(\frac{h}{0.71} \right)^{0.67+(n_s-1)/2}, \quad (47)$$

where the primordial amplitude A_s is defined at comoving wavenumber $k = 0.002 \text{ Mpc}^{-1}$. This formula, similar to that in Hu (2004), is found by varying the parameters in CAMB calculations around the WMAP7 mean values one at a time to evaluate logarithmic derivatives; spot checks indicate that it is accurate to 0.2% over the 2σ range of the WMAP7 errors, and for the range of w and Ω_k variations in Table 1. For models other than flat Λ CDM, one can use this formula to get $\sigma_8(z = 9)$ in GR, assuming that the effect of dark energy at $z > 9$ is negligible, then multiply by $G(z)/G_{\text{GR}}(z = 9)$ to get $\sigma_8(z)$.

For an analytic power spectrum, one can use the approximate formula in Eq. (25) of Eisenstein and Hu (1999), which includes suppression of small scale power by baryonic effects but does not incorporate BAO. This paper defines the power spectrum normalization in terms of a parameter δ_H , related to our growth factor and normalization A_s by

$$\delta_H = \frac{2}{5} A_s^{1/2} \left(\frac{G(z=0)}{\Omega_m} \right) \left(\frac{H_0}{k_{\text{norm}}} \right)^{(n_s-1)/2}. \quad (48)$$

Using the appropriate values for our fiducial WMAP7 flat Λ CDM model [$G(z=0) = 0.76$, $\Omega_m = 0.267$, $A_s = 2.43 \times 10^{-9}$ at $k_{\text{norm}} = 0.002 \text{ Mpc}^{-1}$, $h = 0.71$, $n_s = 0.963$] with this definition of δ_H , the Eisenstein and Hu (1999) formula agrees with the result from CAMB to 2% or better except at the BAO scales, where deviations are up to 10%. One can also use this normalization for the more complex (but still analytic) formulas of Eisenstein and Hu (1998), which do include BAO. We caution that other papers and books (e.g., Dodelson, 2003) have different definitions of δ_H .

There are, of course, degeneracies between the modified gravity parameters G_9 and $\Delta\gamma$ and the $w(z)$ history, since both affect structure growth. However, if $w(z)$ is pinned down well by $D(z)$ and $H(z)$ measurements, then measurements of matter clustering can be used to constrain G_9 and $\Delta\gamma$. The clustering amplitude at a single redshift yields a degenerate combination of these two parameters, but measurements at multiple redshifts or direct measurements of the growth rate via redshift-space distortions can separate them in principle. Of course, there is no guarantee that a modified gravity prediction can be adequately described by G_9 and a constant $\Delta\gamma$, and one might more generally consider (in Eq. (45)), for example, a functional history $\gamma(z)$ analogous to $w(z)$, or a direct multiplicative change to the growth rate $d \ln G/d \ln a$ rather than a change of the growth index γ . However, any constraints inconsistent with $G_9 = 1$, $\Delta\gamma = 0$ after marginalizing over $w(z)$ and cosmological parameters would be suggestive evidence for a breakdown of GR. Even if the measurements themselves are convincing, one must be cautious in the interpretation, since apparent discrepancies could arise from $w(z)$ histories outside the families considered in marginalization or from other violations of the underlying assumptions. To give two examples, “early dark energy” that is dynamically significant at high redshift could cause an apparent $G_9 < 1$, and decay of dark matter into dark energy could cause an apparent $\Delta\gamma < 0$ because the value of $\Omega_m(z)/\Omega_m(z=0)$ would be higher than in the standard picture. In Section 7.7 we discuss other potential signatures of modified gravity, such as scale-dependent growth, discrepancy between masses inferred from lensing and from non-relativistic tracers, and different accelerations in low and high density environments, and we mention other parameterizations that have been used to describe modified gravity models.

While they are not a substitute for full calculations, we find the use of CMB-normalized models like those in this section to be a valuable source of intuition for understanding the impact of distance or structure growth measurements in a (realistic) situation where CMB anisotropies impose tight parameter constraints. To make construction of such model sets

²¹ Albrecht et al. (2009) denote this quantity G_0 instead of G_9 , but we have reserved subscript-0 to refer to $z = 0$ quantities.

easy, we note that for small changes $|1 + w| \lesssim 0.1$ and $|\Omega_k| \lesssim 0.01$, the changes to h required to keep D_* fixed are well approximated by

$$\Delta \ln h \approx -0.5(1 + w) + 8\Omega_k + 0.9|\Omega_k|. \quad (49)$$

The changes to Ω_m and Ω_b are then trivially found by fixing $\Omega_m h^2$ and $\Omega_b h^2$ to their fiducial model values, and the dark energy density follows from $\Omega_\phi = 1 - \Omega_m - \Omega_k - \Omega_r$. The value of $\sigma_{11,\text{abs}}(z = 9)$ is unchanged because $\Omega_m h^2$ and $\Omega_b h^2$ are fixed, while the value of $\sigma_8(z = 9)$ follows from Eq. (46) with the revised Hubble parameter. To compute power spectrum normalizations at other redshifts one uses Eq. (18) with the new $\Omega_m(z)$ implied by Eqs. (3) and (5). The changes to the normalization at $z = 0$ are approximately

$$\Delta \ln \sigma_8(z = 0) \approx -0.4(1 + w) + 0.4\Omega_k - 0.06|\Omega_k|. \quad (50)$$

The coefficients in Eqs. (49) and (50) are chosen to reproduce the values in Table 1; at smaller $|1 + w|$ or $|\Omega_k|$ the best coefficients might be slightly different, but the changes themselves would be smaller.

2.5. Overview of methods

We conclude our “background” material with a short overview of the methods we will describe in detail over the next four sections.

Observations show that Type Ia supernovae have a peak luminosity that is tightly correlated with the shape of their light curves – supernovae that rise and fall more slowly have higher peak luminosity. The intrinsic dispersion around this relation is only about 0.12 mag, allowing each well observed supernova to provide an estimated distance with a 1σ uncertainty of about 6%. Surveys that detect tens or hundreds of Type Ia supernovae and measure their light curves and redshifts can therefore measure the distance–redshift relation $D(z)$ with high precision. Because the supernova luminosity is calibrated mainly by local observations of systems whose distances are inferred from their redshifts, supernova surveys effectively measure $D(z)$ in units of h^{-1} Mpc, not in absolute units independent of H_0 .

Baryon acoustic oscillations provide an entirely independent way of measuring cosmic distance. Sound waves propagating before recombination imprint a characteristic scale on matter clustering, which appears as a local enhancement in the correlation function at $r \approx 150$ Mpc. Imaging surveys can detect this feature in the angular clustering of galaxies in bins of photometric redshift, yielding the angular diameter distance $D(z_{\text{phot}})$. A spectroscopic survey over the same volume resolves the BAO feature in the line-of-sight direction and thereby yields a more precise $D_A(z)$ measurement. Furthermore, measuring the BAO scale in velocity separation allows a direct determination of $H(z)$. Other tracers of the matter distribution can also be used to measure BAO. Because the BAO scale is known in absolute units (based on straightforward physical calculation and parameter values well measured from the CMB), the BAO method measures $D(z)$ in absolute units – Mpc not h^{-1} Mpc – so BAO and supernova measurements to the same redshift carry different information.

The shapes of distant galaxies are distorted by the weak gravitational lensing from matter fluctuations along the line of sight. The typical distortion is only $\sim 0.5\%$, much smaller than the $\sim 30\%$ dispersion of intrinsic galaxy ellipticities, but by measuring the correlation of ellipticities as a function of angular separation, averaged over many galaxy pairs, one can infer the power spectrum of the matter fluctuations producing the lensing. Alternatively, one can measure the average elongation of background, lensed galaxies as a function of projected separation from foreground lensing galaxies to infer the galaxy–mass correlation function of the foreground sample, which can be combined with measurements of galaxy clustering to infer the matter clustering. By measuring the projected matter power spectrum for background galaxy samples at different z , weak lensing can constrain the growth function $G(z)$. However, the strength of lensing also depends on distances to the sources and lenses, so in practice the weak lensing method constrains combinations of $G(z)$ and $D(z)$.

Clusters of galaxies trace the high end of the halo mass function, typically $M \geq 10^{14} M_\odot$. Observationally, one measures the number of clusters as a function of a mass proxy, which directly constrains $dn/(d \ln M dV_c)$, where $dn/d \ln M$ is the halo mass function (Eq. (38)) and dV_c is the comoving volume element at the redshift of interest (Eq. (12)). The mass function at high M is sensitive to the amplitude of matter fluctuations, and therefore to $G(z)$, though this information is mixed with that in the cosmology dependence of the volume element $dV_c \propto D_A^2 H^{-1}$. Clusters can be identified in optical/near-IR surveys that find peaks in the galaxy distribution and measure their richness, in wide-area X-ray surveys that find extended sources and measure their X-ray luminosity and temperature, or in Sunyaev–Zel’dovich (SZ) surveys that find localized CMB decrements and measure their depth. The critical step in any cluster cosmology investigation is calibrating the relation between halo mass and the survey’s cluster observable – richness, luminosity, temperature, SZ decrement – so that the mass function can be inferred from (or constrained by) the distribution of observables. We will argue in Section 6 that the most reliable route to such calibration is via weak lensing, making wide-area optical or near-IR imaging a necessary component of any high-precision cosmic acceleration studies with clusters.

Several of the “alternative” methods described in Section 7 may ultimately play an important role in pinning down the origin of cosmic acceleration, even given the high precision expected from Stage IV supernova, BAO, weak lensing, and cluster surveys. In some cases, such as redshift-space distortions, these alternatives are automatically enabled by the same surveys conducted for BAO or weak lensing. In other cases, such as direct measurement of H_0 , the required observational programs are different in character.

3. Type Ia supernovae

3.1. General principles

Supernovae (which we will often abbreviate to SN or SNe) are the most straightforward tool for studying cosmic acceleration, and they are the tool that directly discovered acceleration in the first place (Riess et al., 1998; Perlmutter et al., 1999; both using local calibration samples from the Calán/Tololo survey, Hamuy et al., 1996). Type Ia supernovae, defined observationally by the absence of hydrogen and presence of SiII in their early-time spectra (Filippenko, 1997), are thought to arise from thermonuclear explosions of white dwarfs, though the evolutionary sequence or sequences that lead to these explosions remains poorly understood. The two broad classes of progenitor models are “single degenerate”, in which a white dwarf accreting from a binary companion is pushed over the Chandrasekhar mass limit, and “double degenerate”, in which gravitational radiation causes an orbiting pair of white dwarfs to merge and exceed the Chandrasekhar mass. The observed supernova population could have contributions from both channels (see Livio, 1999 for a review of Type Ia SN mechanisms).

To a rough approximation, Type Ia SNe are standard candles, with rms dispersion of approximately 0.4 magnitudes in V-band at peak luminosity (Hamuy et al., 1996; Riess et al., 1996). This 0.4-mag scatter can be sharply reduced using an empirical correlation between peak luminosity and light curve shape (LCS) – supernovae with higher peak luminosities decline more slowly after the peak. This correlation, which we will refer to generically as the luminosity–LCS relation, was first quantified by Phillips (1993) based on a handful of objects including the archetypes of low and high luminosity Ia supernovae, SN 1991bg and SN 1991T, respectively. Also important to the refinement of distance determinations was the development of corrections for the correlation between SN color and extinction (Riess et al., 1996; Tripp, 1998; Phillips et al., 1999) and K -corrections for redshifting effects (Kim et al., 1996; Nugent et al., 2002). These were all quickly incorporated into analysis methods such as the Multicolor Light Curve Shape (MLCS; Riess et al., 1996) technique used by the High- z Supernova Search (Schmidt et al., 1998) and the stretch-factor formalism used by the Supernova Cosmology Project (Perlmutter et al., 1997).

With these corrections, the dispersion in well measured optical band peak magnitudes is only ~ 0.12 magnitudes (Hicken et al., 2009b; Folatelli et al., 2010), allowing each well measured supernova to provide a luminosity–distance estimate with $\sim 6\%$ uncertainty. The diversity of SN Ia light curves is not fully understood, and peculiar SNe Ia appear to produce $\sim 5\%$ non-Gaussian tails in the SN Ia distribution (Li et al., 2011). For the bulk of the population, the prevailing picture is that the progenitor explosions produce varying amounts of Ni^{56} , whose radioactivity powers the optical luminosity, and that the correlation of peak luminosity with light curve shape arises from radiative transfer effects (Hoeftlich et al., 1996; Kasen and Woosley, 2007). Recent studies suggest that SN Ia are truly standard candles in the near-IR, with peak luminosities at rest-frame H -band ($1.6 \mu\text{m}$) that have only ~ 0.1 magnitude rms dispersion independent of light curve shape, and with little sensitivity to uncertain reddening laws (Mandel et al., 2009, 2011; Barone-Nugent et al., 2012). This small dispersion in near-IR peak luminosities relative to optical is consistent with theoretical expectations from radiative transfer models (Kasen, 2006).

To measure cosmic expansion with Type Ia SNe, one compares the corrected peak apparent magnitudes of distant supernovae to those of local calibrators at $0.03 < z < 0.1$, a “sweet spot” in which distances inferred from redshifts are insensitive to peculiar velocities and to the assumed densities of dark matter and dark energy. Since the distances to the local calibrators are usually determined from Hubble expansion, this method gives the luminosity distance D_L in units of h^{-1} Mpc. More generally, the SN method yields relative distances in different redshift bins, even if one of those bins is not strictly local. The $D_L(z)$ relation is sensitive to dark energy through Eqs. (7) and (3), and to space curvature through Eqs. (10) and (11). A measurement of N supernovae in a redshift bin with rms observational errors σ_{obs} in peak magnitudes yields an estimate of $D_L(z)$ with fractional statistical error

$$\sigma_{\ln D} = \frac{(\sigma_{\text{int}}^2 + \sigma_{\text{obs}}^2)^{1/2}}{(2 \times 1.086 \times \sqrt{N})}, \quad (51)$$

where σ_{int} is the rms intrinsic scatter, the factor 1.086 converts from magnitudes to natural logarithms, and the factor of two converts from flux uncertainty to distance uncertainty. As discussed in Section 3.4 below, there are many possible sources of systematic uncertainty, including flux calibration, corrections for dust extinction, and possible redshift evolution of the supernova population. Of these, dust extinction looks like it may ultimately be the most difficult to control at the sub-percent level, since even a 0.01-mag $E(B - V)$ color excess corresponds to a 3% suppression of V-band flux. This consideration provides strong motivation for focusing Stage IV supernova surveys on rest-frame near-IR photometry, where dust extinction is a factor of 3 to 8 times smaller compared to the optical and where the small scatter in peak luminosities may help minimize any evolutionary effects.

3.2. The current state of play

Building on the initial discovery of cosmic acceleration, supernova surveys have been a major area of activity in observational cosmology over the last decade. The largest high-redshift ($z \approx 0.4\text{--}1.0$) data sets are those from the ESSENCE survey (Wood-Vasey et al., 2007; Narayan et al., in prep.; ~ 200 spectroscopically confirmed Type Ia SNe) and the CFHT

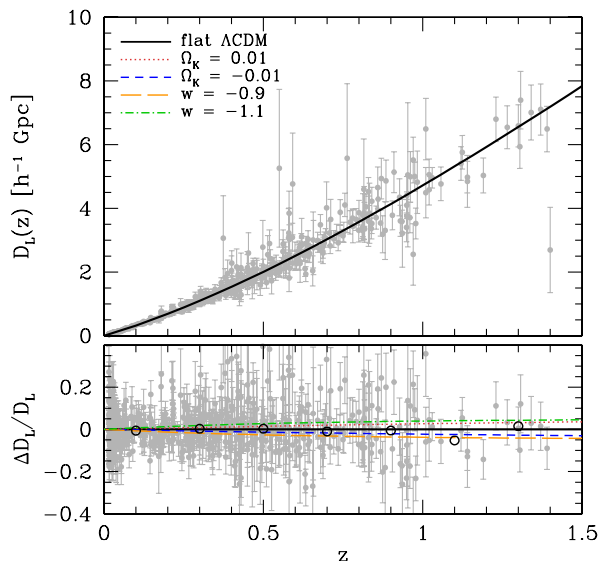


Fig. 5. Luminosity distance vs. redshift for our fiducial cosmological model (solid curves), superposed on supernova measurements from the Union2 compilation (Amanullah et al., 2010). The lower panel shows residuals from the fiducial model prediction for the SN data, with open circles marking medians of the data in $\Delta z = 0.2$ bins and broken curves showing the CMB-normalized variant models described in Table 1. Note that these distances are in h^{-1} Gpc units.

Supernova Legacy Survey (SNLS; Astier et al., 2006; Conley et al., 2011; Sullivan et al., 2011; ~ 500 spectroscopically confirmed Type Ia SNe in the three-year data set SNLS3). At very high redshifts, *HST* surveys (Riess et al., 2004, 2007; Suzuki et al., 2012) have yielded ~ 25 Type Ia SNe at $z > 1.0$, which confirm the expectation that the universe was decelerating at high redshift and limit possible systematic effects from evolution of the supernova population or intergalactic dust extinction. At intermediate redshifts ($0.1 < z < 0.4$), the SDSS-II supernova survey (Frieman et al., 2008; Sako et al., 2008) has discovered and monitored 500 spectroscopically confirmed Type Ia SNe; only the first-year data set (103 SNe) has so far been subjected to a full cosmological analysis (Kessler et al., 2009), but Campbell et al. (2013) present cosmological results from a sample of 752 photometrically classified SDSS-II SNe with spectroscopic host galaxy redshifts, and a joint analysis of the SNLS and SDSS-II samples is in process (J. Frieman, private communication). Finally, the last five years have also seen major efforts to expand the sample of local calibrators and improve their measurements, including rest-frame IR and rest-frame UV photometry (Wood-Vasey et al., 2008; Stritzinger et al., 2011; Contreras et al., 2010; Hicken et al., 2009a).

The greatest cosmological utility from SNe Ia generally comes from the joint use of numerous samples that span a wide range in redshift. To limit systematic errors introduced by combining disparate SN surveys, it is often valuable to recompile a sample from these surveys as homogeneously as possible. This involves applying consistent criteria for inclusion in the sample, light curve fitting with a single algorithm, propagation of errors via covariance matrices, consistent use of K -corrections, and so forth. While any such “survey of surveys” is not unique and may not be optimal for a specific application, these compilations are popular because of their ease of use. Recent examples include the “Gold” sample (Riess et al., 2004, 2007), the “Union” and “Union2” samples (Kowalski et al., 2008; Amanullah et al., 2010), the “Constitution” sample (Hicken et al., 2009a), and the compilation of local, SDSS-II, SNLS3, and *HST* supernovae analyzed by Conley et al. (2011).

Fig. 5 plots luminosity distance measurements from the Union2 compilation over the model predictions shown previously in Fig. 2 (multiplied by $1 + z$ to convert comoving angular diameter distance to luminosity distance). The data are in good agreement with the fiducial cosmological model, and the parameter changes in the bottom panel ($\Omega_k = \pm 0.01$, $1 + w = \pm 0.1$) are at the border of detectability. (Recall that other parameters are adjusted to reproduce the CMB anisotropy of the fiducial model; see Table 1.)

Fig. 6 illustrates model constraints from the Union2 supernova data and WMAP7 CMB data, which we have computed using CosmoMC (Lewis and Bridle, 2002). We use the Union2 covariance matrix that includes correlated systematic error contributions. Panel (a) shows the $(\Omega_m, \Omega_\Lambda)$ plane assuming $w = -1$. CMB and SN constraints are highly complementary in this plane because the former are most sensitive to the total energy density ($\Omega_m + \Omega_\Lambda$) and the latter to the difference between the densities of “attractive” matter and “repulsive” dark energy. Together the two data sets yield tight constraints in this space, $\Omega_m = 0.282 \pm 0.037$, $\Omega_\Lambda = 0.723 \pm 0.030$, consistent with a flat universe. Panel (b) shows the (Ω_m, w) plane, where we now assume spatial flatness and a constant value of w . Here again the SN and CMB data are highly complementary, yielding a tight combined constraint $\Omega_m = 0.270 \pm 0.023$, $w = -1.007 \pm 0.081$, consistent with a cosmological constant. Panel (c) shows the $(w_{0.5}, w_a)$ plane, where we have adopted the 2-parameter dark energy model of Eq. (24); $w_{0.5}$ is the value of w at $z = 0.5$, which is much better determined than the value of w_0 and only weakly correlated with w_a . Here we have assumed spatial flatness and marginalized over uncertainty in Ω_m . CMB and SN data provide only weak

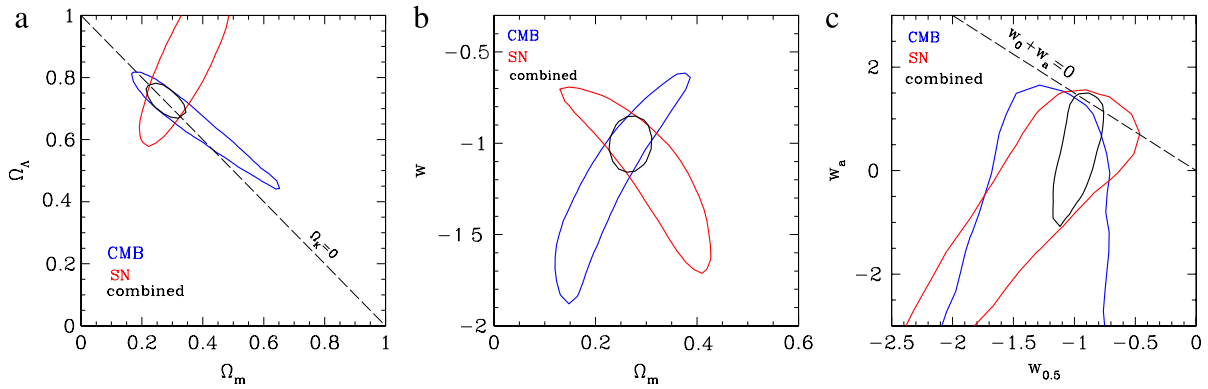


Fig. 6. Constraints from WMAP7 CMB data, Union2 SN data, and the combination of the two, in (a) the $(\Omega_m, \Omega_\Lambda)$ plane assuming $w = -1$, (b) the (Ω_m, w) plane assuming $\Omega_k = 0$, and (c) the $(w_{0.5}, w_a)$ plane assuming $\Omega_k = 0$, where $w_{0.5}$ is the value of w at $z = 0.5$. Contours show 68% confidence intervals. In contrast to panels (a) and (b), the combined contour in (c) is tighter than one would guess from the overlap of the individual contours because the combined data set breaks degeneracies among other parameters that are marginalized over when inferring $w_{0.5}$ and w_a .

constraints individually in this model space, but the combination still provides a good constraint on $w_{0.5}$, with the error on $w_{0.5} = -1.008 \pm 0.132$ only degraded by $\sim 50\%$ compared to panel (b). Constraints on w_a , on the other hand, are very weak. The w and $w_{0.5}$ constraints in panels (b) and (c) would degrade substantially if we allowed non-zero Ω_k ; with this level of flexibility, one must bring in additional data to get useful constraints. However, an H_0 or BAO constraint at the level of current measurements is sufficient to remove most of the sensitivity to Ω_k (Mortonson et al., 2010).

Plots and constraints similar to Figs. 5 and 6 appear in many of the papers cited above. The most up-to-date analysis is that of Conley et al. (2011), who find $w = -0.91^{+0.16}_{-0.20}(\text{stat})^{+0.07}_{-0.14}(\text{sys})$ for SNe alone, assuming a flat universe with constant w and marginalizing over Ω_m . Combining this measurement with other data sets, Sullivan et al. (2011) find $w = -1.016^{+0.077}_{-0.079}$ in combination with 7-year WMAP CMB constraints (similar to the value and error bar quoted above), and $w = -1.061^{+0.069}_{-0.068}$ after adding BAO and H_0 measurements.

There are several indications that current SN cosmology studies are limited by systematic uncertainties associated with the linked issues of dust extinction, SN colors, and photometric calibration. In any cosmological analysis, one uses the color of a supernova relative to a template expectation (derived from a training set) to infer, and correct for, a correlation between color and apparent magnitude arising from dust and/or intrinsic color variations. In the analysis of Wood-Vasey et al. (2007), different priors about host galaxy extinction change the inferred value of w by amounts comparable to the statistical error. When the ratio of extinction to reddening is treated as a free parameter in the cosmological fits, the derived values are typically quite far from those measured for Galactic interstellar dust, e.g., $R_V \equiv A_V/E(B-V) = 1.5 - 2.5$ (Hicken et al., 2009b; Kessler et al., 2009; Sullivan et al., 2011) instead of the mean $R_V = 3.1$ found in the diffuse interstellar medium of the Milky Way (Cardelli et al., 1989). This difference could be a reflection of different kinds of dust along the line of sight to the supernova (e.g., circumstellar dust), but it could also arise from intrinsic color differences among SNe Ia with similar light curve shapes, which would reduce the inferred R_V if they are assumed to arise from reddening. Supporting the latter idea, the distribution of SN colors shows little dependence on host galaxy properties (Kessler et al., 2009; Sullivan et al., 2010), while such dependence might be expected if the color distribution is strongly affected by dust. Chotard et al. (2011), using spectroscopic indicators of luminosity in nearby SNe, infer an extinction law with $R_V = 2.8 \pm 0.3$, consistent with the Galactic value.

One of the main surprises in the first-year analysis of the SDSS-II Supernova Survey (Kessler et al., 2009) was the realization that the two main algorithms developed by other groups for global fitting of SN light curves and cosmological parameters – MLCS2k2 (Jha et al., 2007) and SALT2 (Guy et al., 2007) – initially gave statistically inconsistent cosmological results ($w = -0.76 \pm 0.07$ vs. $w = -0.96 \pm 0.06$, quoting only the statistical errors) when applied to the same data sets, a discrepancy that persisted even if the SDSS-II data themselves were omitted from the fits. Kessler et al. (2009) traced this discrepancy to two factors, one related to calibration data and the other to the treatment of SN colors. For the calibration data, ultraviolet flux measurements in the local sample from the U -band appear inconsistent with those from the g -band at only moderate redshift and suggest a problem with the (observed frame) U -band calibration.²² This problem translates into a difference between fitters because one is trained with U -band data and the other is not. A more subtle difference arises from the determination of the correction to SN brightness from color measurements, specifically whether the correlation can be assumed to be independent of redshift and survey and whether changes in color are due solely to extinction. While these systematic uncertainties will certainly be reduced by larger multi-wavelength data sets and improved analysis methods, the experience from these recent studies argues strongly for using rest-frame IR photometry in precision cosmological studies to circumvent uncertainties related to extinction.

²² Conley et al. (2011) provide further evidence for an error in the local U -band calibration, and they omit these data from their cosmological analysis.

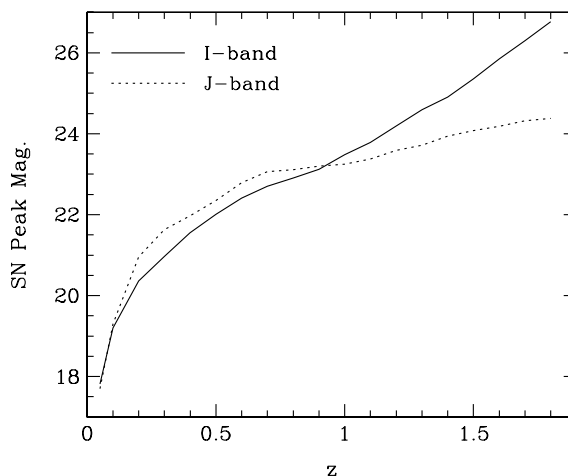


Fig. 7. Peak apparent magnitude of a typical Type Ia supernova as a function of redshift in observed-frame *I*-band (solid) or *J*-band (dotted), from Table 7 of Tonry et al. (2003). The $z > 1.1$ portion of the *I*-band curve and $z < 0.4$ portion of the *J*-band curve rely on extrapolation of the template systems' spectral energy distributions beyond the observed range. Magnitudes are on the Vega system.

3.3. Observational considerations

There are several steps to a supernova cosmology campaign: discovery, monitoring, spectroscopic confirmation, and calibration against low redshift samples. In large area surveys, discovery and monitoring are usually done together, through repeated imaging of a large field of view in multiple bands. A variety of image-differencing techniques can be used to identify SNe (distinguished from other variable objects by their light curves) and measure their magnitudes vs. time. As a rule of thumb, a minimum rest-frame cadence of one observation per ~ 5 days²³ is needed to get adequate measurements of light curve shapes and normalizations, such that statistical errors are dominated by the intrinsic dispersion of SN luminosities and not by observational errors. The required cadence may be somewhat lower in the rest-frame IR, where the dependence on light curve shape is weaker, but one must still have enough data points to determine peak luminosity accurately. At least two bands are needed to measure SN colors and thereby infer dust extinction, though more are better, and multiple colors may prove critical to distinguishing different forms of extinction (interstellar, circumstellar, and intergalactic) from each other and from intrinsic color differences.

Fig. 7, based on Table 7 of Tonry et al. (2003), plots the peak apparent magnitude of a typical Type Ia supernova vs. redshift in observed frame *I* and *J* band. As a rough rule of thumb, a survey with periodic and uniform exposures targeting supernovae at a given redshift should measure to a signal-to-noise ratio of ~ 15 at peak, so that it still usefully measures the SN before or after peak when it is 1.5 magnitudes fainter. This depth ensures that incompleteness for supernovae below the median luminosity does not bias the results and that photometric errors do not dominate over intrinsic scatter in cosmological analysis. Ground-based surveys designed to observe SNe Ia to $z < 0.8$ will typically find ~ 10 SNe Ia per square degree per month.

After discovering SNe, one must determine their type and redshift. The most reliable approach is to obtain their spectra to cross-correlate their spectral features with known templates. Spectral resolution $R \sim 250$ and $S/N \sim 5$ per resolution element are adequate for these purposes, but even at this level spectroscopic follow-up is typically the most resource intensive step of a supernova campaign. For the same telescope aperture, an epoch of spectroscopy requires an order of magnitude more time than an epoch of photometry, and one generally loses the parallelism afforded by photometric monitoring with a large camera (which has several SNe per field of view at a given time). Spectroscopic follow-up of the SNLS3 sample, for example, used more than 1600 h of 8–10 m telescope time (M. Sullivan, private communication).

In principle, photometric redshifts can be used in place of spectroscopic redshifts, and if they are accurate to a fractional distance error $\Delta D/D < 10\%$ they lead to only moderate degradation in statistical accuracy. However, given the degeneracies among redshift, SN color, and dust extinction, and the increased ambition of SN surveys to control systematics, we are skeptical that cosmological SN surveys can achieve the desired accuracy using only broad-band photometric monitoring and spectroscopic follow-up of a small fraction of the sample. An intermediate approach that may work would be to measure the cross-correlation of a supernova SED with the SN Ia spectral features using custom-designed optical filters that are matched to SN spectroscopic features at different redshifts (Scolnic et al., 2009). It also may be possible to make use of subsamples of SNe found in passive (non-star-forming) galaxies, which should host only Type Ia SNe and which allow more accurate photometric redshifts from host galaxies. For type identification, one can also check for a second peak in the rest frame infrared light curve, a morphological feature that is unique to SNe Ia.

²³ Observed-frame time intervals are larger by $1+z$.

Another intermediate approach is to obtain eventual spectroscopic observations of all host galaxies in the cosmological analysis sample but not attempt real-time spectroscopy of all candidate Type Ia supernovae. This scheme still yields precise redshifts, and it provides host galaxy data that can be used to measure and remove correlations between supernova and host galaxy properties (see Section 3.4). While it still requires one faint-object spectrum per supernova, the scheduling demands are much more flexible. One can also apply data quality and other selection cuts before the spectroscopic observations to reduce the total number of spectra required, though one must be careful not to let biases creep in at this stage. With good photometric monitoring and with subsequent spectroscopic redshifts of apparent hosts, Kessler et al. (2010) find that they can identify Type Ia SNe with 70% to 90% confidence from the LCS and color alone, and Bernstein et al. (2012) forecast Type Ia purity as high as 98% for DES-like photometric observations. A moderate amount of real-time supernova spectroscopy may then suffice to assess efficiency and biases. The recent SDSS-II analysis by Campbell et al. (2013) puts this approach into practice, illustrating its promise and its challenges.

Given the photometric and spectroscopic measurements for a selected set of supernovae, one must fit the data set to infer cosmological parameters. Many of the algorithms in current use are descendants of the Multicolor Light Curve Shape (MLCS; Riess et al., 1996) or Spectral Adaptive Light Curve Template (SALT; Guy et al., 2005) methods. In current implementations, MLCS fitters are “trained” on local supernovae to determine the relationships between multi-band light curve shapes and peak absolute magnitudes, and these relationships are applied to distant supernovae to measure $D_L(z)$. SALT-style fitters (which include the SiFTO (Conley et al., 2008) algorithm applied to SNLS3) instead apply a global, simultaneous fit of parameters describing cosmology and the relationship between supernova light curves and absolute magnitude. Of greater practical import, however, is the different treatment of supernova colors in the two methods. MLCS fitters attribute color differences at fixed peak luminosity to dust reddening, and they adopt an explicit prior for the distribution of reddening values. SALT fitters allow scatter in intrinsic colors at fixed peak luminosity and do not attempt to separate intrinsic variations from dust reddening. In reality, there certainly are intrinsic color variations at some level, but there is also useful information in the fact that dust reddening exists and has specific properties, in particular that it cannot be negative. An optimal approach should therefore allow for both effects. Bayesian fitting methods (e.g., Mandel et al., 2009, 2011; March et al., 2011) can in principle incorporate a wide variety of parameterized relationships with explicit priors, including dependences on redshift or host galaxy parameters, which are then marginalized over in cosmological fits. At the level of precision of current SN samples, the differences in fitting methods do matter (e.g., Kessler et al., 2009), so this remains an area of active research. Fortunately, the growing samples of well observed local and distant SNe provide increasingly powerful data to guide this development.

The detailed spectra of SNe could potentially improve their luminosity and/or color calibration relative to photometric light curves alone. For example Foley et al. (2011) find a correlation between intrinsic color and the ejecta velocity inferred from the line width (see also Blondin et al., 2012; Foley, 2012). However, Silverman et al. (2012), considering a variety of spectral indicators, find only marginal evidence for a diagnostic that improves Hubble residuals, and Walker et al. (2011) find similarly ambiguous results. Given the substantial observing time required to measure good spectroscopic diagnostics for high redshift SNe, modest reductions in scatter are unlikely to win over simply observing more supernovae. However, spectral diagnostics merit continued investigation to see whether matching spectral properties between high and low redshift SNe can reduce susceptibility to evolutionary systematics.

3.4. Systematic uncertainties and strategies for amelioration

The largest current supernova surveys have ~ 500 Type Ia supernovae. Future surveys hope to discover and monitor thousands of supernovae, sufficient to yield statistical errors of 0.01 mag or smaller in narrow redshift bins with $\Delta z \sim 0.1$ –0.2. Realizing the statistical power of such surveys will require eliminating or limiting several distinct sources of systematic error. These include flux calibration errors across a wide range of flux and redshift, the systematics associated with SN colors and dust extinction, the possible evolution of the supernova population with redshift, and gravitational lensing. We discuss each of these issues in turn.²⁴

The leverage of SN studies comes from comparing SNe over a wide span of redshift and thus an enormous range of flux; for example, the typical peak I -band magnitude at $z = 0.8$ is 23 mag while the median peak B -band magnitude of the local calibrator sample used in many analyses is 17 mag, implying a ratio of 250 in flux. Maintaining sub-percent accuracy in relative flux calibration over such a range would be challenging under any circumstances, and for SN surveys it is complicated by the fact that (a) local and distant SNe are usually observed with different telescopes equipped with different filters, (b) a given observed-frame filter intercepts a different portion of the SN rest-frame spectral energy distribution (SED) at each redshift, and (c) supernova SEDs are very different from those of the standard stars used for flux calibration in most of astronomy. Conley et al. (2011) identify calibration as the dominant systematic in SNLS3, the only systematic in their analysis that makes a major contribution to their total error budget. Flux calibration uncertainties can be reduced by carefully designing photometric SN surveys with specialized hardware (e.g., tunable lasers, NIST photodiodes and calibration sources; Stubbs and Tonry, 2006) to measure the system throughput *in situ* and by choosing filter systems that provide a good

²⁴ For detailed discussions of systematics in the context of specific contemporary data sets, see, e.g., Wood-Vasey et al. (2007); Kessler et al. (2010) and Conley et al. (2011).

match in rest-frame SED sampling between low- and high-redshift samples. The ACCESS rocket program should improve flux calibration with sub-orbital flights that compare NIST photodiodes to calibration stars (Kaiser et al., 2010). “Self-calibration” that marginalizes over flux-calibration uncertainty can further reduce this systematic error (Kim and Miquel, 2006), but at the price of increasing statistical error.

As already noted in Section 3.2, uncertainties in dust extinction, linked to uncertainties in intrinsic SN colors and in photometric calibration, are already important systematics in SN studies of cosmic acceleration. These uncertainties can likely be reduced with detailed, well calibrated, multi-wavelength observations of large numbers of low redshift SNe, which can characterize the separate dependence of SN colors on luminosity, light curve shape, and time since explosion, and provide constraints on dust extinction laws that are isolated from cosmological inferences. The final analyses of data from the SDSS-II supernova survey (Frieman et al., 2008) and the low-redshift portion of the Carnegie Supernova Project (Hamuy et al., 2006) should allow advances on this front. Analysis techniques that eliminate the most highly reddened SNe can also reduce extinction systematics if they can be applied in a way that does not introduce selection biases; as an extreme example, one can employ only SNe in early-type galactic hosts, which have low amounts of interstellar dust. Perhaps the most important strategy for reducing extinction systematics is to work as far as possible to red/near-IR rest-frame wavelengths, where extinction is low compared to blue/visual wavelengths. Most ground-based SN cosmology studies to date work at rest-frame B (0.4–0.5 μm) or V (0.5–0.6 μm) wavelengths, which transform to observed-frame I -band (0.7–0.9 μm) at $z \approx 0.5$ –0.8. The high-redshift portion of the Carnegie Supernova Project (Freedman et al., 2009) produced a SN Hubble diagram to $z \approx 0.7$ in rest-frame I -band, where systematic errors due to uncertainty in the reddening laws are roughly half that at V -band. Mandel et al. (2009) find that the intrinsic dispersion of peak luminosities is only ~ 0.11 mag at rest-frame H -band (1.5–1.7 μm), where systematics due to extinction are only $\sim 1/6$ that at V -band. However, obtaining rest-frame near-IR photometry for high-redshift supernovae requires space observations due to the high backgrounds seen from the ground (Section 3.5).

Locally observed SNe span a wide range in the age, metallicity, and current star formation rate (SFR) of their host stellar populations. This breadth of host conditions provides a laboratory for the investigation of the evolution of SNe Ia as distance indicators. Recently such an effect was found and calibrated in the form of a modest, $0.03 \text{ mag dex}^{-1}$ relationship between host galaxy stellar mass (a likely tracer of metallicity) and calibrated SN Ia magnitude (Kelly et al., 2010; Lampeitl et al., 2010; Sullivan et al., 2010; see Hicken et al. (2009b) for an analysis with host morphology and Hayden et al. (2013) for an analysis that incorporates star formation rate in an attempt to isolate metallicity). At the level of precision enabled by current surveys, it is necessary to correct for this effect (Conley et al., 2011), but the uncertainty in the correction is not a limiting systematic.

Constraining evolutionary effects to a tenth of σ_{int} (~ 0.01 mag) or better is a challenge. For example, if there are two populations of Type Ia progenitors (e.g., single and double degenerates) that have slightly shifted luminosity–LCS relations, then evolution in the population ratio could produce evolution in the mean relation at a fraction of σ_{int} (see, e.g., Sarkar et al., 2008). A strategy for limiting evolution systematics is to break the SN sample into subsets defined by spectral features, light curve shapes, or host properties and check for consistency of cosmological results, since evolution is unlikely to affect all populations in the same way. A complementary path (Riess and Livio, 2006) is to observe supernovae at $z > 2$, where predicted fluxes relative to low-redshift samples are generally insensitive to dark energy parameters; discrepancies would be an indication of evolutionary effects or of unconventional dark energy models that could be tested by other probes. Finally, we note that any evolutionary corrections may be weaker in the near-IR, both because of the narrower range of luminosities and because of the weaker sensitivity to metal lines (which may itself contribute to the narrower luminosity range) and reddening laws.

Gravitational lensing by intervening large scale structure introduces scatter in observed SN fluxes, at a level of ~ 0.05 magnitudes for sources at $z = 1$ (e.g., Frieman, 1996; Wang, 1999). Flux conservation guarantees that the *mean* flux of the SN population does not change. However, some care is required to ensure that selection effects or weighting schemes do not bias results at the 0.01-mag level, especially as the magnification distribution is highly non-Gaussian (see, e.g., Sarkar et al., 2008a). Since lensing effects are small and calculable, they are unlikely to become a limiting systematic even for the most ambitious future surveys. Analyses that average fluxes of SNe in redshift bins or model the full flux distribution can minimize lensing systematics and may reduce some other systematic effects as well (Wang, 2000; Amendola et al., 2010; Wang et al., 2012).

If rest-frame near-IR photometry can be obtained for large supernova samples, we anticipate that flux calibration uncertainties will ultimately set the floor on systematics. A detailed recent investigation of the *HST* WFC3–IR system implies a limiting calibration uncertainty of ~ 0.02 mag (Riess, 2012). A future mission designed with IR supernova photometry as a key goal could presumably do better, so 0.005–0.02 mag seems a plausible bracket for calibration-limited systematics.

3.5. Space vs. ground

Space observations offer several key advantages for precision supernova cosmology, a point emphasized early on by the SNAP (SuperNova Acceleration Probe) collaboration (e.g., Aldering et al., 2002). The first is the sharp and stable point-spread function (PSF) achievable from space, which greatly increases sensitivity to faint, variable point sources and the precision and accuracy of point-source photometry, especially in the presence of a host galaxy background. Adaptive optics can produce a sharp PSF from the ground, but it is not likely to deliver photometry with 1% precision and an image stable enough to allow host subtraction at random positions on the sky away from bright guide stars. The second advantage is the greater accuracy

and precision of flux calibration achievable from space, with no time-variable atmospheric conditions and (for a well chosen orbit) minimal variations in the telescope environment. The third is the vastly lower sky background in the near-IR. Typical sky backgrounds for ground-based observations are 16, 14, and 13 mag arcsec⁻² at *J*, *H*, and *K* (Vega), while in space they are 6 to 8 mags fainter, limited by the zodiacal light.

It is the last of these advantages that we regard as critical—no improvements in ground-based technology or observing strategy will ever remove the IR sky background. We have already emphasized the key role of rest-frame near-IR photometry in reducing systematics associated with dust extinction, and possibly with evolution. Obtaining rest-frame *J*-band (1.2 μm) photometry of SNe at $z = 0.8$ requires imaging at $\lambda = 2 \mu\text{m}$. A 1.3-m space telescope – the (unobstructed) aperture proposed for *WFIRST* – can make a $S/N=15$ measurement at the peak magnitude of a median $z = 0.8$ supernova at this wavelength in about 20 min. A ground-based 4-m telescope with 0.8" seeing and a typical IR sky background would require multiple nights, and even then the accuracy of photometry would be compromised by variable sky background.

A space-based near-IR telescope also offers the option of discovering and monitoring SNe at substantially higher redshifts, while working at shorter rest-frame wavelengths. However, for the reasons discussed quantitatively in Section 4 and Section 8, we think that the most important role for a mission like *WFIRST* in SN studies is to provide the highest achievable accuracy and precision at $z \leq 0.8$, as part of a combined dark energy program that also includes ambitious BAO and weak lensing surveys. At low redshifts, SNe can achieve a measurement precision unmatched by other methods, but at higher redshifts they cannot match the dark energy sensitivity of large BAO surveys unless they can push statistical and systematic errors well below 0.01 mag (see Table 6 in Section 8.2). The value of a high- z SN program depends critically on whether the systematics at high- z are uncorrelated with those at low- z , in which case the distant SNe provide new information even after the low- z program has saturated its systematics limit, or whether the limiting systematics are correlated across the full redshift range. We discuss this point more quantitatively in Section 8.3.1 below. For a given observing allocation, the maximally efficient use of *WFIRST* SN time may be in a combined ground-space program, with ground-based photometry (in rest-frame optical) providing high-cadence light-curve sampling and color measurements and lower cadence space observations providing the critical, well calibrated, dust-insensitive photometry used for the SN distance determinations.

3.6. Prospects

The next year or two should see the publication of final results from the SDSS-II supernova survey, the five-year SNLS sample, and ESSENCE. The measurements from these large surveys should substantially reduce the statistical errors in the SN Hubble diagram. Perhaps more importantly, they should yield significant reductions of systematic errors because of their high sampling cadence, wide wavelength range, and greater attention to photometric calibration. Large campaigns to discover and monitor local supernovae (e.g., PTF, LOSS, CSP, SN Factory) should also yield better understanding of potential systematics, as well as better local calibration. A new *HST* survey by the Higher- z Team using WFC3 will find more high redshift ($z > 1.5$) SNe, which provide additional leverage on the Hubble diagram and constraints on evolution.

The largest new projects on the near horizon are the SN surveys of PS1 (now underway) and DES (beginning observations in late 2012). Bernstein et al. (2012) discuss the DES strategy in some detail and forecast discovery of up to 4000 Type Ia SNe out to redshift $z = 1.2$. For spectroscopic follow-up, DES aims to observe ~10%–20% of their high- z supernovae but obtain nearly complete spectroscopic host galaxy redshifts for their cosmological sample. A similarly detailed description of the PS1 strategy is not yet available, but in principle PS1 should also be able to discover thousands of Type Ia SNe. In purely statistical terms, a sample of 2000 SNe out to $z = 0.8$ can achieve errors of 0.007 mag in redshift bins of $\Delta z = 0.2$, so both PS1 and DES will almost certainly be limited by systematic rather than statistical errors.

Looking further ahead, LSST is expected to yield samples of tens or even hundreds of thousands of SNe (LSST Science Collaboration, 2009). These photometric samples will certainly swamp spectroscopic follow-up capabilities, and the LSST surveys will again be systematics limited, though the enormous sample size (allowing cross-checks and focus on the most favorable subsamples) and the high-cadence monitoring with high photometric precision across the optical spectrum should reduce systematics below those of PS1 and DES. Finally, if *WFIRST* is completed and launched as per the Astro2010 recommendations, the access to the rest-frame near-IR should yield an unmatched advantage for SN cosmology and the best achievable results in SN dark energy studies.

4. Baryon acoustic oscillations

4.1. General principles

The baryon acoustic oscillation method relies on the imprint left by sound waves in the early universe to provide a feature of known size in the late-time clustering of matter and galaxies. By measuring this acoustic scale at a variety of redshifts, one can infer $D_A(z)$ and $H(z)$. The acoustic length scale can be computed as the comoving distance that the sound waves could travel from the Big Bang until recombination at $z = z_*$ (see descriptions by Hu and Sugiyama, 1996; Eisenstein and Hu, 1998). This is a simple integral

$$r_s = \int_0^{t_*} \frac{c_s(t)}{a(t)} dt = \int_{z_*}^{\infty} \frac{c_s(z)}{H(z)} dz. \quad (52)$$

The behavior of $H(z)$ at $z > z_*$ depends on the ratio of the matter density to radiation density; in simple cosmologies, the radiation sector (photons and neutrinos) is fixed and the ratio is proportional to $\Omega_m h^2$. The sound speed depends on the ratio of radiation pressure to the energy density of the baryon–photon fluid, determined by the baryon-to-photon ratio, which is proportional to $\Omega_b h^2$. Both the matter-to-radiation ratio and the baryon-to-photon ratio are well measured by the relative heights of the acoustic peaks in the CMB anisotropy power spectrum. Analyses of *WMAP* data in the usual Λ CDM cosmological models gives a 1.1% inference of the acoustic scale r_s (Jarosik et al., 2011); *Planck* is expected to shrink this error bar to 0.25%. Note that the acoustic scale is determined in absolute units, Mpc not h^{-1} Mpc.

The acoustic scale is large, about 150 Mpc comoving, because primordial sound waves travel at relativistic speed, maxing out at $c/\sqrt{3}$ at early times when the baryon density is negligible compared to radiation density. The large size of the acoustic scale protects this clustering feature from non-linear structure formation in the low-redshift universe. As discussed below, both cosmological perturbation theory and numerical simulations argue that the scale of the acoustic feature is stable to better than 1% accuracy, making it an excellent standard ruler. The BAO method measures the cosmic distance scale using this ruler. Separations along the line of sight correspond to differences in redshift that depend on the Hubble parameter $H(z)r_s$. Separations transverse to the line of sight correspond to differences in angle that depend on the angular diameter distance $D_A(z)/r_s$.

The challenge of the BAO method is primarily statistical: because this is a weak signal at a large scale, one needs to map enormous volumes of the universe to detect the BAO and obtain a precise distance measurement. Galaxy redshift surveys allow us to make these large three-dimensional maps of the universe, although we will discuss other methods as well.

At low redshift ($z \lesssim 0.5$), the BAO method strongly complements SN measurements because BAO provides an absolute distance scale and a strong connection to the CMB acoustic peaks from $z = 1000$, while SN allow more precise measurements of relative distances and thus offer a more fine-grained view of the distance–redshift relation. At higher redshift ($z \gtrsim 0.5$), the large cosmic volume and the direct access to $H(z)$ make the BAO method an exceptionally powerful probe of dark energy and cosmic geometry.

4.2. The current state of play

The acoustic oscillation phenomenon was identified as a potential effect in the CMB sky in the late 1960s. This was soon extended to the late-time matter power spectrum by (Sakharov, 1966; Peebles and Yu, 1970; Sunyaev and Zel'dovich, 1970); of course, they were considering pure baryon cosmologies, where the effect is very strong. The introduction of adiabatic cold dark matter in the mid-1980's made the predicted late-time acoustic peak very weak (particularly in the $\Omega_m = 1$ scenario), and the acoustic oscillations were primarily studied in the CMB context (Bond and Efstathiou, 1984, 1987; Jungman et al., 1996; Hu and Sugiyama, 1996; Hu and White, 1996; Hu et al., 1997). A resurgence of interest in the dynamics of the early universe post-*COBE* led to the identification of the acoustic scale as a standard ruler, first in the CMB and then in the matter power spectrum (Kamionkowski et al., 1994; Jungman et al., 1996; Hu and Sugiyama, 1996; Eisenstein and Hu, 1998; Meiksin et al., 1999). Fisher matrix forecasts for the combination of CMB and large-scale structure identified the acoustic oscillations as a critical feature in breaking the distance scale degeneracy between Ω_m and H_0 in CMB model fits (Tegmark, 1997; Goldberg and Strauss, 1998; Efstathiou and Bond, 1999; Eisenstein et al., 1998). In particular, the SDSS Luminous Red Galaxy (LRG) sample (Eisenstein et al., 2001)²⁵ was proposed to maximize leverage on the large-scale power spectrum, with BAO as one application.

After the discovery of cosmic acceleration with Type Ia SNe, the focus on the distance scale as a function of redshift became intense. In 2003, several papers appeared discussing the acoustic scale as a standard ruler for the measurement of dark energy in higher redshift galaxy surveys (Eisenstein, 2002; Blake and Glazebrook, 2003; Hu and Haiman, 2003; Linder, 2003; Seo and Eisenstein, 2003). Compelling detections in 2005 intensified these plans (Cole et al., 2005; Eisenstein et al., 2005), with several observational surveys proposed and numerous theoretical investigations. The rapid development of the theory led to the DETF featuring BAO as one of the four leading methods for the study of dark energy (Albrecht et al., 2006).

Early results from the 2dF Galaxy Redshift Survey (2dFGRS) (Percival et al., 2001; Efstathiou et al., 2002; Percival et al., 2002) and the Abell/ACO cluster sample (Miller et al., 1999) gave hints of the acoustic feature in the power spectrum. However, the first convincing detections of BAO came in 2005 from the SDSS Data Release 3 (DR3) and final 2dFGRS samples (Eisenstein et al., 2005; Cole et al., 2005). Eisenstein et al. (2005) measured the large-scale correlation function of SDSS LRGs in the redshift range $0.16 < z < 0.47$ over 3816 square degrees, finding the acoustic peak with 3.4σ significance. As they only measured the monopole of the correlation function, Eisenstein et al. (2005) quoted the distance measurement as a blend of the line-of-sight and transverse distance scale

$$D_V(z) = [D_A(z)]^{2/3} \left[\frac{cz}{H(z)} \right]^{1/3}. \quad (53)$$

Comparing the size of the acoustic scale in SDSS to that in the CMB sky from *WMAP*, they inferred the value of $D_V(0.35)$ divided by the distance to $z = 1089$ with a 1σ uncertainty of 3.7%. (Recall that we use D_A to denote the *comoving* angular

²⁵ Alex Szalay and Jim Annis deserve particular credit for leading this development in the early years.

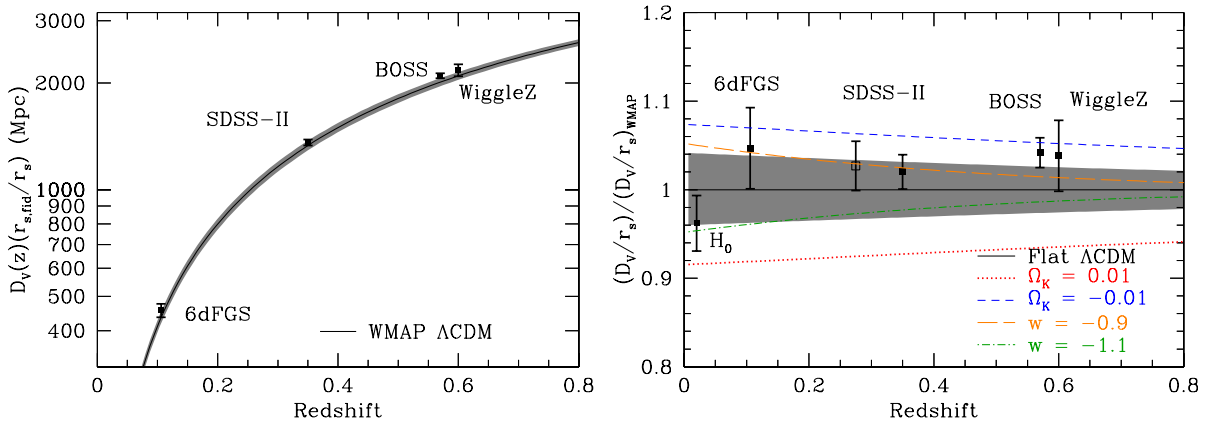


Fig. 8. (Left) The current BAO distance–redshift relation. Individual measurements are of the quantity $D_V(z)/r_s$. We have multiplied by the r_s of the fiducial Λ CDM model to yield a distance; the sound horizon is predicted to 1.1% from WMAP7. In increasing redshift, data points are from the 6dFGS (Beutler et al., 2011), SDSS-II (Padmanabhan et al., 2012; Xu et al., 2012), BOSS (Anderson et al., 2012), and WiggleZ (Blake et al., 2011d). The WiggleZ paper also quotes correlated results from multiple redshift bins, but we have chosen to plot only a single combined data point for each survey so that the measurement errors are uncorrelated. As described in the text, for a fixed choice of $w(z)$ and Ω_k , CMB data allows a prediction for $D_V(z)/r_s$. The flat Λ CDM prediction from the best-fit WMAP7 model is the black line, and the gray region shows the 1σ WMAP7 range. This is not a fit to the data, but rather the vanilla Λ CDM prediction from the CMB data. (Right) The same plot after dividing by the Λ CDM prediction from WMAP7. We have added an open point that shows the measurement from Percival et al. (2010) using a combination of SDSS-II DR7 LRG and Main sample galaxies and 2dFGRS galaxies; the Padmanabhan et al. (2012) measurement from the DR7 LRG data alone has a smaller error bar because of the increased precision afforded by reconstruction. Also shown are the four alternative models from Table 1; here we have suppressed the 1σ range that would surround each line owing to uncertainties in the matter and baryon density. Also shown is the direct H_0 value from Riess et al. (2011); here we have assumed perfect knowledge of the sound horizon, which suppresses a 1.1% uncertainty term between this value and the BAO points. These figures are adapted from the corresponding figures in Anderson et al. (2012). We have omitted the very recent BAO detections from the BOSS Ly α forest at $z \approx 2.3$ (Busca et al., 2012; Slosar et al., 2013), which are also consistent with Λ CDM predictions.

diameter distance.) Cole et al. (2005) measured the power spectrum of 2dFGRS galaxies in the redshift range $0 < z < 0.3$ over 1,800 square degrees. The cosmological fitting analysis detected a baryon fraction of $\Omega_b/\Omega_m = 0.185 \pm 0.046$, the non-zero result indicating a detection of the BAO. The distance precision of the result was quoted as a 4.1% measurement of H_0 .

Since these first detections, the clustering of successively larger SDSS spectroscopic samples has been analyzed by several groups using different methods. Tegmark et al. (2006) analyzed the DR4 LRG and main galaxy samples with a quadratic estimator for the power spectrum and redshift-space distortion. Hütsi (2006) analyzed the monopole of the power spectrum of the LRG data set with the Feldman et al. (1994) (FKP) method. Percival et al. (2007) applied the FKP method to the combined DR5 LRG and main galaxy samples, along with the 2dFGRS sample, to measure the acoustic scale at two different redshifts ($z = 0.20$ and 0.35). Percival et al. (2010) extended this analysis to the final SDSS-II sample (DR7), obtaining an aggregate distance precision of 2.7% to $z = 0.275$. Kazin et al. (2010b) analyzed the DR7 LRG sample with the correlation function (as did Martínez et al., 2009), achieving consistent results. A recent reanalysis of the DR7 sample by Padmanabhan et al. (2012) and Xu et al. (2012) improved the distance precision to 1.9% by applying the reconstruction technique described in Section 4.3.3 below.

New BAO detections have recently been made in three other samples. Beutler et al. (2011) report a 2.4σ detection from the 6-degree Field Galaxy Survey (6dFGS), which covered 17,000 deg 2 of sky, obtaining a 4.5% distance measurement to $z = 0.1$. Stepping beyond $z = 0.5$, the WiggleZ survey (Blake et al., 2011b,d) has used the AAOmega instrument at the Anglo-Australian Telescope to target emission-line galaxies at $0.4 < z < 1.0$. The analysis of the final data set of ~ 800 deg 2 yields BAO detections in three overlapping redshift slices centered on $z = 0.44$, 0.60 , and 0.73 , with an aggregate precision of 3.8%. Anderson et al. (2012) report the first BAO measurements from the SDSS-III BOSS survey (discussed further below), obtaining a 1.7% distance precision to a sample with effective redshift $z = 0.57$.

Combining SDSS-II, WiggleZ, and 6dFGS, Blake et al. (2011d) achieve a 5σ detection of the acoustic peak; Anderson et al. (2012) combine the reconstructed SDSS-II measurement and BOSS measurement to get a 6.7σ detection. Both studies find good agreement between the BAO and SN distance–redshift relations. These BAO measurements are displayed in Fig. 8, which shows D_V as a function of redshift. We can compare this $D_V(z)$ to the relation predicted by WMAP7 under particular assumptions about dark energy and spatial curvature. A given value of $\Omega_m h^2$ and $\Omega_b h^2$ yields a sound horizon r_s . For any fixed choice of Ω_k and $w(z)$, the angular acoustic scale in the CMB then breaks the Ω_m – H_0 degeneracy, which then specifies $D_V(z)$. The left panel shows the WMAP7 prediction for flat Λ CDM, with the gray band marginalizing over 1σ errors in $\Omega_m h^2$ and $\Omega_b h^2$, while the right panel divides by this prediction. The BAO measurements are all in good agreement with the $+1\sigma$ edge of the WMAP7 band; in other words, they are consistent with WMAP7 and Λ CDM but favor a value of $\Omega_m h^2 \approx 0.139$ vs. 0.134. Intriguingly, the BAO data pull in the opposite direction from the $H_0 = 73.8 \pm 2.4$ km s $^{-1}$ Mpc $^{-1}$ measurement of Riess et al. (2011). The discrepancy is only marginally significant at present – less than 2σ assuming Λ CDM – but it illustrates how BAO and direct H_0 measurements can combine to reveal additional physics beyond that in Λ CDM.

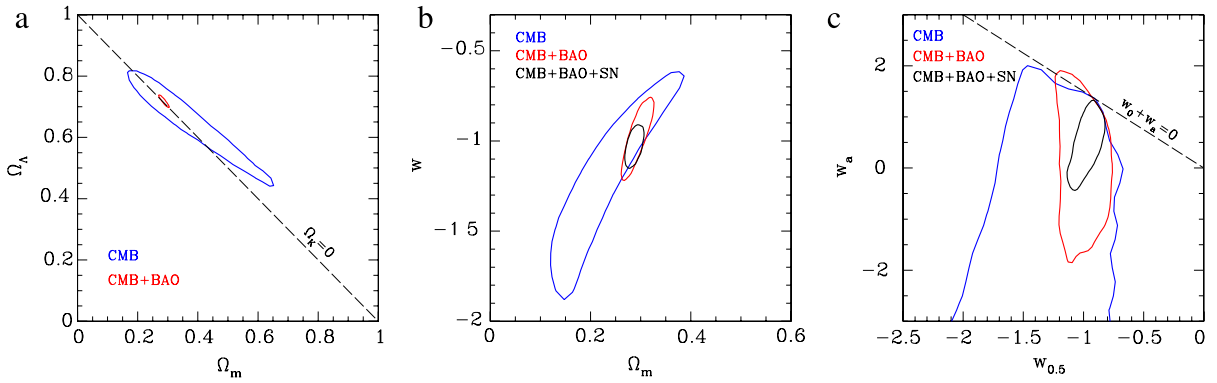


Fig. 9. Constraints from combinations of current BAO data (the four points in the left hand panel of Fig. 8), WMAP7 CMB data, and Union2 SN data in (a) the (Ω_m, Ω_A) plane assuming $w = -1$, (b) the (Ω_m, w) plane assuming $\Omega_k = 0$, and (c) the $(w_{0.5}, w_a)$ plane assuming $\Omega_k = 0$, where $w_{0.5}$ is the value of w at $z = 0.5$. Contours show 68% confidence intervals. We omit the CMB+BAO+SN combination from panel (a) because it is nearly identical to the CMB+BAO combination.

Curves in the right panel show how the comparison to the data would vary with non-zero spatial curvature or $w \neq -1$, using the CMB-normalized models introduced in Section 2.4. One can see that small changes, particularly in spatial curvature, make detectable differences in the prediction, so that comparison of the data to the prediction allows one to measure $w(z)$ and Ω_k . Comparing variations in spatial curvature to variations of constant w , one can see that variations in spatial curvature produce large offsets but relatively small slopes. SN determinations of relative distances can only measure slopes on this graph, whereas absolute distance measurements such as BAO can measure the offset. This illustrates why, in fits to the w - Ω_k model, the CMB+SN combination tends to measure w better while the CMB+BAO combination tends to measure Ω_k better.

Combining the WiggleZ, SDSS+2dFGRS (Percival et al., 2010), and 6dFGS BAO measurements with WMAP7 and the Union-2 SN compilation, Blake et al. (2011d) infer $\Omega_m = 0.289 \pm 0.015$, $H_0 = 68.7 \pm 1.9 \text{ km s}^{-1} \text{ Mpc}^{-1}$, $\Omega_k = -0.004 \pm 0.006$, and $w = -1.03 \pm 0.08$ (where w is assumed to be constant with redshift). Anderson et al. (2012) obtain similar constraints when substituting the BOSS and reconstructed SDSS-II BAO measurements and the SNLS3 SN compilation: $\Omega_m = 0.276 \pm 0.013$, $H_0 = 69.6 \pm 1.7 \text{ km s}^{-1} \text{ Mpc}^{-1}$, $\Omega_k = -0.008 \pm 0.005$, and $w = -1.09 \pm 0.08$. One can think of these inferences approximately as CMB acoustic peak heights measuring $\Omega_m h^2$, the BAO standard ruler then splitting Ω_m and H_0 , the CMB angular acoustic scale measuring Ω_k , and the SNe measuring w . Fig. 9 displays our own constraints derived from these data with CosmoMC (Lewis and Bridle, 2002), with the same parameter space used for the SN and CMB constraints in Fig. 6. While Fig. 6 includes contours for SN alone, it makes little sense to consider BAO constraints independent of CMB data because the latter are needed to calibrate the BAO ruler. We therefore show contours for CMB, CMB+BAO, and CMB+BAO+SN. Consistent with our earlier discussion, CMB+BAO provides much tighter constraints on Ω_k and Ω_m in the $w = -1$ model than CMB+SN (compare the left panels of Figs. 6 and 9), but CMB+SN provides better constraints on w (middle panels). For a w_0 - w_a model with $\Omega_k = 0$ (right panel), the three data sets together yield a good measurement of $w(z = 0.5)$ but still only loose constraints on w_a .

Indications of the acoustic feature have also been found in a sample of higher redshift LRG with photometric redshifts from the SDSS (Padmanabhan et al., 2007; Blake et al., 2007; Crocco et al., 2011; Sawangwit et al., 2011). These analyses produced a 6.5% measurement of the angular diameter distance to $z = 0.5$. An analysis of the maxBCG cluster catalog by Hütsi (2010) also yields a 2–2.5 σ detection.

Other analyses have focused on the anisotropic BAO signal, with the intent of separating $D_A(z)$ and $H(z)$. Okumura et al. (2008) performed a correlation function analysis of the LRG sample from SDSS DR3, achieving a weak indication of the radial BAO. Gaztañaga et al. (2009) analyzed the correlations of the SDSS LRG sample, considering only pairs very close to the line of sight. They claimed a detection of the BAO, thereby measuring $H(z)$; however, the proposed acoustic peak is much higher amplitude than the predicted one, and Kazin et al. (2010a) argue that it is likely to be noise (see Cabré and Gaztañaga, 2011 for a response to this criticism). Chuang and Wang (2012) analyzed the full SDSS DR7 LRG sample with an anisotropic correlation function, finding separate constraints on D_A and H at $z = 0.35$.

The next generation of the SDSS large-scale structure survey is BOSS, the Baryon Oscillation Spectroscopic Survey of SDSS-III. BOSS is observing 1.5 million luminous galaxies (mostly LRGs) out to $z = 0.7$ over 10,000 square degrees (Eisenstein et al., 2011; Dawson et al., 2013), with a selection that triples the number density of LRGs at $z < 0.4$ relative to SDSS-II and extends to a new redshift range with a dense sample at $0.5 < z < 0.7$. The increased sampling should facilitate accurate density-field reconstruction (Section 4.3.3) to boost the BAO performance. BOSS is also surveying the $2 < z < 3$ universe using a grid of quasar sightlines to provide a 3-dimensional view of the Ly α forest, with the goal of detecting BAO in the large-scale clustering of neutral hydrogen at $z \sim 2.5$. This method was proposed by White (2003) and McDonald and Eisenstein (2007). The clustering of Ly α forest flux along single lines of sight is well established as a probe of large-scale structure (see Section 7.6 for a discussion of the underlying theory), and by using cross-correlations among multiple lines of sight one can probe 3-dimensional structure. Observationally this method is attractive because quasars are very luminous

and because each quasar provides ~ 50 measurements of the large-scale density field along its line of sight. Since the BAO peak has an intrinsic rms width of $\sim 8h^{-1}$ Mpc, one need only survey the Ly α forest at modest resolution (a few hundred) to retain full BAO information. Furthermore, one does not need high signal-to-noise ratio spectra, as one gets little gain from photon errors smaller than the intrinsic variation in the small-scale forest. BOSS aims to measure 160,000 spectra of $z > 2$ quasars over 10,000 deg². Using the first third of this data set, Busca et al. (2012) and Slosar et al. (2013) report the first BAO detections in the Ly α forest, and the first detections at any $z > 1$, with precision (2%–3% on an isotropic dilation factor) that is roughly in line with theoretical expectations.

In summary, the BAO feature has been found in eight different samples – 2dFGRS, SDSS LRG, SDSS Main, 6dFGS, WiggleZ, SDSS photometric, BOSS galaxies, and the BOSS Ly α forest – with analyses from several independent research teams and with a variety of methods. The best precision is now slightly below 2%, with excellent agreement with the Λ CDM model.

4.3. Theory of BAO

While the theory of supernova explosions is complicated, the use of Type Ia SNe as distance indicators rests on empirically determined correlations that are largely independent of that theory. With BAO, on the other hand, we are using a standard ruler whose length, imprint on the clustering of observable tracers, and even very existence are derived from theory. We therefore review both the long-established linear theory of BAO and more recent work on non-linear evolution and galaxy bias, and we discuss the implications of this work for analysis of BAO data sets.

4.3.1. Linear theory

Prior to redshifts around 1000, the universe is hot and dense enough that the primordial gas is ionized. The free electrons in this plasma provide enough cross-section to the cosmic microwave background photons via Thomson scattering to produce a mean free time well less than the Hubble time. The result is a close coupling between the electrons, nuclei (baryons), and photons for sufficiently long wavelength perturbations in the early universe. The radiation pressure of the photons is large compared to the gravitational forces in the perturbations, with the result that perturbations in the baryon–photon fluid oscillate as sound waves (Peebles and Yu, 1970; Sunyaev and Zel'dovich, 1970). Diffusion of photons relative to baryons damps these oscillations on comoving scales smaller than $\sim 8h^{-1}$ Mpc, the phenomenon known as Silk damping (Silk, 1968).

After recombination, the mean free time of the photons in the neutral cosmic gas is long compared to the Hubble time. The photons decouple from the perturbations in the baryons and soon become smoothly distributed. The perturbations in the baryons are now subject to gravitational instability, just like the dark matter perturbations.

As with normal sound waves, one can usefully view the BAO phenomenon from different linear basis sets. We first consider the response to a density perturbation at a particular initial location, as illustrated in Fig. 10; see Eisenstein et al. (2007b) and Eisenstein and Bennett (2008) for further description of this view. Primordial perturbations of the adiabatic form predicted by standard inflation models consist of equal fractional density contrasts in all species. The dark matter perturbation grows in place, slowly at first in the radiation dominated epoch, then faster as the universe becomes matter dominated. The baryon–photon perturbation, on the other hand, travels away from its origin as a sound wave. At recombination, the baryon part of the wave is left in a spherical shell centered on the original perturbation. Both the dark matter at the center and the baryons on the shell seed gravitational instability, which grows to form the halos in which galaxies form. We therefore expect the distribution of separations of pairs of galaxies (i.e., the two-point correlation function generated by such perturbations) to show a small enhancement at the radius of the shell, with galaxy concentrations in the central dark matter clumps and in the shells induced by the baryons.

One can equally well view the BAO effect as a standing wave in Fourier space; see Hu and Sugiyama (1996) and Eisenstein and Hu (1998) for this explanation. In Fourier space, the single acoustic scale gives rise to a harmonic sequence of oscillations in the power spectrum. This is easy to understand physically. The power spectrum encodes the response of the universe to a plane wave perturbation. Each crest in the initial wave produces a planar sound wave that travels a distance equal to the acoustic scale. If the wave deposits the baryon perturbation on another crest of the dark matter perturbation, then one gets constructive interference; if the sound wave ends in a dark matter trough, one gets destructive interference. The result is a harmonic relation between the wavelength of the perturbation and the acoustic scale.

Mathematically, this correspondence can be seen by considering that the correlation function and power spectrum are Fourier transform pairs. The Fourier transform of a delta function is a sinusoid, and the smearing of a delta function simply provides a damping envelope to that sinusoid. In the case of the BAO, this smearing is largely due to Silk damping in the early universe and to non-linear structure formation at late times. Both cause the higher harmonics in the power spectrum to be reduced in amplitude or washed out.

While it is secondary to our pedagogical thread, we end with some additional discussion of Fig. 10 and the evolution of the initial point-like density perturbation. First, because the perturbation is in the growing mode, only the density perturbation is localized. The velocity perturbation away from the initial density perturbation has zero divergence but is non-zero; hence it scales as r^{-2} at large radius. As the baryon–photon and neutrino pulses expand, the gravity interior to the shell is weaker than it would have been. This causes the velocity perturbation interior to grow less quickly, creating a non-zero divergence away from the origin, which is why the CDM perturbation grows at non-zero radius. The size of this effect depends on

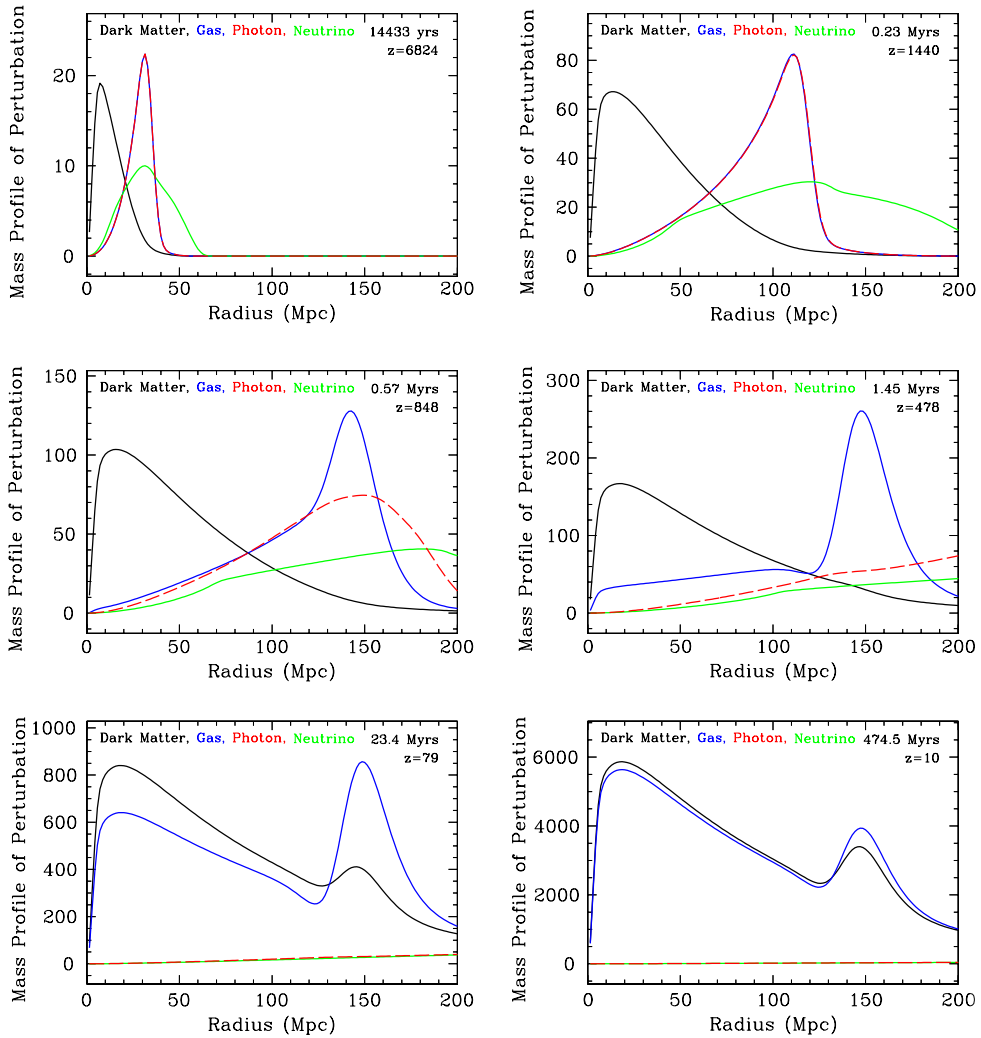


Fig. 10. The generation of the acoustic peak illustrated via the linear-theory response to an initially point-like overdensity at the origin; this figure is reproduced from Eisenstein et al. (2007b). Each panel shows the radial perturbed mass profile in each of the four species: dark matter (black), baryons (blue), photons (red), and neutrinos (green). The redshift and time after the Big Bang are given in each panel. All perturbations are fractional for that species. We have multiplied the radial density profile of the perturbation by the square of the radius in order to yield the mass profile. In detail, we begin with a compact but smooth profile at the origin, which is why the mass profiles go to zero there. As we are using linear theory, the normalization of the amplitude of the perturbation (and thus the absolute scale of the y-axis) is arbitrary. (a) Near the initial time, the photons and baryons are tightly coupled in a spherical traveling wave. (b) The outward-going wave of baryons and relativistic species increases the perturbation of the cold dark matter, similar to raising a wake. (c) At recombination, the photons decouple from the baryons. (d) With recombination complete, the CDM perturbation is near the origin, while the baryonic perturbation is in a shell of 150 Mpc. (e) With pressure forces now small, baryons and dark matter are attracted to these overdensities by gravitational instability. (f) Because most of the growth is drawn from the homogeneous bulk, the baryon fraction converges toward the cosmic mean at late times. Galaxy formation is favored near the origin and at a radius of 150 Mpc. These figures were made by suitable transforms of the transfer functions created by CMBfast (Seljak and Zaldarriaga, 1996; Zaldarriaga and Seljak, 2000).

the radiation to matter density; this transformation of the CDM perturbation is the famous k^{-2} tail of the CDM transfer function (Peebles, 1982). The non-zero velocity perturbation is also the reason why the neutrino perturbation does not remain as a sharp peak. Finally, we note that this description of the behavior is the Green's function of the system. CMB Boltzmann codes typically compute the evolution of individual Fourier standing waves; these are simply combined here to generate the response to a point perturbation rather than a single standing wave.

4.3.2. Non-linear evolution and galaxy clustering bias

The clustering of matter and galaxies undergoes substantial changes at low redshift beyond the growth described by linear perturbation theory. Small-scale structure grows non-linearly, peculiar velocities behave differently from their linear prediction, and galaxies trace the dark matter in a complicated manner. We should worry that these effects might modify the location of the BAO feature relative to the prediction of linear theory, thus distorting our standard ruler (Meiksin et al.,

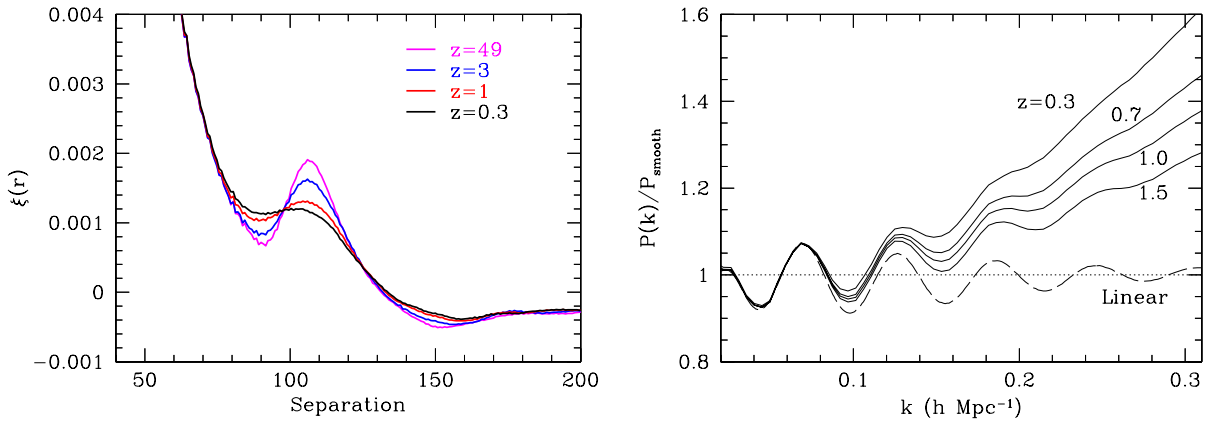


Fig. 11. The effects of non-linear clustering on the BAO. (Left) Redshift-space matter correlation function at four different redshifts from the simulations of Seo and Eisenstein (2005). (Right) Real-space matter power spectra at four different redshifts from the simulations of Seo et al. (2008), divided by a smooth power spectrum so as to reveal the acoustic oscillations. The input linear theory is shown by the dashed line. The effects of non-linear structure formation broaden the acoustic peak in the correlation function. In the power spectrum, this corresponds to a damping of the higher harmonics. Importantly, the boost of broad-band power at late times visible in the power spectrum plot corresponds largely to correlations at scales much smaller than the acoustic peak.

1999; Seo and Eisenstein, 2005; Angulo et al., 2005; Springel et al., 2005; Jeong and Komatsu, 2006; Huff et al., 2007; Angulo et al., 2008; Wagner et al., 2008).

Fortunately, the large scale of the acoustic peak insulates it from most of non-linear structure formation (Eisenstein et al., 2007b). A typical pair of dark matter particles changes its comoving separation by $10h^{-1}$ Mpc (rms value) between high redshift and $z = 0$. These motions broaden the acoustic peak, but the rms displacement is only mildly larger than the $8h^{-1}$ Mpc scale set by Silk damping. The apparent displacement along the line of sight is larger in redshift space, because the peculiar velocity is well correlated with the displacement. Fig. 11 shows the correlation function and power spectrum from N -body simulations; one can see that the acoustic peak in the correlation function becomes broader at low redshift. The corresponding effect in the power spectrum is the decreased amplitude of the wiggles at higher wavenumber. Roughly speaking, one can think of the width of the evolved $\xi(r)$ peak as the quadrature sum of the initial width and the rms pairwise displacement Σ_{NL} (see Orban and Weinberg, 2011, who examine idealized BAO models numerically and analytically). Equivalently, the oscillations in $P(k)$ are damped by a factor $\exp(-k^2 \Sigma_{\text{NL}}^2)$. As discussed in Section 4.3.4, the broadening of the BAO feature does not significantly bias the acoustic scale measurement provided one is using a suitable template-fitting method. However, it does degrade the precision of the measurement for a given survey volume, as it is harder to centroid a broader feature.

To change the acoustic scale itself, one needs instead to move pairs systematically closer or systematically further away. This is a much weaker effect than the rms motion of particles, as it depends on the density variations in 150 Mpc spheres, which are percent level. Moreover, pairs of overdensities fall toward each other and pairs of underdensities fall away from each other, and both situations count equally toward a two-point statistic, causing a partial cancellation.

Padmanabhan and White (2009) compute the change in the acoustic peak location at second-order in gravitational perturbation theory. Crocce and Scoccimarro (2008) have done similar calculations in renormalized perturbation theory. Both calculations reveal a second-order term of the form $d\xi/dr$, which corresponds to moving the acoustic peak. Padmanabhan and White (2009) compute the size of this effect to be around 0.25% at $z = 0$.

N -body simulations reveal a similar story. Seo et al. (2010b) measure the shift in the acoustic scale in a large volume of simulations and detect a shift from $\alpha = 1$ of $0.3\% \pm 0.015\%$ at $z = 0.0$, with a scaling in redshift proportional to the square of the linear growth function as expected for a second order effect (left panel of Fig. 12). Padmanabhan and White (2009) validate their analytic calculation with a similar set of simulations.

Redshift-space distortions have further effects on the BAO signal beyond the extra broadening from the large-scale peculiar velocity. Small-scale velocities, e.g., the Finger of God effect, blurs the measurement of clustering along the line of sight, thereby broadening the acoustic peak. Moreover, the peculiar velocities create anisotropy in the broadband clustering, which must be carefully accounted for when extracting the acoustic scale (Section 4.3.4).

Linear bias, with galaxy density contrast $\delta_g = b\delta_m$, changes the amplitude of $\xi(r)$ or $P(k)$ but not the shape. However, any realistic bias relation must be at least somewhat non-linear, which alters the relative weighting of overdense and underdense regions and should shift the acoustic scale at second order. Early work attempted to measure this shift in simulations (Seo and Eisenstein, 2003; Angulo et al., 2008), but the volume of the simulations was insufficient to get a conclusive detection of the effect. More recently, Padmanabhan and White (2009) explored galaxy bias as the ratio of the second-order to first-order bias term, finding shifts of a few tenths of a percent for reasonable bias cases. Mehta et al. (2011) treated the problem numerically with halo occupation distributions, finding shifts of 0.1% to 0.8% at $z = 1$ depending on the strength of the bias (right panel of Fig. 12). For halo-based models or other prescriptions that tie galaxy bias to the local density field, it

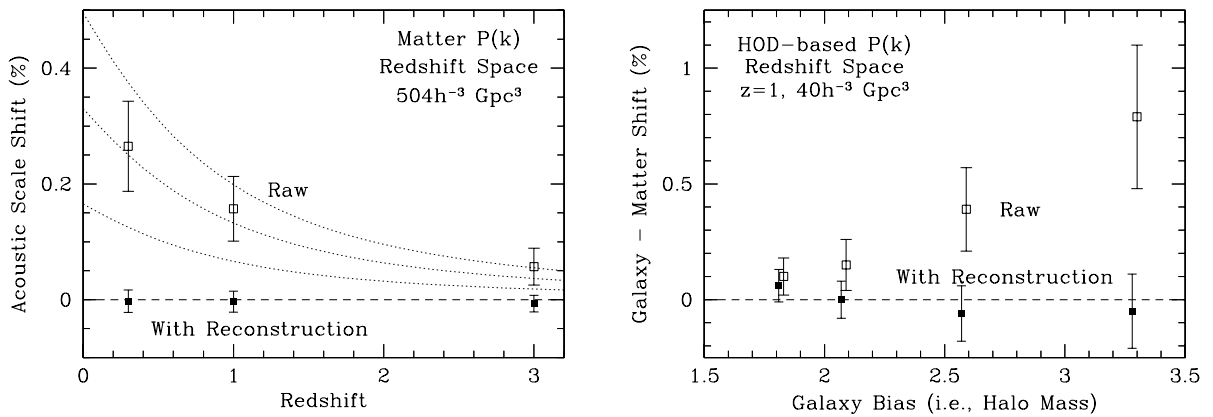


Fig. 12. The shifts of the acoustic scale in cosmological N -body simulations. (Left) Shifts of the acoustic scale in the redshift-space matter power spectrum vs. redshift from Seo et al. (2010b). The open symbols show the acoustic scale shifts prior to reconstruction; the dashed lines show a scaling of the square of the linear growth function. The solid symbols show the shifts after reconstruction is applied. The error bars are derived from the variance among simulations. (Right) Shifts of the acoustic scale in the redshift-space power spectrum of mock galaxy distributions at $z = 1$ from Mehta et al. (2011). The acoustic scale shift from the matter distribution in the same boxes has been subtracted so as to decrease sample variance. Galaxies are placed via HOD prescriptions; increasing mass thresholds leads to lower number densities and higher clustering bias. The open symbols show the shifts prior to reconstruction; the solid symbols, after reconstruction. The errors in the right panel are larger due to the smaller simulated volume and the lower number density of tracers. In all cases of both panels, reconstruction decreases the errors on the acoustic scale and reduces the shift to be consistent with zero. The left panel is based on 63 simulations, each using 576^3 particles in a $2h^{-1}$ Gpc cube. The right panel is based on 40 simulations, each with 1024^3 particles in a $1h^{-1}$ Gpc cube.

therefore appears that bias-induced shifts are small, and corrections of modest fractional accuracy (e.g., to 20% of the shift itself) will suffice to make them negligible. The relevant bias parameters should be tightly constrained by smaller scale clustering measurements and higher order statistics, enabling cross-checks of the model used for correction.

Non-local bias models that tie galaxy formation efficiency directly to the environment on much larger scales (e.g., Babul and White, 1991; Bower et al., 1993) could perhaps induce larger shifts of the acoustic scale. However, such models require fairly extreme physical effects, and they can be readily diagnosed via their impact on clustering at scales below the BAO scale (Narayanan et al., 2000). A survey capable of measuring the acoustic scale to the sub-percent statistical level will provide in its millions of galaxies extensive opportunities to constrain even very general bias models accurately enough to predict the acoustic scale shift to within 10%–20% of its value, sufficient to bring the systematic error below the statistical error.

4.3.3. Reconstruction

By broadening and shifting the BAO feature in $\xi(r)$, non-linear gravitational evolution degrades BAO precision and introduces a possible systematic. Is it possible to remove these effects by “running gravity backwards” to reconstruct the linear density field? The Zel’dovich (1970) approximation – in which particles follow straight line trajectories in comoving coordinates at the rate predicted by linear perturbation theory – captures important aspects of non-linear evolution on large scales (e.g., Weinberg and Gunn, 1990; Melott et al., 1994). Eisenstein et al. (2007a) show that a simple reconstruction scheme based on applying the (reversed) Zel’dovich approximation to the smoothed non-linear density field is remarkably successful at recovering BAO information, effectively shifting the low redshift curves in Fig. 11 back toward the high redshift curves. Fig. 13, from Padmanabhan et al. (2012), illustrates how reconstruction works in the idealized case of an initial perturbation that exactly mimics the “acoustic ring” pattern.

Seo and Eisenstein (2007) and Seo et al. (2010b) investigate the effects of reconstruction in more detail, showing that it noticeably improves the scatter and decreases the shift of the recovered acoustic scale from the matter density field of N -body simulations. The latest simulations demonstrate that the non-linear shift of the scale has been removed to 0.02% or better (see Fig. 12, left). Moreover, comparing the initial conditions to final conditions on a mode-by-mode basis shows that the linear density field has been recovered to roughly double the pre-reconstruction wavenumber. Padmanabhan et al. (2009) analyze the method analytically, revealing the improvement while also noting that the recovered density field is not exactly the linear one.

Mehta et al. (2011) extend this analysis to HOD-based mock galaxy catalogs in simulations. They consider a range of HOD prescriptions and find that the reconstruction of the linear density field is not degraded by this form of galaxy bias and that the shift of the acoustic scale after reconstruction still vanishes, this time to 0.1% precision (Fig. 12, right). This success is not surprising: the halo field traces the matter field fairly accurately on the scales required for reconstruction, so one is correctly estimating and removing the large scale displacements. Non-linear galaxy bias still alters the weighting of convergent and divergent flows, but if the flows are being mostly removed, then it does not matter how they are weighted.

Reconstruction is thus a powerful tool: one is achieving better statistical precision for a given survey, typically by a factor of 1.5 to 2, equivalent to a factor of 2–4 increase in survey size. Meanwhile, one is mitigating the primary systematic error from non-linear clustering and galaxy bias. As an added benefit, one can use the estimate of the large scale displacements

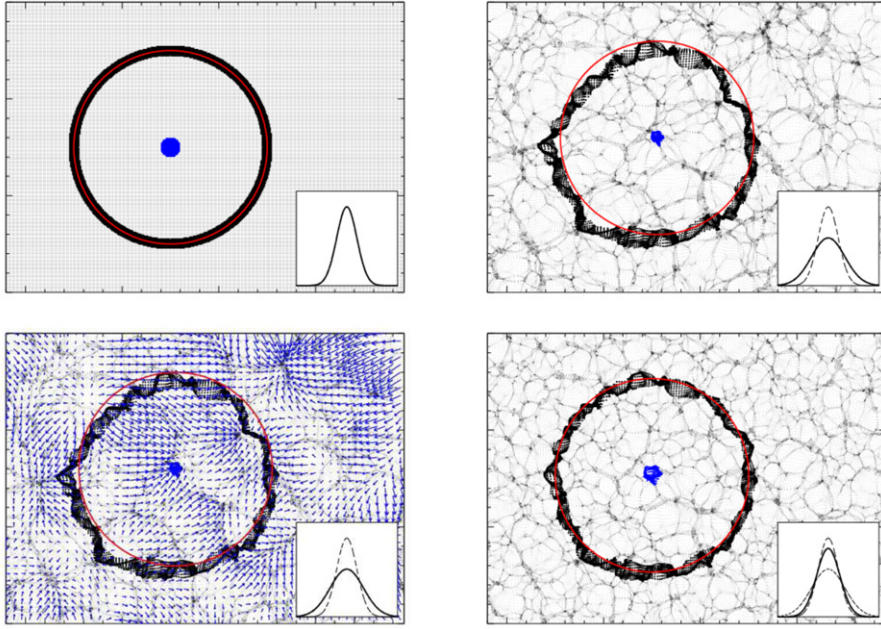


Fig. 13. A pedagogical illustration of how reconstruction can improve the measurement of the acoustic scale; this figure is from Padmanabhan et al. (2012). Each panel shows a thin slice of a cosmological density field. (Top Left) At early times, the density is nearly constant. We mark a set of points at the origin in blue and a ring of points at 150 Mpc in heavy black. We measure the distances between the black points and the centroid of the blue point; the rms of these distances is represented by the Gaussian in the inset. (Top Right) At later times, structure has formed (in this calculation, simply by the Zel'dovich approximation), and the points have moved. The red circle shows the initial radius of the ring, centered on the current centroid of the blue points. The fact that the black points no longer fall on the red ring indicates that the acoustic peak has been broadened. The inset shows that the new rms of the radial distance (solid line) is larger than the original (dashed line). (Bottom Left) Arrows show the Zel'dovich displacements responsible for the structure that has formed. The idea of reconstruction is to estimate these displacements and move the particles back. (Bottom Right) We illustrate this by smoothing the density field by a $10h^{-1}$ Mpc filter and moving the particles back. Because the displacement field is imperfectly estimated, small-scale structure remains. But the black points now fall closer to the red ring, so that the rms of the radial distance is close to the initial (inset). The actual reconstruction algorithm of Padmanabhan et al. (2012) is more complex, but this example shows the basic opportunity. (For interpretation of the references to colour in this figure legend, the reader is referred to the web version of this article.)

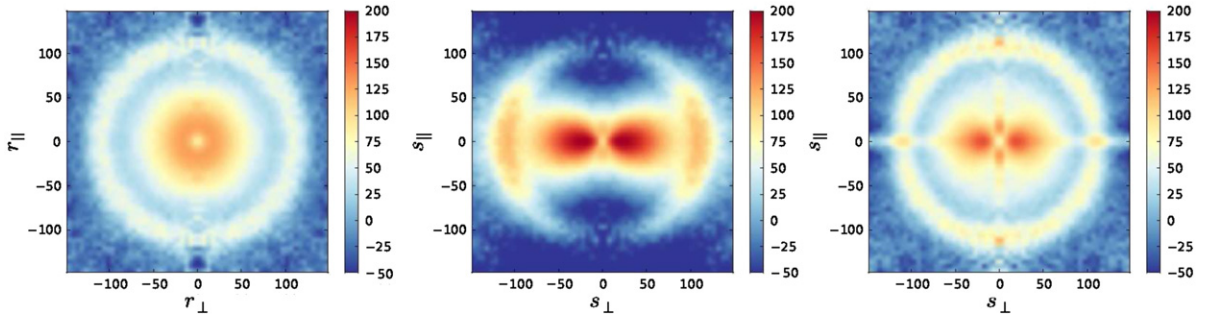


Fig. 14. The ability of reconstruction to correct redshift-space distortion of the BAO feature; figure panels taken from Padmanabhan et al. (2012). The left panel shows contours of the galaxy correlation function from N -body mock catalogs, multiplied by r^2 to enhance the large scale features, as a function of transverse (r_{\perp}) and line-of-sight (r_{\parallel}) separation. Apart from statistical fluctuations, this correlation function is isotropic. The middle panel shows contours of the galaxy correlation function in redshift-space. Peculiar velocities induce anisotropy, breaking the BAO ring into two arcs. The right panel shows the redshift-space correlation function of the galaxy distribution after reconstruction, including peculiar velocity correction at the level of the Zel'dovich approximation, which largely restores the isotropy of the BAO ring.

to remove large-scale redshift-space distortions,²⁶ as illustrated in Fig. 14, which decreases that degradation of the BAO accuracy and also pushes most of the BAO signal into the monopole and quadrupole components of $\xi(\mathbf{s})$ or $P(\mathbf{k})$. Without reconstruction, the redshift-space distortions contain significant terms in the hexadecapole and beyond, and the quadrupolar squashing of the Alcock–Paczynski effect couples to the quadrupole redshift-space distortion to produce BAO signal in the hexadecapole. To the extent that one is recovering the linear density field, one can also hope that the large-scale density

²⁶ The line-of-sight peculiar velocity is, in the Zel'dovich approximation, equal to $f(z)H(z)$ times the line-of-sight component of the 3-d displacement.

field is more Gaussian, which is a major simplification for computing likelihood functions. However, this last property has not been extensively tested.

The first applications of BAO reconstruction to observational data appear in Padmanabhan et al. (2012) and Anderson et al. (2012). For the SDSS-II (DR7) LRG sample, reconstruction shrinks the BAO distance error from 3.5% to 1.9%, equivalent to a factor of three increase in survey volume. It also improves the agreement between the observed and predicted shapes of the correlation function in the BAO regime, thereby increasing the statistical significance of the BAO detection from 3.3σ to 4.2σ . For the BOSS (DR9) sample, reconstruction produces little improvement in the BAO measurement, although this is consistent with the variation among DR9 mock catalogs (see discussion by Anderson et al., 2012).

There is an extensive literature on reconstruction methods for large-scale structure (e.g., Peebles, 1989; Weinberg, 1992; Nusser and Dekel, 1992; Croft and Gaztanaga, 1997; Narayanan and Weinberg, 1998; Mohayaee et al., 2006). Even simple methods appear adequate for BAO recovery, but better reconstruction is valuable for other applications of large-scale structure (Reid et al., 2010). Since BAO surveys are typically sparse, an important area for continuing research is the performance of methods in the presence of both galaxy bias and significant shot noise. The effectiveness of reconstruction as a function of sampling density might have important implications for survey design, favoring different choices compared to the statistical considerations discussed in Section 4.4 below.

4.3.4. Fitting to data

It is worth stressing that “the acoustic scale” is only an approximate description of a more complicated physical situation. For high precision work, we cannot separate the concept of the acoustic scale from the context of a Boltzmann code prediction for the matter power spectrum and CMB anisotropy power spectrum. The sound horizon defined by Eq. (52) does not correspond to the exact maximum of the acoustic peak in the correlation function, nor do the harmonics in the matter power spectrum have an identical scale to those in the CMB anisotropy spectrum. The differences arise from effects such as the fact that photons decouple from the baryons earlier than the baryons decouple from the photons, that the post-recombination matter growing mode is largely set by the velocity perturbation at recombination rather than the density perturbation, and that Silk damping alters the effective redshift of recombination as a function of wavenumber. These effects are accurately calculated in the Boltzmann codes, resulting in precise predictions for the matter and CMB power spectra.

When one wants to extract the acoustic scale (i.e., to measure distance using the BAO standard ruler) from a measurement of the two-point clustering, the appropriate thing to do is to use the predicted clustering for the cosmology one is testing as a template. The optimal plan is then to fit that template to the data over a range of scales using the correct covariance matrix or likelihood. Some early works instead used non-parametric models for the acoustic peak, such as a Gaussian in configuration space or a damped sinusoid in Fourier space (Blake and Glazebrook, 2003), or simply identified the maximum of the correlation function (Guzik et al., 2007; Smith et al., 2008). We believe that, because the acoustic scale is predicted only in the context of an early universe model with parameters taken from fits to CMB data, there is no extra value in avoiding the linear-theory model predictions.

Having said that, one does want to modify the template to allow for effects of non-linear structure formation and perhaps to marginalize over broad-band terms that might enter from scale-dependent clustering bias or velocity bias or from errors in the calibration of one’s survey. This procedure has been carried out by several different authors. For example, Seo and Eisenstein (2007) and Seo et al. (2010b) fit the measured power spectrum to the form

$$P_{\text{measure}}(k) = B(k)P_m(k/\alpha) + A(k), \quad (54)$$

where $A(k)$ and $B(k)$ are smooth functions with parameters to be fit. $P_m(k)$ is the linear theory model with the acoustic oscillations additionally damped by large-scale structure,

$$P_m(k) = \exp(-k^2 \Sigma_{\text{NL}})(P_{\text{lin}}(k) - P_{\text{nw}}(k)) + P_{\text{nw}}(k), \quad (55)$$

where Σ_{NL} is a constant fit from simulations. P_{nw} is the no-wiggle power spectrum from Eisenstein and Hu (1998), hand-crafted to edit out the acoustic oscillations. P_{lin} is the exact linear theory power spectrum; note that $P_m(k)$ goes to this exact linear theory result in the limit of negligible damping ($\Sigma_{\text{NL}} \rightarrow 0$), so the approximate form of $P_{\text{nw}}(k)$ is acceptable. The broadband terms $A(k)$ and $B(k)$ will correct for non-linear power, the shot noise, scale-dependent bias, and any imperfections in the survey. The primary goal for the fit is to measure α , a factor that dilates the scale of the predicted clustering (and of the BAO feature in particular) relative to the observed clustering. A value $\alpha = 1$ indicates agreement with the acoustic scale of the original model. A value $\alpha \neq 1$ indicates that the acoustic scale of the linear-theory model is incorrect or that the distance scale assumed in measuring the galaxy clustering was wrong. Simple alterations of this prescription can be made for fitting the correlation function or mixed-space ω or wavelet statistics (Xu et al., 2010; Arnalte-Mur et al., 2012). This approach thus allows one to fit for the scale of a standard ruler without having to recompute a full predicted power spectrum at every point in parameter space.

This fitting procedure is only compelling to the extent that the recovered value of α is stable (to within the statistical errors) as one varies the prescription for the marginalization of parameters in $A(k)$ and $B(k)$. Too little freedom and one may be biased by broadband tilts and modulations that one has not modeled properly; too much freedom and one will fit out the acoustic signature and reduce the constraining power of the data. Fortunately, the separation between the acoustic scale and the typical non-linear scale and Silk damping scale is large, i.e., the acoustic peak in the correlation function is narrow.

This gives considerable freedom to fit away broadband nuisance terms while not impacting the acoustic peak. Seo et al. (2010b) show stable results for α for various choices, e.g., polynomials of different order. Similarly, α is robust to changes in the choice of Σ_{NL} , so one is not sensitive to how one estimates that parameter in simulations or mock catalogs.

An equivalent method has been used by Percival et al. (2007, 2010), and in related works. Here, one fits a spline to the measured power spectrum and divides by that spline. One does similarly for the template $P_m(k)$ and fits that to the residual spectrum of the data. This is equivalent to taking $B(k)$ to be a spline and setting $A(k) = 0$. Clearly the performance depends on the number of spline points, but there is a broad stable region.

The definition of the acoustic scale as the distance a primordial sound wave could travel before recombination (Eq. (52)) is borne out in such fits. If one fits with the power spectrum from a cosmology that is moderately wrong, then one infers a different α , but this change in α is proportional to the ratio of the acoustic scales, as defined by the sound horizon integral for each cosmology. The stability of this scaling appears to be much better than the statistical errors implied by the surveys that are defining the range of interesting cosmological parameter space (Seo et al., 2010b). In other words, one can use the acoustic scale integral to adjust distance scale measurements of D_A/r_s and Hr_s between different cosmologies within the domain of interest.

Extending these approaches to the anisotropic case so as to extract D_A and H separately is more complicated and has not been fully developed. The primary obstacle is to account for the anisotropic distortions from peculiar velocities. Examples of fit methodologies include Okumura et al. (2008), Padmanabhan and White (2009), Shoji et al. (2009), Chuang and Wang (2012), Kazin et al. (2012), and Xu et al. (2013). The ability of reconstruction to mitigate peculiar velocity distortion (Fig. 14) may be a significant asset for disentangling D_A and H .

With better modeling of non-linear structure and galaxy clustering bias, one could of course extract additional cosmological information from the two-point clustering of galaxies. In particular, one can measure the distance scale from the curvature (i.e., non-power-law form) of the spherically-averaged power spectrum or correlation function. This physical scale arises from the size of the horizon at matter–radiation equality, parameterized as $\Omega_m h^2$ in typical cosmologies. However, this curvature is a much broader feature and thus provides less leverage on distance. Most important, the width of the feature is comparable to the scale itself, implying that one must control all extra broad-band sources of power and scale-dependent galaxy biases in order to extract accurate distance information. This is much more challenging than the BAO application, but it is an important frontier of the field of large-scale structure. In particular, the application of this approach to the quadrupole distortion known as the Alcock–Paczynski effect will be discussed in Section 7.3.

4.4. Observational considerations

4.4.1. Statistical errors

The primary challenge of the BAO method is that very large samples of galaxies (or other tracers) are required to detect the acoustic oscillations and hence measure a distance. Like detecting an emission line in a galaxy spectrum in order to measure a redshift, one must have high enough signal-to-noise to detect the BAO peak or one gets no useful distance information at all. The minimum useful survey volumes are of order $1h^{-3} \text{ Gpc}^3$, which yield a distance precision of about 5%.

The two components of the statistical error are sample variance and shot noise (Kaiser, 1986a). A given survey volume contains only a certain number of Fourier modes; in the periodic box approximation $dN_{\text{modes}}/dk = 4\pi k^2 V / [(2\pi)^3 2]$, where the final factor of 2 in the denominator accounts for the fact that the density field is real. In a Gaussian random field, the real and imaginary parts of each mode are independent with an intrinsic variance of $P(k)/2$. In addition, each mode is imperfectly measured due to shot noise; when treated in the Gaussian approximation (ignoring the 4-point contributions from the Poisson distribution), this raises the variance on the square of the complex norm to $[P(k) + 1/n]^2$, where n is the number density of tracers. The result is that the fractional error bar on the measurement of each mode is $\sigma_p/P = (nP + 1)/nP$. When combining information from modes, we should sum the inverse variances, which are

$$\frac{P^2}{\sigma_p^2} = \left(\frac{nP}{nP + 1} \right)^2. \quad (56)$$

We see that for $n \gg 1/P(k)$ we get unit information from each mode but that the information drops rapidly for $n < 1/P(k)$. We note that the relevant P is the redshift-space power spectrum; this can be substantially larger than the real-space power spectrum for nearly radial large-scale modes, thereby decreasing the shot noise impact on BAO estimation of the Hubble parameter.

The mode-counting argument above neglects boundary effects, effectively assuming that the survey volume is reasonably contiguous with a high filling factor on scales of 150 Mpc. In real space, we can express this as the requirement that the number of pairs of survey galaxies at 150 Mpc separation not be significantly diminished compared to the case of a filled periodic box. In Fourier space, we must ensure that the survey window function not create aliasing between modes in the crests and troughs of the acoustic oscillations.

Converting a power spectrum forecast into constraints on the distance scale requires marginalizing over other cosmological parameters. This has been done with Fisher matrix analyses (Seo and Eisenstein, 2003; Seo and Eisenstein, 2007) or with Monte Carlo approaches (Blake and Glazebrook, 2003; Glazebrook and Blake, 2005; Blake et al., 2006). Several analyses have focused on the anisotropy of the power spectrum in order to measure $H(z)$ and $D_A(z)$ separately.

Table 2
BAO forecasts for a full-sky BAO survey.

z_{\min}	z_{\max}	Volume	% Err $D_A(z)$	% Err $H(z)$	$\Omega_\Lambda(z)$	S/N	σ_w
0.00	0.15	0.33	2.8	4.9	0.708	7.3	0.64
0.15	0.32	2.62	0.95	1.7	0.616	18.2	0.088
0.32	0.51	7.89	0.53	0.96	0.515	27.0	0.036
0.51	0.73	16.5	0.35	0.63	0.413	32.9	0.021
0.73	0.99	28.4	0.26	0.46	0.318	34.9	0.015
0.99	1.28	42.9	0.21	0.36	0.236	33.3	0.013
1.28	1.62	59.0	0.17	0.28	0.170	30.2	0.012
1.62	2.00	75.8	0.14	0.24	0.119	25.2	0.013
2.00	2.44	92.3	0.13	0.21	0.082	20.0	0.014
2.44	2.95	108	0.12	0.18	0.056	15.5	0.016
2.95	3.53	121	0.11	0.17	0.038	11.4	0.020
3.53	4.20	133	0.10	0.15	0.025	8.3	0.025
4.20	4.96	142	0.10	0.15	0.017	5.8	0.033

These forecasts assume a full-sky survey, use $nP = 2$ at $k = 0.2h \text{ Mpc}^{-1}$, and assume reconstruction improvements in the non-linear damping by a factor of 2. Statistical errors scale as $f_{\text{sky}}^{-1/2}$. The first and second columns give the inner and outer edges of redshift bins; the bins have equal width in $\ln(1+z)$. The third column gives the comoving volume of the bin in $h^{-3} \text{ Gpc}^3$, assuming $\Omega_m = 0.25$. The fourth and fifth columns give 1σ fractional errors (in percent) in $D_A(z)$ and $H(z)$, the angular diameter distance to and Hubble parameter at the bin center; note that the errors on these two quantities are 40% correlated. We assume the sound horizon is known. The sixth column gives $\Omega_\Lambda(z)$, i.e., the ratio of the dark energy density to the critical density at that redshift in a Λ -model. Column 7 gives $\Omega_\Lambda(z)H/2\sigma_H$, which is the significance at which one would detect the cosmological constant at redshift z using only the $H(z)$ BAO constraint and assuming perfect knowledge of the matter density and curvature (a good approximation, but not exact). Column 8 shows the error on a constant value of w that would be obtained by comparing the BAO $H(z)$ measurement for this one redshift to the value of ρ_{DE} at $z = 0$, assuming the latter is known perfectly.

Seo and Eisenstein (2007) constructed a fast approximation to the full Fisher matrix calculation using an idealized treatment of the acoustic oscillation, including non-linear structure formation and redshift-space distortions. This method allows forecasts for H and D_A precision as a function of survey redshift, number density, and volume (see their Eq. (26)). Tests with simulations (Seo et al., 2010b; Mehta et al., 2011) have shown this forecast to be accurate to within 10%–20%, with a small trend toward over-optimism at $nP < 1$. Whether this trend is intrinsic to shot noise or to the fact that the low number density models used more massive mass thresholds for halo bias is not clear at present.

Table 2 presents a summary of cosmic variance limited BAO performance. This is a tabulation of the Seo and Eisenstein (2007) forecasts for a full-sky survey, using even binning in $\ln(1+z)$. We assume a shot noise level of $nP = 2$ at $k = 0.2h \text{ Mpc}^{-1}$ (see Section 4.4.3), and that reconstruction has decreased the non-linear displacements by a factor of two in length scale, i.e., reducing the quantity Σ_{NL} in Eq. (55) by a factor of two below its full non-linear value at each redshift. Fig. 15, discussed further in the next section, presents graphical summaries of the main features of Table 2. One can see that the precision available in $D_A(z)$ and $H(z)$ is excellent: of order 0.2% per redshift bin at high redshift. At low redshift, the precision is worse because there is far less cosmic volume. Of course, these statistical errors scale as $f_{\text{sky}}^{-1/2}$, where f_{sky} is the fraction of sky surveyed.

4.4.2. From BAO to dark energy

We will explore how these performance estimates map to dark energy parameter forecasts in Section 8, but here we describe some simplified treatments in order to build intuition. Beginning at low redshift, if we consider that CMB anisotropies give precise values for $\Omega_m h^2$ and the acoustic scale r_s , then a BAO detection near $z = 0$ is measuring a standard ruler and hence H_0 (Eisenstein and Hu, 1998). Combining that with $\Omega_m h^2$ yields Ω_m . No BAO measurement can be strictly at $z = 0$, but the inference of Ω_m and H_0 depends only on the distance scale between $z = 0$ and the survey redshift. Even at $z = 0.35$, this brings in only a mild dependence on w and Ω_k (Eisenstein et al., 2005). Hence, low-redshift BAO measurements offer a strong measurement of Ω_m . Determining Ω_m breaks a key degeneracy for the SN measurements between Ω_m and w .

Moving to higher redshift ($z \gtrsim 1$), we next consider the evolution of the density of dark energy using only the $H(z)$ information from BAO (right panel of Fig. 15). If we know the matter density and spatial curvature perfectly, then the Friedmann equation directly relates the measurement of $H(z)$ to the density of dark energy at that redshift. Considering the null hypothesis of the cosmological constant, we would achieve a detection of the dark energy density with a significance of $\Omega_\Lambda H/2\sigma(H)$, where $\sigma(H)$ is the error on $H(z)$. We next want to consider the variation in the dark energy density. Taking an example in which one assumes the $z = 0$ value is known perfectly, we can translate the error at a given redshift to the error on the exponent of a power-law variation, which can in turn be rewritten as an error on a constant w (Eq. (23)). Of course, a full analysis must include the uncertainties on the matter density, spatial curvature, and $z = 0$ value of Ω_Λ .

Despite the simplifications, Table 2 and Fig. 15 offer some important results for building intuition. We find that the sensitivity of BAO $H(z)$ to dark energy has a broad maximum over the range $0.6 < z < 3.5$. This plateau arises because the declining dynamical importance of dark energy is compensated by the increasing statistical precision afforded by larger comoving volume. For $w = -1$, dark energy is only 10% of the total density at $z = 2$, but a cosmic-variance-limited BAO

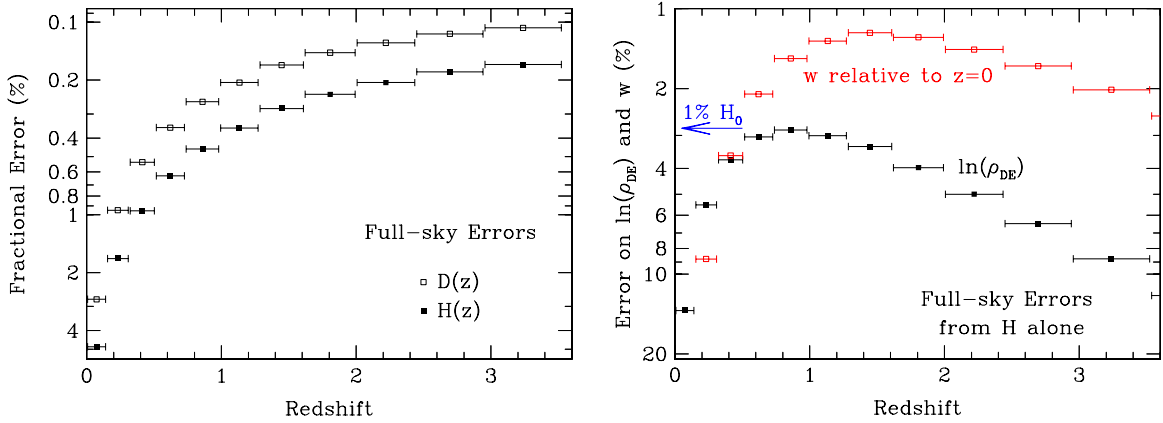


Fig. 15. Illustrative BAO forecasts for a full-sky survey, from Table 2. All errors scale as $f_{\text{sky}}^{-1/2}$; note that y-axes are inverted so that smaller errors appear higher on the plot. (Left) The fractional error on $D_A(z)$ and $H(z)$ in logarithmic redshift bins, as open and solid points, respectively. Note that performance of order 0.2% per bin is possible at high redshift. Here we assume the sound horizon is known. (Right) Illustration of the dark energy leverage available simply from the $H(z)$ information in the previous panel. Assuming perfect knowledge of the matter density (i.e., $\Omega_m H_0^2$) and curvature, measurement of $H(z)$ determines the dark energy density. The solid black points show the resulting fractional errors on the dark energy density as a function of redshift, assuming that the value is close to the cosmological constant. Errors of order 5%, i.e., a $20\text{-}\sigma$ detection of dark energy, are possible at $0.5 < z < 2$, even if the dark energy density is simply constant. The evolution of dark energy can be expressed by comparing the density at high redshift to that at $z = 0$, assuming the latter is known. The open red points give the error on a power-law evolution in $1 + z$, expressed as the error on a constant w . One sees that there is a broad maximum in performance extending out to $z \approx 3$. Of course, we must measure the dark energy density at $z = 0$; the blue arrow shows the fractional error on that density that would result from a 1% measurement of H_0 (which one might get from direct measures or from a combination of BAO and supernovae), assuming perfect knowledge of the matter density. That the blue arrow is comparable to or above the solid points indicates that we can reasonably expect to be limited by our higher redshift data. The open points are optimistic in that we have assumed perfect knowledge of various inputs; the intended lesson is that the large volume and larger redshift lever arm at higher redshift can offset the fact that the dark energy makes up a smaller fraction of the cosmic total. (For interpretation of the references to colour in this figure legend, the reader is referred to the web version of this article.)

measurement can detect that density at $20\text{-}\sigma$ significance. The large lever arm to $z = 0$ translates this into a 1.3% constraint on a constant w model. Of course, if $w > -1$, then ρ_{DE} is higher at high redshift than it is for a cosmological constant, increasing the statistical significance with which BAO can detect it.

Meanwhile, the transverse acoustic scale at $z \sim 2$ and above can be compared to the angular acoustic scale in the CMB to give a combination constraint on early dark energy and the curvature of the universe (McDonald and Eisenstein, 2007). This has considerable value in breaking degeneracies between curvature and dark energy parameters at lower redshift, and it should be considered an important consistency check for the Λ CDM interpretation of the CMB. A clear detection of non-zero curvature would have major implications for inflation, and perhaps for quantum cosmology theories (Gott, 1982; Guth and Nomura, 2012; Kleban and Schillo, 2012). If the Alcock–Paczynski method can be applied at smaller scales to obtain a precise determination of $H(z)D_A(z)$, then the BAO values of $D_A(z)$ can also be used to improve $H(z)$ determinations and thus the dark energy density constraints (see Section 7.3).

4.4.3. Sampling density

The acoustic oscillations in the power spectrum are primarily at wavenumbers $0.1\text{--}0.2h \text{ Mpc}^{-1}$, so we want to design surveys with $nP(k = 0.2h \text{ Mpc}^{-1}) \gtrsim 1$. Furthermore, if one wins sample size proportionally to survey time, then $nP(k) = 1$ is the optimal balance of survey depth to sample volume at a given wavenumber (Kaiser, 1986a). One should beware that this assumption rarely holds in surveys with multi-object instruments: the exposure time is driven by the faintest objects in the survey, so that brighter galaxies are being overexposed in the chosen observation time. Also, the number density is often a function of redshift, so one cannot hit the optimal density everywhere in the survey. Finally, one might care about distance precision differently at different redshifts because of one's specific goals for testing dark energy models. See Parkinson et al. (2007) for a worked example of survey optimization.

For the concordance cosmology, the amplitude of the power spectrum at $k = 0.2h \text{ Mpc}^{-1}$ is about $2700\sigma_{8,g}^2 h^{-3} \text{ Mpc}^3$, where $\sigma_{8,g}^2$ is the variance of the fractional overdensity of the chosen tracer at the survey redshift in spheres of $8h^{-1} \text{ Mpc}$ radius. This implies that we seek number densities around $n = (4 \times 10^{-4} h^3 \text{ Mpc}^{-3}) / \sigma_{8,g}^2$. Fortunately, this is well below the density of L^* galaxies.

Higher galaxy bias is a good thing for the statistical errors of a BAO survey. The power spectrum amplitude scales as the square of the bias, so an early-type galaxy is 3–4 times more valuable (in the sense of boosting nP) than a late-type galaxy. Given that there is no identified risk – higher bias galaxies have larger acoustic scale shifts, but this is correctable (Fig. 12, right) – it makes sense to use higher bias tracers when possible. However, lower bias tracers can be more effective if one can acquire their redshifts sufficiently quickly!

The balance of shot noise to sample variance is more complex in the case of surveys with the Ly α forest or HI intensity mapping. However, the idea is the same: one wants to make a map in which the pixel noise is dominated by sample variance,

but not by much. The power at $k = 0.2h \text{ Mpc}^{-1}$ corresponds roughly to density variance of $8h^{-1} \text{ Mpc}$ spheres. Hence, we seek to measure the density of individual regions of this size to a precision slightly better than the intrinsic rms for such volumes for the chosen tracer (i.e., $b\sigma_8$). If one is measuring too well, one would prefer to do shallower measurements over a wider region. In the case of the Ly α forest, this criterion concerns both the areal density of the quasar sightlines and the signal-to-noise ratio of the spectra (McDonald and Eisenstein, 2007; McQuinn and White, 2011).

4.4.4. Spectroscopic vs. photometric redshifts

Photometric redshifts offer a cheap way to measure many galaxy redshifts and hence to measure the BAO (Seo and Eisenstein, 2003; Glazebrook and Blake, 2005; Dolney et al., 2006; Seo and Eisenstein, 2007). However, the larger errors are a challenge. For velocity errors larger than 1000 km s^{-1} one is smearing out the acoustic scale along the line of sight and failing to measure $H(z)$. Note that this scale is set by the width of the acoustic peak, not by the acoustic scale. One only retains full information with rms precision below 300 km s^{-1} .

To measure $D_A(z)$, in principle precisions of $\sigma_z/(1+z)$ of 4% are enough. Worse precision causes catastrophic degradation because the oscillations in angular power at the front and back of the photometric redshift slab fall out of phase. Redshift precision of 3%–4% yields poor constraints on the BAO per unit volume, with a rule of thumb that one needs ten times more volume for a photometric redshift survey than a spectroscopic survey (Blake and Bridle, 2005; Seo and Eisenstein, 2007). Better redshift precision reduces this gap. At $z < 0.7$, current and ongoing spectroscopic surveys are already covering 1/4 of the sky, so photometric redshift surveys are only competitive at higher redshifts. Extracting large-scale structure and BAO from photometric redshift surveys requires very stringent calibration and more extensive modeling than for spectroscopic surveys. Photometric surveys with many narrow bands offer an intermediate approach between imaging and spectroscopy, which may be advantageous in some regimes (Benítez et al., 2009).

4.4.5. Tracers of structure

As we have seen, BAO surveys require surveys of very large volumes with modest sampling density. One wants to map a wide range of redshift so as to measure the history of expansion. The current generation of surveys are mapping of order 1 million galaxies, and approaching the cosmic variance limit at $z > 1$ requires of order 10^8 galaxies.

We have a lot of freedom in selecting the objects to trace the density field. Usually, we require isotropy of the selection but do not require that the selection be unchanging as a function of redshift. One is seeking to minimize the observational cost for a given well-sampled survey volume. There are many competing considerations (Glazebrook and Blake, 2005). One desires a tracer with a strong spectroscopic signature to allow a redshift determination to about 300 km s^{-1} rms as fast as possible, with few catastrophic redshift errors. One desires a combination of density and clustering bias so that $nP(k = 0.2h \text{ Mpc}^{-1}) \gtrsim 1$. One desires a higher clustering bias, so that the required number density is lower; this allows one to use brighter objects and reduce exposure time. For targeted surveys, one desires that the tracer can be readily selected, so that one does not waste resources on undesired objects. In more detail, one desires photometric redshifts good enough that one can shape the $n(z)$ profile in a way that keeps nP close to unity at high redshift without being swamped by low luminosity objects at low redshift. And, of course, the observed wavelength of the spectroscopic feature determines a great deal about the instrumentation.

Luminous red galaxies are an effective choice at lower redshifts. They have strong absorption features, notably the 4000 Å break, and high surface brightnesses to allow rapid spectroscopy. They have a high bias ($b \sim 2$) to reduce the required number density and hence the number of spectroscopic fibers. They are also easy to select with photometric redshifts: essentially they are the reddest galaxies at a given observed flux (Eisenstein et al., 2001).

As we work to $z = 1$ and beyond, the advantages of using emission-line galaxies increase. Red galaxies are very faint in the optical at $z \gtrsim 1$ because of K corrections, and the 4000 Å break moves into the infrared where the forest of OH sky glow lines makes spectroscopy more difficult. But the star formation rates of normal galaxies at $z > 1$ are about ten times higher than today, and this high star formation produces strong emission lines. These emission lines can be detected even when the stellar continuum cannot, and the galaxies with the strongest lines can be measured in remarkably little time. Spectral resolution of a few thousand is desirable to work between the OH sky glow lines and to resolve the [OII] doublet. The challenge is primarily one of selection, how to use photometric data to pick out the star forming galaxies with the strongest lines. Between the lower clustering bias and the failure rate on weaker-lined systems, one needs to survey many more blue galaxies than red. Current expectations are that the transition point from preferring red galaxies vs. blue is $z \approx 1$ (Glazebrook and Blake, 2005). Slitless spectroscopy offers an alternative route to surveying emission line galaxies, without prior target selection (see Section 4.6).

Clusters of galaxies have been proposed as tracers (Angulo et al., 2005; Hütsi, 2006). These can be readily found from imaging data sets but have the disadvantage that their nP does not reach unity. Also, acquiring spectroscopic redshifts for the clusters imposes requirements similar in area and depth to a red galaxy survey, so the gain in a highly multiplexed fiber survey is much smaller than one would expect based on numbers alone. Quasars have a similar problem of having $nP < 1$, but they are extremely luminous and easy to select. This makes them a possible target for a sparse, wide-field survey at $z > 1$ (Sawangwit et al., 2012), and they are readily added to a multi-fiber survey targeting emission line galaxies or LRGs at other redshifts.

Using the Ly α forest as a tracer is attractive because each spectrum yields many density measurements (effectively about 50) rather than just a single point in a map (White, 2003; McDonald and Eisenstein, 2007; Norman et al., 2009; McQuinn

and White, 2011). One wants to sample the width of the acoustic peak, which is about $20h^{-1}$ Mpc FWHM. This implies that one needs spectral resolution of only a few hundred and moderate angular density of the lines of sight, preferably about 100 per square degree. Quasars of this surface density are much brighter than the Lyman-break galaxies that would be required to match the effective sampling density. As one has little gain from reducing the photon noise errors to below the intrinsic variation of the forest on $10h^{-1}$ Mpc scales, one can afford to use low signal-to-noise ratio spectra. The challenge here is systematics, as one must control the continuum of the quasar and the spectrophotometry of the measurements to utilize the spectral information. It is also possible that theory systematics associated with the state of the IGM enter; so far, IGM uncertainties have not been shown to affect BAO measurements from the forest, but the case has not been investigated as thoroughly as it has for galaxies. The recent detection of BAO in the Ly α forest at a scale and amplitude compatible with theoretical expectations (Busca et al., 2012; Slosar et al., 2013) is already encouraging, but much work remains to demonstrate that systematic effects are below the achievable level of statistical precision.

Star-forming galaxies also can be observed in the radio using the 21 cm line of neutral hydrogen. This is a much weaker line, but future generations of radio interferometers such as the Square Kilometer Array offer phenomenal survey speed because one can synthesize millions of simultaneous beams computationally. Such instruments could in principle achieve spectroscopic samples of 10^9 galaxies out to $z = 2 - 3$ (Abdalla and Rawlings, 2005).

A different concept is that of 21 cm intensity mapping (Peterson et al., 2006; Ansari et al., 2008; Chang et al., 2008; Loeb and Wyithe, 2008; Wyithe et al., 2008; Seo et al., 2010a). Here one does not identify individual galaxies but instead measures the combined emission of the 21 cm line from all galaxies in a volume of order 10 Mpc on a side. The fluctuations in the map encode the large-scale density field and hence the BAO. Relative to an interferometer like the SKA, one uses shorter baselines (around 300 m) and a nearly filled aperture to maintain surface brightness sensitivity.²⁷ Because one is not resolving individual galaxies above the instrumental noise, one is using all of the neutral hydrogen even from low-mass galaxies. In principle, one can map the BAO to the cosmic variance limit out to $z \approx 3$ with new interferometric arrays. The challenge is foreground subtraction, as the cosmic signal is several orders of magnitude below the Galactic and extragalactic emission levels. A first detection of large-scale structure in redshifted 21 cm has been reported by Chang et al. (2010) by cross-correlating with an optical galaxy redshift survey at $z = 0.8$; cross-correlation removes foregrounds that are not themselves correlated with the optical galaxies. For intensity mapping to work on its own, one of course needs to measure the auto-correlation signal.

Unlike for the case of galaxies, diffuse HI mapping does not provide the *mean* level of emission (interferometers are not sensitive to this, and even if they were the Galactic emission would swamp extragalactic HI); therefore δ_{HI} is measured only up to a multiplicative constant. This does *not* present a problem for the BAO technique because one is using the shape and not the amplitude of the power spectrum. It does have an impact on redshift-space distortions (Section 7.2), as without the mean level one cannot turn the observable β into an estimate of the rate of growth of structure $f\sigma_8(z)$. This drawback is, however, also an opportunity to learn about astrophysics: measurement of β_{HI} combined with independent knowledge of $f\sigma_8(z)$ would allow us to infer the mean HI signal and thus obtain the cosmic abundance of neutral gas as a function of time (Wyithe and Brown, 2010).

4.5. Systematic uncertainties and strategies for amelioration

Given that we seek to measure the acoustic scale and hence cosmic distance scale to a high level of precision, it is important to consider the systematic errors that could cause the inferred $D_A(z)/r_s$ and $H(z)r_s$ to be incorrect. We consider three classes of systematic errors: (1) observational errors, in which one mis-measures the large-scale structure of the universe; (2) astrophysical errors, in which our model of large-scale structure for a given cosmology is incorrect; and (3) cosmological errors, in which we mispredict the sound horizon given our measurements because of new cosmological physics, either in the early universe or at late times.

4.5.1. Measurement systematics

The measurement of large-scale structure requires the ability to produce a well-calibrated density map of the universe. The data need not be homogeneous in quality so long as the inhomogeneities are known well enough that one can correct for them statistically.

Observational errors involve imperfections in one's map of the density field. Examples of sources can be photometric miscalibrations of the input catalog, mis-assessments of the incompleteness in the input catalog, redshift failures or errors, incorrect tracking of the target selection, failure to correct for deleterious interactions between targets (e.g., fiber collisions), or imperfect assessment of the redshift distribution of the map. Another class of problems involves understanding of the errors of the map, as one must assess both the statistical properties of the density field and the point sampling of it by galaxies.

Fortunately, these issues have been extensively studied in the general context of the measurement of large-scale structure (e.g., Tegmark et al., 1998). BAO measurement itself is only a particular application of large-scale structure data, and it turns out to be a relatively easy one because the acoustic peak is narrow in scale and hence one has another differential opportunity

²⁷ An interferometer directly measures the Fourier transform (in the transverse direction) of the emission field; antennas separated by a distance L measure Fourier modes with $k_{\perp} = 2\pi L/(\lambda D_A)$.

in the experimental design. That is, one can compare the behavior at 150 Mpc separation to the average of that at 120 and 180 Mpc, so as to remove smooth errors. The only way to produce a non-smooth error is to have a sharply preferred scale in the systematic error.

For galaxy redshift surveys, there is wide expertise in how to calibrate surveys and track their selection functions, and there are many tests that can be employed to look for specific problems. Failing that, residual errors are often intrinsically radial or angular in their nature, so one can reject the purely radial and purely angular modes from a survey (Vogeley and Szalay, 1996; Tegmark et al., 1998). This is a small cost in information content for an intrinsically 3-d field. A more targeted version of this idea is to use angular templates to remove systematic errors with particular angular dependence, e.g., survey depth variations due to sky brightness, seeing, or stellar density (Ho et al., 2008; Ross et al., 2011, 2012). A further related idea is that for a sharp scale in a systematic error to be a real threat, it must be sharp for three dimensional spheres of separation. For example, even if a survey has an error that is modulated on a circular field of view, the diameter of the field affects a range of 3-d separations at a given redshift simply because of the random orientations of pairs to the line-of-sight.

The BAO method is ultimately tied to the separation of galaxies, which depend on astrometric positions and redshifts. These quantities can be exquisitely well measured, and achieving 0.1% precision on one's astrometric and wavelength scale is easy. The concern about systematic errors in the map is that an erroneous tilt in the correlation function would cause one to mismeasure the centroid of the acoustic peak. This is a weaker effect, and one can marginalize against such tilts if one wants, using the techniques in Section 4.3.4.

In short, it is very likely that a reasonable design for a galaxy redshift survey will lead to sufficient accuracy for the BAO method. The greater challenge for such surveys is to control the clustering analysis for the broadband cosmological signals, which require a factor of more than ten better accuracy.

On the other hand, the observational systematics for the Ly α forest and 21 cm intensity mapping techniques are a serious concern. Here we are trying to use every spectral pixel for our mapping data, rather than differencing spectral pixels to measure a single redshift per object. Imperfections in the calibration of the spectra or the subtraction of sky emission or Galactic foregrounds will appear as cosmic structure.

For the Ly α forest, we measure the absorption by assuming that the quasar continuum is intrinsically smooth. However, even an unabsorbed spectrum would have variations due to the intrinsic spectrum of the quasar and any errors in the removal of the sky emissions or flat-fielding of the detector. We do not know the detailed unabsorbed quasar spectrum but instead need to estimate it from the ensemble properties of quasars or from fitting to less absorbed pixels. The BAO signal is a very weak modulation on large scales. Modeling errors far too weak to show up in any one spectrum could inject correlations that bias the BAO scale or simply increase the noise far above the expected sample variance. The most detailed discussions of systematic errors in large-scale Ly α forest measurements are those of McDonald et al. (2006) and Slosar et al. (2011). Measuring the scale of the BAO feature again appears much easier than determining the broad-band shape or absolute amplitude of the power spectrum. Studies to date have not identified observational problems that would prevent high precision BAO measurements, but the field is in its early days.

For 21 cm intensity mapping, we are looking for the correlations of the extragalactic line emission as a function of wavelength (redshift) and sky position. However, the Milky Way is producing synchrotron and free-free emission that is three orders of magnitude higher than the extragalactic signal and highly variable on the sky (Chang et al., 2008, 2010). Fortunately these emission mechanisms are smooth as a function of frequency, unlike the cosmological signal where frequency maps to redshift, which should enable foreground removal (e.g., Liu and Tegmark, 2012). The challenge here is primarily instrumental: undesired features in radio interferometers such as far sidelobes or standing waves in the antenna are strongly frequency dependent and can mimic a cosmological signal if not suppressed. Moreover, the Galactic synchrotron radiation is polarized, and Faraday rotation within the galaxy can lead to strongly wavelength-dependent polarization amplitude (e.g., Haverkorn et al., 2003), so the instrument and software must measure the total intensity and remove Stokes Q and U from their maps – a major challenge given that radio antennas are inherently polarized. The problems are similar to those of the 21 cm mapping of the epoch of reionization, where several experiments are trying to achieve first detections. Projects aimed at $z = 1$ are being started in order to investigate and hopefully control the observational systematics.

4.5.2. Astrophysical systematics

Astrophysical systematic errors are principally due to non-linear structure formation, redshift-space distortions, and galaxy clustering bias. These were discussed in Section 4.3.2. Our understanding of these effects in cold dark matter models has been greatly advanced by numerical simulations and analytic theory over the past decades. Fortunately, the acoustic scale is much larger than the scales of non-linear structure formation and the hydrodynamic effects on galaxy formation. Gravitational forces are by far the dominant effect on 150 Mpc scales, and we can compute these at high accuracy.

Galaxy clustering bias based on halo occupations has been shown to be manageable for the BAO method. The raw shifts of the acoustic scale are below 1%, and they can be reduced below any reasonable detection limit with reconstruction (Mehta et al., 2011), as shown in Fig. 12. Hence, the concern is now for a more complicated clustering bias, e.g., one that couples more directly to the large-scale density field or that features large-scale cooperative effects between galaxies (Bower et al., 1993). But clustering bias is no longer an arbitrary bogeyman. We have many observational probes that should test a bias model: two-point and higher-point clustering over all scales, redshift-space distortion patterns, cross-correlations between types of galaxies, galaxy–galaxy weak lensing maps, and various measures of halo masses. While the simplest formulation

of HOD is surely not the whole story of clustering bias (e.g., Gao et al., 2005; Harker et al., 2006; Gao and White, 2007), the model has passed significant tests. An alternative mechanism that couples to large-scale densities in a very different manner so as to alter the BAO scale will almost certainly produce far more detectable effects on smaller scales.

A possible complication to galaxy biasing at the BAO scale was pointed out by Tseliakhovich and Hirata (2010) and Yoo et al. (2011). At the time of recombination, the pressure of the photons causes the baryonic matter to have a relative velocity compared to the dark matter, with a typical value $v_{bc} \sim 30 \text{ km s}^{-1}$. This relative velocity is largely due to the same standing acoustic waves that produce the BAO feature; it is coherent on scales of a few Mpc and has a feature in its correlation function at 150 Mpc. After recombination, the sound speed in the baryons drops to 6 km s^{-1} , so the relative velocity is supersonic. Tseliakhovich and Hirata (2010) argue that this boosts the effective Jeans mass as small dark matter structures fail to retain baryons, thereby suppressing the formation of the earliest galaxies ($M_{\text{halo}} \sim 10^6 M_{\odot}$ at $z > 10$). This level of suppression depends on the local v_{bc} , which varies on large scales. It is unclear whether this varying suppression causes a detectable imprint on the properties of much more massive galaxies at low redshift; it may be that it is completely erased as galaxy-mass ($> 10^{11} M_{\odot}$) halos form and wipe out the small-scale initial conditions, or it may be that feedback mechanisms such as early metal pollution allow some trace of v_{bc} modulation to survive in structures at $z \ll 10$. In the latter case, it represents a potentially serious concern because (unlike other systematic errors) the modulation contains the BAO scale (Yoo et al., 2011). However, the form of the modulation is predictable, and Yoo et al. (2011) find that the measurements of the galaxy bispectrum would enable the detection and removal of this effect.

Besides gravity, the only physical effect that we reasonably suspect can modulate galaxy properties on large scales is radiation transport. For example, it is predicted that reionization proceeds with bubbles of scales of 10 Mpc for hydrogen and 100 Mpc for He II. This may affect the late-time galaxy density field in non-gravitational ways (McQuinn et al., 2007; Ilev et al., 2008; Mesinger and Furlanetto, 2008; Zheng et al., 2011; Wyithe and Dijkstra, 2011). However, the scale of the reionization bubbles is not sharp enough to mimic the acoustic peak, e.g., any reasonable variation in the luminosity of the ionizing sources will produce a wide spread of bubble sizes. Reionization effects could be a larger issue for the Ly α forest than for galaxy surveys because one is mapping the IGM directly. Simulations of Gpc³ volumes that incorporate models of these reionization effects will be needed to see whether they can detectably influence BAO measurements, but the absence of a sharply preferred scale in reionization should again provide protection if one marginalizes over broad band tilts.

4.5.3. Cosmological systematics

Cosmological effects that alter the sound horizon or the detailed prediction of the linear power spectrum must contend with the fact that the $z = 1000$ universe and the acoustic oscillations themselves are exquisitely well observed in the CMB anisotropies. For example, a change in the recombination history could alter the sound horizon, but this produces correspondingly larger changes in the damping tail of the primary anisotropies (Eisenstein and White, 2004; de Bernardis et al., 2009). Effects such as particle decays that change the expansion history so as to alter the sound horizon affect the gravitational potential of the fluctuations and have large impact on the CMB anisotropies.

Models that combine adiabatic perturbations with smaller isocurvature ones offer additional degrees of freedom to constrain in the CMB. Most such combinations yield differences that can be detected in the acoustic peak structure of the CMB before they affect late-time BAO inferences. However, Mangilli et al. (2010) show that a particular combination of isocurvature modes may exist that can change the sound horizon by a moderate amount before the CMB anisotropies are observably altered. This possibility bears more investigation, e.g., of other late-time observable consequences of such a model (Mangilli et al., 2010; Carbone et al., 2011; Zunckel et al., 2011).

Finally, we note that if the sound horizon or power spectrum template predicted from $z = 1000$ is wrong, then the effect on the BAO distance scale will typically be a multiplicative error across all redshifts. This would alter the inference of $w(z)$, but with a particular redshift dependence that one might choose to be suspicious of if one found it.

In short, while not all cosmological possibilities have been cataloged for their effect on the BAO method, one should always judge such possibilities in light of the CMB as well. The combination of CMB and BAO is likely to be self-diagnosing of new cosmological physics at high redshift. There may be exotica that can slip through this net, but we do not view this potential confusion with dark energy dynamics as a demerit of the method. Large cosmological surveys offer a rich spectrum of possible analyses with which to corroborate our model of structure formation, and the discovery of any discrepancy from vanilla Λ CDM will surely inspire a vigorous search for alternative explanations.

4.6. Space vs. ground

The principal challenge of the BAO method is obtaining the redshifts of millions of faint galaxies. Certainly we can obtain redshifts from the ground for tracers at any redshift; the difficulty is in doing this quickly and cheaply enough.

Most BAO work to date has used multi-fiber spectroscopic surveys at optical wavelengths. This is practical for surveys of order 10^7 galaxies. At $z > 1$, one relies on finding very luminous line emitters, and the desired number of galaxies to reach the cosmic variance limit is of order 10^8 . Routing optical fiber to 10^8 objects is technically very demanding. We expect that fiber-fed optical galaxy redshift surveys will do an excellent job out to $z = 1$ and will make a start at $1 < z < 1.5$, but will not approach the cosmic variance limit at $z > 1$.

Photometric redshifts of either galaxies or clusters are an option to sample a large volume at $z \approx 1$ with upcoming surveys and probably at higher redshifts with deeper surveys like LSST. Redshifts $z < 0.7$ will be done better with funded

spectroscopic programs. One is free to pick a subset of galaxies on which one has better photometric redshift performance. However, photometric redshifts are best when relying on strong breaks, notably the 4000 Å and Lyman break. The former requires near-IR data at $z \gtrsim 1$; the latter requires space UV data at $z \lesssim 3$. As mentioned above, photometric redshifts are not precise enough to capture the BAO $H(z)$ information, which is a large loss at higher redshifts. We expect that the upcoming generation of imaging surveys will be the first to map the BAO at $z \approx 1$ over large areas of the sky. This will achieve an important constraint on $D_A(z)$. Later spectroscopic surveys will improve the $D_A(z)$ measurement and add $H(z)$.

A space mission offers the opportunity for slitless spectroscopy (Glazebrook et al., 2005). This efficiently finds the strongest line emitters over a wide instantaneous field. Slitless spectroscopy of faint objects is only practical in space, where the foreground (or “sky”) emission is low. This is particularly attractive in the near-IR, where the zodiacal background light is low and the $H\alpha$ line from $z > 1$ galaxies is very bright. The UV with Ly α is another opportunity.

At $z > 2$, the Ly α line (whether in emission or in the forest) can penetrate the atmosphere. This offers a renewed opportunity for ground-based work, but only the Ly α forest is likely to be able to approach the cosmic variance limit in the foreseeable future. As described above, this method still has significant uncertainties about its observational and theoretical systematics. Galaxy samples would again require $> 10^8$ objects to reach the cosmic variance limit, a factor of 100 more than planned surveys. The Ly α forest gets undesirably thick at $z > 3.5$, and BAO surveys above this redshift might require a space mission, such as the *Cosmic Inflation Probe* (Melnick et al., 2009).

A 21 cm facility such as the SKA capable of detecting individual high-redshift galaxies is a multi-billion dollar project and hence well in the future, albeit with a large cosmological payoff. We note that not all technical implementations of the SKA permit full-sky mapping, and keeping this option does increase the cost of the correlator. The 21 cm intensity mapping technique is considerably cheaper, but we do not know whether it can achieve the required control of observational systematics. Applying intensity mapping to the reionization epoch could eventually measure the distance scale at $z > 6$ (Mao and Wu, 2008; Rhook et al., 2009).

A space mission that would target of order $10^8 1 < z < 2$ galaxies is the only robust near-term path to approaching the cosmic variance limit for BAO over the enormous comoving volume available in this redshift range. Intensity mapping is an attractive opportunity, but it needs substantially more development before it can be realistically assessed. Ground-based galaxy redshift surveys and Ly α forest surveys will explore $z > 2$, though in the near-term approaching the cosmic variance limit depends on controlling systematic errors in the Ly α forest method, which are not yet understood at the percent or sub-percent level.

4.7. Prospects

In contrast to essentially all of the other observational probes that we consider in this review, we anticipate that even the most ambitious BAO studies will remain limited by statistical errors rather than systematic errors. This assumption could prove incorrect, either because we are overoptimistic about BAO systematics or because we are too pessimistic about other methods. But it does imply a natural long-term target for BAO investigations of cosmic acceleration: survey a large fraction of the entire comoving volume out to $z \approx 3.5$, beyond which the sensitivity to dark energy begins to decline (Table 2), with high enough sampling density that the BAO measurements are limited by sample variance rather than shot noise. No one survey will reach this goal on its own; rather, a variety of projects can gradually map out the available volume by using different facilities and techniques to target different redshift ranges and areas of sky. Surveys that cover the same redshift range with the same technique are *not* redundant unless they cover the same region of the sky. To zeroth order, the primary metric for a BAO survey is the comoving volume that is covered at adequate sampling density, and it makes sense to choose redshift ranges according to observational convenience (though of course one can further optimize both survey strategy and instrument design). Relative to the current state of the art described in Section 4.2 – roughly speaking, analyses that have probed $f_{\text{sky}} = 0.4$ to $z = 0.15$, $f_{\text{sky}} = 0.25$ to $z = 0.45$, and $f_{\text{sky}} = 0.08$ to $z = 0.8$ – BAO surveys have tremendous possibility for growth, with correspondingly great opportunities for improved precision and redshift leverage on $D_A(z)$ and $H(z)$ (Fig. 15).

With the completion of WiggleZ (Parkinson et al., 2012), the only spectroscopic BAO survey currently operating is SDSS-III BOSS (Dawson et al., 2013). BOSS is approximately midway through its five years of spectroscopic observing and will conclude in mid-2014. Forecasts for the galaxy survey predict 1.0% precision on D_A at $z = 0.35$ and $z = 0.6$ and 1.8% precision on $H(z)$ at these redshifts. The Ly α forest survey is expected to yield 4.5% precision on D_A and 2.6% on $H(z)$ at $z = 2.5$. BOSS will provide a solid BAO anchor at low redshift, the first BAO measurements $z > 2$, and the first practical test of the Ly α forest technique.

The Hobby-Eberly Telescope Dark Energy Experiment (HETDEX) is largely funded and currently under construction. HETDEX plans a survey of 800,000 Ly α emission-line galaxies over 420 square degrees at redshifts $1.8 < z < 3.7$, using a blind-pointing strategy with a large set of integral-field spectrographs (Hill et al., 2006). The forecast precision on D_A and H is of order 2% from BAO alone, with additional gain possible if one can take advantage of the increased linearity of the large-scale density field at high redshift to model the full anisotropic clustering signal of the galaxies.

PanSTARRS and DES are two near-term imaging surveys with the depth and area needed to probe BAO at $z \approx 1$. BAO analyses will likely focus on red galaxies as they afford more robust photometric redshifts and the two cameras employ red-sensitive detectors that achieve good depth in the z and y bands. These projects will likely yield the first strong BAO constraints at $z = 1$.

A multitude of more ambitious projects are being planned. On the imaging front, LSST should eventually yield an enormous sample of galaxies with good photometric redshifts, enabling photo- z BAO studies to reach to $z = 2$ and beyond. Two near-term Spanish projects, PAU and JPAS, aim to do shallower imaging with many medium-band filters, designed to achieve high enough redshift precision to recover $H(z)$ information out to $z \approx 1$ (Benítez et al., 2009; Gaztañaga et al., 2012). (PAU would use a new large-format camera built for the William Herschel Telescope while JPAS would use a new telescope dedicated to the project.) This medium-band strategy is intermediate between photometric and spectroscopic approaches.

Returning to spectroscopy, eBOSS, part of a proposed (but not yet fully funded) program of post-2014 surveys on the Sloan 2.5-meter telescope, would extend the BOSS survey in several directions, using higher redshift LRGs (to $z = 0.8$), emission line galaxies, and quasars, including a denser set of $z > 2$ quasars to improve measurements from the Ly α forest. eBOSS would cover 1500–3000 deg² depending on strategy details that are still to be decided. The BigBOSS experiment (Schlegel et al., 2011) would use spectrographs fed by 5000 optical fibers over a 3-degree field on the Mayall 4-meter telescope at Kitt Peak to survey 14,000 deg². For its five-year primary survey, BigBOSS would target luminous red galaxies to $z = 1$ and emission line galaxies to $z = 1.7$, more than 10 million galaxies in total, with sampling density $n_P > 1$ out to $z \approx 1 - 1.2$. BigBOSS would target high redshift quasars with a high enough density to approach the sample variance limit for the Ly α forest method at $2 < z < 3$. The BigBOSS instrument could in principle be moved to the Blanco telescope at CTIO to conduct a similar survey of the southern hemisphere. Alternatively, the DES collaboration has considered a 4000-fiber instrument (DESpec) that would use the DECam optical corrector on the Blanco (Abdalla et al., 2012); this instrument could pursue a similar galaxy redshift survey but would not (in its current design) have the blue wavelength coverage needed to map the Ly α forest. The SuMIRe project proposed for the Subaru 8-meter telescope would use optical/IR prime focus spectrographs fed by 2400 fibers to carry out a large galaxy redshift survey, mapping BAO in the redshift range $0.7 < z < 2.4$. The current baseline program would survey 4 million [OII]-emitting galaxies over 1420 deg². Collectively, these ground-based optical/IR projects could cover a substantial fraction of the sky with fully sampled galaxy surveys to $z \approx 1.2$, provide interesting BAO measurements with lower sampling densities to $z \approx 1.7$, and possibly measure BAO to something approaching the cosmic variance limit at $z = 2-3$ using the Ly α forest.

Both *Euclid* and *WFIRST* plan large BAO surveys as major components of their dark energy science programs, using slitless near-IR spectroscopy to measure redshifts of strong H α emitters. Current incarnations of these plans are described in the *Euclid* Red Book (Laureijs et al., 2011) and the *WFIRST* Science Definition Team's final report (Green et al., 2012), though technical specifications and survey strategies may evolve to some degree prior to launch. The present baseline strategy for *Euclid* has a survey area of approximately 14,000 deg² and redshift range $0.7 < z < 2.0$, while the baseline strategy for *WFIRST* adopts a smaller area (3400 deg²), fainter flux limit, and higher redshift range ($1.3 < z < 2.7$). Green et al. (2012; see their Figs. 24 and 25) attempt a side-by-side comparison of *Euclid* and *WFIRST* BAO performance, using common modeling assumptions that include recent estimates of the luminosity function (Sobral et al., 2013) and clustering bias (Geach et al., 2012) of high-redshift H α emission line galaxies. In their calculations, *Euclid* achieves a sampling density $n_P > 1$ out to $z \approx 0.9$, falling to $n_P \approx 0.15-0.3$ at $z = 1.3-2.0$. *WFIRST* maintains $n_P > 1$ out to $z \approx 2.4$, falling to $n_P \approx 0.5$ at $z = 2.7$. For *Euclid* they forecast fractional errors σ_H/H of 1.3%–1.8% in bins of $\Delta z = 0.1$ out to $z = 1.5$, rising to 2.5% at $z = 2.0$, while for *WFIRST* they forecast $\sigma_H/H = 1.7\%-1.8\%$ (again in $\Delta z = 0.1$ bins) out to $z = 2.4$, rising to 2.4% at $z = 2.7$. These numbers should be taken with a grain of salt, as they depend on uncertain hardware and software performance and on details of survey strategy. For example, a 2.4-meter implementation of *WFIRST* could potentially survey 3–4 times larger area at similar depth (Dressler et al., 2012). By the time these missions are launched, results from earlier dark energy experiments or developments in modeling techniques could well favor alternative strategies, e.g., with deeper sampling but smaller sky area. Furthermore, the *Euclid* and *WFIRST* dark energy programs are both limited by observing time, and either could be more powerful with a longer mission. It is clear, however, that these missions can dramatically improve our knowledge of dark energy evolution at $z = 1-3$.

Shifting wavelengths, several 21 cm intensity mapping experiments for the range $0.8 < z < 3$ are being planned, using different techniques. The CHIME project aims to build a 100 m² filled interferometer using a cylindrical telescope array (Peterson et al., 2006) and conduct a lengthy survey at $0.8 < z < 2.5$. If the foregrounds can be adequately controlled, CHIME would be a powerful demonstrator of the 21 cm method and would yield excellent cosmological information. Other projects include the FFT-based Omniscience (Tegmark and Zaldarriaga, 2010) and the Baryon Acoustic Oscillation Broadband and Broad-beam (BAOBAB) interferometer array (Pofer et al., 2013). Moving beyond intensity mapping, the SKA could enable an HI-redshift survey of a billion galaxies, reaching the sample variance limit over half the sky out to $z = 3$ (Abdalla and Rawlings, 2005), which would be a good approximation to the ultimate BAO experiment.

5. Weak lensing

The subtle distortion of shapes of distant galaxies by gravitational lensing is a powerful probe of both the mass distribution and the global geometry of the universe. It has, however, turned out to be one of the most technically difficult of the cosmological probes. This section will cover the range of applications of weak lensing (which we will sometimes abbreviate to WL), the recent and planned weak lensing surveys, and the technical aspects of weak lensing image processing and control of systematics. By covering the latter subjects in some detail (including some methods that we think have been under-appreciated or under-utilized), we hope to stimulate further progress and be helpful to readers who are already experts in weak lensing.

This section is organized as follows: we begin with a qualitative overview of weak lensing and its uses (Section 5.1). We then go into a mathematical treatment of the various statistics that can be used and their dependences on the background cosmology and matter power spectrum (Section 5.2). We then review the observational results from recent weak lensing surveys (Section 5.3). Section 5.4.1 discusses the statistical errors and cosmological sensitivity of cosmic shear surveys at a rule-of-thumb level; we expect this to be a useful entry point for readers interested in understanding survey design. We then turn to more technical aspects of survey design and analysis, including source redshift estimation and the galaxy populations of optical/near-IR and radio surveys (Sections 5.4.2–5.4.4), CMB lensing (Section 5.4.5), the measurement of galaxy shapes (Section 5.5), and astrophysical uncertainties (Section 5.6). We summarize the major systematic errors and mitigation strategies (Section 5.7). We finally consider the advantages of a space mission for weak lensing (Section 5.8) and prospects for the future (Section 5.9).

Some of the material in this section is technical and in a first reading may be either skipped or skimmed; but given that so much of the promise of weak lensing depends on these issues, we felt compelled to include them. The more technical sections have been denoted with an asterisk (*). They may be thought of as analogous to, e.g., the “Track 2” material in Misner et al. (1973).

5.1. General principles: overview

The images of distant galaxies that we see are distorted by gravitational lensing by foreground structures. In rare cases, such as behind clusters, one observes *strong lensing*: the deflection of light by massive structures can result in multiple images of the same background galaxy. More often, however, images of galaxies are subjected only to *weak lensing*: a small distortion of their size and shape, typically of the order of 1%. Since one does not know the intrinsic size or shape of a given galaxy, weak lensing can only be measured statistically by examining the correlations of shapes in deep and wide sky surveys. However, the payoff if these statistical correlations can be measured is enormous: weak lensing provides a direct measure of the distribution of matter, independent of any assumptions about galaxy biasing. Since this distribution can be predicted theoretically, even in the quasilinear regime, and since its amplitude can be directly used to constrain cosmology (unlike for galaxy surveys where one must marginalize over the bias), weak lensing has great potential as a cosmological probe.

In principle, one may attempt to observe either the shearing of galaxies (shape distortion) or their magnification (size distortion). In practice, the shape distortions have been used much more widely, since the mean shape of galaxies is known (they are statistically round: as many galaxies are elongated on the x -axis as on the y -axis) and the scatter in their shapes is less than the scatter in their sizes.

A variety of statistical approaches have been used to extract information from weak lensing shear (see later subsections for references). The simplest is the angular shear correlation function, or its Fourier transform, the shear power spectrum. These are related to integrals over the matter power spectrum along the line of sight, and as such in the linear regime at low redshift they scale as $\propto \Omega_m^2 \sigma_8^2$.²⁸ Since the angular power spectrum is rather featureless, more information can be extracted via *tomography* – the measurement of the shear correlation function as a function of the redshifts of the galaxies observed, including the use of cross-correlations between redshift slices. Information on the relation between galaxies and matter can be obtained via *galaxy–galaxy lensing*, i.e., the correlation of the density field of nearby galaxies with the lensing shear measured on more distant galaxies. In the linear regime, the galaxy–galaxy lensing signal scales as $\propto b\Omega_m\sigma_8^2$ and thus provides information on the bias of the lensing galaxies, while in the non-linear regime it probes individual galaxy halos and hence places constraints on the halo occupation distribution (Section 2.3). Combination of this with the galaxy clustering signal (which scales as $\propto b^2\sigma_8^2$) enables one to eliminate the bias and measure $\Omega_m\sigma_8$. The scaling of the galaxy–galaxy lensing signal as a function of the source redshift, known as *cosmography*, depends purely on geometric factors and hence can be used to partially²⁹ construct a distance–redshift relation. Finally, the low-redshift matter distribution is non-Gaussian, so higher-order statistics such as the bispectrum or 3-point shear correlation function carry additional information.

For all of the applications of weak lensing to cosmology, deep wide-field imaging is essential. One can see this from a simple order-of-magnitude estimate. For a scatter in galaxy shapes of $\sigma_\gamma \sim 0.2$, measuring a 1% shear with unit signal-to-noise ratio requires ~ 400 galaxies ($0.2/\sqrt{400} \approx 0.01$). Measuring the amplitude of density perturbations to 1% accuracy requires that this be done over $\sim 10^4$ patches of sky, giving a requirement of order 10^7 galaxies, which for a density of 15 resolved galaxies per arcmin² amounts to surveying 200 deg² of sky. This is the scale of the largest current surveys such as CFHTLS; in practice the errors from these surveys are likely to be closer to several percent due to “factors of a few” that we have dropped here, and due to the inclusion of systematic errors. The eventual goal of the weak lensing community is one or more “Stage IV” surveys (such as LSST on the ground and *Euclid* and *WFIRST* in space) that would measure shapes of $\sim 10^9$ galaxies and achieve an additional order of magnitude in precision. Such surveys will have to face the daunting task of reducing systematic errors by another order of magnitude.

There are unfortunately many sources of these systematic errors, and most of the effort of the weak lensing community has been devoted to defeating them. One is the measurement of galaxy shapes: while gravitational lensing by a large-scale

²⁸ Warning: these scalings are altered even at modest redshift, or in the non-linear regime where the exponent of σ_8 becomes closer to 3.

²⁹ The cosmography distance scale suffers from three degeneracies, including the absolute-scale degeneracy that affects supernova measurements; see Section 5.2.7.

density perturbation can coherently align the images of many galaxies, this can also arise from shaking of the telescope or optical aberrations. The accurate determination of the point-spread function (PSF) of the telescope (usually based on observations of stars) and removal of its effects is thus critical. This problem gets much worse if one tries to model galaxies with sizes similar to or smaller than the PSF. High-resolution, stable imaging can help with this problem, motivating placement of future instruments at the best ground-based sites or in space. The determination of redshifts for the large number of source galaxies is also a concern. It is not practical to obtain a robust spectroscopic redshift of every galaxy, and hence “photometric redshifts” – estimates of galaxies’ redshifts based on their broadband colors – are used. These must be calibrated with well-known biases, scatters, and outlier distributions. Finally, there are astrophysical uncertainties: galaxies can suffer “intrinsic alignments” (non-random orientations), and the matter power spectrum may deviate from pure CDM simulations at small scales. Much of our discussion here will be focused on the methodologies that have been developed to suppress systematics at each stage of the observations and analysis.

5.2. Weak lensing principles: mathematical discussion

We will now go into greater detail on the mathematical aspects of weak lensing, both the construction of the weak lensing field and the various statistics that one can extract from it. The modern theoretical formalism of weak lensing traces back largely to the papers of Blandford et al. (1991); Miralda-Escudé (1991), and Kaiser (1992), though one can find roots in the much earlier papers of Kristian and Sachs (1966) and Gunn (1967).

5.2.1. Deflection of light in cosmology

Gravitational lensing gives a mapping from the intrinsic, unlensed image of the sources of light on the sky – the *source plane* – to the actual observable sky – the *image plane*. Our ultimate goal is to extract information about the statistics and redshift dependence of this mapping and use it to constrain cosmological parameters. Our task here is thus two-fold. First, we must derive the mapping function that relates the source to the image plane. However, since we do not know the intrinsic appearance of the sources, we cannot directly infer the lens mapping from observations. Therefore, our second task will be to determine what properties of the lens map can be measured, and with what accuracy.

In a fully general context, the lens mapping can be obtained by taking an observer and following the geodesics corresponding to that observer’s past light cone. We will make some simplifying approximations here, namely that: (i) the space-time is described by a Friedmann–Robertson–Walker metric with scalar perturbations and negligible anisotropic stresses (appropriate for nonrelativistic matter, scalar fields, and Λ); (ii) deflection angles are sufficiently small that we may use the flat-sky approximation; (iii) the evolution of perturbations is slow enough that we may neglect time derivatives of the gravitational potential Φ in comparison to spatial derivatives (i.e., nonrelativistic motion); and (iv) such perturbations are small enough that we may compute the lens mapping only to first order in perturbation theory.³⁰ Within these approximations, we may write the angular coordinates (θ_1, θ_2) of a light ray projected back to comoving distance D_C (see Eq. (7)) in terms of the position (θ_1^i, θ_2^i) in the image plane as³¹

$$\theta_i(D_C) = \theta_i^i - 2 \int_0^{D_C} \mathcal{G}(D_{C1}, D_C) \frac{\partial \Phi}{\partial \theta_i} [D_{C1}, \theta_i(D_{C1})] dD_{C1}, \quad (57)$$

where \mathcal{G} is the Green’s function,

$$\mathcal{G}(D_{C1}, D_C) = \int_{D_{C1}}^{D_C} [D_A(D_{C2})]^{-2} dD_{C2} = \cot_K(D_{C1}) - \cot_K(D_C). \quad (58)$$

Here $\cot_K(D_C)$ is the cotangentlike function,

$$\cot_K(D_C) = \begin{cases} D_C^{-1} & \text{flat} \\ K^{-1/2} \cot(K^{1/2} D_C) & \text{closed} \\ |K|^{-1/2} \coth(|K|^{1/2} D_C) & \text{open,} \end{cases} \quad (59)$$

with the dimensional curvature K defined in Eq. (8), and Φ is the Newtonian gravitational potential.

The potential derivative in Eq. (57) is evaluated at the position of the deflected ray $\theta_i(D_{C1})$, so it represents an implicit solution to the light deflection problem. However, in linear perturbation theory (see our assumption iv above), we may evaluate it at the position of the undeflected ray. This is known as the *Born approximation*. When we do this, it is permissible to pull the angular derivative out of the integral and write

$$\theta_i^S = \theta_i^i + \frac{\partial \psi(D_C, \theta_i^i)}{\partial \theta_i^i}, \quad (60)$$

³⁰ These approximations are sufficient to analyze present power spectrum data, but corrections to (iv) will become necessary in the future.

³¹ The derivation of Eq. (57) can be found in many works, though not always in the same notation. See, e.g., Eq. (6.9) in the classic review by Bartelmann and Schneider (2001). The appendix of Hirata and Seljak (2003a) gives a shorter derivation in more similar notation.

where ψ is the *lensing potential*:

$$\psi(D_C, \theta_i) = -2 \int_0^{D_C} [\cot_K(D_{C1}) - \cot_K(D_C)] \Phi(D_{C1}, \theta_i) dD_{C1}. \quad (61)$$

Here it is important to remember that D_C represents the distance to the sources; one integrates over lens distances D_{C1} .

Eq. (60) provides the mapping from the observed image plane to the source plane, $\theta_i^S(\theta_i^I)$. In what follows, we will assume that this mapping is one-to-one: this is known as the regime of *weak lensing*. In the small portion of sky covered by very massive objects, the alternate regime of *strong lensing* occurs, in which several points in the image plane map to the same point in the source plane. Strong lensing is an important probe of the matter distribution in clusters, but we will not pursue it in this article; we briefly discuss some applications of strong lensing to cosmic acceleration in Section 7.10.

5.2.2. Cosmic shear, magnification, and flexion

We have now accomplished our first task: deriving the lens mapping from the matter distribution. However, we now need a way to classify the observables in the lens mapping. The potential ψ is of course not observable itself: like the Newtonian gravitational potential, its zero-level is arbitrary. Its angular derivative $\partial\psi/\partial\theta_i$ is the *deflection angle*: the difference between the true position of a source θ_i^S and its apparent position θ_i^I . However, since sources (in practice, galaxies) can be at any position, we cannot measure the deflection angle either.

Let us now consider the second derivative of the lensing potential. It is simply the Jacobian of the mapping from image to source plane:

$$\frac{\partial\theta_i^S}{\partial\theta_j^I} = \delta_{ij} + \frac{\partial^2\psi}{\partial\theta_i\partial\theta_j} = \begin{pmatrix} 1 - \kappa - \gamma_+ & -\gamma_\times \\ -\gamma_\times & 1 - \kappa + \gamma_+ \end{pmatrix}. \quad (62)$$

We have separated the 3 independent entries in the symmetric 2×2 matrix of partial derivatives into 3 components: the *magnification* (or *convergence*) κ and the 2 components of *shear*, γ_+ and γ_\times . The magnification has three effects:

- It makes the angular size of a galaxy look larger by a factor of $1 + \kappa$.
- It makes the galaxy appear brighter by a factor of the inverse-determinant of the Jacobian, $1 + 2\kappa$, since lensing conserves surface brightness as dictated by Liouville's theorem.
- It dilutes the number density of galaxies by a factor of $1 - 2\kappa$, since the angular spacing between neighboring galaxies is increased by a factor $1 + \kappa$.

Magnification is a “scalar” in the sense that it is invariant under rotations of the (θ_1, θ_2) coordinate axes.

The shear stretches the galaxy along one axis and squeezes on the other: the image of an intrinsically round galaxy appears elongated along the θ_1 axis if $\gamma_+ > 0$ and along the θ_2 axis if $\gamma_+ < 0$. The γ_\times component stretches and squeezes along the diagonal (45°) axes. The shear is a “spin-2 tensor” in the sense that under a counterclockwise rotation of the coordinate axes by angle δ , it transforms as

$$\begin{pmatrix} \gamma_+ \\ \gamma_\times \end{pmatrix}_{\text{new}} = \begin{pmatrix} \cos 2\delta & \sin 2\delta \\ -\sin 2\delta & \cos 2\delta \end{pmatrix} \begin{pmatrix} \gamma_+ \\ \gamma_\times \end{pmatrix}_{\text{old}}. \quad (63)$$

If all galaxies were round, then each galaxy would provide a direct estimate of the shear, since we could find the values of $(\gamma_+, \gamma_\times)$ that transformed an initially circular galaxy into the observed image. In reality, galaxies come in many shapes, and any such estimate of the shear components will have some standard deviation σ_γ known as the *shape noise*. But in an ensemble average sense galaxies *are* round – there are as many galaxies in the universe elongated along the θ_1 axis as the θ_2 axis. Thus, if we take N galaxies in the same region of sky, we may expect that the shear components in that region can be measured with a standard deviation of $\sim\sigma_\gamma/\sqrt{N}$.³²

Several caveats are in order at this point, and they form the basis for most of the technical problems in weak lensing. One is that a circular galaxy re-mapped by the Jacobian (Eq. (62)) becomes an ellipse, but since in the real sky one does not observe a population of galaxies with homologous elliptical isophotes, there is no unique procedure to estimate the shear. Moreover, real telescopes, even in space, have finite resolution, and the observed image is convolved with a PSF that smears the galaxy and may introduce spurious elongation on some axis. These two problems together are referred to as the *shape measurement* problem. A more fundamental issue is that real galaxies are not randomly oriented: they have preferred directions of orientation that are correlated with each other and with large-scale structure, and thus contaminate statistical measures of the cosmic shear field. This is known as the *intrinsic alignment* problem. Finally, as already mentioned above,

³² As discussed further in Section 5.5.2 below, a typical population of optically imaged galaxies (bulges and randomly oriented disks) has an rms ellipticity $e_{\text{rms}} \sim 0.4$ per component, which translates into an rms shear error $\sigma_\gamma \approx 0.2$ via the shear response factor (Eq. (112)). Because there are two components to shear one might expect to do a factor of $\sqrt{2}$ better in statistical measurements, but in the shear correlation function or power spectrum only one of the two measurable components (the “E-mode” discussed in the next section) contains a cosmological signal at leading order, so the relevant number for order-of-magnitude sensitivity estimates is generally $\sigma_\gamma \approx 0.2$. Similarly, for galaxy–galaxy or cluster–galaxy weak lensing, only the tangential shear contains cosmological information.

relating the lensing potential ψ to the gravitational potential $\Phi(z)$, and hence to cosmological parameters, requires accurate knowledge of the source galaxy redshift distribution, presenting the *photometric redshift calibration* problem. We will discuss all of these problems in Sections 5.4–5.7.

Measuring magnification κ has proven more difficult than measuring shear. One might imagine comparing the size, magnitude, or abundance of galaxies in some region of sky to a typical or “reference” value, but there is a very wide dispersion in galaxy sizes and magnitudes, and since some galaxies are too faint to observe even in deep surveys one cannot measure such a thing as the total number of galaxies. Rather, one can measure the cumulative number of galaxies brighter than some flux threshold, $N(> F)$. If the number counts have a power-law slope α , i.e. $N(> F) \propto F^{-\alpha}$, then magnification will perturb this distribution by a factor

$$N(> F, \text{observed}) \propto [1 + 2(\alpha - 1)\kappa]F^{-\alpha}. \quad (64)$$

There are two competing effects here: in regions of higher magnification the galaxies appear brighter, which gives the $2\alpha\kappa$ factor in Eq. (64), but there is also the dilution of galaxy number, which is responsible for the “ -1 ” term. Unfortunately, for optical galaxies the observed number count slope is close to the critical value $\alpha \approx 1$ for which magnification is not measurable. Moreover, the intrinsic clustering of galaxies gives large fluctuations in the number density that greatly exceed those due to lensing effects. For these reasons, magnification has lagged behind shear as a cosmological probe, and the cosmic magnification signal was not seen until [Scranton et al. \(2005\)](#) measured it using cross-correlation of foreground galaxies and background quasars. [Ménard et al. \(2010\)](#) provide a more detailed analysis, using color information to simultaneously detect lensing magnification and reddening of quasars by dust correlated with intervening galaxies.

The most promising route to utilizing the cosmic magnification signal is to use scaling relations that relate the size of a galaxy (as quantified by, e.g., the half-light radius) to parameters that are magnification-independent and can be measured in photometric surveys ([Bertin and Lombardi, 2006](#)), such as the surface brightness, the Sersic index, or (for AGN) variability amplitude. [Huff and Graves \(2011\)](#) present a first application of this “photometric magnification” method to galaxies, and [Bauer et al. \(2011\)](#) an application to quasars.

After shear and magnification comes the third derivative of the potential, i.e. the variation of shear and convergence across a galaxy. This effect is called the *flexion*, and it manifests itself via asymmetric banana and triangle-like distortions of an initially circular galaxy ([Goldberg, 2005](#)). Flexion has been measured by several groups (e.g. [Leonard et al., 2007](#); [Velander et al., 2011](#); [Leonard et al., 2011](#)), and there is a growing literature on the theory of flexion measurement that parallels the formalism required for shear measurement (e.g. [Massey et al., 2007c](#); [Schneider and Er, 2008](#); [Rowe et al., 2012](#)). However, because of the extra derivative it is sensitive mainly to structure at the very smallest scales, so it is primarily a tool for cluster lensing rather than cosmological applications on larger scales.

5.2.3. Power spectra and correlation functions*

Just as for any other random field in cosmology, one may construct statistics for the cosmic shear field. The most popular are the power spectrum and its real-space equivalent, the correlation function.

To construct the power spectrum, we take the Fourier transform of the shear field,

$$\tilde{\gamma}_{+, \times}(\mathbf{l}) = \int \gamma_{+, \times}(\theta) e^{-i\mathbf{l}\cdot\theta} d^2\theta \leftrightarrow \gamma_{+, \times}(\theta) = \int \tilde{\gamma}_{+, \times}(\mathbf{l}) e^{i\mathbf{l}\cdot\theta} \frac{d^2\mathbf{l}}{(2\pi)^2}. \quad (65)$$

When considering the shear produced by a plane wave perturbation of the lensing potential $\psi(\theta)$, it is convenient to rotate the Fourier-space components from the coordinate axis basis to a basis aligned with the direction of the wavevector, which is a preferred direction in the problem. The rotated components are called the *E*-mode and *B*-mode:

$$\tilde{\gamma}_E(\mathbf{l}) = \cos(2\phi_1)\tilde{\gamma}_+(\mathbf{l}) + \sin(2\phi_1)\tilde{\gamma}_\times(\mathbf{l}) \quad \text{and} \quad \tilde{\gamma}_B(\mathbf{l}) = \cos(2\phi_1)\tilde{\gamma}_\times(\mathbf{l}) - \sin(2\phi_1)\tilde{\gamma}_+(\mathbf{l}), \quad (66)$$

where $\tan \phi_1 = l_2/l_1$, with l_1 and l_2 being the components of \mathbf{l} in the pre-rotated coordinate system. Thus the *E*-mode of the shear field corresponds to galaxies that are stretched in the direction of the wave vector and squashed perpendicular to it, whereas the *B*-mode corresponds to stretching and squashing at 45° angles. One may then define the power spectra:

$$\langle \tilde{\gamma}_E^*(\mathbf{l}) \tilde{\gamma}_E(\mathbf{l}') \rangle = (2\pi)^2 C_{EE}(l) \delta^{(2)}(\mathbf{l} - \mathbf{l}'), \quad (67)$$

and similarly for $C_{EB}(l)$ and $C_{BB}(l)$. Rotational symmetry of structure in the universe guarantees that these depend only on the magnitude of \mathbf{l} and not its direction, and reflection symmetry guarantees that $C_{EB}(l) = 0$.

In order to compute these power spectra, we need to express the Fourier modes in terms of those of the lensing potential. From the definition, Eq. (62), the shear is seen to be the derivative of the deflection angle and hence the second derivative of the lensing potential,

$$\gamma_+(\theta) = -\frac{1}{2} \left(\frac{\partial^2 \psi}{\partial \theta_1^2} - \frac{\partial^2 \psi}{\partial \theta_2^2} \right) \quad \text{and} \quad \gamma_\times(\theta) = -\frac{\partial^2 \psi}{\partial \theta_1 \partial \theta_2}. \quad (68)$$

Using the replacement $\partial/\partial\theta_i \rightarrow il_i$, we find in Fourier space

$$\tilde{\gamma}_+(\mathbf{l}) = \frac{1}{2}(l_1^2 - l_2^2)\tilde{\psi}(\mathbf{l}) = \frac{1}{2}l^2 \cos(2\phi_1)\tilde{\psi}(\mathbf{l}) \quad \text{and} \quad \tilde{\gamma}_\times(\mathbf{l}) = l_1 l_2 \tilde{\psi}(\mathbf{l}) = \frac{1}{2}l^2 \sin(2\phi_1)\tilde{\psi}(\mathbf{l}). \quad (69)$$

Substitution into Eq. (66) implies that

$$\tilde{\gamma}_E(\mathbf{l}) = \frac{1}{2} l^2 \tilde{\psi}(\mathbf{l}) \quad \text{and} \quad \tilde{\gamma}_B(\mathbf{l}) = 0. \quad (70)$$

We thus arrive at the remarkable conclusion that cosmic shear possesses only an E -mode; the B -mode shear must vanish, and we have $C_{BB}(l) = 0$. Confirming this prediction of vanishing B -mode provides a valuable, though not foolproof, test for systematics in WL surveys.

The E -mode shear power spectrum is simply $(l^2/2)^2$ times the lensing potential power spectrum. The latter may be found from the Limber (small-angle) approximation³³ in terms of the Newtonian potential power spectrum, yielding

$$C_{EE}(l) = l^4 \int_0^{D_C} [\cot_K(D_{C1}) - \cot_K(D_C)]^2 \frac{P_\Phi(k = l/D_{A1})}{D_{A1}^2} dD_{C1}. \quad (71)$$

(Here the power spectrum is evaluated at the redshift corresponding to D_{C1} .) We may put this in a more familiar form by recalling Poisson's equation, which tells us that the potential and matter density perturbations are related by

$$P_\Phi(k) = \left[\frac{3}{2} \Omega_m H_0^2 (1+z) \right]^2 k^{-4} P_\delta(k), \quad (72)$$

yielding

$$C_{EE}(l) = \int_0^{D_C} [W(D_{C1}, D_C)]^2 \frac{P_\delta(k = l/D_{A1})}{D_{A1}^2} dD_{C1}, \quad (73)$$

where the *lensing window function*³⁴ is³⁵

$$W(D_{C1}, D_C) = \frac{3}{2} \Omega_m H_0^2 (1+z_1) D_{A1}^2 [\cot_K(D_{C1}) - \cot_K(D_C)] \Theta(D_C - D_{C1}). \quad (74)$$

The window function describes the contributions to lensing of sources at D_C from lens structures at distance D_{C1} . Note that it vanishes as the lens approaches the source ($D_{C1} \rightarrow D_C$). In this equation, D_{A1} is the comoving angular diameter distance (Eq. (9)) to D_{C1} ; in a curved universe $D_{A1} \neq D_{C1}$. Note that in a flat universe, the window function reduces to

$$W_{\text{flat}}(D_{C1}, D_C) = \frac{3}{2} \Omega_m H_0^2 (1+z_1) \frac{D_{C1}(D_C - D_{C1})}{D_C} \Theta(D_C - D_{C1}). \quad (75)$$

One may also define the angular correlation function of the shear for two galaxies separated by angle ϑ . Since the shear is a tensor, this is more complicated than the correlation function for scalars. Without loss of generality, we may rotate the coordinate system so that the galaxies are separated along the θ_1 -axis, and then take the $+$ and \times components of the shear. We then define the shear correlation functions,

$$C_{++}(\vartheta) = \langle \gamma_+(0) \gamma_+(\vartheta) \rangle \quad \text{and} \quad C_{\times\times}(\vartheta) = \langle \gamma_\times(0) \gamma_\times(\vartheta) \rangle. \quad (76)$$

As in the scalar case, these are related to the power spectra:

$$\begin{aligned} C_{++}(\vartheta) &= \langle \gamma_+(0) \gamma_+(\vartheta) \rangle \\ &= \int \frac{d^2\mathbf{l}}{(2\pi)^2} \int \frac{d^2\mathbf{l}'}{(2\pi)^2} \langle \tilde{\gamma}_+(\mathbf{l}) \tilde{\gamma}_+(\mathbf{l}') \rangle \exp(il'\vartheta \cos\phi_{l'}) \\ &= \int \frac{d^2\mathbf{l}}{(2\pi)^2} [\cos^2(2\phi_l) C_{EE}(l) + \sin^2(2\phi_l) C_{BB}(l)] \exp(il\vartheta \cos\phi_l) \\ &= \int_0^\infty \left\{ \frac{J_0(l\vartheta) + J_4(l\vartheta)}{2} C_{EE}(l) + \frac{J_0(l\vartheta) - J_4(l\vartheta)}{2} C_{BB}(l) \right\} \frac{ldl}{2\pi}, \end{aligned} \quad (77)$$

where J_0 and J_4 are spherical Bessel functions. The expression for $C_{\times\times}$ is similar, but with P_{EE} and P_{BB} switched. The correlation function $\{C_{++}(\vartheta), C_{\times\times}(\vartheta)\}$, if measured over all scales, contains exactly the same information as the power spectrum $\{C_{EE}(l), C_{BB}(l)\}$, as one can be derived from the other. Therefore, the choice of which to measure is usually a technical one based on the ease of data processing and handling of covariance matrices. The condition for no B -modes, $C_{BB}(l) = 0 \forall l$, is more complicated in correlation-function space.

³³ See Limber (1953) and Limber (1954) for an introduction to the theory. An exposition in terms of the power spectrum is given by Peebles (1973).

³⁴ Warning: many conventions in use!

³⁵ The Heaviside step function Θ is technically unnecessary in Eq. (74), but it is convenient when considering multiple populations of sources.

An infinite number of other second-order statistics (i.e., expectation values containing two powers of shear) can be constructed, such as the aperture-mass variance (Schneider et al., 1998), ring statistics (Schneider and Kilbinger, 2007), and finite-interval orthogonal basis decompositions (a.k.a. COSEBIs, Schneider et al., 2010). These alternative statistics were introduced because they have useful properties from the point of view of data processing or systematics control – e.g., for separation of E and B modes, or restriction to a particular range of scales – but all of them are expressible as integrals over the power spectrum or correlation function.

Formulas such as (73) and (77) may be generalized to the full sky, as was first done for CMB polarization (Kamionkowski et al., 1997; Zaldarriaga and Seljak, 1997), but for cosmic shear most applications involve small angular scales where the flat-sky approximation suffices.³⁶

Having built the formalism to describe the statistics of weak lensing, we can now consider the proposed ways of using it to measure cosmology. Some methods will depend only on the expansion history of the universe, while others are sensitive to the growth of perturbations.

5.2.4. Method I: cosmic shear power spectrum*

The conceptually simplest approach to using WL is to collect a sample of source galaxies, obtain an estimator for the shear at each galaxy, measure the correlation function or power spectrum, and do a comparison to Eq. (73). Of course not all galaxies are at the same redshift, but there is a probability distribution of distances $p(D_C)$, and the observed mean shear in a particular region of sky is then

$$\gamma_{+, \times}(\theta) = \int_0^{D_{C, \max}} p(D_C) \gamma_{+, \times}(D_C, \theta) dD_C, \quad (78)$$

where $D_{C, \max}$ is the comoving distance to the farthest galaxy in the slice. The power spectrum of this field can then be written as

$$C_{EE}(l) = \int_0^{D_{C, \max}} [W_{\text{eff}}(D_{C1})]^2 \frac{P_\delta(k = l/D_{A1})}{D_{A1}^2} dD_{C1}. \quad (79)$$

This is similar to Eq. (73) with W replaced by an effective window function,

$$W_{\text{eff}}(D_{C1}) = \int_0^{D_{C, \max}} p(D_C) W(D_{C1}, D_C) dD_C, \quad (80)$$

which is simply the usual window function appropriately weighted over the source galaxies.

The cosmic shear power spectrum $C_{EE}(l)$ is sensitive to many cosmological parameters. Being an integral over the matter power spectrum, it is $\propto \sigma_8^2$ in the linear regime, although its behavior in the non-linear regime is closer to $\propto \sigma_8^3$. It also contains two powers of Ω_m , so we expect that the most important dependences in the problem are that the WL power spectrum scales as $\sim \Omega_m^2 \sigma_8^3$. This is qualitatively correct, but the matter power spectrum and the mapping between D_A and D_C at finite redshift contain sensitivities to all of the cosmological parameters, and so a full answer to the question “what does the shear power spectrum constrain?” requires us to actually do the integral to obtain $C_{EE}(l)$.

The sensitivity to every parameter is both a virtue of the WL power spectrum and its greatest fault: the featureless WL power spectrum contains too many parameter degeneracies. One way to break these degeneracies is to combine WL with other probes, as discussed in Section 8. However, there are also ways of using WL that provide additional information and break these degeneracies internally, as we now discuss.

5.2.5. Method II: power spectrum tomography*

We can improve on the WL power spectrum constraints if we can split the source galaxies into redshift slices. In most practical cases, this would be done with photometric redshifts. In this case, instead of having a single power spectrum, we have $N(N+1)/2$ power spectra and cross-spectra; if we denote the slices by $\alpha, \beta \in \{1, 2, \dots, N\}$, then these spectra are

$$C_{EE}^{\alpha\beta}(l) = \int W_{\text{eff}, \alpha}(D_{C1}) W_{\text{eff}, \beta}(D_{C1}) \frac{P_\delta(k = l/D_{A1})}{D_{A1}^2} dD_{C1}, \quad (81)$$

where $W_{\text{eff}, \alpha}$ is the effective window function for the α slice. Note that because the window functions are multiplied, this power spectrum depends only on the matter power spectrum at redshifts closer than that of the nearby slice, i.e. at $z < \min\{z_\alpha, z_\beta\}$. This makes sense because a given lens structure must be in front of both sources to contribute to the shear cross-correlation. Lensing analysis that splits samples by redshift and uses the redshift scalings to constrain cosmology is known as *tomography*.

³⁶ The leading order curved sky correction is the replacement of the scalar wavenumber $||$ with $\sqrt{l(l+1)}$, where here “ l ” is the spherical multipole number. Further corrections are of the order of $1/l^2$ and are most important for the lowest multipoles.

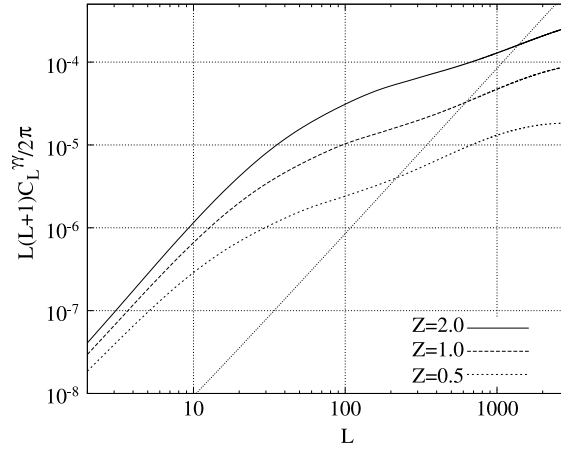


Fig. 16. The E -mode shear power spectra predicted for the WMAP 7-year best fit cosmology ($\Omega_m = 0.265$, $\sigma_8 = 0.8$, $H_0 = 71.9 \text{ km s}^{-1} \text{ Mpc}^{-1}$). The curves show power spectra for sources at $z = 0.5$ (bottom), 1.0, and 2.0 (top). The diagonal line shows the shot noise contribution at a source density of $n_{\text{eff}} = 10 \text{ galaxies per arcmin}^2$; for this power spectrum measurement the shot noise scales as n_{eff}^{-1} . At small scales, where the noise power spectrum exceeds the signal, it is not possible to measure individual structures in the weak lensing map. However, with sufficient sky coverage, high-S/N measurement of the power spectrum or correlation function is still possible (see Section 5.4.1, particularly Eq. (96)).

Like the shear power spectrum, the tomographic spectra are sensitive to both the background geometry and the growth of structure: the shear power spectrum at l depends on the $D_C(z)$ relation, on $P_\delta(k = l/D_A; z)$ as a function of redshift, and on the curvature K .³⁷ With a single power spectrum $C_{EE}(l)$ there is no hope of disentangling these functions with WL alone. One might hope that having the tomographic cross-spectra as a function of z_α and z_β would allow the relevant degeneracies to be broken. Unfortunately, such a program runs into three problems:

- A real WL survey has a maximum source redshift, and there is obviously no sensitivity to structures farther than this.
- There exist exact degeneracies among $\{D_C(z), P_\delta(k = l/D_A; z), K\}$ that lead to exactly the same lensing power spectra for all (l, z_α, z_β) . The most obvious of these is the re-scaling degeneracy: since lensing measures only dimensionless shears, it cannot measure the absolute distance scale, only distance ratios. Two other degeneracies are discussed by Bernstein (2006); see also Section 5.2.7.
- The broad, smooth nature of the lensing window functions $W_{\text{eff},\alpha}(D_C)$ implies near-degeneracies between power spectra at adjacent redshifts. For example, if one were to test a nonstandard cosmology in which $P_\delta(k, z)$ had a rapid oscillation in z superposed on the expected evolution, the rapid oscillation would contribute little to Eq. (81) and would be easily buried by statistical or systematic errors.

Despite these drawbacks, tomographic power spectra have far fewer parameter degeneracies than the shear power spectrum alone. More importantly, having $N(N+1)/2$ power spectra provides many additional opportunities for internal consistency tests and rejection of systematic errors.

Some examples of theoretical tomographic power spectra are shown in Fig. 16.

5.2.6. Method III: galaxy–galaxy lensing*

A third way to use weak lensing is to look not just at the shear power spectrum but at its correlation with the distribution of foreground galaxies. This subject is known as *galaxy–galaxy lensing* (GGL), and it is a powerful probe of the relation between dark matter and galaxies. The angular cross-power spectrum between the galaxies in one redshift slice α (the “foreground” or “lens” slice) and the E -mode shear in a more distant slice β (the “background” or “source” slice) is defined by

$$\langle \tilde{\delta}_g^{\alpha*}(\mathbf{l}) \tilde{\gamma}_E^\beta(\mathbf{l}') \rangle = (2\pi)^2 C_{gE}^{\alpha\beta}(l) \delta^{(2)}(\mathbf{l} - \mathbf{l}'), \quad (82)$$

where δ_g^α is the 2-dimensional projected galaxy overdensity and $\tilde{\delta}_g^\alpha$ is its Fourier transform, and α and β represent redshift slices. It can be computed via Limber’s equation as

$$C_{gE}^{\alpha\beta}(l) = \int p_\alpha(D_{C1}) W_{\text{eff},\beta}(D_{C1}) \frac{P_{g\delta}(k = l/D_{A1})}{D_{A1}^2} dD_{C1}, \quad (83)$$

³⁷ There is also a factor of $\Omega_m H_0^2$ in the window functions, but for now we will assume this combination has been measured accurately from the CMB. Our forecasts in Section 8 marginalize over the uncertainty in this combination, which matters at the precision of Stage IV experiments.

where $P_{g\delta}(k)$ is the 3-dimensional galaxy–matter cross-spectrum. The real-space correlation function of galaxy density and shear is

$$C_{g+}^{\alpha\beta}(\vartheta) = - \int_0^\infty C_{gE}^{\alpha\beta}(l) J_2(l\vartheta) \frac{l dl}{2\pi}. \quad (84)$$

In the case where the foreground galaxy slice (α) is narrow – either due to use of spectroscopic foregrounds or high-quality photo- z s – the probability distribution in Limber’s equation (Eq. (83)) becomes a δ -function, and the galaxy–matter cross-spectrum can be obtained.

One can also measure GGL by computing the mean tangential shear (i.e., shear in the direction orthogonal to the lens–source vector) of background galaxies around foreground galaxies as a function of radius. This view of the measurement is taken in many papers, but it is (almost) mathematically equivalent to correlating the shear field of the background galaxies with the density field of the foreground galaxies.

From the perspective of dark energy studies, the principal advantage of GGL over the shear power spectrum is observational: the shear is being correlated with galaxies rather than itself. A spurious source of shear, e.g. from imperfections in the PSF model, is a source of systematic error in the shear power spectrum, but in GGL it is only a source of noise because it is equally likely to arise in regions of high and low foreground galaxy density. The principal disadvantage of GGL is that its interpretation requires assumptions about the galaxies, which must ultimately be justified empirically.

Galaxy–galaxy lensing can be used in the linear, the weakly non-linear, and the fully non-linear regimes:

- *Linear regime*: In the linear regime, the galaxy–matter cross spectrum is $P_{g\delta}(k) = bP_\delta(k)$, where b is the galaxy bias factor. Thus $C_{gE}^{\alpha\beta}(l)$ is proportional to $b\sigma_8^2$, whereas the galaxy power spectrum is proportional to $(b\sigma_8)^2$. This provides a way to measure the linear bias of the galaxies and hence obtain σ_8 . Unfortunately, one must reach very large scales (tens of Mpc) for linear perturbation theory to be valid at the few percent level of accuracy, and at these scales the signal-to-noise ratio of current GGL results is very low.
- *Weakly non-linear regime*: At scales of order $\sim 10 h^{-1}$ Mpc, non-linear effects simply represent a correction to the linear theory, and one might hope that a judicious combination of observables can remove them. The key is to note that when stochasticity between galaxy and matter densities is included, the GGL signal is proportional to $br\sigma_8^2$, where r is the galaxy–matter cross-correlation coefficient, so all we require to extract b and σ_8 individually from GGL and galaxy clustering observables is a theoretical prediction for the stochasticity. This is a convenient result because simulations show that $r = 1$ is a much better approximation in the weakly non-linear regime than $b = \text{constant}$. This type of analysis is also best done in real space rather than Fourier space so that the 1-halo contributions (see Section 2.3) to both clustering and lensing can be eliminated. A specific outline for how to do this, including the next-order perturbation theory corrections to $r = 1$ and comparison to simulations, is presented by Baldauf et al. (2010).
- *Fully non-linear regime*: GGL can be used on the scale of individual halos ($k \sim 1\text{--}10 \text{ Mpc}^{-1}$) to relate galaxy properties such as luminosity, color, and stellar mass to the properties of the host dark matter halo. Such relations cannot be predicted *ab initio* because of the complicated astrophysics involved. Empirical constraints on these relations are useful for dark energy studies mostly because they enable us to test some of the underlying assumptions of galaxy clustering models. To gain some cosmological power beyond the weakly non-linear regime, one can construct full galaxy HOD models and marginalize over their parameters, using both GGL and galaxy clustering as constraints (Yoo et al., 2006; Leauthaud et al., 2011, 2012). Within the weakly non-linear regime, this approach effectively uses the HOD fits to compute the scale-dependence of br , drawing on the information in the small-scale galaxy clustering to improve the constraints.

Yoo and Seljak (2012) provide an extensive discussion of the cosmological constraints that can be derived from the combination of GGL and galaxy clustering, on small and large scales, in the simplified case where one isolates the population of central galaxies, so that there is one galaxy per dark matter halo.

Cluster–galaxy lensing is similar to GGL, but one takes clusters of galaxies rather than individual galaxies as the reference points (Mandelbaum et al., 2006; Sheldon et al., 2009). We will discuss this idea further in Section 6, arguing that it offers the most reliable route to calibrating cluster mass–observable relations and has the potential to sharpen cosmological parameter constraints significantly. Cluster–galaxy lensing may also be a useful tool for calibrating uncertainties in shear calibration and photometric redshifts, since the shear signal in the cluster regime is stronger and the cluster photometric redshifts themselves are usually well determined.

5.2.7. Method IV: cosmography*

The previous sections motivate us to ask whether there is a way to combine the observational advantages of GGL with the model independence of the shear power spectrum. There is, although there is a large price to pay: one can only obtain geometrical information.

The idea is to consider narrow slices of galaxies centered at redshifts $z_\alpha < z_\beta < z_\gamma$ and measure the lensing of galaxies in slices z_β and z_γ by galaxies in the foreground slice z_α . The ratio of the galaxy–shear cross-spectra is, using Eq. (83),

$$\frac{C_{gE}^{\alpha\beta}(l)}{C_{gE}^{\alpha\gamma}(l)} = \frac{\cot_K D_C(z_\alpha) - \cot_K D_C(z_\beta)}{\cot_K D_C(z_\alpha) - \cot_K D_C(z_\gamma)}. \quad (85)$$

One can see that all dependence on the power spectra and the distribution of galaxies has been canceled, allowing a purely geometric test of cosmology. This is called the *cosmography* or *shear-ratio* test (Jain and Taylor, 2003; Bernstein and Jain, 2004).

One can see from Eq. (85) that cosmography can determine the $\cot_K D_C(z)$ relation up to any affine transformation, i.e. transformations of the form

$$\cot_K D_C(z) \rightarrow a_0 + a_1 \cot_K D_C(z), \quad (86)$$

which leave the ratios of differences of $\cot_K D_C(z)$ s unaffected. (Recall that $\cot_K D_C = 1/D_C$ in a flat universe.) It is clear that a_1 is the familiar overall rescaling degeneracy: cosmography measures only dimensionless ratios and cannot distinguish two models with different H_0 but the same values of Ω_m , w , etc. Precisely the same degeneracy afflicts the supernova $D_L(z)$ relation because the absolute magnitude of a Type Ia supernova is not known *a priori*. The a_0 degeneracy is trickier, arising from the fact that ∞ is not a special distance in lensing problems.³⁸ Finally, since only $\cot_K D_C(z)$ is measured, cosmography cannot by itself provide a model-independent measurement of the curvature of the universe. But aside from these three degeneracies – a_1 , a_0 , and K – the entire geometry of the universe over the range of redshifts observed is measurable.

Unfortunately, the aforementioned degeneracies are similar in functional form to the effects of Ω_m and w , and they have severely limited the application of cosmography thus far. This is particularly true for observations restricted to low redshift: if one Taylor expands the distance as $\tan_K D_C(z) = c_1 z + c_2 z^2 + c_3 z^3 + \dots$ then any cosmological model is degenerate with one that has $(c_1, c_2) = (1, 0)$, and hence one must go through at least the z^3 term before cosmography provides any useful information. For example, at $(z_\alpha, z_\beta, z_\gamma) = (0.25, 0.35, 0.70)$, the difference in the shear ratio (Eq. (85)) between an $\Omega_m = 0.3$ flat Λ CDM cosmology and a pure CDM $\Omega_m = 1$ cosmology is only 1%! In early work (Mandelbaum et al., 2005) cosmography was therefore used as a test for shear systematics rather than a cosmological probe.

The outlook for cosmography is much brighter as we probe to larger redshifts, or if we consider dark energy models with complicated redshift dependences that cannot be mimicked by the degeneracy of Eq. (86). A particularly promising possibility is to use cosmography with lensing of the anisotropies in the CMB ($z = 1100$) to obtain a much longer lever arm (Acquaviva et al., 2008). In principle one can also apply the cosmography method to strong gravitational lenses (see Section 7.10 below). Here the challenge is that different sources probe different locations in the lens, so one must be able to constrain the lens potential extremely well to extract useful cosmographic constraints.

5.2.8. Method V: non-Gaussian statistics*

The primordial density fluctuations in the universe were very nearly Gaussian, as evidenced by the CMB. In this case, the fluctuations are fully described by the power spectrum, and this has become the common language of CMB observations. However, non-linear evolution makes the matter fluctuations and hence the lensing shear in the low-redshift universe highly non-Gaussian on small and intermediate scales. Therefore, many other statistical measures of the shear field have been proposed, the most popular of which is the bispectrum.

The bispectrum is obtained by taking the product of three Fourier modes:

$$\langle \tilde{\gamma}_E^\alpha(\mathbf{l}_1) \tilde{\gamma}_E^\beta(\mathbf{l}_2) \tilde{\gamma}_E^\gamma(\mathbf{l}_3) \rangle = (2\pi)^2 B_{EEE}^{\alpha\beta\gamma}(l_1, l_2, l_3) \delta^{(2)}(\mathbf{l}_1, \mathbf{l}_2, \mathbf{l}_3). \quad (87)$$

Statistical homogeneity forces the three wave vectors involved to sum to zero so the bispectrum is actually a function of the triangle configuration; rotational and reflection symmetry then tell us that it depends only on the side lengths (l_1, l_2, l_3) ,³⁹ which must satisfy the triangle inequality. Because there are 2 shear modes (E and B), there are actually 4 types of bispectrum: EEE , EEB , EBB , and BBB , but only EEE can be produced cosmologically. Limber's equation expresses it in terms of the 3-dimensional matter bispectrum,

$$B_{EEE}^{\alpha\beta\gamma}(l_1, l_2, l_3) = \int W_{\text{eff},\alpha} W_{\text{eff},\beta} W_{\text{eff},\gamma} \frac{B_\delta(l_1/\chi, l_2/\chi, l_3/\chi)}{D_{A1}^4} dD_{C1}. \quad (88)$$

The bispectrum contains information equivalent to the shear 3-point correlation function. The theory of transformations between the two and the implied symmetry properties have been extensively studied (Zaldarriaga and Scoccimarro, 2003; Schneider and Lombardi, 2003; Takada and Jain, 2003; Schneider et al., 2005). Halo model based descriptions of the 3-point function are also available (e.g. Cooray and Hu, 2001).

The original motivation to study the WL shear bispectrum was to break the degeneracy between Ω_m and σ_8 (e.g. Bernardeau et al., 1997; Hui, 1999; Takada and Jain, 2004). At low redshift, and on large scales where perturbation theory applies, the WL power spectrum is proportional to $\Omega_m^2 \sigma_8^2$, whereas the bispectrum is proportional to $\Omega_m^3 \sigma_8^4$; it contains three powers of the shear and hence three powers of Ω_m , but the matter bispectrum is generated by non-linear interactions and is proportional to the square of the matter power spectrum, i.e., to σ_8^4 rather than σ_8^3 . Unfortunately, this route to degeneracy breaking has proven difficult because of the low signal-to-noise ratio and high sampling variance of the bispectrum

³⁸ This is the same reason that the “ ∞ ” setting on the focus knob for a camera is not special.

³⁹ The EEB and BBB bispectra flip sign under reflections of the triangle, and some convention, e.g. that the sides are given in counterclockwise order, must be imposed to avoid ambiguity.

and because the degeneracy directions of the power spectrum and bispectrum are almost parallel in the (Ω_m, σ_8) plane. A more interesting application of the WL bispectrum in future surveys may be as a constraint on modified gravity theories, though this has not yet been well studied.

5.3. The current state of play

Weak lensing as a cosmological probe is only a decade old, although the ideas go back much further. Zwicky (1937) famously suggested gravitational lensing as a tool to determine cluster masses (although the discussion focused on strong lensing). We separately consider here the more recent history of cosmic shear studies, and of galaxy–galaxy lensing as a cosmological probe. Also the techniques and applications associated with lensing outside the optical bandpasses are sufficiently different that we place them in a separate section. Lensing by clusters is considered in the cluster section (Section 6).

5.3.1. Cosmic shear

Kristian (1967) described an initial attempt to measure statistical cosmic shear using photographic plates taken on the Palomar 5 m telescope. He even correctly identified intrinsic alignments as a systematic error, and noted that the distance dependence could be used to separate them from true cosmic shear. Interestingly, the objective of this analysis was to search for cosmological-scale gravitational waves or other large-scale anisotropies (Kristian and Sachs, 1966). The author set a limit on the magnetic part of the Weyl tensor⁴⁰ of $\lesssim 200H_0^{-2}$, which he describes as “about the best that can be done with this kind of measurement”. Fortunately this has not remained the case – indeed it was improved upon by two orders of magnitude by Valdes et al. (1983).

The modern era of lensing studies was introduced by the availability of arrays of large-format CCDs. Mould et al. (1994) searched for cosmic shear and reached percent-level sensitivity, but did not detect a signal. Cosmic shear was finally detected in 2000 by several groups (Wittman et al., 2000; Bacon et al., 2000; Van Waerbeke et al., 2000), and in deeper but narrower data from *HST* (Rhodes et al., 2001; Refregier et al., 2002). Over the same period, several additional square degrees were observed with long exposure times in excellent seeing using ground-based telescopes (Van Waerbeke et al., 2001, 2002; Bacon et al., 2003; Hamana et al., 2003). The first wide-shallow surveys were also carried out from the ground: the 53 deg² Red-Sequence Cluster Survey (Hoekstra et al., 2002) and the 75 deg² CTIO survey (Jarvis et al., 2003). These studies established the existence of cosmic shear, but at a level far below that which would be expected in $\Omega_m \sim 1$ models normalized to the CMB. The large error bars in early studies meant that only a single amplitude could be measured, yielding a constraint on the combination $\sigma_8(\Omega_m/0.3)^\nu$, where the exponent ν varied between 0.3 and 0.7 depending on the scale and depth. In the first detection of the cosmic shear bispectrum, achieved with the VIRMOS-DESCART survey, Pen et al. (2003) measured the skewness of the filtered shear signal and used it in combination with the power spectrum to rule out large- Ω_m , low- σ_8 solutions, finding $\Omega_m < 0.5$ at 90% confidence. The deep COMBO-17 survey first detected the evolution of σ_8 as a function of cosmic time (Bacon et al., 2005).

However, the early studies of cosmic shear were not free of trouble. As one can see from Table 3, while most were broadly in agreement with σ_8 in the 0.7–0.9 range, a detailed comparison shows that the measurements were not all consistent. This discrepancy stimulated discussions about a number of possible ancillary issues with the data, such as the role of intrinsic alignments, whether the source redshift distribution $N(z)$ was properly calibrated, and whether the models for the non-linear power spectrum and assumptions about the $P(k)$ shape parameter Γ could be leading to discrepancies. More seriously, most of the early measurements contained *B*-mode signals at levels not far below the *E*-mode. This was a clear signal of contamination of non-cosmological origin, probably PSF correction residuals. Also, intrinsic alignments of galaxies were detected at high significance even in the linear regime, at a level that represented a potentially serious systematic error even for then-ongoing surveys (Mandelbaum et al., 2006).

It was clear by 2006 that weak lensing was a very hard observational problem and that a great deal of work lay ahead to turn it into a precision cosmological probe. This resulted in a reduction in the rate of new cosmic shear results, the reorganization of the field into larger teams, and detailed looks at systematic errors ranging from optical distortions in telescopes to intrinsic galaxy alignments. Several wide-field optical surveys were ongoing at the time, including the deep 170 deg² CFHT Legacy Survey (for which cosmic shear was a key science driver) and the very deep multiwavelength COSMOS survey with high-resolution optical imaging from *HST*/ACS (Massey et al., 2007b; Schrabback et al., 2010). The CFHTLS presented some early results (Hoekstra et al., 2006; Semboloni et al., 2006a; Fu et al., 2008), but following this there was a rather bleak period of time. No new ground-based wide-field cosmic shear results were published, and no new large surveys were undertaken with *HST*, nor do future large *HST* weak lensing surveys seem likely.⁴¹

In the past five years, however, great progress has been made in overcoming the difficulties that at first appeared so daunting. The community made a massive investment in algorithms to determine and correct for PSF ellipticities (we will

⁴⁰ Equivalent to $\sim\omega^2h$, where ω is the gravitational wave frequency and h is the strain.

⁴¹ The premier lensing instrument on the *HST* (the Advanced Camera for Surveys) failed in January 2007. While its wide-field channel was restored during the 2009 servicing mission, the sky coverage possible with ACS is not competitive with next-generation ground-based surveys, and it seems unlikely a major cosmic shear program will be undertaken with *HST*. Rather, the next major steps in space-based cosmic shear will likely be the *Euclid* mission planned for 2020 and the *WFIRST* mission planned for the early 2020s.

Table 3

A summary of cosmic shear results from the literature obtained in the optical. Note that some of these results are independent analyses or extensions of previous data sets and hence are not independent.

Reference	Telescope/instrument	Area (deg ²)	Number of galaxies	Result
Bacon et al. (2000)	WHT/EEV-CCD	0.5	27k	$\sigma_8 = 1.5 \pm 0.5$ (@ $\Omega_m = 0.3$)
Van Waerbeke et al. (2000)	CFHT/UH8K+CFH12K	1.75	150k	Detection ^a
Wittman et al. (2000)	Blanco/BTC	1.5	145k	Detection ^b
Rhodes et al. (2001)	HST/WFPC2	0.05	4k	$\sigma_8(\Omega_m/0.3)^{0.48} = 0.91^{+0.25}_{-0.30}$
Van Waerbeke et al. (2001)	CFHT/CFH12K	6.5	400k	$\sigma_8(\Omega_m/0.3)^{0.6} = 0.99^{+0.08}_{-0.10}$ (95%CL) ^c
Hoekstra et al. (2002)	CFHT/CFH12K +Blanco/Mosaic II	53	1.78M	$\sigma_8(\Omega_m/0.3)^{0.55} = 0.87^{+0.17}_{-0.23}$ (95%CL)
Refregier et al. (2002)	HST/WFPC2	0.36	31k	$\sigma_8 = 0.94 \pm 0.14$ (@ $\Omega_m = 0.3$, $\Gamma = 0.21$)
Bacon et al. (2003)	Keck II/ESI +WHT	1.6		$\sigma_8(\Omega_m/0.3)^{0.68} = 0.97 \pm 0.13$
Brown et al. (2003)	MPG ESO 2.2m/WFI	1.25		$\sigma_8(\Omega_m/0.3)^{0.49} = 0.72 \pm 0.09^{d,e}$
Jarvis et al. (2003)	Blanco/BTC+Mosaic II	75	2M	$\sigma_8(\Omega_m/0.3)^{0.57} = 0.71^{+0.12}_{-0.16}$ (2σ)
Hamana et al. (2003)	Subaru/SuprimeCam	2.1	250k	$\sigma_8(\Omega_m/0.3)^{0.37} = 0.78^{+0.55}_{-0.23}$ (95%CL)
Rhodes et al. (2004)	HST/STIS	0.25	26k	$\sigma_8(\Omega_m/0.3)^{0.46}(\Gamma/0.21)^{0.13} = 1.02 \pm 0.16$
Heymans et al. (2005)	HST/ACS	0.22	50k	$\sigma_8(\Omega_m/0.3)^{0.65} = 0.68 \pm 0.13$
Massey et al. (2005)	WHT/PFIC	4	200k	$\sigma_8(\Omega_m/0.3)^{0.5} = 1.02 \pm 0.15$
Hoekstra et al. (2006)	CFHT/MegaCam	22	1.6M	$\sigma_8 = 0.85 \pm 0.06$ @ $\Omega_m = 0.3$
Semboloni et al. (2006a)	CFHT/MegaCam	3	150k	$\sigma_8 = 0.89 \pm 0.06$ @ $\Omega_m = 0.3$
Benjamin et al. (2007)	Various ^g	100	4.5M	$\sigma_8(\Omega_m/0.3)^{0.59} = 0.74 \pm 0.04$
Hetterscheidt et al. (2007)	MPG ESO 2.2m/WFI	15	700k	$\sigma_8 = 0.80 \pm 0.10$ @ $\Omega_m = 0.3$
Massey et al. (2007b)	HST/ACS	1.64	200k	$\sigma_8(\Omega_m/0.3)^{0.44} = 0.866^{+0.085}_{-0.068}$
Schrabback et al. (2007)	HST/ACS	0.4	100k	$\sigma_8 = 0.52^{+0.11}_{-0.15}$ (stat) ± 0.07 (sys) @ $\Omega_m = 0.3^f$
Fu et al. (2008)	CFHT/MegaCam	57	1.7M	$\sigma_8(\Omega_m/0.3)^{0.64} = 0.70 \pm 0.04$
Schrabback et al. (2010)	HST/ACS	1.64	195k	$\sigma_8(\Omega_m/0.3)^{0.51} = 0.75 \pm 0.08$
Huff et al. (2011)	SDSS	168	1.3M	$\sigma_8 = 0.636^{+0.109}_{-0.154}$ @ $\Omega_m = 0.265^h$
Lin et al. (2012)	SDSS	275	4.5M	$\sigma_8(\Omega_m/0.3)^{0.7} = 0.64^{+0.08h}_{-0.12}$
Jee et al. (2013)	Mayall+CTIO/Mosaic	20	1M	$\sigma_8 = 0.833 \pm 0.034^i$
Kilbinger et al. (2013)	CFHT/MegaCam	154	4.2M	$\sigma_8(\Omega_m/0.27)^{0.6} = 0.79 \pm 0.03$

^a Consistent with $\Omega_m = 0.3$ (Λ or open), cluster normalized; $\Omega_m = 1$, $\sigma_8 = 1$ excluded.

^b Consistent with Λ CDM or OCDM, but not *COBE* normalized $\Omega_m = 1$.

^c Reanalysis by Van Waerbeke et al. (2002) gives $\sigma_8 = 0.98 \pm 0.06$ ($\Omega_m = 0.3$, $\Gamma = 0.2$, 68%CL).

^d Reanalysis by Heymans et al. (2004) to correct for intrinsic alignments gives $\sigma_8(\Omega_m/0.3)^{0.6} = 0.67 \pm 0.10$.

^e Bacon et al. (2005) used a subset of this data to show that the matter power spectrum increased with time.

^f In the Chandra Deep-Field South; the authors warn that this field was selected to be empty, hence σ_8 may be biased low.

^g A combination of 4 previously published surveys.

^h Both based on the same raw SDSS data, but with analyses and reduction pipelines by 2 different groups.

ⁱ Other parameters fixed to WMAP 7-year values.

review some of these in Section 5.5), and in investigating the physics that determines the PSF, including such complications as atmospheric turbulence (Heymans et al., 2012a). Equally important, these methods were tested in public challenges on simulated data (STEP1, Heymans et al., 2006; STEP2, Massey et al., 2007a; GREAT08, Bridle et al., 2010; GREAT10, Kitching et al., 2010; see further discussion in Section 5.5). Progress was also made on astrophysical systematic errors. We learned that large-scale intrinsic galaxy alignments are strongest for luminous red galaxies (Hirata et al., 2007; Mandelbaum et al., 2011), and that the linear alignment model, once considered a crude analytical tool (Catelan et al., 2001), is in fact an excellent description of the observations of early-type galaxies at $\geq 10h^{-1}$ Mpc scales (Blazek et al., 2011).

As a result of this great effort by the community, the Stage II weak lensing results are finally coming to fruition and yielding large data sets that pass the standard systematics tests (e.g., *B*-modes consistent with zero). Two groups (Lin et al., 2012; Huff et al., 2011) have performed a cosmic shear measurement using the Sloan Digital Sky Survey deep co-added region – a 120-deg long stripe observed many times over the course of three years as part of the SDSS-II supernova survey. These analyses used different methods to co-add their data and correct for the PSF ellipticity, and they imposed different selection cuts and hence had different redshift distributions, yet the results were in agreement (and slightly more than 1σ below the WMAP prediction for σ_8). The largest of the Stage II weak lensing programs was the CFHT Legacy Survey. After a thorough analysis, the lensing results and cosmological implications were recently published (Heymans et al., 2012b; Benjamin et al., 2013; Erben et al., 2012; Kilbinger et al., 2013; Miller et al., 2013). They appear consistent with the standard Λ CDM cosmology with WMAP-derived initial conditions, with the amplitude σ_8 measured to ± 0.03 .

A summary of the current status of optical cosmic shear results is shown in Table 3.

5.3.2. Galaxy–galaxy lensing as a cosmological probe

Like cosmic shear, galaxy–galaxy lensing is an old idea. The earliest astrophysically interesting upper limit was that of Tyson et al. (1984), who used the images of 200,000 galaxies measured by the now-obsolete method of digitizing

photographic plates to exclude extended isothermal halos with $v_c > 200 \text{ km s}^{-1}$ around an apparent magnitude-limited sample of galaxies. Galaxy–galaxy lensing was observed at $\sim 4\sigma$ by Brainerd et al. (1996), the first clear detection of cosmological weak lensing. Their analysis used a total of 3202 lens–source pairs in a field of area 0.025 deg^2 . Several other detections followed this in deep surveys with limited sky coverage (Hudson et al., 1998; Smith et al., 2001; Hoekstra et al., 2003). However the full scientific exploitation of the galaxy–galaxy lensing signal – in contrast to cosmic shear – favors wide-shallow surveys over deep-narrow surveys, since the S/N in the shape-noise limited regime scales as only $\bar{n}_{\text{source}}^{1/2}$ rather than \bar{n}_{source} . Therefore, in the decade of the 2000s the leading galaxy–galaxy lensing surveys became the 92 deg^2 Red-Sequence Cluster Survey (RCS; Hoekstra et al., 2004, 2005; Kleinheinrich et al., 2006) and eventually the 10^4 deg^2 SDSS (references below). The availability of spectroscopic redshifts in the latter allowed the signal from low-redshift galaxies to be stacked in physical rather than angular coordinates, enabling the detection of features as a function of transverse separation. The spectroscopic survey also provided detailed environmental information, measures of star-formation history, and full 3-dimensional clustering data (e.g., correlation lengths and redshift-space distortions) for the lens galaxies.

The SDSS remains the premier galaxy–galaxy lensing survey today, for both galaxy evolution and cosmology applications, and it likely will remain so until DES and HSC results become available. The SDSS Early Data Release, comprising only a few percent of the overall survey, already detected the galaxy–galaxy lensing signal with high significance (Fischer et al., 2000; Mckay et al., 2001). Some of the major results of cosmological importance from the SDSS galaxy–galaxy lensing program have been:

- The galaxy bias can be constrained directly by going to the very largest scales and measuring galaxy–galaxy lensing in the 2-halo regime. By dividing the galaxy clustering signal by the galaxy-mass correlation function, Sheldon et al. (2004) found for L_* galaxies a bias of $b = (1.3 \pm 0.2)(\Omega_m/0.27)r$, where r is the stochasticity (presumably ~ 1 at the largest scales), with no evidence of scale dependence.^{42, 43}
- The measurement of halo masses – or more accurately, HOD parameters (see Section 2.3) – with galaxy–galaxy lensing also enables one to predict the galaxy bias, by using the bias–mass relation $b(M)$. One can in principle use this to constrain cosmological parameters, since the clustering of the lens galaxies can be measured and hence one can obtain $\sigma_{8, \text{gal}} \equiv b\sigma_8$. The results of this analysis on 300,000 lens galaxies at $z \sim 0.1$ were presented by Seljak et al. (2005). The direct constraints on σ_8 itself (with other parameters fixed) were uninteresting because the inferred bias at fixed halo mass is a decreasing function of σ_8 , and the observable product $\sigma_8 b$ is almost independent of σ_8 . However, cosmological parameters that change the shape of the power spectrum can be constrained quite well – e.g., a decrease in small-scale power can make halos rarer and hence decrease b without a compensating change in σ_8 . This breaks degeneracies internal to the CMB alone. Combining with first-year WMAP data, Seljak et al. (2005) found that for the case of three degenerate neutrinos one must have $\sum m_\nu < 0.54 \text{ eV}$ (95%CL).
- The halo mass–concentration relation $c(M)$ (e.g., Bullock et al., 2001) is not in and of itself especially useful as a dark energy probe; it depends somewhat on Ω_m , but also on baryonic physics. Nevertheless, testing it is important for any cosmological application of the 1-halo regime, including cosmic shear (King and Mead, 2011), and galaxy–galaxy lensing is well suited to measuring it at a range of halo masses. (For clusters other techniques are available, such as strong lensing or X-ray measurements.) Mandelbaum et al. (2008) measured this relation across the 10^{12} – $10^{15} M_\odot$ range, finding $c_{200b}(M) = (4.6 \pm 0.7)M_{14}^{-0.13 \pm 0.07}$, where M is the halo mass in units of $10^{14} h^{-1} M_\odot$. The normalization is about 2σ below the theoretical predictions, but the discrepancy may well be a statistical accident, particularly given that other methods have led to larger concentrations.
- Reyes et al. (2010) tested GR by comparing the galaxy-mass correlation function, measured via weak lensing, to the galaxy-velocity correlation function, measured via redshift-space distortions. The SDSS luminous red galaxy sample was chosen due to its large volume. This measurement requires an overlapping spectroscopic and WL survey. They find that

$$E_G = \frac{\Upsilon_{gm}(R)}{\beta \Upsilon_{gg}(R)} = 0.39 \pm 0.06, \quad (89)$$

where Υ is a filtered correlation function (averaged over scales $R = 10$ – $50 h^{-1} \text{ Mpc}$) and β is the redshift-space distortion parameter of Eq. (43). The combination E_G is equal to $\Omega_m/f(z)$ at the redshift of the lenses, for which GR predicts $\Omega_m^{0.45}(z = 0.32) = 0.408 \pm 0.029$. This measurement establishes that the peculiar velocities of galaxies are, to $\sim 15\%$ precision, in agreement with expectations based on the potential structure traced by lensing.

All of these measurements will become possible with much smaller error bars once the Stage III WL experiments are operational. We look forward in particular to much smaller error bars on b/r and E_G derived from the largest scales, as well as improvements on $c(M)$.

⁴² Since lensing measures $\delta\rho$ rather than $\delta\rho/\rho$, there is a factor of Ω_m in this measurement.

⁴³ A re-analysis with the final SDSS imaging data set and improved treatment of the stochasticity is underway.

5.3.3. Lensing outside the optical bands

All wavelengths of light are gravitationally lensed. The optical⁴⁴ is not special in this regard – rather, the emphasis on optical wavelengths has been technological, as this is the cheapest band in which to observe and resolve large numbers of galaxies at cosmological distances and obtain some redshift information. However, advances in technology in other wavebands have resulted in weak lensing being detected at several other wavelengths:

- In the radio, kilometer-scale interferometers are required to resolve extragalactic sources, and at the present time one cannot obtain a radio photo- z because of the featureless synchrotron spectra. However, Chang et al. (2004) detected cosmic shear of extended radio sources using the Very Large Array FIRST survey.
- Lensing of the CMB has been of interest for some time as it provides the most distant possible source screen. The first search was carried out in cross-correlation by Hirata et al. (2004) using luminous red galaxies in SDSS as the lenses and WMAP temperature anisotropies as the sources. The signal was detected three years later with combinations of SDSS and NVSS data, and two additional years of WMAP data (Smith et al., 2007; Hirata et al., 2008). Recently, the Atacama Cosmology Telescope (ACT) carried out a cosmic shear autocorrelation analysis using the CMB as a source and detected the signal at 4σ (Das et al., 2011). While apparently weak, this measurement shows that $\Omega_\Lambda > 0$ using CMB data alone, without assuming a flat universe (Sherwin et al., 2011). The ACT and South Pole Telescope (SPT) collaborations are next planning polarization surveys, which should yield much higher S/N detections of lensing and provide constraints on the neutrino mass.

5.4. Observational considerations and survey design

5.4.1. Statistical errors

The forecasting of statistical errors on the cosmological parameters is much more involved for WL than for supernovae or BAO because of the complex dependence of the observables on the underlying model. Nevertheless, some intuition can be gained by making approximations to enable exact evaluation of the integrals. Specifically, we assume (i) a single source redshift z_s ; (ii) a power-law matter power spectrum,

$$P_\delta(k, z) = 4.2 \times 10^{-4} \sigma_8^2 H_0^{-3} G^2(z) (k/H_0)^{-1.3}, \quad (90)$$

where the slope $k^{-1.3}$ is chosen to match that of the Λ CDM power spectrum at a scale of ~ 10 Mpc and the normalization is chosen to give the correct σ_8 ; (iii) evaluation of the normalization $(1+z)G(z)$ not at the true lens redshift z_l (over which we integrate from 0 to z_s) but at a “typical” lens redshift $z_s/2$; and (iv) a flat universe. Then Eq. (73) gives

$$C_{EE}(l) = 1.1 \times 10^{-3} \sigma_8^2 \left[\left(1 + \frac{z_s}{2}\right) G\left(\frac{z_s}{2}\right) \right]^2 \Omega_m^2 [H_0 D_C(z_s)]^{2.3} l^{-1.3}. \quad (91)$$

The variance per logarithmic range in l is

$$\Delta^2(l) \equiv \frac{l^2}{2\pi} C_{EE}(l) = 1.8 \times 10^{-4} \sigma_8^2 \left[\left(1 + \frac{z_s}{2}\right) G\left(\frac{z_s}{2}\right) \right]^2 \Omega_m^2 [H_0 D_C(z_s)]^{2.3} l^{0.7}; \quad (92)$$

this is a measure of the shear variance at a particular angular scale $\theta \sim l^{-1}$. Recall that $(1+z)G(z)$ varies from ≈ 0.75 at $z = 0$ to one at high redshift (see Fig. 3). Since H_0 enters only in the combination $H_0 D_C(z)$, and $D_C(z) \propto H_0^{-1}$, we see again that the WL signal depend on relative rather than absolute distances.

In practice, Eq. (92) is only a rough guide because of deviations of $P_\delta(k)$ from a power law and the non-linear enhancement of the matter power spectrum on small scales. Nevertheless, we can see several important features:

1. The typical shear, given by $\sqrt{\Delta^2(l)}$, is of order 1% at cosmological distances ($z_s \sim 1$) and degree scales ($l \sim 100$). The shear fluctuations are larger at smaller scales.
2. The shear power spectrum scales as $\propto \sigma_8^2$. Assuming a known background cosmology and source redshift, a measurement of the power spectrum to $X\%$ determines σ_8 to an uncertainty of $\frac{1}{2}X\%$. In the non-linear regime the dependence of the shear power spectrum is closer to σ_8^3 , so in practice the constraint on σ_8 is better than Eq. (92) would suggest.
3. Alternatively, if one assumes perfect knowledge of the growth of structure (hence σ_8 , Ω_m , and G), then the distance $D_C(z_s)$ to the sources can be determined to an uncertainty of $\frac{1}{3}X\%$. Lensing thus acts as a standard “ruler”.
4. Measuring the shear power spectrum as a function of source redshift z_s allows one to measure some combination of the growth function and the distance as functions of redshift. However, one does not measure both separately. In order to simultaneously constrain the functional forms $G(z)$ and $D_C(z)$, lensing must be combined with another cosmological probe.

⁴⁴ By “optical”, we mean to include near-infrared wavelengths $\lambda > 0.7 \mu\text{m}$ at which stars are still the dominant source of luminosity, and which are observed through traditional optical telescopes and with detector technology based on the creation of electron–hole pairs in semiconductors.

5. Systematic errors in any of the terms in Eq. (92) will bias the cosmology results. In particular, a 1% change in z_s , e.g. $1.00 \rightarrow 1.01$, changes the power spectrum by 2%. (This is the result of a full calculation, not evident by simple inspection of the equation.) Therefore, careful estimation of the source redshift distribution is required for a WL survey – a challenge when relying on photometric redshifts for the vast majority of sources.

The statistical uncertainty on the shear power spectrum is determined by two factors: sampling variance at low l and shape noise at high l . Sampling variance uncertainty is associated with the fact that there are only a finite number N of Fourier modes in the survey area, and consequently the fractional uncertainty in the power can be no smaller than $\sqrt{2/N}$ (where the 2 arises because power is the variance of γ_l , not the rms amplitude). If we measure the power spectrum in a bin of width Δl , then the number of modes is $N = 2l\Delta l f_{\text{sky}}$, where f_{sky} is the fraction of the sky observed. This corresponds to a sampling variance uncertainty

$$\frac{\sigma[C_{EE}(l)]}{C_{EE}(l)} = \frac{1}{\sqrt{l\Delta l f_{\text{sky}}}}, \quad \text{sampling variance only.} \quad (93)$$

If we measure modes up to some l_{max} , there are $l_{\text{max}}^2 f_{\text{sky}}$ modes, and the sampling variance uncertainty in the normalization of the power spectrum is $\sqrt{2} f_{\text{sky}}^{-1/2} l_{\text{max}}^{-1}$.

At high l , the errors on the WL power spectrum become dominated not by the number of modes available but by how well each mode can be measured with a finite number of galaxies. Individual galaxies are not round, and so a shear estimator applied to a galaxy has an intrinsic scatter $\sigma_\gamma \sim 0.2$ rms in each component of shear (γ_+ or γ_\times), for typical galaxy populations with rms ellipticity $e_{\text{rms}} \sim 0.4$ per component. This phenomenon is known as *shape noise*. Since it is uncorrelated between distinct galaxies (at least as a first approximation), shape noise produces a white noise (l -independent) power spectrum,⁴⁵

$$C_{EE}^{\text{shape}}(l) = \frac{\sigma_\gamma^2}{\bar{n}_{\text{eff}}}, \quad (94)$$

where \bar{n}_{eff} is the effective number of galaxies per steradian (this is the true number of galaxies with a penalty applied for objects where the observational measurement error on the shear becomes comparable to σ_γ ; see below). Since the cosmic shear $C_{EE}(l)$ is decreasing with l , there is a transition scale l_{tr} where the shape noise becomes comparable to the lensing signal. Using Eq. (92), we estimate

$$l_{\text{tr}} = 1300 \left(\frac{\sigma_8}{0.8} \right)^{1.54} \left[\left(1 + \frac{z_s}{2} \right) G \left(\frac{z_s}{2} \right) \right]^{1.54} \left(\frac{\Omega_m}{0.3} \right)^{1.54} [H_0 D_C(z_s)]^{1.77} \left(\frac{\bar{n}_{\text{eff}}}{20 \text{ arcmin}^{-2}} \right)^{0.77}. \quad (95)$$

At angular scales smaller than $\theta \sim l_{\text{tr}}^{-1}$, lensing cannot detect (at $S/N > 1$) a typical fluctuation in the density field.⁴⁶ Statistical measurements are still possible, however, and the power spectrum can be measured to an accuracy of $\sqrt{2/N} C_{EE}^{\text{shape}}(l)$ where N is the number of modes. Thus, in the shape-noise limited regime,

$$\frac{\sigma[C_{EE}(l)]}{C_{EE}(l)} = \frac{1}{\sqrt{l\Delta l f_{\text{sky}}}} \frac{C_{EE}^{\text{shape}}(l)}{C_{EE}(l)} = \frac{1}{\sqrt{l\Delta l f_{\text{sky}}}} \left(\frac{l}{l_{\text{tr}}} \right)^{1.3}, \quad l > l_{\text{tr}}. \quad (96)$$

One can see from this equation that the fractional uncertainty on $C_{EE}(l)$ in bins of width $\Delta l/l \sim 1$ increases with l for $l > l_{\text{tr}}$. Therefore we arrive at the important conclusion that the power spectrum is best measured at the transition scale l_{tr} : on larger scales sampling variance degrades the measurement even though individual structures are seen at high signal-to-noise ratio (SNR), and on smaller scales shape noise dominates. The aggregate uncertainty in the normalization of the power spectrum is thus of order

$$\frac{\sigma(\text{normalization})}{\text{normalization}} \sim \frac{1}{l_{\text{tr}} \sqrt{f_{\text{sky}}}}. \quad (97)$$

A full-sky experiment⁴⁷ reaching tens of galaxies per arcmin² at redshifts of order unity would have $l_{\text{tr}} \sim 1000$ and so could measure the normalization of the power spectrum to a statistical precision of order 0.1%. This would be an unprecedented measurement of the strength of matter clustering. However, as we will see below, there are substantial statistical and systematic hurdles to such an experiment.

Finally, we consider galaxies measured at finite SNR. In the above analysis, we assumed that each galaxy provided an estimate of the shear with uncertainty σ_γ . At finite SNR there is also measurement noise σ_{obs} , so that each galaxy provides

⁴⁵ We give the E -mode noise here. There is an equal amount of shape noise power in the B -mode, but the lensing B -mode is used only as a systematics test because it contains no cosmological signal to first order.

⁴⁶ High-amplitude features such as clusters may still be visible.

⁴⁷ In practice the Galactic Plane must be avoided, so it is unlikely that optical astronomy would push beyond $f_{\text{sky}} \sim 0.7$ for any cosmological application.

an estimate with error $\sqrt{\sigma_\gamma^2 + \sigma_{\text{obs}}^2}$. Using inverse-variance weighting, in the finite-SNR case the shape noise becomes Eq. (94), with the effective source density

$$\bar{n}_{\text{eff}} = \frac{1}{A} \sum_{i=1}^{N_{\text{gal}}} \frac{\sigma_\gamma^2}{\sigma_\gamma^2 + \sigma_{\text{obs},i}^2}, \quad (98)$$

where A is the survey area and the sum is over the galaxies. This is always less than $\bar{n} = N_{\text{gal}}/A$. The effective source density \bar{n}_{eff} is limited in part by the depth of the survey: $\sigma_{\text{obs},i}$ typically scales with integration time as $\propto t^{-1/2}$, but once $\sigma_{\text{obs},i} \ll \sigma_\gamma$ one no longer continues to gain. How long does this take? In Section 5.5.3, we will show that for nearly circular, Gaussian galaxies⁴⁸

$$\sigma_{\text{obs}} = \frac{1}{\nu} \left(1 + \frac{r_{\text{psf}}^2}{r_{\text{gal}}^2} \right), \quad (99)$$

where r_{psf} and r_{gal} are the half-light radii of the PSF and the galaxy, respectively, and ν is the detection significance (in σ). Thus for galaxies with a similar size as the PSF, we expect to reach $\sigma_{\text{obs}} = 0.1$ (measurement noise half of shape noise) after integrating long enough to see the galaxy at 20σ .

In principle, the summation in Eq. (98) is over all objects detected as extended sources, and any galaxy could be used if its detection significance is high enough. In practice, this is dangerous: while one might hope to obtain $\sigma_{\text{obs}} = 0.1$ on a galaxy with $r_{\text{gal}} = 0.5r_{\text{psf}}$ and a 50σ detection, the “ellipticity measurement” on this galaxy consists of measuring the small deviation of the image from the PSF. Such a procedure tends to magnify systematic errors in the PSF model and is usually unadvisable. Therefore, most WL surveys impose a cutoff on $r_{\text{gal}}/r_{\text{psf}}$ or some similar property.

5.4.2. The galaxy population for optical surveys

The design of a WL survey must begin by considering the population of galaxies. We will focus here on the population in the 3-dimensional space of redshift z , effective radius r_{eff} , and apparent AB magnitude in the I -band (a convenient choice for shape measurement with red-sensitive CCDs from the ground). The plots shown here are based on the mock catalog of Jouvel et al. (2009), which uses real galaxies from the COSMOS survey but fills in missing information for individual galaxies (e.g. redshifts or line fluxes) with photo- z s and models.

Fig. 17 shows the mean surface density of galaxies and the median source redshift as a function of limiting magnitude I_{AB} for effective radius cuts of 0.15", 0.248", and 0.35". In general, one would like to use galaxies larger than the PSF to avoid amplification of systematics when applying a PSF correction to the shapes. The “effective radius” (EE50, for 50% encircled energy) of a typical ground-based PSF is $\sim 0.35''$ under good conditions, corresponding to a FWHM of $\sim 0.7''$. The 0.248" cut is a factor of $\sqrt{2}$ smaller, appropriate if one can make use of galaxies smaller than the PSF or has sufficient étendue to do the entire survey under the very best seeing conditions. Measuring galaxies at $r_{\text{eff}} = 0.15''$ is well beyond present ground-based cosmic shear survey capabilities, for both algorithmic and PSF-determination reasons, and will likely require a space (or balloon) based platform.

5.4.3. Photometric redshifts and their calibration

Modern WL analyses all use photometric redshifts in some way. They are central to tomography and cosmography measurements, and they are also needed in most schemes to remove the intrinsic alignment contamination. In the case of GGL, photo- z s are used to select sources that are actually behind the lens plane (sources in front of the lens are unlensed and dilute the signal, whereas sources at the same redshift as the lens can contribute intrinsic alignments).

One can characterize the photo- z distribution using the joint probability distribution for the photo- z z_p and the true redshift z for some sample of galaxies, $P(z_p, z)$. In the case of lensing, we care about the conditional probability distribution, $P(z|z_p)$. This distribution is sometimes characterized by its conditional bias and scatter,

$$\delta z(z_p) = z_p - \langle z \rangle_{|z_p}, \quad \sigma_z(z_p) = \sqrt{\langle z^2 \rangle_{|z_p} - \langle z \rangle_{|z_p}^2}, \quad (100)$$

but it is always non-Gaussian and in practice there are “outliers” or “catastrophic failures” with $|z - z_p| \sim \mathcal{O}(1)$. The conditional probability distribution is not symmetric: Bayes’ theorem tells us that

$$P(z|z_p) = \frac{P(z)}{P(z_p)} P(z_p|z), \quad (101)$$

so a photo- z that is “unbiased” in the conventional sense of $\langle z_p \rangle|z = z$ may still have $\delta z(z_p) \neq 0$. It is not required that photometric redshifts have $\delta z(z_p) = 0$, but one does need to know the value of $\delta z(z_p)$ to relate observations to model

⁴⁸ For realistic non-Gaussian profiles, the shape measurement error is usually worse by of order 20%.

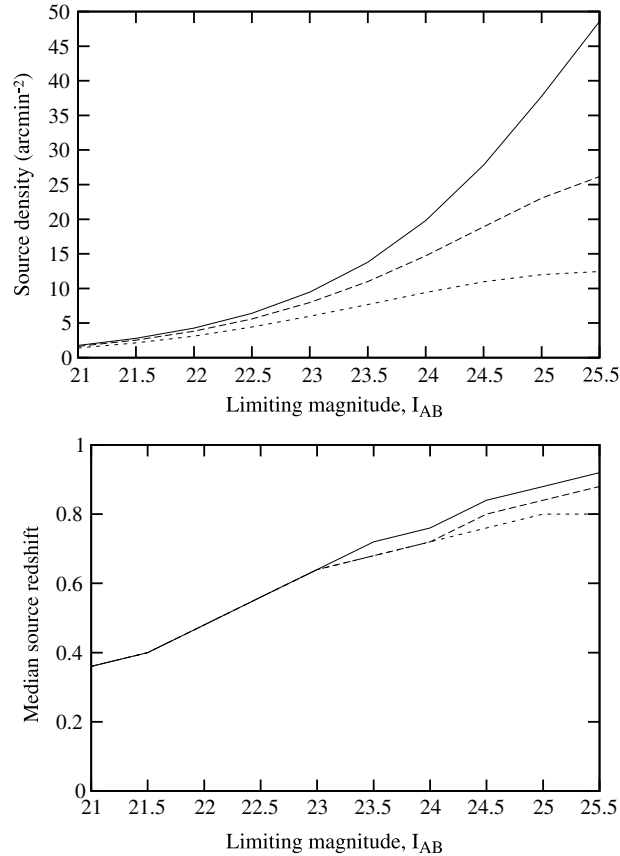


Fig. 17. The mean surface density of galaxies (top panel) and median redshift (bottom panel) as a function of limiting magnitude. The three curves show different r_{eff} cuts: the top curve is a cut at $0.15''$, which might be applied to a space-based survey; the middle curve is a cut at $0.248''$, which would be an optimistic choice from the ground; and the bottom curve is a cut at $0.35''$, a more conservative choice for a ground-based survey with $\sim 0.7''$ seeing (FWHM). For galaxy–galaxy lensing, one could make more aggressive cuts.

parameters. From the simplified example discussed in Section 5.4.1, we can see that a systematic error of ~ 0.01 in $\delta z(z_p)/z_p$ will lead to a normalization error in the matter power spectrum of the order of 2%. Similarly, if 1% of galaxies in a source redshift bin z_s are actually outliers with redshift $z \ll z_s$, they will dilute the expected lensing signal by 1%, and the power spectrum by 2%.

If the full distribution $P(z|z_p)$ is known, then the shear cross-power spectra for any pair of redshift slices can be determined for a given cosmological model. However, the use of photo- z s to suppress intrinsic alignments (Section 5.6.1) does not work if the intrinsic alignments of the outliers are significant, or even if the scatter is large enough that galaxies can evolve significantly within a redshift bin, so there is a strong motivation to reduce them to the minimum level possible. Thus lensing programs must face two challenging problems: (i) obtaining a low outlier rate, and (ii) determining $P(z|z_p)$ to sub-percent precision.

To understand how to reduce the outlier rate, we must investigate how photo- z s work: they take several broad-band fluxes from a galaxy and try to identify spectral features (see Fig. 18). At low redshifts, the strongest feature in the optical part of a galaxy spectrum is the break around $3800\text{--}4000\text{ \AA}$, arising from metal line absorption in early-type galaxies and the Balmer continuum (plus high-order lines) in late-type galaxies. As the redshift of the galaxy increases, this feature moves to the red, and above redshifts of $z \sim 1.3$ it is no longer useful for optical photo- z s (depending on the SNR in z and y bands). At $z \geq 2$, the $\text{Ly}\alpha$ break redshifts into the optical bands and can be used – but it is possible to confuse it with the Balmer/4000 \AA break. This is the principal example of a *photo- z degeneracy*.

The above discussion suggests that to reduce outliers across the whole range of redshifts used for WL surveys ($z = 0$ to ~ 3) one desires coverage from blueward of the Balmer/4000 \AA feature (i.e. a u -band) through the near-IR ($J + H$ bands), so that either the Balmer/4000 \AA feature or $\text{Ly}\alpha$ is robustly identifiable. The optical bands can be easily observed from the ground. As one moves redward, however, the sky brightness as observed from the ground increases rapidly, and obtaining the $J + H$ band photometry matched to the depth of future surveys is only practical from space.

One is then left with the problem of measuring the photo- z error distribution. The most direct and conceptually simplest way to do this is to collect spectroscopic redshifts of a representative subsample of the sources used for WL. This is, however, very expensive in terms of telescope time: many galaxies have weak or absent emission lines (particularly if one restricts to

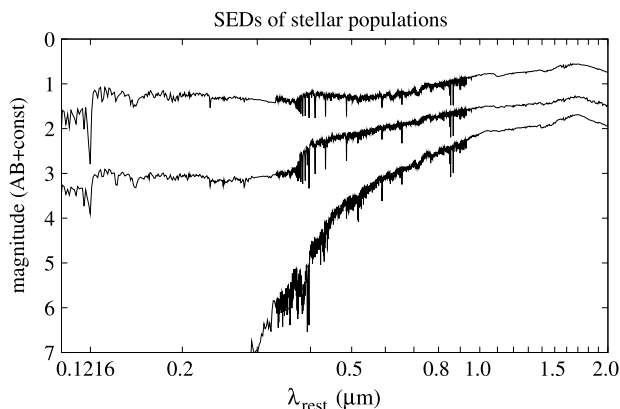


Fig. 18. The SEDs of three stellar populations are shown: a single burst at age 25 Myr (top); a continuous star-forming population of 6 Gyr age (middle); and a single burst at 11 Gyr (bottom). All have solar metallicity. Blueward of Ly α they have been adjusted for an IGM transmission factor of 0.8 (appropriate for $z = 2.25$; see McDonald et al. (2006)), but other corrections (dust, nebular emission) are not included. The models are obtained from Bruzual and Charlot (2003). Note the break at $\sim 0.37\text{--}0.40 \mu\text{m}$ present in all models, albeit with varying shape, strength, and precise location.

the optical range), and so one searches for absorption features of faint ($i \sim 22\text{--}25$) galaxies. Stage III/IV experiments may require $\mathcal{O}(10^5)$ redshifts to calibrate photo-zs at the level of their statistical errors, and we desire sub-percent failure rates because the failures are likely concentrated at specific redshifts. These failure rates are far below those that have actually been achieved by spectroscopic surveys at the desired magnitudes.

An alternative idea (Newman, 2008) is to use the 2-D angular cross-correlation of the photo-z galaxies with a large area spectroscopic redshift survey, which can target brighter galaxies and/or the subset of faint galaxies that have strong emission lines. For a bin of galaxies with photo-z centered on z_p , the amplitude of cross-correlation is proportional to $b_{\text{spec}}(z)b_{\text{phot}}(z, z_p)P(z|z_p)$, where b_{spec} and b_{phot} are the clustering bias factors of the spectroscopic and photo-z galaxies, respectively, at redshift z . The auto-correlations of the spectroscopic and photo-z samples provide additional constraints on the bias factors, and one also has the normalization condition $\int P(z|z_p) dz = 1$ for each z_p bin. The key uncertainty in this approach is constraining the full redshift-dependent $b_{\text{phot}}(z, z_p)$; if the bias varies with photo-z error (e.g., because high-bias red galaxies and low-bias blue galaxies have different photo-z error distributions) then this dependence must be modeled to extract $P(z|z_p)$ (Matthews and Newman, 2010). If one is using intermediate or small scale clustering, then one must also allow for scale-dependent bias and for cross-correlation coefficients lower than unity between different galaxy populations, which would lower the amplitude of cross-correlations relative to auto-correlations. Finally, the approach requires a spectroscopic sample that spans the full redshift range of the photometric sample; a quasar redshift survey may provide sufficient sampling density for probing the high-redshift tail of $P(z|z_p)$. The cross-correlation technique has to date not been used for WL surveys, but it has been used to measure other redshift distributions – see, e.g., the application to radio galaxies by Ho et al. (2008). Adding galaxy–galaxy lensing measurements to the galaxy clustering measurements may improve the robustness and accuracy of the cross-correlation approach and allow some degree of “self-calibration” without relying on an external spectroscopic data set (Zhang et al., 2010).

Overall, the problem of measuring $P(z|z_p)$ to the required accuracy remains one of the greatest challenges for future WL projects. Given the difficulty of assembling an ideal spectroscopic calibration sample, the treatment of photo-z distributions in Stage III and Stage IV WL analyses is likely to involve some combination of direct calibration, cross-correlation calibration, empirically motivated models of galaxy SEDs, and marginalization over remaining uncertainties in parameterized forms of $P(z|z_p)$. Tomographic WL measurements themselves have some power to constrain these distributions (at the cost of some leverage on cosmological parameters), and weak lensing by clusters that have well determined individual redshifts may also be a valuable tool.

5.4.4. Lensing in the radio

An interesting alternative to shape measurement in the optical is to work in the radio part of the spectrum, where late-type galaxies are observable via their synchrotron emission. In order to achieve the required resolution, one needs to use a large interferometer: a fringe spacing of $1''$ is achievable at 1 GHz with a baseline of 60 km. One also needs a large collecting area to obtain high-SNR images on a competitive number of galaxies; the SKA could in principle measure billions of galaxies (Blake et al., 2004). But let us suppose such an interferometer were built. What would it do for WL? In principle, it could solve many problems at once:

- *Shape measurement:* An interferometer directly measures the Fourier transform of the surface brightness of a galaxy, $\tilde{I}(\mathbf{u})$, thereby avoiding the difficulty of interpolating PSF properties from stars. On long baselines, the \mathbf{u} -plane is usually sparsely sampled, i.e., not all values of \mathbf{u} are observed; the Fourier mode $\mathbf{u} = \mathbf{L}_\perp/\lambda$, where \mathbf{L}_\perp is the interferometer baseline projected into the plane of the sky. At a given wavelength, as the Earth rotates, each baseline thus traces out an ellipse in the \mathbf{u} -plane. However, if one combines a finite range of λ and many baselines, one could fill in the \mathbf{u} -plane,

and model-fitting shape measurement techniques can work even with significant coverage gaps. Model-fitting methods were used in the analysis of the FIRST survey at $\lambda = 20$ cm (Chang et al., 2004), which resulted in a 3σ detection of cosmic shear.

- **Redshifts:** Late-type galaxies contain atomic gas, and thus radiate in the H_I 21 cm line. For nearby galaxies ($z < 0.1$) this line has a long history of being used as a redshift indicator. A Stage IV radio interferometer survey could collect hundreds of millions of spectroscopic redshifts in this line out to $z \sim 1-2$, thereby obviating the need to rely on photo- z s and calibrate photo- z error distributions. Conversely, it is not clear that one could make use of the many radio galaxies *not* detected in H_I, as even photometric redshifts for large radio galaxy samples are difficult to obtain at high completeness.
- **Shape noise reduction:** The radio part of the spectrum offers interesting opportunities to reduce shape noise. For example, if one spatially resolved the H_I disk of a galaxy, one could produce a velocity map. A perfect inclined disk has the long axis aligned with the velocity gradient, and if sheared this alignment is destroyed, so a measurement of the velocity gradient provides independent information on the intrinsic shape of the galaxy (Morales, 2006). Another idea is to use the polarization of the synchrotron emission, which tends to be perpendicular to the galactic disk and hence is an indicator of the position angle of the intrinsic minor axis (Brown and Battye, 2011). While promising, these ideas are new, and their practical application to a WL survey may have to await at least a partial SKA.

5.4.5. Lensing of the CMB

It is also possible to do lensing analyses on the CMB. Here there are several advantages: the source redshift is known exactly from cosmological parameters, $z_{\text{src}} = 1100$; theory predicts exactly the statistical distribution of hot and cold spots on the CMB, so there is no intrinsic alignment effect; and the PSF (or “beam” shape) of microwave experiments tends to be far more stable than in the optical. The CMB is a diffuse field rather than a collection of objects (galaxies), so reconstructing the shear requires a different mathematical formalism than for galaxy lensing. The basis for this formalism is two-fold:

- In the presence of lensing by a Fourier mode of the potential $\tilde{\psi}(\mathbf{l})$, the CMB anisotropy field is no longer statistically isotropic: different temperature Fourier modes become correlated, $\langle \tilde{T}^*(\mathbf{l}_1)\tilde{T}(\mathbf{l}_2) \rangle \propto \tilde{\psi}(\mathbf{l}_2 - \mathbf{l}_1)$. These products of temperature modes can be used as estimators of the lensing potential (Hu, 2001).
- A more dramatic effect occurs for CMB polarization. The unlensed CMB polarization is pure E -mode,⁴⁹ i.e., the polarization in each Fourier mode is parallel to the wavevector rather than at a 45° angle. Lensing shear changes the direction of the wavevector \mathbf{l} but not the polarization, so it can generate B -mode shear.

Until recently, because of SNR issues, lensing of the CMB had been detected only in cross-correlation with foreground galaxies (Smith et al., 2007; Hirata et al., 2008; Bleem et al., 2012). The advent of the arcminute-scale CMB experiments ACT and SPT (primarily motivated by cluster cosmology using the SZ effect) has enabled robust detections of the power spectrum of the CMB lensing field (Das et al., 2011; van Engelen et al., 2012).

Because CMB lensing only provides a single source slice, it is unlikely to ever replace galaxy lensing. However, in combination with galaxy lensing, it can provide the most distant source slice for tomography (Hu, 2002b) and cosmography (Acquaviva et al., 2008).

5.5. Measuring shears

So far we have treated shear measurement as a black box: it takes in an image of the galaxy and some knowledge of the instrument, and it returns $\hat{\gamma}_{+, \times}$, an unbiased estimator for the true shear γ with some uncertainty per component σ_γ . This black box is very complicated on the inside, as one needs an accurate and robust *shape measurement algorithm*, and even providing the necessary inputs to such an algorithm, particularly an accurate determination of the PSF, has proven to be difficult. After a brief overview of these algorithms, we describe the idealized problem of measuring shear from an ensemble of galaxy images, then turn to a more detailed discussion of the challenges that arise in practice.

There are two general strategies for shape measurement methods in common use today. One class of methods is to measure moments of galaxies (in real or Fourier space), and relate, e.g., the mean quadrupole moment of galaxies to the shear. These methods started with *ad hoc* “PSF correction” prescriptions, but they have recently evolved toward methods that attempt to statistically close the hierarchy of moments of galaxies and PSFs in a model-independent way. The other class of methods is based on forward modeling: one adopts a model for a galaxy (e.g., an elliptical Sersic profile, or a linear combination of basis images), simulates the observational procedure, and minimizes χ^2 . Both approaches have their advantages and disadvantages. Much of the early WL work used moments-based methods, but for years a generally applicable PSF correction scheme seemed out of reach. Some of the more recent incarnations of the Fourier domain moments-based methods work for arbitrary distributions of galaxy and PSF profiles; however these are less mature in their practical implementation, and they impose stringent requirements on input data quality (e.g., sampling). The forward modeling methods can handle a much wider range of observational defects (e.g., under some circumstances one may even

⁴⁹ Primordial gravitational waves can generate a B -mode on large scales, but such gravitational waves are adiabatically damped on angular scales below a degree. Thus the $\sim 10'$ -scale B -mode should be dominated by lensing.

be able to measure a galaxy containing missing pixels), but they depend on a model for the galaxy being observed; one must carefully assess the impact of an insufficiently general model. Both strategies require exquisite knowledge of the PSF.

Currently there are many algorithms in use in each category. The prototype moments-based method was that of Kaiser, Squires, and Broadhurst (KSB; Kaiser et al., 1995; improved by Luppino and Kaiser, 1997; Hoekstra et al., 1998). Many improvements of these methods have been made – e.g., in computing better conversion factors from shear to quadrupole moments⁵⁰ (Semboloni et al., 2006b). Elliptical-weighted moments and the concept of shear-covariance were introduced by Bernstein and Jarvis (2002) and have been used extensively in SDSS (Hirata and Seljak, 2003b). Further progress was made by moving to moments in Fourier space, where the PSF “correction” becomes trivial (one divides by the Fourier transform of the PSF, at least in the regions where it is nonzero). This has culminated in the development of a shape measurement method that is exact in the high-SNR limit (Bernstein, 2010). We discuss this method and its development in Section 5.5.2. An early example of the model-fitting approach was IM2SHAPE (Bridle et al., 2002). More recently, Bayesian model fits have been introduced that are stable at lower SNR (Miller et al., 2007; Kitching et al., 2008); these are currently being applied to the CFHTLS. The “shapelet” basis (Refregier, 2003; Refregier and Bacon, 2003), derived from energy eigenstates of a 2D quantum harmonic oscillator, is useful in both types of methods. The coefficients in a shapelet decomposition *are* moments, but one may also fit a model galaxy parameterized by its shapelet coefficients.

The various shape measurement algorithms have been tested and compared in blind simulations, such as the Shear Testing Program (STEP1/STEP2; Heymans et al., 2006; Massey et al., 2007a), GREAT08 (Bridle et al., 2010), and GREAT10 (Kitching et al., 2010). In most of these cases, the objective is to minimize both the shear calibration error m (i.e. the error in the response to a given input shear) and the spurious shear c (i.e., the shear measured by the algorithm on an unlensed sample of galaxies). The STEP2 simulations used typical ground-based PSFs and complex galaxy morphologies and found that many of the measurement methods had shear calibration errors $|m|$ of one-to-several percent, and spurious shear $|c|$ ranging from several $\times 10^{-4}$ to several $\times 10^{-3}$. This level of performance should thus be considered typical of the more mature, heavily used shear measurement algorithms, although recent methods have done better. On the other hand, the algorithmic errors are only a portion of the error budget in a WL experiment – most importantly, the early simulation tests did *not* require participants to recover the spatial variability of the PSF. Such a test is currently ongoing as part of the GREAT10 challenge (Kitching et al., 2010). Early results from GREAT10 are now available, but their significance is still being digested.

In the remaining portions of this section we will discuss the mathematical problem of shape measurement (Section 5.5.1) and the basis for *some* of the commonly used methods (Section 5.5.2) and their statistical errors (Section 5.5.3). We cannot of course do justice to every method that has been suggested or used. We have chosen to highlight the recent progress in Fourier-space methods, since in principle they provide an exact solution in the limit of high SNR and are thus ripe for further development and utilization (Bernstein, 2010). There are some biases that can result even for perfect shape measurement (or galaxies measured with a δ -function PSF), including the noise-related biases and selection biases, which are probably present at some level for all known algorithms; these are discussed in Section 5.5.4. Finally Section 5.5.5 describes the determination of the PSF, which is taken as an input for any shape measurement algorithm.

5.5.1. The idealized problem

The idealized shape measurement problem is as follows: we have a galaxy in the source plane whose surface brightness is $f_0(\mathbf{x})$, where \mathbf{x} is a 2-dimensional vector in the plane of the sky. It is first sheared, i.e., the galaxy in the image plane is $f(\mathbf{x}) = f_0(\mathbf{S}\mathbf{x})$, where \mathbf{S} is the shearing matrix,

$$\mathbf{S} = \begin{pmatrix} 1 - \gamma_+ & -\gamma_\times \\ -\gamma_\times & 1 + \gamma_+ \end{pmatrix}. \quad (102)$$

(We assume $|\gamma| \ll 1$ here and work to linear order in γ for simplicity, although higher-order corrections will be important for Stage IV surveys.) We do not observe the actual image on the sky, however – we observe it through an instrument with PSF⁵¹ $G(\mathbf{x})$. The resulting image is

$$I(\mathbf{x}) = [f \star G](\mathbf{x}) = \int_{\mathbb{R}^2} f(\mathbf{x}') G(\mathbf{x} - \mathbf{x}') d^2 \mathbf{x}' = \int_{\mathbb{R}^2} f_0(\mathbf{S}\mathbf{x}') G(\mathbf{x} - \mathbf{x}') d^2 \mathbf{x}'. \quad (103)$$

This equation may also be written in Fourier space: if we define

$$\tilde{I}(\mathbf{u}) = \int_{\mathbb{R}^2} I(\mathbf{x}) e^{-2\pi i \mathbf{u} \cdot \mathbf{x}} d^2 \mathbf{x} \leftrightarrow I(\mathbf{x}) = \int_{\mathbb{R}^2} \tilde{I}(\mathbf{x}) e^{2\pi i \mathbf{u} \cdot \mathbf{x}} d^2 \mathbf{u}, \quad (104)$$

then Eq. (103) simplifies to

$$\tilde{I}(\mathbf{u}) = \tilde{G}(\mathbf{u}) \tilde{f}_0(\mathbf{S}^{-1} \mathbf{u}). \quad (105)$$

⁵⁰ Massey et al. (2007a) Section 3.1.1 give an excellent technical review of the methods derived from KSB.

⁵¹ Here we use the term “PSF” to include not just the image of a point source produced by the telescope optics but also pointing jitter and detector effects. For example, if the detector has square pixels, the PSF is that delivered by the telescope convolved with a square top-hat function.

In practice, the image I is only obtained at discrete values of \mathbf{x} , i.e., at the pixel centers spaced by separation Δ . If the image is oversampled, i.e., if the Fourier transform⁵² of the PSF is zero (or negligible) at wavenumbers above some $|\mathbf{u}|_{\max}$ with $|\mathbf{u}|_{\max} < 1/(2\Delta)$, then it can be sinc-interpolated to recover the full continuous function,

$$I(\mathbf{x}) = \sum_{n_1 n_2} I(n_1 \Delta, n_2 \Delta) \operatorname{sinc} \frac{\pi(x_1 - n_1 \Delta)}{\Delta} \operatorname{sinc} \frac{\pi(x_2 - n_2 \Delta)}{\Delta}. \quad (106)$$

The pixelization thus represents no special difficulty, except that the sinc function has noncompact support and must be smoothly truncated. A second implication of oversampling is that integrals of the form $\int P(\mathbf{x}) I_1(\mathbf{x}) I_2(\mathbf{x}) d^2 \mathbf{x}$, where P is a polynomial in the coordinates and I_1 and I_2 are oversampled functions, can be replaced without error by (infinite) sums over pixels: $\int \rightarrow \Delta^2 \sum$. Again, in practice such sums must be truncated.

We will also define a critical wavenumber u_{crit} , which is the smallest wave number for which there is a Fourier mode with $G(\mathbf{u}) = 0$ with $|\mathbf{u}| = u_{\text{crit}}$. Then we have $G(\mathbf{u}) \neq 0$ for any $|\mathbf{u}| < u_{\text{crit}}$. This critical wavenumber determines the region within the Fourier plane over which deconvolution is possible, and over which measurement of $\tilde{f}(\mathbf{u})$ is possible.

A shape measurement algorithm is a functional $\hat{\gamma}_i[I; G]$, $i \in \{+, \times\}$, that returns a shear estimate. When averaged over a population of galaxies with the same shear, such an algorithm will yield an expectation value

$$\langle \hat{\gamma}_a \rangle = c_a + (\delta_{ab} + m_{ab}) \gamma_b + \mathcal{O}(\gamma^2). \quad (107)$$

Here c_a is called the *additive shear error* and m_{ab} is the *multiplicative shear error* or shear calibration error. An ideal algorithm will have $c_a = m_{ab} = 0$.

Many WL surveys take multiple exposures of each field; if they are oversampled, one may use Eq. (106) to reconstruct a continuous function $I(\mathbf{x})$ for each exposure. If the PSFs in each exposure differ (which they usually do), then to construct a stacked image, one can either apply a convolution kernel to each input image to make the PSFs the same or do a noise-weighted least squares fit to each Fourier mode $\tilde{f}(\mathbf{u})$. If the individual exposures are undersampled (as is likely for space-based data) and appropriately dithered, methods are available in both Fourier space (Lauer, 1999) and real space (Fruchter, 2011; Rowe et al., 2011) to reconstruct a fully-sampled and hence continuous image $I(\mathbf{x})$.⁵³ In either case, the problem is still one of measuring the shear from an ensemble of images of different galaxies. The one exception is that model-fitting shape measurement techniques can operate either on the combined images or via a direct fit to the raw input images. Even in this case, however, with many exposures (as planned for LSST) object detection will have to be carried out on the combined image in order to reach the full survey depth.

One would intuitively expect that shape measurement becomes more difficult when the PSF is larger than the intrinsic size of the galaxy being measured. This is indeed the case. While the idealized problem of measuring shapes in the presence of a PSF is well-defined for any nonzero galaxy size, in practice both statistical and systematic errors blow up when the PSF becomes significantly larger than the galaxy. The extent to which the systematic errors in the high-SNR, $r_{\text{gal}} < r_{\text{psf}}$ regime can be addressed will likely determine the constraining power of large-étendue ground-based WL programs such as that planned for LSST.

5.5.2. Shape measurement algorithms*

The most obvious – but flawed – way to construct a shape measurement algorithm is to simply use the quadrupole moment tensor of a galaxy: one could compute

$$Q_{ij}[I] = \int_{\mathbb{R}^2} I(\mathbf{x})(x_i - \bar{x}_i)(x_j - \bar{x}_j) d^2 \mathbf{x}, \quad (\text{incorrect}) \quad (108)$$

where $\bar{\mathbf{x}}$ is the centroid and the $[I]$ implies that we compute the quadrupole moment on an observed image. It is easily seen from the properties of convolutions that $Q_{ij}[f] = Q_{ij}[I] - Q_{ij}[G]$, i.e., one may obtain the pre-PSF quadrupole moment of a galaxy by subtracting the observed quadrupole moment from that of a PSF. Then one could construct the ellipticities of the galaxy, which are simply the trace-free components of the quadrupole moment normalized by the trace:

$$e_+[f] = \frac{Q_{11}[f] - Q_{22}[f]}{Q_{11}[f] + Q_{22}[f]} \quad \text{and} \quad e_\times[f] = \frac{2Q_{12}[f]}{Q_{11}[f] + Q_{22}[f]}. \quad (109)$$

Since the quadrupole moment of f is simply related to that of f_0 via

$$Q_{ij}[f] = (S^{-1})_{ik} (S^{-1})_{jl} Q_{kl}[f_0], \quad (110)$$

⁵² It is important to recall that the definition of oversampling required for Eq. (106) operates in Fourier space. The commonly used condition for oversampling that the FWHM should exceed 2 pixels is a good rule of thumb for smooth profiles such as a Gaussian, but it is not appropriate for general PSFs.

⁵³ Much of the HST/COSMOS weak lensing work used the ‘‘Drizzle’’ algorithm (Fruchter and Hook, 2002), which in general leads to a slightly different PSF in each pixel. However, this did not represent a limiting systematic for the $\sim 2 \text{ deg}^2$ observed in COSMOS.

we may derive the transformation law for ellipticities under infinitesimal shear:

$$\begin{aligned} e_+[f] &= e_+[f_0] + 2\gamma_+ - e_+[f_0](\gamma_+ e_+[f_0] + \gamma_\times e_\times[f_0]) \quad \text{and} \\ e_\times[f] &= e_\times[f_0] + 2\gamma_\times - e_\times[f_0](\gamma_+ e_+[f_0] + \gamma_\times e_\times[f_0]). \end{aligned} \quad (111)$$

It is then easily seen that the mean ellipticity of a population of galaxies that has an initially isotropic distribution of ellipticities – i.e., $P(e_+, e_\times)$ depends only on the magnitude $\sqrt{e_+^2 + e_\times^2}$ and not on the direction $\arctan(e_\times/e_+)$ – is

$$\langle e_a \rangle = (2 - e_{\text{rms}}^2) \gamma_a, \quad (112)$$

where e_{rms}^2 is the mean square ellipticity per component (+ or \times). Since we work to first order in γ , we may use the mean square ellipticity of the observed sources in Eq. (112). So the galaxy ellipticity divided by $2 - e_{\text{rms}}^2$ is a shear estimator satisfying our desired conditions: by comparison to Eq. (107) there is no additive or multiplicative bias.

The problem with this procedure is that the unweighted quadrupole moment, Eq. (108), involves an integral over the entire sky, with a weight that increases $\propto x^2$ as one moves away from the centroid of the galaxy. Therefore its measurement noise is infinite. It also fails to converge if the wings of the PSF decline as $G(\mathbf{x}) \propto |\mathbf{x}|^{-\alpha}$ for $\alpha \leq 4$, i.e., it fails to converge for all PSFs realized in modern optical telescopes. Therefore Eq. (108) needs modification.

A conceptually simple approach is to do a model fit to each galaxy. If one fits a model of an exponential or de Vaucouleurs profile galaxy with homologous elliptical isophotes, then one can obtain the quadrupole moment $Q_{ij}[f]$ analytically from the model and hence the ellipticity of the galaxy. Modern model-fitting techniques can even fit more general radial profiles, or simultaneously fit bulge + disk models. Model fitting is also robust against many types of nastiness that occur in real data, such as dead pixels, cosmic rays, or non-linear detector effects. However, model fitting assumes that the galaxy actually obeys the model – and especially at $z > 1$, the appearance of galaxies is not simple and they are not describable by simple analytical functions. At present, our best approach to understand what happens when simple model fits are confronted with complex galaxies is with simulations. One can even imagine “re-calibrating” these methods using the simulations, e.g. by subtracting the simulated c_i from each shear and multiplying by the matrix inverse of $\delta_{ij} + m_{ij}$ (see Eq. (107)); but of course one is then relying on the galaxy population in the simulation to closely trace reality.

One could also attempt to do a regularized deconvolution of the galaxy. The most popular such technique is a basis function technique: one writes the galaxy image as $f(\mathbf{x}) = \sum_n b_n \psi_n(\mathbf{x})$, where $\{\psi_n\}$ are a finite basis set and b_n are the fit coefficients; this then becomes a model-fitting problem. A common choice is the “shapelet” basis, where the $\{\psi_n\}$ are the energy eigenmodes of the 2-D quantum harmonic oscillator (polynomials times Gaussians); this requires $(N+1)(N+2)/2$ eigenfunctions to represent the $0 \cdots N$ energy levels (Refregier, 2003; Refregier and Bacon, 2003). This basis is complete in the limit of large N , and the Gaussian endows the basis coefficients with simple transformation properties under translation and shear. Real galaxies often require very large N to be well-represented, however, especially for cuspy profiles.

A final class of ideas has been to note that any ellipticity formula that is *shear-covariant* in the sense of transforming via Eq. (111) enables us to use Eq. (112). For example, suppose that we had the galaxy image f before PSF convolution, and did an unweighted least-squares fit, in the sense of minimizing

$$c = \int_{\mathbb{R}^2} [f(\mathbf{x}) - f_{\text{model}}(\mathbf{x}|\mathbf{p})]^2 d^2\mathbf{x}. \quad (113)$$

Here f_{model} is an elliptical Gaussian fit to the image with free amplitude A , centroid \bar{x}_i , and second moment matrix Q_{ij}^{elfit} (6 parameters). Then Q_{ij}^{elfit} and the ellipticities constructed from it would be shear-covariant – even if the galaxy’s true radial profile does not resemble a Gaussian!⁵⁴ Early work on implementing this idea in the presence of a PSF attempted to determine the second moment matrix of the image on the sky $Q_{ij}^{\text{elfit}}[f]$ from the observed image and the PSF. For example, Gaussian galaxies and PSFs satisfy $Q_{ij}^{\text{elfit}}[f] = Q_{ij}^{\text{elfit}}[I] - Q_{ij}^{\text{elfit}}[G]$, and so “non-Gaussianity corrections” were introduced (Bernstein and Jarvis, 2002; Hirata and Seljak, 2003b) that yielded shear calibration errors of a few percent. But these methods were heuristic, and moreover they suffer from a fundamental limitation: $Q_{ij}^{\text{elfit}}[f]$ depends on very high-wavenumber Fourier modes \mathbf{u} of the image, which are not preserved by the PSF, i.e. $\tilde{G}(\mathbf{u}) = 0$. It is therefore mathematically impossible to determine $Q_{ij}[f]$ from the data in a model-independent manner.

To understand this point more fully, and illustrate a solution, let us imagine that we are doing an unweighted least-squares fit of a parameterized image $f_{\text{model}}(\mathbf{p})$, using Eq. (113). For convenience, we will write the parameters as $\mathbf{p} = \{A, \sigma_{\text{gal}}, \bar{x}_1, \bar{x}_2, e_+, e_\times\}$, where $\sigma_{\text{gal}} = (\det \mathbf{Q})^{1/4}$ is a characteristic scale length of the galaxy,^{1/4} so that they have simple transformation properties under rotations. Written in Fourier space, it becomes

$$c = \int_{\mathbb{R}^2} [\tilde{f}(\mathbf{u}) - \tilde{f}_{\text{model}}(\mathbf{u}|\mathbf{p})]^2 d^2\mathbf{u}, \quad (114)$$

⁵⁴ This is easily seen because the measure $d^2\mathbf{x}$ in Eq. (113) is shear-invariant.

and its minimum is given by the simultaneous solution of the 6 equations

$$0 = \int_{\mathbb{R}^2} \tilde{f}(\mathbf{u}) \frac{\partial \tilde{f}_{\text{model}}(\mathbf{u}|\mathbf{p})}{\partial p_\alpha} d^2\mathbf{u}, \quad (115)$$

where p_α is any of the 6 parameters. The problem occurs because $\partial \tilde{f}_{\text{model}}(\mathbf{u}|\mathbf{p})/\partial p_\alpha$ has support at $|\mathbf{u}| > u_{\text{crit}}$, where we cannot determine $\tilde{f}(\mathbf{u})$.

A solution to this problem has been proposed by Bernstein (2010),⁵⁵ which is in principle exact in the low-noise limit and has been applied to simulations (but not yet to actual data). The key is to work in the Fourier domain, where the effect of the PSF is simple and the effect of the shear is as simple as in real space. We present the solution here in its most general form, and refer the reader to Bernstein (2010) for implementation details. The solution is to replace Eq. (115) with

$$0 = t_\alpha = \int_{\mathbb{R}^2} \tilde{f}(\mathbf{u}) \tilde{W}_\alpha(\mathbf{u}|\mathbf{p}) d^2\mathbf{u}, \quad (116)$$

where $W_1 \cdots W_6$ are weight functions. These should be envisioned to be qualitatively similar to the derivatives in Eq. (115); but the only rules that we will impose are that: (i) the Fourier transforms $\tilde{W}_\alpha(\mathbf{u}|\mathbf{p})$ have compact support, confined to $|\mathbf{u}| < u_{\text{crit}}$; and (ii) they are rotation and translation-covariant, e.g., changing the centroid parameter by $\delta\bar{\mathbf{x}}$ simply translates the function $W_\alpha(\mathbf{x}) \rightarrow W_\alpha(\mathbf{x} - \delta\bar{\mathbf{x}})$, and there is a similar transformation when rotating the ellipticity components.⁵⁶ We do *not* require the W_α to be shear-covariant: indeed, since a large shear can map any mode to another mode with $|\mathbf{u}| > u_{\text{crit}}$, such a requirement would be inconsistent with rule (i). Now we may write Eq. (116) as

$$0 = \int_{|\mathbf{u}| < u_{\text{crit}}} \tilde{I}(\mathbf{u}) \frac{\tilde{W}_\alpha(\mathbf{u}|\mathbf{p})}{\tilde{G}(\mathbf{u})} d^2\mathbf{u}. \quad (117)$$

The combination $\tilde{W}_\alpha/\tilde{G}$ is well-defined, and $\tilde{I}(\mathbf{u})$ is the Fourier transform of the *observed* image, so the parameters \mathbf{p} can be measured from the data.

By rule (ii), we have rotation covariance, so the mean of the ellipticities $\langle \mathbf{e} \rangle$ over an isotropic population of galaxies is zero – even if the PSF is anisotropic. Thus there is no additive bias (except for selection and noise effects – see warnings below). However, dropping shear covariance has come at a price: the ellipticities (e_+ , e_\times) no longer transform according to Eq. (111), and the responsivity coefficient $\langle \mathbf{e} \rangle = \mathcal{R}\gamma$ must be determined. Fortunately, we can evaluate the effect of an infinitesimal shear on Eq. (116): if $\mathbf{S} = \mathbf{1} + \delta\mathbf{S}$, then to first order in $\delta\mathbf{S}$,

$$\delta\tilde{f}(\mathbf{u}) = -u_i [\delta\mathbf{S}]_{ij} \frac{\partial \tilde{f}(\mathbf{u})}{\partial u_j}, \quad (118)$$

and so

$$0 = \delta t_\alpha = - \int_{\mathbb{R}^2} u_i [\delta\mathbf{S}]_{ij} \frac{\partial \tilde{f}(\mathbf{u})}{\partial u_j} \tilde{W}_\alpha(\mathbf{u}|\mathbf{p}) d^2\mathbf{u} + \left\{ \int_{\mathbb{R}^2} \tilde{f}_0(\mathbf{u}) \frac{\partial \tilde{W}_\alpha(\mathbf{u}|\mathbf{p})}{\partial p_\beta} d^2\mathbf{u} \right\} \delta p_\beta. \quad (119)$$

The integral in braces $\{\}$ is simply a 6×6 matrix, which we denote $E_{\alpha\beta}$. Using integration by parts, the tracelessness of $\delta\mathbf{S}$ in the first integral, and the substitution $\tilde{f} \rightarrow \tilde{I}/\tilde{G}$, we then find

$$\delta p_\beta = -[\mathbf{E}^{-1}]_{\beta\alpha} [\delta\mathbf{S}]_{ij} \int_{|\mathbf{u}| < u_{\text{crit}}} \frac{\tilde{I}(\mathbf{u})}{\tilde{G}(\mathbf{u})} u_i \frac{\partial \tilde{W}_\alpha(\mathbf{u}|\mathbf{p})}{\partial u_j} d^2\mathbf{u}, \quad (120)$$

which is well-defined. This equation tells us how the parameters for each galaxy vary under an infinitesimal shear; their ensemble average gives \mathcal{R} . Note that once shear covariance has been dropped, it is only possible to know the responsivity factor \mathcal{R} if one has a sample of real galaxies to observe, since one needs the sample of real galaxies to compute the matrix $E_{\alpha\beta}$.

A related approach to solving the shear calibration problem was suggested by Mandelbaum et al. (2012). They noted that given a high-resolution image of a galaxy (e.g., a space-based image) with PSF G_1 , it is often possible to construct a lower resolution but sheared image of the same galaxy with PSF G_2 in a model-independent way. One can thus directly test *any* shear estimator on the sheared images, and extract the shear calibration factor. Conceptually, the criterion for this to work is that all of the Fourier modes of the image observable using PSF G_2 must be within the band limit of G_1 with enough “padding” to make sure that the shear (which also shears the Fourier plane!) does not bring unobserved high-wavenumber modes not seen with G_1 into the region seen by G_2 . Mathematically, the criterion for this to be possible are that there exist

⁵⁵ See also Kaiser (2000), which contains many of these ideas but seems to have been promptly forgotten by most of the WL community!

⁵⁶ Note that $W_{\bar{\mathbf{x}}}$ must transform as a vector under rotations, and W_e as a spin-2 tensor.

two critical wavenumbers u_c and u_d such that (i) all the power in the low-resolution PSF is below u_c , i.e. $\tilde{G}_2(\mathbf{u}) = 0$ for $|\mathbf{u}| \geq u_c$; (ii) the high-resolution transfer function $\tilde{G}_1(\mathbf{u})$ is far from zero, i.e. $1/\tilde{G}_1(\mathbf{u})$ is well-behaved, at all $|\mathbf{u}| < u_d$; and (iii) $u_c > (1 - \gamma)u_d$. Then one can use the Fourier-domain multiplication:

$$\tilde{I}_2^{(\gamma)}(\mathbf{u}) = \tilde{G}_2(\mathbf{u})\tilde{T}(\mathbf{S}^{-1}\mathbf{u})\tilde{I}_1(\mathbf{S}^{-1}\mathbf{u}), \quad (121)$$

where $\tilde{T}(\mathbf{u}) = 1/\tilde{G}_1(\mathbf{u})$ for wave vectors $|\mathbf{u}| < u_d$. As implemented, this method requires a higher-resolution image of a fair subsample of galaxies, which is not always available. It may however be quite useful in the Stage III ground-based programs, where one might use HST data for the “high resolution” image; see Mandelbaum et al. (2012) for a preliminary application of HST data to shear calibration in SDSS.

5.5.3. Shape measurement errors*

The statistical uncertainty in ellipticity estimation depends on the method used and the radial profile of the galaxy, as well as the sizes of the galaxy and PSF and the SNR. Rules of thumb can be obtained by considering nearly circular Gaussians. Propagating instrument noise through the elliptical Gaussian fitting method, Bernstein and Jarvis (2002) find, in the absence of a PSF,

$$\sigma(e_+[f]) = \sigma(e_\times[f]) = \frac{\sqrt{16\pi n} \sigma_f}{F} = \frac{2}{\nu}, \quad (122)$$

where n is the flux noise variance per unit area, F is the galaxy flux, σ_f is the 1σ width of the galaxy (note: the effective radius of a Gaussian is $1.177\sigma_f$), and ν is the detection SNR in an optimal filter. In the presence of a circular Gaussian PSF, the ellipticity is diluted by

$$\mathbf{e}[I] = \frac{\sigma_f^2}{\sigma_I^2} \mathbf{e}[f] = \frac{\sigma_f^2}{\sigma_f^2 + \sigma_G^2} \mathbf{e}[f], \quad (123)$$

where σ_G is the PSF width and σ_I is the width of the PSF-convolved galaxy image. Furthermore, the detection SNR is reduced because the galaxy is smeared out into an aperture with more noise, so it follows that Eq. (122) should be modified by replacing $\sigma_f \rightarrow \sigma_I$; and, if we want the uncertainty in the pre-PSF galaxy ellipticity, we must divide out the σ_f^2/σ_I^2 factor from Eq. (123). This gives

$$\sigma(e_+[f]) = \sigma(e_\times[f]) = \frac{\sqrt{16\pi n} \sigma_I^3}{F \sigma_f^2} = \frac{2}{\nu} \frac{\sigma_f^2}{\sigma_I^2}. \quad (124)$$

This provides a large advantage for making the PSF smaller than the galaxy: since the noise variance n scales with observing time as t^{-1} , the time required to measure the shape of a galaxy scales as

$$t \propto \sigma_f^6 \propto \left(1 + \frac{\sigma_G^2}{\sigma_f^2}\right)^3; \quad (125)$$

in the limit of a poorly resolved galaxy ($\sigma_f \ll \sigma_G$) a factor of 2 improvement in the PSF provides a factor of 64 gain in speed. However, as the PSF becomes smaller than the galaxy this advantage saturates.

Eq. (123) also illustrates another property of shape measurement: *systematic* errors as well as statistical errors are inflated by having large PSFs. For example, if there is a systematic error in the ellipticity of the observed image I , it propagates to the estimated pre-PSF ellipticity $\mathbf{e}[f]$ with a multiplying factor of $(\sigma_f^2 + \sigma_G^2)/\sigma_f^2$. Therefore there is a systematic advantage to having $\sigma_G \ll \sigma_f$.

The shear uncertainty is a factor of ~ 2 smaller than the ellipticity uncertainty owing to the responsivity factor $2 - e_{\text{rms}}^2$ (Eq. (112)). It does however have a minimum value: the ellipticity of an individual galaxy has an RMS variation of $e_{\text{rms}} \sim 0.4$ per component, so there is a limiting “shape noise” contribution to the shear measurement uncertainty of $\sigma_\gamma \approx 0.2$. There are some ideas for how to circumvent this limit using the color- or scale-dependence of ellipticity (Lombardi and Bertin, 1998; Jarvis and Jain, 2008) or taking advantage of the non-Gaussianity of the ellipticity distribution (Kaiser, 2000; Bernstein and Jarvis, 2002), but there are no clear routes to large improvement for optical galaxies. For galaxies imaged in the HI 21 cm line, one might be able to use kinematic signatures to distinguish random orientation from lensing shear (e.g. Morales, 2006).

5.5.4. Noise rectification and selection biases*

Two pernicious biases can arise even for the “exact” shape measurement algorithms described above: the noise rectification and selection biases.

Noise rectification bias arises whenever a non-linear transformation, such as ellipticity measurement, is applied to noisy data. If we Taylor-expand the mean of the ellipticity measured on the true image I_{obs} around the noiseless image I , we find

$$\langle \mathbf{e}[I_{\text{obs}}] \rangle = \mathbf{e}[I] + \frac{1}{2} \sum_{ab} \frac{\partial^2 \mathbf{e}}{\partial I(\mathbf{x}_a) \partial I(\mathbf{x}_b)} \text{Cov}[I(\mathbf{x}_a), I(\mathbf{x}_b)] + \dots, \quad (126)$$

where the sum is over pairs of pixels in the image, and \mathbf{x}_a and \mathbf{x}_b are positions of those pixels. The bias is proportional to the noise variance, i.e., to $(S/N)^{-2}$ at leading order.

One might at first think that the pixel covariance is described by uncorrelated white noise, which is statistically shear-invariant and thus leads to no bias, but in the presence of a PSF correction [i.e., dividing by $\tilde{G}(\mathbf{u})$] this is no longer the case. The noise rectification bias was first recognized in the context of WL by Kaiser (2000), who showed that because the centroiding of a galaxy is more accurate on the “short” than the “long” axis of the PSF there is a preference for the measured second moment of the galaxy to be elongated along the PSF, even if the PSF correction method is perfect in the deterministic case. This was generalized by Bernstein and Jarvis (2002) to incorporate other noise-related biases and by Hirata and Seljak (2004) to include the effect on shear calibration errors. Eq. (126) provides a unified framework for computing all of these biases to order $(S/N)^{-2}$. At low S/N higher-order terms in the expansion may become important, and the expansion itself may break down, e.g., as fitting algorithms jump to alternate χ^2 minima. It is our judgment that it is best to stay away from this “nonperturbative noise” regime. For a recent investigation of noise rectification bias in the context of current shape-measurement algorithms, see Melchior and Viola (2012).

Selection biases are well-known in astronomy. In our case, they will affect the shear if there is a bias in favor of detecting galaxies in some orientations rather than others, producing an additive shear error, or if selection depends on the magnitude of the ellipticity, which leads to a multiplicative shear error because galaxies are preferentially selected when their intrinsic ellipticity is aligned with the shear (Hirata and Seljak, 2003b). A similar bias results if galaxies are weighted by various properties (e.g., ellipticity uncertainty) that are not shear-invariant. The formalism of Section 5.5.2 can in principle handle this problem if instead of computing $\langle \mathbf{e} \rangle$ we compute $\langle w\mathbf{e} \rangle$ where the weight $w = 0$ for galaxies that are rejected. However, the assessment of selection biases in practice has been addressed through simulations such as the STEP program.

A problem related to selection biases is *blending*: the superposition of images of two galaxies. If the galaxies are at the same redshift, they are affected by the same shear, and an ideal shape measurement algorithm that measures the blend should recover the “correct” answer – indeed, existing WL surveys must contain many sources that are actually blended with their own satellite galaxies. But if the deblending algorithm is not shear-invariant there can be a bias in the shear. Another issue, particularly for ground-based Stage IV experiments that will aim for high source densities at modest resolution and very small statistical errors, is accidental blending of galaxies at different redshifts (and hence different shears).

The general strategy for dealing with these categories of biases is: (1) make choices (e.g., S/N cuts) that keep them small to the extent possible; (2) compute corrections using simulations and/or analytic estimates, and apply them to the measurements; (3) test the accuracy of these corrections in the data by looking for the expected scalings with S/N , source size, and so forth; and (4) marginalize over remaining uncertainties in the corrections.

5.5.5. Determining the PSF and instrument properties

Shape measurement algorithms are only as useful as their inputs: in this case a map of the PSF $G(\mathbf{x})$ at each point in the field. Determining the PSF to sub-percent accuracy is one of the major challenges in WL. Errors in the PSF model introduce correlated structure into the ellipticity field of the galaxies, since residual anisotropy in the PSF determination is interpreted as shear by a shape measurement algorithm.

Fortunately, Nature has provided us with stars, which under typical observing conditions can be treated as point sources. Unfortunately, there is only a finite density of stars in high Galactic latitude fields, typically of order 1 per arcmin², so one must interpolate the PSF to the position of a galaxy. This is a demanding challenge; any error in the interpolated PSF is likely to have spatial structure. It is also not an easy problem, as the PSF is an entire function $G(\mathbf{x}; \theta)$ at every 2-d position θ on the sky, and in contrast to shape measurement, interpolation from stars is underconstrained.⁵⁷ To date, most of the methods applied to real data are heuristic. For example, the SDSS analyses fit a low-order polynomial,

$$G(\mathbf{x}; \theta) = \sum_{i=0}^N \sum_{j=0}^{N-i} \sum_{k=1}^M a_{ijk} \theta_1^i \theta_2^j G^{(k)}(\mathbf{x}), \quad (127)$$

where the $\{G^{(k)}\}$ are the top $M = 3$ principal components of the stellar images, $N = 2$ is the interpolation order, and a_{ijk} are coefficients. Small scale structure in the PSF variation may not be well represented by this approach unless N is large, but if the required number of polynomial coefficients $(N + 1)(N + 2)/2$ exceeds the number of stars in each frame then the method falls apart. If the small-scale structure is repeatable, for example if it is associated with low-order aberrations in the telescope or the topography of the focal plane, then one may make progress by applying PCA to the angular dependence in instrument-fixed coordinates (Jarvis and Jain, 2004), choosing the top K modes out of the space of $(N + 1)(N + 2)/2$ polynomials. Recent work has focused on improved interpolation schemes that outperform polynomials (e.g., Bergé et al., 2012).

For space-based data, one can either build a physical model of the PSF (Rhodes et al., 2006) or use PCA (Jee et al., 2007). However, for ground-based data where the PSF has a large contribution from atmospheric turbulence, the more empirical interpolation schemes have been the methods of choice.

⁵⁷ As a reminder, here \mathbf{x} is used to refer to the location within the image of each star, i.e., of order $\sim 1''$, whereas the independent variable θ accounts for variation across the entire field, of order $\sim 1^\circ$.

Once one has the PSF, one needs a method of quality assessment. We need to be able to determine, or at least bound, the power spectrum of the residual PSF systematics that leak into cosmic shear results. (For GGL, this job is easier because residual PSF anisotropy adds noise but does not correlate with the positions of the galaxies.) One way is to do null tests: one can compute the correlation function of ellipticities of the stars and (supposedly) PSF-corrected galaxies, or search for *B*-mode shear. The latter is not foolproof, as a PSF systematic of *E*-mode type can arise from some aberrations. A very attractive (but underutilized) test is to mask some of the stars in the PSF fitting and compare the interpolated PSFs at their locations to the observed stellar images. There are also methods for using combinations of these correlation functions to test for “overfitting” – the phenomenon in which a too-general PSF model begins to fit noise or small-scale structure in the stellar images, with the effect that the interpolated PSF is actually worse (Rowe, 2010).

Even when this is done, there remain two other errors that have received increasing attention recently, which may cause the PSF of a galaxy to differ from that of a star:

- *Color dependence*: Real PSFs depend on the wavelength of light: a diffraction-limited telescope has a PSF size that scales $\propto \lambda$, seeing through a Kolmogorov atmosphere gives a size $\propto \lambda^{-1/5}$, aberrations introduce λ -dependence into not just the size of the PSF but its morphology and radial profile, real detectors have response functions that depend on wavelength, and in ground-based data atmospheric dispersion acts like a prism and causes a centroid shift with wavelength. Since galaxies have different SEDs than the stars used to fit the PSF (the galaxies are usually redder), the PSF measured from the stars is not always appropriate to the galaxies (Cypriano et al., 2010). Moreover, each galaxy contains a range of SEDs due to differing stellar ages and metallicities and dust columns; and for each of these SEDs there is a different PSF, with the resulting images superposed on the focal plane (Voigt et al., 2012). This represents a major challenge: while the centroid wavelength of galaxies in a typical filter ($\lambda/\Delta\lambda \sim 5$) varies by several percent, Stage IV surveys will require sub-percent shear calibration accuracy, and as yet no WL survey has published a color correction to its PSF at all. While this area requires much more work, in a problem of this complexity prevention is the first step to a cure. For example, one can employ an atmospheric dispersion compensator on the ground, and one can use narrower filters. For smooth spectra or spectra averaged over moderate redshift ranges, the variation of wavelength centroid scales as $\propto \Delta\lambda^2$. The advantage for narrower filters must of course be weighed against the slower survey speed with smaller $\Delta\lambda$. If many observations of a given field are taken under varying conditions, as planned for LSST, one has the intriguing possibility of using the different seeing, focus, or hour angle dependences of these errors to solve them out and distinguish them from shear. A final strategy is to use “calibration samples” of galaxies observed in multiple filters to correct the effect for a lensing survey with a single, wide band (Semboloni et al., 2013).
- *Detector effects*: A CCD image can be altered during readout due to finite *charge-transfer inefficiency*. This results from photoelectrons that temporarily bind to defects (“traps”) in the material, causing each sky object to leave a trail along the readout direction. If not corrected, this can appear as a PSF anisotropy, and it is greater for faint objects than for bright objects because some of the traps saturate, so stellar images tend to underestimate the effect. Charge transfer inefficiency is primarily a concern for space-based data, since the principal cause of traps is radiation damage. Remedies applied to HST data have included empirical corrections to the galaxy ellipticities as a function of row and magnitude, or pixel-level corrections that begin by “undoing” the charge transfer inefficiency before subsequent processing (Massey et al., 2010; Rhodes et al., 2010).
- Near-infrared detectors (as planned for *WFIRST*) suffer from different potential detector-induced systematic errors than CCDs. In particular, since the image is read “in place” on the detector rather than transferred out as on a CCD, there is no charge transfer inefficiency. Instead the major concerns have been *interpixel capacitance* (the sensitivity of the voltage on each pixel to the charge collected in neighboring pixels); *persistence* (a charge trapping and release phenomenon in which each exposure contains a small amount of residual signal from previous exposures); and *reciprocity failure* (a detector exposed to twice the signal for half the time does not produce the same response, which becomes an issue for comparing the images of stars and galaxies of very different magnitudes).

5.6. Astrophysical systematics

The principal advantage of weak lensing is that – despite its technical difficulty – it is directly sensitive to mass. It is thus less affected by astrophysical uncertainties than other probes of cosmic structure such as the galaxy power spectrum or X-ray cluster counts. However, it is not entirely free of astrophysical contamination. The two major sources of uncertainties in this case are intrinsic galaxy alignments, which can mimic the coherent distortion of galaxies by gravitational lensing, and the prediction of the matter power spectrum.

5.6.1. Intrinsic alignments*

We have thus far assumed that the intrinsic ellipticities of galaxies are independent, adding noise but not spurious signal to cosmic shear measurements. However, the orientations of galaxies are determined by physical processes – mergers, torquing by tidal fields from the host halo and large scale structure, etc. – that could produce correlated *intrinsic alignments*. We first describe here the general formalism for the impact of intrinsic alignments, then consider what observations and theory have taught us about them. We conclude by discussing prospects for intrinsic alignment removal.

The field of intrinsic galaxy ellipticities is a tensor function $\mathbf{e}(\mathbf{r}, \hat{\mathbf{n}})$ of position \mathbf{r} and viewing direction $\hat{\mathbf{n}}$. In this sense it is very similar to CMB polarization. In principle it also depends on the type of galaxy under consideration and on the observational details – for example, the B and I -band images of a galaxy could have different ellipticities. We may also discuss either the unweighted intrinsic ellipticity field \mathbf{e}_{unwt} or the field weighted by the galaxies,

$$\mathbf{e}_{\text{wt}}(\mathbf{r}, \hat{\mathbf{n}}) \equiv [1 + g(\mathbf{r})]\mathbf{e}_{\text{unwt}}(\mathbf{r}, \hat{\mathbf{n}}), \quad (128)$$

where $g = (n_{\text{gal}} - \bar{n})/\bar{n}$ is the galaxy overdensity. In what follows, we use \mathbf{e} to denote the galaxy-weighted field \mathbf{e}_{wt} , since this is most closely related to what one observes in a survey.

Like any other field, \mathbf{e} can be Fourier transformed to give $\tilde{\mathbf{e}}(\mathbf{k}, \hat{\mathbf{n}})$, with a power spectrum

$$\langle \tilde{e}_a^*(\mathbf{k}, \hat{\mathbf{n}}) \tilde{e}_b(\mathbf{k}', \hat{\mathbf{n}}') \rangle = (2\pi)^3 \delta^{(3)}(\mathbf{k} - \mathbf{k}') P_{e,ab}(\mathbf{k}, \hat{\mathbf{n}}, \hat{\mathbf{n}}'), \quad (129)$$

where a, b are spin-2 tensor indices. Here we break from the train of reasoning in CMB polarization studies: instead of doing a multipole decomposition of \mathbf{e} , we note that in the Limber approximation (which we use exclusively here) there is only one relevant viewing direction – the direction to the observer – so $\hat{\mathbf{n}} = \hat{\mathbf{n}}'$. Moreover, the Fourier wave vectors that we care about are perpendicular to the line of sight, so $\mathbf{k} \cdot \hat{\mathbf{n}} = 0$. We will thus write this particular configuration as simply $P_{e,ab}(k)$. An E/B mode decomposition is also possible if we rotate the coordinate basis so that the E -component of ellipticity is aligned along the direction of \mathbf{k} and the B -component is at a 45° angle; we then have two ellipticity power spectra, $P_e^{EE}(k)$ and $P_e^{BB}(k)$ (the EB -term vanishes by parity). One can also write correlations of the ellipticity with scalar fields such as the galaxy or matter density. In this case, only the E -mode can be correlated, and we write $P_{e\delta}$, P_{eg} , etc.

The measured shear on the sky is a superposition of the WL shear and the intrinsic ellipticity (converted to shear using the algorithm-specific responsivity factor \mathcal{R}):

$$\gamma_{\text{obs}}(\theta) = \gamma(\theta) + \frac{1}{\mathcal{R}} \int p(D_C) \mathbf{e}(\theta, D_C) dD_C. \quad (130)$$

Limber's equation can then be used to obtain the observed shear power spectrum between the α and β redshift slices. The E -mode contains three terms:

$$C_{EE}^{\alpha\beta}(l; \text{obs}) = C_{EE}^{\alpha\beta}(l; GG) + C_{EE}^{\alpha\beta}(l; GI) + C_{EE}^{\alpha\beta}(l; II), \quad (131)$$

where the GG term is the gravitational lensing shear contribution, II is the intrinsic ellipticity contribution, and GI is the cross-correlation. The GG term is the desired signal and is given by Eq. (81). The other terms are

$$C_{EE}^{\alpha\beta}(l; II) = \frac{1}{\mathcal{R}^2} \int p_\alpha(D_{C1}) p_\beta(D_{C1}) \frac{P_e^{EE}(k = l/D_{A1})}{D_{A1}^2} dD_{C1} \quad (132)$$

and

$$C_{EE}^{\alpha\beta}(l; GI) = \frac{1}{\mathcal{R}} \int [W_{\text{eff},\alpha}(D_{C1}) p_\beta(D_{C1}) + W_{\text{eff},\beta}(D_{C1}) p_\alpha(D_{C1})] \frac{P_{e\delta}(k = l/D_{A1})}{D_{A1}^2} dD_{C1}. \quad (133)$$

There is also an II contribution to the B -mode power spectrum similar to Eq. (132). Since there is no B -mode gravitational shear, there is no GG or GI contribution to the B -mode power spectrum.

Several generic features can be noted from these equations:

- The II contribution to the cross-spectrum is only nonzero if the two redshift distributions overlap, since it arises from intrinsically aligned galaxies at the same redshift. Therefore, if low-scatter photo- z s are available, it can be eliminated. This is one motivation for doing tomography instead of simply measuring the shear power spectrum on a magnitude-limited sample of galaxies.
- The GI contribution is more troublesome. It arises from the lensing of the more distant slice by the same matter field that controls the intrinsic ellipticity of the nearby slice. Inspection of the properties of the window function W_{eff} shows that Eq. (133) is nonzero for *all* redshift distributions, unless either $P_{e\delta}(k) = 0$ or the redshift distributions are δ -functions at the same redshift, which would dramatically enhance II . Thus we are led to conclude that every tomographic power spectrum can suffer intrinsic alignment contributions.
- B -mode “shear” can be generated by intrinsic alignments, and if nonzero $C_{BB}^{\alpha\beta}(l)$ is observed this is one possible explanation (PSF model errors are another). However, it is possible for the intrinsic alignment contribution to the E -mode to be much larger because (i) there is no theoretical reason from galaxy formation to expect $P_e^{EE}(k) \sim P_e^{BB}(k)$ – indeed, we will see below that $P_e^{EE}(k) \gg P_e^{BB}(k)$ may be natural – and (ii) $C_{EE}^{\alpha\beta}(l)$ can also contain a GI term, which for broad redshift distributions usually dominates over II . Therefore a nondetection of B -mode shear does not rule out significant intrinsic alignment contamination.

Before we discuss removal of intrinsic alignments, it is helpful to consider the physics underlying their power spectra. One can distinguish two cases: early-type galaxies, which are triaxial and whose intrinsic ellipticity is presumably related to the direction of the most recent merger or the direction of anisotropic collapse (depending on one's idea of how these galaxies are formed), and late-type galaxies, whose ellipticity is determined by the disk angular momentum (perhaps acquired via tidal torquing during collapse, reshuffled by disk-halo interactions, and perturbed by minor mergers). The detailed physics of these processes remains elusive, but some predictions can still be made by traditional galaxy biasing arguments. For example, if one considers the formation of early-type galaxies in a particular region of the universe, one could argue that at linear order in the large-scale density field a galaxy's formation sequence can be sensitive only to the density and tidal field coming from the linear modes, and to small-scale structure. Since only the tidal field has the correct symmetry properties to be related to an ellipticity, it follows that the ellipticity should be proportional to the tidal field,

$$e_+ = \frac{C_1}{4\pi G\bar{\rho}a^2}(\partial_1^2 - \partial_2^2)\Phi, \quad \text{and} \quad e_\times = \frac{C_1}{4\pi G\bar{\rho}a^2}(2\partial_1\partial_2)\Phi, \quad (134)$$

where C_1 controls the strength of alignment and ∂_1 and ∂_2 denote derivatives along two orthogonal axes on the sky. This implies that the ellipticity traces the density field, and in particular

$$P_e^{EE}(k) = C_1^2 P_\delta(k), \quad P_e^{BB}(k) = 0, \quad \text{and} \quad P_{e\delta} = C_1 P_\delta(k). \quad (135)$$

Eqs. (134), (135) are known as the *linear alignment model* (Catelan et al., 2001). Note that they predict only E -mode intrinsic alignments, because the alignments are linearly sourced by a scalar field.⁵⁸

Observations of LRGs in the SDSS have shown that the galaxy-ellipticity correlation⁵⁹ $w_{ge}(r_p)$ has the same power-law slope as the galaxy correlation function $w_g(r_p) \propto r^{-0.7}$ (Mandelbaum et al., 2006; Hirata et al., 2007), with an amplitude that increases rapidly with LRG luminosity. This is a quantitative success of the linear model. However, on small scales it is not clear how accurate Eq. (135) should be.

For late-type galaxies, it is less clear what to expect. The oldest and most widely discussed model is that disk galaxies acquired their angular momentum from tidal fields acting on nonspherical protogalaxies, an effect that would make the resulting intrinsic ellipticity quadratic in the tidal field: this is known as the *quadratic alignment model* (Pen et al., 2000). This model produces both E and B -mode II signals, but to leading order it predicts $P_{e\delta}(k) = 0$ and hence gives no GI signal (Hirata and Seljak, 2004). However, one should be cautious about this argument for several reasons, most importantly because there has not yet been any quantitative observational confirmation of the scale and configuration dependence predicted by the quadratic model, and additionally because perturbation theory arguments show that the non-linear evolution of the tidal field can generate a linear type alignment (Hui and Zhang, 2008). What is clear from observations is that the alignments of late-type galaxies on large scales, at least as measured by $w_{ge}(r_p)$, are consistent with zero and are certainly much less than for LRGs (Hirata et al., 2007; Mandelbaum et al., 2011).

Detailed assessments of the intrinsic alignment contamination have been made on the basis of SDSS, 2SLAQ, and WiggleZ observations of $w_{ge}(r_p)$ (Hirata et al., 2007; Mandelbaum et al., 2011; Joachimi et al., 2011). These studies show that for surveys of modest depth ($z_{\text{med}} \sim 0.7$) the GI contamination may be up to several percent of the expected cosmic shear signal for late-type galaxies if it is near current upper limits, and it could be tens of percent for LRGs. As one probes to higher source redshifts the level of contamination becomes increasingly uncertain, because there are not yet galaxy surveys at $z \geq 1$ that are capable of probing intrinsic alignments at interesting levels. The II contamination for broad redshift distributions is found to be much less than GI for linear alignment models.

Finally, we consider the methods used to remove intrinsic alignments. One starts with prevention: in the recent COSMOS analysis, Schrabback et al. (2010) suppressed II by throwing out the auto-power spectra of each of their redshift slices with itself, keeping only the cross-spectra. They also suppressed GI by not including LRGs in the foreground redshift slice, since LRGs contribute the most to the contamination. However, it is not clear that sample selection alone will provide sufficient GI rejection for Stage III surveys and beyond. Two general approaches to GI rejection have been proposed, model-independent and model-dependent.

The model-independent GI rejection method is to note that if we have narrow redshift bins, and denote the foreground and background slices by z_α and z_β respectively, then the GI signal depends only on intrinsic alignments at z_α (i.e., in the nearer bin). Then at fixed z_α the GI signal is proportional to

$$C_{EE}^{\alpha\beta}(l; GI) \propto \cot_K D_C(z_\alpha) - \cot_K D_C(z_\beta), \quad (136)$$

which becomes small if $z_\beta - z_\alpha$ is small. This is a different redshift dependence than the GG signal, which is a linear function of $\cot_K D_C(z_\beta)$ but remains finite as $z_\beta \rightarrow z_\alpha$. Hence it could be projected out (Hirata and Seljak, 2004) — e.g., one could take the $\alpha\beta$ shear cross-spectrum at several background bins and extrapolate to z_α . An alternative implementation of this idea is

⁵⁸ If one interprets the model of Eq. (134) as applying to the unweighted ellipticity field, then converting to a galaxy-weighted field introduces a B -mode. However it is much smaller than the E -mode signal and vanishes in the linear regime.

⁵⁹ This has been measured as the line-of-sight integral of the correlation function, $w(r_p)$ where r_p is the transverse separation, which contains the same information as the power spectrum.

nulling (Hirata and Seljak, 2004; Joachimi and Schneider, 2008, 2009), constructing a synthetic redshift slice by weighting of the different z_β whose window function

$$W_{\text{eff, syn}}[D_C(z_\alpha)] = \sum_{\beta} w_{\beta} W[D_C(z_\alpha), D_C(z_\beta)] = 0. \quad (137)$$

Clearly some of the weights w_{β} must be negative. This class of techniques assumes nothing about the physics of intrinsic alignments, but because of the extrapolations or negative weights it can amplify observational systematics, and to date it has not been successfully implemented on real data.

A model-dependent alternative, less demanding in terms of observational systematics, is to construct the 3×3 symmetric matrix of power spectra of the matter, galaxies, and intrinsic ellipticity,

$$\mathbf{P}(k) = \begin{pmatrix} P_{\delta} & P_{g\delta} & P_{e\delta} \\ P_{g\delta} & P_g & P_{eg} \\ P_{e\delta} & P_{eg} & P_e^{EE} \end{pmatrix} (k). \quad (138)$$

This has six free functions of wavenumber, of which one (P_{δ}) can be predicted from cosmological parameters. However, since the tidal field is determined by the matter distribution, if galaxy alignments are really determined by the tidal field then they should not additionally care where the other galaxies are: the conditional probability distribution $\text{Prob}(e|\delta, g) = \text{Prob}(e|\delta)$. In this case, and in the limit of a Gaussian field, one should have the restriction⁶⁰

$$P_{e\delta}(k) = \frac{P_{\delta}(k)}{P_{g\delta}(k)} P_{eg}(k). \quad (139)$$

This relation was assumed by the DETF in their WL parameter forecasts (Albrecht et al., 2006), and if valid it is very useful because it relates the GI contamination ($P_{e\delta}$) to theory (P_{δ}), GGL ($P_{g\delta}$), and galaxy-ellipticity correlations at the same redshift (P_{eg}). Unfortunately, its accuracy is unclear in the non-linear regime, since for non-Gaussian density fields, $\text{Prob}(e|\delta, g) = \text{Prob}(e|\delta)$ no longer implies Eq. (139); an investigation of this in simulations should be a high priority. Nevertheless, Eq. (139) may be usable if the GI correlation for late-type galaxies turns out to be far below current upper bounds, in which case even a crude correction could reduce it to below statistical error bars. Further discussions of this approach and an application to observational data may be found in Bernstein (2009), Joachimi and Bridle (2010) and Kirk et al. (2010).

Intrinsic alignments also represent a contaminant to GGL if the “lens” and “source” redshift distributions overlap; some of the “sources” may then be physically associated with the lens and show an alignment that is a result of galaxy formation physics rather than lensing (Bernstein and Norberg, 2002; Hirata et al., 2004). However, in this case the availability of good photo- z s solves the problem, since for GGL there are only II alignments, which can be eliminated by restricting cross-correlations to non-overlapping redshift slices. Consistency checks between GGL and cosmic shear may provide a useful route to diagnosing the impact of intrinsic alignments on the latter.

5.6.2. Theoretical uncertainties in the matter power spectrum*

An important systematic error in weak lensing is the prediction of the cosmic shear power spectrum, which – although far more theoretically tractable than galaxy clustering – is not free of uncertainty. WL gets most of its information from the non-linear regime, where the only way to accurately predict the power spectrum is using large N -body simulations. At the present time, most WL constraints have used physically motivated fitting formulas calibrated to N -body simulations (e.g., Peacock and Dodds, 1996; Smith et al., 2003), but these have limited accuracy because of the limited resolution and box size of the simulations and the limited ranges of cosmological parameters that have been explored. The situation has improved dramatically in recent years thanks to Moore’s law and the fact that the “interesting” region of parameter space has shrunk considerably. Much improved non-linear matter power spectrum calculations have been obtained from the “Coyote Universe” simulations (Heitmann et al., 2009; Heitmann et al., 2010; Lawrence et al., 2010). Given this progress, and given that the N -body problem is perfectly well-defined mathematically, we expect that the theoretical uncertainty in the power spectrum for pure dark matter models will not be a limiting systematic for WL.

The situation is more complicated when one goes beyond pure dark matter. Baryons make up $\sim 17\%$ of the matter in the universe, and on small scales they do not trace the dark matter. Hydrodynamic simulations can follow them, but one cannot hope to model the processes of cooling, star formation, metal enrichment and feedback from first principles. On quasilinear scales, $k \sim \text{few} \times 0.1h \text{ Mpc}^{-1}$, the largest uncertainty appears to come from clusters, where redistribution of the radial distribution of baryons affects the 1-halo contribution to the power spectrum. Observations of clusters – in particular measurement of cluster concentrations – may help to constrain this effect (Rudd et al., 2008). It has been proposed to either “self-calibrate” the cluster profile effect (Zentner et al., 2008) or incorporate information from cluster-galaxy lensing (Mandelbaum et al., 2008), although this has not yet been necessary for present cosmic shear experiments.

⁶⁰ This is a slightly more general relation than assuming that the galaxies are linearly biased with no stochasticity, in which case one could replace $P_{\delta}(k)/P_{g\delta}(k) \rightarrow 1/b$.

A second uncertainty is associated with the *missing baryon problem* – the fact that most of the baryons that should be in galaxy-sized halos (assuming a cosmic baryon:CDM ratio) are not observed in the stellar, HI, and molecular gas components. If these baryons have been ejected from the host halo, e.g. via galactic winds or AGN feedback, then they could reduce the matter power spectrum. These effects were discussed in an idealized “nightmare scenario” by Levine and Gnedin (2006); more recently, the detailed hydrodynamic simulations of van Daalen et al. (2011) have shown a suppression of the matter power spectrum by 1% at $k = 0.3h/\text{Mpc}$ and 10% at $k = 1h/\text{Mpc}$. These effects are large compared to the statistical errors of Stage IV WL experiments. Worryingly, van Daalen et al. (2011) find that the predictions for the matter power spectrum depend significantly on the treatment of star formation and AGN feedback in the simulations. In their simulations, AGN feedback has the effect of reducing the baryon content of the halos, consistent with X-ray observations of intrahalo gas: the matter power suppression quoted above is thus within the range of “reasonable” rather than “extreme/unrealistic” models.

Semboloni et al. (2011) show that the results of the simulations can be captured by a parameterized halo model for the baryons, so one may be able to use this approach to marginalize over uncertainties, but at the price of reducing the cosmological information derived from WL measurements on these scales. Moreover, their mitigation procedure involves tuning the halo model to the van Daalen et al. (2011) simulations. Therefore one should worry that the removal of baryonic physics-induced bias seen by Semboloni et al. (2011) might not be realized in practice, if the simulation captures the qualitative features of AGN feedback but does not quantitatively reproduce the correct functional form. Zentner et al. (2013) avoid this issue by fitting cosmic shear power spectra based on the van Daalen et al. (2011) simulations using a mitigation procedure tuned to the Rudd et al. (2008) simulations. However they find that this procedure, while successful on simulated Stage III (DES) survey data, is not adequate for the more ambitious task of Stage IV data analysis.

In summary, it is clear that better predictions for baryonic effects in the matter power spectrum, ancillary observations of baryonic gas to constrain the range of outcomes realized in the real universe, and optimal methods for incorporating these effects with minimal damage to cosmological constraints are critical areas for further investigation.

A final issue is the accuracy of the leading-order mapping from $P_\delta(k, z)$ to the shear power spectrum, Eq. (73). Next-order perturbation theory arguments (Krause and Hirata, 2010) suggest that the correction is small, only a few σ for Stage IV experiments. Ultimately, this correction should be computed with ray-tracing simulations that solve the full deflection equation.

5.7. Systematic errors and their amelioration: summary

Summarizing results from our earlier discussion, the principal systematic errors in weak lensing measurements are:

- *PSF correction and shape measurement biases* (Sections 5.5.2–5.5.5): For the typical case of a PSF of a similar size to the galaxy, the correction of the galaxy ellipticity for PSF effects is of order unity, and the desired accuracy is $< 10^{-3}$. This requires both very accurate knowledge of the PSF and appropriate algorithms to correct for it.
- *Redshift distribution uncertainties* (Section 5.4.3): Using source galaxies at a higher redshift increases the WL power spectrum, and hence there is a degeneracy between z_{source} and the inferred cosmological parameters. If the source redshift distribution (or distributions, in the case of a tomographic analysis using photometric redshifts) are not well-calibrated, there is a resulting error in the inferred cosmology.
- *Intrinsic alignments* (Section 5.6.1): The ellipticities of nearby galaxies may be correlated with each other due to formation in a common environment. This “*II* effect” adds to the observed shear power spectrum and represents a systematic error. There can also be cross-correlation of the intrinsic ellipticity of a nearby galaxy at $z = z_1$ with the lensing signal on a more distant galaxy at $z = z_2 > z_1$, since both depend on the tidal field at $z = z_1$. This latter “*GI* effect” contaminates all tomographic cross-power spectra and hence is more difficult to remove than *II*.
- *Matter power spectrum uncertainties* (Section 5.6.2): Predicting $P_m(k, z)$ from a set of cosmological parameters is a nontrivial task. This can now be done accurately for dark matter only cosmologies (assuming that the dark matter behaves as simple CDM), but on small scales the influence of baryonic physics (cooling, feedback, etc.) is difficult to model.

These errors, and the steps to remove them, are not independent – for example, marginalizing out the intrinsic alignment effects can amplify systematic errors in photometric redshifts (Bridle and King, 2007). The development of systematic error budgets and requirements for future surveys thus requires a global analysis of all of the statistical and systematic uncertainties and their possible degeneracies (Bernstein, 2009).

We have described numerous strategies for suppressing most of these effects, but a few features stand out. *First*, exquisite knowledge of the PSF must be achieved through some combination of good engineering (designing a stable telescope and instrument and putting it in the best possible environment), good choice of observing strategy (more dithers and repeat visits), and good algorithms (one needs to generate a homogeneous catalog with well-understood ellipticity errors and selection effects). *Second*, precise photo- z s over the entire range covered by the survey are desirable for characterizing the redshift distribution, and they are *required* if one is to even attempt a model-independent removal of intrinsic alignments – something that has not yet successfully been done. To achieve these photo- z requirements, one wants optical and near-IR photometry to distinguish Balmer/4000 Å breaks from Ly α breaks and spectroscopic samples that span the full range of the WL samples. Cross-correlation against large redshift surveys can be an important tool in photo- z calibration (Newman, 2008).

5.8. Advantages of a space mission

A space platform offers two critical advantages for weak lensing: (i) the availability of a small and stable PSF, and (ii) the low sky brightness in the near-IR, which allows deeper observations. For this reason, weak lensing has been highlighted as an important science objective for the *Euclid* and *WFIRST* space missions.

The small PSF enables the telescope to resolve many more galaxies (see Fig. 17). The space-based PSF size is normally determined by the diffraction limit: for an ideal Airy disk with an unobstructed circular aperture (off-axis telescope), the 50% encircled energy radius EE_{50} is $0.535\lambda/D$. This worsens for obstructed telescopes, reaching $1.25\lambda/D$ in the extreme case of blocking 25% of the area of the telescope entrance. Nevertheless, for typical λ (of order $0.8\ \mu\text{m}$ for a visible mission and $1.5\ \mu\text{m}$ for a near-IR mission) and reasonable telescope size ($D \geq 1.1\ \text{m}$) the EE_{50} radius is several times smaller than the typical $\sim 0.3\text{--}0.4$ arcsec from a good ground-based site. There are additional contributions to the PSF size – charge diffusion, the pixel tophat, aberrations, and pointing jitter – but on a space weak lensing mission these would be designed to be subdominant to diffraction.

A perhaps more important advantage is the *stability* of the PSF on a space mission, which allows for better characterization. The dominant contribution to a ground-based PSF is from atmospheric turbulence, which varies rapidly as a function of time and field position. This is eliminated in space. Moreover, contributions to the optical distortions from temperature variations and gravity loading can be reduced or (in the latter case) eliminated, particularly at the L2 Lagrange point, in a high Earth orbit during periods where shadow is avoided, and/or by using temperature-controlled optics. The three dominant contributions to PSF ellipticity on a space mission are (i) astigmatism, which causes the ellipticity of the PSF to vary with focus position; (ii) coma from misaligned optics, which at second order leads to ellipticity; and (iii) anisotropic pointing jitter. Of these, (i) and (ii) are functions of mirror positions, whose time and field position dependence are controlled by a small number of parameters. The pointing jitter is the least stable – it may be different in every exposure – but it has a controlled position dependence, no color dependence (at least with all-reflective optics), and can be monitored with the same fine guidance sensors used to point the telescope. Therefore a space mission offers the possibility of a PSF whose entire structure is determined by a small number of parameters that can be tracked as a function of time (Ma et al., 2008). This means it provides the best possibility of providing accurate PSF knowledge at every point in every exposure. The diffraction PSF has the unfortunate feature of having a size that is highly color-dependent ($\propto \lambda/D$), and in the presence of aberrations the ellipticity is color-dependent as well. However, in contrast to ground-based observations, the color dependence is controlled by the same wavefront error that determines the PSF morphology.

As already noted, optimal photo- z performance across the entire relevant range of redshifts can be obtained only with continuous coverage from blueward of the $4000\ \text{\AA}$ break (at $z = 0$) through the near-IR. In particular the Balmer/ $4000\ \text{\AA}$ feature is always detected except at very high redshift ($z > 3$), which reduces the number of objects with no breaks identified and provides cleaner separation of the Ly α vs. Balmer/ $4000\ \text{\AA}$ breaks. Collecting photometric data points in the bluer bands (starting at the $\sim 3200\ \text{\AA}$ atmospheric cutoff) is quite reasonable from the ground, and in this area there is no major advantage to a space mission. However, as we move to the red the space mission begins to look much more attractive. From the ground, the near-IR sky brightness (relevant for broadband imaging) is dominated by the decay of OH radicals, which are produced in vibrationally excited states at $\sim 90\ \text{km}$ altitude in the Earth's upper atmosphere (Leinert et al., 1998). The typical sky brightness rises from $18.5\ \text{mag AB arcsec}^{-2}$ in the Z band through $15.4\ \text{mag AB arcsec}^{-2}$ in the H band.⁶¹ In space in the $1\text{--}2\ \mu\text{m}$ region the dominant background is instead scattering of sunlight off of interplanetary dust particles (the “zodiacal light”). The typical brightness is $\sim 23\ \text{mag AB arcsec}^{-2}$ near the ecliptic poles and $21.5\ \text{mag AB arcsec}^{-2}$ in the ecliptic plane (Leinert et al., 1998). Thus in the H band the sky brightness is a factor of $300\text{--}1000$ lower in space, which means that a space telescope with even $\sim 1\ \text{m}^2$ collecting area would outperform the best ground-based telescopes in terms of near-IR imaging survey speed. Note also that because of the altitude of the OH emitting layer, airplane or balloon based platforms cannot access the low background available in space.

5.9. Prospects

The next several years promise to be very exciting for weak lensing as we enter the Stage III era. Two major wide-field ground-based imagers are coming online in the 2012/13 timeframe: the Dark Energy Camera⁶² (DECam) at CTIO in the Southern Hemisphere, and the Hyper Suprime Cam (HSC) on Subaru in the Northern Hemisphere (Miyazaki et al., 2006). These will provide great leaps in étendue, roughly $35\ \text{m}^2\ \text{deg}^2$ for DECam and $70\ \text{m}^2\ \text{deg}^2$ for HSC (vs. $8\ \text{m}^2\ \text{deg}^2$ for CFHT/MegaCam). The Dark Energy Survey (DES; using DECam) plans to observe $5000\ \text{deg}^2$ in the *grizy* bands over five years to ~ 24 th magnitude (10σ r band AB, shallower in y). The HSC plans a somewhat deeper and narrower survey, also in *grizy* ($2000\ \text{deg}^2$, 25 th magnitude 10σ). These projects together will measure the shapes of roughly 300 million galaxies and provide accurate photometric redshifts out to $z \sim 1.3$; this represents a $1\frac{1}{2}$ order of magnitude increase relative to current data sets. We expect that the use of several revisits and shape measurements in multiple bands, as well as incorporating the lessons from Stage II WL projects such as the CFHTLS and SDSS, will provide additional control over systematic errors in

⁶¹ See the WFCAM website, <http://casu.ast.cam.ac.uk/surveys-projects/wfcam>, and beware of Vega to AB conversions, which are significant in the near-IR.

⁶² <http://www.darkenergysurvey.org/>.

shape measurement. With careful attention to the source redshift distribution as well, and the photo- z capability provided by y -band imaging, the Stage III cosmic shear projects (DES and HSC) should reach the 1% level of precision on the amplitude σ_8 , as well as providing high- S/N measurements of its increase as a function of cosmic time. If the stochasticity issue turns out to be tractable, a similar level of precision will be reached by using galaxy–galaxy lensing to constrain the bias of galaxies and infer σ_8 indirectly from galaxy clustering.

The Stage III projects will also mark the completion of the research program of extrapolating the amplitude measured from the CMB forward in time and comparing it to the value of σ_8 measured via WL, and using the agreement of the amplitudes to measure $w(z)$ or test GR. There is a fundamental limitation to this type of comparison coming from reionization: while Planck will measure the CMB power spectrum to very high accuracy, one needs the optical depth τ to convert this into a normalization of the initial perturbations. This seems unlikely to be measured from the CMB E -mode to significantly better than 0.01 due to cosmic variance, foregrounds, and modeling uncertainties (Holder et al., 2003; Mortonson and Hu, 2008; Colombo and Pierpaoli, 2009).⁶³

The completion of the DES and HSC will not, however, mark the end of the road for cosmic shear. Because of the reionization degeneracy, the next step will be to make highly accurate measurements of the *shape* of the signal (dependence on scale and redshift) rather than its amplitude. This is a scientific matter of critical importance: if DES/HSC find a convincing deviation from the expected amplitude of low-redshift structure, one does not know whether this reflects a breakdown of GR at late times (a phenomenon that might be linked to cosmic acceleration) or something that happened to alter the growth of structure between $z \sim 10^3$ and $z \sim$ a few (such as massive neutrinos, though early dark energy would also be a possible explanation). What is needed next is the survey that measures the rate at which the growth of structure is suppressed internally to the low-redshift data. In our Section 8 forecasts we describe deviations from the GR-predicted growth rate using the parameter $\Delta\gamma$ (see Eqs. (15) and (44)), though other choices are possible. Even the Stage III surveys may make only preliminary measurements in this direction. Albrecht et al. (2009) estimated that DES could measure $\Delta\gamma$ to a 1σ accuracy of only 0.2 using the evolution of the WL signal, and our fiducial Stage III forecast in Section 8.3 yields $\sigma_{\Delta\gamma} = 0.148$ (see Table 9). Clusters calibrated by stacked weak lensing might enable a significantly tighter constraint (Section 8.4, Fig. 47), and redshift-space distortions could also enable good measurements of $\Delta\gamma$ (Section 7.2). It is not clear, however, that any method will achieve percent-level measurements of the rate of low redshift structure growth in the 2010 decade. Reaching this goal is one of the major drivers for Stage IV projects using WL and other probes of structure growth. It requires highly accurate, low-systematics shape measurements, of galaxies across a wide range of redshifts, including $z > 1$ where the angular radii of galaxies are small and the shape measurement challenges are immense.

Fortunately, the Stage IV WL experiments are already being planned, although their first light is not expected until ≥ 2020 . There are several approaches. One is the Large Synoptic Survey Telescope (LSST), which would feature a giant-*étendue* ($290 \text{ m}^2 \text{ deg}^2$) telescope dedicated to optical surveys of the Southern Hemisphere. Over a ten-year operating period, LSST would acquire hundreds of images of every point on the sky, which should go a long way toward identifying and removing any residual sources of PSF systematics. The incorporation of 6 bands (*ugrizy*) will likely lead to the best photometric redshifts practical from the ground over such a wide area. LSST will survey the entire extragalactic sky available from the south, perhaps $12,000\text{--}15,000 \text{ deg}^2$. The usable density of source galaxies, particularly at high redshift, is not certain as it depends on both advances in measuring galaxies small compared to the PSF and the quality of photometric redshifts in the notorious $1.3 < z < 2$ range. However, by achieving high S/N on almost every resolved galaxy, LSST is likely to represent the “ultimate experiment” for ground-based optical weak lensing.

An alternative approach is to exploit the small and stable PSF and availability of the near-IR bands from space, as planned for ESA’s *Euclid* mission (scheduled launch in 2020) and the NASA *WFIRST* mission (launch date to be determined; see below). *Euclid* will be a 1.2 m telescope with a 0.5 deg^2 focal plane that will survey $15,000 \text{ deg}^2$ in a parallel WL+BAO mode, with shape measurements performed in a broad red band ($0.55\text{--}0.92 \mu\text{m}$). *Euclid* will have only 3–4 observations of each galaxy, but this is predicted to be acceptable given the much greater stability of *Euclid*’s PSF relative to anything possible on the ground. At ~ 30 galaxies per arcmin², *Euclid* would measure shapes for ~ 1.6 billion galaxies. *Euclid* will also obtain near-IR photometry in three bands, which will be combined with ground-based optical photometry (from LSST where available) for photometric redshifts; the IR imaging is underresolved and will not be used for shape measurements. *WFIRST*, in the “DRM1” configuration described by Green et al. (2012), would be a 1.3 m, unobstructed (i.e., off-axis secondary) infrared space telescope capable of surveying $1400 \text{ deg}^2/\text{yr}$ in a combined WL+BAO mode (4-band imaging and slitless spectroscopy with resolution $\lambda/\Delta\lambda \approx 600$). The baseline WL program has 5–8 exposures in each of three shape measurement filters (J, H, and K), with an effective source density $n_{\text{eff}} = 40 \text{ arcmin}^{-2}$, and in a shorter wavelength filter (Y) that provides additional information for photometric redshifts. (LSST or other ground-based data are again required to provide optical photometry.) Multiple bands provide control of color-dependence of the PSF, and the degree of data redundancy is much higher than in *Euclid* because of the larger number of exposures and the ability to correlate shape measurements in different bands — the WL signal should be achromatic, but many systematics would not be. However, this greater redundancy, and the fact that the telescope is shared with other science programs, comes at the expense of what will likely be a smaller survey. The Green et al. (2012) design reference mission calls for 2.4 years of high-latitude imaging and spectroscopy (out of a 5-year mission

⁶³ In the more distant future, 21 cm measurements may improve our understanding of reionization to the point where this limitation is removed; however such an advanced understanding is not anticipated in the immediate future.

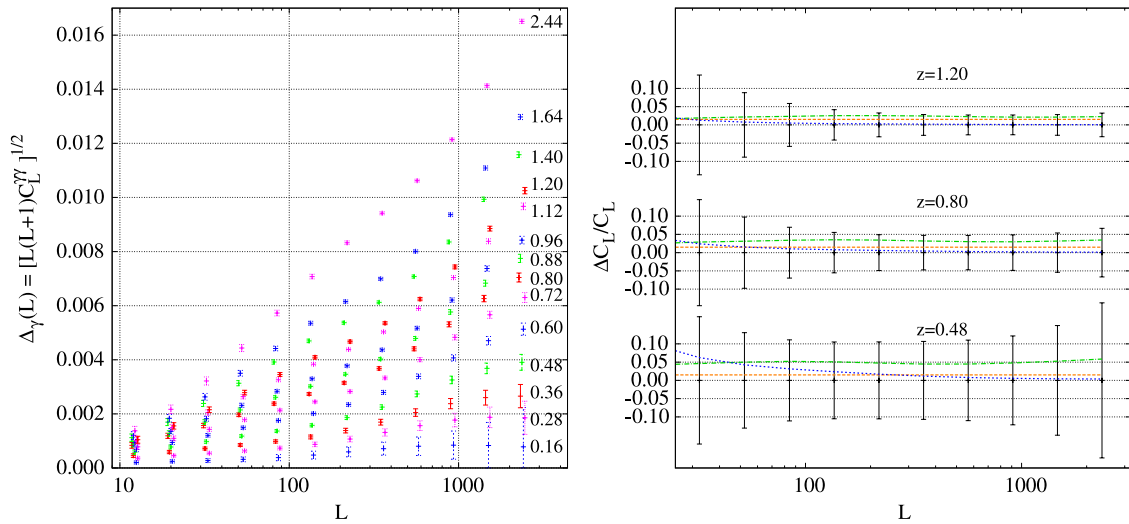


Fig. 19. (Left) The predicted cosmic shear power spectrum and statistical errors in each of 14 photo- z bins assuming a Λ CDM cosmological model with the parameters of Albrecht et al. (2009) and the survey parameters of our fiducial Stage IV WL program. (Right) Impact of systematic errors relative to statistical errors. For three of the photo- z bins from the left panel, error bars show the $\pm 1\sigma$ statistical errors (in bins of width $\Delta \log l = 0.2$ dex), with vertical offsets between bins for clarity. Solid, dashed, and dotted curves show, respectively, the effect of a multiplicative shear calibration bias of $2 \times 10^{-3} \times \sqrt{14}$ (orange), a mean photo- z offset of $2 \times 10^{-3} \times \sqrt{14}$ (green), or an additive shear bias of $3 \times 10^{-4} \times \sqrt{14}$ (blue) per z -bin. (The $\sqrt{14}$ is inserted here since an actual survey would combine all 14 bins.) The power in the additive shear bias was equally distributed in $\ln l$ for the purposes of this plot.

lifetime), which is sufficient to cover 3400 deg^2 .⁶⁴ As mentioned in Section 1.3, the transfer of two 2.4-m on-axis space telescopes from the U.S. National Reconnaissance Office (NRO) to NASA opens an alternative route to *WFIRST*, with initial ideas described by Dressler et al. (2012). While this implementation may not increase the survey area,⁶⁵ the superior angular resolution and light-gathering power of this hardware make it the only plausible option (at least in the optical-NIR bands) to reach source galaxy densities of ~ 70 galaxies/arcmin² over thousands of deg^2 . A detailed study of a 2.4-m implementation of *WFIRST* is ongoing, with a report planned for April 2013.

By the end of the 2020s, we should have a rich data set from all three of these projects (*LSST*, *Euclid*, and *WFIRST*) – and perhaps also from a large-scale radio interferometer such as the SKA. These surveys represent very different approaches to the Stage IV WL problem and will provide for multiple cross-checks of final results and internal cross-correlations of different data sets. The total number of galaxies with accurately measured shapes will probably reach ~ 4 billion, with most observed by at least two instruments and some with all three. Robust measurements of the suppression of the growth of structure to $\sigma_{\Delta\gamma} \approx 0.03$ – a factor of several better than Stage III – should then be possible (see Table 8), as well as tests of other possible deviations from Λ CDM that we have not yet imagined. But a great deal of work will be necessary before then to ensure that the systematic errors are controlled at this level.

For our forecasts in Section 8 we adopt a fiducial Stage IV WL program that assumes an effective source density $n_{\text{eff}} = 23 \text{ arcmin}^{-2}$ over 10^4 deg^2 , for a total of 8.3×10^8 shape measurements in 14 bins of photometric redshift (see Section 8.1 for details). We incorporate (and marginalize over) a multiplicative shear calibration uncertainty of 2×10^{-3} and a mean photo- z uncertainty of 2×10^{-3} ; these are aggregate values, and are larger by $\sqrt{14}$ in each photo- z bin. *LSST* and *Euclid* both anticipate a larger number of shape measurements and thus smaller statistical errors than our fiducial program. The baseline *WFIRST* DRM1 survey has a factor of two fewer shape measurements, but the mission’s technical requirement for shape systematics is a factor of two better. Thus, our fiducial program is conservative relative to the stated goals of all three experiments, though highly ambitious relative to the current state of the field.

For this fiducial Stage IV program, Fig. 19 shows the predicted shear power spectrum and 1σ statistical errors, in each of the 14 photo- z bins. In addition to these auto-spectra, the data allow measurements of $N_{\text{bin}}(N_{\text{bin}} - 1)$ cross-spectra among the bins, providing additional statistical power and tests for intrinsic alignment and other systematics. In a given photo- z bin, the errors in different l bins are independent. However, the errors from one photo- z bin to another are correlated because the same foreground structure can lens galaxies in multiple background redshift shells. We compare the statistical errors to the impact of cosmological parameter changes in Section 8.7. The aggregate statistical precision on the overall

⁶⁴ An additional 0.45 years would be devoted to an imaging and spectroscopic survey for supernovae.

⁶⁵ In wide-field ground-based surveys, an increase in telescope aperture, e.g. $2 \text{ m} \rightarrow 4 \text{ m}$, increases the étendue, resulting in a faster survey at the same seeing-limited resolution. For space-based surveys, the natural choice when receiving a larger telescope is to maintain the same sampling of the PSF (and hence the same f -ratio if the detector properties remain fixed), which results in each pixel subtending a smaller number of arcseconds. The étendue and hence survey speed to reach the same extended-source sensitivity are unchanged if the pixel count is held fixed, but the angular resolution is improved as $\sim \lambda/D$. This is of course an enormous advantage for weak lensing.

amplitude of the WL power spectrum, i.e., on a constant multiplicative factor applied to the auto- and cross-correlations in all photo- z bins, is $\approx 0.21\%$. The corresponding error on σ_8 , treated as a single parameter change, is about three times smaller because the power spectrum scales as σ_8^3 in the regime where it is best measured. The right panel compares the statistical errors in four representative photo- z bins to the effects of a multiplicative shear calibration bias of 2×10^{-3} , a mean photo- z bias of 2×10^{-3} , or an additive shear bias of 3×10^{-4} . We see that systematic errors of this magnitude would be smaller than the statistical errors in an individual photo- z bin, but the overall impact would be larger than the aggregate statistical errors. Thus, for our fiducial assumptions the Stage IV program is systematics limited rather than statistics limited, but not by an enormous factor. Even though our assumptions for this fiducial program are arguably conservative, it would achieve powerful constraints on the cosmic expansion history and the history of structure growth, as discussed in Section 8.

Is there a future for WL beyond Stage IV, both in terms of science motivation and technical capability? It seems unlikely that there would be a follow-on experiment that consists of simply a super-size LSST, *Euclid*, or *WFIRST*, particularly given that these experiments will come within a factor of a few of the cosmic variance limit at several tens of galaxies per arcmin². Rather the more distant future would have to involve new technology and a new science case not subject to the usual limitations. An example might be to look for lensing by primordial gravitational waves, which is not practical using galaxies as sources (Dodelson et al., 2003) but is at least in principle possible using highly-redshifted 21 cm radiation as the source, even for tensor-to-scalar ratios as low as 10^{-9} (Book et al., 2012). But we have now entered the speculative realm of post-2030 science and technology, where our ability to forecast the future is of limited reliability. We thus conclude our discussion of weak lensing here.

6. Clusters of galaxies

6.1. General principles

Galaxy clusters have a long and storied history as cosmological probes. They provided the first line of evidence for the existence of dark matter (Zwicky, 1933; Smith, 1936), and cluster mass-to-light ratio measurements suggested that the matter density in the universe was sub-critical ($\Omega_m < 1$) as far back as the early 1970's (see Gott et al., 1974, and references therein). The evidence for low Ω_m was substantially strengthened by baryon fraction measurements (White et al., 1993; Evrard, 1997), and by the discovery of massive clusters at high ($z \approx 0.8$) redshift (e.g., Henry, 1997; Eke et al., 1998; Donahue et al., 1998). Today, clusters remain an important cosmological tool, capable of testing cosmology in a variety of ways. Here we focus on cluster abundances as a tool for constraining the growth of structure in the matter distribution. Tight geometrical constraints from BAO and supernovae in turn yield tight predictions for structure growth assuming GR to be correct. Deviations from these predictions, revealed by weak lensing or by clusters, would constitute direct evidence for modified gravity as the driver of accelerated expansion. The excellent review by Allen et al. (2011) discusses other cosmological applications of clusters and examines recent cluster abundance results in detail (see also the earlier review by Voit, 2005); we summarize recent work in Section 6.2 but devote most of our attention to methods for Stage III and Stage IV cluster surveys. Other recent reviews in the field include Kravtsov and Borgani (2012), who review the physics of cluster formation with emphasis on the insights gained from hydrodynamic cosmological simulations, and Kneib and Natarajan (2011), who review strong and weak lensing by clusters.

The basic idea of cluster abundance studies is to compare the predicted space density of massive halos (Fig. 1) to the observed space density of clusters, which can be identified via optical, X-ray, or CMB observables that should correlate with halo mass. In optical searches, the basic observable is the richness, the number of galaxies in a specified luminosity and color range within a fiducial radius (typically taken to be the estimated virial radius of the halo). In X-ray searches, the luminosity L_X , temperature T_X , and inferred gas mass M_{gas} all provide observable indicators of halo mass. In CMB searches, clusters can be characterized by the central or integrated value of the flux decrement Y_{SZ} produced by the Sunyaev-Zel'dovich (1970; hereafter SZ) effect: Compton up-scattering of CMB photons by hot electrons in the intracluster medium. The product $Y_X = T_X M_{\text{gas}}$ defines an X-ray observable that should scale with Y_{SZ} , and numerical simulations predict that Y_X tracks halo mass more closely than temperature or gas mass alone (Kravtsov et al., 2006).

The first applications of this approach were made by Peebles et al. (1989) and Evrard (1989), who used observed cluster abundances to argue against an $\Omega_m = 1$ CDM cosmological model (see also Kaiser, 1986b, 1991, who compared the observed evolution of X-ray clusters to predictions of a self-similar model with $\Omega_m = 1$). Halo abundance is sensitive to the amplitude of the matter power-spectrum σ_8 and the matter density Ω_m . The mean matter content in a sphere of comoving radius $8h^{-1}$ Mpc is $\approx 2 \times 10^{14} M_\odot$. Thus, cluster-mass halos form from the gravitational collapse of fluctuations on about this scale, and their abundance naturally tracks σ_8 . Moreover, because the total mass of each collapsed volume scales linearly with Ω_m , the number of halos at a given mass can be raised either by raising σ_8 , so that fluctuations are larger, or by raising Ω_m , so that the mass associated with each perturbation is larger. The quantity most tightly constrained by cluster abundances is a combination of the form $\sigma_8 \Omega_m^q$, with $q \approx 0.4$ (White et al., 1993). The degeneracy between σ_8 and Ω_m can be broken by measuring abundances at a variety of masses. This argument also holds at higher redshift, so one can think of cluster abundances as primarily constraining $\sigma_8(z) \Omega_m^q$, modulated by the additional cosmological dependence of the volume element $dV_C(z) \propto D_A^2 H^{-1} d\Omega dz$, and by any intrinsic dependence of cluster observables on the distance-redshift relations. Note that, as elsewhere in this article, Ω_m always refers to the $z = 0$ value unless $\Omega_m(z)$ is written explicitly.

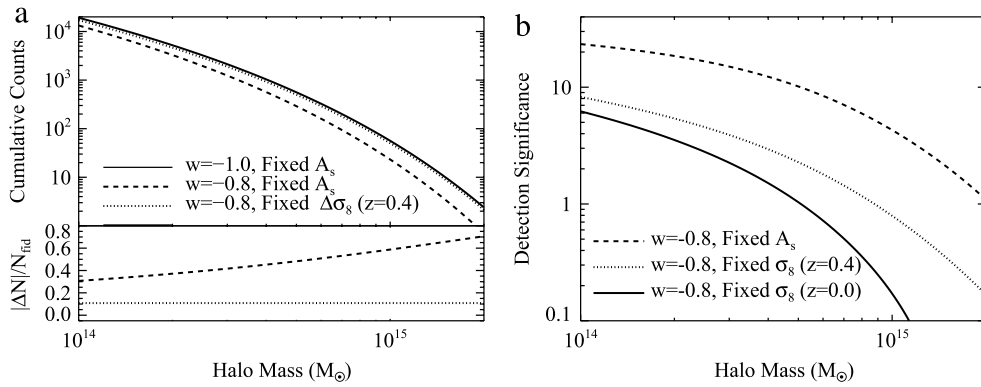


Fig. 20. (a) Cumulative halo counts as a function of limiting mass for a 10^4 deg^2 survey in a redshift slice $z = 0.4 \pm 0.05$. The solid line shows the fiducial model from Table 1. The dashed line corresponds to $w = -0.8$ with the amplitude of the primordial matter power spectrum held fixed. The dotted line has $w = -0.8$, but holds $\sigma_8(z = 0.4)$ fixed. Residuals relative to the fiducial model are shown in the bottom panel. The small, nearly constant offset of the dotted line is sourced by the dark energy dependence of the comoving volume element dV_c . (b) The significance with which this hypothetical halo sample could distinguish the fiducial model from the alternatives in panel (a) as a function of mass threshold, using the statistical error of Eq. (140). The dot-dashed line shows an additional model in which $\sigma_8(z = 0)$ is held fixed. Even though the high mass end of the halo mass function depends most strongly on cosmology, the statistical power of the cluster abundances is dominated by the low mass end because of the much lower measurement errors.

We illustrate these ideas in Fig. 20. Panel (a) shows the expected halo abundance as a function of the limiting mass in a redshift slice $z = 0.35\text{--}0.45$ subtending 10^4 deg^2 . Plots for other redshift slices are qualitatively similar. For this plot, and throughout the rest of this section unless otherwise noted, halo mass refers to the mass enclosed within a sphere whose mean interior overdensity is $\Delta = 200$ relative to the mean matter density of the universe. The solid line is the abundance in our fiducial model (see Table 1), while the dashed line shows the corresponding halo abundance when setting $w = -0.8$ and holding Ω_m and the primordial power spectrum amplitude $A_s(k = 0.002 \text{ Mpc}^{-1})$ fixed. Unlike in Fig. 1, this choice does not leave the CMB observables fixed, but it better illustrates the intrinsic sensitivity of cluster abundances. For $w = -0.8$, dark energy becomes dynamically important earlier than for $w = -1$, suppressing growth and lowering $\sigma_8(z = 0.4)$ from 0.66 to 0.62. This sharply reduces the halo abundance, by $\approx 30\%$ at a threshold of $10^{14} M_{\odot}$ and by $\approx 60\%$ at $10^{15} M_{\odot}$. If we raise A_s so as to hold $\sigma_8(z = 0.4)$ fixed, then the $w = -1$ and $w = -0.8$ models differ by a nearly constant factor of 1.1, which is the ratio of the comoving volumes of the redshift slices in the two cases. This volume effect is clearly weaker than the overall scaling of halo abundances with σ_8 .

While the mean halo abundance becomes more sensitive to $\sigma_8(z)$ at higher masses, the statistical precision with which one can measure $\sigma_8(z)$ decreases with increasing mass because of the larger Poisson fluctuations for rarer clusters. This point is illustrated in Fig. 20b, which shows the statistical significance at which a 10^4 deg^2 , $z = 0.35\text{--}0.45$ cluster survey would distinguish the models shown in panel (a). For reference, we also show the case in which σ_8 is held fixed at $z = 0$, which reduces model differences because the growth and volume element effects act in opposite directions. We discuss statistical errors in cluster abundances, including the role of sample variance, in Section 6.3.1. The key conclusion from Fig. 20b is that lower mass clusters allow stronger model discrimination.

Cluster cosmology requires making an explicit link between the theoretically predicted population of halos as a function of mass and an observed population of clusters. This problem is complicated by the fact that the halo population is usually characterized using dark matter simulations, whereas clusters are identified using baryonically-sourced signatures such as the presence of galaxy overdensities, extended X-ray emission, or SZ decrements (see Section 6.3.2). The lower mass limit probed by cluster abundance experiments is partly set by the detection thresholds intrinsic to each method, but also by the difficulty of characterizing the relation between low mass halos and poor clusters. Different researchers adopt varying definitions of halos and of clusters. Within a reasonable range, such variation is acceptable, provided each study is self-consistent and the halo–cluster relation is accurately characterized. In recent years, numerical studies have mostly shifted from the friends-of-friends algorithm used in earlier work (e.g., Efstathiou et al., 1988) to spherical overdensity definitions (e.g., Tinker et al., 2008), thus avoiding the tendency of the friends-of-friends method to occasionally link distinct mass concentrations via narrow bridges (see More et al., 2011, and references therein for a more detailed discussion). Halo boundaries are typically drawn at overdensities $\Delta \approx 100\text{--}500$, where clusters are in approximate dynamical equilibrium and where mass predictions are fairly robust to baryonic physics. The overdensity Δ can be quoted relative to the mean matter density of the universe at the cluster redshift or relative to the critical density at that redshift. In this section, we will adopt $\Delta = 200$ with respect to the mean density as our definition unless otherwise specified.

The principal challenge to precision cosmology with clusters is not cluster identification *per se*, but the accurate calibration of the relation between cluster observables (e.g., richness, X-ray luminosity, SZ decrement) and halo masses. Fig. 21 illustrates this point by flipping the x and y axes of panel (a) in Fig. 20, thus plotting the mass threshold at fixed cluster abundance for the different cosmological models. Changing from $w = -1$ to $w = -0.8$ while holding A_s fixed changed the predicted abundances by 30%–60%, but the corresponding change in mass threshold is only about 20%. For fixed $\sigma_8(z = 0.4)$,

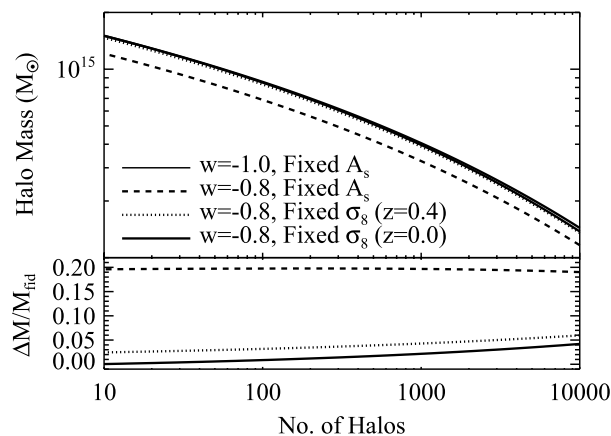


Fig. 21. Halo mass thresholds as a function of cumulative number counts, i.e. flipping the x and y axes of Fig. 20a. The x-axis shows the number of halos predicted in a 10^4 deg^2 survey in a redshift slice $z = 0.4 \pm 0.05$. The lower panel shows the fractional change in mass threshold relative to the fiducial cosmological model.

the 15% change in abundance corresponds to a 2.5%–6% change in mass threshold. These, then, are the levels of accuracy in mass calibration that must be attained to distinguish between the two $w = -0.8$ models and our fiducial $w = -1$ model. The issue of mass calibration will arise repeatedly in this section, especially in Sections 6.3.3 and 6.4.3.

In principle, cluster abundances are sensitive to $\sigma_8(z)$, Ω_m , and the comoving volume element dV_C , as well as any inherent sensitivity of the relation between cluster mass and cluster observables on the distance–redshift relations. To simplify our discussion, we will usually assume that a combination of other data sets (CMB, SN, BAO, WL, etc.) will determine both Ω_m and $dV_C(z)$ at higher precision than that achievable from cluster abundances. Consequently, we will focus on the sensitivity of cluster abundances to $\sigma_8(z)$ while holding Ω_m , $dV_C(z)$, and the angular and luminosity distances fixed. In practice, we expect our assumption should be a good one as far as the comoving volume element and the distances are concerned. However, the sensitivity attainable with clusters is high enough that holding Ω_m fixed may be incorrect in detail. We will discuss this point in Section 6.6 and again in Section 8.4.

Many cluster cosmology papers quote masses in $h^{-1} M_\odot$ because observational mass estimates (and, to some extent, theoretical predictions) scale inversely with h . However, at non-zero redshift many other parameters also come into play, and h is itself one of the parameters constrained by dark energy experiments. Thus, we have elected to quote masses in M_\odot rather than $h^{-1} M_\odot$. In a similar vein, we will switch most of our subsequent discussion from σ_8 to $\sigma_{11, \text{abs}}$, the rms fluctuation on a scale of $R = 11 \text{ Mpc}$ (equal to σ_8 for $h = 0.727$). For some observables (e.g., the X-ray estimated gas mass M_{gas} , the inferred cluster mass is sensitive to the angular diameter distance $D_A(z)$ and this dependence itself provides useful cosmological constraints; this point is discussed by Allen et al. (2011) but we will not address it further here. Our primary focus is the statistical precision with which cluster abundances constrain $\sigma_{11, \text{abs}}(z)$, and the level at which systematic uncertainties must be controlled to achieve these statistical limits. In Section 6.6 we compare the precision potentially attainable with clusters to forecasts (described in Section 8) from fiducial Stage III and Stage IV CMB+SN+BAO+WL programs.

6.2. The current state of play

Most cluster cosmology studies of the past decade have been based on X-ray catalogs, with typical cluster samples numbering in the several tens to few hundreds of clusters. The vast majority of these catalogs rely on *ROSAT* data – either from the *ROSAT* All-Sky Survey (RASS; Voges et al., 1999) or from serendipitous detections in pointed observations – though there are also samples selected based on *XMM-Newton* and *Chandra* imaging. Table 4 summarizes some of the main X-ray catalogs that have been employed in these studies. The recently approved XXL survey will add $\approx 50 \text{ deg}^2$ of imaging, contributing ≈ 600 clusters out to $z = 1$ and above. The next big step forward for X-ray samples is the *eROSITA* mission, which should identify $\approx 80,000$ galaxy clusters at high confidence (see Section 6.5).

The largest existing cluster samples are optically selected, using either spectroscopic or photometric galaxy catalogs. The former benefit from much finer spatial resolution along the line of sight. They tend to be shallow, with typical $z \lesssim 0.2$ (Merchán and Zandivarez, 2002; Kochanek et al., 2003; Miller et al., 2005; Merchán and Zandivarez, 2005; Berlind et al., 2006; Yang et al., 2007; Li and Yee, 2008; Blackburne and Kochanek, 2012), though high redshift spectroscopic catalogs do exist (Gerke et al., 2005; Coil et al., 2006). Photometric cluster catalogs hail back as far as the original Abell (1958) catalog, which contained upwards of 2500 systems and served as the primary basis of cluster studies for decades. Though many recent photometric catalogs have focused on narrow but deep survey data ($z \lesssim 1$, e.g., Gonzalez et al., 2001; Gladders and Yee, 2005; Milkeraitis et al., 2010; Adami et al., 2010), the SDSS has led to the publication of several moderately deep ($z \lesssim 0.5$) and wide catalogs, which can contain upwards of 50,000 clusters (e.g. Koester et al., 2007; Wen et al., 2009; Hao

Table 4
X-ray cluster catalogs.

Catalog/Reference	Type of survey	No. of clusters	Redshift limit
BCS (Ebeling et al., 2000)	Wide/shallow	107	0.3
NORAS (Böhringer et al., 2000)	Wide/shallow	378	0.3
HIFLUGCS (Reiprich and Böhringer, 2002)	Wide/shallow	63	0.2
WARPS (Perlman et al., 2002)	Narrow/deep	34	0.8
SHARC (Burke et al., 2003)	Narrow/deep	48	0.7
160 deg ² (Mullis et al., 2003)	Narrow/deep	201	0.7
REFLEX (Böhringer et al., 2004)	Wide/shallow	447	0.3
400 deg ² (Burenin et al., 2007)	Narrow/deep	287	0.8
MACS (Ebeling et al., 2010)	Wide/shallow	34	0.6
MCXC (Piffaretti et al., 2011)	Compilation	1783	0.8
XCS (Lloyd-Davies et al., 2011)	Narrow/deep	1022/3669 ^a	0.8

Note: All cluster catalogs included above are drawn from *ROSAT* data, except for XCS, which is a serendipitous cluster search in *XMM-Newton* archival data (see Mehtens et al., 2012, for the first data release). Wide/shallow survey catalogs refer to cluster searches in the *ROSAT* All-Sky Survey (RASS), whereas narrow/deep catalogs are drawn from pointed *ROSAT* or *XMM-Newton* observations. MCXC is a compilation of various X-ray cluster catalogs. The characteristic high redshift limit shown is not the redshift of the highest redshift cluster in the sample, but rather a redshift that contains $\gtrsim 90\%$ of the galaxy clusters. The highest cluster redshifts can be significantly higher than the redshift quoted, as expected for flux limited surveys.

^a 1022 is the number of galaxy clusters with ≥ 300 photons, allowing for T_x estimates. 3669 is the number of 4σ cluster candidates.

et al., 2010; Szabo et al., 2011). Extensions that reach out to $z \approx 1$ over 1000 deg² or more from current or near future photometric surveys – such as RCS-2, DES, Pan-STARRS, and HSC – will expand samples to the hundreds of thousands.

One limiting factor that affects these optical cluster finding experiments is that the 4000 Å break in the spectrum of early-type galaxies shifts into the near-IR at $z \approx 1$, making optical detection challenging above this redshift. This difficulty can be overcome with IR adaptations of optical cluster finding techniques. Today, there are two independent efforts aiming to detect galaxy clusters using IR data: the IRAC Shallow Cluster Survey (ISCS; Eisenhardt et al., 2008) and the *Spitzer* Adaptation of the Red-Sequence Cluster Survey (SPARCS; Wilson et al., 2006). Both surveys have discovered and spectroscopically confirmed candidate galaxy clusters out to redshift $z \lesssim 1.5$ (e.g., Stanford et al., 2005; Brodwin et al., 2006; Eisenhardt et al., 2008; Muzzin et al., 2009; Wilson et al., 2009; Demarco et al., 2010), with some recent detections reaching $z \lesssim 2$ (Stanford et al., 2012; Zeimann et al., 2012). Additionally, some of these systems have also been detected in X-rays and/or SZ (Brodwin et al., 2011; Andreon and Moretti, 2011; Brodwin et al., 2012). These early results are encouraging and suggest that IR detection of high redshift clusters can play an important role in the future of cluster cosmology.

While detections of the SZ effect in known galaxy clusters date back as early as 1976 (Gull and Northover, 1976), it is only recently that instrumentation advances have made large scale SZ searches feasible. The first three successful cluster SZ surveys – using the South Pole Telescope (SPT), the Atacama Cosmology Telescope (ACT), and the *Planck* satellite – are all currently ongoing. All three projects have released SZ-selected cluster samples (Vanderlinde et al., 2010; Marriage et al., 2011; Planck Collaboration et al., 2011a; Williamson et al., 2011; Reichardt et al., 2013). These samples tend to be of very massive clusters (see Fig. 27) and, in the case of ACT and SPT, extend to $z \approx 2$, with the upper limit set by the lack of massive galaxy clusters above this redshift. For ACT and SPT, this redshift coverage is limited only by the abundance of such massive objects at high redshift. *Planck* is limited in part by its relatively large beam, but it has the important benefit of being an all sky survey, which results in a larger cluster yield overall. Based on the sensitivity estimates shown in Fig. 27, we anticipate ~ 700 clusters in 2500 deg² for SPT and $\sim 11,000$ over the full sky for *Planck*. We emphasize, however, that these numbers can easily shift by factors of ~ 2 – 3 depending on the signal-to-noise cut adopted for cluster identification. In contrast to optical and X-ray techniques, there is not likely to be a major leap forward in SZ capabilities in the next few years, so the SPT, ACT, and *Planck* samples will probably remain the largest SZ cluster samples available for the next decade. That said, the limiting masses of SZ cluster samples will go down as these and other facilities conduct deeper surveys focused on CMB polarization (e.g., ACTPol and SPTPol).

Existing cluster cosmology constraints have come primarily from X-ray data (see, e.g., Henry, 2000; Reiprich and Böhringer, 2002; Schuecker et al., 2003; Allen et al., 2003; Pierpaoli et al., 2003), reflecting the fact that X-ray observables can be related to mass via simulations and/or analytic approximations and by hydrostatic modeling for well observed clusters. All three of the most recent X-ray analyses yielded tight, consistent cosmological constraints, which can be summarized as $\sigma_8(\Omega_m/0.25)^{0.45} = 0.80 \pm 0.03$ (Henry et al., 2009; Vikhlinin et al., 2009; Mantz et al., 2010). Cosmological analyses from optical samples have typically been less constraining because of uncertain mass calibration (see, e.g., Bahcall et al., 2003; Gladders et al., 2007; Wen et al., 2010). However, recent work that uses stacked weak lensing analysis for mass calibration (Johnston et al., 2007; Mandelbaum et al., 2008; Sheldon et al., 2009) has allowed optical samples to achieve the same level of precision as X-ray samples (Rozo et al., 2010), with comparable levels of systematic error. Constraints from SZ selected samples are emerging (Vanderlinde et al., 2010; Sehgal et al., 2011; Reichardt et al., 2013), and while they are currently

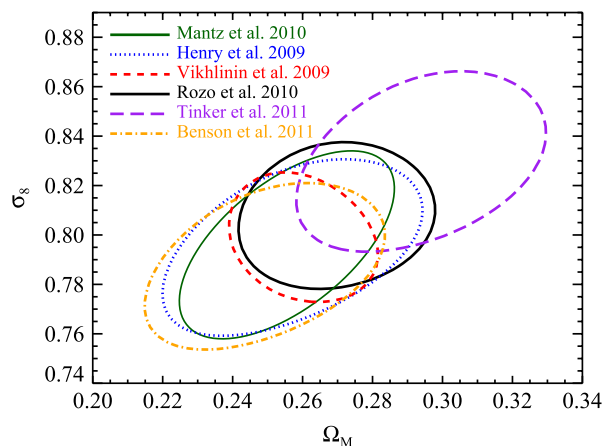


Fig. 22. Comparison of the 68% confidence regions derived from galaxy cluster abundances and WMAP CMB data by various groups. The first three error ellipses – using quoted uncertainties from Mantz et al. (2010), Henry et al. (2009), and Vikhlinin et al. (2009) – all come from X-ray selected cluster samples. The Rozo et al. (2010) ellipse comes from an optically selected cluster sample with stacked weak lensing mass calibration. The Tinker et al. (2012) constraint uses the same optical clusters and mass calibration, but relies on galaxy clustering and mass-to-number ratios to derive cosmological constraints, making it essentially an independent cross-check. The Benson et al. (2013) ellipse comes from the SPT selected cluster sample.

weak because of the relatively large uncertainty in the SZ-mass scaling relation, the extensive follow-up campaigns that are currently underway will reduce this scaling uncertainty and bring these constraints to a level comparable to those from optical and X-ray cluster catalogs (e.g. High et al., 2012; Hoekstra et al., 2012; Planck Collaboration, 2013; Rozo et al., 2012d).

Regardless of the wavelength of choice, current cluster abundance constraints are limited not by the number of clusters but by uncertainty in mass calibration. Fig. 22 shows the cluster abundance constraints from several recent analyses. Because the current X-ray and optical mass calibrations are fundamentally different (hydrostatic vs. weak lensing), the excellent agreement illustrated in Fig. 22 provides a strong test of systematic uncertainties. However, the results from the Planck Collaboration et al. (2011b) have sounded a cautionary note, as the optical mass estimates used to derive cosmological parameters in Rozo et al. (2010) appear to be inconsistent with SZ data (see also Draper et al., 2012). Biesiadzinski et al. (2012) have attributed this inconsistency to miscentering, while Angulo et al. (2012) point out the importance of systematics covariance. Rozo et al. (2012c,b,a) argue that the optical, X-ray, and SZ data can be reconciled by considering, in addition to these effects, the systematics of X-ray temperature measurements indicated by the offsets among estimates from different groups, and departures from hydrostatic equilibrium at the level predicted by hydrodynamic cosmological simulations (e.g., Nagai et al., 2007). Regardless of how this issue is ultimately resolved, it is clear that further tightening cosmological constraints will require a significant improvement in our ability to estimate cluster masses.

On this last count, we note that Fig. 22 also includes cosmological constraints from an analysis by Tinker et al. (2012) that does not rely on cluster abundances. Tinker et al. (2012) use a halo occupation model (see Section 2.3) fit to SDSS galaxy clustering, which yields a prediction for the mass-to-number ratio of clusters⁶⁶ as a function of σ_8 and Ω_m . While this analysis uses the same weak lensing mass calibration as Rozo et al. (2010), the method is less sensitive to the mass scale and is entirely independent of abundance uncertainties, making it a largely independent measurement and a powerful systematics cross-check. The same approach can be adapted to future, deeper photometric surveys. We also note that stacked weak lensing measurements for clusters can be extended far beyond the virial radius (Sheldon et al., 2009), into the regime where they measure the large scale cluster-mass cross-correlation function, and that these large scale measurements can also be used to constrain cosmological parameters (Zu et al., 2013).

6.3. Observational considerations

6.3.1. Expected numbers and cosmological sensitivity

Fig. 23a shows the expected cluster counts in our fiducial cosmological model for a variety of limiting masses, as a function of the limiting redshift z of a 10^4 deg^2 survey. (Note that these are lower limits on mass but upper limits on redshift.) Panel (b) shows number counts in redshift bins of width ± 0.05 ; e.g., at $z = 0.15$, we show the halo counts in the redshift bin $[0.1, 0.2]$. We maintain this redshift binning convention throughout. Together, these two figures give a broad-brush sense for the typical sample sizes and redshift distribution of galaxy clusters as a function of limiting mass and redshift.

Assuming halo masses can be adequately measured, the statistical error in cluster abundances is the sum in quadrature of Poisson noise and sample variance (Hu and Kravtsov, 2003),

$$(\Delta N)^2 = N + \bar{b}^2 N^2 \sigma^2(V). \quad (140)$$

⁶⁶ Analogous to mass-to-light ratio, but with galaxy number instead of integrated luminosity.

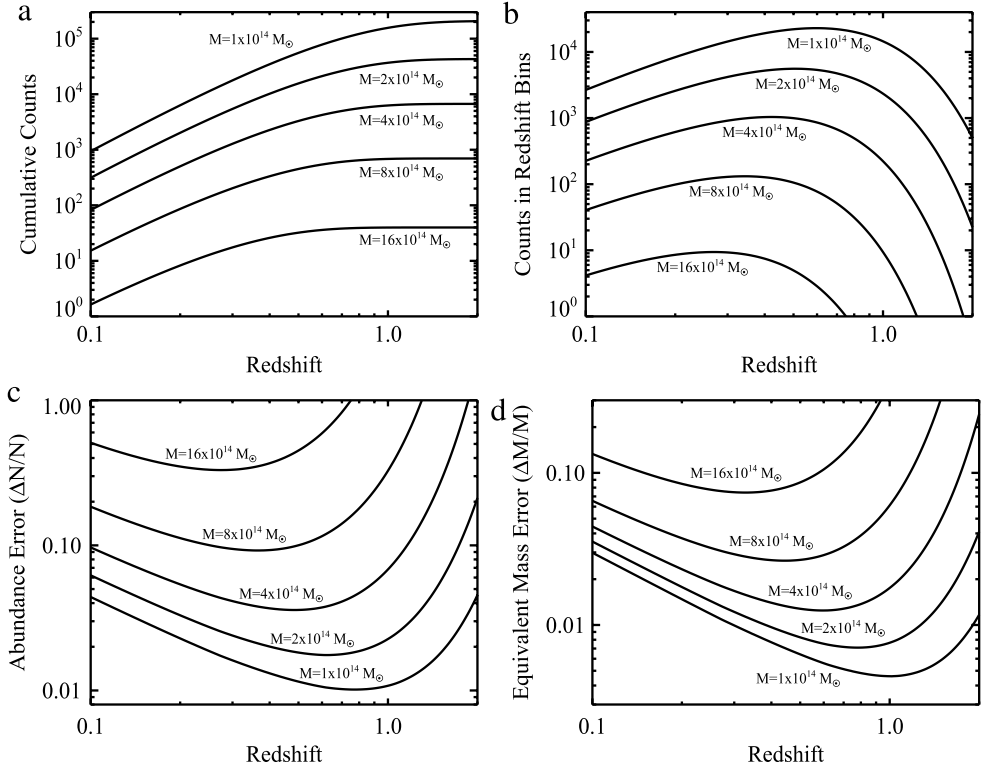


Fig. 23. (a) Cumulative halo number counts above the indicated mass thresholds M as a function of the limiting survey redshift. We assume the fiducial cosmological model from Table 1, and survey area of 10^4 deg^2 . (b) Counts above the mass threshold in redshift bins $z = z_c \pm 0.05$. (c) Statistical error in the number of clusters above the mass threshold from Eq. (140), again in redshift bins $z = z_c \pm 0.05$. (d) The mass accuracy required to ensure that cosmological constraints are limited by the statistical precision in the number of galaxy clusters rather than by uncertainties in mass estimation.

Here, N is the mean number of halos in the volume of interest, \bar{b} is the mean bias of the halos, and $\sigma^2(V)$ is the variance of the matter density field over the survey volume.⁶⁷ Fig. 23c shows the fractional error $\Delta N/N$ for the fiducial model, again for redshift bins $z = z_c \pm 0.05$ where z_c is the central redshift of the bin. Sample variance becomes larger than Poisson variance below a transition mass $\sim 4 \times 10^{14} M_\odot$ at $z = 0.1$ and $\sim 10^{14} M_\odot$ at $z = 1$. However, the statistical error is never more than a factor ~ 2 above the $N^{-1/2}$ Poisson expectation (see Fig. 26), and total statistical errors should scale with survey area roughly as $(A/10^4 \text{ deg}^2)^{-1/2}$. For any mass threshold the statistical error first decreases with redshift, as the number of clusters grows with the increasing comoving volume per Δz . This trend flattens when the clusters become exponentially rare, at which point further increase in redshift leads to a precipitous drop in the number of clusters and a corresponding rise in Poisson errors. These competing effects lead to the characteristic U-shape of the curves in Fig. 23c.

Fig. 23d converts these statistical abundance errors to equivalent errors in mass by dividing $\Delta N/N$ by the logarithmic slope of the cumulative halo mass function, $\alpha = -d \ln N/d \ln M$, which ranges between 2 and 5 depending on redshift and mass. While observational samples are not thresholded exactly in mass, the sensitivity of cluster abundances to an overall shift in the mean mass at fixed observable is well captured by this heuristic argument. In order for clusters to saturate the statistical limit in the abundances, the uncertainty in mass calibration must be smaller than this $\Delta M/M$. For a 10^4 deg^2 survey and $M \geq 8 \times 10^{14} M_\odot$, a mass accuracy of 3%–10% (depending on z) suffices. By $M \approx 2 \times 10^{14} M_\odot$, however, the accuracy requirement has sharpened to $\lesssim 1\%$. (This last number agrees well with the more detailed analysis of Cunha and Evrard (2010) for a mass threshold of $10^{14.2} M_\odot$; see in particular the top panels in their Fig. 2.) Achieving such accuracy is a tall order, and current studies are clearly limited by the systematic uncertainty in cluster masses rather than abundance statistics. Note that the required accuracy scales roughly as $(A/10^4 \text{ deg}^2)^{-1/2}$, and it applies to the overall mass scale (i.e., the mean of the mass–observable relation) rather than the mass of any individual system.

Fig. 24 translates the errors on cluster abundance from Fig. 23 to errors on the matter power spectrum amplitude $\sigma_{11,\text{abs}}(z)$, again for a 10^4 deg^2 survey with $z = z_c \pm 0.05$ bins. For simplicity, we assume that Ω_m , the comoving volume element $dV_c(z)$, and the power spectrum shape are perfectly known from independent data (CMB+SN+BAO+WL), so that $\sigma_{11,\text{abs}}(z)$ is the single cosmological parameter controlling the cluster abundance. As discussed in Section 6.1, if the uncertainty in Ω_m is non-negligible, then it is the combination $\sigma_8(z)\Omega_m^q$ that is constrained instead. Panel (a) shows the case

⁶⁷ For example, in our fiducial cosmology at $z = 0.6$, the matter variance in a volume of $\Delta z = 0.1$ and area $10,000 \text{ deg}^2$ is $\sigma(V) \approx 0.2\%$, and the mean halo bias is ≈ 3.0 and ≈ 5.7 for mass thresholds of $10^{14} M_\odot$ and $4 \times 10^{14} M_\odot$, respectively.

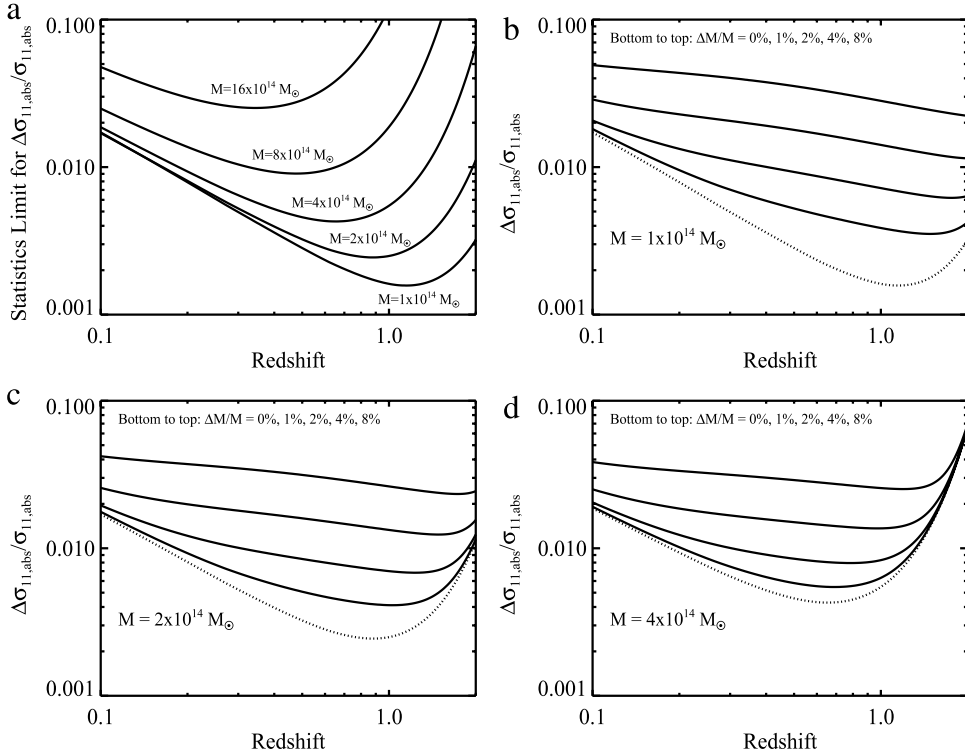


Fig. 24. (a) Statistical error on $\sigma_{11,\text{abs}}(z)$ as a function of redshift, in redshift bins $z = z_c \pm 0.05$, for different mass thresholds as labeled. We assume a 10^4 deg^2 survey area, and the fiducial cosmological model. We also assume that Ω_m , the shape of the matter power spectrum, and the comoving volume element dV_c are perfectly known from independent data (CMB+SN+BAO+WL). Panels (b)–(d) refer to specific mass thresholds as labeled. In each panel the solid curves show the effect of different mass calibration uncertainties as labeled while the dotted curve assume the perfect mass calibration values (i.e., number statistics limited) from panel (a). For reference, the uncertainty in $\sigma_{11,\text{abs}}(z)$ that we forecast for a fiducial CMB+SN+BAO+WL program is $\sim 1\%$ for Stage IV data sets and $\sim 2\%$ – 3% for Stage III data sets (see Sections 6.6 and 8.4).

where mass calibration errors are negligible. The errors on $\sigma_{11,\text{abs}}(z)$ roughly track the abundance errors $\Delta N/N$ in Fig. 23, but because the sensitivity of the abundance to $\sigma_{11,\text{abs}}(z)$ at fixed mass increases with increasing redshift, the best constraint on $\sigma_{11,\text{abs}}(z)$ comes at a higher redshift than the one at which $\Delta N/N$ is minimized. The remaining panels show the impact of 1%, 2%, 4%, and 8% mass calibration errors for three different threshold masses.

The basic features in Fig. 24 are simple to understand at a quantitative level, starting from the knowledge that cluster abundances constrain the combination $\sigma_{11,\text{abs}}(z)\Omega_m^q$ with $q \approx 0.4$. Since the mass of a collapsed volume scales linearly with Ω_m , a shift of the mass scale by a constant factor is nearly degenerate with a change of Ω_m by the same factor. Together these scalings imply $\sigma_{11,\text{abs}}(z) \propto M^q$, where M is the mass scale at fixed abundance, making $\Delta \ln \sigma_{11,\text{abs}}(z) \approx q \Delta \ln M$ for a survey limited by mass calibration uncertainty $\Delta \ln M$. For a survey limited by halo statistics, the corresponding effective mass error is $(\Delta \ln M)_{\text{eff}} = \alpha^{-1} \Delta \ln N$ where $\alpha = -d \ln N / d \ln M \approx 2\text{--}5$ is the slope of the cumulative halo mass function, so in this case $\Delta \ln \sigma_{11,\text{abs}}(z) \approx q \alpha^{-1} \Delta \ln N$. Combining the two limits we arrive at

$$\Delta \ln \sigma_{11,\text{abs}}(z) \approx q \times \max [\Delta \ln M, \alpha^{-1} \Delta \ln N]. \quad (141)$$

The above expression fits the data in Fig. 24 with better than 30% accuracy (typically $\lesssim 15\%$).

Fig. 25 plots the value of the degeneracy exponent q as a function of limiting mass and redshift. In the Press and Schechter (1974) theory of the halo mass function, the cumulative abundance is set by the probability that a point in a Gaussian field of variance $\sigma^2(M)$ exceeds the critical threshold $\delta_c \approx 1.69$ for spherical collapse (see Section 2.3), so that $N \propto [1 - \text{erf}(\delta_c / \sqrt{2}\sigma(M))]$. Putting in the $\sigma(M, z)$ relation for a Λ CDM power spectrum yields a logarithmic derivative $d \ln N / d \ln \sigma \equiv \alpha_\sigma \approx 5 - 9$ depending on mass and redshift. Because cluster abundances are degenerate in Ω_m/M , the logarithmic derivative of cluster abundances relative to Ω_m is the same as the slope α of the mass function (but with opposite sign), so locally the cumulative mass function scales as

$$N(m) \propto [\sigma_{11,\text{abs}}(z)]^{\alpha_\sigma} \Omega_m^{-\alpha} = [\sigma_{11,\text{abs}}(z) \Omega_m^{-\alpha/\alpha_\sigma}]^{\alpha_\sigma}. \quad (142)$$

We see that halo abundances are degenerate in $\sigma_{11,\text{abs}}(z) \Omega_m^q$ with $q = -\alpha/\alpha_\sigma \approx 3/7 \approx 0.4$. We plot the ratio α/α_σ – computed using the Tinker et al. (2008) mass function rather than the Press–Schechter mass function – in Fig. 25.

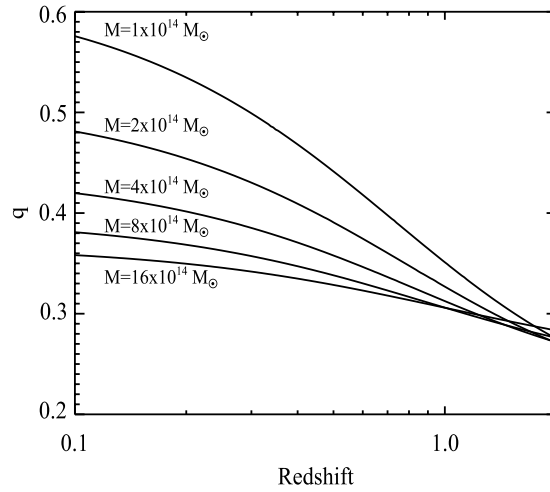


Fig. 25. The degeneracy exponent q as a function of redshift for a series of threshold masses. The parameter q is the exponent in $\sigma_{11,\text{abs}}(z)\Omega_m^q$ that holds the abundance of galaxy clusters above the quoted threshold mass at the appropriate redshift bin fixed for small, oppositely directed changes in $\sigma_{11,\text{abs}}(z)$ and Ω_m .

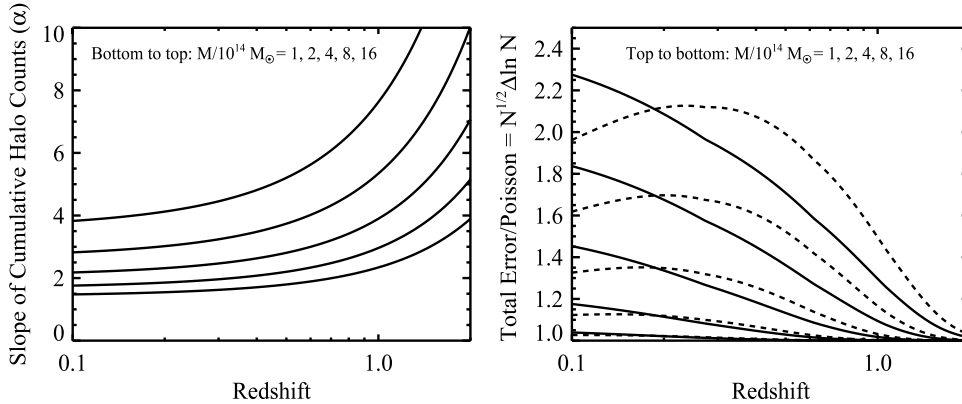


Fig. 26. *Left:* Logarithmic derivative $\alpha = -d \ln N / d \ln M$ of the cumulative halo counts, as a function of redshift, for five mass thresholds as labeled. *Right:* The ratio of the total (Poisson + sample variance) error in the halo counts $\Delta \ln N$ to the Poisson error $N^{-1/2}$. Solid lines assume a survey area of 10,000 deg^2 , while dashed lines correspond to 100 deg^2 . In conjunction with Fig. 25 and Eq. (141), these figures allow one to quickly estimate how well $\sigma_{11,\text{abs}}(z)$ can be constrained at each redshift by a galaxy cluster sample with N clusters.

A cluster abundance analysis becomes limited by mass scale uncertainty rather than halo abundance statistics when $\Delta \ln M > \alpha^{-1} \Delta \ln N$. If we approximate the error as Poisson, $\Delta \ln N = N^{-1/2}$, then an experiment is limited by mass uncertainty if the sample size is $N \geq (\alpha \Delta \ln M)^{-2}$. Current systematic uncertainties in mass calibration are $\approx 10\%$, which for $\alpha \approx 3$ corresponds to $N \approx 10$. Thus, cluster abundance studies are limited by uncertainty in the overall mass scale even for samples with as few as ≈ 10 – 20 galaxy clusters. For cluster samples with $N \approx 10^3$ (10^4), the accuracy required in mass estimation for an experiment to be dominated by halo statistics is $\approx 1\%$ (0.3%). So that one may apply the rule-of-thumb estimates derived in this section, Fig. 26 plots the mass-function slope α and the ratio of the total error $\Delta \ln N$ to the Poisson uncertainty $N^{-1/2}$. Note that abundance errors including sample variance almost never exceed twice the Poisson error and are often much closer. Using Figs. 25 and 26 along with Eq. (141), one can quickly estimate how well an experiment with given number of galaxy clusters N can constrain $\sigma_{11,\text{abs}}(z)$.

If Ω_m and $dV_c(z)$ are not perfectly known, then cluster abundances will constrain a combination of cosmological parameters rather than the matter fluctuation amplitude alone. Predicted abundances are proportional to $dV_c(z)$, so for an experiment dominated by uncertainty in the mass scale, uncertainty in the volume element will affect the interpretation if $\Delta \ln dV_c \gtrsim \alpha \Delta \ln M$, the effective abundance uncertainty. SN and BAO surveys should typically yield uncertainties below this limit, so we expect regarding $dV_c(z)$ as known to be an adequate approximation for our purposes, though it may fail for sufficiently powerful cluster surveys. Since a pure shift in Ω_m is equivalent to a shift in mass scale, uncertainties in Ω_m are relevant if $\Delta \ln \Omega_m \gtrsim \Delta \ln M$, where we have again assumed the experiment in question is dominated by the mass error $\Delta \ln M$. If the uncertainty in Ω_m is larger than this critical scale, then clusters will effectively constrain $\sigma_{11,\text{abs}}(z)\Omega_m^q$ rather than $\sigma_{11,\text{abs}}(z)$ alone. Eq. (141) will still hold, but one must replace $\Delta \ln \sigma_{11,\text{abs}}(z)$ by $\Delta \ln [\sigma_{11,\text{abs}}(z)\Omega_m^q]$. Current fractional uncertainties

in Ω_m from CMB and other observables are $\sim 10\%$, comparable to mass calibration systematics. Future studies will reduce Ω_m uncertainties, but they may remain significant compared to improved mass calibration errors in cluster surveys.

We have focused our discussion here on cumulative cluster abundances – i.e., space densities of clusters above a mass threshold – while observational analyses usually examine the differential distribution as a function of observable mass-proxies. Differential distributions are useful for breaking degeneracies (e.g., among $\sigma_{11, \text{abs}}$, Ω_m , and dV_c), and for constraining “nuisance parameters” such as the scatter of the observable–mass relation. However, for single-parameter constraints on $\sigma_{11, \text{abs}}(z)$, we expect that our analysis of the cumulative abundance uncertainties provides an accurate guide, as it makes use of the single number best determined by the data for any given mass threshold and redshift range. We anticipate that observational analyses will continue to concentrate mainly on differential distributions, but cumulative distributions are more amenable to the kind of rule-of-thumb estimates that we try to develop throughout this section, so they provide a more intuitive way of understanding the cosmological information content of cluster surveys.

6.3.2. Cluster finding

Each of the three main methods for finding galaxy clusters – optical, X-ray, and SZ – has its own virtues and deficiencies. The principal advantage of optical surveys is sheer statistics, reflecting the low mass threshold for optical detection; clusters with masses as low as $5 \times 10^{13} M_\odot$ are capable of hosting significant galaxy overdensities. Near-future surveys (RCS-2, DES, HSC, Pan-STARRS) should find $\approx 10^5$ systems in areas of 10^3 – 10^4 deg^2 out to $z \approx 1$. On a longer time scale (≈ 10 years), surveys with LSST should increase the available cluster samples by another factor of 5–10, due both to larger area ($\approx 20,000 \text{ deg}^2$) and to deeper imaging, which should allow cluster detection out to $z \approx 1.5$. Finally, cluster searches in the IR are capable of finding galaxy clusters out to $z \approx 2$, but large survey areas to this depth will only be achievable with the advent of *Euclid* and/or *WFIRST*. With the stacked weak lensing mass calibration that we advocate in Section 6.3.3, the calibration accuracy scales with cluster number as $N^{-1/2}$, so enormous samples are statistically advantageous even if mass uncertainties dominate the error budget.

The main drawback for optical cluster detection is projection effects, i.e., chance alignments of multiple low mass halos along the line of sight that are misidentified as a single massive galaxy cluster. While this systematic has been drastically suppressed in modern surveys with multi-band photometry and photometric redshift estimators, one still expects 5%–20% of photometrically selected clusters to suffer from serious projection effects (Cohn et al., 2007; Rozo et al., 2011a). The importance of projection effects increases with decreasing mass, so we expect it is projection effects rather than survey depths that will ultimately set the detection mass threshold for optical cluster finding in future surveys.

Unlike optical studies, X-ray cluster searches are nearly free from projection effects. This robustness to the presence of structures along the line of sight reflects the fact that X-ray emission scales as density-squared, which enhances the relative contrast of a cluster in the sky, and it is the principal reason that X-rays are considered the cleanest method for selecting galaxy clusters. The main difficulty for X-ray selection is a technological one, specifically, the need for space-based observatories. A dramatic leap forward in capabilities will happen with the launch of *eROSITA*, which should detect $\approx 10^5$ galaxy clusters over the full sky out to $z = 1$ and beyond, ensuring that X-rays will continue to play a critical role in the development of cosmologically relevant cluster samples over the coming decade. On a longer time scale, further improvements would require X-ray observatories that reach lower flux limits with higher angular resolution, both of which are needed to detect large numbers of systems at $z \gtrsim 1$.

The primary advantage of SZ searches is that they do not suffer from cosmological dimming. The SZ signature arises from up-scattering of CMB photons by the hot intra-cluster plasma, and because the number of up-scattered photons does not depend on the distance to the cluster the signal is roughly redshift independent. In practice, the SZ signal is not exactly redshift independent because of residual sensitivity to the relative size of the cluster and the beam of the telescope. Unfortunately, achieving sufficient sensitivity to detect low mass clusters in SZ is technologically very challenging. For instance, the current SPT, ACT, and *Planck* surveys are expected to be complete at all redshifts above mass thresholds of $7 \times 10^{14} M_\odot$, $10^{15} M_\odot$, and $2 \times 10^{15} M_\odot$ respectively (Vanderlinde et al., 2010; Marriage et al., 2011; Planck Collaboration et al., 2011a); while these limits will go down, they will not reach thresholds comparable to those of X-ray or optical cluster selection. Consequently, while these experiments are currently the best avenue to probe the $z \approx 1$ massive cluster population, on a 3–5 year time scale the focus of cluster detection is likely to shift toward optical and X-ray. To our knowledge, there are no current plans to develop a new generation of SZ survey instruments that would dramatically improve upon the capabilities of current experiments for cluster detection, at least compared to the differences in optical (e.g., DES vs. SDSS) and X-ray (*eROSITA* vs. *ROSAT*). However, both SPTpol and ACTpol should lead to significantly lower mass thresholds for SZ cluster detection than the current SPT and ACT cluster samples.

Fig. 27 showcases the difference of the cluster populations from the various selection methods, where we have limited ourselves to wide surveys (1000 deg^2 or higher) and have shown only a handful of representative selection functions. The top row shows the selection functions for existing or ongoing surveys, while the bottom-row shows the selection for future surveys. The left panels shows the limiting mass as a function of redshift for each of the surveys considered, while the right panels shows the number above the limiting mass in a redshift bin of width $\Delta z = 0.1$, accounting for survey area. We emphasize that in practice cluster samples never have a sharp mass threshold; the curves shown in Fig. 27 are only roughly indicative of the mass and redshift ranges probed. The number of clusters detected depends in detail on the selection cuts applied, and small changes in threshold translate to larger changes in abundance, so factor-of-two deviations from the projections in Fig. 27 would not be particularly surprising.

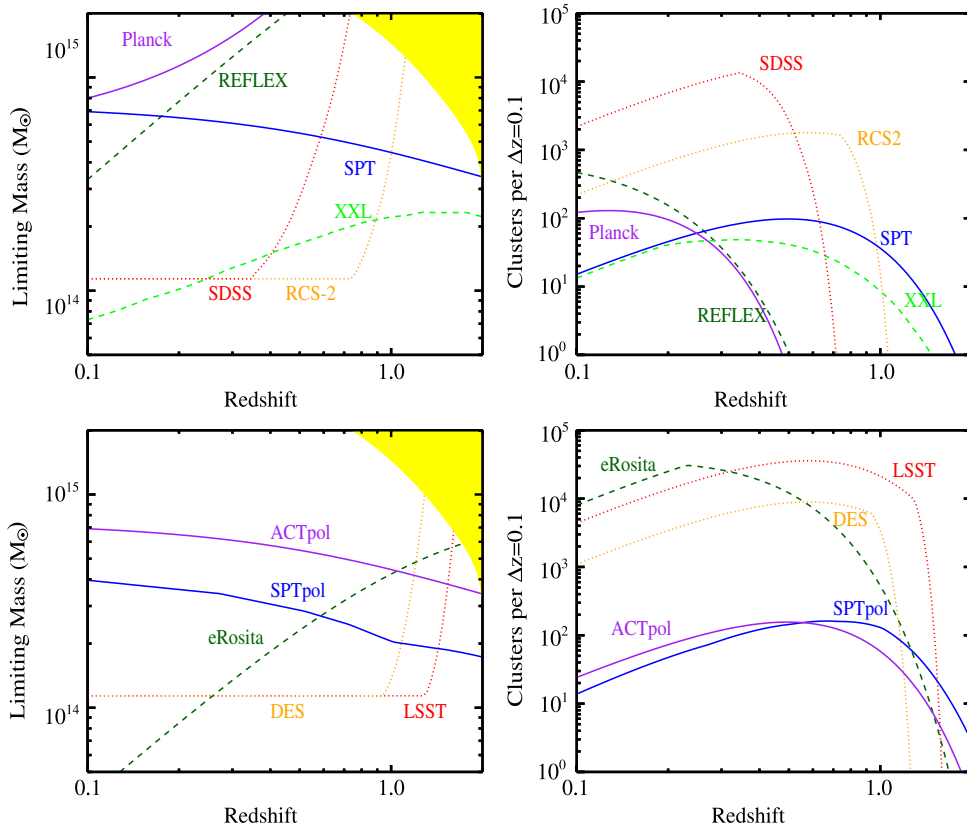


Fig. 27. Selection function for several representative cluster samples, as labeled. The top panels show surveys that are completed or currently ongoing. The bottom panels show future surveys. Left panels show the limiting mass as a function of redshift, while right panels show the number of galaxy clusters above the limiting mass in redshift bins of width $\Delta z = 0.1$. The yellow region in the left panels corresponds to the area in parameter space where one expects fewer than one galaxy cluster above the mass and redshift under consideration. For the abundance plot, we consider the appropriate area for each of the surveys: 30,000 deg² for the *eROSITA* and *Planck* cluster samples, 10,000 deg² for the REFLEX sample, 20,000 deg² for LSST, 10,000 deg² for SDSS, 5000 deg² for DES, 1000 deg² for RCS-2, 2500 deg² for SPT, 600 deg² for SPTpol, and 4000 deg² for ACTpol. The current ACT survey (not plotted) is similar to SPT, with a somewhat higher mass threshold and a 1000 deg² survey area. Different line types are used only to aid visual discrimination. (For interpretation of the references to colour in this figure legend, the reader is referred to the web version of this article.)

For the optical detection threshold we have assumed that projection effects limit useful cluster catalogs to a minimum richness $\lambda = 15$ in the algorithm of Rykoff et al. (2012), which counts galaxies of luminosity $L \geq 0.2L_*$. To account for mass-richness scatter, we choose an effective mass threshold that yields approximately the same space density as this richness threshold. The sharp upturn occurs when $0.2L_*$ matches the magnitude limit of the survey. In SZ we see that the SPT mass threshold (kindly provided by the SPT collaboration, and normalized to a total cluster yield of ≈ 700 clusters at full depth) is only mildly sensitive to redshift. The gentle decrease in limiting mass with increasing z reflects the fact more distant clusters subtend smaller angles that better match the SPT beam size, and that clusters are hotter at fixed mass with increasing redshift. For *Planck*, conversely, the decreasing angular size of clusters reduces sensitivity at higher redshift because the beam itself is large. The curve shown is a rough estimate of the *Planck* Early SZ sample (Planck Collaboration et al., 2011a), though the final selection will go considerably lower in mass, because of both deeper data and lower S/N cuts. The SPTpol curve is similar to SPT, but it reaches lower masses over a smaller area, while the ACTpol curve reaches similar noise levels to SPT ($\approx 20 \mu\text{K}$, Niemack et al., 2010) over a larger area. (ACTpol also plans a separate survey, deeper and narrower than SPTpol.) Turning to X-rays, the REFLEX, XXL, and *eROSITA* curves all show the increase of mass threshold with redshift characteristic of flux-limited surveys. The XXL selection is that of Valageas et al. (2011) scaled to match the observed density of C1 clusters in the XMM-LSS field (Pacaud et al., 2007), while the *eROSITA* threshold represents a flux limit $\approx 4 \times 10^{-14}$ erg s⁻¹, corresponding to ≈ 50 photon counts (Pillepich et al., 2012). The mass limit is higher by a factor of ≈ 3 for clusters reaching 300 photon counts.

Current wide X-ray samples are largely limited to massive systems at moderate redshifts, but narrow/deep samples reaching $z \approx 1$ and above do exist. By comparison, the SDSS reaches lower mass over large areas of the sky, but it only extends to $z \approx 0.5$. RCS-2 reaches $z \approx 1$, but over a smaller (though still quite significant) area. The *Planck* SZ survey is largely limited to massive, moderate redshift systems, while the SPT SZ survey has the best current sensitivity to high redshift clusters. In the near future, DES will extend the range of optical identification to $z \approx 1$ over a large area, but *eROSITA* should ultimately produce a larger sample. While DES has a lower mass threshold over the range $0.3 < z < 1$, the

larger (all-sky) area of *eROSITA* leads to a larger cluster total, and *eROSITA* should continue to detect clusters at $z > 1$ where the DES sensitivity declines rapidly. On a longer time scale, LSST will push the optical selection limit to $z \approx 1.5$, increasing the number of $z > 1$ galaxy clusters by one to two orders of magnitude.

Another proposed method for detecting galaxy clusters is to search for peaks in the weak lensing shear field. However, while massive halos produce local shear peaks, shear peak statistics are known to suffer from severe projection effects: many peaks arise from the superposition of multiple halos along the line of sight. Consequently, shear peak selection is not a particularly effective method for selecting clusters of galaxies. That said, the shear peak abundance is an observable that can be predicted from numerical simulations in much the same way as the halo mass function, and this approach may well yield useful cosmological constraints (e.g., [Marian et al., 2009](#); [Dietrich and Hartlap, 2010](#)). For the remainder of this review, however, we focus on abundances of clusters identified by optical, X-ray, or SZ methods. We emphasize that stacked weak lensing mass calibration of clusters identified by other methods is *not* equivalent to shear peak statistics, since cluster methods use the additional information afforded by baryonic density peaks to drastically reduce the impact of projection effects on cluster selection.

6.3.3. Calibrating the observable–mass relation

The biggest challenge for cluster cosmology is characterizing the observable–mass relation $P(X|M, z)$, where X is a cluster observable that is correlated with mass (e.g., richness, Y_{SZ} , L_X) and $P(X|M, z)$ is the probability that a halo of mass M at redshift z is detected as a cluster with observable X . This relation is usually described by parameters that specify the mean relation, the rms scatter, and perhaps a measure of skewness or kurtosis, all of which can evolve with redshift. There are three general approaches to determining these parameters: simulations, direct calibration, and statistical calibration.

In the simulation approach, one relies on numerical simulations to calibrate the observable–mass relation (e.g. [Vanderlinde et al., 2010](#); [Sehgal et al., 2011](#)). The main difficulty that simulation methods face is our incomplete understanding of baryonic physics, particularly galaxy formation feedback processes. These difficulties can be minimized by defining new X-ray observables that are expected to be robust to these details, and through careful exploration of the sensitivity of the observable–mass relation to the physics that goes into the simulations (e.g., [Nagai et al., 2007](#); [Rudd and Nagai, 2009](#); [Stanek et al., 2010](#); [Fabjan et al., 2011](#); [Battaglia et al., 2012](#)). The simulations themselves are steadily improving thanks to increased computer power, more sophisticated algorithms, and the availability of better data to test the input physics. Despite these trends, we think it unlikely that simulations will achieve the $\sim 0.5\%$ – 2% level of accuracy required for cluster abundance experiments to become statistics dominated in the next ten years.

The second approach to calibrating the observable–mass relation is the direct method, in which a small subset of galaxy clusters have X-ray hydrostatic mass estimates and/or weak lensing mass estimates that are taken to represent “true” masses. The observable–mass relation is directly calibrated on this small subset of galaxy clusters, then applied to the general cluster population ([Vikhlinin et al., 2009](#); [Mantz et al., 2010](#)). Unfortunately, hydrostatic mass estimates are themselves problematic because non-thermal pressure support (bulk motions, magnetic fields, cosmic rays) is expected to bias them at the $\approx 10\%$ – 20% level ([Lau et al., 2009](#); [Meneghetti et al., 2010](#)), and it is not clear that these biases can be predicted at the required level of accuracy. We therefore suspect that hydrostatic estimates will play a steadily decreasing role in future cluster abundance experiments. Weak lensing mass estimates of individual clusters can in principle be unbiased in the mean, but they are typically available only for the most massive galaxy clusters in a given sample because of limited signal-to-noise ratio. In addition, even if the WL shape noise is small, halo orientation and large scale structure introduce irreducible noise in the mass estimates of individual clusters at the 20% – 30% level ([Becker and Kravtsov, 2011](#)). Nonetheless, ambitious efforts to achieve accurate weak lensing masses for substantial samples (≈ 50) of X-ray or SZ-selected clusters are likely to play a key role in improving cluster cosmological constraints over the next few years ([Hoekstra et al., 2012](#); [von der Linden et al., 2012](#)).

The final approach to calibrating the observable–mass relation is statistical: instead of relying on precise mass estimates of a subsample of galaxy clusters, the relation is calibrated using additional observables for the full sample that correlate with mass. One such statistical method uses the spatial clustering of the clusters themselves, as characterized by the variance of counts-in-cells ([Lima and Hu, 2004](#)) or by the cluster correlation function or power spectrum ([Schuecker et al., 2003](#); [Majumdar and Mohr, 2004](#); [Hütsi and Lahav, 2008](#)). Because the bias of halo clustering depends on mass ([Fig. 1](#)), the amplitude and scale-dependence of clustering provides information about the mass–observable relation. Operationally, one parameterizes this relation, then uses standard likelihood methods to jointly fit for both cosmology and the $P(X|M, z)$ parameters ([Hu and Cohn, 2006](#); [Holder, 2006](#)). These types of analyses are often referred to as “self-calibration” because they do not require “direct” mass calibration data. However, we think the descriptor “statistical mass calibration” is more accurate.

The other statistical method we consider is stacked weak lensing, wherein one measures the mean tangential shear of background galaxies around galaxy clusters in a bin of fixed observable. In other words, the stacked weak lensing signal is the cluster-shear correlation function, which can be inverted to yield the mean 3-d mass profile of clusters in the bin ([Johnston et al., 2007](#)). Because this measurement allows one to stack many clusters, one can easily obtain high signal-to-noise measurements even for low mass clusters and large angular distances ([Mandelbaum et al., 2008](#); [Sheldon et al., 2009](#)). Since the underlying halo population is randomly oriented relative to the line of sight, stacked weak lensing mass calibration does not suffer from orientation biases so long as the cluster identification itself does not preferentially select halos oriented along a particular direction or aligned with line-of-sight structure. However, orientation biases in the cluster selection method will probably exist to some degree, and they must be calibrated carefully on simulations. Finally, because this method relies on

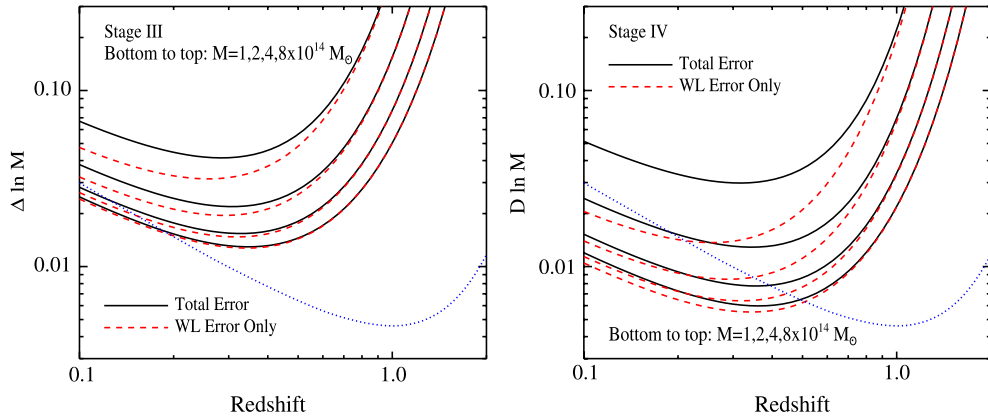


Fig. 28. Mass uncertainty from stacked weak lensing calibration as a function of redshift, assuming only WL shape noise (dashed red curves) and including sample variance due to intrinsic scatter between WL mass and halo mass (solid curves). For Stage III data (left) we assume $\sigma_e = 0.4$ and $\bar{n}_g = 10$ galaxies/arcmin², while for Stage IV (right) we assume $\sigma_e = 0.3$ and $\bar{n}_g = 30$ galaxies/arcmin². For both cases we assume a 10^4 deg² survey, and the redshift bin width is $z = z_c \pm 0.05$. Each curve corresponds to a different mass threshold as labeled. The blue dotted line shows the mass error corresponding to a statistics-limited cluster survey with a threshold mass of $10^{14} M_\odot$, as per Fig. 23. The intersection between the blue dotted line and the lowest solid black line marks the redshift at which a cluster abundance experiment with a threshold mass of $10^{14} M_\odot$ transitions from being dominated by the statistical error in cluster abundance (at low redshift) to the error in the weak lensing mass calibration (at high redshift).

stacking all galaxy clusters, it only provides information about the mean of the mass–richness relation, so additional data are required to provide tight constraints on the scatter.⁶⁸

Fig. 28 shows the error in mass calibration that can be achieved using stacked weak lensing for both “Stage III” (left panel) and “Stage IV” (right panel) observations, calculated via the methodology described by Rozo et al. (2011b). Briefly, we assume a source redshift distribution appropriate for DES-like survey depth, and we sum over all annuli within the radius $2R_{200}$, which is a rough approximation for the location of the one-to-two halo transition of the matter correlation function using the Hayashi and White (2008) model. (Other studies, e.g. Tavio et al. (2008), also find that one-halo regime of the mass profile extends well beyond R_{200} .) For our Stage III estimates we assume an intrinsic shape noise $\sigma_e = 0.4$ and source galaxy surface density $\bar{n}_g = 10$ arcmin⁻², while for Stage IV we assume $\sigma_e = 0.3$ and $\bar{n}_g = 30$ arcmin⁻². Note that the corresponding tangential shear error is $\sigma_\gamma \approx \sigma_e/\sqrt{2}$. These values correspond roughly to expectations for DES data and *Euclid*/*WFIRST* data, respectively; the lower σ_e for the latter reflects higher image quality, though the partition of this improvement between σ_e and \bar{n}_g is somewhat arbitrary. LSST falls between these two cases but closer to Stage IV. We assume that clusters have NFW mass profiles (Navarro et al., 1996), and we include the decrease in background source density with increasing cluster redshift. In all cases, the redshift distribution is set to

$$F(z) \propto z^2 \exp[-(z/z_*)^2] \quad (143)$$

with $z_* = 0.5$. This is appropriate for DES and underestimates the redshift depth for LSST, which will result in a slight overestimate of the statistical uncertainties for Stage IV experiments, particularly at the highest redshift bins.

In each panel of Fig. 28, dashed red curves show the error from shape noise alone, while solid curves include the intrinsic scatter between noiseless WL mass estimates and true three-dimensional halo masses, a consequence of non-spherical mass distributions, which we add in quadrature to the shape noise assuming an intrinsic scatter per cluster of $\sigma_{wl} = 0.3$ (Becker and Kravtsov, 2011). The two curves separate when the number of sources is high enough to measure individual clusters with $S/N \sim 3$. We assume the stacked weak lensing signal uses all halos within a redshift bin $z = z_c \pm 0.05$ and above a given mass threshold as labeled. The forecast mass errors are marginalized over concentration. The improvement in precision with decreasing mass is driven by the rapid increase in the number of halos as the mass threshold decreases. For mass thresholds $1 - 2 \times 10^{14} M_\odot$, calibration at the 1%–2% level is achievable in principle with Stage III data and at the sub-percent level with Stage IV data. These are errors per $\Delta z = \pm 0.05$ bin, so if one assumes a smooth, parameterized evolution of $P(X|M, z)$ it may be possible to constrain the overall normalization more tightly. Conversely, some forms of WL systematics (e.g., uncertainty in the shear calibration or source redshift distribution) could introduce mass calibration errors correlated across redshift bins. The results in Fig. 28 are broadly consistent with those from the more detailed treatment by Oguri and Takada (2011).

Comparing Figs. 23d and 28, we see that Stage IV weak lensing data can in principle calibrate the mean relation well enough that a 10^4 deg² cluster survey would be limited by the statistical uncertainty in abundance for $z \lesssim 0.5$, though mass

⁶⁸ The distinction between statistical calibration via stacked weak lensing and direct calibration using weak lensing mass measurements is not a sharp one, and both methods share the virtue that the relation between mass and weak lensing signal is governed by well understood gravitational physics. By “stacked weak lensing” we mean to emphasize the case where (a) the WL measurements come from a large area imaging survey that overlaps the cluster catalog (and may have been used to create it) rather than from cluster-by-cluster follow-up observations, and (b) the S/N of the mass measurement for any individual cluster may be ≤ 1 , though the S/N for the ensemble is high.

calibration error would dominate at higher redshift. (The abundance error and weak lensing calibration error both scale with area as $A^{-1/2}$.) The statistics limit for $M = 10^{14} M_\odot$ from Fig. 23d is shown in Fig. 28 as the blue dotted line. Stage III weak lensing data fall short of this goal by a factor ~ 3 , but they can still achieve powerful constraints on $\sigma_{11,\text{abs}}(z)$ (see Fig. 30).

The general trends in Fig. 28 can be understood using simple arguments. For a singular isothermal sphere (SIS) of velocity dispersion $\sigma_v \propto M^{1/3}$, the tangential shear is $\gamma(\theta) = \theta_E/2\theta$, where θ is the angular distance to the cluster center, and θ_E is the Einstein radius. The Einstein radius is related to the velocity dispersion via (Fort and Mellier, 1994)

$$\theta_E = 4\pi \left(\frac{\sigma_v}{c}\right)^2 \frac{D_{ls}}{D_s} \approx 0.07 \text{ arcmin} \left(\frac{\sigma_v}{550 \text{ km s}^{-1}}\right)^2 \left(\frac{D_{ls}/D_s}{0.5}\right), \quad (144)$$

where D_s is the distance to the source, D_{ls} is the distance to the source as seen from the lens, and we have scaled to a typical value of their ratio. We have also scaled Eq. (144) to the (1-dimensional) velocity dispersion of a $2 \times 10^{14} M_\odot$ cluster at $z = 0.5$. Each source galaxy gives a low S/N estimate of γ and hence of $\theta_E = 2\theta\gamma$. The variance of this estimate is $\text{Var}(\hat{\theta}_E) = 2\theta^2\sigma_e^2$, where $\sigma_e = \sqrt{2}\sigma_\gamma$ is the WL shape noise. The number of source galaxies in a logarithmic angular interval $d \ln \theta$ is $2\pi\bar{n}_g\theta^2 d \ln \theta$, so each such interval contributes equally to the S/N on θ_E , from θ_{\min} where the weak lensing approximation fails to θ_{\max} , the angular extent of the cluster. The variance of the estimate for an individual cluster is thus

$$\text{Var}(\hat{\theta}_E) = \frac{2\theta^2\sigma_e^2}{2\pi\bar{n}_g\theta^2 \ln(\theta_{\max}/\theta_{\min})}, \quad (145)$$

and the variance for N clusters is smaller by N . As representative values we take $\theta_E = 0.07$ arcmin, $\theta_{\min} = 5\theta_E = 0.35$ arcmin (so $\gamma_{\max} = 0.1$), and $\theta_{\max} = 6.5$ arcmin, the angle subtended by a radius $R = 2R_{200}$ at $z = 0.5$ (for $M = 2 \times 10^{14} M_\odot$), yielding $\ln(\theta_{\max}/\theta_{\min}) \approx 3$. Since $\theta_E \propto \sigma_v^2 \propto M^{2/3}$, $\Delta \ln M = 1.5 \Delta \ln \theta_E$, with $\Delta \ln \theta_E = \theta_E^{-1} [\text{Var}(\hat{\theta}_E)]^{1/2}$. Putting these results together yields a total shape noise error at $z = 0.5$ of

$$\Delta \ln M \approx 1.5N^{-1/2} \left[\frac{\sigma_e^2}{\pi\bar{n}_g\theta_E^2 \ln(\theta_{\max}/\theta_{\min})} \right]^{1/2} \quad (146)$$

$$\approx 6 \times 10^{-3} \left(\frac{N}{4000}\right)^{-1/2} \left(\frac{\sigma_e}{0.3}\right) \left(\frac{M}{2 \times 10^{14} M_\odot}\right)^{-2/3} \left(\frac{\bar{n}_g}{30 \text{ arcmin}^{-2}}\right)^{-1/2} \left(\frac{D_{ls}/D_s}{0.5}\right)^{-1}. \quad (147)$$

This error estimate is 25% smaller than the value plotted in Fig. 28 (which shows $\Delta \ln M \approx 0.008$ at $z = 0.5$ from shape noise alone), in part because the surface density of sources *behind* the clusters is lower than \bar{n}_g , and in part because marginalizing over the NFW concentration parameter further increases the mass error. Including the dependence of N on mass threshold, Eq. (146) implies

$$\Delta \ln M_{\text{shape}} \propto \theta_E^{-1} N^{-1/2} \propto M^{-2/3+\alpha/2}, \quad (148)$$

where α is the mass function slope shown in Fig. 26. For $\alpha \geq 4/3$, which is always satisfied for $M \geq 10^{14} M_\odot$, the increase in abundance at lower masses outweighs the lower S/N per cluster, yielding higher precision at lower mass threshold as seen in Fig. 28. To obtain the total noise, one simply adds the intrinsic weak-lensing noise $\sigma_{\text{wl}}N^{-1/2}$ in quadrature to the shape noise.

Multi-wavelength studies of galaxy clusters also allow for statistical mass calibration from cross-correlation studies. Just as the clustering of clusters is a mass-dependent observable, so too are the abundance functions of different observables. Consequently, overlapping surveys allow for the possibility of measuring the abundance of galaxy clusters as a function of two observables X_1 and X_2 . While an overall shift in the normalization of the multi-variate observable–mass relation $P(X_1, X_2|M)$ is still degenerate with cosmology, the addition of the clustering signal – which depends on cluster masses directly – allows one to jointly calibrate $P(X_1, X_2|M)$ while still improving the cosmological constraints relative to those derived from a single observable (Cunha, 2009). The improvement is driven by the fact that using two cluster observables simultaneously allows one to better constrain the scatter of the observable–mass relation (see also Stanek et al., 2010). Given the large overlap between many of the currently ongoing or near future cluster surveys (e.g., DES fully overlaps with SPT), we expect this type of analysis to become increasingly important in the coming decade.

It remains to be seen whether statistical calibration of the mean observable–mass relation via clustering can compete with stacked weak lensing calibration, but we suspect that the answer is no based on the following approximate argument. If the cluster bias factor is measured with uncertainty $\Delta \ln b$, then the corresponding mass scale uncertainty is $\Delta \ln M \approx \eta^{-1} \Delta \ln b$, where $\eta \equiv d \ln b/d \ln M \approx 0.4\text{--}0.5$ is the logarithmic slope of the bias–mass relation for cluster mass halos. We have computed $\Delta \ln b$ for an optimally weighted measurement of cluster pairs in a wide radial bin, $20 \text{ Mpc} < R < 100 \text{ Mpc}$ (comoving), considering *only* Poisson pair count errors, not sample variance errors. For our usual $\Delta z = 0.1$ redshift bin over 10^4 deg^2 , centered at $z = 0.5$, we find that the corresponding $\Delta \ln M$ rises from 6% for a $10^{14} M_\odot$ threshold to $\sim 50\%$ for a $4 \times 10^{14} M_\odot$ threshold, much worse than our estimated errors for Stage III stacked weak lensing calibration shown in Fig. 28. Cross-correlation with a much denser galaxy sample might evade this argument by allowing higher precision bias measurements, but sample variance will set a floor to these errors, and the bias of the cross-correlation sample must also

be known. Our expectation is that clustering may well help constrain the scatter given mass constraints from weak lensing, but that it will prove insufficiently powerful to pin down the mass scale of clusters on its own.

In practice, the distinction between simulation, direct, and statistical mass calibration is somewhat artificial. One can use simulation and direct mass calibration to place priors on the observable–mass relations, then use statistical methods to arrive at the final constraint. High quality observations of individual clusters can provide important information about the scatter of the observable–mass relation, a quantity that is only indirectly constrained via statistical calibration methods. Conversely, we expect that only statistical methods, and particularly stacked weak lensing, are likely to achieve the $\approx 1\%$ mass scale accuracy demanded by Stage IV experiments. To the extent that this is true, optical imaging of galaxy clusters will be a necessary component of all future cluster surveys, not just for redshifts, but also for cluster mass calibration. Conversely, imaging surveys conducted for WL studies of cosmic acceleration will automatically enable cluster studies.

With spectroscopic follow-up data or an overlapping galaxy redshift survey, one can also try to calibrate cluster observable–mass relations using virial mass estimators (Heisler et al., 1985), “hydrostatic” estimators for the galaxy population (Carlberg et al., 1997), or “velocity caustics” that mark the boundary between galaxies bound to the cluster potential and galaxies above the escape velocity (Regös and Geller, 1989; Diaferio, 1999; Rines et al., 2003). The key systematic issue for this approach is the possible influence of galaxy formation physics on the velocity field and velocity dispersion profile, though Diaferio (1999) argues that these effects should be small for velocity caustics. These approaches can again be applied in either a “direct” mode for individual clusters or a “statistical” mode using velocity distributions measured for large samples. Studies to date have not established the robustness of these methods at the few-percent level needed for future progress, but with the large spectroscopic surveys underway or planned for dark energy measurements the approach merits further investigation (e.g., White et al., 2010; Saro et al., 2012). Zu and Weinberg (2012) show that the mean radial infall profile for clusters can be extracted from measurements of the redshift-space cluster–galaxy cross-correlation function, which may provide a practical route to implementation. Even if the calibration precision from redshift-space distortions is lower than that from stacked weak lensing, comparison of the two enables tests of modified gravity models that predict differences between the potentials affecting lensing and non-relativistic motions (see Section 7.7).

6.4. Systematic uncertainties and strategies for amelioration

If X is a cluster observable correlated with mass, and $P(X|M, z)$ the mass–observable relation discussed in Section 6.3.3, then the expected number of clusters in a volume V at redshift z above a threshold X_{\min} is

$$N(X_{\min}, z) = \int_{X_{\min}}^{\infty} dX \frac{dN}{dX} = \int_{X_{\min}}^{\infty} dX \int_0^{\infty} dM V(z) \frac{dn(z)}{dM} P(X|M, z), \quad (149)$$

where $dn(z)/dM$ is the halo mass function at redshift z . From Eq. (149) we can identify several sources of potential systematic uncertainties: errors in cluster redshifts, incompleteness and contamination that produce extended non-Gaussian tails of $P(X|M, z)$, the form and calibration of the “core” of $P(X|M, z)$, and the theoretical prediction of dn/dM itself. We discuss each of these categories in turn.

6.4.1. Redshift uncertainties

Eq. (149) implicitly assumes that all clusters are assigned the correct redshifts. As cluster samples grow to the tens and even hundreds of thousands, obtaining spectroscopic redshifts for all systems becomes impractical, and photometric redshifts are essential. Fortunately, clusters contain many galaxies with uniform (red-sequence) colors, allowing precise and accurate photo- z 's. Lima and Hu (2007) estimated the level at which the bias and scatter of photometric redshift errors must be controlled in a Stage III dark energy experiment so as to not degrade cosmological information, finding that the rms scatter must be held to $\sigma_z \leq 0.03$ and that any bias in the mean photo- z must be held below $\Delta z = 0.003$. Current cluster photometric redshift estimates have a dispersion of ≈ 0.01 (e.g. Koester et al., 2007), so controlling the scatter at the 0.03 level is not particularly problematic. The bias on the mean is more challenging, but current catalogs do achieve close to the necessary accuracy. For instance, the bias of the SDSS maxBCG catalog, measured by comparing cluster photo- z 's to spectroscopic redshifts, is ≈ 0.004 (Koester et al., 2007). We expect these successes will still hold as we push to higher redshifts, so cluster photometric redshift errors are unlikely to be a significant source of systematic uncertainty in abundance studies, at least for samples below $z \approx 1$. Above this redshift, the 4000 Å break feature in the spectrum of early-type galaxies red-shifts into the IR, and the photometric redshift accuracy will become more difficult to control at the required level unless near IR data are available. X-ray and SZ cluster samples require deep multi-band optical imaging and/or spectroscopic follow-up to achieve these errors. In particular, while the use of iron lines in X-ray spectroscopy has proven to a reliable indicator of cluster redshift (e.g. Yu et al., 2011), the accuracy achieved by these methods is only of order ≈ 0.03 , with a not-insignificant outlier fraction, and even then this requires a significant number of photon counts. Nevertheless, for high redshift systems without IR data this information is often the only indicator of a cluster's redshift, and it can therefore play a critical role.

6.4.2. Contamination and incompleteness: the tails of $P(X|M, z)$

Eq. (149) assumes a one-to-one match between halos and observable clusters. In practice, any observed cluster catalog suffers some degree of contamination, the presence of systems whose true halo mass is far below the value suggested by the observable X . Cluster catalogs are also affected by incompleteness, halos whose corresponding observable X is anomalously

low so that they are assigned masses far below their true masses, or perhaps fail to make it into the catalog at all. Thus, we can think of contamination and incompleteness as characterizing the extended non-Gaussian tails of $P(X|M, z)$.

Significant levels of contamination and incompleteness can be tolerated provided that they are well calibrated. A contamination fraction C increases the estimated cluster abundance by a factor $(1 + C)$ relative to the true value, while an incompleteness fraction I reduces the estimated abundance by a factor $(1 - I)$. To prevent them becoming the limiting factor in cluster abundance measurements, the product $(1 + C)(1 - I)$ must be determined to a fractional accuracy that is smaller than the uncertainty in the cluster space density, roughly $N^{-1/2}$ if limited by cluster statistics or $\alpha \Delta \ln M$ if limited by mass calibration uncertainty.

Contamination can also impact mass calibration (Cohn et al., 2007; Erickson et al., 2011). In the simplest case, if \bar{M} is the mean mass of a sample of clusters selected by some range of observable and contaminating clusters have mass $M \ll \bar{M}$, they dilute the sample and reduce the mean mass inferred from calibration by a factor $(1 + C)$. Incompleteness, on the other hand, should not affect the estimated mean mass of a galaxy cluster sample, provided that the reason a cluster of given X fails to be detected is not correlated with its halo mass. Keeping the impact of contamination uncertainty sub-dominant requires that the contamination level be known to $\Delta C \approx \Delta \ln(1 + C) \leq \Delta \ln M$. This is a stiffer requirement than that on the product $(1 - I)(1 + C)$, by a factor of $\alpha \approx 3$, so it will be more difficult to achieve in practice.

Different cluster finding techniques are sensitive to different sources of contamination and incompleteness. In X-rays, the principal contaminants are X-ray point sources (AGNs), which can be effectively removed from cluster catalogs by demanding that galaxy clusters be detected as spatially extended emission. With this cut, the fraction of galaxy clusters where AGNs have a significant impact on the cluster emission is $\lesssim 5\%$ (Burenin et al., 2007; Mantz et al., 2010). The few percent contamination level of today's X-ray cluster surveys is not an important systematic relative to mass calibration uncertainty. However, the demands will be stiffer for *eROSITA*, so whether AGN contamination will continue to be a negligible systematic in the future remains to be seen. Incompleteness (in the sense of clusters that reside in non-Gaussian tails) is a source of possible concern, since *eROSITA* will probe significantly lower cluster masses than current X-ray surveys, and the regularity of the intracluster medium could break down at lower halo masses because of greater importance of radiative cooling or galaxy and AGN feedback. However, *Chandra* studies of group-scale systems show that the scaling relations of galaxy clusters extend down to $M \approx 4 \times 10^{13} M_{\odot}$ (Sun et al., 2009), so *eROSITA* should be able to use the vast majority of all X-ray selected groups and clusters for cosmological investigations. As usual, the largest open question is accuracy of the mass calibration.

Because SZ clusters work in the low S/N limit, with typical detections being $\approx 5\sigma$, SZ cluster samples typically can contain a few false detections – sources that do not correspond to massive galaxy clusters but rather reflect the stochastic nature of the CMB and/or instrumental noise. However both of these sources of stochasticity can be very well characterized, so we do not expect them to be a limiting systematic: their impact on $P(X|M, z)$ is calculable. Radio emission by point sources and/or dusty star forming galaxies can systematically reduce the SZ signal of clusters, but these effects are expected to fall below the 10% level (e.g., Vanderlinde et al., 2010). Further study of the ongoing SZ surveys will better illuminate the impact that such sources can have on cosmological constraints from SZ cluster samples. Contamination by intrinsic CMB fluctuations and point sources are both mitigated by multi-frequency observations, since the SZ effect has a distinct spectral signature. While contamination and incompleteness of SZ samples remains an area of active research, we think these effects are unlikely to compete with mass calibration as a limiting uncertainty.

For optical cluster searches the primary source of contamination is projection effects – two or more small halos lining up to produce the apparent galaxy overdensity of a larger halo. These projections can arise from truly random superpositions or from galaxies or groups that lie in the same filamentary structure but not within the virial radius of a common halo. Even with galaxy spectroscopic redshifts, projection effects in the optical can produce contamination levels of 5%–20% depending on the richness threshold (Cohn et al., 2007; Rozo et al., 2011a); in a direct comparison of optical and X-ray catalogs, Andreon and Moretti (2011) conclude that the contamination of the former is 10% or less. The principal reason that projection effects are more important in optical catalogs than in X-ray or SZ catalogs is that optical catalogs tend to reach significantly lower mass thresholds at high redshift, which results in higher surface densities of clusters and therefore stronger projection effects. In fact, projection effects may well set the lower mass threshold at which cosmological analyses with optical clusters are possible. We anticipate that incompleteness and contamination can be adequately modeled through the use of realistic mock catalogs constructed using numerical simulations, provided they are constructed to match the clustering data of the survey under consideration. These mock catalogs can be analyzed using the same algorithms applied to the observational data, allowing one to quantitatively characterize the impact of projection effects. Many of the most recent optical analysis draw on such detailed mock catalogs, but greater accuracy will be needed for next generation surveys.

The impact of contamination on weak lensing mass calibration is somewhat subtle, and probably weaker than the naive expectation of depressing the estimated mass by $(1 + C)$ through dilution. When superposed galaxy groups masquerade as a single more massive cluster, their projected mass distributions are also superposed, and the lensing signal from this blend may be close to the signal that would come from a cluster of the combined richness. The net impact must again be evaluated with detailed mock catalogs.

6.4.3. Calibrating the core of $P(X|M, z)$

In addition to characterizing extended tails of the mass–observable relation, one must calibrate the “core” of $P(X|M, z)$, where scatter arises from physical variations in cluster properties at fixed halo mass, from observational noise, and from

low level contamination that produces small random fluctuations in the observable. These effects are typically assumed to produce a log-normal form of $P(X|M, z)$, i.e., Gaussian scatter in $\ln X$ at fixed M . The calibration task is then to determine the mean relation $\langle \ln X|M, z \rangle$ and the variance $\text{Var}(\ln X|M, z)$, and to characterize any deviations from log-normal form that are large enough to affect the predicted abundance. As the notation indicates, the relation can evolve with redshift, and the scatter and non-Gaussianity may depend on halo mass at fixed redshift.

We consider each of the relevant terms in turn, starting with the mean observable–mass relation. We have already expressed our view that statistical calibration methods, and stacked weak lensing in particular, are the most promising route to meeting the stringent demands of next-generation cluster surveys. Cunha et al. (2009) and Oguri and Hamana (2011) show that this approach allows the mass and redshift dependence of $\langle \ln X|M, z \rangle$ and $\text{Var}(\ln X|M, z)$ to be parameterized in an extremely flexible way while retaining enough information to yield strong cosmological constraints.

If the mean mass–observable relation is calibrated using stacked weak lensing, then the systematic effects discussed for WL in Section 5.7 are also sources of uncertainty for cluster studies. In particular, errors in the source galaxy redshift distribution and/or shear calibration will shift the inferred cluster mass scale. For these systematics to be insignificant, the rule of thumb is that the uncertainty in the mean inverse critical surface density $\langle \Sigma_{\text{crit}}^{-1} \rangle$ of the source galaxies and the error in the shear calibration must be smaller than the mass errors plotted in Fig. 28, divided by 1.5. The 1.5 factor comes in because an error in $\langle \Sigma_{\text{crit}}^{-1} \rangle$ or shear calibration uniformly biases the recovered cluster density profile and therefore biases the estimate of R_{200} . A bias b in the mass at a fixed aperture becomes roughly a bias $b^{1.5}$ in the estimated virial mass. Typically, a systematic error $\Delta \bar{z}$ in the mean redshift of sources produces a corresponding error $\sim \Delta \bar{z}/2$ in $\langle \Sigma_{\text{crit}}^{-1} \rangle$. Recent work suggests that controlling photometric redshifts at the level required for weak lensing mass calibration of galaxy clusters is possible (Sheldon et al., 2012). Importantly, because cluster weak lensing depends on the mean tangential shear around cluster centers, some forms of cosmic shear systematics are automatically averaged away and therefore not relevant for weak lensing mass calibration of galaxy clusters. For instance, errors that are coherent on scales larger than cluster diameters (typically a few arcmin) but incoherent on still larger scales will be averaged out in a stacked lensing measurement. Moreover, because the weak lensing signal about galaxy clusters is stronger than cosmic shear, uncertainties that appear for very low shear values (e.g., additive biases) are less important. All in all, the demands on weak lensing systematics for stacked weak lensing calibration of galaxy clusters are likely to be lower than those for cosmic shear.

There are some systematics specific to stacked cluster lensing, the most significant of which is cluster mis-centering. If the observationally determined center of a cluster does not match the location of the center of the dark matter halo that one would select in simulations, then the observed mean tangential shear about the assigned center will differ from the theoretical expectation. Cluster mis-centering should not be problematic in X-ray experiments with high angular resolution, as gas in hydrostatic equilibrium traces the underlying gravitational potential. While a few exceptions will arise, such as the famed Bullet Cluster (Clowe et al., 2006), the frequency of these systems is low. For similar reasons, centroiding of SZ systems is expected to be fairly robust. The mis-centering problem is most difficult in the optical, where the center is typically chosen to be a specific galaxy but the choice of galaxy is not necessarily obvious; X-ray studies of SDSS maxBCG clusters suggest that the mis-centered fraction is about 30% (Andreon and Moretti, 2011). Mis-centering is currently one of the dominant systematics in stacked cluster lensing, introducing uncertainties at the $\approx 5\%$ – 10% level (Johnston et al., 2007). There are ongoing efforts aimed at improving cluster centering (George et al., 2012). Oguri and Takada (2011) find that marginalizing over parameters that describe mis-centering does not significantly dilute the cosmological power of cluster abundance studies, so it may be that future analyses will simply treat mis-centering via an additional set of nuisance parameters. Alternative weak lensing estimators can be constructed to avoid mis-centering biases in the inner regions of clusters (Mandelbaum et al., 2010). Other potential biases that affect stacked cluster lensing are modulation of the source population by lensing magnification, non-linear shear corrections, and source density modulation due to obscuration by cluster members (see Rozo et al., 2011b; Hartlap et al., 2011). These effects can also have impact on cosmic shear experiments.

Turning to scatter, we can show that the magnitude of the variance $\text{Var}(\ln X|M, z)$ is degenerate with the mass scale through a simple argument. Suppose the observable of interest is a mass estimator $X = M_{\text{obs}}$, where the subscript indicates the observationally estimated cluster mass. The observed abundance is

$$\frac{dn}{d \ln M_{\text{obs}}} = \int d \ln M \frac{dn}{d \ln M} P(M_{\text{obs}}|M, z). \quad (150)$$

For a power-law mass function $dn/d \ln M = AM^{-\alpha} = A \exp(-\alpha \ln M)$ and log-normal scatter of variance $\sigma^2 = \langle (\ln M_{\text{obs}} - \ln M)^2 \rangle$, one can readily compute the observed abundance by completing the square, finding

$$\frac{dn}{d \ln M_{\text{obs}}} = A \exp\left(-\alpha \ln M_{\text{obs}} - \frac{1}{2}\alpha^2\sigma^2\right). \quad (151)$$

From Eq. (151) it is evident that a shift in mass $\Delta \ln M$ is degenerate with a shift in the variance $\Delta \sigma^2 = 2\alpha^{-1}\Delta \ln M$. (For a more rigorous argument that arrives at the same conclusion, see Lima and Hu, 2005.) Thus, if the mass scale is controlled with an accuracy $\Delta \ln M$, then the scatter must be controlled with an accuracy $\Delta \sigma^2 = 2\alpha^{-1}\Delta \ln M$. If we further set $\Delta \sigma^2 = 2\sigma \Delta \sigma$, we arrive at $\Delta \sigma = \alpha^{-1}\sigma^{-1}\Delta \ln M$. The fractional accuracy with which σ must be known to avoid competing with $\Delta \ln M$ scales as σ^{-2} , so the requirement is much less demanding if the scatter is smaller to begin with.

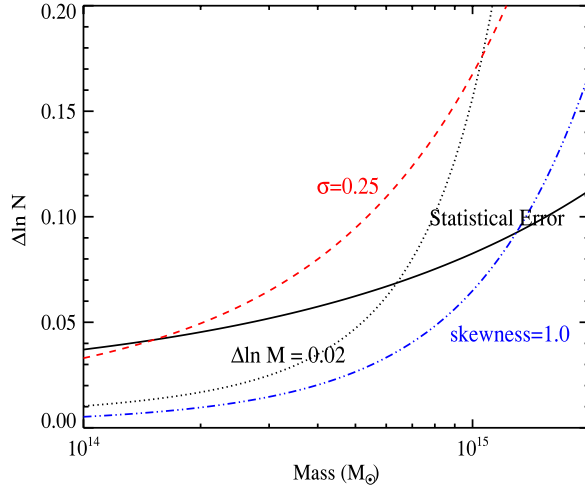


Fig. 29. Relative change in cluster abundances at $z = 0.6$ as a function of mass due to a 2% bias in the mass ($\Delta \ln M = 0.02$), raising the log-normal scatter σ from 0.2 to 0.25, or introducing skewness $\gamma = 1$ in $P(X|M, z)$ (solid, dashed, and dot-dashed curves, respectively). The statistical error in number counts for $A = 10^4 \text{ deg}^2$ is shown by the dotted line. The sensitivity of $\Delta \ln N$ to systematic errors in the mass, scatter, or skewness can be estimated using the rule-of-thumb approximations in Eqs. (154)–(156).

As an illustrative example, we set $\alpha = 3$ and $\sigma = 0.2$, which is roughly appropriate for SZ and likely slightly optimistic for optical. We find that the uncertainty due to errors in the scatter becomes comparable to that from errors in the mass when $\Delta \sigma \approx 1.7 \Delta \ln M$. For Stage III experiments with weak lensing calibration, yielding $\Delta \ln M \approx 2\%$, the scatter needs to be known at the $\Delta \sigma \approx 0.04$ level, a value in agreement with the more rigorous estimate by Rozo et al. (2011b) and likely to be achievable in the near future (see, e.g., Rykoff et al., 2012). If Stage IV experiments reach 0.5% precision, the corresponding uncertainty in the scatter must be below 0.01 (absolute, not fractional), which is difficult to achieve from an *ab initio* calculation but may be possible with statistical calibration methods.

Finally, we must consider the possibility that, in addition to extended tails reflecting contamination and incompleteness, the core of $P(X|M, z)$ deviates from log-normal form. This problem was considered by Shaw et al. (2008), whose discussion we paraphrase here. An observable–mass relation can be approximated by

$$P(\ln X|M) = G(x) - \frac{\gamma}{6} \frac{d^3 G}{dx^3} + \frac{\kappa}{24} \frac{d^4 G}{dx^4} + \dots \quad (152)$$

known as the Edgeworth expansion. Here G is a Gaussian of zero mean and unit standard deviation, $x = (\ln X - \langle \ln X \rangle) / [\text{Var}(\ln X|M, z)]^{1/2}$, γ is the skewness of the distribution, and κ is the kurtosis. For a power-law mass function $dn/d \ln M \propto M^{-\alpha}$, it is straightforward to check that the resulting cluster abundance is

$$\frac{dn}{dX} = \int dM \frac{dn}{dM} P(X|M) = \left(\frac{dn}{dX} \right)_0 \left[1 + \frac{\alpha^3 \sigma^3}{6} \gamma + \frac{\alpha^4 \sigma^4}{24} \kappa + \dots \right], \quad (153)$$

where $(dn/dX)_0$ is the abundance for a purely log-normal distribution. (Note that this α is also the logarithmic slope of the cumulative halo mass function $d \ln N / d \ln M$ that appears in our earlier discussion.)

Setting $\alpha = 3$ and assuming 10% scatter for X-ray masses, a 3% correction to the abundance – equivalent to a 1% correction in the mass – requires extreme non-Gaussianity with $\gamma \approx 7$ or $\kappa \approx 90$. Numerical simulations, on the other hand, predict distributions of X-ray observables that are close to log-normal (see, e.g., Stanek et al., 2010, Fig. 8; Fabjan et al., 2011, Fig. 3). We therefore do not expect X-ray studies to be sensitive to departures from a log-normal $P(X|M, z)$. For $[\text{Var}(\ln X|M, z)]^{1/2} = 0.2$, typical for SZ and perhaps achievable for optical, a 3% abundance change arises from $\gamma \approx 0.8$ or $\kappa \approx 6$, still quite large deviations from Gaussianity. For $[\text{Var}(\ln X|M, z)]^{1/2} = 0.4$ these numbers drop to 0.1 and 0.35, respectively, so with this level of scatter a moderate degree of non-Gaussianity can have noticeable impact on the predicted abundances. For example, a Poisson distribution for a cluster with $\langle N \rangle = 10$ galaxies corresponds to a skewness $\gamma \approx 0.3$. This discussion demonstrates the value of finding improved optical richness estimators that have lower scatter relative to mass (Roza et al., 2009; Rykoff et al., 2012).

Fig. 29 shows the impact that various elements of $P(X|M, z)$ can have on the recovered cluster counts. For illustrative purposes, we assume that X is an observed mass and show the change in the observed mass function due to changes in $P(M_{\text{obs}}|M, z)$. For our reference model, we assume M_{obs} is unbiased and has log-normal scatter $\sigma = 0.2$, and we compute the cumulative cluster counts above M_{obs} for our fiducial cosmology at $z = 0.6$ in a redshift bin of width $\Delta z = 0.1$. Results at other redshifts are qualitatively similar.

Solid, dashed, and dot-dashed curves show the change in the cumulative number counts $\Delta \ln N$ if M_{obs} is biased by 2% ($\Delta \ln M = 0.02$), if the scatter is increased from $\sigma = 0.2$ to $\sigma = 0.25$, or if the skewness is increased from $\gamma = 0$ to $\gamma = 1$

using the Edgeworth expansion. For reference, we also show the statistical error on the cluster counts for $A = 10^4 \text{ deg}^2$ as a dotted line. The details of $P(X|M, z)$ affect the recovered cluster counts, and the impact is larger at higher masses than at lower masses. Moreover, the relative impact of skewness to scatter and of scatter to bias is mass dependent, with lower masses being more robust to uncertainties in the scatter and skewness. This is as expected: the shallower the slope of the mass function, the less important the details of $P(X|M, z)$. The systematic offsets in Fig. 29 are well approximated (to $\approx 10\%$ and 30% for scatter and skewness respectively) by the rule-of-thumb calculations we have described above, specifically

$$\Delta \ln N_{\text{predicted}} = \alpha \Delta \ln M, \quad (154)$$

$$\Delta \ln N_{\text{predicted}} = \alpha^2 \sigma \Delta \sigma, \quad (155)$$

$$\Delta \ln N_{\text{predicted}} = \frac{1}{6} \alpha^3 \sigma^3 \Delta \gamma. \quad (156)$$

Given the values of $\Delta \ln N$ and α expected for a survey (Fig. 26; typical values $\Delta \ln N \approx N^{-1/2}$ and $\alpha \approx 3$), one can use Eqs. (154)–(156) to infer the uncertainties $\Delta \ln M$, $\Delta \sigma$, and $\Delta \gamma$ required to keep a cosmological analysis limited by abundance statistics.

6.4.4. Theoretical systematics

Predicting observed cluster counts via Eq. (149) requires knowledge of the halo mass function dn/dM for any cosmological model under consideration. If the fractional uncertainty in dn/dM exceeds the observational error in cluster counts $\Delta \ln N$, or if the equivalent mass scale uncertainty exceeds the mass calibration error $\Delta \ln M$, then cosmological constraints will be limited by theoretical uncertainty rather than by observational errors. The study of Tinker et al. (2008) finds agreement in dn/dM at the $\lesssim 5\%$ level among multiple simulations by different groups for a Λ CDM cosmological model with WMAP3 parameters. This is roughly the level required for large area surveys of $M > 4 \times 10^{14} M_\odot$ clusters in $\Delta z = 0.1$ bins, though higher accuracy is needed for lower mass thresholds (for detailed discussion see Cunha and Evrard, 2010; Wu et al., 2010). The formula (39) describes Tinker et al.'s $z = 0$ results accurately, but at redshifts $z = 0.5$ – 2.5 they find deviations of $\sim 10\%$ – 30% from this “universal” prescription. While these deviations are themselves numerically calibrated, their existence suggests that the mass function may depend on the dark energy model even when expressed in terms of the $\sigma(M)$ relation as in Eq. (39). In addition, consistency in halo definitions is clearly critical. For instance, Bhattacharya et al. (2011) find that mass functions in their suite of Λ CDM simulations – which are calculated using friends-of-friends halo finders – deviate by up to 10% from a fitting formula calibrated on their Λ CDM simulation suite. It seems likely that Stage III and certainly Stage IV experiments will need to move to emulator based methods with comprehensive N -body libraries (e.g., Lawrence et al., 2010) rather than simple fitting formulas.

While further N -body work is needed to interpret future surveys, dark matter evolution is straightforward in principle, and the problem should yield to sufficient applications of computational force. Baryonic evolution is potentially a thornier issue. Some X-ray studies suggest a depletion of baryonic mass (stars + hot gas) relative to the universal Ω_b/Ω_m ratio by 20% – 30% within the $\Delta = 500 \rho_c$ radius, with systematically larger depletion in less massive clusters (e.g., Giodini et al., 2009). For $\Omega_b/\Omega_m = 0.17$, a 20% deviation in baryonic mass is a 3.4% deviation in total mass, and thus comparable to or larger than the statistical mass calibration errors achievable with stacked weak lensing (Fig. 28), as well as the precision required to achieve the statistical limits of large cluster surveys (Fig. 23d). Hydrodynamic simulations can explain baryon depletions comparable to those observed (Young et al., 2011), but the magnitude and even the sign of the baryonic effects depend on the star formation and feedback physics (e.g., Stanek et al., 2009; Cui et al., 2012). Furthermore, because the baryons influence the dark matter profile, they can have substantial impact ($\sim 15\%$) on the total mass within a high overdensity threshold (e.g., the $\Delta = 500 \rho_{\text{crit}}$ threshold frequently adopted in X-ray analyses; see Stanek et al., 2009). In all of these simulations the corrections are smaller at larger radii, so defining halo boundaries at lower overdensity (such as the $\Delta = 200 \bar{\rho}$ convention used here) is beneficial in this respect.

It may be possible to calibrate baryonic effects well enough with simulations and detailed observations of selected systems to remove them as a source of systematic uncertainty, but this problem will require concerted effort, particularly when Stage IV experiments get underway. By the same token, if stacked weak lensing is the primary mass calibration tool, then one must also develop robust theoretical models for predicting the weak gravitational lensing signal, which in turn requires that the halo-mass correlation function be characterized at the same level as $\Delta \ln M$. Current analytical models are accurate only at the $\approx 10\%$ – 20% level (Hayashi and White, 2008), so this is another area that requires further theoretical study.

A final caveat related to the halo mass function is that primordial non-Gaussianity could alter its form (e.g., Weinberg and Cole, 1992; Dalal et al., 2008; Grossi et al., 2009; Loverde and Smith, 2011; D’amico et al., 2011) and thereby change the cluster abundances predicted for a given dark energy model (e.g., Cunha et al., 2010; Pillepich et al., 2012). Of course, evidence for non-Gaussian initial conditions would be exciting in its own right, with important implications for early-universe physics. However, it appears that the levels of non-Gaussianity that would have significant impact on cluster abundances are already ruled out by other constraints, unless one allows the magnitude of the non-Gaussianity to be scale-dependent (e.g., Hoyle et al., 2011; Paranjape et al., 2011). Given the strong theoretical prior for Gaussian initial conditions and the multiple observational probes that could detect and characterize primordial non-Gaussianity if it exists, we think it unlikely that non-Gaussianity will limit the power of cluster abundances as a probe of dark energy and modified gravity.

6.5. Space vs. ground

As discussed in Section 6.2, X-ray observations, possible only from space, have played a central role in nearly all cluster cosmological studies to date. The *ROSAT* All-Sky Survey has been the basis for many of the cluster samples used in these studies (Table 4). Pointed observations with a variety of telescopes, especially *XMM-Newton* and *Chandra*, have been the basis of mass calibration for X-ray observables and the source of most empirical knowledge about the physics of the intracluster gas. Ongoing *XMM-Newton* surveys will expand the dynamic range and size of X-ray catalogs over the next few years. The most important advance will come with the *eROSITA* mission (Merloni et al., 2012), which should produce the definitive all-sky survey of massive ($M \gtrsim 4 \times 10^{14} M_\odot$) clusters out to $z \approx 1$, with an extended tail of higher redshift clusters reaching $z \approx 2$. Follow-up X-ray studies at higher angular resolution will help better assess point-source contamination and will improve the mass calibration of the *eROSITA* catalog. For comparable numbers of clusters, X-ray catalogs offer significant advantages over SZ or optical catalogs because of the low scatter expected between X-ray observables and halo mass, which reduces sensitivity to uncertainties in the width and form of the observable–mass relation (Section 6.4.3).

For SZ searches, ground-based telescopes have higher sensitivity than space observatories because of their larger collecting area and higher angular resolution. The larger beam size of the *Planck* observatory (≈ 5 arcmin) relative to SPT and ACT (≈ 1 arcmin) reduces its ability to detect high redshift systems. Nonetheless, the all-sky nature of *Planck* observations is an important asset, and the *Planck* catalog of high mass clusters will be useful both for direct cosmological constraints and for cross-correlation studies with clusters identified at other wavelengths. Thus, we view the *Planck*, SPT, and ACT surveys as highly complementary. Any future CMB space mission designed to probe inflation physics and primordial gravity waves would also produce a much more sensitive all-sky SZ cluster catalog, provided it achieved high angular resolution.

Turning to optical searches, space observatories provide little advantage for cluster detection at $z \lesssim 1$, since cluster detection does not gain much from the improved image resolution achievable from space. However, as discussed in Section 6.3.2, space-based near-IR imaging is highly desirable for extending (rest-frame) optical cluster catalogs to $z \approx 2$. In the near future, such searches will rely on *Spitzer* data, as in the case of ISCS (Eisenhardt et al., 2008), SpARCS (Wilson et al., 2006), and the recently approved 100 deg² *Spitzer* – SPT Deep Field. Additional IR data is or will soon be available from surveys like VHS, UKIDSS, and *WISE*, which may allow for high redshift cluster finding (Gettings et al., 2012). The VIKING survey, covering ≈ 1500 deg², should be sufficiently deep to allow for robust cluster detection at $z > 1$. In the longer term, IR imaging from *Euclid* and/or *WFIRST* could make a key contribution to high redshift cluster surveys. High redshift cluster detection should also be feasible with extremely deep optical imaging from the ground, like that planned for LSST, which should reach $z \approx 1.5$.

In the long run, however, the most important contribution of space observations to cluster cosmology will come via weak lensing mass calibration rather than cluster finding. The statistical error of WL mass calibration scales as $\bar{n}_g^{-1/2}$, where \bar{n}_g is the source surface density. As can be seen from Fig. 28, a surface density $\bar{n}_g \approx 30$ arcmin⁻² is required to reduce mass calibration error below the statistical abundance error, and even then only for $z \lesssim 0.5$. This source density is expected for an optical space mission like *Euclid*, but it is probably higher than can be achieved by ground-based observations, even with the depth and image quality of LSST. The cluster counting error and mass calibration error both scale with survey area as $A^{-1/2}$, so the area effect cancels out if the cluster and WL surveys overlap completely. If the cluster survey covers a larger area (e.g., the all-sky *eROSITA* catalog), then the WL source density required to saturate the halo statistics limit is even higher. Reaching the calibration accuracy allowed by the source galaxy statistics also requires excellent control of shape measurement systematics, generally expected to be lower from a space-based platform, and photo- z systematics, which probably require space-based IR imaging to achieve the stringent demands implied by Fig. 28. More generally, if the error in WL mass calibration sets the ultimate limit of cluster measurements of fluctuation growth, as we have speculated it will, then the achievable error on $\sigma_{11,\text{abs}}(z)$ scales as $\bar{n}_g^{-1/2}$, or as $(\Delta\gamma)_{\text{sys}}^{-1}$ if the WL measurements are themselves limited by a shear measurement systematic $(\Delta\gamma)_{\text{sys}}$.

6.6. Prospects

We expect cluster abundance studies to undergo substantial and steady improvements over the next decade and beyond. In the near term ($\lesssim 3$ years), we anticipate advances in X-ray, SZ, and optical cluster studies. The XMM Cluster Survey (XCS) and XMM XXL Survey will yield much larger X-ray cluster samples at $z \gtrsim 0.3$. *Planck* will produce the definitive all-sky SZ catalog of massive clusters out to $z \lesssim 0.7$, while SPT and ACT will probe $z \gtrsim 0.7$ cluster populations over thousands of square degrees for the first time. In the optical, continuing studies with the SDSS will lead to improved cluster finders and richness estimators, as well as improved weak lensing calibration thanks to better centering and better source photometric redshifts. On a comparable time scale, the RCS-2 survey will obtain g , r , and z imaging to a nominal depth of $r \approx 24.8$ (roughly 2 magnitudes deeper than SDSS) over 1000 deg², yielding the first large area optical cluster catalog extending to $z \approx 1$. Relative to the results shown in Fig. 22, these X-ray, SZ, and optical studies will improve the low redshift σ_8 – Ω_m constraint and extend it, at somewhat lower precision, to $z \approx 0.5$ – 1 . At the same time, improved calibration and cross-checks among surveys will test for and reduce remaining sources of systematic error.

In the medium term (≈ 3 – 8 years), several new optical surveys will cover thousands of deg² with greater depth than SDSS and larger area and/or more photometric bands than RCS-2. These include the Kilo-Degree Survey (KIDS, 1500 deg²

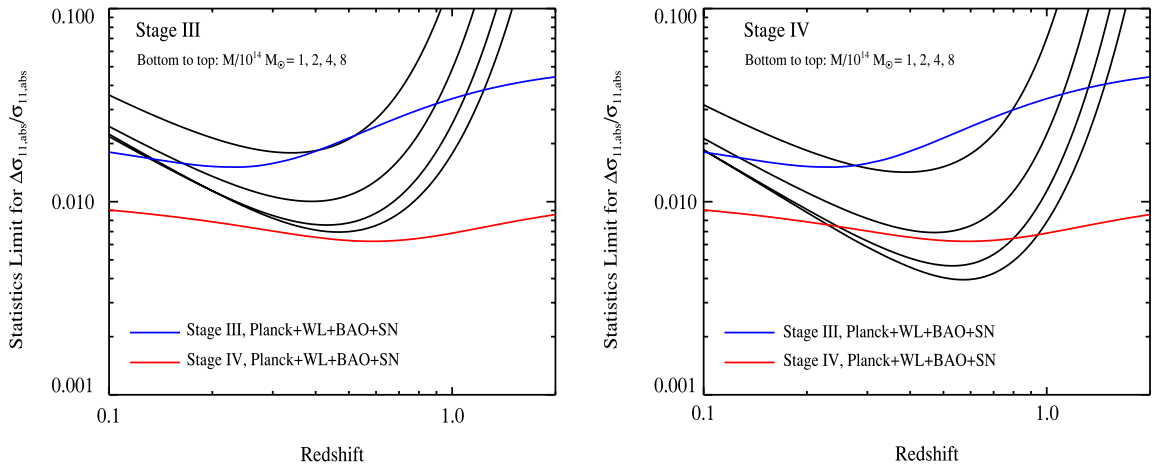


Fig. 30. Error on $\sigma_{11,abs}(z)$ achievable by measuring cluster abundances in a redshift bin $z = z_c \pm 0.05$ in a 10^4 deg^2 , assuming mass calibration via stacked weak lensing with Stage III or Stage IV source densities. We assume that all geometric cosmological parameters – most significantly the comoving volume element and the matter density parameter Ω_m – are held fixed, being effectively constrained by a joint CMB+SN+BAO+WL experiment. Also shown for comparison are the forecast constraints on $\sigma_{11,abs}(z)$ derived from such a joint analysis using our fiducial Stage III and Stage IV surveys, assuming a w_0-w_a parameterization of dark energy and allowing deviations from GR parameterized by G_9 and $\Delta\gamma$ (see Section 8.4 for details).

in *ugriz*), DES (5000 deg^2 in *grizY*), PS1 (15,000 deg^2 in *grizY*), and the Hyper-Suprime Camera survey (HSC, 1500 deg^2 in *grizY*). These surveys should significantly improve the cosmological constraints relative to RCS-2, thanks to higher cluster numbers, lower statistical errors in weak lensing mass calibration, and better control of photometric redshift uncertainties. The VIKING survey will cover 1500 deg^2 at near-IR wavelengths (*ZYJHK_s*) at sufficient depth to allow cluster identification and accurate photometric redshifts at $z = 1-2$. In addition, all of these surveys will overlap with *Planck*, and often with either the ACT or SPT surveys, which can further enhance the utility of both sets of catalogs. DES in particular is designed to cover the entire footprint of the SPT SZ survey.

With launch expected 2013–2014, *eROSITA* will produce the ultimate all-sky catalog of massive clusters (see Section 6.5). The optical imaging surveys will allow weak lensing calibration of the *eROSITA* mass–observable relations, with multiple independent surveys affording larger overlap area and thus more precise calibration. This combination of X-ray selection and optical WL calibration offers bright prospects for the coming decade of cluster cosmology. Optical surveys will further extend this leverage by probing cluster abundances to masses below those probed by *eROSITA*.

On a longer timescale, LSST plans to image 20,000 deg^2 of high-latitude sky in six bands (*ugrizY*), with each single pass comparable in depth to the medium-term surveys described above and co-added data reaching 2.5–3 magnitudes deeper. The increased depth of LSST should allow one to cleanly select galaxy clusters out to $z \approx 1.5$. While the greater dynamic range of the cluster catalogs will be an asset in itself, LSST’s most important contribution to cluster cosmology will be in the form of improved WL mass calibration, both for *eROSITA* and for LSST’s own clusters. *Euclid* could provide even better WL calibration over a similar sky area, while *WFIRST* should achieve a high WL source density but over a smaller survey area. The IR sensitivity of *Euclid* and/or *WFIRST* should also enable cluster searches at $z \approx 2$ and beyond.

We have argued throughout this section that mass calibration will be the likely limiting factor in cluster studies of cosmic acceleration, and that stacked weak lensing is the most promising avenue to achieve accurate mass calibration. Fig. 30 combines information from Figs. 24 and 28, showing the fractional error on $\sigma_{11,abs}(z)$ in $\Delta z = 0.1$ bins that can be achieved with a 10^4 deg^2 cluster survey, using the WL mass calibration errors we have forecast for Stage III (left panel) or Stage IV (right panel) source densities. With Stage III lensing calibration, errors on $\sigma_{11,abs}(z)$ are below 1% at $z \approx 0.5$ for cluster mass thresholds of $1 - 2 \times 10^{14} M_{\odot}$, and $\sim 1.5\%$ for a mass threshold of $4 \times 10^{14} M_{\odot}$. With Stage IV lensing calibration, the peak sensitivity is better than 0.5% for the lower mass thresholds and better than 1% for the $4 \times 10^{14} M_{\odot}$ threshold.

The additional red and blue curves in Fig. 30 show the forecast constraints on $\sigma_{11,abs}(z)$ for a fiducial Stage III (blue) or Stage IV (red) program combining SN, BAO, WL, and CMB data as discussed in Section 8. These forecasts assume a w_0-w_a dark energy model and allow departures from GR-predicted growth described by an overall multiplicative offset G_9 and a growth index deviation $\Delta\gamma$ (see Section 2.2). The fiducial programs are defined in Section 8.1. If WL systematics are controlled at the level assumed in these fiducial programs then they should be negligible for cluster mass calibration relative to statistical errors, so we have not included them in computing $\Delta \ln M$.

From Fig. 30 we see that a 10^4 deg^2 cluster survey with Stage III WL calibration data can easily exceed the $\sigma_{11,abs}(z)$ precision expected from the Stage III CMB+SN+BAO+WL program, by as much as a factor of ≈ 3 for a threshold of $10^{14} M_{\odot}$. Similarly, cluster constraints with Stage IV WL calibration improve on the fiducial Stage IV $\sigma_{11,abs}(z)$ precision without clusters by a factor of ≈ 2 . The visual impression that clusters can outperform the fiducial program only at $z \approx 0.4-0.8$ but perform worse at high and low redshifts is artificial, since the CMB+SN+BAO+WL curves assume a smooth growth model while the cluster constraints in Fig. 30 are those that can be achieved from galaxy clusters within each individual redshift

bin. For Fig. 30 we have assumed that errors on Ω_m and $dV_c(z)$ are negligible. While the assumption for $dV_c(z)$ should prove reasonably accurate, the forecast CMB+SN+BAO+WL errors on Ω_m (4% and 1% for Stage III and Stage IV, respectively) are larger than our assumed WL mass calibration errors for $M \lesssim 2 \times 10^{14} M_\odot$ (see Fig. 28). In practice, therefore, the fractional errors in Fig. 30 would apply not to $\sigma_{11,\text{abs}}(z)$ but to the parameter combination $\sigma_{11,\text{abs}}(z)\Omega_m^q$, with $q \approx 0.4$. We return to these points in Section 8.4 below, where we discuss the improvements in constraints on the dark energy equation of state and on G_0 and $\Delta\gamma$ achievable with clusters.

If some alternative mass calibration method proves better than stacked weak lensing, then the situation could be even better than Fig. 30 suggests. This would be especially true for Stage III, where the WL source density is the clear limiting factor on the overall error. For our assumed Stage IV source density, the uncertainty from WL mass calibration is already close to the statistical uncertainty in cluster counts at $z \lesssim 0.6$. Conversely, the situation would be worse than Fig. 30 suggests if some other systematic uncertainty – e.g., contamination, miscentering, theory, or WL photo- z calibration – makes it impossible to achieve the statistical limits of the WL mass calibration.

In summary, our analysis indicates that cluster abundances with masses calibrated by stacked weak lensing could provide strong tests of cosmic acceleration models, beyond those afforded by the 2-point WL statistics described in Section 5. However, achieving this potential requires that mass calibration uncertainties be controlled at the 1%–3% level for Stage III and at the 0.5%–1.5% level for Stage IV. We see no obvious show stoppers, but the challenge is a demanding one.

7. Alternative methods

In Sections 3–6, we have reviewed in detail the four observational methods that have been most widely discussed, and applied, as probes for the origin of cosmic acceleration. We now review more briefly some of the other techniques for testing cosmic acceleration models. In some cases, surveys conducted for SN, BAO, or WL studies will automatically provide the data needed for these alternative methods. For example, redshift-space distortions (Section 7.2) and the Alcock–Paczynski effect (Section 7.3) can be measured in galaxy redshift surveys designed for BAO measurements, and synoptic surveys designed for Type Ia supernovae will discover other transients that might provide alternative distance indicators (Section 7.4). Just as cluster investigations will increase the cosmological return from WL surveys, these methods will increase the return from BAO or SN surveys. The potential gains are large, but they are uncertain because the level of theoretical or observational systematics for these methods has not yet been comprehensively explored. In Section 8.5 we will examine how precisely our fiducial Stage III or Stage IV CMB+SN+BAO+WL programs predict the observables of these methods, setting targets for the precision and accuracy they should achieve to make major contributions to cosmic acceleration studies.

Some of the other methods described below require completely different types of observations or experiments, falling outside of the “survey mode” that characterizes the methods we have discussed so far. Compared to the combined SN+BAO+WL+CL approach, these methods may yield more limited information or be sensitive only to certain classes of acceleration models, but they can provide high-precision tests of the standard Λ CDM model, and they could yield surprising results that would give strong guidance to the physical origin of acceleration.

7.1. Measurement of the Hubble constant at $z \approx 0$

As emphasized by Hu (2005), a precise measurement of the Hubble constant, when combined with CMB data, allows a powerful test of dark energy models and tightened constraints on cosmological parameters. In effect, the CMB and H_0 provide the longest achievable lever arm for measuring the evolution of the cosmic energy density, from $z \approx 1100$ to $z = 0$. The sensitivity of H_0 to dark energy is illustrated in Fig. 2, which shows that a change $\Delta w = \pm 0.1$ alters the predicted value of H_0 by 5% in $\Omega_k = 0$ models that are normalized to produce the same CMB anisotropies. More generally, a low redshift determination of the Hubble constant combined with *Planck*-level CMB data constrains w with an uncertainty that is twice the fractional uncertainty in H_0 , assuming constant w and flatness. The challenge for future H_0 studies is to achieve the percent-level statistical and systematic uncertainties needed to remain competitive with other cosmic acceleration methods. Freedman and Madore (2010) review recent progress in H_0 determinations and prospects for future improvements; the past five years have seen substantial advances in both statistical precision and reduction of systematic uncertainties.

One of the defining goals of the *Hubble Space Telescope* was to measure H_0 to an accuracy of 10%. The H_0 Key Project achieved this goal, with a final estimate $H_0 = 72 \pm 8 \text{ km s}^{-1} \text{ Mpc}^{-1}$ (Freedman et al., 2001), where the error bar was intended to encompass both statistical and systematic contributions. This estimate used Cepheid-based distances to relatively nearby ($D < 25 \text{ Mpc}$) galaxies observed with WFPC2 to calibrate a variety of secondary distance indicators – Type Ia supernovae, Type II supernovae, the Tully–Fisher relation of disk galaxies, and the fundamental plane and surface-brightness fluctuations of early-type galaxies. These secondary indicators were in turn applied to galaxies “in the Hubble flow”, meaning galaxies at large enough distance ($D \approx 40\text{--}400 \text{ Mpc}$) that their peculiar velocities v_{pec} did not contribute significant uncertainty when computing $H_0 = v/d$. The Cepheid period–luminosity (P – L) relation was calibrated to an adopted distance modulus of $18.50 \pm 0.10 \text{ mag}$ for the Large Magellanic Cloud (LMC). The uncertainty in adjusting the LMC optical P – L relation to the higher characteristic metallicities of calibrator galaxies was an important contributor to the final error budget; Freedman et al. (2001) adopted a $\pm 0.2 \text{ mag/dex}$ uncertainty in the metallicity dependence, implying a $\sim 0.07 \text{ mag}$ systematic uncertainty in the correction (3.5% in distance). Another important systematic was the uncertainty in

differential measurements of Cepheid fluxes and colors over a wide dynamic range along the distance ladder. The uncertainty of the LMC distance itself was also a significant fraction of the error budget.

A number of subsequent developments have allowed substantial improvements in the measurement of H_0 (see Riess et al., 2009, 2011; Freedman and Madore, 2010; Freedman et al., 2012). The recent determination of $H_0 = 73.8 \pm 2.4 \text{ km s}^{-1} \text{ Mpc}^{-1}$ by Riess et al. (2011) yields a 1σ uncertainty of only 3.3%, including all identified sources of systematic uncertainty and calibration error. One important change in this analysis is a shift to Cepheid calibration based on the maser distances to NGC 4258 (Herrnstein et al., 1999; Humphreys et al., 2008, in press) and on parallaxes to Galactic Cepheids measured with *Hipparcos* (van Leeuwen et al., 2007) and with the *HST* fine-guidance sensors (Benedict et al., 2007). These calibrations circumvent the statistical and systematic uncertainties in the LMC distance, and they directly calibrate the P – L relation in the metallicity range typical of calibrator galaxies, albeit with a sample of only ~ 10 stars reaching an error-on-the-mean of 2.8% in the case of Milky Way parallaxes. A second improvement is more than doubling the sample of “ideal” Type Ia SNe – with modern photometry, low-reddening, typical properties, and caught before maximum – from the two available to Freedman et al. (2001) to eight. Of all secondary distance indicators, Type Ia supernovae have the smallest statistical errors, and probably the smallest systematic errors, and they can be tied to large samples of supernovae observed at distances that are clearly in the Hubble flow. Riess et al. (2009, 2011) use Type Ia supernovae exclusively in their H_0 estimates. Third, Cepheid observations at near-IR wavelengths ($1.6 \mu\text{m}$) have reduced uncertainties associated with extinction and the dependence of Cepheid luminosity on metallicity (Riess et al., 2012). Finally, relative calibration uncertainties of Cepheid photometry obtained with different instruments and photometric systems along the distance ladder have been mitigated by the use of a single instrument, *HST*’s WFC3, for a large fraction of the data.

Extending the trend toward longer wavelength calibration, Freedman et al. (2011) and Scowcroft et al. (2011) argue that $3.6 \mu\text{m}$ measurements – possible with *Spitzer* and eventually with *JWST* – minimize systematic uncertainties in the Cepheid distance scale because of low reddening and weak metallicity dependence. Monson et al. (2012) calibrate the $3.6 \mu\text{m}$ P – L zero-point against Galactic Cepheid samples, including the Benedict et al. (2007) parallax sample, and thereby infer the distance modulus to the LMC as a test of the optical Cepheid P – L relation and its metallicity correction. Freedman et al. (2012) use these Milky Way parallaxes to calibrate the optical Cepheid P – L relation and then recalibrate the Key Project data set to infer H_0 ; this determination still relies on optical, WFPC2 Cepheid data (and the associated metallicity corrections and flux and color zero-point uncertainties), and the Key Project SN Ia calibrator sample includes several SNe with photographic photometry or high extinction. Sorce et al. (2012) use the Tully and Fisher (1977) relation in the *Spitzer* $3.6 \mu\text{m}$ band, normalized to the Monson et al. (2012) LMC distance, to recalibrate the SN Ia absolute magnitude scale and thereby infer H_0 . Suyu et al. (2012a) infer H_0 from gravitational lens time delays for two well constrained systems, an approach that sidesteps the traditional distance ladder entirely (see Section 7.10 for further discussion). These four recent H_0 determinations (Riess et al., 2011; Freedman et al., 2012; Sorce et al., 2012; Suyu et al., 2012a) agree with each other to better than 2%. While the data used for the first three are only partly independent, this level of consistency is nonetheless an encouraging indicator of the maturity of the field. With the precision of H_0 measurements already at a level that allows critical tests of dark energy models in combination with CMB, BAO, and SN data (see, e.g., Anderson et al., 2012), a key challenge for the field is convergence on error budgets that neither underrepresent the power of the data nor understate systematic uncertainties.

Over the next decade, it should be possible to reduce the uncertainty in direct measurement of H_0 to approach the one-percent level. One crucial step will be the 1% to 5% parallax calibration of hundreds of long-period Galactic Cepheids within 5 kpc by the *Gaia* mission, setting the fundamental calibration of the multi-wavelength P – L relation and, to some degree, its metallicity dependence on a solid geometrical base with distance precision easily better than 1%. New Milky Way parallax measurements using the spatial scanning capability of *HST* may achieve this precision even sooner. Discovery of additional galaxies with maser distances (like NGC 4258) may also improve the Cepheid calibration or, if they are in the Hubble flow, may provide a direct determination of the Hubble constant (see Reid et al., 2013 for a recent measurement of UGC 3789 and Greenhill et al., 2009 for additional candidates). The other key step will be the Cepheid calibration of more Type Ia supernovae, which occur at a rate of one per 2–3 years in the range $D < 35 \text{ Mpc}$ accessible to *HST* with WFC3. *JWST* could increase this range to $D < 60 \text{ Mpc}$, quadrupling the rate of usable supernovae. Ultimately a sample of 20 to 30 calibrations of the SN Ia luminosity is needed to reduce the sample size contribution to uncertainty in H_0 below 1%. With firmer P – L calibration and a larger Type Ia sample, the remaining uncertainty in H_0 is likely to be dominated by systematic uncertainty in the linearity of the photometric systems observing nearby and distant Cepheids. This may be minimized by the careful construction of “flux ladders”, analogous to distance ladders but used to compare the measurements of disparate flux levels. Additional contributions to the determination of H_0 with few percent precision could come from “golden” lensing systems, infrared Tully–Fisher distances, surface brightness fluctuation measurements further into the Hubble flow, Sunyaev–Zel’dovich effect measurements, and local volume measurements of BAO.

We discuss the potential contribution of H_0 measurements to dark energy constraints in Sections 8.3 and 8.5 below. Already, the combination of the 3% measurement of Riess et al. (2011) with CMB data alone yields $w = -1.08 \pm 0.10$, assuming a flat universe with constant w . The limitation of H_0 is, of course, that it is a single number at a single redshift, so while it can test any well specified dark energy model, it provides little guidance on how to interpret deviations from model predictions. However, precision H_0 measurements can significantly increase the constraining power of other measurements: for our fiducial Stage IV program described in Section 8, assuming a w_0 – w_a model for dark energy, a 1% H_0 measurement would raise the DETF Figure of Merit by 40%. A direct measurement of H_0 also has the potential to reveal departures from the

smooth evolution of dark energy enforced by the w_0-w_a parameterization. In essence, the dark energy model transfers the absolute distance calibration from moderate redshift BAO measurements down to $z = 0$, but unusual low redshift evolution of dark energy can break this link, shifting H_0 away from its expected value. A precise determination of H_0 , coupled to a $w(z)$ parameterization that allows low-redshift variation, could reveal recent evolution of dark energy and definitively answer the basic question, “Is the universe *still* accelerating?”

7.2. Redshift-space distortions

As discussed in Section 2.3, peculiar velocities make large scale galaxy clustering anisotropic in redshift space (Kaiser, 1987). In linear theory, the relation between the real-space matter power spectrum $P(k)$ and the redshift-space galaxy power spectrum $P_g(k, \mu)$ at redshift z follows Eq. (43): $P_g(k, \mu) = [b_g(z) + \mu^2 f(z)]^2 P(k)$, where $b_g(z)$ is the galaxy bias factor, $f(z)$ is the logarithmic growth rate of fluctuations, and μ is the cosine of the angle between the wavevector \mathbf{k} and the line of sight. The strength of the anisotropy is governed by distortion parameter $\beta = f(z)/b_g(z)$, which has been measured for a variety of galaxy redshift samples (e.g., Cole et al., 1995; Peacock et al., 2001; Hawkins et al., 2003; Okumura et al., 2008). By modeling the full redshift-space galaxy power spectrum one can extract the parameter combination $f(z)\sigma_8(z)$, the product of the matter clustering amplitude and the growth rate (see Percival and White, 2009, who provide a clear review of the physics of redshift-space distortions and recent theoretical developments). Like any galaxy clustering measurement, statistical errors for redshift-space distortion (RSD) come from the combination of sample variance – determined by the finite number of structures present in the survey volume – and shot noise in the measurement of these structures (see Section 4.4.1). Optimal weighting of galaxies based on their host halo masses can reduce the effects of shot noise below the naive expectation from Poisson statistics (Seljak et al., 2009; Cai and Bernstein, 2012; Hamaus et al., 2012). However, sample variance has a large impact on RSD measurements because filaments and walls extend for many tens of Mpc with specific orientations, so even in real space one would find isotropic clustering only after averaging over many such structures. McDonald and Seljak (2009) show that one can partly beat the limits imposed by sample variance by analyzing multiple galaxy populations with distinct bias factors in the same volume, which allows one to extract information from the b_g -dependence of the amplitude $\delta_g(\mathbf{k}, \mu)$ of each individual mode, rather than just the variance of the modes. Bernstein and Cai (2011) provide a nicely pedagogical discussion of this idea.

Anisotropy of clustering in galaxy redshift surveys thus offers an alternative to weak lensing and cluster abundances as a tool for measuring the growth of structure. While WL and clusters constrain the amplitude of matter clustering and yield growth rate constraints from measurements at multiple redshifts, redshift-space distortions directly measure the rate at which structure is growing at the redshift of observation; the coherent flows responsible for RSD are the same flows that are driving the growth of fluctuations (Eq. (42)). Recent observational analyses include the measurement of Guzzo et al. (2008) from the VIMOS-VLT Deep Survey (VVDS), $f(z) = 0.91 \pm 0.36$ at $z \approx 0.8$, the measurement of Samushia et al. (2012) from SDSS DR7, obtaining $\sim 10\%$ constraints on $f(z)\sigma_8(z)$ at $z = 0.25$ and $z = 0.37$, the measurement of Blake et al. (2011a) from the WiggleZ survey, obtaining $\sim 10\%$ constraints in each of four redshift bins from $z = 0.1$ to $z = 0.9$, the measurement of Reid et al. (2012) from BOSS, obtaining a $\sim 8\%$ constraint at $z = 0.57$, and the local measurement of Beutler et al. (2012) from the 6dFGS, obtaining a $\sim 13\%$ constraint at $z = 0.067$. All of these measurements assume Λ CDM geometry when inferring $f(z)\sigma_8(z)$, and their derived growth parameters are consistent with Λ CDM predictions.

Redshift-space distortions can be measured with much higher precision from future redshift surveys designed for BAO studies. These measurements can improve constraints on dark energy models assuming GR to be correct, and they can be used to constrain (or reveal) departures from GR by testing consistency of the growth and expansion histories. The key challenge in modeling RSD is accounting for non-linear effects, including non-linear or scale-dependent bias between galaxies and matter, at the level of accuracy demanded by the measurement precision. The linear theory formula (43) is an inadequate approximation even on scales of $50h^{-1}$ Mpc or more (Cole et al., 1994; Hatton and Cole, 1998; Scoccimarro, 2004) because of a variety of non-linear effects, including the “finger-of-God” (FoG) distortions in collapsing and virialized regions, which are opposite in sign from the linear theory distortions. Their effects are commonly modeled by adding an incoherent small scale velocity dispersion to the linear theory distortions, but this model is physically incomplete, and it typically leaves 5%–10% systematic errors in β estimates (Hatton and Cole, 1998). Higher order perturbation theory can be used to refine the large scale predictions (Scoccimarro, 2004), but this does not capture the small scale dispersion effects, which are themselves significantly different for galaxies vs. dark matter. Tinker et al. (2006) and Tinker (2007) advocate an approach based on halo occupation modeling, which has the virtue of adopting an explicit, self-consistent physical description that can encompass linear, quasi-linear, and fully non-linear scales. However, the model is complicated, and it is presently implemented using numerically calibrated fitting formulas that may not generalize to all cosmologies. Following similar lines, Reid and White (2011) present a simpler and more fully analytic scheme for computing redshift-space clustering of halos, which may prove sufficiently accurate for the large scales probed by future surveys. Hikage et al. (2011) suggest using galaxy–galaxy lensing to estimate the radial distribution of tracer galaxies in their dark matter halos and combining with the virial theorem to predict the FoG profile. Other recent discussions of analytic or numerically calibrated models of non-linear RSD, from different perspectives, include Taruya et al. (2010), Jennings et al. (2011), Seljak and McDonald (2011), Jennings (2012) and Okumura et al. (2012); this is a highly active area of current research.

Linear theory RSD depends only on the growth parameters $f(z)\sigma_8(z)$, but testing non-GR models such as $f(R)$ gravity with RSD may require full numerical simulations to capture non-linear effects in these models (e.g., Jennings et al., 2012a;

Li et al., 2013). While analytic models are convenient when fitting data to extract parameter values and errors, there is no problem of principle in using brute-force numerics to compute RSD predictions, for either GR or modified gravity models. The fundamental question is the limit on the accuracy of predictions that will be imposed by uncertainties in galaxy formation physics, such as the relative velocity dispersions of galaxies and dark matter within halos. These limits are poorly understood at present.

Since the number of Fourier modes in a 3-dimensional volume increases as k^3 , the precision of clustering measurement is generally higher on smaller scales, at least until one hits the shot noise limits of the tracer population. Forecasts of cosmological constraints from RSD remain uncertain because it is not clear how small a scale and how high a precision one can go to before being limited by theoretical modeling systematics. The impact of theoretical systematics is often characterized implicitly in terms of a maximum wavenumber k_{\max} used in the modeling. As one goes to larger k_{\max} the non-linear effects are larger, and the demands on modeling them accurately become more stringent because the statistical precision is higher. One can think of k_{\max} as representing the crossover scale where theoretical uncertainties become comparable to the statistical uncertainty, a scale that depends on the survey volume as well as the modeling accuracy itself. Most forecasts (including ours below) assume that modeling is perfect up to k_{\max} but uses no information from higher k . In practice, analyses may continue to high k but marginalize over systematic uncertainties, leading to an “effective” value of k_{\max} that determines the strength of the RSD constraints.

Plausible assumptions suggest promising prospects for future RSD experiments. For example, assuming a maximum k equal to $0.075h \text{ Mpc}^{-1}$ at $z = 0$ and tracking the non-linear scale k_{nl} at higher redshifts, White et al. (2009) predict 1σ errors on $f(z)\sigma_8(z)$ of a few percent per $\Delta z = 0.1$ redshift bin out to $z = 0.6$ from the SDSS-III BOSS survey, and for a space-based survey that achieves a high galaxy density⁶⁹ out to $z = 2$ they predict errors per $\Delta z = 0.1$ that drop from $\sim 1\%$ at $z = 0.8$ to $\sim 0.2\%$ at $z = 1.9$. These forecasts incorporate the McDonald and Seljak (2009) method for beating sample variance. Reid and White (2011) examine BOSS RSD forecasts in more detail, considering the impact of modeling uncertainties. They forecast a 1σ error on $f(z)\sigma_8(z)$ at $z = 0.55$ of 1.5% using correlation function measurements down to a comoving scale $s_{\min} = 10h^{-1} \text{ Mpc}$, rising to 3% if the minimum scale is $s_{\min} = 30h^{-1} \text{ Mpc}$. (The corresponding wavenumber scale is $k_{\max} \approx 1.15\pi/s_{\min}$.) These forecasts assume marginalization over a nuisance parameter σ_v characterizing the small scale velocity dispersion. They improve by a factor of ~ 1.5 if σ_v is assumed to be known perfectly, demonstrating the potential gains from a method (like that of Tinker, 2007) that can use smaller scale measurements to pin down the impact of velocity dispersions. More generally, small scale clustering may be useful to pin down the nuisance parameters of large scale RSD models and therefore improve the precision of the cosmological parameter measurements (Tinker et al., 2006).

At the percent level there is another potential systematic error in RSD if the selection function has an orientation dependence (e.g., due to fiber aperture or self-extinction by dust in the target galaxy) and galaxies are aligned by the large-scale tidal field. This exactly mimics RSD, even in the linear regime (Hirata, 2009), but fortunately the effect seems to be negligible for present surveys. Orientation-dependent selection is predicted to be a larger effect for high- z Ly α emitters (Zheng et al., 2011), since there the radiation can resonantly scatter in the IGM and must make its way out through the large-scale velocity flows surrounding the galaxy; at very high redshift ($z = 5.7$) simulations predict an order unity effect. The implications for Ly α emitters at more modest redshift will become clear with the HETDEX survey.

In Section 8.5.3 we show that our fiducial Stage IV program (CMB+SN+BAO+WL) constrains $\sigma_8(z)f(z)$ to a 1σ precision of 2% at $z = 0.5$ and 1% at $z \gtrsim 1$ if we assume a w_0 - w_a dark energy model with G_0 and $\Delta\gamma$ as parameters to describe departures from GR. Thus, RSD measurements with this level of precision or better can significantly improve the figure-of-merit for dark energy constraints and sharpen tests of GR, even in a combined program that includes powerful weak lensing constraints. Much weaker RSD measurements could still make a significant contribution to Stage III constraints. Forecasts of the contribution of redshift-space distortions to constraints from specific Stage IV experiments (a BigBOSS-like ground-based survey and a *Euclid*- or *WFIRST*-like space-based survey) are presented by Stril et al. (2010), Wang et al. (2010) and Wang et al. (2013).

To provide guidance for our forecast discussions in Section 8, we have used the publicly available code of White et al. (2009) to predict errors on $f(z)\sigma_8(z)$ for different assumptions about survey parameters and modeling limitations. The solid curves in Fig. 31 show predicted fractional errors per $\Delta z = 0.1$ redshift bin assuming a survey with $f_{\text{sky}} = 0.25$ and a sampling density that yields $nP(k = 0.2h \text{ Mpc}^{-1}) = 2$, the same assumptions that we make for our fiducial Stage IV BAO program (see Section 8.1). In contrast to BAO forecasts, which depend only on the combination nP , RSD forecasts also depend separately on the bias evolution $b_g(z)$ because more strongly biased tracers exhibit weaker anisotropy (lower β) and therefore provide less leverage on $f(z)\sigma_8(z)$. Here we have assumed strongly biased tracers (such as luminous red galaxies) at $z < 0.9$ and weaker bias (appropriate to emission line galaxies) at $z > 0.9$; specifically, we adopt $b_g(z)\sigma_8(z) = 1.3$ at $z < 0.9$ (motivated by Reid et al., 2012) and $b_g(z)\sigma_8(z) = 0.6$ at $z > 0.9$, corresponding to $b_g = 1.5$ at $z = 1.5$ (see Orsi et al., 2010 and Geach et al., 2012). This change in assumed bias factor produces the sharp drop in the forecast error at $z = 0.9$. Maintaining $nP = 2$ would, of course, require a corresponding jump in galaxy density for $z > 0.9$. Upper and lower curves correspond to $k_{\max} = 0.1h \text{ Mpc}^{-1}$ and $0.2h \text{ Mpc}^{-1}$, respectively. In either case, the forecast error drops with

⁶⁹ We caution that the space densities assumed by White et al. (2009) are much higher than those that *Euclid* or *WFIRST* is likely to achieve, so these RSD precision forecasts may prove overoptimistic. Recent forecasts in the specific context of *Euclid* and *WFIRST* appear in Majerotto et al. (2012) and Green et al. (2012), respectively.

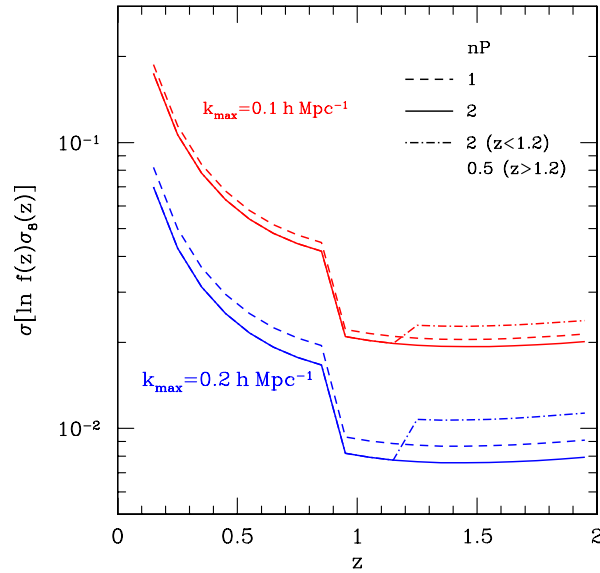


Fig. 31. Forecast errors on $f(z)\sigma_8(z)$ per $\Delta z = 0.1$ redshift bin from an RSD survey with $f_{\text{sky}} = 0.25$, computed with the code of White et al. (2009). For simplicity, we assume linear theory up to $k_{\text{max}} = 0.1 h \text{ Mpc}^{-1}$ (upper) or $k_{\text{max}} = 0.2 h \text{ Mpc}^{-1}$ (lower) and no information from smaller scales. Solid and dashed curves show sampling densities $nP = 2$ and $nP = 1$, respectively, and dot-dashed curves show a case where nP drops from 2 to 0.5 at $z = 1.2$. The sharp drop at $z = 0.9$ reflects an assumed change in bias factors from a high value (appropriate to absorption-line galaxies) at low z to a lower value (appropriate to emission-line galaxies) at high z .

increasing redshift out to $z = 0.9$ because of the larger comoving volume per $\Delta z = 0.1$ bin, then stays roughly constant from $z = 0.9$ – 2 .

For $k_{\text{max}} = 0.2 h \text{ Mpc}^{-1}$ and $nP = 2$, the error per bin is about 0.8% from $z = 0.9$ – 2 . Lowering the sampling density from $nP = 2$ to $nP = 1$ degrades the fractional error by about 12.5%, equivalent to a 25% reduction in f_{sky} . The dot-dashed curve shows the case in which we assume $nP = 2$ for $z < 1.2$ and $nP = 0.5$ for $z > 1.2$, where emission line galaxy redshifts become increasingly difficult to obtain from the ground and the dominant samples may eventually come from slitless spectroscopic surveys with *Euclid* and *WFIRST*. In this case, the high redshift error increases by $\sim 40\%$. Reducing nP has less impact for $k_{\text{max}} = 0.1 h \text{ Mpc}^{-1}$ because structure at this larger scale is more fully sampled, leaving sample variance as the dominant source of measurement uncertainty.

Fig. 31 highlights the critical role of modeling uncertainty in determining the ultimate cosmological return from RSD measurements. If we assume $k_{\text{max}} = 0.1 h \text{ Mpc}^{-1}$ instead of $k_{\text{max}} = 0.2 h \text{ Mpc}^{-1}$, then the errors for $nP = 2$ are larger by a factor ~ 2.5 , only slightly less than the factor $(0.2/0.1)^{3/2} = 2.83$ suggested by a pure mode counting argument. In both cases we have assumed that k_{max} is constant with redshift in comoving coordinates, in contrast to White et al. (2009) who assume that it scales with k_{nl} , and this difference largely accounts for the substantially larger errors that we forecast at high redshift. It is not clear which assumption is more appropriate, since it is not clear whether the scale at which modeling uncertainties dominate will be set by non-linearity in the matter clustering, which tracks k_{nl} , or by non-linearity in the biased galaxy clustering, which stays roughly constant in comoving coordinates because of compensation between $b_g(z)$ and $\sigma_8(z)$. While our $k_{\text{max}} = 0.2 h \text{ Mpc}^{-1}$, $nP = 2$ case yields 0.8% errors per bin at $z > 0.9$, the actual demand on modeling accuracy is tighter by $\sqrt{N_{\text{bin}}} \sim 3.3$ because a systematic modeling error would be likely to affect all bins coherently.

Our forecasts here include only $P(k)$ modeling, not the additional gains that are potentially available by applying the McDonald and Seljak (2009) method to tracer populations with different bias factors in the same volume. High redshift surveys may not yield galaxy samples with a wide range of bias, but at $z < 1$ this approach could reduce errors significantly relative to those presented here.

For the calculations in Fig. 31, we have set the small scale velocity dispersion $\sigma_v = 0$, i.e., we have assumed pure linear theory up to $k = k_{\text{max}}$. Setting $\sigma_v = 300 \text{ km s}^{-1}$ produces only mild degradation of the errors, much smaller than the difference between $nP = 1$ and $nP = 2$. However, marginalizing over σ_v , or more generally over parameters that describe non-linear effects, could degrade precision significantly unless smaller scale data can be used to constrain these parameters. Conversely, modeling to higher k_{max} can yield substantially tighter errors. In experiments with σ_v fixed to 300 km s^{-1} , we find that the $k_{\text{max}}^{3/2}$ scaling holds at the factor-of-two level up to $k_{\text{max}} \sim 1 h \text{ Mpc}^{-1}$, so the potential gains are large. This analysis thus confirms the key point of this section: RSD analyses of the same redshift surveys conducted for BAO could provide powerful constraints on dark energy and stringent tests of GR growth predictions, but exploiting this potential will require development of theoretical modeling methods that are accurate at the sub-percent level in the moderately non-linear regime.

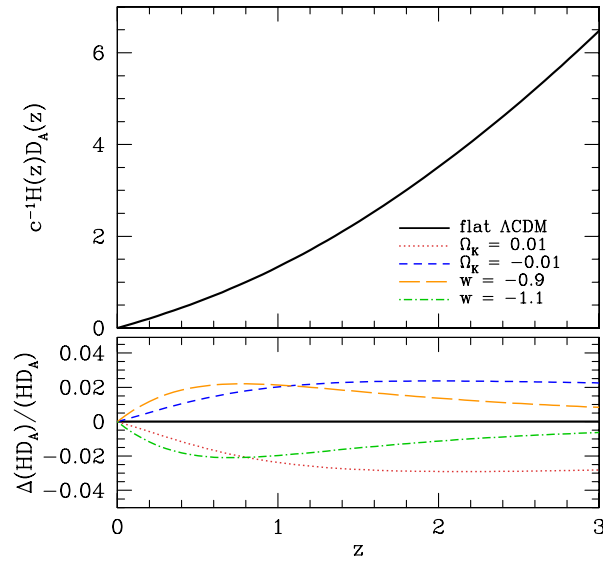


Fig. 32. Evolution of the parameter combination $H(z)D_A(z)$ constrained by the Alcock–Paczynski test, for the same suite of CMB-normalized models shown in Fig. 2.

7.3. The Alcock–Paczynski test

The translation from angular and redshift separations to comoving separations depends on $D_A(z)$ and $H(z)$, respectively. Therefore, even if peculiar velocities are negligible, clustering in redshift space will appear anisotropic if one adopts an incorrect cosmological model – specifically, one with an incorrect value of the product $H(z)D_A(z)$. Alcock and Paczynski (1979; hereafter AP) proposed an idealized cosmological test using this idea, based on a hypothetical population of intrinsically spherical galaxy clusters. The AP test can be implemented in practice by using the amplitude of quasar or galaxy clustering to identify equivalent scales in the angular and redshift dimensions (Ballinger et al., 1996; Matsubara and Suto, 1996; Popowski et al., 1998; Matsubara and Szalay, 2001) or by using anisotropy of clustering in the Ly α forest (Hui et al., 1999; Mcdonald and Miralda-Escudé, 1999). AP measurements provide a cosmological test in their own right, and they allow high-redshift distance measurements to be translated into constraints on $H(z)$, which is a more direct measure of energy density. Recently Blake et al. (2011c) have measured the AP parameter $H(z)D_A(z)$ from galaxy clustering in the WiggleZ survey, obtaining 10%–15% precision in each of four redshift bins out to $z = 0.8$, and Reid et al. (2012) have obtained $\sim 6\%$ precision at $z = 0.55$ from BOSS galaxies, improving to $\sim 3.5\%$ if they assume that the growth rate (and hence the peculiar velocity distortion) has the value predicted by Λ CDM. Both results are consistent with flat- Λ geometry for WMAP7 values of Ω_m .

Fig. 32 shows the evolution of $c^{-1}H(z)D_A(z)$ for the same set of CMB-normalized models shown earlier in Figs. 2–4. At low redshift, the model dependence resembles that of $H(z)/ch$ (lower left panel of Fig. 2), but deviations are reduced in amplitude because of partial cancellation between $H(z)$ and $D_A(z) \propto \int_0^z dz' H^{-1}(z')$. At high redshift $\Omega_k = \pm 0.01$ has a larger impact than $1 + w = \pm 0.1$. Note that negative space curvature (positive Ω_k) tends to increase D_A , but because the CMB normalization lowers Ω_m (see Table 1) and thus $H(z)/H_0$, the net effect is to decrease $H(z)D_A(z)$. In Section 8.5.2 we show that our fiducial Stage IV program predicts $H(z)D_A(z)$ with an accuracy of $\sim 0.15\%$ – 0.3% , assuming a w_0 – w_a dark energy model. AP measurements at this level could significantly improve dark energy constraints. For Stage III, the predictions are considerably weaker, $\sim 0.5\%$ – 0.9% .

Like redshift-space distortion measurements, the AP test is automatically enabled by redshift surveys conducted for BAO. In practice the two effects must be modeled together (see, e.g., Matsubara, 2004), and the principal systematic uncertainty for AP measurements is the uncertainty in modeling non-linear redshift-space distortions. At present, it is difficult to forecast the likely precision of future AP measurements because there have been no rigorous tests of the accuracy of redshift-space distortion corrections at the level of precision reachable by such surveys. If one assumes that redshift-space distortions can be modeled adequately up to $k \sim k_{nl}$ then the potential gain from AP measurements is impressively large. For example, Wang et al. (2010) find that using the full galaxy power spectrum in a space-based emission-line redshift survey increases the forecast value of the DETF FoM by a factor of ~ 3 relative to the BAO measurement alone; this gain is not broken down into separate contributions, but we suspect that a large portion comes from AP.⁷⁰ In the context of HETDEX, Shoji et al. (2009) show that the AP test substantially improves the expected cosmological constraints relative to BAO analysis alone, even after marginalizing over linear RSD and a small-scale velocity dispersion parameter. The appendix to that paper presents analytic formalism for incorporating AP and RSD constraints into Fisher matrix analyses.

⁷⁰ Since RSD and AP both depend on modeling the broadband $P(k, \mu)$, it is difficult even in principle to separate the two types of constraints in an observational analysis.

Halo occupation methods (see Section 2.3) provide a useful way of approaching peculiar velocity uncertainties in AP measurements. Observations and theory imply that galaxies reside in halos, and on average the velocity of galaxies in a halo should equal the halo’s center-of-mass velocity because galaxies and dark matter feel the same large scale acceleration. However, the dispersion of satellite galaxy velocities in a halo could differ from the dispersion of dark matter particle velocities by a factor of order unity, and central galaxies could have a dispersion of velocities relative to the halo center-of-mass (van den Bosch et al., 2005; Tinker et al., 2006). To be convincing, an AP measurement must show that it is robust (relative to its statistical errors) to plausible variations in the halo occupation distribution and to plausible variations in the velocity dispersion of satellite and central galaxies. Alternatively, the AP errors can be marginalized over uncertainties in these multiple galaxy bias parameters, drawing on constraints from the observed redshift-space clustering.

BAO measurements from spectroscopic surveys in some sense already encompass the AP effect, since they use the location of the BAO scale as a function of angular and redshift separations to separately constrain $D_A(z)$ and $H(z)$. The presence of a feature at a particular scale makes the separation of the AP effect from peculiar velocity RSD much more straightforward (see Fig. 6 of Reid et al., 2012). However, the addition of a high-precision AP measurement from smaller scales could significantly improve the BAO cosmology constraints. BAO measurements typically constrain $D_A(z)$ better than $H(z)$ because there are two angular dimensions and only one line-of-sight dimension. However, at high redshift $H(z)$ is more sensitive to dark energy than $D_A(z)$, since $H(z)$ responds directly to $u_\phi(z)$ through the Friedmann equation (3) while $D_A(z)$ is an integral of $H_0/H(z')$ over all $z' < z$. An AP measurement would allow the BAO measurement of $D_A(z)$ to be “transferred” to $H(z)$, thus yielding a better measure of the dark energy contribution. Blake et al. (2011c) have recently implemented a similar idea by using their AP measurements in the WiggleZ survey to convert SN luminosity distances into $H(z)$ determinations.

The AP test can be implemented with measures other than the power spectrum or correlation function. One option is to use the angular distribution of small scale pairs of quasars or galaxies (Phillipps, 1994; Marinoni and Buzzi, 2010), though peculiar velocities still affect this measure, in a redshift- and cosmology-dependent way (Jennings et al., 2012b). A promising recent suggestion is to use the average shape of voids in the galaxy distribution; individual voids are ellipsoidal, but in the absence of peculiar velocities the mean shape should be spherical (Ryden, 1995; Lavaux and Wandelt, 2010). Typical voids are of moderate scale ($R \sim 10h^{-1}$ Mpc) and have a large filling factor f , so the achievable precision in a large redshift survey is high if the sampling density is sufficient to allow accurate void definition. A naive estimate for the error on the mean ellipticity of voids with rms ellipticity ϵ_{rms} in a survey volume V is $\sigma_{\bar{\epsilon}} \sim \epsilon_{\text{rms}} (fV / \frac{4}{3}\pi R^3)^{-1/2} \approx 6 \times 10^{-4} (\epsilon_{\text{rms}}/0.3) (fV / 1 h^{-3} \text{Gpc}^3)^{-1/2} (R/10h^{-1} \text{Mpc})^{-3/2}$, if the galaxy density is high enough to make the shot noise contribution to the ellipticity scatter negligible on scale R . Peculiar velocities have a small, though not negligible, impact on void sizes and shapes (Little et al., 1991; Ryden and Melott, 1996; Lavaux and Wandelt, 2012), so one can hope that the uncertainty in this impact will be small, but this hope has yet to be tested. Assuming statistical errors only, Lavaux and Wandelt (2012) estimate that a void-based AP constraint from a *Euclid*-like redshift survey would provide several times better dark energy constraints than the BAO measurement from the same data set, mainly because the scale of voids is so much smaller than the BAO scale. Sutter et al. (2012) have recently applied the AP test to a void catalog constructed from the SDSS DR7 redshift surveys, though with this sample the statistical errors are too large to yield a significant detection of the predicted effect.

7.4. Alternative distance indicators

In Sections 3 and 4 we have discussed the two most well established methods for measuring the cosmological distance scale beyond the local Hubble flow: Type Ia supernovae and BAO. These two methods set a high bar for any alternative distance indicators. Type Ia supernovae are highly luminous, making them relatively easy to discover and measure at large distances. Once corrected for light curve duration, local Type Ia’s have a dispersion of 0.1–0.15 mag in peak luminosity despite sampling stellar populations with a wide range of age and metallicity, and extreme outliers are apparently rare (Li et al., 2011). Thus far, surveys are roughly succeeding in achieving the \sqrt{N} error reduction from large samples, though progress on systematic uncertainties will be required to continue these gains. The BAO standard ruler is based on well understood physics, and it yields distances in absolute units. “Evolutionary” corrections (from non-linear clustering and galaxy bias) are small and calculable from theory.

Core collapse supernovae exhibit much greater diversity than Type Ia supernovae, which is not surprising given the greater diversity of their progenitors. However, Type IIP supernovae, characterized by a long “plateau” in the light curve after peak, show a correlation between expansion velocity (measured via spectral lines) and the bolometric luminosity of the plateau phase, making them potentially useful as standardized candles with ~ 0.2 mag luminosity scatter (Hamuy and Pinto, 2002; see Maguire et al., 2010 for a recent discussion). Unfortunately, as distance indicators Type IIP supernovae appear to be at least slightly inferior to Type Ia supernovae on every score: they are less luminous, the scatter is larger, the fraction of outliers may be larger, and they arise in star-forming environments that are prone to dust extinction. With the existence of cosmic acceleration now well established by multiple methods, we are skeptical that Type IIP supernovae can make a significant contribution to refinement of dark energy constraints.

The door for alternative distance indicators is more open beyond $z = 1$, the effective limit of most current SN and BAO surveys. Gamma-ray bursts (GRBs) are highly luminous, so they can be detected to much higher redshifts than optical supernovae; the current record holder is at $z \approx 8.2$ (Tanvir et al., 2009; Salvaterra et al., 2009). GRBs are extremely diverse

and highly beamed, but they exhibit correlations (Amati, 2006; Ghirlanda et al., 2006) between equivalent isotropic energy and spectral properties (such as the energy of peak intensity) or variability. These correlations can be used to construct distance–redshift diagrams for those systems with redshift measured via spectroscopy of afterglow emission or of host galaxies (e.g., Schaefer, 2007; see Demianski and Piedipalumbo, 2011 for a recent review and discussion). While GRBs reach to otherwise inaccessible redshifts, we are again skeptical that they can contribute to our understanding of dark energy because of statistical limitations and susceptibility to systematics. It has taken detailed observations of many hundreds of Type Ia supernovae, local and distant, to understand their systematics and statistics. The number of GRBs with spectroscopic redshifts is ~ 100 , and the spectroscopic sample may be a biased subset of the full GRB population because of the requirement of a bright optical afterglow or identified host galaxy.

Quasars are another tool for reaching high redshifts, drawing on empirical correlations between line equivalent widths and luminosity (Baldwin, 1977) or between luminosity and the broad line region radius R_{BLR} (Bentz et al., 2009). For example, Watson et al. (2011) have recently proposed reverberation mapping (which measures R_{BLR}) of large quasar samples to constrain dark energy models. The high redshift quasar population is systematically different (in black hole mass and host galaxy environment) from lower redshift calibrators. Quasar spectral properties appear remarkably stable over a wide span of redshift (Steffen et al., 2006), and the dependence of R_{BLR} on luminosity is driven primarily by photoionization physics. However, in the event of a “surprising” result from quasar distance indicators, one would have to be prepared to argue that subtle (e.g., 10% or smaller) changes with redshift were a consequence of cosmology rather than evolution. Of course, quasar distance indicators also face the same challenges of photometric calibration, k -corrections, and dust extinction that affect supernova studies.

Radio galaxies have been employed as a standard (or at least standardizable) ruler for distance–redshift studies, drawing on empirically tested theoretical models that connect the source size to its radio properties (Daly, 1994; Daly and Guerra, 2002). Analysis of 30 radio galaxies out to $z = 1.8$ gives results consistent with those from Type Ia supernovae (Daly et al., 2009). The number of radio galaxies to which this technique can be applied is limited, and the model assumptions used to translate observables into distance estimates are fairly complex (see Daly et al., 2009, Section 2.1). We therefore expect that both statistical and systematic limitations will prevent this method from becoming competitive with supernovae and BAO.

In Section 8.5.4 we show forecast distance errors for our fiducial Stage III and Stage IV experimental programs, presenting a target for alternative methods. If one assumes a w_0 – w_a model then the constraints are very tight, with errors below $\sim 0.25\%$ at Stage IV and $\sim 0.5\%$ at Stage III. However, with a general $w(z)$ model the constraints become much weaker outside the redshift range directly measured by Type Ia SNe or BAO. In particular, our Stage IV forecasts presume large BAO surveys at $z > 1$, and if these do not come to fruition there is much more room for alternative indicators at high redshift.

7.5. Standard sirens

Gravitational wave astronomy opens an entirely different route to distance measurement, with an indicator that is grounded in fundamental physics (Schutz, 1986). The basic concept is illustrated by considering a nearly Newtonian binary system of two black holes with total mass M and reduced mass μ , in a nearly circular orbit at separation a . The gravitational wave luminosity of such a source is

$$L_{\text{GW}} = \frac{32G^4\mu^2M^3}{5c^5a^5}. \quad (157)$$

If one can measure the angular velocity of the orbit⁷¹ $\omega = \sqrt{GM/a^3}$, its rate of change due to inspiral as the binary loses energy $\dot{\omega}/\omega = 96G^3\mu M^2/5c^5a^4$, and the orbital velocity $v = \sqrt{GM/a}$ (using relativistic corrections to the emitted waveform), one has enough information to solve for a , M , and μ . One can therefore calculate L_{GW} from the measured observables and compare to the measured energy flux to infer distance. In practice, one would need to solve for other dimensionless parameters such as the eccentricity and the orientation of the orbit, black hole spins, and source position on the sky. The solution is not trivial (!), but gravitational waveforms from relativistic binaries encode this information in higher harmonics and modulation of the signal due to precession (Arun et al., 2007). Because of the analogy between gravitational wave observations and acoustic wave detection, this approach is often referred to as the “standard siren” method.

There are several practical obstacles to gravitational wave cosmology. First, of course, gravitational waves from an extragalactic source must be detected. The most promising near-term possibility is nearby ($z \ll 1$) neutron star binaries, which should be detected by the ground-based Advanced LIGO detector (to start observations in ~ 2014) and upgraded VIRGO detector, and which could be used to measure H_0 . The space-based gravitational wave detector LISA (possible launch in the 2020 decade) is designed to allow high S/N measurements of the mergers of massive black holes at the centers of galaxies at $z \sim \mathcal{O}(1)$, which would enable a full Hubble diagram $D_L(z)$ to be constructed. A second complication is that gravitational wave observations yield a distance but do not give an independent source redshift. One thus needs an identification of the host galaxy, and given the angular positioning accuracy of gravitational wave observations this will generally require identification of an electromagnetic transient that accompanies the gravitational wave burst. Possibilities

⁷¹ The observed frequency of the gravitational wave is 2ω because the source is a quadrupole, producing two crests and two troughs per orbit.

include GRBs resulting from neutron star mergers (Dalal et al., 2006) and the optical, X-ray, or radio signatures of the response of an accretion disk to a massive black hole merger (Milosavljevic and Phinney, 2005; Lippai et al., 2008). However, both the event rates and the characteristics of the electromagnetic signatures are poorly understood at present. One can also make identifications statistically using large scale structure (Macleod and Hogan, 2008). A third complication, important for the high S/N observations expected from *LISA*, is that weak lensing magnification becomes a dominant source of noise at $z \gtrsim 1$, inducing a scatter in distance of several percent per observed source (Markovic, 1993; Holz and Linder, 2005; Jonsson et al., 2007). By taking advantage of the non-Gaussian shape of the lensing scatter, one can reduce the error on the mean by a factor $\sim 2\text{--}3$ below the naive σ/\sqrt{N} expectation (Hirata et al., 2010; Shang and Haiman, 2011), so samples of a few dozen well observed sources could yield sub-percent distance scale errors.

Nissanke et al. (2010) forecast constraints on H_0 from next-generation ground-based gravitational wave detectors, including Monte Carlo simulations of parameter recovery from neutron star–neutron star and neutron star–black hole mergers. They find that H_0 can be constrained to 5% for 15 NS–NS mergers with GRB counterparts and a network of three gravitational wave detectors. While the event rate is highly uncertain, tens of events per year are quite possible and could lead to percent-level constraints on H_0 a decade or so from now. Taylor and Gair (2012) discuss the prospects for a network of “third generation” ground-based interferometers, which could detect $\sim 10^5$ double neutron star binaries.

It remains to be seen whether standard sirens can compete with other distance indicators in the LIGO/VIRGO and *LISA* era. Looking further ahead, Cutler and Holz (2009) show that an interferometer mission designed to search for gravitational waves from the inflation epoch in the 0.03–3 Hz range, such as the *Big Bang Observer* (*BBO*, Phinney et al., 2004) or the Japanese *Decigo* mission (Kawamura et al., 2008), would detect hundreds of thousands of compact star binaries out to $z \sim 5$. The arc-second level resolution would be sufficient to identify the host galaxies for most binaries even at high z , enabling redshift determinations through follow-up observations. With the S/N expected for *BBO*, the error in luminosity distance for most of these standard sirens would be dominated by weak lensing magnification, and the \sqrt{N} available for beating down this scatter would be enormous. Indeed, Cutler and Holz (2009) argue that the dispersion of distance estimates as a function of separation could itself be used to probe structure growth via the strength of the WL effect. For the *BBO* case, Cutler and Holz (2009) forecast errors of $\sim 0.1\%$, 0.01, and 0.1 on H_0 , w_0 , and w_a when combining with a *Planck* CMB prior, assuming a flat universe. Because the distance indicator is rooted in fundamental physics, there are no obvious systematic limitations to this method provided the calibration of the gravitational wave measurements themselves is adequate.

7.6. The Ly α forest as a probe of structure growth

The Ly α forest is an efficient tool for mapping structure at $z \approx 2\text{--}4$ because each quasar spectrum provides many independent samples of the density field along its line of sight. (At lower redshifts Ly α absorption moves to UV wavelengths unobservable from the ground, and at higher redshifts the forest becomes too opaque to trace structure effectively.) The relation between Ly α absorption and matter density is non-linear and to some degree stochastic. However, the physics of this relation is straightforward and fairly well understood, in contrast to the more complicated processes that govern galaxy formation. We have previously discussed the Ly α forest as a method of measuring BAO at $z > 2$, which requires only that the forest provide a linearly biased tracer of the matter distribution on ~ 150 Mpc scales. However, by drawing on a more detailed theoretical description of the forest, one can use Ly α flux statistics to infer the amplitude of matter fluctuations and thus measure structure growth at redshifts inaccessible to weak lensing or clusters.

The Ly α forest is described to surprisingly good accuracy by the Fluctuating Gunn–Peterson Approximation (FGPA, Weinberg et al., 1998; see also Gunn and Peterson, 1965; Rauch et al., 1997; Croft et al., 1998), which relates the transmitted flux $F = \exp(-\tau_{\text{Ly}\alpha})$ to the dark matter overdensity $\rho/\bar{\rho}$, with the latter smoothed on approximately the Jeans scale of the diffuse intergalactic medium (IGM) where gas pressure supports the gas against gravity (Schaye, 2001). Most gas in the low density IGM follows a power-law relation between temperature and density, $T = T_0(\rho/\bar{\rho})^\alpha$ with $\alpha \lesssim 0.6$, which arises from the competition between photo-ionization heating and adiabatic cooling (Katz et al., 1996; Hui and Gnedin, 1997). The Ly α optical depth is proportional to the hydrogen recombination rate, which scales as $\rho^2 T^{-0.7}$ in the relevant temperature range near 10^4 K. This line of argument leads to the relation

$$F = \exp(-\tau_{\text{Ly}\alpha}) \approx \exp[-A(\rho/\bar{\rho})^{2-0.7\alpha}]. \quad (158)$$

The constant A depends on a combination of parameters that are individually uncertain (see Croft et al., 1998; Peebles et al., 2010), and the value of α depends on the IGM reionization history, so in practice these parameters must be inferred empirically from the Ly α forest observables. However, even after marginalizing over these parameters there is enough information in the clustering statistics of the flux F to constrain the shape and amplitude of the matter power spectrum (e.g., Croft et al., 2002; Viel et al., 2004; McDonald et al., 2006). Ly α forest surveys conducted for BAO allow high precision measurements of flux correlations on smaller scales, so they have the statistical power to achieve tight constraints on matter clustering.

There are numerous physical complications not captured by Eq. (158). On small scales, absorption is smoothed along the line of sight by thermal motions of atoms. Peculiar velocities add scatter to the relation between flux and density, though this effect is mitigated if one uses the redshift-space $\rho/\bar{\rho}$ in Eq. (158). Gas does not perfectly trace dark matter, so $(\rho/\bar{\rho})_{\text{gas}}$ is not identical to $(\rho/\bar{\rho})_{\text{DM}}$. Shock heating and radiative cooling push some gas off of the temperature–density relation. All

of these effects can be calibrated using hydrodynamic cosmological simulations, and since the physical conditions are not highly non-linear and the effects are moderate to begin with, uncertainties in the effects are not a major source of concern.

A more serious obstacle to accurate predictions is the possibility that inhomogeneous IGM heating – especially heating associated with helium reionization, which is thought to occur at $z \approx 3$ – produces spatially coherent fluctuations in the temperature–density relation that appear as extra power in Ly α forest clustering, or makes the relation more complicated than the power law that is usually assumed (Mcquinn et al., 2011; Meiksin and Tittley, 2012). Fluctuations in the ionizing background radiation can also produce extra structure in the forest, though this effect should be small on comoving scales below ~ 100 Mpc (Mcquinn et al., 2011). On the observational side, the primary complication is the need to estimate the unabsorbed continuum of the quasar, relative to which the absorption is measured. (In our notation, F is the ratio of the observed flux to that of the unabsorbed continuum.) For statistical analysis of a large sample, the continuum does not have to be accurate on a quasar-by-quasar basis, and there are strategies (such as measuring fluctuations relative to a running mean) for mitigating any bias caused by continuum errors (see, e.g., Slosar et al., 2011). Nonetheless, residual uncertainties from continuum determination can be significant compared to the precision of measurements.

A discrepancy between clustering growth inferred from the Ly α forest and cosmological models favored by other data would face a stiff burden of proof, to demonstrate that the Ly α forest results were not biased by the theoretical and observational systematics discussed above. However, complementary clustering statistics and different physical scales have distinct responses to systematics and to changes in the matter clustering amplitude, so it may be possible to build a convincing case. For example, the bispectrum (Mandelbaum et al., 2003; Viel et al., 2004) and flux probability distribution (e.g., Lidz et al., 2006) provide alternative ways to break the degeneracy between mean absorption and power spectrum amplitude and to test whether a given model of IGM physics is really an adequate description of the forest. Ly α forest tests will assume special importance if other measures indicate discrepancies at lower redshifts with the growth predicted by GR combined with simple dark energy models. Growth measurements at $z \sim 3$ from the Ly α forest could then play a critical role in distinguishing between modified gravity explanations and models with unusual dark energy history. Because it probes high redshifts and moderate overdensities, the Ly α forest can also constrain the primordial power spectrum on small scales that are inaccessible to other methods. The resulting lever arm may be powerful for detecting or constraining the scale-dependent growth expected in some modified gravity models, as discussed further in the next section.

7.7. Other tests of modified gravity

We have concentrated our discussion of modified gravity on tests for consistency between measured matter fluctuation amplitudes and growth rates – from weak lensing, clusters, and redshift-space distortions – with the predictions of dark energy models that assume GR. However, “not General Relativity” is a broad category, and there are many other potentially observable signatures of modified gravity models. For an extensive review of modified gravity theories and observational tests, we refer the reader to Jain and Khoury (2010). We follow their notation and discussion in our brief summary here.

In Newtonian gauge, the spacetime metric with scalar perturbations can be written in the form

$$ds^2 = -(1 + 2\psi)dt^2 + (1 - 2\phi)a^2(t)dl^2, \quad (159)$$

which is general to any metric theory of gravity. If the dominant components of the stress–energy tensor have negligible anisotropic stress, then the Einstein equation of GR predicts that $\psi = \phi$, i.e., the same gravitational potential governs the time–time and space–space components of the metric. We have made this assumption implicitly in the WL discussion of Section 5. Anisotropic stress should be negligible in the matter-dominated era, and most proposed forms of dark energy (e.g., scalar fields) also have negligible anisotropic stress. Therefore, one generic form of modified gravity test is to check for the GR-predicted consistency between ψ and ϕ . For example, if the Ricci curvature scalar R in the GR spacetime action $S \propto \int d^4x \sqrt{-g}R$ is replaced by a function $f(R)$, then ψ and ϕ are generically unequal. In the forecasts of Section 8 we focus on GR-deviations described by the G_9 and $\Delta\gamma$ parameters that characterize structure growth (Section 2.2), but an alternative approach parametrizes the ratios of ψ and ϕ to their GR-predicted values (see Koivisto and Mota, 2006; Bean and Tangmatitham, 2010; Daniel and Linder, 2010, and references therein). The G_9 and $\Delta\gamma$ formulation is well matched to observables that can be measured by large surveys, but the potentials formulation is arguably closer to the physics of modified gravity.

The main approach to testing the consistency of ψ and ϕ exploits the fact that the gravitational accelerations of non-relativistic particles are determined entirely by ψ but the paths of photons depend on $\psi + \phi$. Thus, an inequality of ψ and ϕ should show up observationally as a mismatch between mass distributions estimated from stellar or gas dynamics and mass distributions estimated from gravitational lensing. (In typical modified gravity scenarios, it is then the lensing measurement that characterizes the true mass distribution.) The approximate agreement between X-ray and weak lensing cluster masses already rules out large disagreements between ψ and ϕ . A systematic statistical approach to this test, employing the techniques discussed in Section 6, could probably sharpen it to the few percent level, limited by the theoretical uncertainty in converting X-ray observations to absolute masses. To reach high precision on cosmological scales, the most promising route is to test for consistency between growth measurements from redshift-space distortions, which respond to the non-relativistic potential ψ , and growth measurements from weak lensing. Implementing an approach suggested by Zhang et al. (2007) and Reyes et al. (2010) present a form of this test that draws on redshift-space distortion measurements of

SDSS luminous red galaxies by Tegmark et al. (2006) and galaxy–galaxy lensing measurements of the same population. The precision of the test in Reyes et al. (2010) is only $\sim 30\%$, limited mainly by the redshift–space distortion measurement, but this is already enough to rule out some otherwise viable models. In the long term, this approach could well be pushed to the sub-percent level, with the limiting factors being the modeling uncertainty in redshift–space distortions and systematics in weak lensing calibration. Similar tests on the $\sim \text{kpc}$ scales of elliptical galaxies have been carried out by Bolton et al. (2006) and Schwab et al. (2010).

Some modified gravity models allow Ψ and Φ to depend on scale and/or time, yielding an “effective” gravitational constant $G_{\text{Newton}} \rightarrow G_{\text{Newton}}(k, t)$ (where k denotes Fourier wavenumber). Scale-dependent gravitational growth will alter the shape of the matter power spectrum relative to that predicted by GR for the same matter and radiation content. Precise measurements of the galaxy power spectrum shape can constrain or detect such scale-dependent growth. Uncertainties in the scale-dependence of galaxy bias may be the limiting factor in this test, though departures from expectations could also arise from non-standard radiation or matter content or an unusual inflationary power spectrum, and these effects may be difficult to disentangle from scale-dependent growth. The lever arm for determining the power spectrum shape can be extended by using the Ly α forest or, in the long term, redshifted 21 cm maps to make small-scale measurements. Time-dependent G_{Newton} would alter the history of structure growth, leading to non-GR values of G_9 or $\Delta\gamma$, but it could also be revealed by quite different classes of tests. For example, the consistency of big bang nucleosynthesis with the baryon density inferred from the CMB requires G_{Newton} at $t \approx 1$ s to equal the present day value to within $\sim 10\%$ (Yang et al., 1979; Steigman, 2010). Variation of G_{Newton} over the last 12 Gyr would also influence stellar evolution, and it is therefore constrained by the Hertzsprung–Russell diagram of star clusters (deg’Innocenti et al., 1996) and by helioseismology (Guenther et al., 1998).

Departures from GR are very tightly constrained by high-precision tests in the solar system, and many modified gravity models require a screening mechanism that forces them toward GR in the solar system and Milky Way environment.⁷² Screening may be triggered by a deep gravitational potential, in which case the strength of gravity could be significantly different in other cosmological environments. For a generic class of theories, the value of G_{Newton} would be higher by $4/3$ in unscreened environments, allowing order unity effects (see, for example, the discussion of $f(R)$ gravity by Chiba (2003) and DGP gravity by Lue (2006)). Chang and Hui (2011) suggest tests with evolved stars, which could be screened in the dense core and unscreened in the diffuse envelope; the stars should be located in isolated dwarf galaxies so that the gravitational potential of the galaxy, group, or supercluster environment does not trigger screening on its own. Hui et al. (2009) and Jain and Vanderplas (2011) propose testing for differential acceleration of screened and unscreened objects in low density environments (e.g., stars vs. gas, or dwarf galaxies vs. giant galaxies), in effect looking for macroscopic and order unity violations of the equivalence principle. Jain (2011) provides a systematic, high-level review of these ideas and their implications for survey experiments, emphasizing the value of including dwarf galaxies at low redshifts within large survey programs.

Evidence for modified gravity could emerge from some very different direction, such as high precision laboratory or solar system tests, tests in binary pulsar systems, or gravity wave experiments. In many of these areas, technological advances allow potentially dramatic improvements of measurement precision – for example, the proposed STEP satellite could sharpen the test of the equivalence principle by five orders-of-magnitude (Overduin et al., 2009). Modified gravity or a dark energy field that couples to non-gravitational forces could also lead to time-variation of fundamental “constants” such as the fine-structure constant α . Unfortunately, there are no “generic” predictions for the level of deviations in these tests, so searches of this sort necessarily remain fishing expeditions. However, the existence of cosmic acceleration suggests that there may be interesting fish to catch.

7.8. The integrated Sachs–Wolfe effect

On large angular scales, a major contribution to CMB anisotropies comes from gravitational redshifts and blueshifts of photon energies (Sachs and Wolfe, 1967). In a universe with $\Omega_{\text{tot}} = \Omega_m = 1$, potential fluctuations $\delta\Phi \sim G\delta M/R$ stay constant because (in linear perturbation theory) δM and R both grow in proportion to $a(t)$. In this case, a photon’s gravitational energy shift depends only on the difference between the potential at its location in the last scattering surface and its potential at earth. However, once curvature or dark energy becomes important, δM grows slower than $a(t)$, potential wells decay, and photon energies gain a contribution from an integral of the potential time derivative ($\dot{\Psi} + \dot{\Phi}$ in the notation of Section 7.7) known as the Integrated Sachs–Wolfe (ISW) effect. In more detail, one should distinguish the early ISW effect, associated with the transition from radiation to matter domination, from the late ISW effect, associated with the transition to dark energy domination. The ISW effect depends on the history of dark energy, which determines the rate at which potential wells decay. It can also test whether anisotropy is consistent with the GR prediction – in particular whether the Ψ and Φ potentials are equal as expected.

As an observational probe, the ISW effect has two major shortcomings. First, it is significant only on large angular scales, where cosmic variance severely and unavoidably limits measurement precision. (On scales much smaller than the horizon, potential wells do not decay significantly in the time it takes a photon to cross them.) Second, even on these large scales

⁷² To give one example, the Shapiro delay of radio waves passing near the Sun, measured to agree with GR to five decimal places (Bertotti et al., 2003), is reduced in theories of gravity that contain scalar fields, but the effect could be suppressed by scalar self-interaction in dense environments.

the ISW contribution is small compared to primary CMB anisotropies. The second shortcoming can be partly addressed by measuring the cross-correlation between the CMB and tracers of the foreground matter distribution, which separates the ISW effect from anisotropies present at the last scattering surface. The initial searches, yielding upper limits on Ω_{Λ} , were carried out by cross-correlating COBE CMB maps with the X-ray background (mostly from AGN, which trace the distribution of their host galaxies) as measured by HEAO (Boughn et al., 1998; Boughn and Crittenden, 2004). The WMAP era, combined with the availability of large optical galaxy samples with well-characterized redshift distributions, led to renewed interest in ISW and to the first marginal-significance detections (Fosalba et al., 2003; Scranton et al., 2003; Afshordi et al., 2004; Boughn and Crittenden, 2004; Fosalba and Gaztañaga, 2004; Nolta et al., 2004)

Realizing the cosmological potential of the ISW effect requires cross-correlating the CMB with large scale structure tracers over a range of redshifts at the largest achievable scales, and properly treating the covariance arising from the redshift range and sky coverage of each data set. Ho et al. (2008) used 2MASS objects ($z < 0.2$), photometrically selected SDSS LRGs ($0.2 < z < 0.6$) and quasars ($0.6 < z < 2.0$), and NVSS radio galaxies, finding an overall detection significance of 3.7σ . Giannantonio et al. (2008) used a similar sample (but with a different SDSS galaxy and quasar selection, and with the inclusion of the HEAO X-ray background maps) and found a 4.5σ detection of ISW. Both of these measurements are consistent with the “standard” Λ CDM cosmology.⁷³ Zhao et al. (2010) utilize the Giannantonio et al. (2008) measurement in combination with other data to test for late-time transitions in the potentials Φ and Ψ , finding consistency with GR.

Giannantonio et al. (2008) estimate that a cosmic variance limited experiment could achieve a 7–10 σ ISW detection. Because of the low S/N ratio, the ISW effect does not add usefully to the precision of parameter determinations within standard dark energy models, but it could reveal signatures of non-standard models. Early dark energy – dynamically significant at the redshift of matter–radiation equality – can produce observable CMB changes via the early ISW effect (Doran et al., 2007; de Putter et al., 2009 discuss the related problem of constraining early dark energy via CMB lensing). Perhaps the most interesting application of ISW measurements is to constrain, or possibly reveal, inhomogeneities in the dark energy density (see Section 2.2), which produce CMB anisotropies via ISW and are confined to large scales in any case (see de Putter et al., 2010). However, it is not clear whether even exotic models can produce an ISW effect that is distinguishable from the Λ CDM prediction at high significance. Measuring the ISW cross-correlation requires careful attention to angular selection effects in the foreground catalogs, but these effects should be controllable, and independent tracers allow cross-checks of results. Since the prediction of conventional dark energy models is robust compared to expected statistical errors, a clear deviation from that prediction would be a surprise with important implications.

7.9. Cross-correlation of weak lensing and spectroscopic surveys

Our forecasts in Section 7.2 incorporate an ambitious Stage IV weak lensing program, and in Section 8.5.3 we consider the impact of adding an independent measurement of $f(z)\sigma_8(z)$ from redshift-space distortions in a spectroscopic galaxy survey, finding that a 1%–2% measurement can significantly improve constraints on the growth-rate parameter $\Delta\gamma$ relative to our fiducial program. However, some recent papers (Bernstein and Cai, 2011; Gaztañaga et al., 2012; Cai and Bernstein, 2012) suggest that a combined analysis of overlapping weak lensing and galaxy redshift surveys can yield much stronger dark energy and growth constraints than an after-the-fact combination of independent WL and RSD measurements.

The analysis envisioned in these papers involves measurement of all cross-correlations among the WL shear fields (and perhaps magnification fields) in tomographic bins, the angular clustering of galaxies in photo- z bins of the imaging survey, and the redshift-space clustering of galaxies in redshift bins of the spectroscopic survey, as well as auto-correlations of these fields. While the forecast gains emerge from detailed Fisher-matrix calculations, the essential physics (Bernstein and Cai, 2011; Gaztañaga et al., 2012) appears to be absolute calibration of the bias factor of the spectroscopic galaxies via their weak lensing of the photometric galaxies (galaxy–galaxy lensing, Section 5.2.6). This calibration breaks degeneracy in the modeling of RSD, and it effectively translates the spectroscopic measurement of the galaxy power spectrum into a normalized measurement of the matter power spectrum. While the second technique can also be applied to galaxy clustering in the photometric survey, using photo- z 's, the clustering measurement in a spectroscopic survey is much more precise because there are more modes in 3-d than in 2-d. The cross-correlation approach is more powerful if the spectroscopic survey includes galaxies with a wide range of bias factors (McDonald and Seljak, 2009), e.g., a mix of massive absorption-line galaxies and lower mass emission-line galaxies.

These studies are still in an early phase, and it remains to be seen what gains can be realized in practice. The largest synergistic impact arises when the WL and RSD surveys are comparably powerful in their individual measurements of growth parameters (Cai and Bernstein, 2012). Stochasticity in the relation between the galaxy and mass density fields depresses cross-correlations relative to auto-correlations, a potentially important theoretical systematic, though stochasticity is expected to be small at large scales, and corrections can be computed with halo-based models that are constrained by small and intermediate-scale clustering. Conversely, it may be possible to realize these gains even when the weak lensing and spectroscopic surveys do not overlap, by calibrating the bias of a photometric sample that has the same target selection criteria as the spectroscopic sample. Gaztañaga et al. (2012) also investigate the possibility of implementing these techniques in a narrow-band imaging survey with large numbers of filters, which is effectively a low-resolution

⁷³ The Ho et al. (2008) measurement is almost 2σ above Λ CDM, but we attribute no special significance to this!

spectroscopic survey. They find that most of the gains of a spectroscopic survey are achieved if the rms photo- z uncertainty is $\Delta z/(1+z) \lesssim 0.0035$, while larger uncertainties degrade the results.

7.10. Strong gravitational lenses

Strong gravitational lenses can be employed to measure expansion history in a variety of ways. One is to simply count the number of lenses as a function of angular separation and (when available) redshift — the predicted counts depend on dark energy because the probability of lensing goes up when path lengths are larger (Kochanek, 1996). This approach requires a large sample of lenses with well understood statistical characteristics and selection biases. Observationally it is a stiff challenge, but the more fundamental difficulty is that the predicted counts also depend on the evolution of the mass distribution, in particular that of the early-type galaxies that dominate the lensing statistics. For example, Oguri et al. (2012) derive constraints from a sample of 19 strong lenses found from 50,000+ source quasars in the SDSS, and while the analysis yields a robust detection of dark energy, the cosmological parameter values are significantly degenerate with uncertainties in the evolution of the galaxy velocity function. The latter can be addressed to some degree with measurements of galaxy velocity dispersions, but even then one is left with uncertainty in the exact relation between the observable stellar velocity dispersion and the potential well depth that is important for lensing. With a sufficiently large sample of lenses one can “self-calibrate” by using the full distribution as a function of angular separation and redshift, though one still relies on direct galaxy counts for an overall normalization. While future imaging surveys will yield much larger samples of lens candidates (which can then be confirmed spectroscopically), we suspect that the systematic uncertainties in interpreting lens counts will be too large for this method to be competitive as a dark energy probe — rather, it will probe the dynamical history of galaxy assembly. The number of giant cluster arcs as a function of curvature radius and redshift offers an alternative form of the “lens counting” test that depends on both geometry and structure growth (e.g., Horesh et al., 2011), but one must again understand the detailed mass assembly history of the central regions of massive halos to derive dark energy constraints (Killedar et al., 2012).

A second approach is to use angular positions of multiple sources with different (known) redshifts to obtain distance ratios, a strong-lensing version of the cosmography test discussed in Section 5.2.7. Clusters of galaxies are the best targets for this approach, as they sometimes have large numbers of lensed sources (see Soucail et al., 2004 and Jullo et al., 2010 for representative observational applications). The difficulty is that the sources with different redshifts also probe different locations in the lens potential, so to derive cosmological results one needs strong constraints on substructure in the lens cluster and in the foreground and background mass distributions. Meneghetti et al. (2005) and D’Aloisio and Natarajan (2011) discuss some of the theoretical issues in this approach and their implications for data requirements. Obtaining strong cosmological constraints from cosmographic analysis of cluster lenses will be observationally demanding, and mass modeling uncertainties may be a limiting systematic.

The most promising of the strong-lensing approaches uses time delay measurements, which attach an absolute scale to the angular separations and redshifts measured for a gravitational lens. Predicted time delays scale as H_0^{-1} , and more generally with the angular diameter distance relation $D_A(z)$. The critical systematic is again the uncertainty in the total mass and mass distribution of the lens, which enters predictions of the angular positions and time delays. Given the observed positions, a time-delay measurement determines a degenerate combination of the distance scale (H_0^{-1}) and the surface mass density of the lens within the Einstein radius (Kochanek et al., 2003), so a dynamical measurement, usually the stellar velocity dispersion, is required to break the degeneracy and isolate the cosmological information. When the sources are resolved (i.e., galaxies rather than AGN in the optical, or jets mapped with VLBI), or when the multiplicity of images is unusually high, then reproducing the data places more stringent constraints on the mass distributions (e.g., Suyu et al., 2012b). In the best cases, distance scale constraints at the $\sim 5\%$ level, after marginalizing over uncertainties in the mass distribution, are achievable for an individual lens (e.g., Suyu et al., 2010, 2012a). Careful measurements and modeling of a number of well constrained lenses could lead to high aggregate precision, adding significant power to tests of dark energy models (Coe and Moustakas, 2009; Linder, 2011). The critical question from the point of view of dark energy is whether the mass modeling uncertainties are independent from system to system, so that the net uncertainty drops as $1/\sqrt{N}$, or whether global uncertainties in the approach to mass modeling impose a systematic floor. The answer to this question should become clearer as the current generation of cosmological time-delay analyses proceeds.

7.11. Galaxy ages

In principle the age of the universe is an observable that can probe cosmic expansion history. The integral that determines age,

$$t(z) = \int_z^\infty \frac{dz'}{1+z'} H^{-1}(z'), \quad (160)$$

is similar to the integral for comoving distance (Eq. (7)), except that it extends from z to ∞ instead of 0 to z . The conflict between the ages of globular clusters and the value of t_0 in a decelerating universe was one of the significant early arguments

for cosmic acceleration, and a number of authors have employed ages of high-redshift galaxies or clusters of galaxies as a constraint on dark energy models (e.g., Lima and Alcaniz, 2000; Jimenez et al., 2003; Capozziello et al., 2004).

Jimenez and Loeb (2002) proposed using *differential* ages of galaxies at different redshifts to measure, in effect, $H(z)$. Observational studies thus far have concentrated on the massive ellipticals, as these have the fewest complications (dust, ongoing star formation). This differential approach removes some of the uncertainties in the population synthesis models, but it relies on identifying a population of galaxies at one redshift that is just an aged version of a population at a higher redshift, or accounting for the evolutionary corrections that arise from mergers, low-level star formation, and movement of galaxies into or out of the passive population. The state-of-the-art observational study is the analysis of $\sim 11,000$ early-type galaxies from several large surveys by Moresco et al. (2012). They report measurements of $H(z)$ in eight bins out to $z \approx 1$, with uncertainties of $\sim 5\%$ – 15% per bin including estimated systematic errors. At low ($z < 0.3$) redshift, Moresco et al. (2011) analyzed a sample of 14,000 early type galaxies from the SDSS, obtaining $H_0 = 72.6 \pm 2.9$ (stat) ± 2.3 (syst) $\text{km s}^{-1} \text{Mpc}^{-1}$, compatible with other estimates of H_0 and competitive in precision. These papers provide extensive discussions of systematic uncertainties and argue that they can be well controlled. Nonetheless, the reliance on population synthesis and galaxy evolution models means that this method will face a stiff burden of proof if it finds a discrepancy with simple dark energy models or other observational analyses, particularly if the differences are at the sub-percent level that is the target of future dark energy experiments.

7.12. Redshift drift

The redshift of a comoving source changes as the universe expands. Sandage (1962) was the first to propose this “redshift drift” as a cosmological test, but he noted that it appeared far beyond the capabilities of existing experimental techniques. Loeb (1998) repopularized the idea, noting that high-resolution spectrographs on large telescopes could potentially measure the effect in absorption-line spectra of high-redshift quasars. Quercellini et al. (2012) provide an extensive review of the redshift-drift method and other forms of “real-time cosmology” experiments. The expected change in redshift over a time interval Δt , expressed as an apparent velocity shift, is

$$\Delta v \equiv \frac{c \Delta z}{1+z} = c H_0 \Delta t \left[1 - \frac{H(z)/H_0}{1+z} \right], \quad (161)$$

which vanishes for a coasting universe with $H(z)/H_0 = (1+z)^{-1}$. For our fiducial cosmological model, the predicted change over a $\Delta t = 10$ year observational span is $+1.32 \text{ cm s}^{-1}$, -1.21 cm s^{-1} , and -3.66 cm s^{-1} for sources at $z = 2, 3$, and 4 , respectively. Corasaniti et al. (2007) estimate that observations of 240 quasars over a span of 30 years using the CODEX spectrograph proposed for the European Extremely Large Telescope could measure $H(z)$ over $z = 2$ – 5 with an aggregate precision of $\approx 2\%$ (see Liske and Codex Team, 2006 and Balbi and Quercellini, 2007 for similar discussions and Liske et al., 2008 for detailed calculations of CODEX performance). The BAO component of the fiducial Stage IV program that we present in Section 8.1 (which assumes 25% sky coverage and errors that are 1.8 times those of linear theory sample variance) yields errors of 0.6%–0.7% in $H(z)$ per bin of 0.07 in $\ln(1+z)$ at $z = 2$ – 3 (see Table 6). The fiducial BAO program would thus be much more powerful than the redshift-drift approach, but it is not yet clear that high-redshift BAO surveys of this volume will prove practical.

7.13. Alternative methods: summary

Of the methods described in this section, redshift-space distortion is the one that seems almost guaranteed to have a broad-ranging impact in future studies of cosmic acceleration. Because of its direct sensitivity to $f(z)$ and its use of non-relativistic tracers, RSD is a valuable complement to weak lensing and clusters as a probe of structure growth. The redshift surveys ongoing or planned for BAO measurements will automatically enable RSD measurements with high statistical precision over a significant range in redshift. The primary systematics for RSD are associated with theoretical modeling uncertainties, and these are likely to diminish with time as more sophisticated techniques are developed, numerical simulations become more powerful, and galaxy clustering measurements provide more detailed tests of the models. The AP method may also amplify the return from BAO redshift surveys, perhaps by a large factor, depending on the success of modeling non-linear velocity distortions.

The $z = 0$ Hubble constant is only a single number, but it is an important one, as it determines the current critical density and the current expansion rate, with the maximal leverage against the CMB at $z \approx 1100$. Ongoing technical developments seem to offer a realistic path to achieving H_0 measurements with 1%–2% uncertainty, tight enough to make significant contributions to dark energy constraints even in the era of Stage IV experiments. *JWST* and *Gaia* represent dramatic improvements in technological capabilities for H_0 studies, perhaps allowing progress to the sub-percent level.

The impact of the other methods discussed here is more difficult to predict. In some cases, interesting results at the few-percent level are already in hand but it is still too early to say whether the limiting systematics can be reduced to the percent or sub-percent level required for long-term progress. In other cases, such as precision gravity tests, there are clear paths to radically improved measurements, but these will provide useful clues or tests only for a limited class of cosmic acceleration models.

The one method that looks like it could ultimately outperform even Stage IV experiments is that of standard sirens applied to compact star binaries (Section 7.5), because of the opportunity to measure hundreds of thousands of distances by a technique that has no obvious limiting systematics. This approach requires extraordinary technological advances, which are unlikely to be achieved in the next decade, and perhaps not in the next two decades. However, the most precise mapping of the expansion history of the universe might ultimately come from spacetime ripples rather than electromagnetic waves.

8. A balanced program on cosmic acceleration

Having discussed many observational methods individually, we now turn to what we might hope to learn from them in concert. To the extent that this report has an underlying editorial theme, it is the value of a balanced observational program that pursues multiple techniques at comparable levels of precision. In our view, there is much more to be gained by doing a good job on three or four methods than by doing a maximal job on one at the expense of the others. This is *not* a “try everything” philosophy – moving forward from where we are today, an observational method is interesting only if it has reasonable prospects of achieving percent- or sub-percent-level errors, both statistical and systematic, on observables such as $H(z)$, $D(z)$, and $G(z)$. The successes of cosmic acceleration studies to date have raised the field’s entry bar impressively high.

A balanced strategy is important both for cross-checking of systematics and for taking advantage of complementary information. Regarding systematics, the next generation of cosmic acceleration experiments seek much higher precision than those carried out to date, so the risk of being limited or biased by systematic errors is much higher. Most methods allow internal checks for systematics – e.g., comparing distinct populations of SNe, measuring angular dependence and tracer dependence of BAO signals, testing for B -modes and redshift-scaling of WL – but conclusions about cosmic acceleration will be far more convincing if they are reached independently by methods with different systematic uncertainties. Two methods only provide a useful cross-check of systematics if they have comparable statistical precision; otherwise a result found only in the more sensitive method cannot be checked by the less sensitive method.

Regarding information content, we have already emphasized the complementarity of SN and BAO as distance determination methods. SN have unbeatable statistical power at $z \lesssim 0.6$, while BAO surveys that map a large fraction of the sky with adequate sampling can achieve higher precision at $z \gtrsim 0.8$. Overlapping SN and BAO measurements provide independent physical information because the former measure relative distances and the latter absolute distances (h^{-1} Mpc vs. Mpc), and the value of h is itself a powerful dark energy diagnostic in the context of CMB constraints (see Section 7.1 and Section 8.5.1). WL, clusters, and redshift-space distortions provide independent constraints on expansion history, at levels that can be competitive with SN and BAO, and they provide sensitivity to structure growth. Without structure probes, we would have little hope of clues that might locate the origin of acceleration in the gravitational sector rather than the stress–energy sector, and we would, more generally, reduce the odds of “surprises” that might push us beyond our current theories of cosmic acceleration.

The primary purpose of this section is to present quantitative forecasts for a program of Stage IV dark energy experiments and to investigate how the forecast constraints depend on the performance of the individual components of such a program. Our forecasts are analogous to those of the DETF (Albrecht et al., 2006), updated with a more focused idea of what a Stage IV program might look like, and updated in light of subsequent work on parameterized models and figures of merit for dark energy experiments, most directly that of the JDEM Figure-of-Merit Science Working Group (FoMSWG; Albrecht et al., 2009). In Section 8.1 we summarize our assumptions about the fiducial program. In Section 8.2 we describe the methodology of our forecasts, in particular the construction of Fisher matrices for the fiducial program. In Section 8.3 we present results for the fiducial program and for variants in which one or more components of this program are made significantly better or worse. We also compare these results to forecasts of a “Stage III” program represented by experiments now underway or nearing their first observations.

We have elected to focus on SN, BAO, and WL as the components of these forecasts, for two reasons. First, it is more straightforward (though still not easy) to define the expected statistical and systematic errors for these methods than for others. Second, the most promising alternative methods – clusters, redshift-space distortions, and the Alcock–Paczynski effect – will be enabled by the *same* data sets obtained for WL and BAO studies. It is therefore reasonable to view these as auxiliary methods that may improve the return from these data sets (perhaps by substantial factors) rather than as drivers for the observational programs themselves. In Sections 8.4 and 8.5 we present forecasts for how well the fiducial CMB+SN+BAO+WL programs predict the observables of these and other alternative methods, providing a target for how well they must perform to add new information beyond that in our primary probes. In some cases we find that plausible levels of performance could substantially improve tests of cosmic acceleration models. In Section 8.6 we focus on the precision with which our fiducial program measures fundamental observables, and we discuss aggregate precision as a useful, nearly model-independent way of characterizing the power of an experiment and the level of systematics control required to realize it. Section 8.7 provides a high-level summary, discussing the potential yield from programs that combine CMB, SN, BAO, and WL measurements with additional constraints from clusters, redshift-space distortions, and direct H_0 determinations.

8.1. A fiducial program

As discussed in Section 1.3, Astro2010 and the European Astronet report have placed high priority on ground- and space-based dark energy experiments. The Stage III experiments currently underway will already allow much stronger tests of

cosmic acceleration models, and Stage IV facilities built over the next decade should advance the field much further still. Our Stage IV program corresponds roughly to the goals recommended by the Cosmology and Fundamental Physics panel report of Astro2010.

For SN studies, we anticipate that Stage IV efforts will be limited not by statistical errors but by systematics associated with photometric calibration, dust extinction, and evolution of the SN population. For our fiducial program, we assume that SN surveys will achieve net errors (statistical + systematic) of 0.01 mag for the mean distance modulus in each of three redshift bins of width $\Delta z = 0.2$ extending from $z = 0.2$ to a maximum redshift $z_{\max} = 0.8$ (see discussion in Section 3.4). We also assume the existence of a local SN sample at $z = 0.05$ with the same 0.01 mag net error. High quality observations could yield a smaller systematic error in the local sample, but we suspect that the most challenging systematic for this local calibration will be transferring it to the more distant bins. We treat the bin-to-bin errors as uncorrelated, though this is clearly an approximation to systematic errors that are correlated at nearby redshifts and gradually decorrelate as one considers differing redshift ranges and observed-frame wavelengths. Even with 0.15 mag errors per SN, achieving this level of statistical error requires only 225 SNe per bin, and we expect that the error per SN can be reduced by working at red/IR wavelengths and by selecting sub-populations based on host galaxy type, spectral properties, and light curve shape. For purely ground-based efforts, we consider our 0.01 mag floor for systematic errors to be somewhat optimistic, given the challenges of dust extinction corrections and photometric calibration. However, a space-based program at rest-frame near-IR wavelengths, enabled by *WFIRST*, could plausibly achieve better than 0.01 mag systematics. We suspect that it will be hard to push calibration and evolution systematics below 0.005 mag even with *WFIRST*, and pushing statistical errors below this level begins to place severe demands on spectroscopic capabilities, unless purely photometric information can be used to identify populations with scatter below 0.1 mag per SN. We also consider the impact of increasing z_{\max} beyond 0.8, though we argue that this is beneficial mainly when one is hitting a systematics floor at lower z and high- z observations have uncorrelated systematics.

For BAO, the primary metric of statistical constraining power is the total comoving volume mapped spectroscopically with a sampling density high enough to keep shot-noise sub-dominant. There are several projects in the planning stages that could map significant fractions of the comoving volume available out to $z \approx 3$. These include the near-IR spectroscopic components of *Euclid* and *WFIRST*, ground-based optical facilities such as BigBOSS, DESpec, and SuMIRe PFS, and radio intensity-mapping experiments (see Section 4.7). For our fiducial program, we assume that these projects will collectively map 25% of the comoving volume out to $z = 3$, with errors a factor of 1.8 larger than the linear theory sample variance errors.⁷⁴ We specifically assume full redshift coverage from $z = 0-3$ with $f_{\text{sky}} = 25\%$ sky fraction, but other combinations of redshift coverage and f_{sky} that have the same total comoving volume yield similar results. The factor 1.8 accounts for imperfect sampling (hence non-negligible shot-noise) and for non-linear degradation of the BAO signal. It approximates the effects of sampling with $n_P = 2$ and using reconstruction (Section 4.3.3) to remove 50% but not 100% of the non-linear Lagrangian displacement of tracers. We implicitly assume that theoretical systematics associated with location of the BAO peak will remain below this level, an assumption we consider reasonable but not incontrovertible based on the discussion in Section 4.5.

For WL, the primary metric of statistical constraining power is the total number of galaxies that have well measured shapes and good enough photometric redshifts to allow accurate model predictions and removal of intrinsic alignment systematics. For our fiducial case, we assume a survey of 10^4 deg^2 achieving an effective surface density of 23 galaxies per arcmin² with $z_{\text{med}} = 0.84$, corresponding to $I_{\text{AB}} < 25$ and $r_{\text{eff}} > 0.25''$. The effective galaxy number is 8.3×10^8 . *Euclid* plans a 14,000 deg² imaging survey and can likely achieve this surface density or slightly higher. LSST will survey a still larger area, and it might or might not achieve this effective surface density, depending on how low a value of $r_{\text{eff}}/r_{\text{PSF}}$ it can work to before shape measurements are systematics dominated. The *WFIRST* design reference mission (Green et al., 2012; DRM1) would achieve $n_{\text{eff}} \approx 40 \text{ arcmin}^{-2}$ but would only image 3400 deg² in its 2.4-year high-latitude survey, thus measuring about 4.8×10^8 galaxy shapes. An extended *WFIRST* mission, or an implementation of *WFIRST* using one of the NRO 2.4-m telescopes (Dressler et al., 2012), could potentially reach 10^4 deg^2 . Even individually, therefore, any one of these projects may well exceed the number of shape measurements assumed in our fiducial program, and collectively they will almost certainly do so. We compute constraints from cosmic shear in 14 bins of photometric redshift and from the shear-ratio test described in Section 5.2.7, but we do not incorporate higher order lensing statistics or galaxy-shear cross-correlations. We include information up to multipole $l_{\max} = 3000$, beyond which statistical power becomes limited at this surface density and systematic uncertainties associated with non-linear evolution and baryonic effects become significant.

Forecasting the systematic uncertainties in Stage IV WL experiments is very much a shot in the dark. Systematic errors are already comparable to statistical errors in surveys of 100 deg², so lowering them to the level of statistical errors in a 10^4 deg^2 survey that has higher galaxy surface density requires more than an order of magnitude improvement. We therefore consider a “fiducial” and an “optimistic” case for WL systematics. For the fiducial case, we incorporate (and marginalize over) aggregate uncertainties of 2×10^{-3} in shear calibration and 2×10^{-3} in the mean photo- z , with errors in each redshift bin larger by $\sqrt{14}$ but uncorrelated across bins. We also incorporate intrinsic alignment uncertainty as described by Albrecht et al. (2009, Section 2h of Appendix A), which includes marginalization over both GI and II components (see Section 5.6.1). For our “optimistic” case we adopt no specific form of the systematic errors but simply assume that they will double the

⁷⁴ This is equivalent to assuming linear theory sample variance over a fractional volume $25\%/1.8^2 = 7.7\%$.

statistical errors throughout. At an order of magnitude level, we can see that the optimistic case corresponds to a global fractional error $\sigma \sim 2N_{\text{mode}}^{-1/2} \sim 2f_{\text{sky}}^{-1/2}l_{\text{max}}^{-1} = 1.3 \times 10^{-3}$, significantly lower than the fiducial case assumption of 2×10^{-3} errors for shear and photo- z calibration (which, roughly speaking, combine in quadrature to make a 2.8×10^{-3} multiplicative uncertainty). However, at scales and redshifts where the statistical errors are large, multiplying them by two can be a larger change than adding the shear-calibration and photo- z systematics. As a result, there will be some measures (e.g., the error on Ω_k) for which our “optimistic” program performs slightly worse than our fiducial program. Of course, WL experiments that achieved the statistical limits of several $\times 10^9$ source galaxies – possible in principle – would be several times more powerful than even our optimistic scenario.

8.2. Forecasting constraints

The fiducial program outlined above provides a baseline for evaluating improvement in the determination of the cosmological parameters relative to current constraints. We use a Fisher matrix analysis to quantify this improvement and to study the complementarity of the main probes of cosmic acceleration. Since our knowledge of the exact design of future surveys and the systematic errors they will face is inherently imperfect, we also consider the effect of varying the precision of each technique in our forecasts, including both pessimistic and optimistic cases for SN, BAO, and WL data.

Quantifying the impact of each probe on our understanding of cosmic acceleration requires metrics for evaluating progress. The precision with which the dark energy equation of state (and its possible time dependence) can be measured is a common choice; while not the only quantity of interest, it is clearly a central piece of the puzzle. One of the main quantities we use below is the DETF figure of merit defined in Eq. (26), $\text{FoM} = [\sigma(w_p)\sigma(w_a)]^{-1}$. The FoM indicates how well an experiment determines the dark energy equation of state parameter and its derivative dw/da at the pivot redshift z_p , and it thereby indicates the ability to detect deviations from the standard Λ CDM model with $w_p = -1$ and $w_a = 0$. When one considers experiments of increasing power, $\sigma(w_p)$ and $\sigma(w_a)$ tend to shrink in concert, so the DETF FoM scales roughly as an inverse variance and therefore increases linearly with data volume when statistical errors dominate. If the error of every individual measurement (e.g., each D_L or $H(z)$ measurement) goes down by $\sqrt{2}$, then the FoM doubles.

While the DETF FoM is relatively simple to evaluate for a particular experiment, it omits much of the information that will be available from future experiments, including some potentially important clues to the nature of cosmic acceleration. For example, the true dark energy dynamics may be considerably more complicated than what the two-parameter linear model can accommodate, so that constraints on w_0 and w_a may yield incomplete or misleading results. Additionally, the equation of state alone is insufficient to describe the full range of possible alternatives to the standard cosmological model. For example, modified gravity theories can mimic the effect of any particular equation of state evolution on the Hubble expansion rate and the distance–redshift relation while altering the rate of growth of large-scale structure (e.g., Lue et al., 2004; Song et al., 2007). Including such possibilities requires extra parameters that describe changes in the growth history that are independent of equation of state variations, as discussed in Section 2.2. Other standard parameters of the cosmological model, such as the spatial curvature and the Hubble constant, are important due to degeneracies with the effects of cosmic acceleration that can limit the precision of constraints on the dark energy equation of state.

To include more general variations of the equation of state as well as altered growth of structure from modifications to GR on large scales, we adopt the JDEM FoMSWG parameterization (Albrecht et al., 2009). The equation of state in this parameterization is allowed to vary independently in each of 36 bins of width $\Delta a = 0.025$ extending from the present to $a = 0.1$ ($z = 9$). Specifically, the equation of state has a constant value of w_i at $(1 - 0.025i) < a < [1 - 0.025(i - 1)]$, for $i = 1, \dots, 36$. At earlier times, the equation of state is assumed to be $w = -1$, although the impact of this assumption is typically quite small since dark energy accounts for a negligible fraction of the total density at $z > 9$ in most models. Modifications to the linear growth function of GR $G_{\text{GR}}(z)$ are included through the parameters G_9 and $\Delta\gamma$ as defined in Eqs. (44) and (45). These parameters describe the change relative to GR in the normalization of the growth of structure at $z = 9$ and in the growth rate at $z < 9$, respectively. Adding these to the binned w_i values and the standard Λ CDM parameters, the full set is

$$\mathbf{p} = (w_1, \dots, w_{36}, \ln G_9, \Delta\gamma, \Omega_m h^2, \Omega_b h^2, \Omega_k h^2, \Omega_\phi h^2, \ln A_s, n_s, \Delta\mathcal{M}), \quad (162)$$

where the primordial amplitude A_s is defined at $k = 0.05 \text{ Mpc}^{-1}$. $\Delta\mathcal{M}$ is an overall offset in the absolute magnitude scale of Type Ia supernovae. The Hubble constant is determined by these parameters through $h^2 = \Omega_m h^2 + \Omega_k h^2 + \Omega_\phi h^2$. We compute our forecasts at the fiducial parameter values chosen by the FoMSWG to match CMB constraints from the 5-year release of WMAP data (Komatsu et al., 2009); these are listed in Table 5. These parameters are similar but not identical to those of the model used in Section 2 (Table 1), which is based on WMAP7. Note that spatially flat Λ CDM and GR are assumed for the fiducial model.

We use a Fisher matrix analysis to estimate the constraints on these parameters from the fiducial program defined in Section 8.1 and its variations. The Fisher matrix for each experiment consists of a model of the covariance matrix for the observable quantities and derivatives of these quantities with respect to the parameters. We compute the latter numerically with finite differences and confirm the results using analytic expressions when possible.

We model SN data as measurements of the average SN magnitude in each of several redshift bins and in a low-redshift calibration sample. While our fiducial case assumes that the net magnitude error is uncorrelated from one bin to the next,

Table 5
Fiducial model for forecasts.

w_1	...	w_{36}	$\ln G_9$	$\Delta\gamma$	$\Omega_m h^2$	$\Omega_b h^2$	$\Omega_k h^2$	$\Omega_\phi h^2$	$\ln A_s$	n_s	$\Delta\mathcal{M}$
−1	...	−1	0	0	0.1326	0.0227	0	0.3844	−19.9628	0.963	0

we also consider the impact of including a correlated component of the error by defining the SN covariance matrix as

$$C_{\alpha\beta}^{\text{SN}} = \begin{cases} \sigma_{m,u}^2 \delta_{\alpha\beta}, & \alpha = 1 \text{ or } \beta = 1, \\ \sigma_{m,u}^2 \left(\frac{0.2}{\Delta z}\right) \delta_{\alpha\beta} + \sigma_{m,c}^2 \exp\left(-\frac{|z_\alpha - z_\beta|}{\Delta z_c}\right), & \alpha > 1 \text{ and } \beta > 1, \end{cases} \quad (163)$$

where Δz is the bin width, $\sigma_{m,u}$ is the uncorrelated error in a bin of width $\Delta z = 0.2$ (or in the local sample at redshift z_1), $\sigma_{m,c}$ is the correlated error with correlation length Δz_c , and the net error in each bin z_α ($\alpha > 1$) is $\sigma_m = \sqrt{\sigma_{m,u}^2 + \sigma_{m,c}^2}$. In general these errors are redshift dependent, but here we assume that they are constant for simplicity. We do not consider possible correlations between the local SN sample and the high-redshift bins. For the fiducial forecasts we take $\sigma_{m,c} = 0$, so the covariance matrix is diagonal. The SN Fisher matrix is then computed as a sum over redshift bins

$$F_{ij}^{\text{SN}} = \sum_{\alpha,\beta} \frac{\partial m(z_\alpha)}{\partial p_i} (C_{\alpha\beta}^{\text{SN}})^{-1} \frac{\partial m(z_\beta)}{\partial p_j}, \quad (164)$$

where $m(z_\alpha) = 5 \log[H_0(D_L(z_\alpha))] + \mathcal{M}$ is the average magnitude in the bin and the derivatives are taken with respect to the parameters of Eq. (162).

For BAO we divide the observed volume into bins of equal width in $\ln(1+z)$, assumed to be uncorrelated, and compute the Fisher matrix

$$F_{ij}^{\text{BAO}} = \sum_{\mu,\nu,\alpha} \frac{\partial r_\mu(z_\alpha)}{\partial p_i} [C_{\mu\nu}^{\text{BAO}}(z_\alpha)]^{-1} \frac{\partial r_\nu(z_\alpha)}{\partial p_j}, \quad (165)$$

where the measurement vector $\mathbf{r}(z_\alpha) \equiv \{D(z_\alpha)/r_s, H(z_\alpha)r_s\}$, the sum is over $\mu, \nu = 1, 2$ and $\alpha = 1, \dots, N_{\text{bin}}$, and r_s is the sound horizon at recombination (see Section 2.3), for which we use the fitting formula from Hu (2005),

$$r_s \approx (144.4 \text{ Mpc}) \left(\frac{\Omega_m h^2}{0.14}\right)^{-0.252} \left(\frac{\Omega_b h^2}{0.024}\right)^{-0.083}. \quad (166)$$

We estimate the covariance matrix in each redshift bin using the BAO forecast code by Seo and Eisenstein (2007), which provides estimates of the fractional error on distance and the Hubble expansion rate at each redshift (relative to r_s), $\sigma_{\ln(D/r_s)} = \sqrt{C_{11}^{\text{BAO}}}/(D/r_s)$ and $\sigma_{\ln(Hr_s)} = \sqrt{C_{22}^{\text{BAO}}}/(Hr_s)$, respectively, as well as the cross correlation $r = C_{12}^{\text{BAO}}/\sqrt{C_{11}^{\text{BAO}}C_{22}^{\text{BAO}}}$. For our default forecasts, we start with the linear theory cosmic variance predictions, corresponding to the limit of perfect sampling of the density field within the observed volume and no degradation of the signal due to non-linear effects. To approximate the effects of finite sampling and non-linearity, we increase these errors by a factor of 1.8 for our fiducial forecasts, which leads to parameter constraints comparable to what would be expected with sampling $nP = 2$ and reconstruction that halves the effects of non-linear evolution. In Table 6 we list the volume for $f_{\text{sky}} = 0.25$ and fiducial BAO covariance matrix elements for 20 redshift slices from $0 \leq z \leq 3$. The results we obtain are only weakly dependent on the number of redshift bins chosen to divide up the total volume.

The WL Fisher matrix is based on the methodology described by Albrecht et al. (2009), where the explicit formulas are given. It includes both power spectrum tomography and cross-correlation cosmography (redshift scaling of the galaxy–galaxy lensing signal), but makes no assumption about the galaxy bias. The galaxies are sliced into $N_z = 14$ redshift bins and we consider power spectra in $N_\ell = 18$ bins logarithmically spaced over $10 < \ell < 10^4$. We consider all power spectra and cross-spectra of the galaxies g_i and the E -mode shear γ_i^E . This leads to $2N_z$ scalar fields on the sky, and hence $N_{2\text{pt}} = 2N_z(2N_z + 1)/2 \times N_\ell$ bins in the power spectrum matrix.⁷⁵ The length $N_{2\text{pt}}$ vector \mathbf{C} of power spectra incorporates all 2-point information.

Our task is now to construct a model both for \mathbf{C} and for its covariance matrix Σ , and then to construct the Fisher matrix for parameters \mathbf{p} :

$$F_{ij} = \frac{\partial \mathbf{C}^T}{\partial p^i} \Sigma^{-1} \frac{\partial \mathbf{C}}{\partial p^j}, \quad (167)$$

⁷⁵ Since we neglect magnification bias, some of these spectra, e.g. the correlation of high-redshift galaxies with low-redshift shear, are zero for all cosmological models.

Table 6
BAO errors for the fiducial program.

z_{\min}	z_{\max}	$V[(\text{Gpc}/h)^3]$	$\sigma_{\ln(D/r_s)}[\%]$	$\sigma_{\ln(Hr_s)}[\%]$
0.000	0.072	0.010	13.386	21.881
0.072	0.149	0.075	4.895	8.002
0.149	0.231	0.217	2.873	4.697
0.231	0.320	0.449	1.997	3.265
0.320	0.414	0.781	1.515	2.476
0.414	0.516	1.218	1.213	1.983
0.516	0.625	1.761	1.009	1.649
0.625	0.741	2.407	0.863	1.410
0.741	0.866	3.148	0.754	1.233
0.866	1.000	3.970	0.672	1.098
1.000	1.144	4.860	0.607	0.992
1.144	1.297	5.799	0.556	0.909
1.297	1.462	6.770	0.514	0.841
1.462	1.639	7.758	0.481	0.785
1.639	1.828	8.745	0.453	0.740
1.828	2.031	9.718	0.429	0.702
2.031	2.249	10.664	0.410	0.670
2.249	2.482	11.576	0.393	0.643
2.482	2.732	12.443	0.379	0.620
2.732	3.000	13.261	0.368	0.601

Column 3 gives the volume of the redshift slice for $f_{\text{sky}} = 0.25$. In all redshift slices, errors on D/r_s and Hr_s are correlated with correlation coefficient $r = 0.409$.

where T denotes a matrix transpose. Systematic errors may be incorporated as either nuisance parameters \mathbf{p} (marginalized over some prior) or as additional contributions to Σ :

$$\Sigma_{ij} \rightarrow \Sigma_{ij} + \sigma_{\varpi}^2 \frac{\partial C_i}{\partial \varpi} \frac{\partial C_j}{\partial \varpi}, \quad (168)$$

where ϖ is the amplitude of some systematic and σ_{ϖ} is the amount over which it is marginalized.

We incorporate in Σ the following contributions:

- The Gaussian covariance matrix.
- The 1-halo contribution to the shear 4-point function, given by Eq. (A9) of [Albrecht et al. \(2009\)](#).
- Galaxy bias and stochasticity, fully marginalized⁷⁶ in each bin of ℓ and z .
- The II intrinsic alignment term, obtained by fully marginalizing out the shear auto-correlations in each redshift slice.
- The GI intrinsic alignment term. It is assumed that Eq. (139) will allow estimation of $P_{e\delta}(k)$ and removal of this term in the linear and weakly non-linear regimes (taken to be $\ell < 10^{2.5}$). At smaller scales, we impose a weak prior that the GI not exceed present upper limits. This is implemented as

$$\frac{\sigma[P_{e\delta}(k)]}{P_{\delta}(k)} = 0.003 \sqrt{N_{\ell, \text{nonlin}}(N_z - 1)}, \quad (169)$$

where the square root is introduced to prevent many bins from being used to “average down” this systematic ([Albrecht et al., 2009](#)).

The photometric redshift errors (one bias parameter for each bin) and shear calibration errors (also one bias parameter for each bin) are treated as nuisance parameters in the parameter vector \mathbf{p} and are marginalized out before combining with other cosmological probes.

The forecasts for the main SN, BAO, and WL probes are supplemented by the expected constraints from upcoming CMB measurements provided by the *Planck* satellite. We adopt the Fisher matrix \mathbf{F}^{CMB} constructed by the FoMSWG, which includes cosmological constraints from the 70, 100, and 143 GHz channels of *Planck* with $f_{\text{sky}} = 0.7$, assuming that data collected at other frequencies will be used for foreground removal. The noise level and beam size for each channel comes from the *Planck* Blue Book ([Planck Collaboration, 2006](#)). Information from secondary anisotropies of the CMB is not included in this Fisher matrix; in particular, constraints from the ISW effect (Section 7.8) are removed by requiring the angular diameter distance to the CMB to be matched exactly, as described in [Albrecht et al. \(2009\)](#). Additionally, the large-scale ($\ell < 30$) polarization angular power spectrum and temperature–polarization cross power spectrum, which mainly contribute to constraints on the optical depth to reionization τ , are excluded from the forecast and replaced by a Gaussian prior with width $\sigma_{\tau} = 0.01$. This prior accounts for uncertainty in τ due to limited knowledge of the redshift dependence of reionization, which is not included in the simplest models of the CMB anisotropies. Although τ does not appear in the parameter set for

⁷⁶ i.e. with sufficiently wide prior that no significant information remains.

the Fisher matrices, marginalization over τ in the CMB constraints contributes to the uncertainty on the primordial power spectrum amplitude A_s , which in turn affects predictions for the growth of large-scale structure.

Combined constraints on cosmological parameters are obtained simply by adding the Fisher matrices of the individual probes, i.e. $\mathbf{F} = \mathbf{F}^{\text{SN}} + \mathbf{F}^{\text{BAO}} + \mathbf{F}^{\text{WL}} + \mathbf{F}^{\text{CMB}}$. Then the forecast for the parameter covariance is $\mathbf{C} = \mathbf{F}^{-1}$, and in particular the uncertainty on a given parameter p_i after marginalizing over the error on all other parameters is $\sqrt{[\mathbf{F}^{-1}]_{ii}}$.

Computing the Fisher matrix in the FoMSWG parameter space with a large number of independent bins for $w(z)$ gives us the flexibility to project these forecasts onto a number of simpler parameterizations, including the w_0 – w_a model for the purposes of computing the FoM. To change from the original parameter set \mathbf{p} to some new set \mathbf{q} , we compute

$$\tilde{F}_{kl} = \sum_{ij} \frac{\partial p_i}{\partial q_k} F_{ij} \frac{\partial p_j}{\partial q_l}, \quad (170)$$

which gives the Fisher matrix $\tilde{\mathbf{F}}$ for the new parameterization. In particular, projection from bins w_i to w_0 and w_a involves the derivatives $\partial w_i / \partial w_0 = 1$ and $\partial w_i / \partial w_a = z / (1 + z)$. We also compute the pivot redshift z_p and the uncertainty in the equation of state at that redshift, w_p . Given the 2×2 covariance matrix C_{ij} for w_0 and w_a (marginalized over the other parameters), the pivot values are computed as (Albrecht et al., 2009)

$$z_p = -\frac{C_{12}}{C_{12} + C_{22}}, \quad (171)$$

$$\sigma_{w_p} = C_{11} - \frac{C_{12}^2}{C_{22}},$$

where the first index corresponds to w_0 and the second to w_a .

One drawback to the w_0 – w_a parameterization is that constraints on $w(z)$ at high redshift are coupled to those at low redshift by the form of the model; for example, if observations determine the value of the equation of state perfectly at $z = 0$ and at $z = 0.1$, then it is completely determined at high redshift even in the absence of high redshift data. To specifically address questions related to the ability of dark energy probes to constrain dark energy at low redshift vs. high redshift, we define an alternative but equally simple parameterization in which $w(z)$ takes constant, independent values in each of two bins at $z \leq 1$ and $z > 1$. The projection onto this parameterization using Eq. (170) requires the derivatives $\partial w_i / \partial w(z \leq 1) = \Theta(1 - z_i)$ and $\partial w_i / \partial w(z > 1) = 1 - \Theta(1 - z_i)$, where $\Theta(x)$ is the Heaviside step function equal to 0 for $x < 0$ and 1 for $x \geq 0$.

Principal components (PCs) of the dark energy equation of state provide another way to determine which features of the equation of state evolution are best constrained by a given combination of experiments (Huterer and Starkman, 2003; Hu, 2002a; Huterer and Cooray, 2005; Wang and Tegmark, 2005; Dick et al., 2006; Simpson and Bridle, 2006; de Putter and Linder, 2008; Tang et al., 2011; Crittenden et al., 2009; Mortonson et al., 2009b; Kitching and Amara, 2009; Maturi and Mignone, 2009). We compute the PCs for each forecast case by taking the total Fisher matrix for the original parameter set (Eq. (162)) and marginalizing over all parameters other than the 36 binned values of w_i . If we call the Fisher matrix for the w_i parameters \mathbf{F}^w , then the PCs are found by diagonalizing \mathbf{F}^w :

$$\mathbf{F}^w = \mathbf{Q}\mathbf{\Lambda}\mathbf{Q}^T, \quad (172)$$

where \mathbf{Q} is an orthogonal matrix whose columns are eigenvectors of \mathbf{F}^w and $\mathbf{\Lambda}$ is a diagonal matrix containing the corresponding eigenvalues of \mathbf{F}^w . Up to an arbitrary normalization factor, the eigenvectors are equal to the PC functions $\mathbf{e}_i = (e_i(z_1), e_i(z_2), \dots)$ which describe how the binned values of $w(z)$ are weighted with redshift. Here we adopt the normalization of Albrecht et al. (2009),

$$\sum_{k=1}^{36} e_i(z_k) e_j(z_k) = \sum_{k=1}^{36} e_k(z_i) e_k(z_j) = (\Delta a)^{-1} \delta_{ij}, \quad (173)$$

where $\Delta a = 0.025$ is the bin width; for $i = j$ this condition approximately corresponds to $\int_{0.1}^1 da [e_i(a)]^2 = 1$. With this convention, the columns of \mathbf{Q} are $(\Delta a)^{1/2} \mathbf{e}_i$. The PCs rotate the original set of parameters to a set of PC amplitudes $\mathbf{Q}^T(\mathbf{1} + \mathbf{w})$ with elements

$$\beta_i = (\Delta a)^{1/2} \sum_{j=1}^{36} e_i(z_j) (1 + w_j). \quad (174)$$

Combining Eqs. (173) and (174), we can construct $w(z)$ in each redshift bin from a given set of PC amplitudes as

$$w_i = -1 + \sum_{j=1}^{36} \alpha_j e_j(z_i), \quad (175)$$

Table 7
Key to forecast variations.

$Any \times 4$	Quadruple fiducial errors (divide Fisher matrix by 16)
$Any \times 2$	Double fiducial errors (divide Fisher matrix by 4)
$Any/2$	Halve fiducial errors (multiply Fisher matrix by 4)
SN-III	Stage III-like SN: total magnitude error of 0.02 per $\Delta z = 0.2$ bin over $0.2 \leq z \leq 0.8$ and in local sample at $z = 0.05$
SN z_{\max}	Increase max. redshift to $z_{\max} = 1.6$ (7 bins with $\Delta z = 0.2$ and 0.01 mag. error)
SN-local	Omit local sample at $z = 0.05$
SNcx	Correlated errors: $\sigma_{m,u} = \sigma_{m,c} = 0.007$, $\Delta z_c = 0.2$, with x bins over $0.2 \leq z \leq 0.8$
BAO-III	Stage III-like BAO, approximating forecasts for BOSS LRGs+HETDEX: (D/r_s , Hr_s) errors of (1.0%, 1.8%) at $z = 0.35$, (1.0%, 1.7%) at $z = 0.6$, and (0.8%, 0.8%) at $z = 2.4$. These are “BAO only” forecasts for BOSS and “full power spectrum” forecasts for HETDEX
BAO z_{\max}	Reduce maximum redshift to $z_{\max} = 2$ (20 bins), retaining $f_{\text{sky}} = 0.25$
WL-opt	“Optimistic” Stage IV case (total error = $2 \times$ statistical)
WL-III	Stage III-like WL, approximating forecasts for DES: 5000 deg 2 and $n_{\text{eff}} = 9 \text{ arcmin}^{-2}$
CMB-W9	Fisher matrix forecast for 9-year WMAP data

where $\alpha_i \equiv (\Delta a)^{1/2} \beta_i$. The accuracy with which the α_i can be determined from the data is given by the eigenvalues of \mathbf{F}^w , $\sigma_i \equiv \sigma_{\alpha_i} = (\Delta a / \Delta_{ii})^{1/2}$, and the PCs are numbered in order of increasing variance (i.e. $\sigma_{i+1} > \sigma_i$).

For constraints that are marginalized over the w_i parameters, we impose a weak prior on w_i as suggested by Albrecht et al. (2009) to reduce the dependence of forecasts for $\Delta\gamma$ on the poorly-constrained high redshift w_i values, since arbitrarily large fluctuations in $w(z)$ can alter the high redshift growth rate. We include a weak Gaussian prior with width $\sigma_{w_i} = \Delta w / \sqrt{\Delta a}$ by adding to the total Fisher matrix

$$F_{ij}^{\text{prior}} = \begin{cases} \sigma_{w_i}^{-2} \delta_{ij}, & i \leq 36, \\ 0, & i > 36, \end{cases} \quad (176)$$

assuming that the parameters are ordered as in Eq. (162) with $p_1 = w_1, p_2 = w_2$, etc. For most forecasts, we use a default prior width of $\Delta w = 10$ ($\sigma_{w_i} \approx 63$), which approximately corresponds to requiring that the average value of $|1 + w|$ in all bins does not exceed 10. In the next section we also consider how constraints on certain parameters change with a narrower prior of $\Delta w = 1$. For priors wider than the default choice, the Fisher matrix computations are subject to numerical effects arising from the use of a finite number of w_i bins to approximate continuous variations in $w(z)$, so we do not present results with weaker priors than $\Delta w = 10$. Note that the construction of PCs of $w(z)$ as described above does not include such a prior on w_i .

8.3. Results: forecasts for the fiducial program and variations

8.3.1. Constraints in simple $w(z)$ models

We begin with forecasts for which the 36 $w(z)$ bins are projected onto the simpler w_0 - w_a parameter space. Tables 7–10 give the forecast 1σ uncertainties for the fiducial program and numerous variations. Each forecast case is labeled by a list of the Fisher matrices that are added together, and the basic variations we consider are simple rescalings of the total errors for each probe; for example, [SN/2, BAO $\times 4$, WL-opt, CMB] includes the fiducial SN data with the total error halved (i.e. the Fisher matrix multiplied by 4), 4 times the fiducial BAO errors, the optimistic version of the WL forecast, and the fiducial Planck CMB Fisher matrix. Note that /2 denotes a more powerful program and $\times 2$ denotes a less powerful program. The key in Table 7 describes other types of variations of the fiducial probes. In some cases we omit a probe entirely, e.g. [SN, BAO, WL] sums the fiducial Fisher matrices of the three main probes but does not include the Planck CMB priors. Note that even though we assume a specific systematic error component in computing certain Fisher matrices (in particular, \mathbf{F}^{WL}), the cases with rescaled errors simply multiply each Fisher matrix by a constant factor and thus do not distinguish between statistical and systematic contributions to the total error.

Constraints on the equation of state are given in Tables 8–10 by the DETF FoM and the error on w_p . The rule of thumb that $\sigma_{w_a} \equiv (\text{FoM} \times \sigma_{w_p})^{-1} \approx 10\sigma_{w_p}$ holds at the $\sim 30\%$ level for most of the forecast variations we consider – i.e., at the best-constrained redshift, the value of w is typically determined a factor of ten better than the value of its derivative. The forecast tables also list the uncertainty in the high redshift equation of state ($w(z) > 1$) for the alternative parameterization where $w(z)$ takes independent, constant values at $z \leq 1$ and $z > 1$. Note that all of these $w(z)$ constraints are marginalized over uncertainties in G_9 and $\Delta\gamma$, so they do not assume that structure growth follows the GR prediction.

For the fiducial program outlined in Section 8.1, the DETF FoM is projected to be around 600–800, depending on whether the WL forecast uses the default systematic error model or the optimistic model. This is roughly an order of magnitude larger than the FoM forecast for a combination of Stage III experiments (e.g. see Table 9, rows 2–3) and nearly two orders

Table 8
Forecast uncertainties for variations of the fiducial program.

	Forecast case	z_p	σ_{w_p}	FoM	$\sigma_{w(z>1)}$	$10^3 \sigma_{\Omega_k}$	$10^2 \sigma_H$	$\sigma_{\Delta\gamma}$	$\sigma_{\ln G_9}$
1	[SN, BAO, WL, CMB]	0.46	0.014	664	0.051	0.55	0.51	0.034	0.015
2	[SN, BAO, WL-opt, CMB]	0.39	0.013	789	0.049	0.64	0.42	0.026	0.016
3	[BAO, WL, CMB]	0.63	0.017	321	0.054	0.56	0.99	0.034	0.015
4	[SN-III, BAO, WL, CMB]	0.57	0.016	433	0.053	0.56	0.75	0.034	0.015
5	[SN \times 4, BAO, WL, CMB]	0.61	0.017	353	0.054	0.56	0.91	0.034	0.015
6	[SN \times 2, BAO, WL, CMB]	0.57	0.016	433	0.053	0.56	0.75	0.034	0.015
7	[SN/2, BAO, WL, CMB]	0.32	0.010	1197	0.049	0.55	0.32	0.034	0.015
8	[SNz _{max} , BAO, WL, CMB]	0.42	0.011	841	0.050	0.55	0.40	0.034	0.015
9	[SN-local, BAO, WL, CMB]	0.59	0.016	376	0.053	0.56	0.85	0.034	0.015
10	[SNc3, BAO, WL, CMB]	0.46	0.014	652	0.051	0.55	0.51	0.034	0.015
11	[SNc6, BAO, WL, CMB]	0.46	0.014	663	0.051	0.55	0.51	0.034	0.015
12	[SNc12, BAO, WL, CMB]	0.46	0.014	667	0.051	0.55	0.50	0.034	0.015
13	[SN, WL, CMB]	0.26	0.022	152	0.321	2.13	0.72	0.038	0.022
14	[SN, BAO-III, WL, CMB]	0.32	0.019	299	0.120	1.19	0.57	0.035	0.017
15	[SN, BAO \times 4, WL, CMB]	0.30	0.020	245	0.145	1.16	0.65	0.036	0.018
16	[SN, BAO \times 2, WL, CMB]	0.36	0.018	380	0.087	0.76	0.58	0.035	0.016
17	[SN, BAO/2, WL, CMB]	0.50	0.010	1222	0.033	0.47	0.39	0.034	0.014
18	[SN, BAOz _{max} , WL, CMB]	0.42	0.014	547	0.071	0.66	0.52	0.034	0.015
19	[SN, BAO, CMB]	0.41	0.016	539	0.059	0.78	0.53	–	–
20	[SN, BAO, WL-III, CMB]	0.41	0.016	543	0.058	0.77	0.52	0.145	0.048
21	[SN, BAO, WL \times 4, CMB]	0.42	0.016	553	0.057	0.75	0.53	0.126	0.031
22	[SN, BAO, WL \times 2, CMB]	0.43	0.015	587	0.055	0.68	0.52	0.065	0.020
23	[SN, BAO, WL/2, CMB]	0.48	0.012	815	0.047	0.45	0.47	0.018	0.012
24	[SN, BAO, WL-opt \times 4, CMB]	0.41	0.016	556	0.058	0.76	0.52	0.085	0.022
25	[SN, BAO, WL-opt \times 2, CMB]	0.41	0.015	606	0.055	0.73	0.49	0.045	0.018
26	[SN, BAO, WL-opt/2, CMB]	0.37	0.009	1397	0.040	0.52	0.30	0.017	0.013
27	[SN, BAO, WL]	0.31	0.020	368	0.075	7.82	1.48	0.037	6.697
28	[SN, BAO, WL, CMB-W9]	0.43	0.015	592	0.055	1.07	0.53	0.036	0.019

Forecasts in this table vary the assumptions about a single probe at a time from the fiducial program. With the exception of $w(z > 1)$, a w_0-w_a model for the dark energy equation of state is assumed for all parameter uncertainties here and in Tables 9 and 10. All forecasts allow for deviations from GR parameterized by $\Delta\gamma$ and G_9 .

Table 9
Forecast uncertainties for variations of the fiducial program (continued).

	Forecast case	z_p	σ_{w_p}	FoM	$\sigma_{w(z>1)}$	$10^3 \sigma_{\Omega_k}$	$10^2 \sigma_H$	$\sigma_{\Delta\gamma}$	$\sigma_{\ln G_9}$
1	[SN, BAO, WL, CMB]	0.46	0.014	664	0.051	0.55	0.51	0.034	0.015
2	[SN-III, BAO-III, WL-III, CMB]	0.42	0.032	131	0.137	1.36	0.96	0.147	0.051
3	[SN-III, BAO-III, WL-III, CMB-W9]	0.33	0.039	92	0.174	2.41	1.01	0.148	0.064
4	[SN \times 4, BAO \times 4, WL \times 4, CMB]	0.51	0.048	52	0.179	1.32	1.98	0.128	0.033
5	[SN \times 2, BAO \times 2, WL \times 2, CMB]	0.49	0.026	188	0.095	0.85	1.00	0.065	0.021
6	[SN/2, BAO/2, WL/2, CMB]	0.43	0.007	2439	0.027	0.34	0.26	0.018	0.011
7	[SN/2, BAO/2, WL-opt, CMB]	0.34	0.008	1832	0.035	0.55	0.26	0.023	0.014
8	[SN-III, BAO-III, WL, CMB]	0.44	0.026	169	0.126	1.20	0.89	0.035	0.017
9	[SN \times 4, BAO \times 4, WL, CMB]	0.50	0.034	85	0.157	1.18	1.49	0.037	0.019
10	[SN \times 4, BAO \times 2, WL, CMB]	0.57	0.026	153	0.093	0.77	1.28	0.035	0.016
11	[SN \times 4, BAO/2, WL, CMB]	0.57	0.011	891	0.033	0.47	0.53	0.034	0.014
12	[SN \times 2, BAO \times 4, WL, CMB]	0.41	0.029	132	0.151	1.17	1.01	0.037	0.018
13	[SN \times 2, BAO \times 2, WL, CMB]	0.49	0.023	218	0.090	0.76	0.92	0.035	0.016
14	[SN \times 2, BAO/2, WL, CMB]	0.55	0.011	966	0.033	0.47	0.49	0.034	0.014
15	[SN/2, BAO \times 4, WL, CMB]	0.25	0.012	499	0.142	1.15	0.47	0.036	0.017
16	[SN/2, BAO \times 2, WL, CMB]	0.27	0.011	735	0.084	0.76	0.39	0.035	0.016
17	[SN/2, BAO/2, WL, CMB]	0.38	0.008	1921	0.032	0.47	0.27	0.034	0.014
18	[SNz _{max} , BAOz _{max} , WL, CMB]	0.40	0.012	694	0.069	0.66	0.42	0.034	0.015

Same as Table 8, but varying two or three probes at a time from the fiducial specifications.

of magnitude larger than current, “Stage II” FoM values (~ 10). The equation of state in the w_0-w_a parameterization is best measured by the fiducial set of Stage IV experiments at a redshift $z_p \approx 0.5$ with a 1σ precision of $\sigma_{w_p} \approx 0.014$, and the time variation of $w(z)$ is determined to within $\sigma_{w_a} \approx 0.11$. The fiducial program also yields impressive constraints of 5.5×10^{-4} on Ω_k and $0.51 \text{ km s}^{-1} \text{ Mpc}^{-1}$ on H_0 . Forecast 1σ errors for the modified gravity parameters are 0.034 on $\Delta\gamma$ and 0.015 on $\ln G_9$. We caution, however, that the Ω_k , H_0 , and G_9 errors (but not the $\Delta\gamma$ error) are sensitive to our assumption of the w_0-w_a parameterization (see Figs. 36–40). CMB constraints make a critical contribution – the FoM drops from 664 to 368 if they are omitted entirely (Table 8, line 27) – but the difference between *Planck* precision and anticipated WMAP9 precision is modest (line 28) except for Ω_k , where it is a factor of two.

Table 10
Forecast uncertainties for variations of the fiducial program (continued).

	Forecast case	z_p	σ_{w_p}	FoM	$\sigma_{w(z>1)}$	$10^3 \sigma_{\Omega_k}$	$10^2 \sigma_h$	$\sigma_{\Delta\gamma}$	$\sigma_{\ln G_9}$
1	[SN, BAO, WL, CMB]	0.46	0.014	664	0.051	0.55	0.51	0.034	0.015
2	[SN, BAO-III, WL-III, CMB]	0.29	0.022	239	0.129	1.35	0.59	0.147	0.051
3	[SN, BAO \times 4, WL \times 4, CMB]	0.28	0.022	185	0.165	1.30	0.77	0.128	0.033
4	[SN, BAO \times 4, WL \times 2, CMB]	0.28	0.021	200	0.159	1.26	0.73	0.067	0.023
5	[SN, BAO \times 4, WL/2, CMB]	0.35	0.016	373	0.115	0.98	0.54	0.020	0.014
6	[SN, BAO \times 4, WL-opt, CMB]	0.29	0.015	361	0.102	1.21	0.57	0.042	0.020
7	[SN, BAO \times 2, WL \times 4, CMB]	0.34	0.019	328	0.092	0.90	0.62	0.127	0.031
8	[SN, BAO \times 2, WL \times 2, CMB]	0.35	0.019	340	0.090	0.85	0.61	0.065	0.021
9	[SN, BAO \times 2, WL/2, CMB]	0.40	0.015	502	0.078	0.67	0.51	0.019	0.013
10	[SN, BAO \times 2, WL-opt, CMB]	0.33	0.014	506	0.072	0.83	0.49	0.033	0.017
11	[SN, BAO/2, WL \times 4, CMB]	0.43	0.012	926	0.041	0.65	0.40	0.126	0.031
12	[SN, BAO/2, WL \times 2, CMB]	0.45	0.011	1010	0.038	0.59	0.40	0.064	0.020
13	[SN, BAO/2, WL/2, CMB]	0.54	0.008	1585	0.028	0.34	0.38	0.018	0.012
14	[SN, BAO/2, WL-opt, CMB]	0.43	0.010	1251	0.035	0.55	0.35	0.023	0.015
15	[SN-III, BAO, WL-III, CMB]	0.54	0.019	346	0.060	0.77	0.79	0.146	0.048
16	[SN \times 4, BAO, WL \times 4, CMB]	0.60	0.020	277	0.060	0.75	0.99	0.126	0.031
17	[SN \times 4, BAO, WL \times 2, CMB]	0.60	0.019	298	0.058	0.68	0.97	0.065	0.020
18	[SN \times 4, BAO, WL/2, CMB]	0.59	0.014	486	0.049	0.45	0.75	0.018	0.012
19	[SN \times 4, BAO, WL-opt, CMB]	0.47	0.014	568	0.049	0.64	0.56	0.026	0.016
20	[SN \times 2, BAO, WL \times 4, CMB]	0.54	0.019	351	0.059	0.75	0.79	0.126	0.031
21	[SN \times 2, BAO, WL \times 2, CMB]	0.55	0.018	375	0.057	0.68	0.78	0.065	0.020
22	[SN \times 2, BAO, WL/2, CMB]	0.56	0.013	567	0.048	0.45	0.65	0.018	0.012
23	[SN \times 2, BAO, WL-opt, CMB]	0.45	0.014	619	0.049	0.64	0.52	0.026	0.016
24	[SN/2, BAO, WL \times 4, CMB]	0.28	0.011	998	0.056	0.74	0.33	0.126	0.031
25	[SN/2, BAO, WL \times 2, CMB]	0.30	0.011	1061	0.053	0.67	0.33	0.065	0.020
26	[SN/2, BAO, WL/2, CMB]	0.35	0.009	1430	0.045	0.44	0.30	0.018	0.012
27	[SN/2, BAO, WL-opt, CMB]	0.30	0.010	1242	0.049	0.64	0.30	0.026	0.015

Continuation of Table 9.

Fig. 33 illustrates the key results of our forecasting investigation, highlighting many aspects of the interplay among the three observational probes. In the upper left panel, the solid curve shows how the FoM changes as the total SN errors vary from four times fiducial to half fiducial, keeping the other probes (BAO, WL, and CMB) fixed at their fiducial levels. Other curves show the effect of doubling WL or BAO errors or switching to the optimistic WL forecast. The lower panels show analogous results from varying the BAO or WL errors, while the upper right panel shows the effect of changing the maximum redshift of the SN program. Over the range of variations plotted in Fig. 33, the FoM varies from just over 100 to almost 1400.

The scaling of the FoM with the forecast errors is not uniform among the three main probes. Starting from the fiducial program, the effect of doubling or halving errors is greater for BAO than for SN, and greater for SN than for WL. This scaling implies that BAO data provide the greatest leverage in these forecasts. However, the hierarchy of the three probes is sensitive to the assumptions about each experiment; in particular, assuming the optimistic version of WL errors promotes WL from having the least leverage on the FoM to having the most leverage. More generally, the fact that varying the errors of any individual probe changes the FoM noticeably demonstrates the complementarity of the methods.

Unlike many previous FoM forecasts, we marginalize over the structure growth parameters $\Delta\gamma$ and $\ln G_9$, which tends to increase the uncertainties on w_0 and w_a . In most cases, the difference between the marginalized constraints and ones obtained under the assumption of GR ($\Delta\gamma = \ln G_9 = 0$) is small, but the difference is greater if WL contributes significantly to expansion history constraints; for example, for the fiducial program, the change in the FoM due to assuming GR is only $664 \rightarrow 771$, whereas with the WL-opt forecast the change is $789 \rightarrow 1119$.

The local calibrator sample plays an important role in the SN constraints. Omitting the measurement at $z = 0.05$ reduces the FoM from $664 \rightarrow 376$ (Table 8, line 9). Even replacing it with a measurement over a broad low-redshift bin $0 < z < 0.2$, still with an error of 0.01 mag, reduces the FoM from $664 \rightarrow 533$ because it increases degeneracy between the supernova absolute magnitude scale and dark energy parameters. Reducing the redshift of the calibrator sample below 0.05 makes little further difference, and at lower redshifts peculiar velocity uncertainties may become too large to remove with high precision. It is also interesting to ask whether it is better to go after SNe at high redshifts or to focus on reducing the errors on SN data at low redshifts. Comparing the upper panels of Fig. 33, we find that the benefit from reducing errors is typically greater than that from obtaining SNe beyond $z \sim 1$, at least for the FoM. For example, reducing the error per redshift bin from 0.01 mag (the fiducial value) to 0.005 mag raises the FoM by a factor of 1.80, but increasing the maximum redshift from 0.8 to 1.6 raises the FoM by only 1.27 (see Table 8). If BAO errors are doubled, the FoM drops substantially, but SN errors still have much greater leverage than SN maximum redshift.

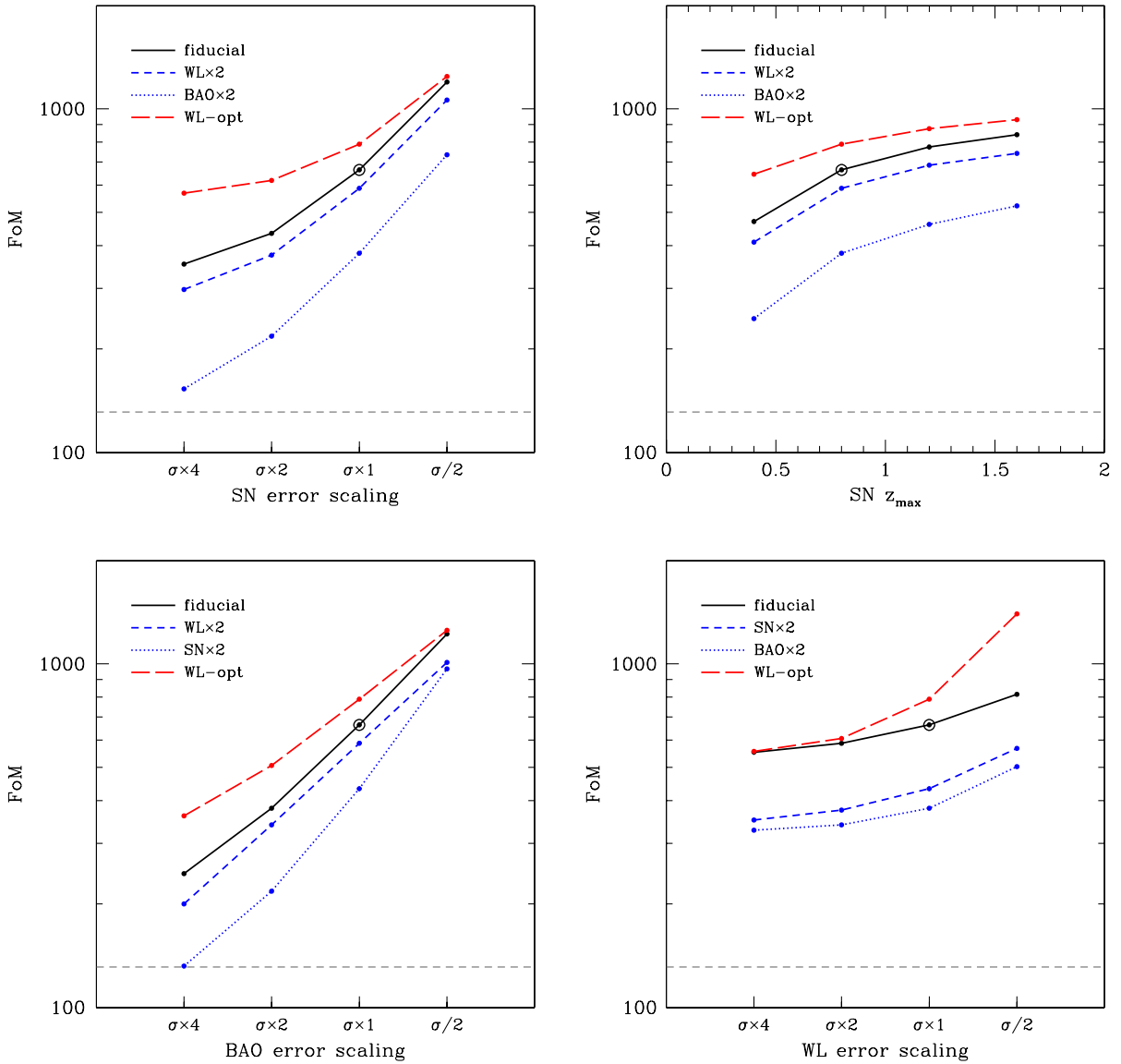


Fig. 33. The DETF FoM, $(\sigma_{w_p} \sigma_{w_a})^{-1}$, for the fiducial program and simple variants. In each panel, the open circle marks the FoM of the fiducial program. In the upper left panel, the other points along the solid curve show the effect of scaling the error on the SN measurements by factors of 2 or 4 while keeping errors for other probes fixed at their fiducial values. Dotted, short-dashed, and long-dashed curves show the effect of, respectively, doubling the BAO errors, doubling the WL errors, or adopting the optimistic WL forecasts in which systematic errors are simply twice the statistical errors. Other panels show analogous results, but instead of scaling the total SN error they scale the total BAO error (lower left), the total WL error (lower right), or the maximum redshift of the SN constraints (upper right). In each panel, the dashed gray line marks the forecast performance of Stage III probes (including *Planck*) with FoM = 131.

The weak dependence of $w(z)$ constraints on the maximum SN redshift extends to other parameters as well. Fig. 34 compares the effect on 1σ errors of varying the maximum SN redshift to that of varying the maximum BAO redshift. For the w_0-w_a model, the errors on all parameters are relatively insensitive to changes in the maximum SN redshift at $z \gtrsim 1$, but the errors on w_a and Ω_k decrease by a factor of a few as the maximum BAO redshift increases from $z = 1$ to $z = 3$. Likewise, the high redshift equation of state $w(z > 1)$ can be determined much more precisely as BAO data extend to higher redshifts, but it depends little on the maximum SN redshift. For the fiducial Stage IV forecasts, only the Hubble constant error depends significantly on the depth of SN observations (assuming a w_0-w_a model). More pessimistic assumptions about the achievable BAO errors enhance the importance of high redshift SNe for determining w_p (dotted line in Fig. 34), but the dependence of other parameters on z_{\max} for the SN data remains weak.

In practice, the impact of the maximum SN redshift on dark energy constraints will depend crucially on the behavior of systematic errors. We have assumed in our forecasts here that the error per redshift bin stays constant as the maximum SN redshift increases, but in reality higher redshift SNe are likely to have larger systematic errors associated with them,

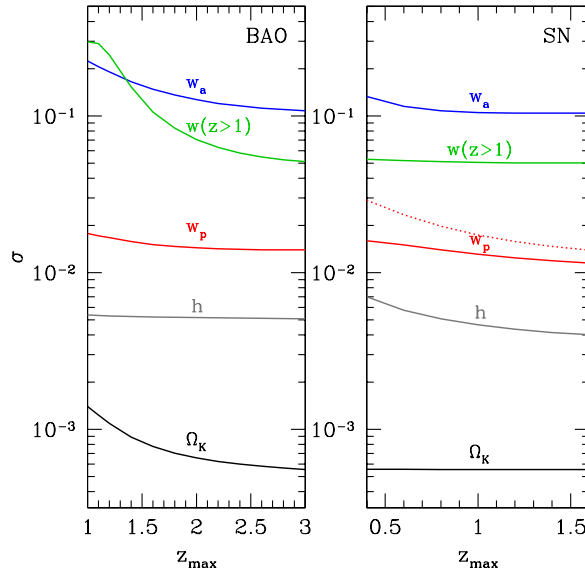


Fig. 34. Variation of 1σ parameter errors with the maximum redshift for BAO at fixed f_{sky} (left) or for SN with fixed error per $\Delta z = 0.2$ redshift bin (right). For the solid curves, fiducial Stage IV forecasts are assumed for all other probes. The dotted curve in the right panel shows the scaling of $\sigma(w_p)$ with SN z_{max} assuming 4 times larger BAO errors (BAO $\times 4$). The plotted errors assume a w_0 - w_a parameterization (except for $w(z > 1)$).

which would diminish the gains from high redshift SNe even more than indicated by the flattening of curves in Fig. 33. However, once the systematic errors at $z < 0.8$ are saturated, then pushing to higher redshift may be the only way to continue improving the SN constraints. The gain from the higher redshift SNe then depends on whether their systematics are *uncorrelated* with those at lower redshift, so that they indeed provide new information. While there has been considerable recent progress in understanding and accounting of systematic errors in SN cosmology, there has been little exploration to date of the correlation of systematics across redshift bins. The correlation of systematics may vary with details of experimental design (e.g., flux calibration), and it also depends on aspects of the Type Ia supernova population that are, as yet, poorly understood (e.g., whether there is a mix of single-degenerate and double-degenerate progenitors that changes with redshift). To optimize a specific experiment, one must assess both the expected behavior of systematics and the observing time required to discover SNe at different redshifts and to measure them with adequate photometric and spectroscopic precision. The SDT report for *WFIRST* (Green et al., 2012) provides a worked example: with a two-tier strategy (shallow wide fields and narrow deep fields), the CMB+SN FoM increases steadily as the maximum redshift is increased from 0.8 to 1.7 at (roughly) fixed observing time, assuming systematics that are uncorrelated among redshift bins. However, reducing the systematics by a factor of two (from ≈ 0.02 mag per $\Delta z = 0.1$ bin to ≈ 0.01 mag) has a larger impact than raising z_{max} from 0.8 to 1.7. The contrast is less stark than in our Fig. 33 because the reduction in *total* error is less than a factor of two; with the smaller systematic errors, the *WFIRST* DRM1 SN survey would be mainly statistics limited.

The behavior in Fig. 33 can be approximately understood in terms of the aggregate measurement precision, a notion we discuss at greater length in Section 8.6 below. The local ($z = 0.05$) SN bin serves mainly to calibrate the SN absolute magnitude, so in our fiducial program there are three $\Delta z = 0.2$ redshift bins with cosmological information. Increasing z_{max} to 1.6 changes the number of non-local bins from three to seven, improving aggregate precision by $\sim \sqrt{7/3}$, and the impact on the FoM is roughly half the impact of reducing errors by a factor of two while retaining $z_{\text{max}} = 0.8$. If we increase z_{max} to 1.6 but simultaneously inflate the errors of the non-local bins by $\sqrt{7/3}$, thus keeping the aggregate precision of the $z > 0.1$ measurements fixed, then the FoM rises to 749, a 13% improvement over the fiducial case, vs. a 26% improvement if we increase z_{max} to 1.6 at constant per-bin error. In this sense, roughly half of the improvement when extending the redshift limit comes from tightening the aggregate statistical precision by adding new bins, and half the improvement comes from the greater leverage afforded by a wider redshift range. A similar calculation for $z_{\text{max}} = 1.2$ (where the corresponding FoM improvements over the fiducial case are 9% and 17%) leads to the same conclusion. Ultimately, however, the trade between extending the redshift range of a SN survey vs. improving the observations at lower redshift depends on aspects of observational and evolutionary systematics that are still poorly understood. This remains an important issue for near-term investigation with the much more comprehensive data sets that are now becoming available.

8.3.2. Constraints on structure growth parameters

While the DETF FoM is a useful metric for studying the impact of variations in each of the dark energy probes, it does not tell the whole story. Deviations from the standard model might show up in other sectors of the parameter space; for example, a detection of non-GR values for the growth parameters $\Delta\gamma$ and G_0 could point to a modified gravity explanation for cosmic acceleration that would not be evident from measurements of $w(z)$ alone. Thus, even the less optimistic version of

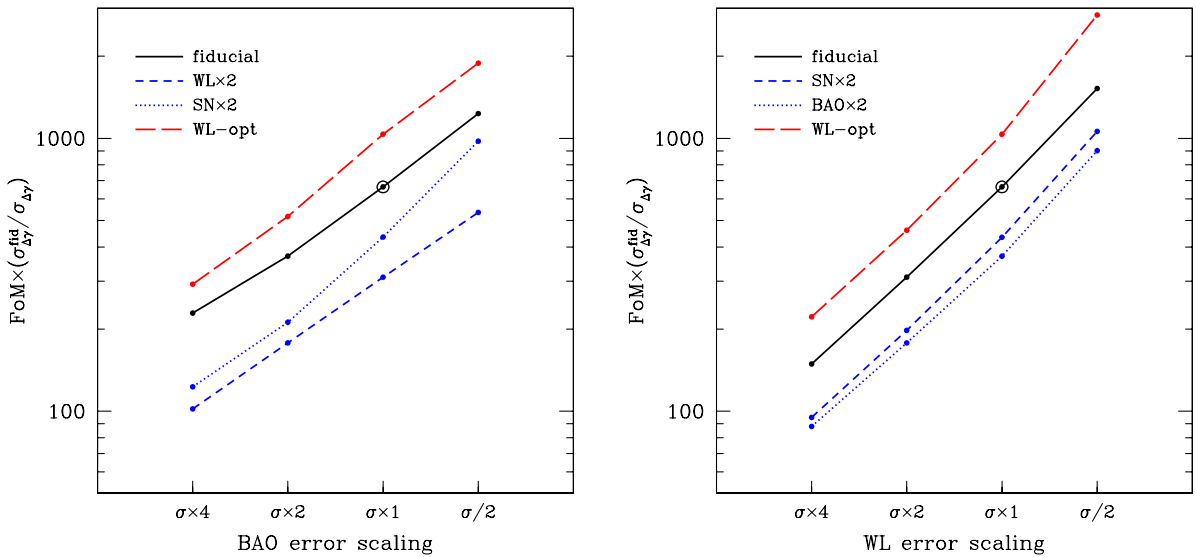


Fig. 35. FoM scaling with BAO errors (left) and WL errors (right) including changes in the error on $\Delta\gamma$, normalized to the forecast uncertainty for the fiducial program, $\sigma_{\Delta\gamma}^{\text{fid}} = 0.034$. The fiducial Stage IV forecast is marked by an open circle. For the Stage III forecast, $\text{FoM} \times (\sigma_{\Delta\gamma}^{\text{fid}} / \sigma_{\Delta\gamma}) = 30$.

the WL experiment, which adds relatively little to the $w(z)$ constraints obtained by the combination of fiducial SN, BAO, and CMB forecasts, is a critical component of a program to study cosmic acceleration because of its unique role in determining the growth parameters $\Delta\gamma$ and G_9 .

The impact of various experiments on the structure growth parameters is more evident if we extend the DETF FoM to include $\Delta\gamma$ in addition to w_0 and w_a . As shown in Fig. 35, the scaling of this new FoM with respect to WL errors (and, to a lesser extent, BAO errors) is much steeper than it is for the usual FoM (Fig. 33). We do not show the scaling with SN errors or z_{max} , since those assumptions do not affect the expected uncertainties for $\Delta\gamma$ and G_9 (see Table 8, lines 3–12). One could also consider versions of the FoM that include uncertainties in G_9 and that account for the correlations between the structure growth parameters and the dark energy equation of state.

The complementarity between the SN, BAO, and WL techniques is further demonstrated in Figs. 36–38, which show the forecast 68% confidence level contours in the $w_{0.5}-w_a$ and $\Delta\gamma-\ln G_9$ planes after marginalizing over other parameters. Instead of w_0 we plot $w_{0.5}$, the equation-of-state parameter at $z = 0.5$, because it is much less correlated with w_a for most of the forecast scenarios. In every panel, the blue ellipse shows the error contour of the fiducial forecast while other ellipses show the effect of varying the errors of the indicated method. The opposite orientation of ellipses in Figs. 36 and 37 demonstrates the complementary sensitivity of SN and BAO to $w(z)$: the SN data are mainly sensitive to the equation of state at low redshift, whereas BAO data measure the equation of state at higher redshift. However, the sensitivity to the beyond-GR growth parameters comes entirely from WL data, which provide the only direct measurements of growth, and the strength of the $\Delta\gamma$ and G_9 constraints depends directly on the WL errors, as shown in Fig. 38. Conversely, these constraints are very weakly sensitive to the SN or BAO errors (Figs. 36 and 37), showing that the uncertainties are dominated by the growth measurements themselves rather than residual uncertainty in the expansion history. Inspection of Table 8 shows that the $\Delta\gamma$ constraints are essentially linear in the WL errors, while the $\ln G_9$ constraints scale more slowly.

Although the w_0-w_a parameterization is flexible enough to describe a wide variety of expansion histories, it is too simple to account for all possibilities; in particular, $w(z)$ is restricted to functions that are smooth and monotonic over the entire history of the universe. Because many cosmological parameters are partially degenerate with the dark energy evolution, assumptions about the functional form of $w(z)$ can strongly affect the precision of constraints on other parameters. As an example of this model dependence, the right panels of Figs. 36–38 show how the constraints on the growth parameters weaken (dashed curves) if one allows the 36 binned w_i values to vary independently instead of assuming that they conform to the w_0-w_a model. While $\Delta\gamma$ forecasts are only mildly affected by the choice of dark energy modeling, constraints on the $z = 9$ normalization parameter G_9 depend strongly on the form of $w(z)$. This dependence follows from the absence of data probing redshifts $3 \lesssim z < 9$ in the fiducial Stage IV program. In the w_0-w_a model, dark energy evolution is well determined even at high redshifts, since the two parameters of the model can be measured from data at $z < 3$, and thus the growth function at $z = 9$ is closely tied to the low redshift growth of structure measured by WL. However, allowing $w(z)$ to vary independently at high redshift where it is unconstrained by data decouples the low and high redshift growth histories, and therefore G_9 can no longer be determined precisely. In fact, the constraints on G_9 in that case depend greatly on the chosen prior on w_i (taken to be the default prior of $\sigma_{w_i} = 10/\sqrt{\Delta a}$ in Figs. 36–38). One important consequence of this dependence on the $w(z)$ model is that an apparent breakdown of GR via $G_9 \neq 1$ might instead be a sign that the chosen dark energy parameterization is too restrictive.

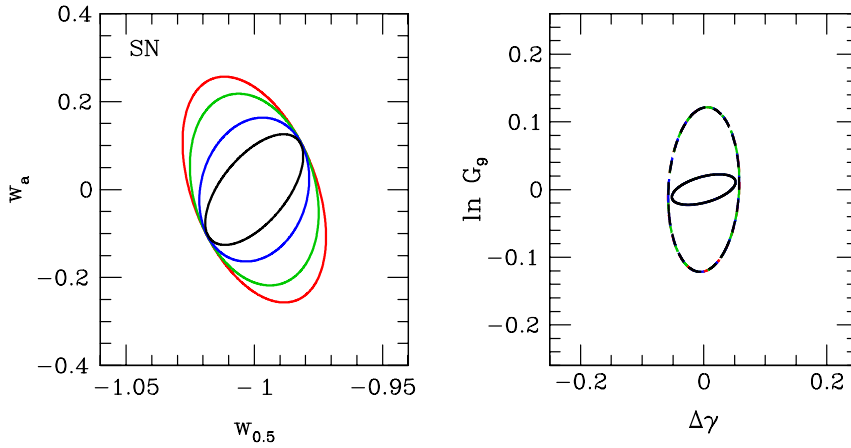


Fig. 36. Forecast constraints (68% confidence levels) for dark energy and growth parameters, varying errors on SN data: fiducial $\times 4$ (red), $\times 2$ (green), $\times 1/2$ (blue), and $/2$ (black). In all cases, the fiducial forecasts are used for the other probes (BAO, WL, CMB). Contours in the left panel use the value of the equation of state at $z = 0.5$ (close to the typical pivot redshift), $w_{0.5} = w_0 + w_a/3$. Dashed contours in the right panel show the errors on growth parameters for the binned $w(z)$ parameterization, with the default priors corresponding to deviations of $\lesssim 10$ in the average value of w . Solid contours assume a w_0 – w_a parameterization. In both cases, the G_9 and $\Delta\gamma$ constraints are essentially independent of the SN errors. (For interpretation of the references to colour in this figure legend, the reader is referred to the web version of this article.)

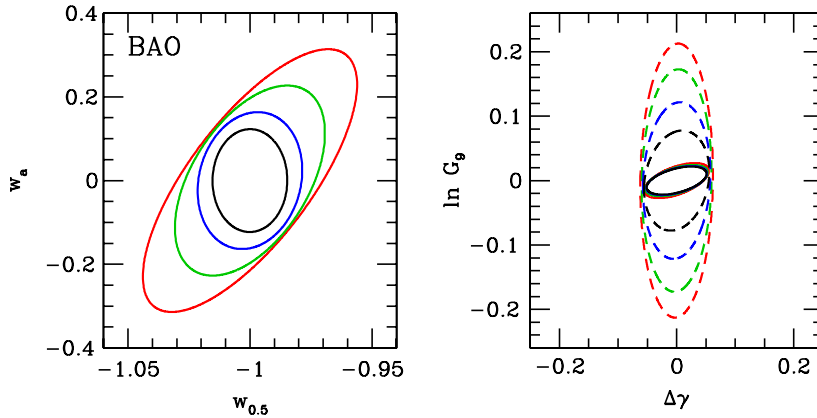


Fig. 37. Same as Fig. 36, but varying BAO errors from fiducial $\times 4$ (red) to fiducial/2 (black). (For interpretation of the references to colour in this figure legend, the reader is referred to the web version of this article.)

8.3.3. Dependence on the $w(z)$ model and binning of data

Other parameters are also affected to varying degrees by the choice of $w(z)$ model and the priors on the model parameters. Fig. 39 shows how errors on Ω_k and h are affected by relaxing assumptions about dark energy evolution. For the fiducial program and minor variants, Ω_k is very weakly correlated with w_0 and w_a , resulting in similar errors on curvature for the w_0 – w_a and Λ CDM models. However, generalizing the dark energy parameterization to include independent variations in 36 redshift bins can degrade the precision of Ω_k measurements by an order of magnitude or more. In that case, the error on Ω_k is very sensitive to the chosen prior on the value of w_i in each bin, and it improves little as the BAO errors decrease. This dependence on priors reflects the fact that curvature is most correlated with the highest redshift w_i values, which are poorly constrained by the fiducial combination of data. Relative to curvature, constraints on the Hubble constant are affected more by the choice of dark energy parameterization but less by priors on w_i in the binned $w(z)$ model.

Fig. 40 shows the dependence of σ_{σ_h} on the precision of SN data for various dark energy parameterizations (σ_{Ω_k} is nearly independent of the SN errors for this range of variations around the fiducial forecast; see Table 8). If we assume a w_0 – w_a model for dark energy, Hubble constant errors strongly depend on the precision of SN data. However, Fig. 40 shows that either decreasing or increasing the number of dark energy parameters can almost completely eliminate the dependence of σ_h on the SN data. In the case of the simpler Λ CDM model, the combination of the fiducial BAO, WL, and CMB forecasts is sufficient to precisely determine all of the model parameters, and adding information from SN data has a negligible effect on the parameter errors. Adding w_0 and w_a to the model introduces degeneracies between these dark energy parameters and other parameters, including h . Since constraints from SN data help to break these degeneracies, reducing SN errors can significantly improve measurement of the Hubble constant in the w_0 – w_a model.

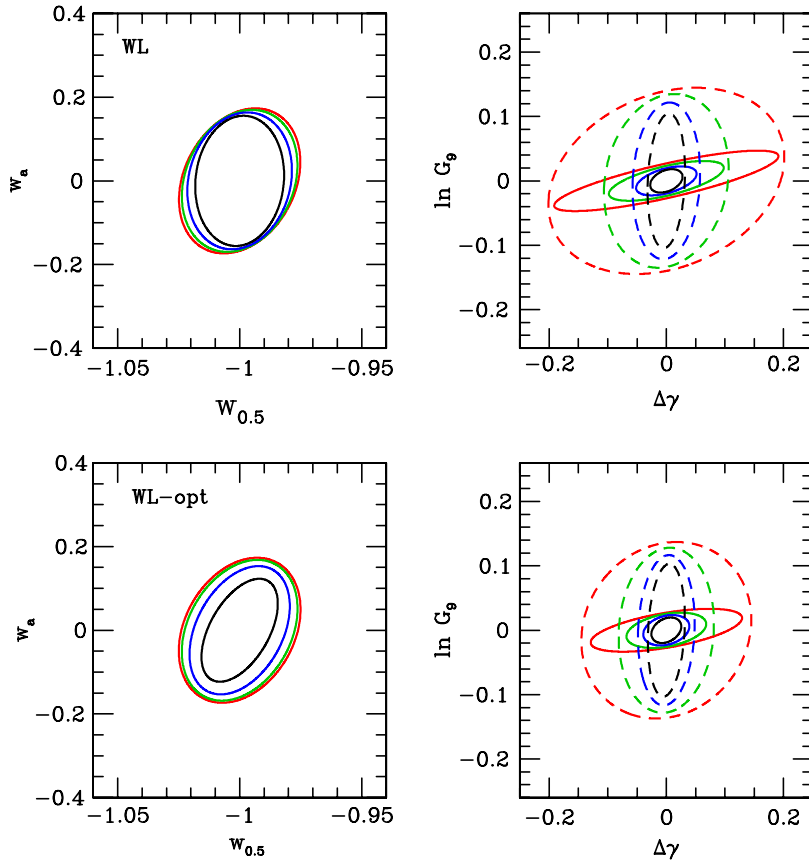


Fig. 38. Same as Fig. 36, but varying WL errors from fiducial $\times 4$ (red) to fiducial/2 (black). Lower panels assume the optimistic WL forecasts. (For interpretation of the references to colour in this figure legend, the reader is referred to the web version of this article.)

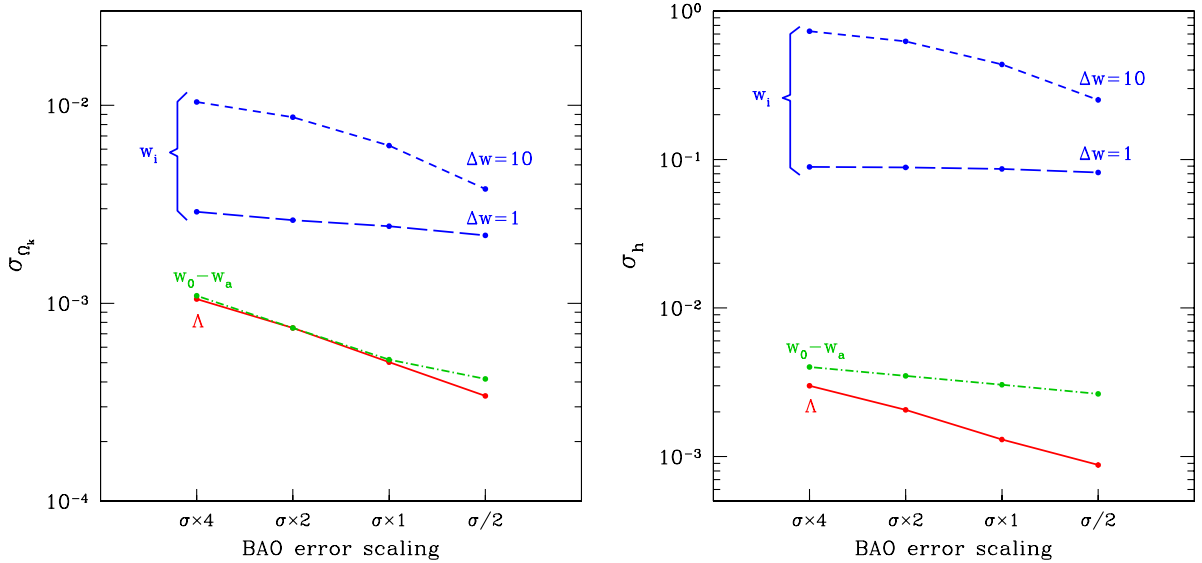


Fig. 39. Dependence of σ_{Ω_k} (left) and σ_h (right) on BAO errors for various dark energy parameterizations and priors. For the w_i curves, the equation of state varies independently in 36 bins with Gaussian priors of width $\sigma_{w_i} = \Delta w / \sqrt{\Delta a}$. The fiducial versions of the Stage IV SN, WL, and CMB data are included in all cases.

As one continues to add more dark energy parameters to the model, the degeneracies between these parameters and h increase, but another effect arises that diminishes the impact of SN data on σ_h . Measurement of the Hubble constant requires

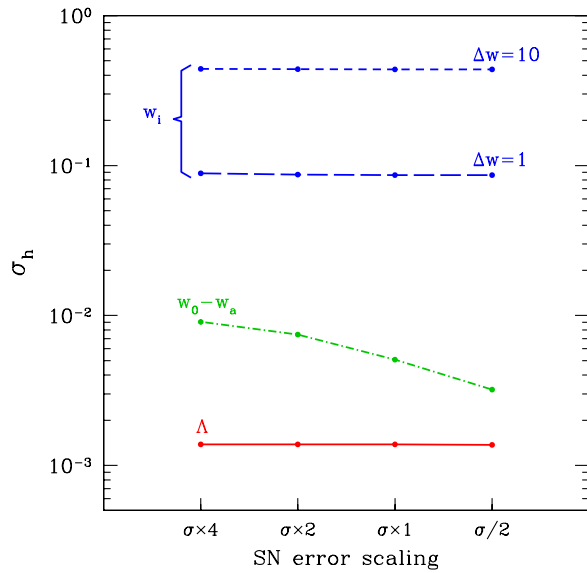


Fig. 40. Dependence of σ_h on SN errors for various dark energy parameterizations and priors, including the fiducial BAO, WL, and CMB forecasts.

relating observed quantities at $z > 0$ (e.g. SN distances) to the expansion rate at $z = 0$. In the case of Λ CDM or the w_0 - w_a model, the assumed dark energy evolution is simple enough that this relation between $z = 0$ and low-redshift observations is largely set by the model. However, when we specify $w(z)$ by a large number of independent bins in redshift, this relation must instead be determined by the data. Since SN data are only sensitive to relative changes in distances, the lowest-redshift w_i value (centered at $z \approx 0.01$) is strongly degenerate with h (Mortonson et al., 2009a). This degeneracy is partially broken by the local SN sample at $z = 0.05$: removing it from the forecasts increases the error on h from 0.44 to 0.48 in the binned $w(z)$ parameterization, and from 0.0051 to 0.0085 in the w_0 - w_a model. SNe at even lower redshifts are more sensitive to the Hubble constant, but they also have larger systematic uncertainties due to peculiar velocities.

For BAO data, the choice of redshift bin width affects forecasts for models with general equation-of-state variations. Measurements of $H(z)$ and $D(z)$ in narrower bins are better able to constrain rapid changes in $w(z)$. They can also reduce uncertainty in the Hubble constant by about a factor of two, and in other parameters such as Ω_K , $\ln G_9$, and $\Delta\gamma$ by a smaller amount, relative to measurements in wide bins. However, in practice one cannot reduce the bin size indefinitely, since each bin must contain enough objects to be able to robustly identify and locate the BAO peak; for example, requiring that the bin be at least wide enough to contain pairs of objects separated by $\sim 100h^{-1}$ Mpc along the line of sight sets a lower limit of $\Delta z/(1+z) \gtrsim 0.03$. We do not attempt to optimize the choice of bins for the simplified forecasts in this section, but we note that binning schemes in analyses of BAO data aimed at constraining general $w(z)$ variations should be chosen with care to avoid losing information about dark energy evolution and other parameters. Similar concerns are likely to apply for WL data as well.

8.3.4. Constraints on $w(z)$ in the general model

So far, in the context of general dark energy evolution we have only considered the forecast errors on parameters such as h and Ω_K that are partially degenerate with $w(z)$. But how accurately can $w(z)$ itself be measured when we do not restrict it to specific functional forms? Since the errors on w_i values in different bins are typically strongly correlated with each other, it is not very useful to simply give the expected w_i errors, marginalized over all other parameters. Instead, we can consider combinations of the w_i that are independent of one another and ask how well each of these combinations can be measured by the fiducial program of observations.

As mentioned in Section 2.2, many methods for combining $w(z)$ bins into independent (or nearly independent) components have been proposed. Here we adopt the principal component (PC) decomposition of the dark energy equation of state. Starting from the Fisher matrix for the combined acceleration probes, the PCs are computed by first marginalizing the Fisher matrix over everything except for the w_i parameters and then diagonalizing the remaining matrix, as described above in Section 8.2. The shapes of the three best-measured PCs for the fiducial program (with both fiducial and optimistic WL assumptions) and some simple variations are plotted in Fig. 41. In general, the structure of the PCs is similar in all cases; for example, the combination of w_i that is most tightly constrained is typically a single, broad peak at $z < 1$, while the next best-determined combination is the difference between $w(z \sim 0.1)$ and $w(z \sim 1)$. However, variations in the forecast assumptions slightly alter the shape of each PC and, in particular, shift the redshifts at which features in the PC shapes appear. Changes in the location of the peak in the first PC mirror the dependence of the pivot redshift z_p for the w_0 - w_a model in Tables 8–10, with improved SN data decreasing the peak redshift and improved BAO data increasing it. The direction and magnitude of these shifts reflects the redshift range that a particular probe is most sensitive to and the

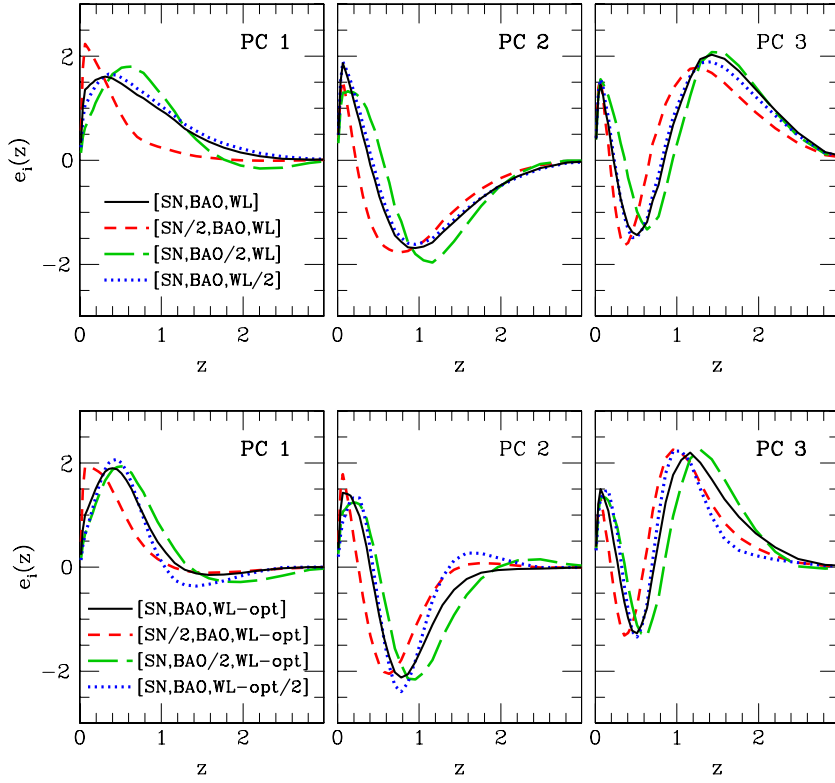


Fig. 41. The three best-measured PCs for the fiducial program (solid curves) and from programs with SN, BAO, or WL errors halved (as labeled). The top row uses the fiducial version of the WL forecast, while the bottom row uses the optimistic WL forecast with reduced systematic errors. Although not indicated in the plot legends, all forecasts here include the default *Planck* CMB Fisher matrix. For all PCs shown here, $e_i(z)$ is nearly zero for $3 < z < 9$.

Table 11
Errors on PC amplitudes for the fiducial program.

i	σ_i^{fid}	σ_i^{opt}									
1	0.011	0.009	10	0.135	0.102	19	0.442	0.378	28	1.652	1.810
2	0.017	0.014	11	0.143	0.116	20	0.779	0.413	29	2.285	2.217
3	0.026	0.019	12	0.168	0.137	21	0.824	0.436	30	3.243	2.973
4	0.038	0.026	13	0.180	0.150	22	0.939	0.531	31	6.540	6.785
5	0.052	0.036	14	0.185	0.160	23	0.978	0.609	32	12.43	19.20
6	0.067	0.047	15	0.216	0.179	24	1.212	0.725	33	16.59	24.78
7	0.083	0.062	16	0.252	0.240	25	1.307	0.892	34	25.17	46.41
8	0.099	0.074	17	0.310	0.244	26	1.457	1.036	35	59.32	94.09
9	0.115	0.089	18	0.323	0.308	27	1.587	1.561	36	74.12	118.0

σ_i^{fid} refers to errors for the fiducial Stage IV program (CMB+SN+BAO+WL) and σ_i^{opt} to the optimistic WL case (CMB+SN+BAO+WL-opt).

degree to which that probe contributes to the total constraints on $w(z)$. Note that so far we have only considered the impact of forecast assumptions on the functional form of PCs, and not on the precision with which each PC can be measured. In general, altering the forecast model changes both the PC shapes and PC errors, which complicates the comparison among expected PC constraints from different sets of forecasts.

Comparing the top and bottom rows of panels in Fig. 41, we see again the contrast between the fiducial WL forecast and the “WL-opt” forecast with reduced systematic errors. In the former case, decreasing WL errors by a factor of two has a negligible effect on the PC shapes relative to similar reductions in SN or BAO errors. However, when we take WL-opt as the baseline forecast the PCs depend more on the precision of WL measurements and less on that of the SN or BAO data.

The full set of PCs for the fiducial program is shown in Fig. 42, and the forecast errors on the PC amplitudes are listed in Table 11. The best-measured, lowest-variance PCs vary smoothly with redshift, corresponding to averaging $w(z)$ over fairly broad ranges in z . There is a clear trend of increasingly high frequency oscillations for higher PCs. Visual inspection of Fig. 42 shows that the sum of the number of peaks and the number of troughs in the PC is equal to the index of the PC, a pattern that continues at least up to PC 13. Higher PCs often change sign between adjacent z bins. High frequency oscillations in $w(z)$ are poorly measured by any combination of cosmological data because the evolution of the dark energy density, which

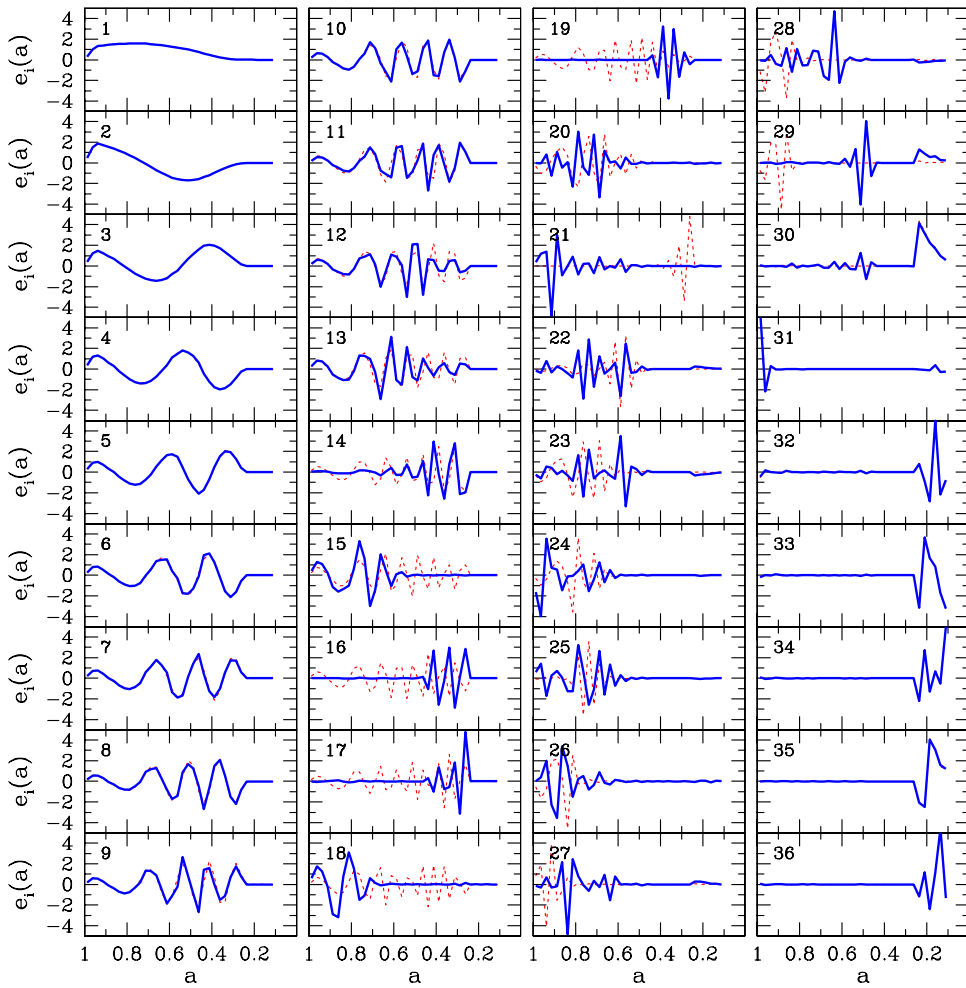


Fig. 42. PCs for the fiducial program (solid curves). Dotted curves double the number of bins used for BAO data from the default choice of 20 to 40.

determines $H(z)$, depends on an integral of $w(z)$ (Eq. (22)), and $D(z)$ and $G(z)$ depend (approximately) on integrals of $H(z)$. Rapid oscillations in $w(z)$ tend to cancel out in these integrals. Many of the most poorly-measured PCs depend on the chosen BAO binning scheme, since narrower BAO bins can better sample rapid changes in $w(z)$. As an example, we show how the PCs of the fiducial program are affected by doubling the number of BAO bins in Fig. 42.

The maximum redshift probed by SN, BAO, and WL data, primarily set by the highest-redshift BAO constraint at $z = 3$ in our forecasts, imprints a clear signature in the set of PCs in Fig. 42. At high redshift, specifically $z > 3$ ($a < 0.25$), the first 29 PCs have almost no weight. Conversely, PCs 30 and 32–36 only vary significantly at high redshift and are nearly flat for $z < 3$; additionally, the errors on these PCs are many times larger than those of the first 29 PCs.⁷⁷ Thus, $w(z)$ variations above and below $z = 3$ are almost completely decoupled from each other in the fiducial forecasts, and the high-redshift variations are effectively unconstrained. CMB data limit the equation of state at $z > 3$ to some extent, for example, through comparison of the measured distance to the last scattering surface with the distance to $z = 3$ measured in BAO data. However, such constraints are very weak when split among several independent $w(z)$ bins at high redshift. Furthermore, since the dark energy density typically falls rapidly with increasing redshift, variations in $w(z)$ at high redshift are intrinsically less able to affect observable quantities than low-redshift variations, resulting in reduced sensitivity to the high-redshift equation of state even in the presence of strong constraints at earlier epochs. Likewise, variations in $w(z)$ at even higher redshifts of $z > 9$, where we assume that w is fixed to -1 , are unlikely to significantly affect constraints on $w(z)$ at low redshift.⁷⁸

⁷⁷ Note that our w_1 parameterization has exactly $(0.25-0.1)/0.025 = 6$ bins at $3 < z < 9$ and 30 bins at $z < 3$. PC 31 parameterizes variations in the lowest redshift bin w_1 , which is poorly constrained as discussed in Section 8.3.3.

⁷⁸ This partly depends on the choice of fiducial model at which the Fisher matrix used to construct the PCs is computed. Taking a fiducial model with a larger dark energy density at high redshift than in Λ CDM makes the low-redshift PC shapes more sensitive to assumptions about the high-redshift equation of state (e.g., de Putter and Linder, 2008).

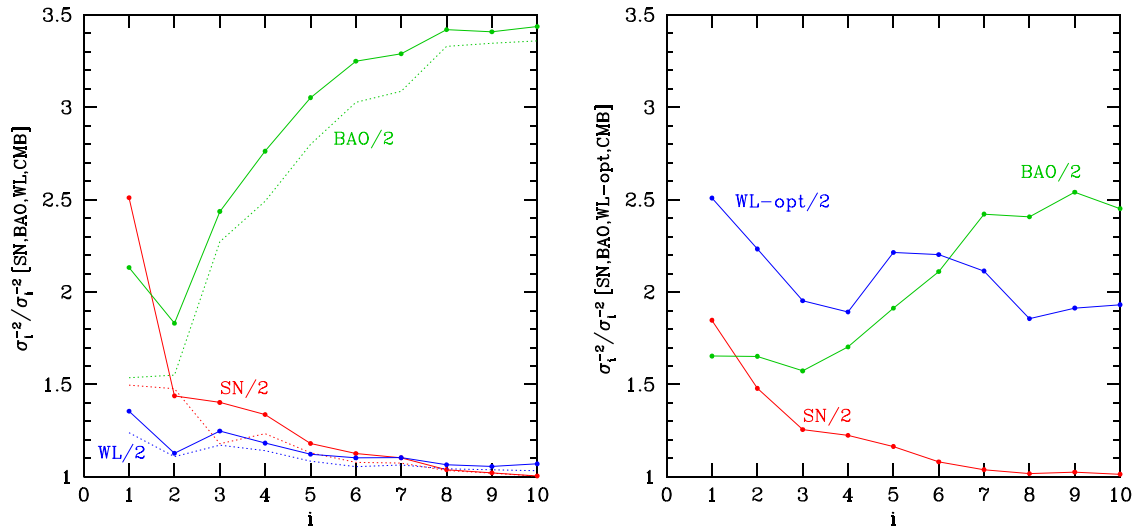


Fig. 43. Ratios of inverse variances of PC amplitudes for variants of the fiducial program to the fiducial inverse variances (points and solid curves). Each variant divides SN, BAO, or WL errors by a factor of 2 while keeping other probes fixed at the fiducial errors. The left panel assumes the default WL forecast and the right panel assumes the optimistic version. Dotted curves in the left panel use $\hat{\sigma}_i$ instead of σ_i , which describes how well the amplitudes of the fiducial set of PCs are expected to be measured by some variant of the fiducial forecast.

Fig. 43 shows how the inverse variance σ_i^{-2} of the 10 best-measured $w(z)$ PCs increases relative to the fiducial program if we halve the errors on the SN, BAO, or WL data. Following Albrecht et al. (2009), when computing these ratios $\sigma_{(2)i}^{-2}/\sigma_{(1)i}^{-2}$ (where 1 denotes the fiducial program and 2 the improved program), we first limit PC variances to unity by making the substitution $\sigma_i^{-2} \rightarrow 1 + \sigma_i^{-2}$, so that uninteresting improvements in the most poorly-measured PCs do not count in favor of a particular forecast. We caution that, as noted earlier, the PC shapes themselves are changing as we change the errors assumed in the forecast, so $\sigma_{(2)i}^{-2}$ and $\sigma_{(1)i}^{-2}$ are not variances of identical $w(z)$ components. However, as shown in Fig. 41, these changes are not drastic if we consider factor-of-two variations about our fiducial program.

The differences in σ_i^{-2} ratios among improvements in SN, BAO, and WL errors is striking. Relative to the fiducial program, reduced SN errors mainly contribute to knowledge of the first few PCs. For the fiducial WL systematics, reducing WL errors helps to better measure several of the highest-variance PCs in the plot ($i > 10$), but it makes little difference to the well measured PCs. Reducing BAO errors tightens constraints on nearly all of the PCs, with the greatest impact in the intermediate range between the SN and WL contributions. Assuming the optimistic WL errors gives much greater weight to WL improvements, which now produce the largest improvement in the first five PCs (right panel of Fig. 43). The trends for reducing SN or BAO errors are similar to before, but the magnitude of their effect is smaller because they are competing with tighter WL constraints. The behavior of the σ_i^{-2} ratios of the best-measured PCs mirrors that shown for the DETF FoM in Fig. 33. With the fiducial WL systematics, BAO measurements have the greatest leverage, followed by SN, and the impact of reducing WL errors is small. With the optimistic WL systematics, on the other hand, reducing WL errors makes the largest difference, followed by BAO, followed by SN.

Dotted curves in the left hand panel show the σ_i^{-2} ratios when we fix the PCs to be those of the fiducial program. In this case, the PC errors for the improved programs are no longer uncorrelated, but the correlation coefficient of errors among any pair of PCs is less than 0.5 in nearly all cases. Results are similar to before except for the first component (first two components for BAO). These, of course, show less improvement when they are fixed to be those of the fiducial program rather than shifting to be the components best determined by the improved data. Fig. 44 shows the expected improvements in σ_i^{-2} between our fiducial Stage III and Stage IV programs. Consistent with the DETF FoM plots in Fig. 33, the expected improvements are dramatic, and considerably more so with the optimistic WL assumptions.

The DETF FoM compresses constraints in the w_0-w_a model to a single number. Similar figures of merit for PC constraints have been defined in the literature, in various forms, each of which may be useful for different purposes. These include the determinant of \mathbf{F}^w , which characterizes the total volume of parameter space allowed by a particular combination of experiments in analogy to the DETF FoM for the w_0-w_a parameter space, and the sum of the inverse variances of the PCs, which is typically less sensitive than the determinant to changes in the errors of the most weakly constrained PCs (Huterer and Turner, 2001; Bassett, 2005; Albrecht et al., 2006; Albrecht and Bernstein, 2007; Wang, 2008; Barnard et al., 2008; Albrecht et al., 2009; Crittenden et al., 2009; Amara and Kitching, 2011; Mortonson et al., 2010; Shapiro et al., 2010; Trotta et al., 2011; March et al., 2011).

Examples of these FoMs for the fiducial program and the variants considered in Fig. 43 are listed in Table 12. Here we allow the PC basis to change with the forecast assumptions, so \mathbf{F}^w is diagonal and $\det \mathbf{F}^w = \prod_{i=1}^{36} \sigma_i^{-2}$. As with the ratios of PC variances in Fig. 43, we restrict the variances to be less than unity by replacing $\sigma_i^{-2} \rightarrow 1 + \sigma_i^{-2}$. The other FoM,

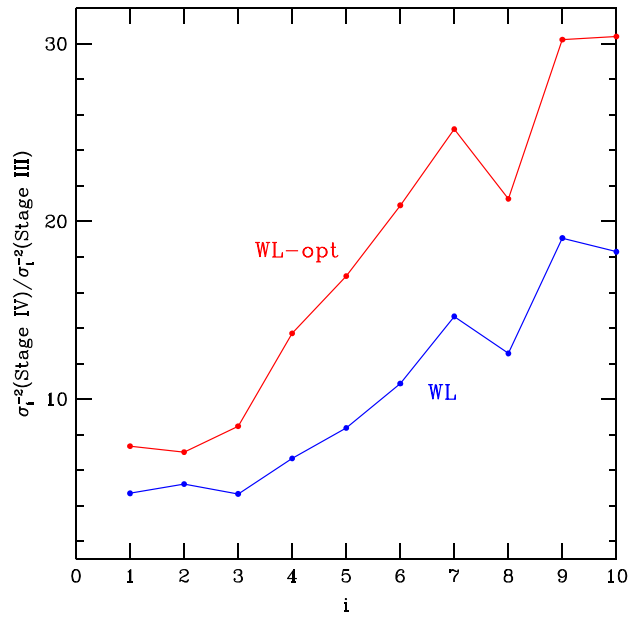


Fig. 44. Ratios of inverse variances of PC amplitudes of Stage IV to those of Stage III, assuming either the fiducial or optimistic versions of the Stage IV WL forecast.

Table 12
Comparison of figures of merit for selected forecasts.

Forecast case	$\log_{10} \prod_{i=1}^{36} (1 + \sigma_i^{-2})^{1/2}$	$(\sum_{i=1}^{36} \sigma_i^{-2})^{1/2}$	$[\sigma(w_p)\sigma(w_a)]^{-1}$
[SN, BAO, WL, CMB]	20.2	124	664
[SN/2, BAO, WL, CMB]	20.8	176	1197
[SN, BAO/2, WL, CMB]	26.0	186	1222
[SN, BAO, WL/2, CMB]	21.6	140	816
[SN, BAO, WL-opt, CMB]	23.0	157	789
[SN/2, BAO, WL-opt, CMB]	23.4	199	1242
[SN, BAO/2, WL-opt, CMB]	27.9	205	1251
[SN, BAO, WL-opt/2, CMB]	26.0	240	1397

computed as the sum of inverse variances, requires no such prior because PCs with large variances contribute negligibly to the sum. Note that the choice of PC FoM definition can affect decisions about whether one experiment or another is optimal; for example, halving WL errors (assuming fiducial systematics) relative to the fiducial model increases the $\det \mathbf{F}^w$ FoM more than halving SN errors, but the opposite is true for the sum of inverse variances, which favors improvements in the best-measured PCs and more closely tracks the DETF FoM. In this case, at least, we regard the latter measure as a better diagnostic, since the improvements for PCs that are poorly measured in any case seem unlikely to reveal departures from a cosmological constant or other simple dark energy models. Another virtue of $\sum \sigma_i^{-2}$ (the square of the quantity tabulated in Table 12) is its sensible scaling with measurement precision. If the error of all the individual cosmological measurements (e.g., D_L values and WL power spectrum amplitude) is dropped by a factor of two, as expected if experiments are statistically limited and data volume is increased by a factor of four, then each σ_i will drop by a factor of two and $\sum \sigma_i^{-2}$ will go up by a factor of four, scaling with data volume just like the DETF FoM. For $\det \mathbf{F}^w$, on the other hand, the FoM will go up by $\approx 2^N$, where N is the number of PCs that have σ_i significantly below one, so there is no obvious scaling with data volume.

The disagreement between different PC FoMs in Table 12 highlights one of the difficulties with using PCs or related methods for evaluating the potential impact of future experiments. Forecasts for PCs provide a wealth of information in both the redshift-dependent shapes of the PCs and the expected errors on their amplitudes, but it is often difficult to interpret what this information implies about cosmic acceleration. Given a set of forecasts for PCs, one can easily compute the expected constraints on any specific model for $w(z)$ by expressing the model in terms of the PC amplitudes (Eq. (174)); this is a potentially useful application, but it makes very limited use of the available information.

More generally, we can use the forecast PC shapes and errors to try to visualize what types of $w(z)$ variations are allowed by a certain combination of experiments. One approach is to generate several random $w(z)$ curves that would be consistent with the forecast measurements. This method is easily implemented with the PCs because the errors on different PC amplitudes are uncorrelated. One can generate a random realization of $w(z)$ by simply drawing an amplitude α_i from a Gaussian distribution with mean zero and width σ_i , then using Eq. (175) to compute $w(z)$ corresponding to the randomly-drawn α_i values.

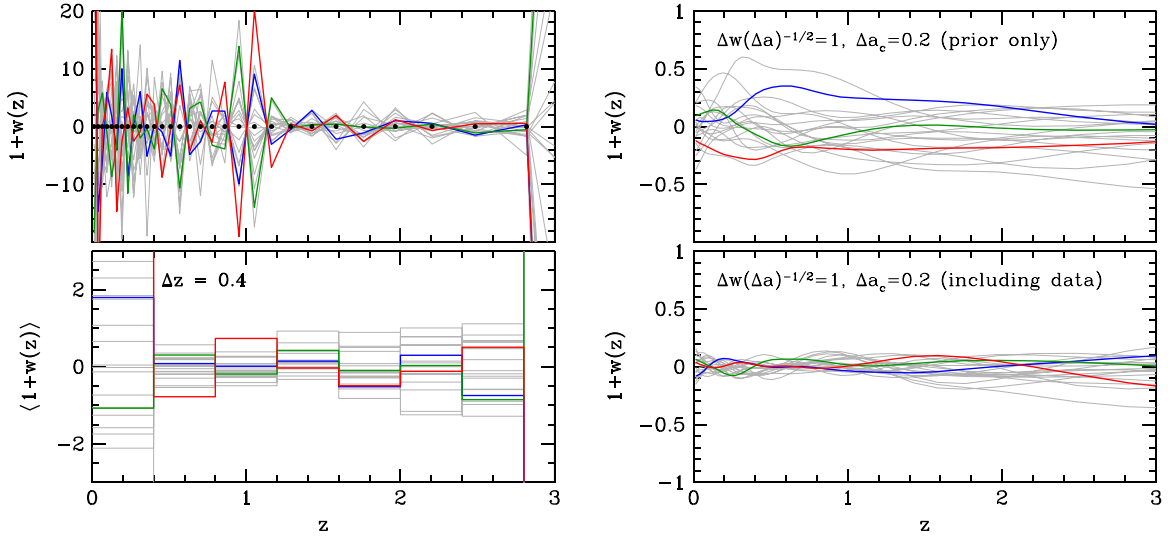


Fig. 45. Reconstruction of $w(z)$ from PC constraints. *Left:* 20 randomly-generated models that would be indistinguishable from a cosmological constant using the fiducial program of experiments. Three of the 20 models are highlighted (in red, green, and blue) to more clearly show examples of the evolution with redshift. The lower panel shows the average of $1 + w(z)$ in bins of width $\Delta z = 0.4$ for the same models as in the upper panel. Points along the $w(z) = -1$ line in the upper panel mark the centers of the bins in which $w(z)$ is allowed to vary in our forecasts. *Right:* $w(z)$ reconstruction including a prior of the form in Eq. (178). The upper panel shows a random selection of models consistent with this prior, but without including any data, and the lower panel shows examples of models that are allowed by both the prior and the data assumed in the fiducial program.

In the upper left panel of Fig. 45, we use this method to plot several $w(z)$ models using the fiducial program PC shapes and errors from Fig. 42 and Table 11, respectively. We cut off the plot at $z = 3$, since $w(z)$ variations at higher redshifts are essentially unconstrained by the fiducial experiments. Even at lower redshifts, though, the allowed $w(z)$ variations are enormous, with w_i values often changing by 10 or more from one bin to the next. (Recall that our prior corresponds to a Gaussian of width $\sigma_{w_i} \approx 63$ per bin, Eq. (172).) Compared to the $\sim 1.5\%$ constraints on w_p in the w_0-w_a model, this forecast looks rather depressing. The consequence of allowing the equation of state to be a free function of redshift is that it is nearly impossible to say with any certainty what the value of w is at any specific redshift, because rapid oscillations in $w(z)$ have tiny effects on observables. The allowed range of variations would be even larger if we considered a model with finer Δa bins.

The large variations of $w(z)$ in Fig. 45 are driven by the poorly constrained PCs, which have many oscillations in $w(z)$, peak-to-peak amplitudes $|\Delta w| \sim 4$, and normalization uncertainties $\sigma_i \sim 0.1-2.3$ (see Fig. 42 and Table 11). The lower left panel of Fig. 45 shows these $w(z)$ realizations averaged over bins of width $\Delta z = 0.4$, which vastly reduces the range of variations, especially at $z \sim 1$. However, the dispersion of $w(z)$ in the bins centered at $z = 0.6$ and $z = 1$ is still about 0.3. Adding a precise, independent measurement of H_0 reduces the uncertainty in $w(z)$ in the lowest-redshift bin, but it has little effect at higher redshifts (see Section 8.5.1).

Instead of averaging $w(z)$ over wide redshift bins, one can impose a theoretical prejudice for models with smoothly-varying equations of state by adding an off-diagonal prior to the Fisher matrix, imposing correlations among the w_i that are closely separated in redshift. Here we follow Crittenden et al. (2009), but we modify their method to use scale factor rather than redshift as the independent variable (see also Crittenden et al., 2012), adopting a correlation function

$$\xi(|a_i - a_j|) = \frac{(\Delta w)^2}{\pi \Delta a_c} \left[1 + \left(\frac{a_i - a_j}{\Delta a_c} \right)^2 \right]^{-1}, \quad (177)$$

where Δw sets the amplitude of allowed $w(z)$ variations and Δa_c is the correlation length. Following the calculation in Crittenden et al. (2009), the covariance matrix for the w_i bins, which is the inverse of the prior Fisher matrix for those parameters, is

$$[F_{ij}^{\text{prior}}]_{(i,j \leq 36)}^{-1} = \frac{(\Delta w)^2 \Delta a_c}{\pi \Delta a^2} \left[x_+ \tan^{-1} x_+ + x_- \tan^{-1} x_- - 2\bar{x} \tan^{-1} \bar{x} + \ln \left(\frac{1 + \bar{x}^2}{\sqrt{(1 + x_+^2)(1 + x_-^2)}} \right) \right], \quad (178)$$

where $\bar{x} = |i - j| \Delta a / \Delta a_c$, $x_+ = (|i - j| + 1) \Delta a / \Delta a_c$, and $x_- = (|i - j| - 1) \Delta a / \Delta a_c$. In the limit $\Delta a_c \rightarrow 0$, this reduces to our default diagonal prior on the w_i parameters with width $\sigma_{w_i} = \Delta w / \sqrt{\Delta a}$.

The upper right panel of Fig. 45 shows models randomly drawn from this prior with $\Delta w / \sqrt{\Delta a} = 1$ and $\Delta a_c = 0.2$. The influence of the correlation function is clearly evident in the smoother, lower-amplitude variations of $w(z)$ in these models, and yet the range of possible models is still much greater than for simpler parameterizations like w_0-w_a . Combining this

prior with the assumed data set of the fiducial Stage IV program, we obtain the $w(z)$ realizations plotted in the lower right panel of Fig. 45. Even more so than averaging $w(z)$ in wide redshift bins, including this type of prior significantly narrows the constraints on $w(z)$. While the particular smoothness prior of (177) is certainly not unique, this approach of combining PC constraints dictated by the data sets with theoretically motivated priors on the behavior of $w(z)$ – perhaps based on an underlying model for the potential $V(\phi)$ – may be the most valuable application of the PC approach.

Our constraints on general $w(z)$ models account for the possibility of modified gravity by marginalizing over the structure growth parameters $\Delta\gamma$ and $\ln G_9$. If we instead restrict our analysis to GR by fixing $\Delta\gamma = \ln G_9 = 0$, the main effect is that the dark energy equation of state at high redshifts, $w(3 < z < 9)$, is better constrained because the CMB measurement of the power spectrum amplitude at $z \sim 1000$ can be more directly related to WL measurements of growth at lower redshifts. Because of the additional CMB constraint on the distance to the last scattering surface, $w(3 < z < 9)$ is strongly correlated with Ω_k , and therefore assuming GR considerably improves the determination of spatial curvature in the binned $w(z)$ parameterization. For our fiducial forecasts, assuming $\Delta\gamma = \ln G_9 = 0$ lowers σ_{Ω_k} by a factor of ~ 3 ($0.0075 \rightarrow 0.0023$); note that this is still several times larger than the error in Ω_k for the simpler Λ CDM or w_0 – w_a forecasts.

8.4. Forecasts for clusters

We have concentrated so far on the constraints expected for combinations of CMB, SN, BAO, and WL data, as all of these methods are well studied and are likely to play a central role in Stage III and Stage IV studies of cosmic acceleration. For other methods we adopt a simplified approach, first asking how well our fiducial CMB+SN+BAO+WL programs should predict the basic observables of these methods, then showing how different levels of precision on these observables would affect constraints on equation-of-state and growth parameters. We describe our methodology more fully in the next section (Section 8.5), but we begin with a discussion of clusters, where our analysis of stacked weak lensing calibration (Section 6.3.3) gives a clear quantitative target for measurement precision.

Fig. 46a shows the predicted fractional error (1σ) in $\sigma_8(z)$ for the fiducial Stage III and Stage IV experimental programs discussed in Section 8.3, and for the Stage IV program with optimistic WL errors. All curves assume a w_0 – w_a dark energy parameterization, and for each case the lower, thinner curve shows the forecast assuming GR to be correct while the upper, bolder curve allows GR deviations parameterized by G_9 and $\Delta\gamma$. Roughly speaking, we would expect a measurement with precision better than that shown by the upper curve to significantly improve tests for GR deviations and a measurement with precision better than that shown by the lower curve to significantly improve w_0 – w_a constraints when assuming GR to be correct. For Stage IV programs we predict $\sigma_8(z)$ constraints at the 0.75%–1% level over the full redshift range $0 < z < 3$, with little difference between the fiducial and optimistic WL assumptions. In fact, the “optimistic” WL assumptions lead to slightly larger errors in $\sigma_8(z)$ than the fiducial assumptions because for this quantity doubling the statistical errors has a larger impact than adding 2×10^{-3} shear calibration and photo- z errors (see Section 8.1). For Stage III, the predicted $\sigma_8(z)$ errors are about 1.2% assuming GR, but they are much larger if we allow GR deviations, especially at $z > 0.8$. Even for Stage IV, the good constraints at high z rely on the assumption of a w_0 – w_a equation of state, which allows precise low redshift WL measurements to be extrapolated to high redshift. The direct measurements of $z > 1$ clustering amplitude are considerably weaker.

Fig. 46b plots $\sigma_{11,\text{abs}}(z)$ errors, which are tighter than the $\sigma_8(z)$ errors by $\sim 30\%$ – 50% because uncertainty in h contributes noticeably to the latter. In Section 6.6 we estimated the errors on $\sigma_{11,\text{abs}}(z)$ achievable with a 10^4 deg² cluster survey with weak lensing mass calibration, assuming Stage III (10 arcmin^{−2}) or Stage IV (30 arcmin^{−2}) effective source densities and survey depths. For a mass threshold of $2 \times 10^{14} M_\odot$ the $\sigma_{11,\text{abs}}(z)$ errors at $z \approx 0.5$ are $\sim 1\%$ and $\sim 0.5\%$, respectively, below the corresponding Stage III and Stage IV errors shown in Fig. 46b. Furthermore, these cluster errors are per $\Delta z = 0.1$ redshift bin, so constraints on the clustering amplitude in a smoothly evolving model can be substantially better if the cluster errors are not correlated across redshifts. (The statistical errors should be uncorrelated, but some forms of weak lensing systematics could affect many redshift bins in the same direction.)

The cluster errors shown earlier in Fig. 30 were derived assuming perfect knowledge of Ω_m , with $\sigma_{11,\text{abs}}(z)$ as the single parameter controlling the cluster abundance at each redshift. In practice, cluster abundances constrain a parameter combination that is approximately $\sigma_{11,\text{abs}}(z)\Omega_m^{0.4}$, as discussed in Section 6. The fractional errors in Ω_m from our fiducial CMB+SN+BAO+WL programs are 2.7% (Stage III), 1.4% (Stage IV), and 1.2% (Stage IV with WL-opt), making $\Omega_m^{0.4}$ uncertainties comparable to the fractional errors in $\sigma_{11,\text{abs}}(z)$. Fig. 46c shows the predicted fractional errors in $\sigma_{11,\text{abs}}(z)\Omega_m^{0.4}$, which in some ranges are significantly larger than those for $\sigma_{11,\text{abs}}(z)$. Finally, Fig. 46d shows our forecast errors on $\sigma_{11,\text{abs}}(z)\Omega_m^{0.4}$ from a 10^4 deg² cluster survey in which errors are limited by weak lensing mass calibration statistics. Here we have simply set the fractional errors from clusters on $\sigma_{11,\text{abs}}(z)\Omega_m^{0.4}$ equal to the ones we derived earlier on $\sigma_{11,\text{abs}}(z)$, which should be a good but not perfect approximation. Comparing Figs. 46c and 46d shows that cluster errors are competitive with those expected from the CMB+SN+BAO+WL combination for cluster mass thresholds of ~ 4 – $8 \times 10^{14} M_\odot$ at Stage III or 1 – $4 \times 10^{14} M_\odot$ at Stage IV.

Fig. 47 shows the potential improvement in equation-of-state and growth parameter determinations from including the cluster constraints on $\sigma_{11,\text{abs}}(z)\Omega_m^{0.4}$. We assume that these constraints have independent errors in each $\Delta z = 0.1$ bin. Upper panels show the effect of adding Stage III cluster constraints (dotted curves in Fig. 46d) to the Stage III CMB+SN+BAO+WL Fisher matrix. Even adding clusters with an $8 \times 10^{14} M_\odot$ mass threshold substantially improves the errors on G_9 and $\Delta\gamma$, and reducing the mass threshold to 1 – $2 \times 10^{14} M_\odot$ produces substantial further gains. Somewhat surprisingly, the cluster

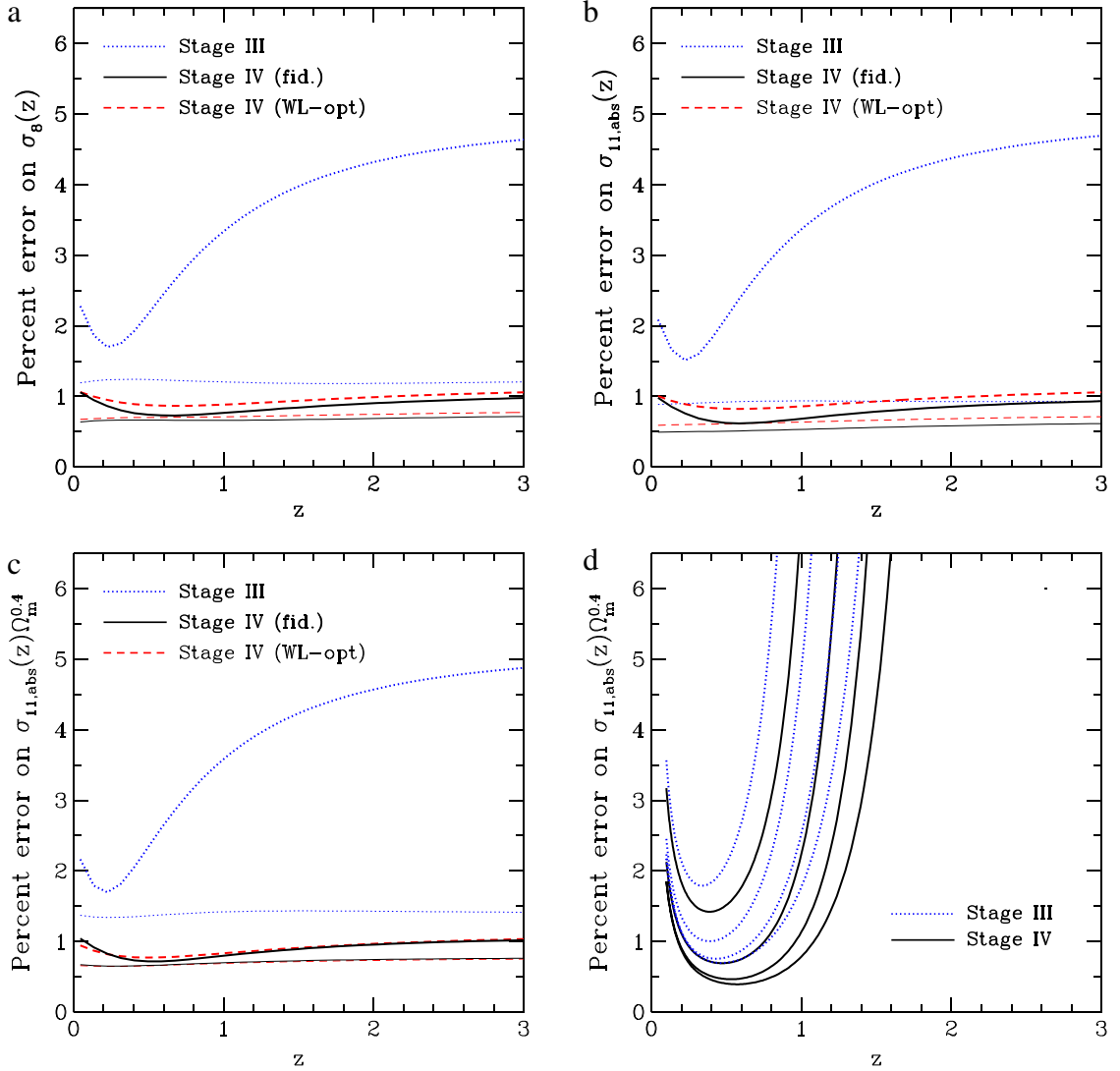


Fig. 46. (a) Predicted fractional errors (1σ) on $\sigma_8(z)$ from our fiducial Stage III (dotted) and Stage IV (solid) CMB+SN+BAO+WL programs, and from the Stage IV program with optimistic WL systematic assumptions (dashed). All curves assume a w_0 - w_a dark energy parameterization. For each case, the lower, thin curve shows the forecast assuming GR is correct and the upper, thick curve shows the forecast allowing GR deviations parameterized by G_9 and $\Delta\gamma$. (b) Like (a), but for $\sigma_{11,\text{abs}}(z)$, the rms matter fluctuation in spheres of radius 11 Mpc (instead of $8h^{-1}$ Mpc). (c) Like (b), but for the parameter combination $\sigma_{11,\text{abs}}(z)\Omega_m^{0.4}$ that approximates the quantity best constrained by cluster abundances. (d) Predicted fractional errors in $\sigma_{11,\text{abs}}(z)\Omega_m^{0.4}$ from cluster abundances in a 10^4 deg 2 survey calibrated by stacked weak lensing mass estimates with Stage III ($n_{\text{eff}} = 10$ arcmin $^{-2}$) and Stage IV ($n_{\text{eff}} = 30$ arcmin $^{-2}$) source surface densities and survey depths (dotted and solid curves, respectively). From top to bottom, curves correspond to cluster mass thresholds of 8, 4, 2, and $1 \times 10^{14} M_\odot$.

constraints also lead to significantly smaller errors on the equation-of-state parameter $w_{0.5}$ and slightly smaller errors on w_a . This improvement largely reflects the additional information about Ω_m , which allows the distance and $H(z)$ constraints from other probes to translate more directly into $w(z)$ constraints. We have checked that fixing Ω_m exactly would produce a still greater improvement in $(w_{0.5}, w_a)$ than the gain we have forecast from clusters, while making little difference to the $(G_9, \Delta\gamma)$ errors.

For Stage IV (middle and bottom panels), where we now assume the Stage IV cluster mass constraints, an $8 \times 10^{14} M_\odot$ cluster sample produces little improvement over CMB+SN+BAO+WL in G_9 and $\Delta\gamma$, but it still leads to noticeable improvement in $w_{0.5}$. A $1 - 2 \times 10^{14} M_\odot$ cluster sample produces substantial gains in both the equation-of-state and growth parameters. As in the Stage III case, much of the improvement in the equation of state comes from the Ω_m information provided by clusters. However, the cluster constraints reduce the $w_{0.5}$ error even if Ω_m is held fixed, so some of this improvement arises from another source, probably by allowing some WL information to be effectively transferred from growth to distance. Adding our Stage IV, $10^{14} M_\odot$ cluster constraint to the fiducial Stage IV program increases the DETF FoM from 664 to 1258, and it increases the modified FoM $[\sigma(w_p)\sigma(w_a)]^{-1} \times [0.034/\sigma(\Delta\gamma)]$ (Fig. 35) from 664 to 1955. For the

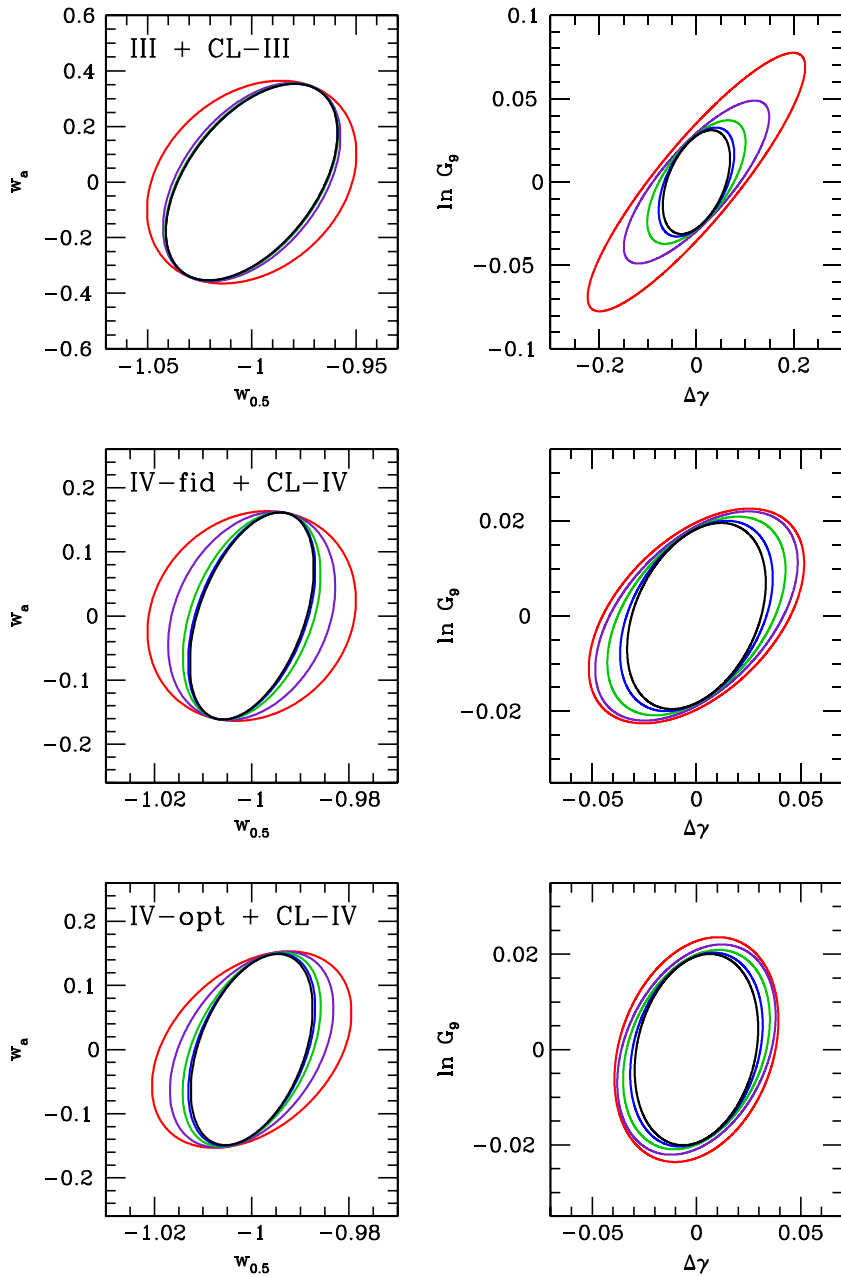


Fig. 47. Predicted constraints (1σ) on the equation-of-state parameters $w_{0.5} = w(z = 0.5)$ and w_a (left panels) and the growth parameters G_9 and $\Delta\gamma$ (right panels) from our fiducial CMB+SN+BAO+WL programs combined with cluster abundance measurements of $\sigma_{11,\text{abs}}(z)\Omega_m^{0.4}$ with the precision shown in Fig. 46d. Top panels show Stage III clusters with Stage III CMB+SN+BAO+WL, while middle and bottom panels show Stage IV clusters combined with the fiducial and WL-opt Stage IV programs, respectively. Note the change in axis scale between the top and middle/lower panels. In each panel, the outermost contour shows the constraints without clusters, and the remaining contours show the constraints for cluster mass thresholds of 8, 4, 2, and $1 \times 10^{14} M_\odot$ (outer to inner).

WL-opt program, the improvements are $789 \rightarrow 1363$ and $1037 \rightarrow 2380$, respectively. For Stage III CMB+SN+BAO+WL, adding Stage III clusters leads to improvements of $131 \rightarrow 183$ (FoM) and $30 \rightarrow 137$ (modified FoM).

Our treatment here is simplified because we have ignored the impact of volume-element changes on the cluster abundance and have set the scaling index of $\sigma_{11,\text{abs}}(z)\Omega_m^q$ to a constant value $q = 0.4$ instead of including its redshift and mass dependence. More importantly, we have assumed that errors in the cluster abundance will be dominated by the statistical errors in the weak lensing calibration of the mean mass scale, not increased by marginalizing over uncertainties in mass-observable scatter, incompleteness, contamination, or theoretical predictions. The effective mass calibration uncertainties we are assuming are those in Fig. 28. These are probably pessimistic at $z \gtrsim 1$, where the weak lensing calibration

error exceeds 10% but one could likely use other calibration methods (including direct comparison to theory) to do better; thus, we are underplaying the potential contribution of high-redshift clusters. Our approximate calculations confirm the conclusions of Oguri and Takada (2011) that clusters calibrated with stacked weak lensing can make an important contribution to testing cosmic acceleration models, even in the era of Stage IV dark energy experiments. Fig. 46 also provides a target for other methods of measuring the matter clustering amplitude, such as the Ly α forest (Section 7.6).

8.5. Forecasts for alternative methods

We now turn to some of the alternative probes discussed previously in Section 7. For each technique, we first focus on the question of complementarity with the primary methods by asking how well the observable quantity measured by a particular technique is *already* known given the fiducial combination of SN, BAO, WL, and CMB data. These predictions provide benchmarks that any additional measurement must reach in order to contribute significantly to constraints on dark energy or modified gravity parameters. In many cases, the precision of the predictions depends strongly on the chosen parameterization of deviations from the standard paradigm of Λ CDM and GR. We will generally assume a w_0 – w_a model for the results in this section, but we note that if one adopts a more general parameterization of dark energy then the predictions are normally weaker, and thus the value of alternative probes is potentially greater.

The covariance matrix for a set of observables \mathbf{X} measured by a particular alternative probe can be computed straightforwardly using the covariance matrix of the cosmological parameters given by the inverse of the total Fisher matrix for SN, BAO, WL, and CMB data,

$$C_{ij}^{\mathbf{X}} = \sum_{k,l} \frac{\partial X_i}{\partial p_k} F_{kl}^{-1} \frac{\partial X_j}{\partial p_l}, \quad (179)$$

where \mathbf{p} is either the full set of parameters in Eq. (162) or the reduced set with w_0 and w_a replacing the 36 w_i bins; in the latter case, \mathbf{F} is the Fisher matrix for the w_0 – w_a parameterization computed using Eq. (170). We compute the full covariance matrices for the alternative methods, but the plots in the following sections only show the predicted uncertainties $\sigma_{X_i} = \sqrt{C_{ii}^{\mathbf{X}}}$ and do not reflect the fact that errors on the observables may be correlated.

In addition to computing how well the fiducial SN, BAO, WL, and CMB constraints predict each observable that would be measured by the alternative techniques, we provide several examples to show the improvement in the FoM and other parameters that would result from a specific measurement of that observable. For these tests, we only consider the impact of measurement of a single quantity X at a time, so the total Fisher matrix is modified simply by adding the term

$$F_{ij}^{\text{alt}} = \sigma_X^{-2} \frac{\partial X}{\partial p_i} \frac{\partial X}{\partial p_j}, \quad (180)$$

where σ_X is the assumed uncertainty in the measurement of X .

8.5.1. The Hubble constant

For the Hubble constant, the predicted uncertainty from the fiducial probes is simply the value of σ_{H_0} that comes out of the Fisher matrix forecasts of the previous section. Assuming a w_0 – w_a dark energy model, the expected precision on H_0 is 0.7% for the fiducial Stage IV forecasts and small variations of those forecasts, and 1.3% for Stage III (see Tables 8–10). These are challenging, but probably attainable, targets for future efforts to independently measure H_0 .

In Fig. 48, we show the effect on the DETF FoM of adding a prior on H_0 to the fiducial Stage III and IV forecasts. In all cases, adding a prior with precision that matches the uncertainty one would have in the absence of the prior increases the FoM by $\sim 40\%$. The uncertainties in other cosmological parameters are affected little by the inclusion of an independent H_0 measurement, as discussed in Section 7.1.

For a more general dark energy parameterization such as the binned w_i values, predictions for σ_{H_0} can be orders of magnitude weaker than they are for w_0 – w_a or Λ CDM (see Figs. 39 and 40). In this case an independent, local measurement of H_0 is vital for accurate determination of the Hubble constant. However, H_0 priors do not significantly improve dark energy constraints in this case; an H_0 constraint limits the range of $w(z)$ in the lowest-redshift bin, but since $w(z=0)$ is only weakly correlated with the equation of state at higher redshifts by SN, BAO, WL, and CMB data, the impact of an additional H_0 measurement on the equation of state at $z > 0$ is small. The improvement in the DETF FoM in Fig. 48 is largely a consequence of the restrictions that the w_0 – w_a parameterization places on the evolution of $w(z)$ between $z=0$ and higher redshifts. Of course, a discrepancy between directly measured H_0 and a w_0 – w_a prediction would already provide the crucial insight that w_0 – w_a is inadequate; it just would not give further direction about the evolution of $w(z)$.

8.5.2. The Alcock–Paczynski test

For the AP test (Section 7.3), we consider the observable $H(z)D_A(z)$. Since Stage IV BAO data provide tight constraints on both $H(z)$ and $D_A(z)$, which are further strengthened by the SN, WL, and CMB measurements, it is not surprising that the product $H(z)D_A(z)$ is predicted very precisely in the combined forecasts. The left panel of Fig. 49 shows that the uncertainty

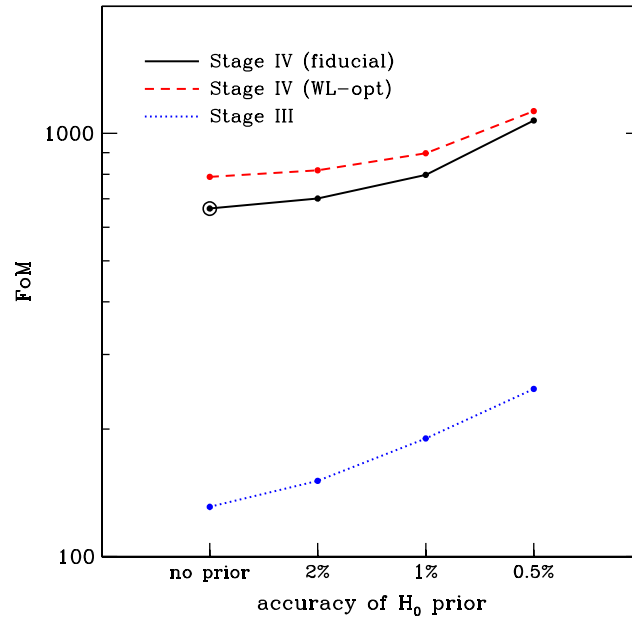


Fig. 48. Dependence of the DETF FoM on the accuracy of additional measurements of the Hubble constant for Stage III and IV forecasts from Section 8.3. The fiducial Stage IV program with $\text{FoM} = 664$ is marked by an open circle.

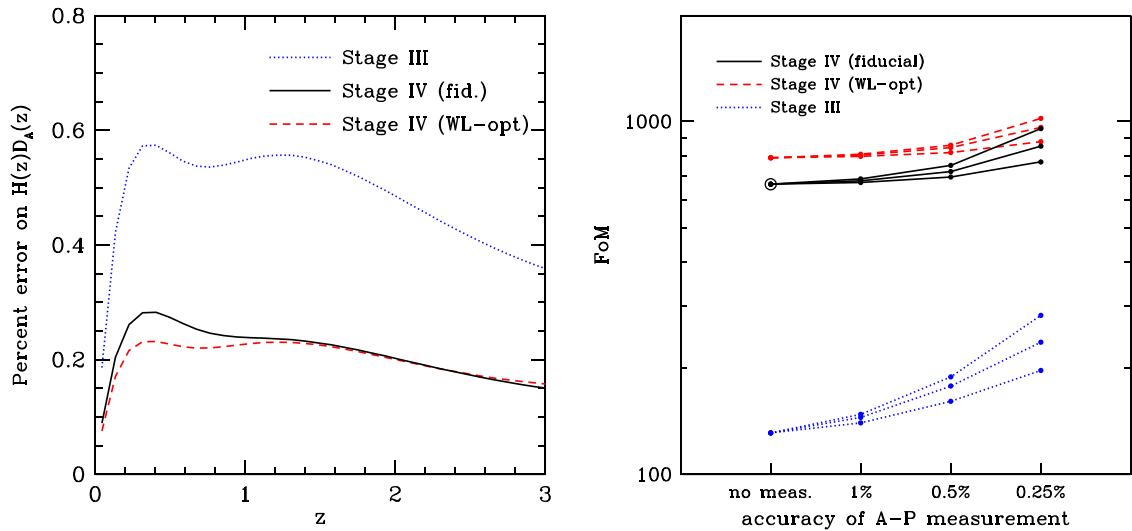


Fig. 49. *Left:* Predicted fractional error (1σ) of the AP parameter $H(z)D_A(z)$ from our fiducial Stage III and Stage IV CMB+SN+BAO+WL programs, assuming a w_0-w_a dark energy parameterization. *Right:* Dependence of the DETF FoM on additional measurements of $H(z)D_A(z)$ at a single redshift. For each forecast, the three curves from top to bottom assume AP measurements at $z = 0.5$, $z = 1$, and $z = 2$, respectively.

in the AP observable is $\sim 0.2\%$ at $0 < z < 3$ for Stage IV data, and it is still predicted to sub-percent accuracy with Stage III data. Independent measurements of the AP observable that are significantly less precise than these predictions would contribute little to cosmological constraints. Note that these results are for a w_0-w_a dark energy model. If we instead use independently-varying $w(z)$ bins, the uncertainty in the AP observable for the Stage IV forecasts increases to $\sim 1\%$ at $1 < z < 3$ and becomes much larger at both lower and higher redshifts, although the exact precision of the predictions in this case depends strongly on the detailed forecast assumptions such as the prior on w_i in each bin or the number of bins used for BAO data.

In the right panel of Fig. 49, we show the improvement in the DETF FoM (assuming the w_0-w_a parameterization) when various measurements of the AP observable are added to the fiducial Stage III and IV forecasts. Since the predictions for $H(z)D_A(z)$ are weakest at $z \lesssim 0.5$, a direct measurement of the AP observable at those redshifts has a greater impact on the

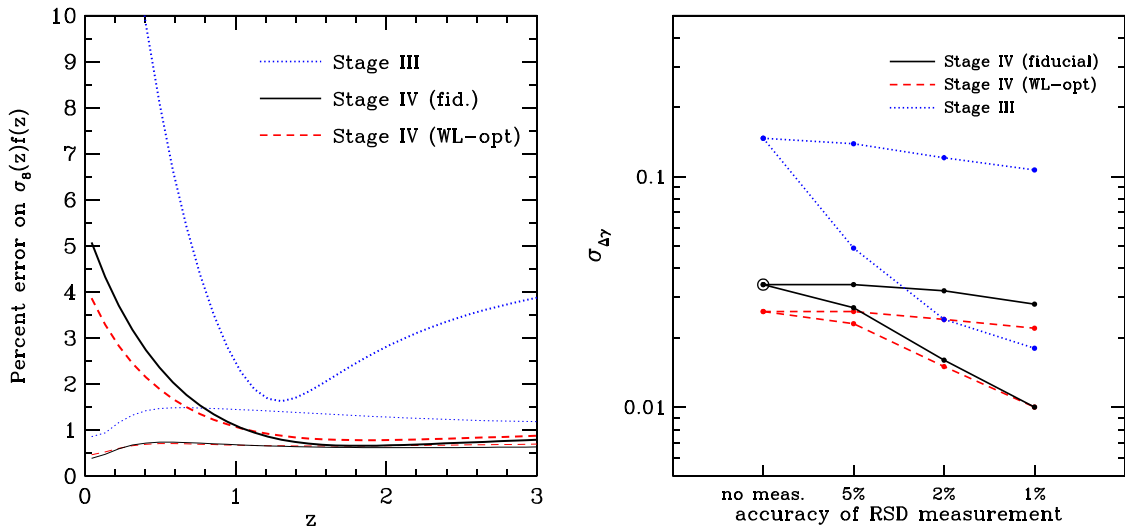


Fig. 50. *Left:* Predicted fractional error (1σ) of the RSD observable $\sigma_8(z)f(z)$ from our fiducial Stage III and Stage IV CMB+SN+BAO+WL programs, assuming a w_0 - w_a dark energy parameterization. The lower, thin curves for each forecast additionally assume GR by fixing $\Delta\gamma = \ln G_9 = 0$. *Right:* Improvement in the 1σ uncertainty on $\Delta\gamma$ from an additional RSD measurement at a single redshift. For each forecast, the lower and upper curves assume RSD measurements at $z = 0.2$ and $z = 1$, respectively.

FoM than measurements at higher redshifts.⁷⁹ A 1% measurement of $H(z)D_A(z)$ at $z = 0.5$ increases the Stage III FoM by about 13%; a similar improvement in the Stage IV FoM requires an accuracy of 0.5% at the same redshift. While the demands suggested by Fig. 49 appear stiff, large redshift surveys in principle have the information to achieve very high precision on $H(z)D_A(z)$. The challenge is lowering systematics to the level needed to achieve this precision.

8.5.3. Redshift-space distortions

For redshift-space distortions (RSD; Section 7.2), the relevant observable is $\sigma_8(z)f(z)$. WL data provide some limits on this observable by constraining the structure growth parameters $\Delta\gamma$ and (in combination with the CMB) G_9 , and through their constraints on the expansion history all of the acceleration probes contribute indirectly to the predicted growth history. The resulting predictions for Stage III and IV programs are plotted in the left panel of Fig. 50. We show predictions both for the general case where we marginalize over the structure growth parameters and for GR ($\Delta\gamma = \ln G_9 = 0$).

With the assumption of GR, the RSD observable is predicted to 1%–2% accuracy for Stage III and 0.5%–1% accuracy for Stage IV. If we allow modifications to GR through $\Delta\gamma$ and G_9 , however, the uncertainty at $z < 1$ increases dramatically. This change is mainly tied to the freedom to alter the growth rate $f(z)$ at low redshift by varying $\Delta\gamma$. Note that the effect of $\Delta\gamma$ vanishes at high redshift because $\Omega_m(z)$ approaches unity and therefore $f(z) \rightarrow f_{GR}(z)$ (see Eq. (44)). At $z \gtrsim 2$, uncertainty in G_9 significantly weakens Stage III predictions of the RSD observable, but the effect on Stage IV predictions is much smaller.

The DETF FoM can be improved by the addition of precise RSD measurements if we assume GR; for example, the fiducial Stage IV (Stage III) FoM increases by $\sim 10\%$ – 15% with a 1% (2%) RSD constraint at $z = 1$. Without assuming GR, the additional information from an RSD measurement at a single redshift goes mainly into constraining the structure growth parameters (and thus *testing* GR). In this case, the FoM improvement from percent-level RSD constraints is $\lesssim 10\%$. However, percent-level measurements in several redshift bins can still have an important impact on the FoM.

Low-redshift measurements of the RSD observable can contribute significantly to constraints on $\Delta\gamma$, as shown in the right panel of Fig. 50. For Stage III forecasts, 1%–2% RSD measurements at $z = 0.2$ reduce the error in $\Delta\gamma$ by nearly an order of magnitude, reaching an uncertainty comparable to that expected from the Stage IV probes. Likewise, the Stage IV constraint on $\Delta\gamma$ can be improved by a factor of a few by the addition of percent-level RSD measurements. At higher redshifts, the impact of RSD observations on the $\Delta\gamma$ uncertainty is greatly reduced due to the diminishing effect of $\Delta\gamma$ on the growth rate at high z . This reduced sensitivity at high z is in some sense an artifact of the $\Delta\gamma$ parameterization; the error on $\Delta\gamma$ is larger than the error on $\ln f$ by a factor $|(d \ln f / d \Delta\gamma)^{-1}| = |[\ln \Omega_m(z)]^{-1}|$, which for the fiducial cosmological model of Table 7 is 1.02 at $z = 0.2$ [where $\Omega_m(z) = 0.373$] and 3.23 at $z = 1$ [where $\Omega_m(z) = 0.734$].

We have computed but not plotted the impact of RSD measurements on the growth normalization parameter G_9 . For Stage IV, the uncertainty in G_9 is little affected by adding RSD measurements at any redshift. For Stage III, 1%–2% measurements of $\sigma_8(z)f(z)$ can reduce the fractional error in G_9 by up to a factor of two. As discussed in Section 7.7, some

⁷⁹ Note, however, that either decreased SN errors or increased BAO errors for any of these forecasts would reduce the difference between the predictions at $z < 1$ and at $z > 1$.

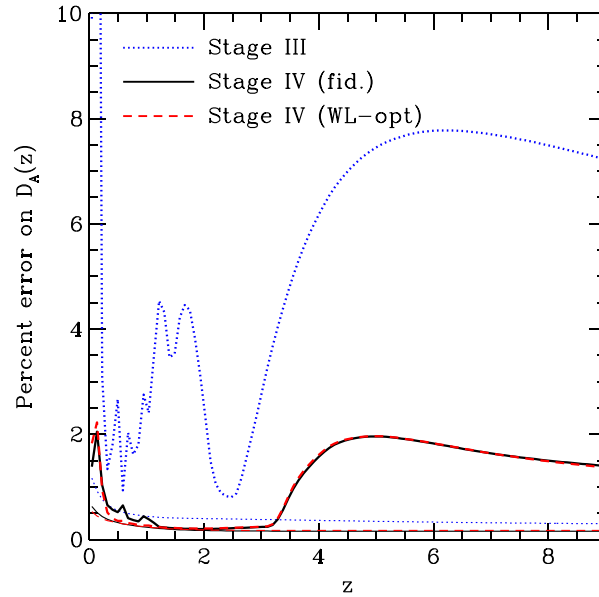


Fig. 51. Predicted fractional error (1σ) on the distance $D_A(z)$ from our fiducial Stage III and Stage IV CMB+SN+BAO+WL programs and the Stage IV program with optimistic weak lensing assumptions. For each case, the lower, thin curve assumes a w_0-w_a dark energy parameterization, while the upper, thick curve represents our binned $w(z)$ model.

modified gravity theories predict a mismatch between measures of structure using non-relativistic tracers, which respond to the Newtonian potential Ψ (Eq. (159)), and measures based on weak lensing, which responds to $\Psi + \Phi$, the sum of the Newtonian potential and space curvature. Consistency between RSD and WL, or cluster masses calibrated by weak lensing, tests for deviations of this sort, in addition to the G_0 and $\Delta\gamma$ constraints obtained by combining the measurements assuming $\Psi = \Phi$.

8.5.4. Distances

As a target for alternative distance indicator methods (Section 7.4) and standard sirens (Section 7.5), Fig. 51 plots the predicted fractional error on the angular diameter distance from our fiducial Stage III and Stage IV CMB+SN+BAO+WL programs. If we assume a w_0-w_a model then the constraints are tight, better than $\approx 0.25\%$ for Stage IV and $\approx 0.5\%$ for Stage III at all $z > 0.5$. However, the highest redshift distance measurements included in our forecasts (other than CMB) are BAO measurements at $z = 3$, so when we change to our general $w(z)$ model the distance errors at $z > 4$ become dramatically worse, $\approx 2\%$ for Stage IV and $\approx 8\%$ for Stage III. Furthermore, our Stage III forecast assumes a 0.8% distance measurement from HETDEX at $z = 2.4$, which we consider somewhat optimistic because it assumes that the full power spectrum shape can be used rather than the BAO scale alone. At $z < 2$ the Stage III curve has a jagged structure that depends to some degree on the specific choices we have made in binning and in assigning BAO/WL measurements to particular redshifts.

The message to take away is that Stage III distance errors for the general $w(z)$ model should be in the 1%–2% range at $z < 1$, the 3%–5% range at $1 < z < 2$, and the 6%–8% range at $z > 4$, with the errors at $2 < z < 4$ depending on the strength of BAO measurements from Ly α emission line galaxies (HETDEX) or the Ly α forest (BOSS). On the Stage III timescale, alternative distance measurements at $z > 1$ with few percent precision could reveal otherwise hidden departures from the w_0-w_a model. For Stage IV, where we assume powerful BAO experiments extending to $z = 3$, the demands on alternative distance indicators are much stiffer. Even for the general $w(z)$ model, alternative measures at $z > 4$ must reach 2% precision to be competitive. The Stage IV distance errors in this model become large at $z < 0.25$, similar to the several percent errors in H_0 seen in Fig. 40. As already discussed in Section 8.5.1, precise low redshift distance measurements have the potential to reveal late-time departures from smooth $w(z)$ evolution.

8.6. Observables and aggregate precision

We have characterized the performance of the fiducial program and its variants in terms of their ability to constrain parameterized models, from the specific ($w_0-w_a + GR$) to the general ($w(z_i), G_0, \Delta\gamma$). An alternative, more model-agnostic approach to characterizing the power of an experiment is via the aggregate precision with which it measures its basic observable. We have already introduced this idea at a few points, most notably in our discussion of BAO. By “aggregate precision” we mean the fractional (1σ) error on an overall factor that multiplies the observable in all redshift bins (and, if applicable, angular or mass bins). For the simple case of an observable O with independent fractional measurement errors

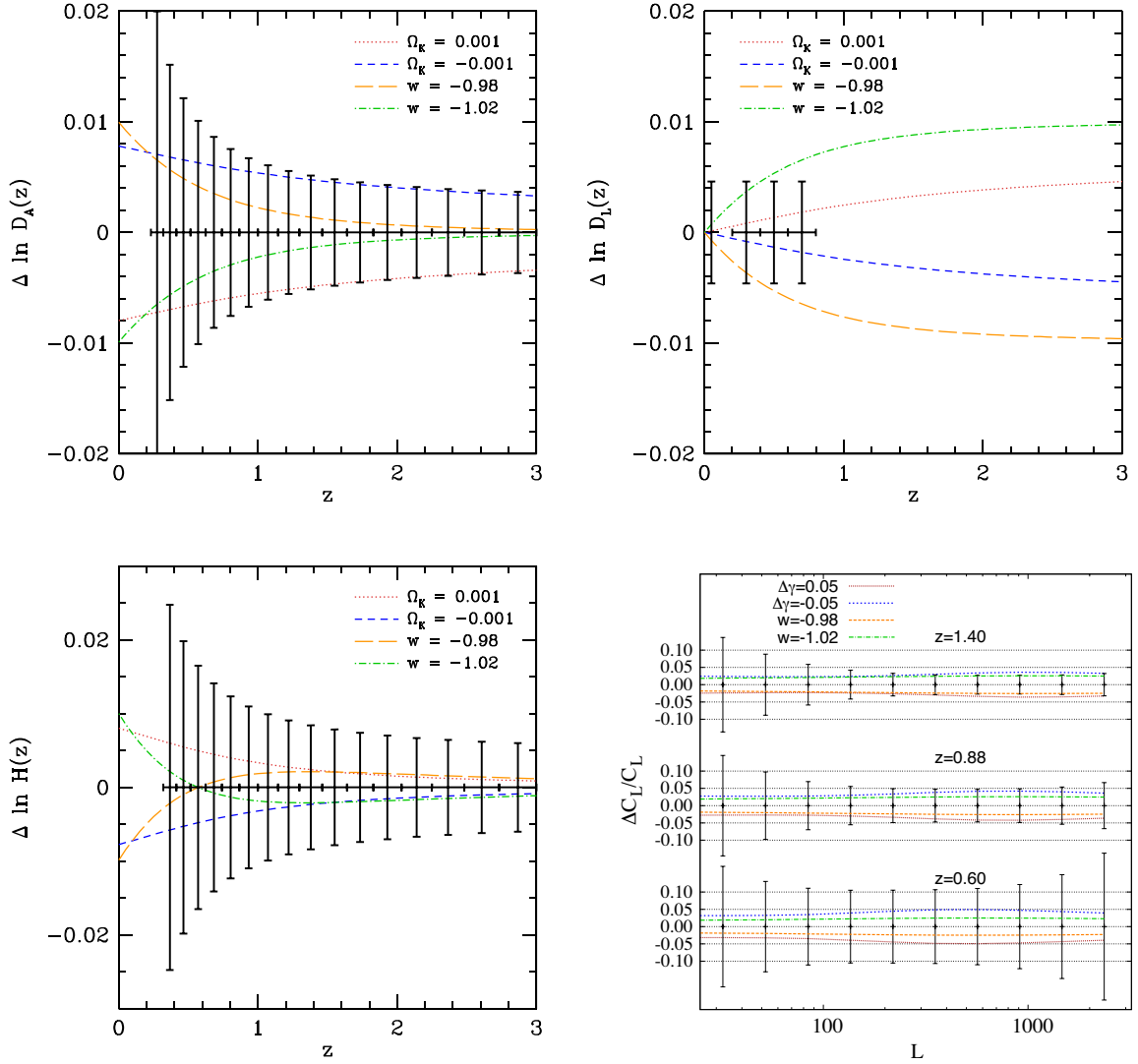


Fig. 52. Forecast errors for fiducial Stage IV SN, BAO, and WL programs, compared to model deviations from fiducial Λ CDM. The top panels show the forecast fractional errors in angular diameter distance from BAO (left) and luminosity distance from SNe (right), in absolute (Mpc) and relative (h^{-1} Mpc) units, respectively. The lower left panel shows the $H(z)$ error from BAO. The errors are uncorrelated from bin to bin, though the $D_A(z)$ and $H(z)$ errors in each bin are correlated with each other. Curves show the fractional changes in the predicted relations relative to the fiducial cosmology for CMB-normalized models with $1 + w = \pm 0.02$ or $\Omega_k = \pm 0.001$, as labeled. Marginalization over \mathcal{M} and H_0 allows arbitrary vertical offsets to the model curves in the SN panel without changing other cosmological parameters. The lower right panel shows forecast statistical errors (no systematics) in the cosmic shear power spectrum for three of the 14 source photometric redshift bins, in bins of $\Delta \log l = 0.2$ dex. Statistical errors are approximately uncorrelated for different l -bins at a given z , but errors in different z -bins are correlated. Curves show the fractional change in the predicted spectrum in models with $1 + w = \pm 0.02$ or $\Delta\gamma = \pm 0.05$.

$\Delta \ln O(z_i)$ in N redshift bins, the aggregate precision follows from the quadrature combination of the individual errors:

$$\Delta \ln O_{\text{agg}} = \left(\sum_{i=1}^N [\Delta \ln O(z_i)]^{-2} \right)^{-1/2}. \quad (181)$$

One important virtue of forecasting an experiment's aggregate precision is that it focuses one's attention on the required control of systematics, especially systematics that are correlated across redshift bins.

Fig. 52 plots the errors on the observables in our fiducial SN, BAO, and WL programs. For SN (upper right), we adopt independent errors of 0.01 mag in each of four redshift bins, corresponding to fractional errors in luminosity distance of 0.46%. The aggregate measurement precision is therefore $\Delta \ln D_{L,\text{agg}} = 0.23\%$. This is equal to the aggregate precision forecast for the SN component of the *WFIRST* design reference mission (DRM1) forecast by Green et al. (2012) for their

“optimistic” assumption about SN systematics.⁸⁰ However, the measurement in the $z = 0.05$ bin goes mainly to constraining the nuisance parameter \mathcal{M} , the SN absolute magnitude scale, so it is arguably better to characterize our fiducial program’s aggregate precision as $0.46\%/\sqrt{3} = 0.27\%$, which is closer to that of the “conservative” *WFIRST* forecast (0.32%). More generally, we note that large local calibrator samples are likely to achieve high statistical precision, and the systematic uncertainty in relating this local sample to fainter, redshifted samples will play a crucial role in determining the cosmological performance of the SN program.

The left panels show the fractional errors predicted on $D_A(z)$ and $H(z)$ for the fiducial BAO program, as tabulated in Table 6. These error bars decrease with increasing redshift because of the greater comoving volume per $\Delta \ln(1+z)$ bin at high redshift. Comparison of the D_L and D_A panels nicely illustrates the complementarity of SN and BAO as low and high redshift probes, respectively, though recall that they provide distinct information even at the same redshift because of relative vs. absolute calibration. The aggregate precision of the BAO measurement is $\Delta \ln D_{A,\text{agg}} = 0.13\%$, tighter than that from SNe because of the larger number of bins. Statistical errors in $H(z)$ are larger by a factor of 1.6 in each redshift bin, so the aggregate precision of the $H(z)$ measurement is lower by the same factor, $\Delta \ln H_{\text{agg}} = 0.21\%$. The D_A and $H(z)$ errors are correlated, with a correlation coefficient of ≈ 0.41 in each redshift bin.

Achieving the goals of our fiducial BAO program – sampling the equivalent of $f_{\text{sky}} = 0.25$ with $nP \approx 2$ out to $z = 3$ – will require multiple experiments probing different redshifts and regions of sky. While BigBOSS, *Euclid*, and *WFIRST* all plan to measure BAO in the range $1 < z < 2$, it is not clear that they can achieve $f_{\text{sky}} = 0.25$ with $nP \approx 2$ even collectively. *Euclid* plans to survey $\approx 14,000 \text{ deg}^2$ over the range $0.7 < z < 2$ in its 6.25-year primary mission, but the forecasts in Green et al. (2012), which are based on the *Euclid* instrument sensitivity of Laureijs et al. (2011) and the $H\alpha$ luminosity function and galaxy bias measurements of Sobral et al. (2013) and Geach et al. (2012), imply that *Euclid* will reach $nP < 0.5$ at $z > 1.2$. BigBOSS plans to survey $14,000 \text{ deg}^2$ in the northern hemisphere, and a southern hemisphere equivalent could increase the area to $24,000 \text{ deg}^2$ (limited in the end by Galactic extinction). Sampling density forecasts are more uncertain for BigBOSS than for *Euclid*; Schlegel et al. (2011) predict $nP > 2$ out to $z \approx 1.05$ and $nP > 0.5$ out to $z \approx 1.35$, falling to $nP = 0.35$ by $z = 1.65$.⁸¹ The *WFIRST* DRM1 of Green et al. (2012), with 2.4 years devoted to high-latitude imaging and spectroscopy, is projected to achieve $nP \gtrsim 1$ from $1.3 < z < 2.0$, declining to $nP \approx 0.5$ at $z = 2.7$. However, the survey area is only 3400 deg^2 , so a substantially extended mission would be required to reach 10^4 deg^2 , and the depth is still $nP < 2$. An implementation of *WFIRST* using one of the NRO 2.4-m telescopes could plausibly survey 10^4 deg^2 with $nP = 1 - 2$, depending on the instrument field of view and the time allocated to the spectroscopic survey (Dressler et al., 2012). In concert with ground-based surveys covering $z \lesssim 1.2$ and $z > 2$, this offers the best current prospect of achieving something close to our fiducial BAO program on the Stage IV timescale. Breakthroughs in 21 cm intensity mapping (see Section 4.4.5) could also lead to major progress on this timescale.

As a context for assessing these projected measurement errors, curves in these panels show the impact of changing w or Ω_k in “CMB-normalized” models, as described in Section 2.4. These curves are similar to those in Fig. 2, but here we have adopted much smaller parameter changes, $1 + w = \pm 0.02$ or $\Omega_k = \pm 0.001$, in line with the tight constraints expected for Stage IV experiments.⁸² Note that a model that skirts the top of the 1σ error bars in N_{bin} redshift bins would be ruled out at the $N_{\text{bin}}^{1/2}$ - σ level. However, while one can see the partial tradeoff between curvature and w , these plots do not capture the impact of degeneracy with other parameters such as Ω_m and w_a . The behavior of the curves is explained in Section 2.4 so we will not repeat it here, but one can see the complementarity of SN and BAO distance measurements in constraining w and curvature, respectively, and the roughly constant sensitivity of BAO $H(z)$ measurements at $1 < z < 3$ to a change in the equation of state. Some caution is required in interpreting the SN panel because marginalizing over H_0 and \mathcal{M} allows the model curves to be offset vertically with no change in other parameters, so the direct information about w and Ω_k resides in the slopes of the curves relative to the data points.

Analogous to the SN and BAO panels of Fig. 52, the lower right panel shows the projected 1σ statistical errors of the WL power spectrum in logarithmic bins $\Delta \log l = 0.2$ dex, for three of the 14 tomographic bins of source photometric redshift. Several caveats are in order. First, while the statistical errors in different l bins at fixed redshift are independent, errors among redshift bins are correlated because structure at redshift z_l contributes to the lensing of all background shells at $z_s > z_l$. Second, systematics in shape measurement or photometric redshift calibration will typically produce errors that are correlated across both redshift and angle; here we have plotted only statistical errors. Third, in addition to the 11 auto-correlation power spectra not shown here, our fiducial program includes 14×13 shear cross-power spectra, and cross-spectra between shear fields and galaxy density fields. All of these provide cosmological information, albeit with correlated errors and some loss of constraining power through marginalization over galaxy bias and intrinsic alignments. Finally, the shear power spectrum depends on both geometry and structure growth: for sources at z_s lensed by matter at z_l , the expected shear depends on $D_A(z_l)$, $D_A(z_s)$, and $\sigma_8(z_l)$.

⁸⁰ Specifically, that forecast assumes uncorrelated systematic errors of $0.01(1+z)/1.8 \text{ mag}$ in $16 \Delta z = 0.1$ redshift bins out to $z = 1.7$. The total errors have roughly comparable statistical and systematic contributions.

⁸¹ Schlegel et al. (2011) use a different convention, quoting nP for the redshift-space power spectrum at $k = 0.14h \text{ Mpc}^{-1}$ and $\mu = 0.6$ instead of the real-space power spectrum at $k = 0.2h \text{ Mpc}^{-1}$. We have quoted the numbers from their Table 2.3 as is, with no conversion to our nP convention and no independent assessment of the sampling density the instrument is likely to achieve.

⁸² These models have $h = 0.7030$ ($w = -0.98$), $h = 0.7171$ ($w = -1.02$), $h = 0.7157$ ($\Omega_k = 0.001$) and $h = 0.7045$ ($\Omega_k = -0.001$). Other parameters can be computed from the conditions $\Omega_b h^2 = 0.02268$, $\Omega_c h^2 = 0.1119$, and $\Omega_\phi = 1 - \Omega_c - \Omega_b - \Omega_k$.

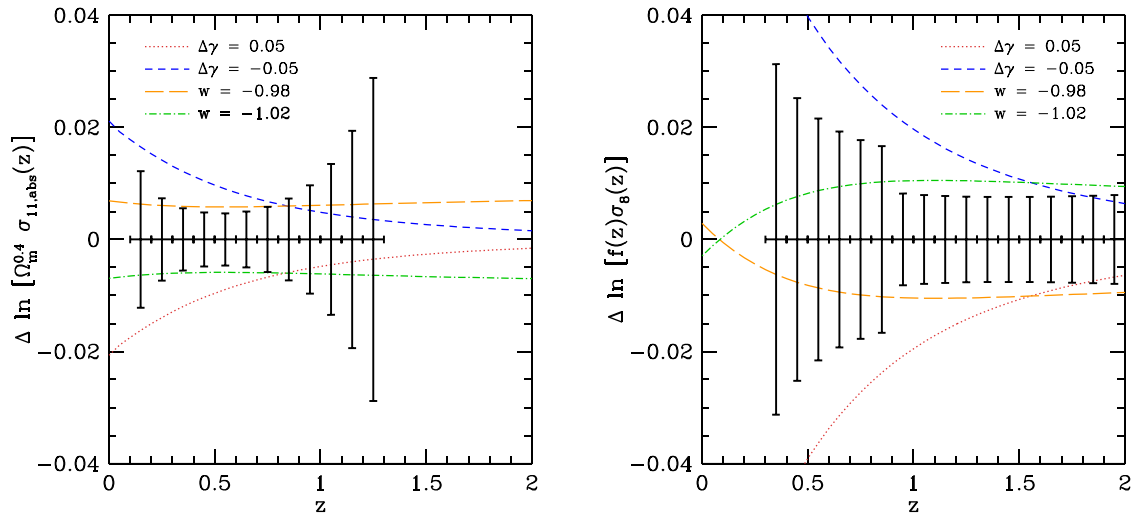


Fig. 53. Forecast errors for fiducial Stage IV cluster (left) and RSD (right) programs, with the assumptions described in the text. Curves show the predicted deviations from our fiducial Λ CDM model for CMB-normalized models with $1 + w = \pm 0.02$ and $\Delta\gamma = \pm 0.05$.

Correlated errors, the multitude of auto- and cross-correlations, and the linked parameter dependences mean one cannot characterize the information content of WL measurements as simply as that of SN or BAO measurements. We can nonetheless define an aggregate precision as the fractional error on the matter fluctuation amplitude σ_8 with all other parameters – and thus $D_A(z)$, $H(z)$, and $G(z)$ – held fixed. From Eq. (92) one can see that the fractional error on an overall scaling of $D_A(z)$ with fixed matter clustering would be similar to this fractional error on σ_8 with fixed geometry. For our fiducial Stage IV WL program we find an aggregate precision on σ_8 of 0.33%, where our calculation includes marginalization over the assumed 2×10^{-3} systematic uncertainties in shear calibration and photometric redshift offsets (and over parameters describing intrinsic alignments). The uncertainty in this case is dominated by these systematics, and the aggregate error is close to the quadrature sum (0.28%) of these two fractional contributions. For the optimistic WL case, with total errors double the statistical errors (and thus double those plotted in Fig. 52), the aggregate precision on σ_8 is 0.14%. If we assumed purely statistical errors, as plotted in Fig. 52, then the aggregate precision would of course be a factor of two higher. As already discussed in Section 8.1, it is likely that LSST, *Euclid*, and *WFIRST* will collectively, and perhaps even individually, exceed the performance of our fiducial Stage IV program as far as statistical errors are concerned. The key question is whether they will achieve the tight level of systematics control that we assume. In principle these experiments could collectively achieve an aggregate precision several times better than that of even our optimistic WL forecast, with cross-checks between them testing for any experiment-specific systematics.

For a given photo- z bin, the statistical errors per $\Delta \log l = 0.2$ dex bin shown in Fig. 52 shrink slowly with increasing l because of decreased cosmic variance, then grow slowly as shape noise errors become dominant (see Section 5.4.1). Errors are smaller for the higher photo- z bins because of the larger numbers of source galaxies the larger foreground volume. Orange and green curves show the impact of $1 + w = \pm 0.02$ variations, which is comparable to the 1σ error per $\Delta \ln l$ bin for $z_p = 0.88$ and $z_p = 1.40$. Red and blue curves show the impact of setting the growth index parameter to $\Delta\gamma = \pm 0.05$, with all other cosmological parameters fixed. Because the logarithmic growth rate is $f(z) \approx [\Omega_m(z)]^{\gamma + \Delta\gamma}$, a negative $\Delta\gamma$ corresponds to faster growth and thus higher C_l . These $\Delta\gamma$ and $1 + w$ changes have effects of similar magnitude but with different redshift dependence, so in principle WL measurements can break the degeneracy between them. In practice, the strongest degeneracy breaking will likely come from combining WL data with SN and BAO constraints, which are independent of $\Delta\gamma$.

Fig. 53 presents error forecasts for two other probes of structure growth, clusters and redshift-space distortions. The cluster errors are based on Fig. 30, assuming stacked weak lensing mass calibration of $M > 2 \times 10^{14} M_\odot$ clusters over 10^4 deg^2 with a WL source density of 30 arcmin^{-2} . While Fig. 30 is couched in terms of errors on $\sigma_{11,\text{abs}}(z)$ with other parameters held fixed, here we assume (as in Section 8.4) that the constrained quantity is $\Omega_m^{0.4} \sigma_{11,\text{abs}}(z)$, with the same fractional error; we caution that this is only an approximate characterization of the constraints from clusters. If the errors are dominated by WL shape noise and random cluster orientations, as assumed here, then they should be essentially uncorrelated among redshift bins. The aggregate precision for the cluster program is 0.20%, and since this is comparable to that of our other fiducial programs, it is not surprising that clusters have a significant impact on the expected uncertainties in equation-of-state and growth parameters (Section 8.4). Achieving this high aggregate precision would demand tight control of the systematics discussed in Section 6.4, including the effects of contamination, incompleteness, and mis-centering, the impact of mass-observable scatter, and the prediction of the mass function and stacked WL profiles in the presence of baryonic effects.

The RSD error bars in Fig. 53 are those shown previously by the lower solid curve in Fig. 31, computed with the forecasting code of White et al. (2009). They assume a galaxy sample like that of our fiducial BAO program out to $z = 2$ and full use

of information up to comoving $k = k_{\max} = 0.2h \text{ Mpc}^{-1}$ at each redshift. The sharp change in errors at $z = 0.9$ is due to the assumed drop in bias factor as surveys transition from absorption-line galaxies to emission-line galaxies. The aggregate precision on $f(z)\sigma_8(z)$ is 0.22%, again comparable to that of our other fiducial programs. The ranges $z > 1.4$ and $z < 1.4$ make equal contributions to this precision. As discussed in Section 7.2, we expect the dominant systematic uncertainty for RSD to lie in theoretical prediction of the RSD signal in the presence of non-linear gravitational evolution and galaxy bias, not the measurements themselves. To realize the full statistical power of Stage IV galaxy redshift surveys, these theoretical uncertainties must be controlled at the 0.2%-level. The White et al. (2009) forecasts, which assume that k_{\max} scales with the non-linear wavelength $k_{\text{nl}}(z)$ of the matter power spectrum, yield smaller errors at high redshift and an aggregate precision of 0.10%.

Curves in Fig. 53 again show the effect of isolated parameter changes with $1+w = \pm 0.02$ and $\Delta\gamma = \pm 0.05$. In isolation, either of these changes would be strongly ruled out by either the fiducial cluster program or the fiducial RSD program with the assumptions adopted here. For clusters, the impact of the w changes is comparable to the 1σ error bar per $\Delta z = 0.1$ redshift bin over the range $0.2 < z < 0.8$. The impact of $\Delta\gamma$ changes exceeds the 1σ error at all $z < 0.8$. For RSD, the $\Delta\gamma = \pm 0.05$ impact exceeds the 1σ per-bin error at all $z < 1.7$. In these CMB-normalized models, where changes to w and Ω_m have counteracting effects on $f(z)$, the sensitivity of RSD to a constant- w change is greatest at high redshifts. The impact of $\Delta w = \pm 0.02$ exceeds the per-bin 1σ error for $z \geq 0.9$.

Quantities like the DETF FoM and errors on $\Delta\gamma$ or $\ln G_9$ are useful for optimizing choices in a well defined experimental program, e.g., area vs. depth or the value of different target classes in a spectroscopic survey. However, since we have little idea where deviations from GR+ Λ are likely to show up (if they are there at all), we think that aggregate precision, including the effects of systematics, is a comparably useful tool for providing seat-of-the-pants guidance in a more general situation. For a given level of aggregate precision, a measurement at low redshift will typically have more direct sensitivity to dark energy, a measurement at high redshift will typically have more direct sensitivity to curvature, and measurements over a range of redshifts are needed to constrain dark energy evolution. However, given the degeneracies among parameters (especially w , Ω_m , and Ω_k) and the powerful impact of CMB constraints, it is difficult to identify a specific redshift range as the optimal one to probe. For a given method and a given facility, it makes sense to start where the pickings are easy, in terms of gaining precision relative to existing knowledge, and move to more difficult terrain when required. This assessment must also include consideration of where one can most readily control systematics, which is often but not always at low redshift. Extending the redshift range of a method increases leverage for breaking degeneracies and constraining dark energy evolution, but the more important impact is often to improve the method's aggregate precision by bringing in measurements with decorrelated errors. As we have emphasized repeatedly, a full program should employ multiple methods to take advantage of their complementary information content and redshift sensitivity and to cross-check for unrecognized systematics. Fortunately, Figs. 52 and 53 show that several methods have the potential to achieve 0.1%–0.3% aggregate precision in Stage IV experiments, a dramatic improvement on the $\sim 1\%$ –5% precision that represents the current state of the art for these methods.

8.7. Prospects with many probes

Section 8.3 demonstrates the power of a combined CMB+SN+BAO+WL experimental program, while Sections 8.4–8.6 show that other probes could add substantial further sensitivity to dark energy or modified gravity. Drawing these results together, we show in Fig. 54 the result of combining our fiducial CMB+SN+BAO+WL programs with representative performance estimates for clusters, redshift-space distortions, and direct H_0 measurement. (While the AP test could also play an important role, we consider current understanding of its systematic uncertainty too limited to allow even representative performance estimates.) Top, middle, and bottom panels show inverse errors on w_p , w_a , and $\Delta\gamma$, respectively, assuming a w_0 – w_a model with G_9 and $\Delta\gamma$ as beyond-GR growth parameters. Black bars show the results of combining all of these probes, while colored bars show the cumulative impact of successively omitting individual probes (see further explanation below).

For Stage IV we assume our fiducial CMB, SN, BAO, and WL constraints, the cluster and RSD constraints described in Section 8.6 (Fig. 53), and an H_0 constraint with precision of 1%. For Stage III we adopt the CMB+SN+BAO+WL errors summarized in Table 7. (Note, in particular, that our assumed Stage III SN errors are 0.02 mag per $\Delta z = 0.2$ bin and our Stage IV errors are 0.01 mag per bin, with the same error for the local calibrator sample at $z = 0.05$. For these plots, though not for others in the paper, we also include the Union2 SN constraints when computing Stage III and Stage IV.) For Stage III clusters we assume 5000 deg^2 and a source density of 10 arcmin^{-2} for mass calibration (both appropriate to DES), while keeping the mass threshold at $2 \times 10^{14} M_\odot$. For H_0 we assume 2% errors, and for RSD we take the White et al. (2009) forecasts for BOSS. Finally, for current data we take WMAP CMB errors, Union2 SN errors, and the BAO data and errors described in Section 4.2. We adopt the RSD errors reported by Blake et al. (2011a) from WiggleZ (see Section 7.2). We also include a 3% error on H_0 , and a 4% error on $\sigma_8 \Omega_m^{0.4}$ to represent clusters and weak lensing (see Section 6.2).

Beginning with the black bars representing the full combinations, we see that these projections predict improvements of more than an order-of-magnitude for each of the three parameters – w_p , w_a , and $\Delta\gamma$ – between current knowledge and Stage IV results. These combinations yield 1σ errors of approximately 0.005 on w_p , 0.1 on w_a , and 0.01 on $\Delta\gamma$, testing the Λ CDM model far more stringently than it has been tested to date. Stage III projections are roughly the geometric mean of current and Stage IV constraints in all cases.

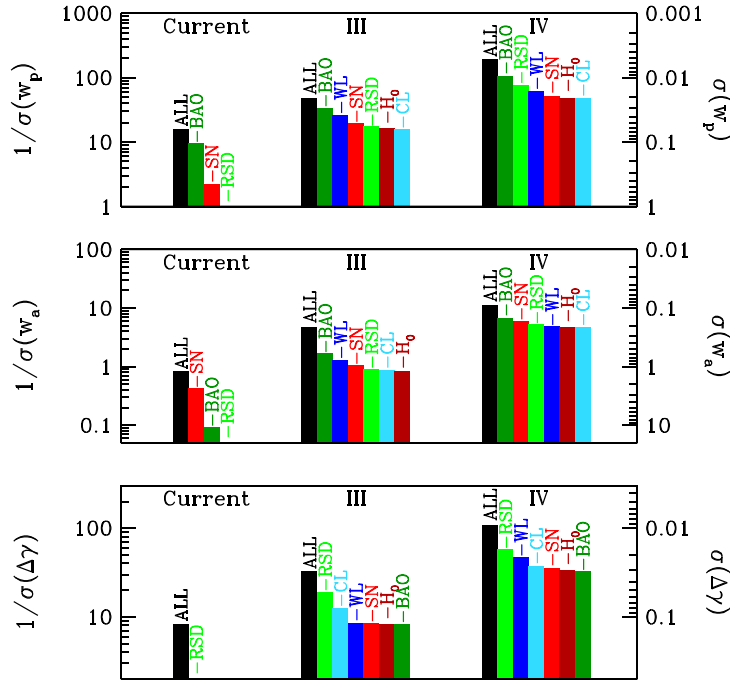


Fig. 54. Forecasts for inverse 1σ errors (left axis; errors themselves on the right axis) on w_p , w_a , and $\Delta\gamma$ from combining our fiducial CMB+SN+BAO+WL programs with additional constraints from redshift-space distortions (RSD), clusters (CL), and direct H_0 measurements. See text for a description of the errors assumed for Current (left), Stage III (middle), and Stage IV (right) forecasts. Black bars show the results of combining all of these probes. Colored bars show the cumulative impact of dropping probes in succession (“–BAO” should be read as “minus BAO”, for example). When a Stage IV probe is “dropped” it is set to its Stage III precision, and when a Stage III probe is “dropped” it is set to its current precision. CMB constraints are always retained.

It is interesting to ask what the different methods contribute to this performance, but there is no unique way to decompose a constraint into a sum of individual contributions, and the apparent relative importance of different components depends on how the decomposition is done. We have attempted one form of “even-handed” decomposition by dropping individual probes in succession, beginning with the probe whose omission causes the largest increase in the parameter error, then the probe that causes the largest increase after the first probe has already been dropped, and so forth. However, when we “drop” a probe we do not omit it entirely; rather, we set the error for that probe in the Stage IV forecast equal to the value we previously assumed for the Stage III forecast, or we set the error in the Stage III forecast equal to the value adopted for current data. Thus, for example, the dark green bar in the upper right shows the impact on $\sigma(w_p)$ of replacing the Stage IV BAO constraints with the Stage III BAO constraints. The light green bar next to it shows the impact of *also* setting the RSD constraint to the Stage III value, the dark blue bar the impact of also setting the WL constraint to the Stage III value, and so forth. To give one more example, the light blue bar in the middle of the bottom panel shows the error on $\Delta\gamma$ using Stage III WL+SN+BAO+ H_0 but current constraints for RSD and clusters. If the Stage III WL improvement is also dropped (dark blue bar) then there is no improvement over current knowledge of $\Delta\gamma$ because none of the remaining probes (SN, BAO, H_0) directly measures structure growth. We *always* include CMB constraints, with WMAP9 errors for current and *Planck* errors for Stage III and Stage IV. By construction, the rightmost colored bar for a given stage matches the black bar of the previous stage, since we have then set all probes back to their value in the previous stage.

We caution against reading too much into the ordering of probes in Fig. 54 because it depends in detail on our assumptions about the expected errors of the individual components; furthermore, a probe only gains in this plot based on its *differential* improvement between current performance and Stage III or between Stage III and Stage IV. The detailed examination of CMB+SN+BAO+WL in Tables 8–10 and the associated figures provides much more nuanced information. These caveats notwithstanding, Fig. 54 demonstrates several interesting points. In present data, BAO make the largest contribution to w_p constraints and SNe to w_a constraints,⁸³ though it is really the combination of the two with CMB data that is required to achieve interesting constraints in a model space that allows w_p , w_a , and Ω_k to vary simultaneously. BAO become more powerful in our fiducial Stage III and Stage IV programs, making the largest contribution to both the w_p and w_a constraints. Current constraints on $\Delta\gamma$ rely entirely on RSD, as the cluster constraint on $\sigma_8\Omega_m^{0.4}$ is degenerate with G_9 . With our adopted error forecast, RSD remains the most powerful contributor to $\Delta\gamma$ constraints at Stage III and Stage IV, outweighing both WL

⁸³ Interestingly, the roles of BAO and SNe in the current w_p constraint are reversed relative to the original arXiv posting of our article because of the inclusion of the new SDSS DR7 and BOSS measurements, both published in 2012.

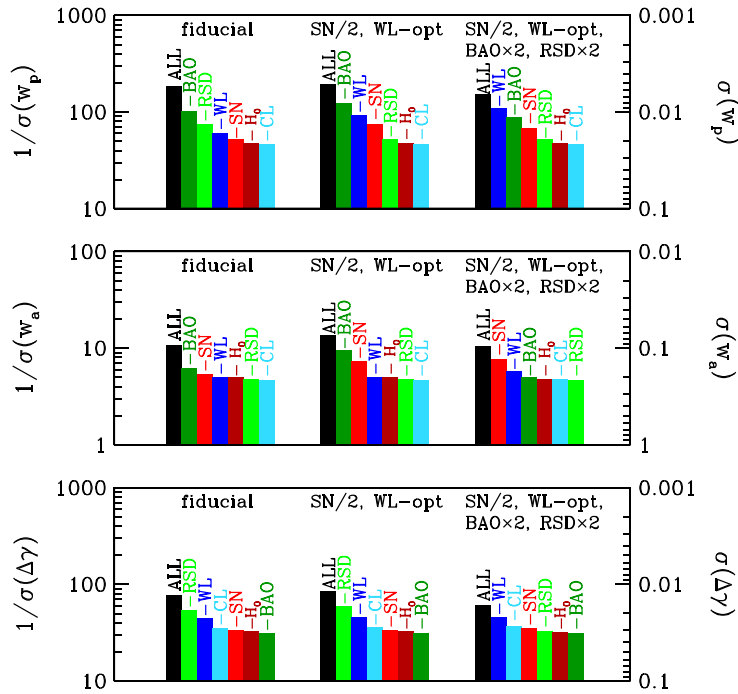


Fig. 55. Like Fig. 54, but showing variations on the Stage IV fiducial program. The middle column shows forecasts with the optimistic WL systematics and SN errors reduced by a factor of two. The right column shows the effect of, additionally, doubling the errors on RSD and BAO. The left column repeats the fiducial case from Fig. 54 for reference.

and clusters. Indeed, with these errors Stage IV RSD also makes an important contribution to the w_p measurement. WL and clusters make significant contributions to $\Delta\gamma$ constraints but have limited impact on w_p and w_a .

Fig. 55 shows two variants on the fiducial Stage IV case. In the middle column we consider a combined program with SN errors improved by a factor of two and the optimistic WL systematics. The forecast errors on w_p , w_a , and $\Delta\gamma$ shrink by 6%, 21%, and 8%, respectively. WL and SN now leapfrog RSD as contributors to the w_p error, though they still contribute less than BAO. The improvement in w_a is driven by the supernova improvement, though BAO remains the largest contributor. The right column shows the effect of, additionally, doubling the errors on BAO and RSD, since our fiducial assumptions for these programs are perhaps overoptimistic compared to the capabilities of planned Stage IV experiments. The forecast errors are larger than they are for the fiducial case but by moderate amounts, 20% (w_p), 14% (w_a), and 28% ($\Delta\gamma$). WL leapfrogs BAO to become the strongest contributor to w_p precision, while SN and WL both leapfrog BAO for w_a . With doubled measurement errors, RSD makes only a modest contribution to the parameter constraints, even for $\Delta\gamma$.

Perhaps the most important message to take from Figs. 54 and 55 is that these six probes together with CMB measurements provide a tight web of constraints on cosmic acceleration models, and that even if one or two methods prove disappointing, there are others (including ones not shown in this plot) to take up slack. We have focused much of our review on the stiff challenges of controlling systematic errors at the level demanded by future dark energy experiments. However, given the ingenuity of the community in devising and refining analysis methods, we are optimistic that the powerful data sets provided by these experiments will ultimately lead to constraints at the high end of our forecasts.

9. Conclusions

The first evidence for dark matter emerged from studies of galaxy clusters in the 1930s (Zwicky, 1933), and the dark matter problem assumed a central position in cosmology after technological advances allowed dynamical measurements in the outer regions of individual galaxies (Rubin and Ford, 1970; Rogstad and Shostak, 1972; see review by Faber and Gallagher (1979)). Because it clusters on small scales, dark matter has a rich phenomenology, and detailed studies of galaxies, galaxy clusters, large scale structure, the Ly α forest, and the CMB have largely pinned down its properties even though we have yet to identify the dark matter particle or particles. The implications of the dark matter problem have proven even more profound than might have been imagined in the 1930s, pointing the way to an entirely new form of matter whose cosmic mean density exceeds that of all baryonic material by a ratio of 6:1. There are now several plausible ideas of what dark matter might be — ideas that are rooted in well motivated extensions of the standard model of particle physics and that (at least in some cases) naturally explain the observed density of dark matter (Bertone et al., 2005). With experimental methods advancing on many fronts, there are good reasons to hope that dark matter will soon be identified in particle accelerators, detected directly in underground experiments, or detected indirectly via its annihilation into γ -rays, neutrinos, or cosmic rays.

Evidence for cosmic acceleration began to emerge in the early 1990s, and it rapidly evolved into a near-airtight case following the supernova discoveries of the late 1990s (see Section 1.1). Whether the cause is a new energy component or a breakdown of GR, the implications of cosmic acceleration are dramatic, even more so than those of dark matter. Cosmic acceleration may ultimately provide clues to the nature of quantum gravity, or to the structure of the universe on scales beyond the Hubble volume, or to its history over times longer than the Hubble time. There are already many theories of cosmic acceleration, but none of them offers a convincing explanation of the observed magnitude of the effect, and nearly all of them were introduced to explain the observed acceleration, rather than emerging naturally out of fundamental physics models. In contrast to dark matter, most models of dark energy predict that it is phenomenologically poor, affecting the overall expansion history of the universe but little else. That impression could yet prove incorrect: other signatures of “cosmic acceleration physics” might appear in small-scale gravitational experiments, in the behavior of gravity in different large scale environments, or in non-gravitational interactions.

While the solution to the cosmic acceleration problem could come from a surprising direction, including theory, there is a clear experimental path forward through increasingly precise measurements of expansion history and growth of structure. Relative to current knowledge, Stage IV experiments can improve the measurement of basic cosmological observables – $H(z)$, $D(z)$, and $G(z)$ – by one to two orders of magnitude. Correspondingly, they can achieve a 1–2 order-of-magnitude improvement in constraints on w , 2–3 orders-of-magnitude improvement in the DETF figure-of-merit, and still greater gains in higher dimensional parameterizations, including tests of GR violations. Any robust deviation from a cosmological constant model would have profound implications, and the greater the precision and detail with which such a deviation is characterized, the greater the direction for understanding its cause.

We have reviewed in considerable detail the four leading methods – supernovae, BAO, weak lensing, and clusters – and we have briefly discussed some of the emerging new methods, whose capabilities and limitations are as yet less thoroughly explored. We have also investigated the complementarity of these methods for constraining theories of cosmic acceleration. We have spent little time on the CMB as it has little *direct* constraining power on these theories, but it does provide crucial constraints on other cosmological parameters that are essential to precision tests. We now conclude our article with an editorial recap of our main takeaway points.

Type Ia supernovae have unbeatable precision for measuring distances at $z \lesssim 0.5$. Future surveys can readily achieve statistical errors of 0.01 mag or less (0.5% in distance) averaged over bins of $\Delta z = 0.2$. The challenge is getting systematic uncertainties at or below the level of such statistical errors. In our view, the key systematics for SN studies are imperfect photometric calibration, evolution in the population of SNe represented at different redshifts, and the effects of dust extinction. The first can be addressed by careful technical design, of the instruments used for SN surveys and of the observing and calibration procedures. The second can be addressed by obtaining high quality observations of the SNe and their host galaxies that allow one to match the properties of high and low redshift systems. The third is best addressed by working in the rest-frame near-IR, where extinction is low. Rest-frame IR observations may also mitigate evolution systematics and improve statistical errors, since current observations indicate that the scatter in SN luminosities is smaller in the near-IR than in the optical.

The BAO method complements the SN method in several ways. SN measure distance ratios relative to local calibrators (i.e., distances in h^{-1} Mpc), while BAO measure absolute distances (in Mpc) assuming a calibration of the sound horizon. SN and BAO measurements at the same redshift therefore provide complementary information, effectively constraining H_0 , which is itself sensitive to acceleration when combined with CMB data. Spectroscopic BAO measurements that sample a constant fraction of the sky become *more* precise at high redshift because they cover a greater comoving volume and because they measure $H(z)$ directly in addition to $D_A(z)$. (Of course, they also require a larger number of tracers to probe these larger volumes, and the tracers themselves are fainter at higher redshifts.) Cosmic variance limited BAO surveys have roughly constant sensitivity to dark energy over the range $1 < z < 3$ because the decreasing dynamical impact of dark energy at higher redshifts is balanced by the greater BAO measurement precision. Furthermore, the BAO method is the only one that we expect to be statistics-limited even with Stage IV surveys. Non-linear matter clustering and non-linear galaxy bias may shift the BAO peak by more than the statistical errors of Stage IV experiments, but the shifts can be computed using theoretical models that are constrained by the smaller scale clustering data, and moderate fractional accuracy in these corrections is enough to keep any uncertainty in the corrections well below the statistical errors. Thus, we see the main challenge for the BAO method as finding ways to efficiently map the available structure. There are several promising ideas, both ground-based and space-based, and Stage IV BAO constraints will likely come from a union of several approaches covering different redshift ranges.

Weak lensing measurements provide sensitivity to both the distance–redshift relation and the growth of structure. The statistical precision achievable with future facilities is very high, so the challenge is reducing systematic uncertainties to a level that does not overwhelm these statistical errors. The most important problem is reducing multiplicative shape measurement biases to the level of $\sim 10^{-3}$ or below, which requires (among other things) determining the PSF that affects the galaxy images to very high accuracy. This is an area of highly active research, and it is not yet clear what approach will prove most successful; we have advocated pursuit of a Fourier method that becomes exact in the limit of high S/N ratio. Since most shape measurement systematics depend inversely on the ratio r_{50}/r_{PSF} of galaxy size to PSF radius, one can mitigate these systematics by restricting the analysis to larger galaxies, but this gives up statistical precision by reducing the surface density of usable sources. The second major challenge for WL studies is the measurement and calibration of photometric redshift distributions, characterizing both their means and their outlier fractions at the $\sim 10^{-3}$ level or below. Meeting this

challenge requires optical and near-IR imaging for robust identification of spectral breaks, and large spectroscopic calibration data sets. The third systematics challenge for WL is intrinsic alignment of galaxies. With continuing theoretical work and good photometric redshifts, we believe that this systematic can be kept subdominant, but it remains a challenging problem. WL measurements are rich with observables, including higher order statistics and varied combinations of galaxy–galaxy lensing, galaxy clustering, and tomography. Despite the field’s formidable technical obstacles, we think it quite possible that constraints from WL surveys will eventually exceed current forecasts because these additional observables provide cosmological sensitivity and/or allow systematic uncertainties to be calibrated away.

Cluster abundance measurements provide an alternative route to measuring the growth of structure and thus testing the consistency of GR growth predictions. In addition, by reducing uncertainty in Ω_m and breaking other degeneracies, cluster abundance measurements can sharpen the equation-of-state constraints from SN, BAO, and WL distance measurements. The key challenge for cluster cosmology is achieving unbiased and precise calibration of the cluster mass scale. Realizing the statistical power of future surveys requires absolute mass calibration accurate at the 0.5%–1% level. In our view, this is only achievable with weak lensing, because the baryonic physics associated with other observables is too uncertain to predict them this accurately from first principles. We thus see cluster studies as a natural byproduct of WL surveys and in some sense as a specialized branch of WL, one that takes advantage of the strong additional information afforded by knowing the locations of peaks in the optical galaxy density, X-ray flux, or SZ decrement. If WL provides the fundamental mass calibration, then the shape measurement and photometric redshift uncertainties that affect WL also affect cluster methods.

While all of these methods can be pursued at ambitious levels from the ground, all would benefit from the capabilities of a space mission, especially from the capability of wide-field near-IR imaging and spectroscopy, which is possible at the necessary depth only from space. For SN, a space platform provides the greater stability and sharp PSF needed for highly accurate photometric calibration, and it allows observations in the rest-frame near-IR, which is crucial for minimizing extinction systematics and may be valuable for reducing evolution systematics. For BAO, near-IR spectroscopy allows emission-line galaxy surveys over the huge comoving volume from $1.2 \lesssim z \lesssim 2$, which is difficult to probe with ground-based optical or IR observations. (Intensity-mapping radio methods may be able to probe this redshift range from the ground, but this approach still has significant technological hurdles to overcome.) For WL, space observations allow the deep near-IR photometry that is essential for robust and accurate photometric redshifts, and they provide stable imaging with a sharp PSF that enables accurate shape measurements for a high surface-density source population. The above considerations motivated both *WFIRST* and the IR capabilities of *Euclid*. Space-based optical imaging, the other major element of *Euclid*, allows a significantly sharper PSF and thus potentially more powerful WL measurements, if the systematic errors are sufficiently well controlled. More generally, space-based WL measurements can employ a higher galaxy surface density than ground-based surveys to the same photometric depth, both because the PSF itself is smaller and because greater stability and the absence of atmospheric effects should allow accurate measurements down to a smaller ratio of r_{50}/r_{PSF} .

The current generation of “Stage III” experiments such as BOSS, PS1, DES, HSC, and HETDEX are collectively pursuing all of these methods, and they should achieve dark energy constraints substantially better than those that exist today. It is crucial that the next generation, Stage IV experiments maintain, collectively, a balanced program that includes SN, BAO, and WL, as well as other methods (clusters, Alcock–Paczynski, redshift-space distortions) that can be applied to the same data sets. There is much more to be gained, and much lower risk, from doing a good job on all three methods than from doing a maximal job on one at the expense of the others. A balanced program takes advantage of the methods’ complementary information content and areas of sensitivity, and it allows the best cross-checks for systematic errors. It is becoming standard practice to trade systematic uncertainties for statistical errors by parameterizing their impact and marginalizing — e.g., over an uncertain shear calibration multiplier or photometric redshift offset. While this is a powerful strategy for removing biases due to “known unknowns”, it does not protect against “unknown unknowns”. Any conclusion about cosmic acceleration will be more compelling if it is demonstrated by independent methods, and the more interesting the conclusion, the more crucial this independent confirmation will be.

In Section 8 we have provided quantitative forecasts for a fiducial Stage IV program and for many variants upon it. Our fiducial SN program assumes 0.01 mag mean errors for a local calibrator sample at $z = 0.05$ and in three bins of $\Delta z = 0.2$ at $0.2 < z < 0.8$, uncorrelated from bin to bin. Our fiducial BAO program assumes mapping 1/4 of the sky to $z = 3$, with errors that are $1.8\times$ the linear theory sample variance errors over this volume. Different combinations of redshift range and sky coverage that have the same comoving volume yield nearly the same results. Our fiducial WL program assumes statistical errors of a $\sim 10^9$ -galaxy imaging survey (more precisely, 10^4 deg^2 with 23 galaxies/arcmin²), and systematic errors of 2×10^{-3} in shear calibration and photometric redshift calibration. We also consider an optimistic case in which the total (systematic + statistical) errors are simply double the statistical errors, which effectively corresponds to total errors ~ 2 – 3 times smaller than those of the fiducial case. Our fiducial program corresponds fairly closely to the one recommended by the Astro2010 Cosmology and Fundamental Physics panel, and it is a reasonable, probably conservative forecast of what could be achieved by a combination of LSST, *Euclid*/*WFIRST*, and ground-based BAO and SN surveys.

To quantify the expected performance of this program and its variants, we considered two dark energy models, one with $w_a = w_0 + w_a(1 - a) = w_p + w_p(a_p - a)$, where $a_p = (1 + z_p)^{-1}$ is the expansion factor at which w is best constrained, and a second with $w(a)$ allowed to vary freely in each of 36 bins of $\Delta a = 0.025$, reaching to $z = 9$. In both cases we allowed deviations from GR-predicted growth rates characterized by an overall multiplicative offset G_9 in $G(z)$ and by a shift $\Delta\gamma$ in the logarithmic growth rate $d \ln G/d \ln a \propto [\Omega_m(a)]^{\gamma + \Delta\gamma}$. We focused principally on the expected errors in w_p , w_a , $\Delta\gamma$, and G_9 , including the DETF FoM defined as $(\sigma_{w_p} \sigma_{w_a})^{-1}$. While principal components (PCs) of the general $w(a)$ model allow a

much richer characterization of the dark energy history (and its uncertainties), we regard the combination of the DETF FoM and the $\Delta\gamma$ error to be as good as any alternative for characterizing the strength of a combined program.

The primary results of our forecasting investigation appear in Tables 8–10 and, in distilled form, in Figs. 33 and 38. The FoM of our fiducial program is 664, more than five times better than our Stage III forecast and a roughly 50-fold improvement on current knowledge. Within the adopted parameterization, 1σ errors on individual parameters are 0.014 on w_p , 0.11 on w_a , 0.034 on $\Delta\gamma$, 0.015 on $\ln G_9$, 5.5×10^{-4} on Ω_k , and 5.1×10^{-3} on h . All three methods contribute significantly to these constraints. For our fiducial assumptions, BAO have the greatest leverage on the DETF FoM, in the sense that halving the BAO errors produces the greatest increase in the FoM while doubling the BAO errors produces the greatest decrease. WL has the least leverage, which implies that the fiducial BAO and SN measurements constrain the expansion history well enough that the WL measurements add relatively little constraining power. However, the error on $\Delta\gamma$ scales nearly linearly with the WL errors, since all of the information on growth comes from the WL measurements. (Note that we scale the *total* WL errors, equivalent to multiplying systematic and statistical errors by the same factor.) Conversely, changing the SN or BAO errors has almost no impact on the $\Delta\gamma$ constraint.

Changing to our optimistic assumptions about WL systematics (total errors equal to twice the statistical errors), while retaining the fiducial SN and BAO assumptions, raises the FoM from 664 to 789 and lowers the $\Delta\gamma$ error from 0.034 to 0.026. For the optimistic systematics model, WL measurements have the *greatest* leverage on the DETF FoM instead of the least, and the $\Delta\gamma$ errors continue to scale approximately linearly with the WL errors. Thus, our conclusions about the power of WL relative to BAO and SN depend significantly on the assumed importance of WL systematics, which is difficult to predict at present.

When we move from the w_0-w_a model to the general $w(z)$ model, the forecast errors on $\Delta\gamma$ barely change, since it is constrained by differential measurements of matter clustering over the redshift range of our fiducial data sets. The errors on G_9 , on the other hand, expand dramatically, because even within GR the overall amplitude of structure can be shifted by the behavior of $w(z)$ outside of our constrained redshift range (i.e., at $z > 3$). If the amplitude of matter clustering proved inconsistent with that of a w_0-w_a , $G_9 = 1$ model, it would definitely indicate something interesting, but this measurement alone would not show whether the unusual behavior arises from a violation of GR or from unexpected behavior of $w(z)$ at high redshift.

For variations around our fiducial program, the impact of reducing the errors of SN measurements is greater than the impact of increasing the redshift range of these measurements. For example, reducing the error per redshift bin from 0.01 mag to 0.005 mag increases the FoM from 664 to 1197, while increasing the maximum redshift from 0.8 to 1.6 only raises the FoM to 841. These scalings imply that the highest priority for SN studies is to minimize statistical and systematic errors at $z < 1$, and that pushing to higher redshifts is a lower priority until the reduction in $z < 1$ systematics has been saturated. At fixed f_{sky} , BAO constraints have a stronger dependence on maximum redshift, because at higher z the BAO measurements become more precise and the importance of the direct $H(z)$ measurements grows.

We have not incorporated cluster abundances into our primary forecasts, but we have investigated how precisely our fiducial Stage III and Stage IV programs (CMB+SN+BAO+WL) predict the parameter combination $\sigma_{11,\text{abs}}(z)\Omega_m^{0.4}$ that is best constrained by cluster abundances. For a w_0-w_a dark energy model, the forecast precision is $\sim 1.5\%$ for Stage III and $\sim 0.75\%$ for Stage IV if we assume GR is correct. If we allow GR deviations parameterized by G_9 and $\Delta\gamma$, then the forecast precision degrades significantly, especially for Stage III at $z > 0.5$. Our analysis in Section 6.3.3 indicates that clusters calibrated by stacked weak lensing should be able to achieve higher precision on $\sigma_{11,\text{abs}}(z)\Omega_m^{0.4}$. When we add the anticipated cluster constraints for a 10^4 deg^2 survey with a $10^{14}M_\odot$ mass threshold, assuming that calibration errors are limited by weak lensing statistics, we find that the DETF FoM grows by a factor of 1.4 at Stage III and 1.9 at Stage IV relative to the fiducial CMB+SN+BAO+WL program. The error on $\Delta\gamma$ decreases by a factor of 3.2 for Stage III and by 1.6 for Stage IV. Cluster studies will be enabled automatically by large WL surveys, which can be used to identify clusters as optical galaxy concentrations and to provide mass calibration for clusters identified by any method (X-ray, SZ, optical). If they can achieve the limits imposed by weak lensing statistics, they can add considerable leverage to tests of dark energy models and deviations from GR.

We have adopted a similar strategy for some of the alternative probes discussed in Section 7. For a w_0-w_a dark energy model, the forecast precision on H_0 is 0.7% from our fiducial Stage IV program, 1.3% for Stage III. A direct measurement of H_0 with 1% precision would improve the DETF FoM of the fiducial Stage IV program by 20%; a 2% measurement would improve the Stage III FoM by 15%. The forecast constraint on H_0 degrades, dramatically, to $\sim 60\%$ in our general $w(z)$ model, since large changes in w at low redshift can affect H_0 significantly while having minimal impact on probes at higher redshift. Thus, a discrepancy between direct measurements and H_0 constraints from CMB+SN+BAO+WL data could be a diagnostic for unusual low- z evolution of dark energy.

The Alcock–Paczynski parameter $H(z)D_A(z)$ is constrained to $\sim 0.2\%$ – 0.3% by our fiducial Stage IV program over the redshift range $0.2 < z < 3$, setting a demanding target for AP tests. The corresponding precision forecast for Stage III is $\sim 0.5\%$. Redshift-space distortions and galaxy clustering can measure the parameter combination $\sigma_8(z)f(z)$, which is constrained by our Stage IV fiducial program to about 5% at $z \approx 0.1$, 2.5% at $z = 0.5$, and $\sim 1\%$ beyond $z = 1$, numbers that improve only slightly for the optimistic weak lensing systematics. For Stage III, the constraints at a given redshift are considerably weaker. In all cases the constraints are tighter if we assume GR ($\Delta\gamma = 0$, $G_9 = 1$), but the main purpose of redshift-space distortion analyses would be to test GR growth, so we regard the looser constraints as the more relevant targets for such analyses. This level of precision appears within reach of large galaxy redshift surveys

if theoretical systematics can be adequately controlled, making redshift-space distortions a potentially powerful addition to the arsenal of cosmic acceleration probes. While WL and redshift-space distortions both probe structure growth, they have different dependences on the two distinct potentials that enter the GR spacetime metric (see Section 7.7), so a discrepancy between them could reveal a GR-deviation that might not be captured by $\Delta\gamma$ alone. Galaxy redshift surveys designed for BAO measurements should allow redshift-space distortion analyses (and AP tests) as an automatic by-product, which may greatly increase their science return. Precise measurements of the shape of the galaxy power spectrum could also reveal signs of scale-dependent growth, another possible consequence of modified gravity models, though these may be difficult to distinguish from other factors that affect the power spectrum shape (see Section 7.7).

The aggregate precision of our fiducial Stage IV program measurements, in the sense described in Section 8.6, is 0.23% in D_L (from SN), 0.13% in D_A (from BAO), 0.21% in H (also from BAO), and 0.33% in σ_8 for fixed geometry (for fiducial WL; optimistic WL yields 0.14%). For the fiducial Stage IV cluster program with weak lensing mass calibration we forecast 0.20% aggregate precision on $\sigma_8(z)\Omega_m^{0.4}$, while our fiducial Stage IV RSD forecast yields 0.22% aggregate precision on $f(z)\sigma_8(z)$. The ultimate limits on H_0 and Alcock–Paczynski measurements are still difficult to predict, but sub-percent precision appears well within reach on the Stage IV timescale. These forecasts represent a dramatic advance over the current state of the art, which is roughly 1%–5% for distance measurements (SN, BAO, H_0) and $\sim 5\%$ for structure growth measurements (σ_8 , $f(z)$). The cosmological measurements of the past two decades have established a “standard model” of cosmology based on inflation, cold dark matter, a cosmological constant, and a flat universe. The measurements of the next two decades will test that model far more stringently than it has been tested to date.

The future of cosmic acceleration studies depends partly on the facilities built to enable them, partly on the ingenuity of experimenters and theorists in controlling systematic errors and fully exploiting their data sets, and partly on the kindness of nature. The next generation of experiments could merely tighten the noose around $w = -1$, ruling out many specific theories but leaving us no more enlightened than we are today about the origin of cosmic acceleration. However, barely a decade after the first supernova measurements of an accelerating universe, it seems unwise to bet that we have uncovered the last “surprise” in cosmology. Equally important, the powerful data sets required to study cosmic acceleration support a broad range of astronomical investigations. These observational efforts are natural next steps in a long-standing astronomical tradition: mapping the universe with increasing precision over ever larger scales, from the solar system to the Galaxy to large scale structure to the CMB. These ever growing maps have taught us extraordinary things – that gravity is a universal phenomenon, that we live in a galaxy populated by 100 billion stars, that our galaxy is one of 100 billion within our Hubble volume, that our entire observable universe has expanded from a hot big bang 14 billion years in the past, that the dominant form of matter in the universe is non-baryonic, and that the early universe was seeded by Gaussian (or nearly Gaussian) fluctuations that have grown by gravity into all of the structure that we observe today. We hope that the continuation of this tradition will lead to new insights that are equally profound.

We gratefully acknowledge the many mentors, collaborators, and students with whom we have learned this subject over the years. For valuable comments and suggestions on the draft manuscript, we thank Joshua Frieman, Dragan Huterer, Chris Kochanek, Andrey Kravtsov, Mark Sullivan, and Alexey Vikhlinin. We also thank the many readers who sent comments in response to the original arXiv posting of the article, which led to numerous improvements in the text and referencing. We gratefully acknowledge support from the National Science Foundation, the National Aeronautics and Space Administration, the Department of Energy Office of Science, including NSF grants AST-0707725, AST-0707985, AST-0807337, and AST-1009505, NASA grant NNX07AH11G1320, and DOE grants DE-FG03-02-ER40701 and DE-SC0006624. DW acknowledges the hospitality of the Institute for Advanced Study and the support of an AMIAS membership during critical phases of this work. MM was supported by the Center for Cosmology and Astro-Particle Physics (CCAPP) at Ohio State University. CH acknowledges additional support from the Alfred P. Sloan Foundation and the David & Lucile Packard Foundation. ER was supported by the NASA Einstein Fellowship Program, grant PF9-00068.

Appendix. Glossary of acronyms and facilities

Note that we have not repeated the acronyms of X-ray surveys listed in Table 4.

ACS:	Advanced Camera for Surveys (on Hubble Space Telescope)
ACT:	Atacama Cosmology Telescope
ADEPT:	Advanced Dark Energy Physics Telescope
AP:	Alcock–Paczynski
BAO:	Baryon Acoustic Oscillations
BOSS:	Baryon Oscillation Spectroscopic Survey
BigBOSS:	Big Baryon Oscillation Spectroscopic Survey
CCD:	Charge Coupled Device
CDM:	Cold Dark Matter
CFHT:	Canada–France–Hawaii Telescope
CFHTLS:	Canada–France–Hawaii Telescope Legacy Survey
Chandra:	Chandra X-ray Observatory (NASA)

CHIME: Canadian Hydrogen Intensity Mapping Experiment
CMB: Cosmic Microwave Background
COBE: Cosmic Background Explorer
COSMOS: Cosmic Evolution Survey (from Hubble Space Telescope)
CSP: Carnegie Supernova Project
DES: Dark Energy Survey
DESpec: Dark Energy Spectrograph
DESTINY: Dark Energy Space Telescope
DETF: Dark Energy Task Force
DUNE: Dark Universe Explorer
EE50: Encircled Energy 50%
eROSITA: extended Roentgen Survey with an Imaging Telescope Array
ESA: European Space Agency
ESSENCE: Equation of State: SupErNovae trace Cosmic Expansion
Euclid: Euclid dark energy space mission (ESA)
FKP: Feldman–Kaiser–Peacock (1994) $P(k)$ estimation method
FFT: Fast Fourier Transform
FIRST: Faint Images of the Radio Sky at Twenty-Centimeters (from the VLA)
FWHM: Full Width at Half Maximum
Gaia: Gaia astrometry mission (ESA)
GR: General Relativity
HEAO: High-Energy Astrophysics Observatory (NASA)
HETDEX: Hobby-Eberly Telescope Dark Energy Experiment
HOD: Halo Occupation Distribution
HSC: Hyper-Suprime Camera (for Subaru Telescope)
HST: Hubble Space Telescope
IGM: Intergalactic Medium
IRAC: Infrared Array Camera (on Spitzer Space Telescope)
ISCS: IRAC Shallow Cluster Survey
JDEM: Joint Dark Energy Mission
JEDI: Joint Efficient Dark-energy Investigation
JPAS: Javalambre Physics of the Accelerating Universe Astrophysical Survey
JWST: James Webb Space Telescope
KIDS: Kilo-Degree Survey
LCS: Light Curve Shape
LIGO: Laser Interferometer Gravitational Wave Observatory
LOSS: Lick Observatory Supernova Survey
LRG: Luminous Red Galaxy
LSST: Large Synoptic Survey Telescope
NASA: National Aeronautics and Space Administration
NOAO: National Optical Astronomy Observatories
NVSS: NRAO VLA Sky Survey
Pan-STARRS: Panoramic Survey Telescope and Rapid Response System
PAU: Physics of the Accelerating Universe
PCA: Principal Component Analysis
Planck: Planck CMB satellite (ESA)
PS1: Pan-STARRS 1
PSF: Point Spread Function
PTF: Palomar Transient Factory
RASS: ROSAT All Sky Survey
RCS: Red-Sequence Cluster Survey
ROSAT: Roentgen Satellite
SDSS: Sloan Digital Sky Survey
SED: Spectral Energy Distribution
SFR: Star Formation Rate
SKA: Square Kilometer Array
SN: Supernova
SNAP: Supernova Acceleration Probe
SNLS: Supernova Legacy Survey (part of CFHTLS)
SNR: Signal-to-Noise Ratio
SPT: South Pole Telescope

STEP: Satellite Test of Equivalence Principle
 SuMIRe: Subaru Measurement of Images and Redshifts
 2SLAQ: 2dF and SDSS Large Area Quasar survey
 VHS: VISTA Hemisphere Survey
 VLBI: Very Long Baseline Interferometry
 VIKING: VISTA Kilo-Degree Infrared Galaxy Survey
 VIRGO: VIRGO gravity wave observatory
 VVDS: VIMOS-VLT Deep Survey
 UKIDSS: UKIRT Infrared Deep Sky Survey
 WFC3: Wide-Field Camera 3 (on Hubble Space Telescope)
 WFPC2: Wide-Field and Planetary Camera 2 (on Hubble Space Telescope)
 WFIRST: Wide Field Infrared Survey Telescope
 WiggleZ: WiggleZ galaxy redshift survey
 WISE: Wide-field Infrared Survey Explorer
 WL: Weak Lensing
 WMAP: Wilkinson Microwave Anisotropy Probe (NASA)
 XMM-Newton: X-ray Multi-Mirror Mission

References

- Abazajian, K.N., Adelman-McCarthy, J.K., Agüeros, M.A., Allam, S.S., Allende Prieto, C., An, D., et al., 2009. The seventh data release of the Sloan Digital Sky Survey. *ApJS* 182 (Jun.), 543–558.
- Abdalla F., Annis J., Bacon D., Bridle S., Castander F., Colless M., et al. 2012. The dark energy spectrometer (DESPEC): a multi-fiber spectroscopic upgrade of the dark energy camera and survey for the Blanco telescope. arXiv:1209.2451.
- Abdalla, F.B., Rawlings, S., 2005. Probing dark energy with baryonic oscillations and future radio surveys of neutral hydrogen. *MNRAS* 360 (Jun.), 27–40.
- Abell, G.O., 1958. The distribution of rich clusters of galaxies. *ApJS* 3 (May), 211–+.
- Acquaviva, V., Hajian, A., Spergel, D.N., Das, S., 2008. Next generation redshift surveys and the origin of cosmic acceleration. *Phys. Rev. D* 78, 043514.
- Adami, C., Durret, F., Benoist, C., Coupon, J., Mazure, A., Meneux, B., et al., 2010. Galaxy structure searches by photometric redshifts in the CFHTLS. *A&A* 509 (Jan.), A81+.
- Afshordi, N., Loh, Y.-S., Strauss, M.A., 2004. Cross-correlation of the cosmic microwave background with the 2MASS galaxy survey: signatures of dark energy, hot gas, and point sources. *Phys. Rev. D* 69 (8), 083524.
- Albrecht A., Amendola L., Bernstein G., Clowe D., Eisenstein D., Guzzo L., et al. 2009. Findings of the joint dark energy mission figure of merit science working group. arXiv:0901.0721.
- Albrecht, A., Bernstein, G., 2007. Evaluating dark energy probes using multidimensional dark energy parameters. *Phys. Rev. D* 75, 103003.
- Albrecht, A., Bernstein, G., Cahn, R., Freedman, W.L., Hewitt, J., Hu, W., et al., 2006. Report of the Dark Energy Task Force. arXiv:astro-ph/0609591.
- Alcock, C., Paczynski, B., 1979. An evolution free test for non-zero cosmological constant. *Nature* 281, 358–359.
- Aldering, G., Akerlof, C.W., Amanullah, R., Astier, P., Barrelet, E., Bebek, C., et al., 2002. Overview of the supernova/acceleration probe (SNAP). In: Society of Photo-Optical Instrumentation Engineers (SPIE) Conference Series, vol. 4835. pp. 146–157.
- Allen, S.W., Evrard, A.E., Mantz, A.B., 2011. Cosmological parameters from observations of galaxy clusters. *ARA&A* 49 (Sep.), 409–470.
- Allen, S.W., Schmidt, R.W., Fabian, A.C., Ebeling, H., 2003. Cosmological constraints from the local X-ray luminosity function of the most X-ray-luminous galaxy clusters. *MNRAS* 342 (Jun.), 287–298.
- Amanullah, R., Lidman, C., Rubin, D., Aldering, G., Astier, P., Barbary, K., Supernova Cosmology Project., 2010. Spectra and Hubble space telescope light curves of six type Ia supernovae at $0.511 < z < 1.12$ and the Union2 compilation. *ApJ* 716 (Jun.), 712–738.
- Amara, A., Kitching, T.D., 2011. Figures of merit for testing standard models: application to dark energy experiments in cosmology. *MNRAS* 413 (May), 1505–1514.
- Amati, L., 2006. The Ep, *i*-Eiso correlation in GRBs: updated observational status, re-analysis and main implications. *MNRAS* 372, 233–245.
- Amendola, L., Kainulainen, K., Marra, V., Quartin, M., 2010. Large-scale inhomogeneities may improve the cosmic concordance of supernovae. *Phys. Rev. Lett.* 105 (12), 121302.
- Amendola, L., Quercellini, C., Giallongo, E., 2005. Constraints on perfect fluid and scalar field dark energy models from future redshift surveys. *MNRAS* 357, 429–439.
- Anderson, L., Aubourg, E., Bailey, S., Bizyaev, D., Blanton, M., Bolton, A.S., et al., 2012. The clustering of galaxies in the SDSS-III baryon oscillation spectroscopic survey: baryon acoustic oscillations in the data release 9 spectroscopic galaxy sample. *MNRAS* 427 (Dec.), 3435–3467.
- Andreon, S., Moretti, A., 2011. Do X-ray dark or underluminous galaxy clusters exist? *A&A* 536 (Dec.), A37.
- Angulo, R., Baugh, C.M., Frenk, C.S., Bower, R.G., Jenkins, A., Morris, S.L., 2005. Constraints on the dark energy equation of state from the imprint of baryons on the power spectrum of clusters. *MNRAS* 362 (Sep.), L25–L29.
- Angulo, R.E., Baugh, C.M., Frenk, C.S., Lacey, C.G., 2008. The detectability of baryonic acoustic oscillations in future galaxy surveys. *MNRAS* 383 (Jan.), 755–776.
- Angulo, R.E., Springel, V., White, S.D.M., Jenkins, A., Baugh, C.M., Frenk, C.S., 2012. Scaling relations for galaxy clusters in the millennium-XXL simulation. *MNRAS* 426 (Nov.), 2046–2062.
- Ansari R., Le Goff J., Magneville C., Moniez M., Palanque-Delabrouille N., Rich J., Ruhlmann-Kleider V., Yèche C., 2008. Reconstruction of HI power spectra with radio-interferometers to study dark energy. arXiv:0807.3614.
- Armendariz-Picon, C., Mukhanov, V.F., Steinhardt, P.J., 2001. Essentials of *k*-essence. *Phys. Rev. D* 63, 103510.
- Arnalte-Mur, P., Labatie, A., Clerc, N., Martínez, V.J., Starck, J.-L., Lachièze-Rey, M., Saar, E., Paredes, S., 2012. Wavelet analysis of baryon acoustic structures in the galaxy distribution. *A&A* 542 (Jun.), A34.
- Arun, K.G., Iyer, B.R., Sathyaprakash, B.S., Sinha, S., Broeck, C.V.D., 2007. Higher signal harmonics, LISA's angular resolution and dark energy. *Phys. Rev. D* 76, 104016.
- Astier, P., Guy, J., Regnault, N., Pain, R., Aubourg, E., Balam, D., et al., 2006. The supernova legacy survey: measurement of Ω_M , Ω and *w* from the first year data set. *A&A* 447 (Feb.), 31–48.
- Astier, P., Pain, R., 2012. Observational evidence of the accelerated expansion of the universe. *Comptes Rendus Physique* 13 (Jul.), 521–538.
- Babul, A., White, S.D.M., 1991. Quasar-modulated galaxy clustering in a cold dark matter universe. *MNRAS* 253 (Dec.), 31P–34P.
- Bacon, D.J., Massey, R.J., Refregier, A.R., Ellis, R.S., 2003. Joint cosmic shear measurements with the Keck and William Herschel telescopes. *MNRAS* 344, 673.
- Bacon, D.J., Refregier, A.R., Ellis, R.S., 2000. Detection of weak gravitational lensing by large-scale structure. *MNRAS* 318, 625.
- Bacon, D.J., Taylor, A.N., Brown, M.L., Gray, M.E., Wolf, C., Meisenheimer, K., Dye, S., Wisotzki, L., Borch, A., Kleinheinrich, M., 2005. Evolution of the dark matter distribution with three-dimensional weak lensing. *MNRAS* 363 (Nov.), 723–733.

- Bahcall, N.A., Dong, F., Bode, P., Kim, R., Annis, J., McKay, T.A., et al., 2003. The cluster mass function from early sloan digital sky survey data: cosmological implications. *ApJ* 585 (Mar.), 182–190.
- Balbi, A., Quercellini, C., 2007. The time evolution of cosmological redshift as a test of dark energy. *MNRAS* 382 (Dec.), 1623–1629.
- Baldauf, T., Smith, R.E., Seljak, U., Mandelbaum, R., 2010. An algorithm for the direct reconstruction of the dark matter correlation function from weak lensing and galaxy clustering. *Phys. Rev. D* 81, 063531.
- Baldwin, J.A., 1977. Luminosity indicators in the spectra of quasi-stellar objects. *ApJ* 214 (Jun.), 679–684.
- Ballinger, W.E., Peacock, J.A., Heavens, A.F., 1996. Measuring the cosmological constant with redshift surveys. *MNRAS* 282, 877–888.
- Barausse, E., Matarrese, S., Riotto, A., 2005. Effect of inhomogeneities on the luminosity distance–redshift relation: Is dark energy necessary in a perturbed universe? *Phys. Rev. D* 71 (6), 063537.
- Bardeen, J.M., Bond, J.R., Kaiser, N., Szalay, A.S., 1986. The statistics of peaks of Gaussian random fields. *ApJ* 304, 15–61.
- Barnard, M., Abrahamse, A., Albrecht, A., Bozek, B., Yashar, M., 2008. A measure of the impact of future dark energy experiments based on discriminating power among quintessence models. *Phys. Rev. D* 78, 043528.
- Barone-Nugent, R.L., Lidman, C., Wyithe, J.S.B., Mould, J., Howell, D.A., Hook, I.M., et al., 2012. Near-infrared observations of type Ia supernovae: the best known standard candle for cosmology. *MNRAS* 425 (Sep.), 1007–1012.
- Bartelmann, M., Schneider, P., 2001. Weak gravitational lensing. *Phys. Rept.* 340, 291–472.
- Bassett, B.A., 2005. Optimizing cosmological surveys in a crowded market. *Phys. Rev. D* 71 (8), 083517.
- Battaglia, N., Bond, J.R., Pfrommer, C., Sievers, J.L., 2012. On the cluster physics of Sunyaev–Zel’dovich and X-ray surveys. I. The influence of feedback, non-thermal pressure, and cluster shapes on Y–M scaling relations. *ApJ* 758 (Oct.), 74.
- Bauer, A.H., Seitz, S., Jerke, J., Scalzo, R., Rabinowitz, D., Ellman, N., Baltay, C., 2011. Measuring lensing magnification of quasars by large scale structure using the variability–luminosity relation. *ApJ* 732 (May), 64.
- Baumann, D., Nocolis, A., Senatore, L., Zalduendo, M., 2012. Cosmological non-linearities as an effective fluid. *JCAP* 7 (Jul.), 51.
- Bean, R., Doré, O., 2004. Probing dark energy perturbations: the dark energy equation of state and speed of sound as measured by WMAP. *Phys. Rev. D* 69 (8), 083503.
- Bean, R., Tangmatitham, M., 2010. Current constraints on the cosmic growth history. *Phys. Rev. D* 81, 083534.
- Becker, M.R., Kravtsov, A.V., 2011. On the accuracy of weak-lensing cluster mass reconstructions. *ApJ* 740 (Oct.), 25.
- Belenkiy, A., 2012. Alexander Friedmann and the origins of modern cosmology. *Phys. Today* 65 (Oct.), 38–43.
- Benedict, G.F., et al., 2007. Hubble space telescope fine guidance sensor parallaxes of galactic cepheid variable stars: period–luminosity relations. *AJ* 133, 1810–1827.
- Benítez, N., Gaztañaga, E., Miquel, R., Castander, F., Moles, M., Crocco, M., et al., 2009. Measuring baryon acoustic oscillations along the line of sight with photometric redshifts: the PAU survey. *ApJ* 691 (Jan.), 241–260.
- Benjamin, J., Heymans, C., Semboloni, E., van Waerbeke, L., Hoekstra, H., Erben, T., Gladders, M.D., Hetterscheidt, M., Mellier, Y., Yee, H.K.C., 2007. Cosmological constraints from the 100–deg² weak-lensing survey. *MNRAS* 381 (Oct.), 702–712.
- Benjamin, J., Van Waerbeke, L., Heymans, C., Kilbinger, M., Erben, T., Hildebrandt, H., et al., 2013. CFHTLenS tomographic weak lensing: quantifying accurate redshift distributions. *MNRAS* 431, 1547.
- Bennett, C.L., Halpern, M., Hinshaw, G., Jarosik, N., Kogut, A., Limon, M., et al., 2003. First-year Wilkinson microwave anisotropy probe (WMAP) observations: preliminary maps and basic results. *ApJS* 148 (Sep.), 1–27.
- Benson, B.A., de Haan, T., Dudley, J.P., Reichardt, C.L., Aird, K.A., Andersson, K., et al., 2013. Cosmological constraints from Sunyaev–Zel’dovich–Selected clusters with X-ray observations in the first 178 square degrees of the south pole telescope survey. *ApJ* 763, 147.
- Bentz, M.C., Peterson, B.M., Netzer, H., Pogge, R.W., Vestergaard, M., 2009. The radius–luminosity relationship for active galactic nuclei: the effect of host-galaxy starlight on luminosity measurements II. The full sample of reverberation–mapped AGNs. *ApJ* 697, 160–181.
- Bergé, J., Price, S., Amara, A., Rhodes, J., 2012. On point spread function modelling: towards optimal interpolation. *MNRAS* 419 (Jan.), 2356–2368.
- Berlind, A.A., Frieman, J., Weinberg, D.H., Blanton, M.R., Warren, M.S., Abazajian, K., et al., 2006. Percolation galaxy groups and clusters in the SDSS redshift survey: identification, catalogs, and the multiplicity function. *ApJS* 167 (Nov.), 1–25.
- Berlind, A.A., Weinberg, D.H., 2002. The Halo occupation distribution: towards an empirical determination of the relation between galaxies and mass. *ApJ* 575, 587–616.
- Bernardeau, F., van Waerbeke, L., Mellier, Y., 1997. Weak lensing statistics as a probe of Ω and power spectrum. *A&A* 322 (Jun.), 1–18.
- Bernstein, G., 2006. Metric tests for curvature from weak lensing and baryon acoustic oscillations. *ApJ* 637 (Feb.), 598–607.
- Bernstein, G.M., 2009. Comprehensive two-point analyses of weak gravitational lensing surveys. *ApJ* 695, 652–665.
- Bernstein, G.M., 2010. Shape measurement biases from underfitting and ellipticity gradients. *MNRAS* 406 (Aug.), 2793–2804.
- Bernstein, G.M., Cai, Y.-C., 2011. Cosmology without cosmic variance. *MNRAS* 416 (Oct.), 3009–3016.
- Bernstein, G.M., Jain, B., 2004. Dark energy constraints from weak lensing cross-correlation cosmography. *ApJ* 600, 17–25.
- Bernstein, G.M., Jarvis, M., 2002. Shapes and shears, stars and smears: optimal measurements for weak lensing. *AJ* 123, 583–618.
- Bernstein, G.M., Norberg, P., 2002. Shape alignments of satellite galaxies. *AJ* 124 (Aug.), 733–736.
- Bernstein, J.P., Kessler, R., Kuhlmann, S., Biswas, R., Kovacs, E., Aldering, G., et al., 2012. Supernova simulations and strategies for the dark energy survey. *ApJ* 753 (Jul.), 152.
- Bertin, G., Lombardi, M., 2006. Looking at the fundamental plane through a gravitational lens. *ApJ* 648, L17–L20.
- Bertone, G., Hooper, D., Silk, J., 2005. Particle dark matter: evidence, candidates and constraints. *Phys. Rep.* 405 (Jan.), 279–390.
- Bertotti, B., Iess, L., Tortora, P., 2003. A test of general relativity using radio links with the Cassini spacecraft. *Nature* 425 (Sep.), 374–376.
- Beutler, F., Blake, C., Colless, M., Jones, D.H., Staveley-Smith, L., Campbell, L., Parker, Q., Saunders, W., Watson, F., 2011. The 6dF galaxy survey: baryon acoustic oscillations and the local Hubble constant. *MNRAS* 416 (Oct.), 3017–3032.
- Beutler, F., Blake, C., Colless, M., Jones, D.H., Staveley-Smith, L., Poole, G.B., Campbell, L., Parker, Q., Saunders, W., Watson, F., 2012. The 6dF galaxy survey: $z \approx 0$ measurements of the growth rate and σ_8 . *MNRAS* 423 (Jul.), 3430–3444.
- Bhattacharya, S., Heitmann, K., White, M., Lukić, Z., Wagner, C., Habib, S., 2011. Mass function predictions beyond Λ CDM. *ApJ* 732 (May), 122–+.
- Biesiadzinski, T., McMahon, J., Miller, C.J., Nord, B., Shaw, L., 2012. Impact of systematics on SZ-optical scaling relations. *ApJ* 757 (Sep.), 1.
- Blackburne, J.A., Kochanek, C.S., 2012. The structure of 2MASS galaxy clusters. *ApJ* 744 (Jan.), 76.
- Blake, C., Bridle, S., 2005. Cosmology with photometric redshift surveys. *MNRAS* 363 (Nov.), 1329–1348.
- Blake, C., Brough, S., Colless, M., Contreras, C., Couch, W., Croom, S., et al., 2011a. The WiggleZ dark energy survey: the growth rate of cosmic structure since redshift $z = 0.9$. *MNRAS* 415 (Aug.), 2876–2891.
- Blake, C., Collister, A., Bridle, S., Lahav, O., 2007. Cosmological baryonic and matter densities from 600000 SDSS luminous red galaxies with photometric redshifts. *MNRAS* 374 (Feb.), 1527–1548.
- Blake, C., Davis, T., Poole, G.B., Parkinson, D., Brough, S., Colless, M., et al., 2011b. The WiggleZ dark energy survey: testing the cosmological model with baryon acoustic oscillations at $z = 0.6$. *MNRAS* 415 (Aug.), 2892–2909.
- Blake, C., Glazebrook, K., 2003. Probing dark energy using baryonic oscillations in the galaxy power spectrum as a cosmological ruler. *ApJ* 594 (Sep.), 665–673.
- Blake, C., Glazebrook, K., Davis, T.M., Brough, S., Colless, M., Contreras, C., et al., 2011c. The WiggleZ dark energy survey: measuring the cosmic expansion history using the Alcock–Paczynski test and distant supernovae. *MNRAS* 418 (Dec.), 1725–1735.
- Blake, C., Kazin, E.A., Beutler, F., Davis, T.M., Parkinson, D., Brough, S., et al., 2011d. The WiggleZ dark energy survey: mapping the distance–redshift relation with baryon acoustic oscillations. *MNRAS* 1598–+.
- Blake, C., Parkinson, D., Bassett, B., Glazebrook, K., Kunz, M., Nichol, R.C., 2006. Universal fitting formulae for baryon oscillation surveys. *MNRAS* 365 (Jan.), 255–264.
- Blake, C.A., Abdalla, F.B., Bridle, S.L., Rawlings, S., 2004. Cosmology with the square kilometre array. *New Astron. Rev.* 48, 1063–1077.

- Blanchard, A., 2010. Evidence for the fifth element astrophysical status of dark energy. *Astron. Astrophys. Rev.* 18, 595–645.
- Blandford, R.D., Saust, A.B., Brainerd, T.G., Villumsen, J.V., 1991. The distortion of distant galaxy images by large-scale structure. *MNRAS* 251 (Aug.), 600–627.
- Blazek, J., McQuinn, M., Seljak, U., 2011. Testing the tidal alignment model of galaxy intrinsic alignment. *JCAP* 1105, 010.
- Bleem, L.E., van Engelen, A., Holder, G.P., Aird, K.A., Armstrong, R., Ashby, M.L.N., et al., 2012. A measurement of the correlation of galaxy surveys with CMB lensing convergence maps from the south pole telescope. *ApJ Lett.* 753 (Jul.), L9.
- Block D.L., 2011. A Hubble eclipse: lemaître and censorship. *arXiv:1106.3928*.
- Blondin, S., Matheson, T., Kirshner, R.P., Mandel, K.S., Berlind, P., Calkins, M., et al., 2012. The spectroscopic diversity of type Ia supernovae. *AJ* 143 (May), 126.
- Böhringer, H., Schuecker, P., Guzzo, L., Collins, C.A., Voges, W., Cruddace, R.G., et al., 2004. The ROSAT-ESO flux limited X-ray (REFLEX) galaxy cluster survey. V. The cluster catalogue. *A&A* 425 (Oct.), 367–383.
- Böhringer, H., Voges, W., Huchra, J.P., Mclean, B., Giacconi, R., Rosati, P., et al., 2000. The northern ROSAT all-sky (NORAS) galaxy cluster survey. I. X-ray properties of clusters detected as extended X-ray sources. *ApJS* 129 (Aug.), 435–474.
- Bolton, A.S., Rappaport, S., Burles, S., 2006. Constraint on the post-Newtonian parameter γ on galactic size scales. *Phys. Rev. D* 74 (6), 061501.
- Bond, J.R., Cole, S., Efstathiou, G., Kaiser, N., 1991. Excursion set mass functions for hierarchical Gaussian fluctuations. *ApJ* 379, 440.
- Bond, J.R., Efstathiou, G., 1984. Cosmic background radiation anisotropies in universes dominated by nonbaryonic dark matter. *ApJ Lett.* 285 (Oct.), L45–L48.
- Bond, J.R., Efstathiou, G., 1987. The statistics of cosmic background radiation fluctuations. *MNRAS* 226 (Jun.), 655–687.
- Book, L., Kamionkowski, M., Schmidt, F., 2012. Lensing of 21-cm fluctuations by primordial gravitational waves. *Phys. Rev. Lett.* 108 (21), 211301.
- Boughn, S.P., Crittenden, R.G., 2004. The large-scale bias of the hard X-ray background. *ApJ* 612 (Sep.), 647–651.
- Boughn, S.P., Crittenden, R.G., Turok, N.G., 1998. Correlations between the cosmic X-ray and microwave backgrounds: constraints on a cosmological constant. *NewA* 3 (Jul.), 275–291.
- Bower, R.G., Coles, P., Frenk, C.S., White, S.D.M., 1993. Cooperative galaxy formation and large-scale structure. *ApJ* 405 (Mar.), 403–412.
- Boyle, L.A., Caldwell, R.R., Kamionkowski, M., 2002. Spintessence! New models for dark matter and dark energy. *Phys. Lett. B* 545 (Oct.), 17–22.
- Brainerd, T.G., Blandford, R.D., Smail, I., 1996. Measuring galaxy masses using galaxy–galaxy gravitational lensing. *ApJ* 466, 623.
- Brandenberger R.H., 2002. Back reaction of cosmological perturbations and the cosmological constant problem. *hep-th/0210165*.
- Bridle, S., Balan, S.T., Bethge, M., Gentile, M., Harmeling, S., Heymans, C., et al., 2010. Results of the GREAT08 challenge: an image analysis competition for cosmological lensing. *MNRAS* 405 (Jul.), 2044–2061.
- Bridle, S., King, L., 2007. Dark energy constraints from cosmic shear power spectra: impact of intrinsic alignments on photometric redshift requirements. *New J. Phys.* 9, 444.
- Bridle, S.L., Kneib, J.-P., Bardeau, S., Gull, S.F., 2002. Bayesian galaxy shape estimation. In: Natarajan, P. (Ed.), *The Shapes of Galaxies and their Dark Halos*. pp. 38–46.
- Brodwin, M., Brown, M.J.I., Ashby, M.L.N., Bian, C., Brand, K., Dey, A., et al., 2006. Photometric redshifts in the IRAC shallow survey. *ApJ* 651 (Nov.), 791–803.
- Brodwin, M., Gonzalez, A.H., Stanford, S.A., Plagge, T., Marrone, D.P., Carlstrom, J.E., et al., 2012. IDCS J1426.5+3508: Sunyaev–Zel’dovich measurement of a massive infrared-selected cluster at $z = 1.75$. *ApJ* 753 (Jul.), 162.
- Brodwin, M., Stern, D., Vikhlinin, A., Stanford, S.A., Gonzalez, A.H., et al., 2011. X-ray emission from two infrared-selected galaxy clusters at $z > 1.4$ in the IRAC shallow cluster survey. *ApJ* 732 (May), 33.
- Brown, M.L., Battye, R.A., 2011. Polarization as an indicator of intrinsic alignment in radio weak lensing. *MNRAS* 410 (Jan.), 2057–2074.
- Brown, M.L., Taylor, A.N., Bacon, D.J., Gray, M.E., Dye, S., Meisenheimer, K., Wolf, C., 2003. The shear power spectrum from the COMBO-17 survey. *MNRAS* 341 (May), 100–118.
- Bruzual, G., Charlot, S., 2003. Stellar population synthesis at the resolution of 2003. *MNRAS* 344, 1000.
- Bucher, M., Goldhaber, A.S., Turok, N., 1995. An open universe from inflation. *Phys. Rev. D* 52, 3314–3337.
- Buchert, T., 2011. Toward physical cosmology: focus on inhomogeneous geometry and its non-perturbative effects. *Classical Quantum Gravity* 28 (16), 164007.
- Bullock, J.S., Kolatt, T.S., Sigad, Y., Somerville, R.S., Kravtsov, A.V., Klypin, A.A., Primack, J.R., Dekel, A., 2001. Profiles of dark haloes: evolution, scatter and environment. *MNRAS* 321 (Mar.), 559–575.
- Burenin, R.A., Vikhlinin, A., Hornstrup, A., Ebeling, H., Quintana, H., Mescheryakov, A., 2007. The 400 square degree ROSAT PSPC Galaxy cluster survey: catalog and statistical calibration. *ApJS* 172 (Oct.), 561–582.
- Burke, D.J., Collins, C.A., Sharples, R.M., Romer, A.K., Nichol, R.C., 2003. The southern SHARC catalogue: a ROSAT survey for distant galaxy clusters. *MNRAS* 341 (Jun.), 1093–1108.
- Busca N.G., Delubac T., Rich J., Bailey S., Font-Ribera A., Kirkby D., et al. 2012. Baryon Acoustic Oscillations in the Ly- α forest of BOSS quasars. *arXiv:1211.2616*.
- Cabr e, A., Gazta aga, E., 2011. Have baryonic acoustic oscillations in the galaxy distribution really been measured? *MNRAS* 412 (Mar.), L98–L102.
- Cai, Y.-C., Bernstein, G., 2012. Combining weak-lensing tomography and spectroscopic redshift surveys. *MNRAS* 422 (May), 1045–1056.
- Caldwell, R.R., Linder, E.V., 2005. The limits of quintessence. *Phys. Rev. Lett.* 95, 141301.
- Campbell, H., D’andrea, C.B., Nichol, R.C., Sako, M., Smith, M., Lampeitl, H., et al., 2013. Cosmology with photometrically-classified type Ia supernovae from the SDSS-II supernova survey. *ApJ* 763, 88.
- Capozziello, S., Cardone, V.F., Funaro, M., Andreon, S., 2004. Constraining dark energy models using the lookback time to galaxy clusters and the age of the universe. *Phys. Rev. D* 70 (12), 123501.
- Capozziello, S., Fang, L.Z., 2002. Curvature quintessence. *Internat. J. Modern Phys. D* 11, 483–491.
- Carbone, C., Mangilli, A., Verde, L., 2011. Isocurvature modes and Baryon acoustic oscillations II: gains from combining CMB and large scale structure. *JCAP* 9 (Sep.), 28–+.
- Cardelli, J.A., Clayton, G.C., Mathis, J.S., 1989. The relationship between infrared, optical, and ultraviolet extinction. *ApJ* 345 (Oct.), 245–256.
- Carlberg, R.G., Yee, H.K.C., Ellingson, E., Morris, S.L., Abraham, R., Gravel, P., et al., 1997. The average mass profile of galaxy clusters. *ApJ Lett.* 485 (Aug.), L13.
- Carlson, J., White, M., Padmanabhan, N., 2009. A critical look at cosmological perturbation theory techniques. *Phys. Rev. D* 80, 043531.
- Carroll S.M., 2003. Why is the universe accelerating? *astro-ph/0310342*.
- Carroll, S.M., Duvvuri, V., Trodden, M., Turner, M.S., 2004. Is cosmic speed-up due to new gravitational physics? *Phys. Rev. D* 70 (4), 043528.
- Catelan, P., Kamionkowski, M., Blandford, R.D., 2001. Intrinsic and extrinsic galaxy alignment. *MNRAS* 320 (Jan.), L7–L13.
- Chaboyer, B., 1998. The age of the universe. *Phys. Rept.* 307, 23–30.
- Chaboyer, B., Demarque, P., Kernan, P.J., Krauss, L.M., 1996. A lower limit on the age of the universe. *Science* 271 (Feb.), 957–961.
- Chang, P., Hui, L., 2011. Stellar structure and tests of modified gravity. *ApJ* 732, 25.
- Chang, T.-C., Pen, U.-L., Bandura, K., Peterson, J.B., 2010. An intensity map of hydrogen 21-cm emission at redshift $z \sim 0.8$. *Nature* 466 (Jul.), 463–465.
- Chang, T.-C., Pen, U.-L., Peterson, J.B., McDonald, P., 2008. Baryon acoustic oscillation intensity mapping of dark energy. *Phys. Rev. Lett.* 100 (9), 091303–+.
- Chang, T.-C., Refregier, A., Helfand, D.J., 2004. Weak lensing by large-scale structure with the FIRST radio survey. *ApJ* 617, 794–810.
- Chevallier, M., Polarski, D., 2001. Accelerating universes with scaling dark matter. *Internat. J. Modern Phys. D* 10, 213–223.
- Chiba, T., 2003. $1/R$ gravity and scalar-tensor gravity. *Phys. Lett. B* 575 (Nov.), 1–3.
- Chotard, N., Gangler, E., Aldering, G., Antilogus, P., Aragon, C., Bailey, S., 2011. The reddening law of type Ia supernovae: separating intrinsic variability from dust using equivalent widths. *A&A* 529 (May), L4. Nearby Supernova Factory.
- Chuang, C.-H., Wang, Y., 2012. Measurements of $H(z)$ and $D_A(z)$ from the two-dimensional two-point correlation function of Sloan Digital Sky Survey luminous red galaxies. *MNRAS* 426 (Oct.), 226–236.
- Clowe, D., Brada c, M., Gonzalez, A.H., Markevitch, M., Randall, S.W., Jones, C., Zaritsky, D., 2006. A direct empirical proof of the existence of dark matter. *ApJ Lett.* 648 (Sep.), L109–L113.

- Coe, D., Moustakas, L.A., 2009. Cosmological constraints from gravitational lens time delays. *ApJ* 706 (Nov.), 45–59.
- Cohn, J.D., Evrard, A.E., White, M., Croton, D., Ellingson, E., 2007. Red-sequence cluster finding in the millennium simulation. *MNRAS* 382 (Dec), 1738–1750.
- Coil, A.L., Gerke, B.F., Newman, J.A., Ma, C., Yan, R., Cooper, M.C., Davis, M., Faber, S.M., Guhathakurta, P., Koo, D.C., 2006. The DEEP2 galaxy redshift survey: clustering of groups and group galaxies at $z \sim 1$. *ApJ* 638 (Feb.), 668–685.
- Cole, S., Fisher, K.B., Weinberg, D.H., 1994. Fourier analysis of redshift space distortions and the determination of Ω . *MNRAS* 267, 785.
- Cole, S., Fisher, K.B., Weinberg, D.H., 1995. Constraints on Ω from the IRAS redshift surveys. *MNRAS* 275, 515.
- Cole, S., Kaiser, N., 1989. Biased clustering in the cold dark matter cosmogony. *MNRAS* 237 (Apr.), 1127–1146.
- Cole, S., Percival, W.J., Peacock, J.A., Norberg, P., Baugh, C.M., Frenk, C.S., et al., 2005. The 2dF galaxy redshift survey: power-spectrum analysis of the final data set and cosmological implications. *MNRAS* 362 (Sep.), 505–534.
- Cole, S., Weinberg, D.H., Frenk, C.S., Ratra, B., 1997. Large-scale structure in COBE-normalized cold dark matter cosmogonies. *MNRAS* 289, 37.
- Colombo, L.P.L., Pierpaoli, E., 2009. Model independent approaches to reionization in the analysis of upcoming CMB data. *NewAst* 14 (Apr.), 269–276.
- Committee on the Physics of the Universe, 2003. *Connecting Quarks with the Cosmos: Eleven Science Questions for the New Century*. National Academies Press, Washington, D.C.
- Conley, A., Guy, J., Sullivan, M., Regnault, N., Astier, P., Balam, D., et al., 2011. Supernova constraints and systematic uncertainties from the first three years of the supernova legacy survey. *ApJS* 192 (Jan.), 1–+.
- Conley, A., Sullivan, M., Hsiao, E.Y., Guy, J., Astier, P., Balam, D., et al., 2008. SiFTO: an empirical method for fitting SN Ia light curves. *ApJ* 681 (Jul.), 482–498.
- Conroy, C., Wechsler, R.H., Kravtsov, A.V., 2006. Modeling luminosity-dependent galaxy clustering through cosmic time. *ApJ* 647, 201–214.
- Contreras, C., Hamuy, M., Phillips, M.M., Folatelli, G., Suntzeff, N.B., Persson, S.E., et al., 2010. The Carnegie supernova project: first photometry data release of low-redshift type Ia supernovae. *AJ* 139 (Feb.), 519–539.
- Cooray, A., Hu, W., 2001. Weak gravitational lensing bispectrum. *ApJ* 548 (Feb.), 7–18.
- Copeland, E.J., Sami, M., Tsujikawa, S., 2006. Dynamics of dark energy. *Internat. J. Modern Phys. D* 15, 1753–1935.
- Corasaniti, P.-S., Huterer, D., Melchiorri, A., 2007. Exploring the dark energy redshift desert with the Sandage-Loeb test. *Phys. Rev. D* 75, 062001.
- Crittenden, R.G., Pogosian, L., Zhao, G.-B., 2009. Investigating dark energy experiments with principal components. *JCAP* 0912, 025.
- Crittenden, R.G., Zhao, G.-B., Pogosian, L., Samushia, L., Zhang, X., 2012. Fables of reconstruction: controlling bias in the dark energy equation of state. *JCAP* 2 (Feb.), 48.
- Crocce, M., Gaztañaga, E., Cabré, A., Carnero, A., Sánchez, E., 2011. Clustering of photometric luminous red galaxies - I. Growth of structure and baryon acoustic feature. *MNRAS* 417 (Nov.), 2577–2591.
- Crocce, M., Scoccimarro, R., 2008. Nonlinear evolution of baryon acoustic oscillations. *Phys. Rev. D* 77 (2), 023533–+.
- Croft, R.A.C., Gaztanaga, E., 1997. Reconstruction of cosmological density and velocity fields in the Lagrangian Zel'dovich approximation. *MNRAS* 285 (Mar.), 793–805.
- Croft, R.A.C., Weinberg, D.H., Katz, N., Hernquist, L., 1998. Recovery of the power spectrum of mass fluctuations from observations of the Lyman-alpha forest. *ApJ* 495, 44.
- Croft, R.A.C., et al., 2002. Towards a precise measurement of matter clustering: Lyman- alpha forest data at redshifts 2–4. *ApJ* 581, 20–52.
- Cui, W., Borgani, S., Dolag, K., Murante, G., Tornatore, L., 2012. The effects of baryons on the halo mass function. *MNRAS* 423 (Jul.), 2279–2287.
- Cunha, C., 2009. Cross-calibration of cluster mass observables. *Phys. Rev. D* 79 (6), 063009–+.
- Cunha, C., Huterer, D., Doré, O., 2010. Primordial non-Gaussianity from the covariance of galaxy cluster counts. *Phys. Rev. D* 82 (2), 023004.
- Cunha, C., Huterer, D., Frieman, J.A., 2009. Constraining dark energy with clusters: complementarity with other probes. *Phys. Rev. D* 80 (6), 063532–+.
- Cunha, C.E., Evrard, A.E., 2010. Sensitivity of galaxy cluster dark energy constraints to halo modeling uncertainties. *Phys. Rev. D* 81 (8), 083509.
- Cutler, C., Holz, D.E., 2009. Ultrahigh precision cosmology from gravitational waves. *Phys. Rev. D* 80 (10), 104009–+.
- Cypriano, E.S., Amara, A., Voigt, L.M., Bridle, S.L., Abdalla, F.B., Réfrégier, A., Seiffert, M., Rhodes, J., 2010. Cosmic shear requirements on the wavelength dependence of telescope point spread functions. *MNRAS* 405 (Jun.), 494–502.
- Dalal, N., Doré, O., Huterer, D., Shirokov, A., 2008. Imprints of primordial non-Gaussianities on large-scale structure: scale-dependent bias and abundance of virialized objects. *Phys. Rev. D* 77 (12), 123514.
- Dalal, N., Holz, D.E., Hughes, S.A., Jain, B., 2006. Short GRB and binary black hole standard sirens as a probe of dark energy. *Phys. Rev. D* 74, 063006.
- D'Aloisio, A., Natarajan, P., 2011. Cosmography with cluster strong lenses: the influence of substructure and line-of-sight haloes. *MNRAS* 411 (Mar.), 1628–1640.
- Daly, R.A., 1994. Cosmology with powerful extended radio sources. *ApJ* 426 (May), 38–50.
- Daly, R.A., Guerra, E.J., 2002. Quintessence, cosmology, and FRIB radio galaxies. *AJ* 124, 1831.
- Daly, R.A., Mory, M.P., O’dea, C.P., Kharb, P., Baum, S., Guerra, E.J., Djorgovski, S.G., 2009. Cosmological studies with radio galaxies and supernovae. *ApJ* 691 (Feb.), 1058–1067.
- D’Amico, G., Musso, M., Noreña, J., Paranjape, A., 2011. An improved calculation of the non-Gaussian halo mass function. *JCAP* 2 (Feb.), 1.
- Daniel, S.F., Linder, E.V., 2010. Confronting general relativity with further cosmological data. *Phys. Rev. D* 82, 103523.
- Das, S., Sherwin, B.D., Aguirre, P., Appel, J.W., Bond, J.R., Carvalho, C.S., et al., 2011. Detection of the power spectrum of cosmic microwave background lensing by the atacama cosmology telescope. *Phys. Rev. Lett.* 107 (2), 021301.
- Dawson, K.S., Schlegel, D.J., Ahn, C.P., Anderson, S.F., Aubourg, É., Bailey, S., et al., 2013. The baryon oscillation spectroscopic survey of SDSS-III. *AJ* 145 (Jan.), 10.
- de Bernardis, F., Bean, R., Galli, S., Melchiorri, A., Silk, J.I., Verde, L., 2009. Delayed recombination and standard rulers. *Phys. Rev. D* 79 (4), 043503–+.
- de Bernardis, P., Ade, P.A.R., Bock, J.J., Bond, J.R., Borrill, J., Boscaleri, A., et al., 2000. A flat Universe from high-resolution maps of the cosmic microwave background radiation. *Nature* 404 (Apr.), 955–959.
- de Putter, R., Huterer, D., Linder, E.V., 2010. Measuring the speed of dark: detecting dark energy perturbations. *Phys. Rev. D* 81, 103513.
- de Putter, R., Linder, E.V., 2008. To bin or not to bin: decorrelating the cosmic equation of state. *Astropart. Phys.* 29, 424–441.
- de Putter, R., Zahn, O., Linder, E.V., 2009. CMB lensing constraints on neutrinos and dark energy. *Phys. Rev. D* 79 (6), 065033–+.
- DeDeo, S., Caldwell, R.R., Steinhardt, P.J., 2003. Effects of the sound speed of quintessence on the microwave background and large scale structure. *Phys. Rev. D* 67 (10), 103509.
- degl’Innocenti, S., Fiorentini, G., Raffelt, G.G., Ricci, B., Weiss, A., 1996. Time-variation of Newton’s constant and the age of globular clusters. *A&A* 312 (Aug.), 345–352.
- Demarco, R., Wilson, G., Muzzin, A., Lacy, M., Surace, J., Yee, H.K.C., Hoekstra, H., Blindert, K., Gilbank, D., 2010. Spectroscopic confirmation of three red-sequence selected galaxy clusters at $z = 0.87, 1.16,$ and 1.21 from the SpARCS survey. *ApJ* 711 (Mar.), 1185–1197.
- Demianski, M., Piedipalumbo, E., 2011. Standardizing the gamma-ray bursts with the Amati $E_{p,i}-E_{iso}$ relation: the updated Hubble diagram and implications for cosmography. *MNRAS* 415 (Aug.), 3580–3590.
- DiAferio, A., 1999. Mass estimation in the outer regions of galaxy clusters. *MNRAS* 309 (Nov.), 610–622.
- Dick, J., Knox, L., Chu, M., 2006. Reduction of cosmological data for the detection of time-varying dark energy density. *JCAP* 0607, 001.
- Dicke, R., Peebles, P., 1979. General relativity. In: Hawking, S., Israel, W. (Eds.), *An Einstein Centenary Survey*. Cambridge University Press, Cambridge, UK.
- Dicke, R.H., Peebles, P.J.E., Roll, P.G., Wilkinson, D.T., 1965. Cosmic black-body radiation. *ApJ* 142, 414–419.
- Dietrich, J.P., Hartlap, J., 2010. Cosmology with the shear-peak statistics. *MNRAS* 402 (Feb.), 1049–1058.
- Dodelson, S., 2003. *Modern Cosmology*. Academic Press, Amsterdam.
- Dodelson, S., Rozo, E., Stebbins, A., 2003. Primordial gravity waves and weak lensing. *Phys. Rev. Lett.* 91, 021301.
- Dolney, D., Jain, B., Takada, M., 2006. Baryon oscillations and dark-energy constraints from imaging surveys. *MNRAS* 366 (Mar.), 884–898.
- Donahue, M., Voit, G.M., Gioia, I., Lupino, G., Hughes, J.P., Stocke, J.T., 1998. A very hot, high-redshift cluster of galaxies: more trouble for $\omega = 1$. *ApJ* 502 (Aug.), 550–+.

- Doran, M., Robbers, G., Wetterich, C., 2007. Impact of three years of data from the Wilkinson Microwave Anisotropy Probe on cosmological models with dynamical dark energy. *Phys. Rev. D* 75 (2), 023003–+.
- Draper, P., Dodelson, S., Hao, J., Rozo, E., 2012. Sunyaev–Zel’dovich signal of the maxBCG SDSS galaxy clusters in WMAP. *Phys. Rev. D* 85 (2), 023005.
- Dressler A., Spergel D., Mountain M., Postman M., Elliott E., Bendek E., et al. 2012. Exploring the NRO opportunity for a Hubble-sized wide-field near-IR space telescope — NEW WFIRST. arXiv:1210.7809.
- Dvali, G.R., Gabadadze, G., Porrati, M., 2000. 4D gravity on a brane in 5D Minkowski space. *Phys. Lett.* B485, 208–214.
- Ebeling, H., Edge, A.C., Allen, S.W., Crawford, C.S., Fabian, A.C., Huchra, J.P., 2000. The ROSAT brightest cluster sample - IV. The extended sample. *MNRAS* 318 (Oct.), 333–340.
- Ebeling, H., Edge, A.C., Mantz, A., Barrett, E., Henry, J.P., Ma, C.J., van Speybroeck, L., 2010. The X-ray brightest clusters of galaxies from the massive cluster survey. *MNRAS* 407 (Sep.), 83–93.
- Efstathiou, G., 1995. An anthropic argument for a cosmological constant. *MNRAS* 274 (Jun.), L73–L76.
- Efstathiou, G., Bond, J.R., 1999. Cosmic confusion: degeneracies among cosmological parameters derived from measurements of microwave background anisotropies. *MNRAS* 304 (Mar.), 75–97.
- Efstathiou, G., Frenk, C.S., White, S.D.M., Davis, M., 1988. Gravitational clustering from scale-free initial conditions. *MNRAS* 235 (Dec.), 715–748.
- Efstathiou, G., Moody, S., Peacock, J.A., Percival, W.J., Baugh, C., Bland-Hawthorn, J., et al., 2002. Evidence for a non-zero Λ and a low matter density from a combined analysis of the 2dF Galaxy Redshift Survey and cosmic microwave background anisotropies. *MNRAS* 330 (Feb.), L29–L35.
- Efstathiou, G., Sutherland, W.J., Maddox, S.J., 1990. The cosmological constant and cold dark matter. *Nature* 348, 705–707.
- Einstein, A., 1917. Cosmological considerations in the general theory of relativity. *Sitzungsber. Preuss. Akad. Wiss. Berlin (Math. Phys.)* 1917, 142–152.
- Eisenhardt, P.R.M., Brodwin, M., Gonzalez, A.H., Stanford, S.A., Stern, D., Barmby, P., et al., 2008. Clusters of galaxies in the first half of the universe from the IRAC shallow survey. *ApJ* 684 (Sep.), 905–932.
- Eisenstein, D., 2002. Large-scale structure and future surveys. In: Brown, M.J.I., Dey, A. (Eds.), *Next Generation Wide-Field Multi-Object Spectroscopy*. In: *Astronomical Society of the Pacific Conference Series*, vol. 280. 35–+.
- Eisenstein, D., White, M., 2004. Theoretical uncertainty in baryon oscillations. *Phys. Rev. D* 70 (10), 103523–+.
- Eisenstein, D.J., Annis, J., Gunn, J.E., Szalay, A.S., Connolly, A.J., Nichol, R.C., et al., 2001. Spectroscopic target selection for the sloan digital sky survey: the luminous red galaxy sample. *AJ* 122 (Nov.), 2267–2280.
- Eisenstein, D.J., Bennett, C.L., 2008. Cosmic sound waves rule. *Physics Today* 61 (4), 040000–+.
- Eisenstein, D.J., Hu, W., 1998. Baryonic features in the matter transfer function. *ApJ* 496 (Mar.), 605–+.
- Eisenstein, D.J., Hu, W., 1999. Power spectra for cold dark matter and its variants. *ApJ* 511 (Jan.), 5–15.
- Eisenstein, D.J., Hu, W., Tegmark, M., 1998. Cosmic complementarity: H 0 and Omega M from combining cosmic microwave background experiments and redshift surveys. *ApJ Lett.* 504 (Sep.), L57+.
- Eisenstein, D.J., Seo, H.-J., Sirko, E., Spergel, D.N., 2007a. Improving cosmological distance measurements by reconstruction of the baryon acoustic peak. *ApJ* 664 (Aug.), 675–679.
- Eisenstein, D.J., Seo, H.-J., White, M., 2007b. On the robustness of the acoustic scale in the low-redshift clustering of matter. *ApJ* 664 (Aug.), 660–674.
- Eisenstein, D.J., Weinberg, D.H., Agol, E., Aihara, H., Allende Prieto, C., Anderson, S.F., et al., 2011. SDSS-III: massive spectroscopic surveys of the distant universe, the milky way, and extra-solar planetary systems. *AJ* 142 (Sep.), 72–+.
- Eisenstein, D.J., et al., 2005. Detection of the baryon acoustic peak in the large-scale correlation function of SDSS luminous red galaxies. *ApJ* 633, 560–574.
- Eke, V.R., Cole, S., Frenk, C.S., Patrick Henry, J., 1998. Measuring Omega₀ using cluster evolution. *MNRAS* 298 (Aug.), 1145–1158.
- Erben T., Hildebrandt H., Miller L., van Waerbeke L., Heymans C., Hoekstra H., et al. 2012. CFHTLenS: the Canada–France–Hawaii telescope lensing survey — imaging data and catalogue products. arXiv:1210.8156.
- Erickson, B.M.S., Cunha, C.E., Evrard, A.E., 2011. Influence of projection in cluster cosmology studies. *Phys. Rev. D* 84 (10), 103506.
- Erickson, J.K., Caldwell, R.R., Steinhardt, P.J., Armendariz-Picon, C., Mukhanov, V., 2002. Measuring the speed of sound of quintessence. *Phys. Rev. Lett.* 88 (12), 121301.
- Evrard, A.E., 1989. Biased cold dark matter theory — Trouble from rich clusters? *ApJ Lett.* 341 (Jun.), L71–L74.
- Evrard, A.E., 1997. The intracluster gas fraction in X-ray clusters — Constraints on the clustered mass density. *MNRAS* 292 (Dec.), 289–+.
- Faber, S.M., Gallagher, J.S., 1979. Masses and mass-to-light ratios of galaxies. *ARA&A* 17, 135–187.
- Fabjan, D., Borgani, S., Rasia, E., Bonafede, A., Dolag, K., Murante, G., Tornatore, L., 2011. X-ray mass proxies from hydrodynamic simulations of galaxy clusters - I. *MNRAS* 416 (Sep.), 801–816.
- Feldman, H.A., Kaiser, N., Peacock, J.A., 1994. Power-spectrum analysis of three-dimensional redshift surveys. *ApJ* 426 (May), 23–37.
- Ferreira, P.G., Joyce, M., 1997. Structure formation with a self-tuning scalar field. *Phys. Rev. Lett.* 79 (Dec.), 4740–4743.
- Filippenko, A.V., 1997. Optical spectra of supernovae. *ARA&A* 35, 309–355.
- Fischer, P., McKay, T.A., Sheldon, E., Connolly, A., Stebbins, A., Frieman, J.A., et al., 2000. Weak lensing with sloan digital sky survey commissioning data: the galaxy-mass correlation function to 1 H⁻¹ Mpc. *AJ* 120 (Sep.), 1198–1208.
- Folatelli, G., Phillips, M.M., Burns, C.R., Contreras, C., Hamuy, M., Freedman, W.L., et al., 2010. The carnegie supernova project: analysis of the first sample of low-redshift type-Ia supernovae. *AJ* 139 (Jan.), 120–144.
- Foley, R.J., 2012. The relation between ejecta velocity, intrinsic color, and host-galaxy mass for high-redshift type Ia supernovae. *ApJ* 748 (Apr.), 127.
- Foley, R.J., Sanders, N.E., Kirshner, R.P., 2011. Velocity evolution and the intrinsic color of type Ia supernovae. *ApJ* 742 (Dec.), 89.
- Fort, B., Mellier, Y., 1994. Arc(let)s in clusters of galaxies. *A&A Rev.* 5, 239–292.
- Fosalba, P., Gaztañaga, E., 2004. Measurement of the gravitational potential evolution from the cross-correlation between WMAP and the APM galaxy survey. *MNRAS* 350 (May), L37–41.
- Fosalba, P., Gaztañaga, E., Castander, F.J., 2003. Detection of the integrated Sachs–Wolfe and Sunyaev–Zel’dovich effects from the cosmic microwave background-galaxy correlation. *ApJ Lett.* 597 (Nov.), L89–L92.
- Freedman, W.L., Burns, C.R., Phillips, M.M., Wyatt, P., Persson, S.E., Madore, B.F., et al., 2009. The Carnegie supernova project: first near-infrared Hubble diagram to $z \sim 0.7$. *ApJ* 704 (Oct.), 1036–1058.
- Freedman, W.L., Madore, B.F., 2010. The Hubble constant. *ARA&A* 48 (Sep.), 673–710.
- Freedman, W.L., Madore, B.F., Gibson, B.K., Ferrarese, L., Kelson, D.D., Sakai, S., et al., 2001. Final results from the Hubble Space Telescope key project to measure the Hubble constant. *ApJ* 553 (May), 47–72.
- Freedman, W.L., Madore, B.F., Mould, J.R., Hill, R., Ferrarese, L., et al., 1994. Distance to the Virgo cluster galaxy M100 from Hubble Space Telescope observations of cepheids. *Nature* 371 (Oct.), 757–762.
- Freedman, W.L., Madore, B.F., Scowcroft, V., Burns, C., Monson, A., Persson, S.E., Seibert, M., Rigby, J., 2012. Carnegie Hubble program: a mid-infrared calibration of the Hubble constant. *ApJ* 758 (Oct.), 24.
- Freedman, W.L., Madore, B.F., Scowcroft, V., Monson, A., Persson, S.E., Seibert, M., Rigby, J.R., Sturch, L., Stetson, P., 2011. The carnegie Hubble program. *AJ* 142 (Dec.), 192.
- Freese, K., 2005. Cardassian expansion: dark energy density from modified Friedmann equations. *New Astron. Rev.* 49, 103–109.
- Freese, K., Lewis, M., 2002. Cardassian expansion: a model in which the universe is flat, matter dominated, and accelerating. *Phys. Lett.* B540, 1–8.
- Friedmann, A., 1922. On the curvature of space. *Z. Phys.* 10, 377.
- Friedmann, A., 1924. On the possibility of a world with constant negative curvature of space. *Z. Phys.* 21, 326.
- Frieman, J.A., 1996. Weak lensing and the measurement of q_0 ; from type Ia supernovae. *Comments Astrophys.* 18, 323.
- Frieman, J.A., Bassett, B., Becker, A., Choi, C., Cinabro, D., Dejongh, F., et al., 2008. The sloan digital sky survey-II supernova survey: technical summary. *AJ* 135 (Jan.), 338–347.
- Frieman, J.A., Hill, C.T., Stebbins, A., Waga, I., 1995. Cosmology with ultralight pseudo nambu-goldstone bosons. *Phys. Rev. Lett.* 75, 2077–2080.

- Frieman, J.A., Turner, M., Huterer, D., 2008. Dark energy and the accelerating universe. *Ann. Rev. A&A* 46, 385–432.
- Fruchter, A.S., 2011. A new method for band-limited imaging with undersampled detectors. *PASP* 123 (Apr.), 497–502.
- Fruchter, A.S., Hook, R.N., 2002. Drizzle: a method for the linear reconstruction of undersampled images. *PASP* 114, 144–152.
- Fu, L., Semboloni, E., Hoekstra, H., Kilbinger, M., van Waerbeke, L., Tereno, I., et al., 2008. Very weak lensing in the CFHTLS wide: cosmology from cosmic shear in the linear regime. *A&A* 479 (Feb.), 9–25.
- Gao, L., Springel, V., White, S.D.M., 2005. The age dependence of halo clustering. *MNRAS* 363 (Oct.), L66–L70.
- Gao, L., White, S.D.M., 2007. Assembly bias in the clustering of dark matter haloes. *MNRAS* 377 (Apr.), L5–L9.
- Gaztañaga, E., Cabré, A., Hui, L., 2009. Clustering of luminous red galaxies - IV. Baryon acoustic peak in the line-of-sight direction and a direct measurement of $H(z)$. *MNRAS* 399 (Nov.), 1663–1680.
- Gaztañaga, E., Eriksen, M., Crocce, M., Castander, F.J., Fosalba, P., Martí, P., Miquel, R., Cabré, A., 2012. Cross-correlation of spectroscopic and photometric galaxy surveys: cosmology from lensing and redshift distortions. *MNRAS* 422 (Jun.), 2904–2930.
- Geach, J.E., Sobral, D., Hickox, R.C., Wake, D.A., Smail, I., Best, P.N., Baugh, C.M., Stott, J.P., 2012. The clustering of $H\alpha$ emitters at $z = 2.23$ from HiZELS. *MNRAS* 426 (Oct.), 679–689.
- George, M.R., Leauthaud, A., Bundy, K., Finoguenov, A., Ma, C.-P., Rykoff, E.S., Tinker, J.L., Wechsler, R.H., Massey, R., Mei, S., 2012. Galaxies in X-ray groups. II. A weak lensing study of halo centering. *ApJ* 757 (Sep.), 2.
- Gerke, B.F., Newman, J.A., Davis, M., Marinoni, C., Yan, R., Coil, A.L., et al., 2005. The DEEP2 galaxy redshift survey: first results on galaxy groups. *ApJ* 625 (May), 6–22.
- Gettings, D.P., Gonzalez, A.H., Stanford, S.A., Eisenhardt, P.R.M., Brodwin, M., Mancone, C., et al., 2012. The massive distant clusters of WISE survey: the first distant galaxy cluster discovered by WISE. *ApJ Lett.* 759 (Nov.), L23.
- Ghirlanda, G., Chisellini, G., Firmani, C., 2006. Gamma ray bursts as standard candles to constrain the cosmological parameters. *New J. Phys.* 8, 123.
- Giannantonio, T., Scranton, R., Crittenden, R.G., Nichol, R.C., Boughn, S.P., Myers, A.D., Richards, G.T., 2008. Combined analysis of the integrated Sachs–Wolfe effect and cosmological implications. *Phys. Rev. D* 77 (12), 123520.
- Giodini, S., Pierini, D., Finoguenov, A., Pratt, G.W., Boehringer, H., Leauthaud, A., et al., 2009. Stellar and total baryon mass fractions in groups and clusters since redshift 1. *ApJ* 703 (Sep.), 982–993.
- Gladders, M.D., Yee, H.K.C., 2005. The red-sequence cluster survey. I. The survey and cluster catalogs for patches RCS 0926+37 and RCS 1327+29. *ApJS* 157 (Mar.), 1–29.
- Gladders, M.D., Yee, H.K.C., Majumdar, S., Barrientos, L.F., Hoekstra, H., Hall, P.B., Infante, L., 2007. Cosmological constraints from the red-sequence cluster survey. *ApJ* 655 (Jan.), 128–134.
- Glazebrook, K., Baldry, I., Moos, W., Kruk, J., McCandliss, S., 2005. Monster redshift surveys through dispersive slitless imaging: The baryon oscillation probe. *NewAR* 49 (Nov.), 374.
- Glazebrook, K., Blake, C., 2005. Measuring the cosmic evolution of dark energy with baryonic oscillations in the galaxy power spectrum. *ApJ* 631 (Sep.), 1–20.
- Goldberg, D.M., Bacon, D.J., 2005. Galaxy–galaxy flexion: weak lensing to second order. *ApJ* 619, 741–748.
- Goldberg, D.M., Strauss, M.A., 1998. Determination of the baryon density from large-scale galaxy redshift surveys. *ApJ* 495 (Mar.), 29–+.
- Gonzalez, A.H., Zaritsky, D., Dalcanton, J.J., Nelson, A., 2001. The las campanas distant cluster survey: the catalog. *ApJS* 137 (Nov.), 117–138.
- Gott, J.R., Slepian, Z., 2011. Dark energy as double N-flation - observational predictions. *MNRAS* 416 (Sep.), 907–916.
- Gott III, J.R., 1982. Creation of open universes from de Sitter space. *Nature* 295 (Jan.), 304–306.
- Gott III, J.R., Schramm, D.N., Tinsley, B.M., Gunn, J.E., 1974. An unbound universe. *ApJ* 194 (Dec.), 543–553.
- Green, J., Schechter, P., Baltay, C., Bean, R., Bennett, D., Brown, R., et al., 2012. Wide-Field InfraRed Survey Telescope (WFIRST): Final Report of Science Definition Team. [arXiv:1208.4012](https://arxiv.org/abs/1208.4012).
- Green, S.R., Wald, R.M., 2011. New framework for analyzing the effects of small scale inhomogeneities in cosmology. *Phys. Rev. D* 83 (8), 084020.
- Greenhill, L., Humphreys, E., Hu, W., Macri, L., Murphy, D., Masters, K., Hagiwara, Y., Kobayashi, H., Murata, Y., 2009. Estimation of the Hubble constant and constraint on descriptions of dark energy. In: *Astro2010 White Paper*. [arXiv:0902.4255](https://arxiv.org/abs/0902.4255).
- Griest, K., 2002. Toward a possible solution to the cosmic coincidence problem. *Phys. Rev. D* 66, 123501.
- Gross, M.A.K., Somerville, R.S., Primack, J.R., Holtzman, J., Klypin, A., 1998. Cold dark matter variant cosmological models - I. Simulations and preliminary comparisons. *MNRAS* 301 (Nov.), 81–94.
- Grossi, M., Verde, L., Carbone, C., Dolag, K., Branchini, E., Iannuzzi, F., Matarrese, S., Moscardini, L., 2009. Large-scale non-Gaussian mass function and halo bias: tests on N -body simulations. *MNRAS* 398 (Sep.), 321–332.
- Guenther, D.B., Krauss, L.M., Demarque, P., 1998. Testing the constancy of the gravitational constant using helioseismology. *ApJ* 498 (May), 871–+.
- Gull, S.F., Northover, K.J.E., 1976. Detection of hot gas in clusters of galaxies by observation of the microwave background radiation. *Nature* 263 (Oct.), 572–+.
- Gunn, J.E., 1967. On the propagation of light in inhomogeneous cosmologies. I. Mean effects. *ApJ* 150 (Dec.), 737.
- Gunn, J.E., Gott III, J.R., 1972. On the infall of matter into cluster of galaxies and some effects on their evolution. *ApJ* 176, 1–19.
- Gunn, J.E., Peterson, B.A., 1965. On the density of neutral hydrogen in intergalactic space. *ApJ* 142, 1633.
- Guth, A.H., 1981. The inflationary universe: a possible solution to the horizon and flatness problems. *Phys. Rev. D* 23, 347–356.
- Guth, A.H., Nomura, Y., 2012. What can the observation of nonzero curvature tell us? *Phys. Rev. D* 86 (2), 023534.
- Guy, J., Astier, P., Baumont, S., Hardin, D., Pain, R., Regnault, N., et al., 2007. SALT2: using distant supernovae to improve the use of type Ia supernovae as distance indicators. *A&A* 466 (Apr.), 11–21.
- Guy, J., Astier, P., Nobili, S., Regnault, N., Pain, R., 2005. SALT: a spectral adaptive light curve template for type Ia supernovae. *A&A* 443 (Dec.), 781–791.
- Guzik, J., Bernstein, G., Smith, R.E., 2007. Systematic effects in the sound horizon scale measurements. *MNRAS* 375 (Mar.), 1329–1337.
- Guzzo, L., Pierleoni, M., Meneux, B., Branchini, E., Le Fèvre, O., Marinoni, C., et al., 2008. A test of the nature of cosmic acceleration using galaxy redshift distortions. *Nature* 451 (Jan.), 541–544.
- Hamana, T., Miyazaki, S., Shimasaku, K., Furusawa, H., Doi, M., Hamabe, M., et al., 2003. Cosmic shear statistics in the supprime-cam 2.1 square degree field: constraints on Ω_m and σ_8 . *ApJ* 597 (Nov.), 98–110.
- Hamaus, N., Seljak, U., Desjacques, V., 2012. Optimal weighting in galaxy surveys: application to redshift–space distortions. *Phys. Rev. D* 86 (10), 103513.
- Hamilton, A.J.S., 1998. Linear redshift distortions: a review. In: Hamilton, D. (Ed.), *The Evolving Universe*. In: *Astrophysics and Space Science Library*, vol. 231. p. 185.
- Hamuy, M., Folatelli, G., Morrell, N.I., Phillips, M.M., Suntzeff, N.B., Persson, S.E., et al., 2006. The Carnegie supernova project: the low-redshift survey. *PASP* 118 (Jan.), 2–20.
- Hamuy, M., Phillips, M.M., Suntzeff, N.B., Schommer, R.A., Maza, J., Aviles, R., 1996. The absolute luminosities of the calan/tololo type IA supernovae. *AJ* 112 (Dec.), 2391.
- Hamuy, M., Pinto, P.A., 2002. Type II supernovae as standardized candles. *ApJ* 566, L63–L65.
- Hanany, S., Ade, P., Balbi, A., Bock, J., Borrill, J., Boscaleri, A., et al., 2000. MAXIMA-1: a measurement of the cosmic microwave background anisotropy on angular scales of $10' - 5^\circ$. *ApJ Lett.* 545 (Dec.), L5–L9.
- Hao, J., McKay, T.A., Koester, B.P., Rykoff, E.S., Rozo, E., et al., 2010. A GMBCG galaxy cluster catalog of 55,424 rich clusters from SDSS DR7. *ApJS* 191 (Dec.), 254–274.
- Harker, G., Cole, S., Helly, J., Frenk, C., Jenkins, A., 2006. A marked correlation function analysis of halo formation times in the millennium simulation. *MNRAS* 367 (Apr.), 1039–1049.
- Hartlap, J., Hilbert, S., Schneider, P., Hildebrandt, H., 2011. A bias in cosmic shear from galaxy selection: results from ray-tracing simulations. *A&A* 528 (Apr.), A51+.
- Hatton, S.J., Cole, S., 1998. Modelling the redshift–space distortion of galaxy clustering. *MNRAS* 296, 10–20.

- Haverkorn, M., Katgert, P., de Bruyn, A.G., 2003. Multi-frequency polarimetry of the galactic radio background around 350 MHz. I. A region in Auriga around $l = 161$ deg, $b = 16$ deg. *A&A* 403 (Jun.), 1031–1044.
- Hawkins, E., Maddox, S., Cole, S., Lahav, O., Madgwick, D.S., Norberg, P., et al., 2003. The 2dF galaxy redshift survey: correlation functions, peculiar velocities and the matter density of the Universe. *MNRAS* 346 (Nov.), 78–96.
- Hayashi, E., White, S.D.M., 2008. Understanding the halo-mass and galaxy-mass cross-correlation functions. *MNRAS* 388 (Jul.), 2–14.
- Hayden, B.T., Gupta, R.R., Garnavich, P.M., Mannucci, F., Nichol, R.C., Sako, M., 2013. The fundamental metallicity relation reduces type Ia SN Hubble residuals more than host mass alone. *ApJ* 764, 191.
- Heisler, J., Tremaine, S., Bahcall, J.N., 1985. Estimating the masses of galaxy groups — alternatives to the virial theorem. *ApJ* 298 (Nov.), 8–17.
- Heitmann, K., Higdon, D., White, M., Habib, S., Williams, B.J., Lawrence, E., Wagner, C., 2009. The coyote universe. II. Cosmological models and precision emulation of the nonlinear matter power spectrum. *ApJ* 705 (Nov.), 156–174.
- Heitmann, K., White, M., Wagner, C., Habib, S., Higdon, D., 2010. The coyote universe I: precision determination of the nonlinear matter power spectrum. *ApJ* 715, 104–121.
- Henry, J.P., 1997. A measurement of the density parameter derived from the evolution of cluster X-ray temperatures. *ApJ Lett.* 489 (Nov.), L1+.
- Henry, J.P., 2000. Measuring cosmological parameters from the evolution of cluster X-ray temperatures. *ApJ* 534 (May), 565–580.
- Henry, J.P., Evrard, A.E., Hoekstra, H., Babul, A., Mahdavi, A., 2009. The X-ray cluster normalization of the matter power spectrum. *ApJ* 691 (Feb.), 1307–1321.
- Herrnstein, J.R., Moran, J.M., Greenhill, L.J., Diamond, P.J., Inoue, M., Nakai, N., Miyoshi, M., Henkel, C., Riess, A., 1999. A geometric distance to the galaxy NGC4258 from orbital motions in a nuclear gas disk. *Nature* 400 (Aug.), 539–541.
- Hetterscheidt, M., Simon, P., Schirmer, M., Hildebrandt, H., Schrabback, T., Erben, T., Schneider, P., 2007. GaBoDS: the Garching-Bonn deep survey. VII. Cosmic shear analysis. *A&A* 468 (Jun.), 859–876.
- Heymans, C., Brown, M., Heavens, A., Meisenheimer, K., Taylor, A., Wolf, C., 2004. Weak lensing with COMBO-17: estimation and removal of intrinsic alignments. *MNRAS* 347 (Jan.), 895–908.
- Heymans, C., Brown, M.L., Barden, M., Caldwell, J.A.R., Jahnke, K., Peng, C.Y., et al., 2005. Cosmological weak lensing with the HST GEMS survey. *MNRAS* 361 (Jul.), 160–176.
- Heymans, C., Rowe, B., Hoekstra, H., Miller, L., Erben, T., Kitching, T., van Waerbeke, L., 2012a. The impact of high spatial frequency atmospheric distortions on weak-lensing measurements. *MNRAS* 421 (Mar.), 381–389.
- Heymans, C., van Waerbeke, L., Miller, L., Erben, T., Hildebrandt, H., Hoekstra, H., et al., 2012b. CFHTLenS: the Canada–France–Hawaii telescope lensing survey. *MNRAS* 427 (Nov.), 146–166.
- Heymans, C., van Waerbeke, L., Bacon, D., Berge, J., Bernstein, G., Bertin, E., et al., 2006. The shear testing programme - I. Weak lensing analysis of simulated ground-based observations. *MNRAS* 368 (May), 1323–1339.
- Hicken, M., Challis, P., Jha, S., Kirshner, R.P., Matheson, T., Modjaz, M., et al., 2009a. CfA3: 185 type Ia supernova light curves from the CfA. *ApJ* 700 (Jul.), 331–357.
- Hicken, M., Wood-Vasey, W.M., Blondin, S., Challis, P., Jha, S., Kelly, P.L., Rest, A., Kirshner, R.P., 2009b. Improved dark energy constraints from ~ 100 new CfA supernova type Ia light curves. *ApJ* 700 (Aug.), 1097–1140.
- High, F.W., Hoekstra, H., Leethochawalit, N., de Haan, T., Abramson, L., Aird, K.A., et al., 2012. Weak-lensing mass measurements of five galaxy clusters in the south pole telescope survey using Magellan/Megacam. *ApJ* 758 (Oct.), 68.
- Hikage, C., Takada, M., Spergel, D.N., 2011. Using galaxy–galaxy weak lensing measurements to correct the finger of God. *MNRAS* 1979.
- Hill, G.J., Macqueen, P.J., Palunas, P., Kelz, A., Roth, M.M., Gebhardt, K., Grupp, F., 2006. VIRUS: A hugely replicated integral field spectrograph for HETDEX. *NewAR* 50 (Jun.), 378–381.
- Hirata, C.M., 2009. Tidal alignments as a contaminant of redshift space distortions. *MNRAS* 399 (Oct.), 1074–1087.
- Hirata, C.M., Ho, S., Padmanabhan, N., Seljak, U., Bahcall, N.A., 2008. Correlation of CMB with large-scale structure: II. Weak lensing. *Phys. Rev. D* 78, 043520.
- Hirata, C.M., Holz, D.E., Cutler, C., 2010. Reducing the weak lensing noise for the gravitational wave Hubble diagram using the non-Gaussianity of the magnification distribution. *Phys. Rev. D* 81, 124046.
- Hirata, C.M., Mandelbaum, R., Ishak, M., Seljak, U., Nichol, R., Pimblett, K.A., Ross, N.P., Wake, D., 2007. Intrinsic galaxy alignments from the 2SLAQ and SDSS surveys: luminosity and redshift scalings and implications for weak lensing surveys. *MNRAS* 381 (Nov.), 1197–1218.
- Hirata, C.M., Mandelbaum, R., Seljak, U., Guzik, J., Padmanabhan, N., Blake, C., et al., 2004. Galaxy–galaxy weak lensing in the Sloan Digital Sky Survey: intrinsic alignments and shear calibration errors. *MNRAS* 353 (Sep.), 529–549.
- Hirata, C.M., Padmanabhan, N., Seljak, U., Schlegel, D., Brinkmann, J., 2004. Cross-correlation of CMB with large-scale structure: weak gravitational lensing. *Phys. Rev. D* 70, 103501.
- Hirata, C.M., Seljak, U., 2003a. Analyzing weak lensing of the cosmic microwave background using the likelihood function. *Phys. Rev. D* 67, 043001.
- Hirata, C.M., Seljak, U., 2003b. Shear calibration biases in weak lensing surveys. *MNRAS* 343, 459–480.
- Hirata, C.M., Seljak, U., 2004. Intrinsic alignment–lensing interference as a contaminant of cosmic shear. *Phys. Rev. D* 70, 063526.
- Hirata, C.M., Seljak, U., 2005. Can superhorizon cosmological perturbations explain the acceleration of the universe? *Phys. Rev. D* 72 (8), 083501.
- Ho, S., Hirata, C., Padmanabhan, N., Seljak, U., Bahcall, N., 2008. Correlation of CMB with large-scale structure. I. Integrated Sachs–Wolfe tomography and cosmological implications. *Phys. Rev. D* 78 (4), 043519.
- Hoeflich, P., Khokhlov, A., Wheeler, J.C., Phillips, M.M., Suntzeff, N.B., Hamuy, M., 1996. Maximum brightness and postmaximum decline of light curves of type Ia supernovae: a comparison of theory and observations. *ApJ Lett.* 472 (Dec.), L81.
- Hoekstra, H., Franx, M., Kuijken, K., Carlberg, R.G., Yee, H.K.C., 2003. Lensing by galaxies in CNOC2 fields. *MNRAS* 340 (Apr.), 609–622.
- Hoekstra, H., Franx, M., Kuijken, K., Squires, G., 1998. Weak lensing analysis of CL 1358+62 using Hubble Space Telescope observations. *ApJ* 504 (Sep.), 636–+.
- Hoekstra, H., Hsieh, B.C., Yee, H.K.C., Lin, H., Gladders, M.D., 2005. Virial masses and the baryon fraction in galaxies. *ApJ* 635, 73–85.
- Hoekstra, H., Mahdavi, A., Babul, A., Bildfell, C., 2012. The Canadian cluster comparison project: weak lensing masses and SZ scaling relations. *MNRAS* 427 (Dec.), 1298–1311.
- Hoekstra, H., Mellier, Y., van Waerbeke, L., Semboloni, E., Fu, L., Hudson, M.J., Parker, L.C., Tereno, I., Benabed, K., 2006. First cosmic shear results from the Canada–France–Hawaii telescope wide synoptic legacy survey. *ApJ* 647 (Aug.), 116–127.
- Hoekstra, H., Yee, H.K.C., Gladders, M.D., 2002. Constraints on Ω_m and σ_8 from weak lensing in RCS fields. *ApJ* 577, 595–603.
- Hoekstra, H., Yee, H.K.C., Gladders, M.D., 2004. Properties of galaxy dark matter halos from weak lensing. *ApJ* 606, 67–77.
- Hogg, D.W., 1999. Distance measures in cosmology. arXiv:astro-ph/9905116.
- Holder, G., 2006. Likelihood functions for galaxy cluster surveys. arXiv:astro-ph/0602251.
- Holder, G.P., Haiman, Z., Kaplinghat, M., Knox, L., 2003. The reionization history at high redshifts. II. Estimating the optical depth to Thomson scattering from cosmic microwave background polarization. *ApJ* 595 (Sep.), 13–18.
- Holz, D.E., Linder, E.V., 2005. Safety in numbers: gravitational lensing degradation of the luminosity distance–redshift relation. *ApJ* 631, 678–688.
- Horesh, A., Maoz, D., Hilbert, S., Bartelmann, M., 2011. Lensed arc statistics: comparison of Millennium simulation galaxy clusters to Hubble Space Telescope observations of an X-ray selected sample. *MNRAS* 418 (Nov.), 54–63.
- Hoyle, B., Jimenez, R., Verde, L., 2011. Implications of multiple high-redshift galaxy clusters. *Phys. Rev. D* 83 (10), 103502.
- Hu, W., 1998. Structure formation with generalized dark matter. *ApJ* 506 (Oct.), 485–494.
- Hu, W., 2001. Angular trispectrum of the cosmic microwave background. *Phys. Rev. D* 64 (8), 083005.
- Hu, W., 2002a. Dark energy and matter evolution from lensing tomography. *Phys. Rev. D* 66, 083515.
- Hu, W., 2002b. Dark synergy: gravitational lensing and the CMB. *Phys. Rev. D* 65, 023003.
- Hu, W., 2005. Dark energy probes in light of the CMB. *ASP Conf. Ser.* 339, 215.
- Hu, W., Cohn, J.D., 2006. Likelihood methods for cluster dark energy surveys. *Phys. Rev. D* 73, 067301.

- Hu, W., Haiman, Z., 2003. Redshifting rings of power. *Phys. Rev. D* 68 (6), 063004.
- Hu, W., Jain, B., 2004. Joint galaxy-lensing observables and the dark energy. *Phys. Rev. D* 70, 043009.
- Hu, W., Kravtsov, A.V., 2003. Sample variance considerations for cluster surveys. *ApJ* 584, 702–715.
- Hu, W., Sugiyama, N., 1996. Small-scale cosmological perturbations: an analytic approach. *ApJ* 471 (Nov.), 542–+.
- Hu, W., Sugiyama, N., Silk, J., 1997. The physics of microwave background anisotropies. *Nature* 386 (Mar), 37–43.
- Hu, W., White, M., 1996. Acoustic signatures in the cosmic microwave background. *ApJ* 471 (Nov.), 30–+.
- Hubble, E., 1929. A relation between distance and radial velocity among extra-galactic nebulae. *Proc. Nat. Acad. Sci.* 15, 168–173.
- Hudson, M.J., Gwyn, S.D.J., Dahle, H., Kaiser, N., 1998. Galaxy-galaxy lensing in the Hubble Deep Field: the halo Tully-Fisher relation at intermediate redshift. *ApJ* 503, 531.
- Huff, E., Schulz, A.E., White, M., Schlegel, D.J., Warren, M.S., 2007. Simulations of baryon oscillations. *Astropart. Phys.* 26 (Jan), 351–366.
- Huff E.M., Eifler T., Hirata C.M., Mandelbaum R., Schlegel D., Seljak U., 2011. Seeing in the dark – II. Cosmic shear in the Sloan Digital Sky Survey. arXiv:1112.3143.
- Huff E.M., Graves G.J., 2011. Magnificent magnification: exploiting the other half of the lensing signal. arXiv:1111.1070.
- Hui, L., 1999. Weighing the cosmological energy contents with weak gravitational lensing. *ApJ Lett.* 519 (Jul.), L9–L12.
- Hui, L., Gnedin, N.Y., 1997. Equation of state of the photoionized intergalactic medium. *MNRAS* 292, 27.
- Hui, L., Nicolis, A., Stubbs, C., 2009. Equivalence principle implications of modified gravity models. *Phys. Rev. D* 80, 104002.
- Hui, L., Stebbins, A., Burles, S., 1999. A geometrical test of the cosmological energy contents using the Lyman-alpha forest. *ApJ* 511, L5–9.
- Hui, L., Zhang, J., 2008. Density-ellipticity correlations, galaxy-galaxy lensing, and the importance of non-gaussianity in intrinsic alignment. *ApJ* 688 (Dec.), 742–756.
- Humphreys, E.M.L., Reid, M.J., Greenhill, L.J., Moran, J.M., Argon, A.L., 2008. Toward a new geometric distance to the active galaxy NGC 4258. II. Centripetal accelerations and investigation of spiral structure. *ApJ* 672 (Jan.), 800–816.
- Humphreys, E.M.L., Reid, M.J., Moran, J.M., Greenhill, L.J., Argon, A.L., 2013. Toward a new geometric distance to NGC 4258. III. Final results and the Hubble constant. *ApJ* (in press).
- Huterer, D., Cooray, A., 2005. Uncorrelated estimates of dark energy evolution. *Phys. Rev. D* 71, 023506.
- Huterer, D., Starkman, G., 2003. Parameterization of dark-energy properties: a principal-component approach. *Phys. Rev. Lett.* 90, 031301.
- Huterer, D., Turner, M.S., 1999. Prospects for probing the dark energy via supernova distance measurements. *Phys. Rev. D* 60 (8), 081301.
- Huterer, D., Turner, M.S., 2001. Probing dark energy: methods and strategies. *Phys. Rev. D* 64 (12), 123527.
- Hütsi, G., 2006. Acoustic oscillations in the SDSS DR4 luminous red galaxy sample power spectrum. *A&A* 449 (Apr.), 891–902.
- Hütsi, G., 2010. Power spectrum of the maxBCG sample: detection of acoustic oscillations using galaxy clusters. *MNRAS* 401 (Feb.), 2477–2489.
- Hütsi, G., Lahav, O., 2008. The cluster-galaxy cross spectrum. An additional probe of cosmological and halo parameters. *A&A* 492 (Dec.), 355–365.
- Iliev, I.T., Shapiro, P.R., McDonald, P., Mellema, G., Pen, U.-L., 2008. The effect of the intergalactic environment on the observability of Ly α emitters during reionization. *MNRAS* 391 (Nov.), 63–83.
- Jain, B., 2011. Designing surveys for tests of gravity. *R. Soc. Lond. Philos. Trans. Series A* 369 (Dec.), 5081–5089.
- Jain, B., Khoury, J., 2010. Cosmological tests of gravity. *Annals Phys.* 325, 1479–1516.
- Jain, B., Taylor, A., 2003. Cross-correlation tomography: measuring dark energy evolution with weak lensing. *Phys. Rev. Lett.* 91, 141302.
- Jain, B., Vanderplas, J., 2011. Tests of modified gravity with dwarf galaxies. *JCAP* 1110, 032.
- Jain, B., Zhang, P., 2008. Observational tests of modified gravity. *Phys. Rev. D* 78 (6), 063503.
- Jarosik, N., Bennett, C.L., Dunkley, J., Gold, B., Greason, M.R., et al., 2011. Seven-year Wilkinson Microwave Anisotropy Probe (WMAP) Observations: sky maps, systematic errors, and basic results. *ApJS* 192 (Feb.), 14–+.
- Jarvis, M., Bernstein, G.M., Fischer, P., Smith, D., Jain, B., Tyson, J.A., Wittman, D., 2003. Weak-lensing results from the 75 square degree cerro tololo inter-American observatory survey. *AJ* 125 (Mar), 1014–1032.
- Jarvis M., Jain B., 2004. Principal component analysis of PSF variation in weak lensing surveys. arXiv:astro-ph/0412234.
- Jarvis, M., Jain, B., 2008. On combining lensing shear information from multiple filters. *JCAP* 1 (Jan.), 3.
- Jee, M.J., Blakeslee, J.P., Sirianni, M., Martel, A.R., White, R.L., Ford, H.C., 2007. Principal component analysis of the time- and position-dependent point-spread function of the advanced camera for surveys. *PASP* 119 (Dec.), 1403–1419.
- Jee, M.J., Tyson, J.A., Schneider, M.D., Wittman, D., Schmidt, S., Hilbert, S., 2013. Cosmic shear results from the deep lens survey. I. Joint constraints on Ω_M and σ_8 with a two-dimensional Analysis. *ApJ* 765 (Mar), 74.
- Jenkins, A., Frenk, C.S., Pearce, F.R., Thomas, P.A., Colberg, J.M., White, S.D.M., Couchman, H.M.P., Peacock, J.A., Efstathiou, G., Nelson, A.H., 1998. Evolution of structure in cold dark matter universes. *ApJ* 499 (May), 20–+.
- Jennings, E., 2012. An improved model for the non-linear velocity power spectrum. *MNRAS* 427 (Nov.), L25–L29.
- Jennings, E., Baugh, C.M., Li, B., Zhao, G.-B., Koyama, K., 2012a. Redshift-space distortions in f(R) gravity. *MNRAS* 425 (Sep.), 2128–2143.
- Jennings, E., Baugh, C.M., Pascoli, S., 2011. Modelling redshift space distortions in hierarchical cosmologies. *MNRAS* 410 (Jan.), 2081–2094.
- Jennings, E., Baugh, C.M., Pascoli, S., 2012b. Testing dark energy using pairs of galaxies in redshift space. *MNRAS* 420 (Feb.), 1079–1091.
- Jeong, D., Komatsu, E., 2006. Perturbation theory reloaded: analytical calculation of nonlinearity in baryonic oscillations in the real-space matter power spectrum. *ApJ* 651 (Nov.), 619–626.
- Jha, S., Riess, A.G., Kirshner, R.P., 2007. Improved distances to type Ia supernovae with multicolor light curve shapes: MLC2k2. *ApJ* 659, 122–148.
- Jimenez, R., Loeb, A., 2002. Constraining cosmological parameters based on relative galaxy ages. *ApJ* 573, 37–42.
- Jimenez, R., Verde, L., Treu, T., Stern, D., 2003. Constraints on the equation of state of dark energy and the Hubble constant from stellar ages and the cosmic microwave background. *ApJ* 593 (Aug.), 622–629.
- Joachimi, B., Bridle, S.L., 2010. Simultaneous measurement of cosmology and intrinsic alignments using joint cosmic shear and galaxy number density correlations. *A&A* 523 (Nov.), A1.
- Joachimi, B., Mandelbaum, R., Abdalla, F.B., Bridle, S.L., 2011. Constraints on intrinsic alignment contamination of weak lensing surveys using the MegaZ-LRG sample. *A&A* 527 (Mar), A26.
- Joachimi, B., Schneider, P., 2008. The removal of shear-ellipticity correlations from the cosmic shear signal via nulling techniques. *A&A* 488 (Sep.), 829–843.
- Joachimi, B., Schneider, P., 2009. The removal of shear-ellipticity correlations from the cosmic shear signal. Influence of photometric redshift errors on the nulling technique. *A&A* 507 (Nov.), 105–129.
- Johnston D.E., Sheldon E.S., Wechsler R.H., Rozo E., Koester B.P., Frieman J.A., McKay T.A., Evrard A.E., Becker M.R., Annis J., 2007. Cross-correlation weak lensing of SDSS galaxy clusters II: cluster density profiles and the mass-richness relation. arXiv:0709.1159.
- Jonsson, J., Dahlen, T., Goobar, A., Mortzell, E., Riess, A., 2007. Tentative detection of the gravitational magnification of type Ia supernovae. *JCAP* 0706, 002.
- Jouvel, S., Kneib, J.-P., Ilbert, O., Bernstein, G., Arnouts, S., Dahlen, T., et al., 2009. Designing future dark energy space missions. I. Building realistic galaxy spectro-photometric catalogs and their first applications. *A&A* 504 (Sep.), 359–371.
- Jullo, E., Natarajan, P., Kneib, J.-P., D’alioisio, A., Limousin, M., Richard, J., Schimd, C., 2010. Cosmological constraints from strong gravitational lensing in clusters of galaxies. *Science* 329 (Aug.), 924–927.
- Jungman, G., Kamionkowski, M., Kosowsky, A., Spergel, D.N., 1996. Weighing the universe with the cosmic microwave background. *Phys. Rev. Lett.* 76 (Feb.), 1007–1010.
- Kaiser M.E., Kruk J.W., Mccandliss S.R., Sahnou D.J., Barkhouser R.H., Van Dixon W., et al. 2010. ACCESS: enabling an improved flux scale for astrophysics. arXiv:1001.3925.
- Kaiser, N., 1984. On the spatial correlations of Abell clusters. *ApJ* 284, L9–L12.
- Kaiser, N., 1986a. A sparse-sampling strategy for the estimation of large-scale clustering from redshift surveys. *MNRAS* 219 (Apr.), 785–790.
- Kaiser, N., 1986b. Evolution and clustering of rich clusters. *MNRAS* 222 (Sep.), 323–345.
- Kaiser, N., 1987. Clustering in real space and in redshift space. *MNRAS* 227, 1–27.

- Kaiser, N., 1991. Evolution of clusters of galaxies. *ApJ* 383 (Dec.), 104–111.
- Kaiser, N., 1992. Weak gravitational lensing of distant galaxies. *ApJ* 388 (Apr.), 272–286.
- Kaiser, N., 2000. A new shear estimator for weak-lensing observations. *ApJ* 537 (Jul.), 555–577.
- Kaiser, N., Squires, G., Broadhurst, T.J., 1995. A Method for weak lensing observations. *ApJ* 449, 460–475.
- Kamionkowski, M., Kosowsky, A., Stebbins, A., 1997. Statistics of cosmic microwave background polarization. *Phys. Rev. D* 55 (Jun.), 7368–7388.
- Kamionkowski, M., Spergel, D.N., Sugiyama, N., 1994. Small-scale cosmic microwave background anisotropies as probe of the geometry of the universe. *ApJ Lett.* 426 (May), L57+.
- Kasen, D., 2006. Secondary maximum in the near-infrared lightcurves of type Ia supernovae. *ApJ* 649, 939–953.
- Kasen, D., Woosley, S.E., 2007. On the origin of the type Ia supernova width-luminosity relation. *ApJ* 656, 661–665.
- Katz, N., Weinberg, D.H., Hernquist, L., 1996. Cosmological simulations with TreeSPH. *ApJS* 105, 19.
- Kawamura, S., Ando, M., Nakamura, T., Tsubono, K., Tanaka, T., Funaki, I., et al., 2008. The Japanese space gravitational wave antenna - DECIGO. *J. Phys. Conf. Ser.* 122 (1), 012006.
- Kazin, E.A., Blanton, M.R., Scoccimarro, R., Mcbride, C.K., Berlind, A.A., 2010a. Regarding the line-of-sight baryonic acoustic feature in the sloan digital sky survey and baryon oscillation spectroscopic survey luminous red galaxy samples. *ApJ* 719 (Aug.), 1032–1044.
- Kazin, E.A., Blanton, M.R., Scoccimarro, R., Mcbride, C.K., Berlind, A.A., Bahcall, N.A., et al., 2010b. The baryonic acoustic feature and large-scale clustering in the sloan digital sky survey luminous red galaxy sample. *ApJ* 710 (Feb.), 1444–1461.
- Kazin, E.A., Sánchez, A.G., Blanton, M.R., 2012. Improving measurements of $H(z)$ and $D_A(z)$ by analysing clustering anisotropies. *MNRAS* 419 (Feb.), 3223–3243.
- Kelly, P.L., Hicken, M., Burke, D.L., Mandel, K.S., Kirshner, R.P., 2010. Hubble residuals of nearby type Ia supernovae are correlated with host galaxy masses. *ApJ* 715, 743–756.
- Kessler, R., Bassett, B., Belov, P., Bhatnagar, V., Campbell, H., Conley, A., et al., 2010. Results from the supernova photometric classification challenge. *PASP* 122 (Dec.), 1415–1431.
- Kessler, R., et al., 2009. First-year sloan digital sky survey-II (SDSS-II) supernova results: Hubble diagram and cosmological parameters. *ApJS* 185, 32–84.
- Kilbinger, M., Fu, L., Heymans, C., Simpson, F., Benjamin, J., Erben, T., et al., 2013. CFHTLenS: Combined probe cosmological model comparison using 2D weak gravitational lensing. *MNRAS* 430, 2200.
- Killedar, M., Borgani, S., Meneghetti, M., Dolag, K., Fabjan, D., Tornatore, L., 2012. How baryonic processes affect strong lensing properties of simulated galaxy clusters. *MNRAS* 427 (Nov.), 533–549.
- Kim, A., Goobar, A., Perlmutter, S., 1996. A generalized K correction for type Ia supernovae: comparing R band photometry beyond $z = 0.2$ with B, V, and R band nearby photometry. *PASP* 108, 190.
- Kim, A.G., Miquel, R., 2006. Optimal extraction of cosmological information from supernova data in the presence of calibration uncertainties. *Astropart. Phys.* 24, 451–458.
- King, L.J., Mead, J.M.G., 2011. The mass-concentration relationship of virialized haloes and its impact on cosmological observables. *MNRAS* 416 (Oct.), 2539–2549.
- Kirk, D., Bridle, S., Schneider, M., 2010. The impact of intrinsic alignments: cosmological constraints from a joint analysis of cosmic shear and galaxy survey data. *MNRAS* 408 (Nov.), 1502–1515.
- Kitching T., Balan S., Bernstein G., Bethge M., Bridle S., Courbin F., et al. 2010. Gravitational lensing accuracy testing 2010 (GREAT10) challenge handbook. arXiv:1009.0779.
- Kitching, T.D., Amara, A., 2009. Fisher matrix decomposition for dark energy prediction. *MNRAS* 398 (Oct.), 2134–2142.
- Kitching, T.D., Miller, L., Heymans, C.E., van Waerbeke, L., Heavens, A.F., 2008. Bayesian galaxy shape measurement for weak lensing surveys - II. Application to simulations. *MNRAS* 390 (Oct.), 149–167.
- Kleban, M., Schillo, M., 2012. Spatial curvature falsifies eternal inflation. *JCAP* 6 (Jun.), 29.
- Kleinheinrich, M., Schneider, P., Rix, H.-W., Erben, T., Wolf, C., Schirmer, M., Meisenheimer, K., Borch, A., Dye, S., Kovacs, Z., Wisotzki, L., 2006. Weak lensing measurements of dark matter halos of galaxies from COMBO-17. *A&A* 455 (Aug.), 441–451.
- Kneib, J.-P., Natarajan, P., 2011. Cluster lenses. *A&A Rev.* 19 (Nov.), 47.
- Kochanek, C.S., 1996. Is there a cosmological constant? *ApJ* 466 (Aug.), 638.
- Kochanek, C.S., White, M., Huchra, J., Macri, L., Jarrett, T.H., Schneider, S.E., Mader, J., 2003. Clusters of galaxies in the local universe. *ApJ* 585 (Mar), 161–181.
- Koester, B.P., McKay, T.A., Annis, J., Wechsler, R.H., Evrard, A., Bleem, L., et al., 2007. A MaxBCG catalog of 13,823 galaxy clusters from the sloan digital sky survey. *ApJS* 660 (May), 239–255.
- Koivisto, T., Mota, D.F., 2006. Dark energy anisotropic stress and large scale structure formation. *Phys. Rev. D* 73 (8), 083502.
- Kolb E.W., Matarrese S., Notari A., Riotto A., 2005. Primordial inflation explains why the universe is accelerating today. arXiv:hep-th/0503117.
- Komatsu, E., Dunkley, J., Nolta, M.R., Bennett, C.L., Gold, B., Hinshaw, G., et al., 2009. Five-year Wilkinson microwave anisotropy probe observations: cosmological interpretation. *ApJS* 180 (Feb.), 330–376.
- Komatsu, E., Smith, K.M., Dunkley, J., Bennett, C.L., Gold, B., Hinshaw, G., et al., 2011. Seven-year Wilkinson microwave anisotropy probe (WMAP) observations: cosmological interpretation. *ApJS* 192 (Feb.), 18.
- Kowalski, M., Rubin, D., Aldering, G., Agostinho, R.J., Amadon, A., Amanullah, R., et al., 2008. Improved cosmological constraints from new, old, and combined supernova data sets. *ApJ* 686 (Oct.), 749–778.
- Krause, E., Hirata, C.M., 2010. Weak lensing power spectra for precision cosmology. Multiple-deflection, reduced shear, and lensing bias corrections. *A&A* 523 (Nov.), A28.
- Krauss, L.M., Turner, M.S., 1995. The cosmological constant is back. *Gen. Rel. Grav.* 27, 1137–1144.
- Kravtsov, A.V., Berlind, A.A., Wechsler, R.H., Klypin, A.A., Gottlöber, S., Allgood, B., Primack, J.R., 2004. The dark side of the Halo occupation distribution. *ApJ* 609 (Jul.), 35–49.
- Kravtsov, A.V., Borgani, S., 2012. Formation of galaxy clusters. *ARA&A* 50 (Sep.), 353–409.
- Kravtsov, A.V., Vikhlinin, A., Nagai, D., 2006. A new robust low-scatter X-ray mass indicator for clusters of galaxies. *ApJ* 650 (Oct.), 128–136.
- Kristian, J., 1967. On the cosmological distortion effect. *ApJ* 147 (Mar), 864.
- Kristian, J., Sachs, R.K., 1966. Observations in cosmology. *ApJ* 143 (Feb.), 379.
- Kujat, J., Linn, A.M., Scherrer, R.J., Weinberg, D.H., 2002. Prospects for determining the equation of state of the dark energy: what can be learned from multiple observables? *ApJ* 572 (Jun.), 1–14.
- Kunz, M., Sapone, D., 2007. Dark energy versus modified gravity. *Phys. Rev. Lett.* 98 (12), 121301.
- Lampeitl, H., Smith, M., Nichol, R.C., Bassett, B., Cinabro, D., Dilday, B., et al., 2010. The effect of host galaxies on type Ia supernovae in the SDSS-II supernova survey. *ApJ* 722 (Oct.), 566–576.
- Larson, D., Dunkley, J., Hinshaw, G., Komatsu, E., Nolta, M.R., Bennett, C.L., et al., 2011. Seven-year Wilkinson Microwave Anisotropy Probe (WMAP) observations: power spectra and WMAP-derived parameters. *ApJS* 192 (Feb.), 16.
- Lau, E.T., Kravtsov, A.V., Nagai, D., 2009. Residual gas motions in the intracluster medium and bias in hydrostatic measurements of mass profiles of clusters. *ApJ* 705 (Nov.), 1129–1138.
- Lauer, T.R., 1999. Combining undersampled dithered images. *PASP* 111 (Feb.), 227–237.
- Laureijs R., Amiaux J., Arduini S., Auguères J., Brinchmann J., Cole R., et al. 2011. Euclid definition study report. arXiv:1110.3193.
- Lavaux, G., Wandelt, B.D., 2010. Precision cosmology with voids: definition, methods, dynamics. *MNRAS* 403, 1392–1408.
- Lavaux, G., Wandelt, B.D., 2012. Precision cosmography with stacked voids. *ApJ* 754 (Aug.), 109.
- Lawrence, E., Heitmann, K., White, M., Higdon, D., Wagner, C., Habib, S., Williams, B., 2010. The coyote universe. III. simulation suite and precision emulator for the nonlinear matter power spectrum. *ApJ* 713 (Apr.), 1322–1331.

- Leauthaud, A., Tinker, J., Behroozi, P.S., Busha, M.T., Wechsler, R.H., 2011. A theoretical framework for combining techniques that probe the link between galaxies and dark matter. *ApJ* 738 (Sep.), 45.
- Leauthaud, A., Tinker, J., Bundy, K., Behroozi, P.S., Massey, R., Rhodes, J., et al., 2012. New constraints on the evolution of the stellar-to-dark matter connection: a combined analysis of galaxy–galaxy lensing, clustering, and Stellar mass functions from $z = 0.2$ to $z = 1$. *ApJ* 744 (Jan.), 159.
- Leinert, C., Bowyer, S., Haikala, L.K., Hanner, M.S., Hauser, M.G., Levasseur-Regourd, A.-C., et al., 1998. The 1997 reference of diffuse night sky brightness. *A&AS* 127 (Jan.), 1–99.
- Lemaître, G., 1927. Un Univers homogène de masse constante et de rayon croissant rendant compte de la vitesse radiale des nébuleuses extra-galactiques. *Annales de la Societe Scientifique de Bruxelles* 47, 49–59.
- Leonard, A., Goldberg, D.M., Haaga, J.L., Massey, R., 2007. Gravitational shear, flexion, and strong lensing in Abell 1689. *ApJ* 666 (Sep.), 51–63.
- Leonard, A., King, L.J., Goldberg, D.M., 2011. New constraints on the complex mass substructure in Abell 1689 from gravitational flexion. *MNRAS* 413 (May), 789–804.
- Levine, R., Gnedin, N.Y., 2006. AGN outflows and the matter power spectrum. *ApJ* 649, L57–L60.
- Lewis, A., Bridle, S., 2002. Cosmological parameters from CMB and other data: a Monte Carlo approach. *Phys. Rev. D* 66 (10), 103511–+.
- Lewis, A., Challinor, A., Lasenby, A., 2000. Efficient computation of CMB anisotropies in closed FRW models. *ApJ* 538, 473–476.
- Li, B., Hellwing, W.A., Koyama, K., Zhao, G.-B., Jennings, E., Baugh, C.M., 2013. The non-linear matter and velocity power spectra in $f(R)$ gravity. *MNRAS* 428 (Jan.), 743–755.
- Li, I.H., Yee, H.K.C., 2008. Finding galaxy groups in photometric-redshift space: the probability friends-of-friends algorithm. *AJ* 135 (Mar), 809–822.
- Li, W., Leaman, J., Chornock, R., Filippenko, A.V., Poznanski, D., Ganeshalingam, M., Wang, X., Modjaz, M., Jha, S., Foley, R.J., Smith, N., 2011. Nearby supernova rates from the Lick Observatory Supernova Search - II. The observed luminosity functions and fractions of supernovae in a complete sample. *MNRAS* 412 (Apr.), 1441–1472.
- Lidz, A., Heitmann, K., Hui, L., Habib, S., Rauch, M., Sargent, W.L.W., 2006. Tightening constraints from the Ly α forest with the flux probability distribution function. *ApJ* 638 (Feb.), 27–44.
- Lightman, A.P., Schechter, P.L., 1990. The Omega dependence of peculiar velocities induced by spherical density perturbations. *ApJS* 74 (Dec.), 831–+.
- Lima, J.A.S., Alcaniz, J.S., 2000. Constraining the cosmic equation of state from old galaxies at high redshift. *MNRAS* 317 (Oct.), 893–896.
- Lima, M., Hu, W., 2004. Self-calibration of cluster dark energy studies: counts in cells. *Phys. Rev. D* 70 (4), 043504–+.
- Lima, M., Hu, W., 2005. Self-calibration of cluster dark energy studies: observable-mass distribution. *Phys. Rev. D* 72, 043006.
- Lima, M., Hu, W., 2007. Photometric redshift requirements for self-calibration of cluster dark energy studies. *Phys. Rev. D* 76 (12), 123013–+.
- Limber, D.N., 1953. The analysis of counts of the extragalactic nebulae in terms of a fluctuating density field. *ApJ* 117 (Jan.), 134.
- Limber, D.N., 1954. The analysis of counts of the extragalactic nebulae in terms of a fluctuating density field. II. *ApJ* 119 (May), 655.
- Lin, H., Dodelson, S., Seo, H.-J., Soares-Santos, M., Annis, J., Hao, J., Johnston, D., Kubo, J.M., Reis, R.R.R., Simet, M., 2012. The SDSS co-add: cosmic shear measurement. *ApJ* 761 (Dec.), 15.
- Linde, A.D., 1987. Eternally existing self-reproducing inflationary universe. *Physica Scripta* Volume T 15, 169–175.
- Linder, E.V., 2003. Baryon oscillations as a cosmological probe. *Phys. Rev. D* 68 (8), 083504–+.
- Linder, E.V., 2003a. Exploring the expansion history of the universe. *Phys. Rev. Lett.* 90, 091301.
- Linder, E.V., 2003b. Mapping the dark energy equation of state. *arXiv:astro-ph/0311403*.
- Linder, E.V., 2005. Cosmic growth history and expansion history. *Phys. Rev. D* 72, 043529.
- Linder, E.V., 2007. Theory challenges of the accelerating universe. *J. Phys. A* 40, 6697.
- Linder, E.V., 2010. Frontiers of dark energy. *arxiv:1009.14111*.
- Linder, E.V., 2011. Lensing time delays and cosmological complementarity. *Phys. Rev. D* 84 (12), 123529.
- Linder, E.V., Huterer, D., 2005. How many dark energy parameters? *Phys. Rev. D* 72, 043509.
- Lippai, Z., Frei, Z., Haiman, Z., 2008. Prompt shocks in the gas disk around a recoiling supermassive black hole binary. *ApJ Lett.* 676 (Mar), L5–L8.
- Liske, J., Codex Team., 2006. The Cosmological Dynamics Experiment. In: *ESA Special Publication*, vol. 637.
- Liske, J., Grazian, A., Vanzella, E., Dessauges, M., Viel, M., Pasquini, L., et al., 2008. Cosmic dynamics in the era of extremely large telescopes. *MNRAS* 386 (May), 1192–1218.
- Little, B., Weinberg, D.H., Park, C., 1991. Primordial fluctuations and non-linear structure. *MNRAS* 253 (Nov.), 295–306.
- Liu, A., Tegmark, M., 2012. How well can we measure and understand foregrounds with 21-cm experiments? *MNRAS* 419 (Feb.), 3491–3504.
- Livio M., 1999. The progenitors of type Ia supernovae. *arXiv:astro-ph/9903264*.
- Livio, M., 2011. Lost in translation: mystery of the missing text solved. *Nature* 479 (Nov.), 171–173.
- Lloyd-Davies, E.J., Romer, A.K., Mehtens, N., Hosmer, M., Davidson, M., Sabirli, K., et al., 2011. The XMM cluster survey: X-ray analysis methodology. *MNRAS* 418 (Nov.), 14–53.
- Loeb, A., 1998. Direct measurement of cosmological parameters from the cosmic deceleration of extragalactic objects. *ApJ* 499, L111–L114.
- Loeb, A., Wyithe, J.S.B., 2008. Possibility of precise measurement of the cosmological power spectrum with a dedicated survey of 21cm emission after reionization. *Phys. Rev. Lett.* 100 (16), 161301–+.
- Lombardi, M., Bertin, G., 1998. Improving the accuracy of mass reconstructions from weak lensing: local shear measurements. *A&A* 330 (Feb.), 791–800.
- Loverde, M., Smith, K.M., 2011. The non-Gaussian halo mass function with f_{NL} , g_{NL} and τ_{NL} . *JCAP* 8 (Aug.), 3.
- LSST Science Collaboration. 2009. LSST science book, Version 2.0. *arXiv:0912.0201*.
- Lue, A., 2006. The phenomenology of Dvali Gabadadze Porrati cosmologies. *Phys. Rep.* 423 (Jan.), 1–48.
- Lue, A., Scoccimarro, R., Starkman, G., 2004. Differentiating between modified gravity and dark energy. *Phys. Rev. D* 69 (4), 044005.
- Luppino, G.A., Kaiser, N., 1997. Detection of weak lensing by a cluster of galaxies at $z = 0.83$. *ApJ* 475, 20.
- Ma, Z., Bernstein, G., Weinstein, A., Sholl, M., 2008. Diagnosing space telescope misalignment and jitter using stellar images. *PASP* 120 (Dec.), 1307–1317.
- MacLeod, C.L., Hogan, C.J., 2008. Precision of Hubble constant derived using black hole binary absolute distances and statistical redshift information. *Phys. Rev. D* 77, 043512.
- Maddox, S.J., Efstathiou, G., Sutherland, W.J., Loveday, J., 1990. Galaxy correlations on large scales. *MNRAS* 242, 43–49.
- Maguire, K., Kotak, R., Smartt, S.J., Pastorello, A., Hamuy, M., Bufano, F., 2010. Type II-P supernovae as standardized candles: improvements using near-infrared data. *MNRAS* 403 (Mar), L11–L15.
- Majerotto, E., Guzzo, L., Samushia, L., Percival, W.J., Wang, Y., de la Torre, S., et al., 2012. Probing deviations from general relativity with the Euclid spectroscopic survey. *MNRAS* 424 (Aug.), 1392–1408.
- Majumdar, S., Mohr, J.J., 2004. Self-calibration in cluster studies of dark energy: combining the cluster redshift distribution, the power spectrum, and mass measurements. *ApJ* 613 (Sep.), 41–50.
- Mandel, K.S., Narayan, G., Kirshner, R.P., 2011. Type Ia supernova light curve inference: hierarchical models in the optical and near-infrared. *ApJ* 731 (Apr.), 120.
- Mandel, K.S., Wood-Vasey, W.M., Friedman, A.S., Kirshner, R.P., 2009. Type Ia supernova light-curve inference: hierarchical bayesian analysis in the near-infrared. *ApJ* 704 (Oct), 629–651.
- Mandelbaum, R., Blake, C., Bridle, S., Abdalla, F.B., Brough, S., Colless, M., et al., 2011. The WiggleZ dark energy survey: direct constraints on blue galaxy intrinsic alignments at intermediate redshifts. *MNRAS* 410 (Jan.), 844–859.
- Mandelbaum, R., Hirata, C.M., Ishak, M., Seljak, U., Brinkmann, J., 2006. Detection of large scale intrinsic ellipticity-density correlation from the Sloan Digital Sky Survey and implications for weak lensing surveys. *MNRAS* 367, 611–626.
- Mandelbaum, R., Hirata, C.M., Leauthaud, A., Massey, R.J., Rhodes, J., 2012. Precision simulation of ground-based lensing data using observations from space. *MNRAS* 420 (Feb.), 1518–1540.
- Mandelbaum, R., Hirata, C.M., Seljak, U., Guzik, J., Padmanabhan, N., Blake, C., Blanton, M.R., Lupton, R., Brinkmann, J., 2005. Systematic errors in weak lensing: application to SDSS galaxy–galaxy weak lensing. *MNRAS* 361 (Aug.), 1287–1322.

- Mandelbaum, R., McDonald, P., Seljak, U., Cen, R., 2003. Precision cosmology from the Lyman α forest: power spectrum and bispectrum. *MNRAS* 344 (Sep.), 776–788.
- Mandelbaum, R., Seljak, U., Baldauf, T., Smith, R.E., 2010. Precision cluster mass determination from weak lensing. *MNRAS* 405 (Jul.), 2078–2102.
- Mandelbaum, R., Seljak, U., Hirata, C.M., 2008. A halo mass–concentration relation from weak lensing. *JCAP* 8 (Aug.), 6–+.
- Mangilli, A., Verde, L., Beltran, M., 2010. Isocurvature modes and baryon acoustic oscillations. *JCAP* 10 (Oct.), 9–+.
- Mantz, A., Allen, S.W., Rapetti, D., Ebeling, H., 2010. The observed growth of massive galaxy clusters - I. Statistical methods and cosmological constraints. *MNRAS* 406 (Aug.), 1759–1772.
- Mantz, A., Allen, S.W., Rapetti, D., Ebeling, H., 2010. The observed growth of massive galaxy clusters I: statistical methods and cosmological constraints. *MNRAS* 406, 1759–1772.
- Mao, X.-C., Wu, X.-P., 2008. Signatures of the baryon acoustic oscillations on 21 cm emission background. *ApJ Lett.* 673 (Feb.), L107–L110.
- March, M.C., Trotta, R., Amendola, L., Huterer, D., 2011. Robustness to systematics for future dark energy probes. *MNRAS* 415, 143–152.
- March, M.C., Trotta, R., Berkes, P., Starkman, G.D., Vaudrevange, P.M., 2011. Improved constraints on cosmological parameters from Type Ia supernova data. *MNRAS* 418 (Dec.), 2308–2329.
- Marian, L., Smith, R.E., Bernstein, G.M., 2009. The cosmology dependence of weak lensing cluster counts. *ApJ Lett.* 698 (Jun.), L33–L36.
- Marinoni, C., Buzzi, A., 2010. A geometric measure of dark energy with pairs of galaxies. *Nature* 468 (Nov.), 539–541.
- Markovic, D., 1993. On the possibility of determining cosmological parameters from measurements of gravitational waves emitted by coalescing, compact binaries. *Phys. Rev. D* 48, 4738–4756.
- Marriage, T.A., Acquaviva, V., Ade, P.A.R., Aguirre, P., Amiri, M., Appel, J.W., et al., 2011. The atacama cosmology telescope: Sunyaev–Zel’dovich-selected galaxy clusters at 148 GHz in the 2008 survey. *ApJ* 737 (Aug.), 61.
- Martel, H., Shapiro, P.R., Weinberg, S., 1998. Likely values of the cosmological constant. *ApJ* 492, 29.
- Martin, J., 2012. Everything you always wanted to know about the cosmological constant problem (but were afraid to ask). *C. R. Phys.* 13 (Jul.), 566–665.
- Martínez, V.J., Arnalte-Mur, P., Saar, E., de la Cruz, P., Pons-Bordería, M.J., Paredes, S., Fernández-Soto, A., Tempel, E., 2009. Reliability of the detection of the baryon acoustic peak. *ApJ Lett.* 696 (May), L93–L97.
- Massey, R., Heymans, C., Bergé, J., Bernstein, G., Bridle, S., Clowe, D., et al., 2007a. The shear testing programme 2: factors affecting high-precision weak-lensing analyses. *MNRAS* 376 (Mar), 13–38.
- Massey, R., Refregier, A., Bacon, D., Ellis, R., 2005. An enlarged cosmic shear survey with the William Herschel telescope. *MNRAS* 359, 1277–1286.
- Massey, R., Rhodes, J., Leauthaud, A., Capak, P., Ellis, R., Koekemoer, A., et al., 2007b. COSMOS: three-dimensional weak lensing and the growth of structure. *ApJS* 172 (Sep.), 239–253.
- Massey, R., Rowe, B., Refregier, A., Bacon, D.J., Bergé, J., 2007c. Weak gravitational shear and flexion with polar shapelets. *MNRAS* 380 (Sep.), 229–245.
- Massey, R., Stoughton, C., Leauthaud, A., Rhodes, J., Koekemoer, A., Ellis, R., Shaghoulain, E., 2010. Pixel-based correction for Charge Transfer Inefficiency in the Hubble space telescope advanced camera for surveys. *MNRAS* 401 (Jan.), 371–384.
- Matsubara, T., 2004. Correlation function in deep redshift space as a cosmological probe. *ApJ* 615, 573–585.
- Matsubara, T., Suto, Y., 1996. Cosmological redshift distortion of correlation functions as a probe of the density parameter and the cosmological constant. *ApJ* 470, L1–L5.
- Matsubara, T., Szalay, A.S., 2001. Constraining the cosmological constant from large-scale redshift–space clustering. *ApJ Lett.* 556 (Aug.), L67–L70.
- Matthews, D.J., Newman, J.A., 2010. Reconstructing redshift distributions with cross-correlations: tests and an optimized recipe. *ApJ* 721, 456–468.
- Maturi, M., Mignone, C., 2009. An optimal basis system for cosmology: data analysis and new parameterisation. *A&A* 508, 45M.
- McDonald, P., Eisenstein, D.J., 2007. Dark energy and curvature from a future baryonic acoustic oscillation survey using the Lyman- α forest. *Phys. Rev. D* 76 (6), 063009–+.
- McDonald, P., Miralda-Escudé, J., 1999. Measuring the cosmological geometry from the Lyman-alpha forest along parallel lines of sight. *ApJ* 518 (Jun.), 24–31.
- McDonald, P., Seljak, U., 2009. How to measure redshift–space distortions without sample variance. *JCAP* 0910, 007.
- McDonald, P., Seljak, U., Burles, S., Schlegel, D.J., Weinberg, D.H., Cen, R., et al., 2006. The Ly α forest power spectrum from the sloan digital sky survey. *ApJS* 163 (Mar), 80–109.
- Mckay T.A., Sheldon E.S., Racusin J., Fischer P., Seljak U., Stebbins A., et al. 2001. Galaxy mass and luminosity scaling laws determined by weak gravitational lensing. *arXiv:astro-ph/0108013*.
- Mcquinn, M., Hernquist, L., Lidz, A., Zaldarriaga, M., 2011. The signatures of large-scale temperature and intensity fluctuations in the Lyman-alpha Forest. *MNRAS* 415, 977–992.
- Mcquinn, M., Hernquist, L., Zaldarriaga, M., Dutta, S., 2007. Studying reionization with Ly α emitters. *MNRAS* 381 (Oct.), 75–96.
- Mcquinn, M., White, M., 2011. On estimating Ly α forest correlations between multiple sightlines. *MNRAS* 415 (Aug.), 2257–2269.
- Mehrtens, N., Romer, A.K., Hilton, M., Lloyd-Davies, E.J., Miller, C.J., et al., 2012. The XMM cluster survey: optical analysis methodology and the first data release. *MNRAS* 423 (Jun.), 1024–1052.
- Mehta, K.T., Seo, H.-J., Eckel, J., Eisenstein, D.J., Metchnik, M., Pinto, P., Xu, X., 2011. Galaxy bias and its effects on the baryon acoustic oscillation measurements. *ApJ* 734 (Jun.), 94–+.
- Meiksin, A., Tittley, E.R., 2012. The impact of helium reionization on the structure of the intergalactic medium. *MNRAS* 423 (Jun.), 7–25.
- Meiksin, A., White, M., Peacock, J.A., 1999. Baryonic signatures in large-scale structure. *MNRAS* 304 (Apr.), 851–864.
- Melchior, P., Viola, M., 2012. Means of confusion: how pixel noise affects shear estimates for weak gravitational lensing. *MNRAS* 424, 2757–2769.
- Melnick, G.J., Bromm, V., Fazio, G.G., Gebhardt, K., Jaffe, D.T., Komatsu, E., et al., 2009. The Cosmic Inflation Probe (CIP) - Updated. In: *American Astronomical Society Meeting Abstracts #213*. In: *Bulletin of the American Astronomical Society*, vol. 41, p. 481.08.
- Melott, A.L., Pellman, T.F., Shandarin, S.F., 1994. Optimizing the Zel’dovich approximation. *MNRAS* 269 (Aug.), 626.
- Ménard, B., Scranton, R., Fukugita, M., Richards, G., 2010. Measuring the galaxy-mass and galaxy-dust correlations through magnification and reddening. *MNRAS* 405 (Jun.), 1025–1039.
- Meneghetti, M., Jain, B., Bartelmann, M., Dolag, K., 2005. Constraints on dark energy models from galaxy clusters with multiple arcs. *MNRAS* 362 (Oct.), 1301–1310.
- Meneghetti, M., Rasia, E., Merten, J., Bellagamba, F., Ettori, S., Mazzotta, P., Dolag, K., Marri, S., 2010. Weighing simulated galaxy clusters using lensing and X-ray. *A&A* 514 (May), A93+.
- Merchán, M., Zandivarez, A., 2002. Galaxy groups in the 2dF galaxy redshift survey: the catalogue. *MNRAS* 335 (Sep.), 216–222.
- Merchán, M.E., Zandivarez, A., 2005. Galaxy groups in the third data release of the sloan digital sky survey. *ApJ* 630 (Sep.), 759–763.
- Merloni A., Predehl P., Becker W., Böhringer H., Boller T., Brunner H., German eROSITA Consortium. Sep. 2012. eROSITA Science Book: Mapping the Structure of the Energetic Universe. *arXiv:1209.3114*.
- Mesinger, A., Furlanetto, S.R., 2008. Ly α emitters during the early stages of reionization. *MNRAS* 386 (Jun.), 1990–2002.
- Milkeraitis, M., van Waerbeke, L., Heymans, C., Hildebrandt, H., Dietrich, J.P., Erben, T., 2010. 3D-Matched-Filter galaxy cluster finder - I. Selection functions and CFHTLS Deep clusters. *MNRAS* 406 (Jul.), 673–688.
- Miller, A.D., Caldwell, R., Devlin, M.J., Dorwart, W.B., Herbig, T., Nolta, M.R., Page, L.A., Puchalla, J., Torbet, E., Tran, H.T., 1999. A Measurement of the angular power spectrum of the cosmic microwave background from $l = 100$ to 400. *ApJ Lett.* 524 (Oct.), L1–L4.
- Miller, C.J., Nichol, R.C., Reichart, D., Wechsler, R.H., Evrard, A.E., et al., 2005. The C4 clustering algorithm: clusters of galaxies in the sloan digital sky survey. *AJ* 130 (Sep.), 968–1001.
- Miller, L., Heymans, C., Kitching, T.D., 2013. Bayesian galaxy shape measurement for weak lensing surveys - III. Application to the Canada–France–Hawaii telescope lensing survey. *MNRAS*.
- Miller, L., Kitching, T.D., Heymans, C., Heavens, A.F., van Waerbeke, L., 2007. Bayesian galaxy shape measurement for weak lensing surveys - I. Methodology and a fast-fitting algorithm. *MNRAS* 382 (Nov.), 315–324.

- Milosavljevic, M., Phinney, E.S., 2005. The afterglow of massive black hole coalescence. *ApJ* 622, L93–L96.
- Miralda-Escudé, J., 1991. The correlation function of galaxy ellipticities produced by gravitational lensing. *ApJ* 380 (Oct.), 1–8.
- Misner, C.W., Thorne, K.S., Wheeler, J.A., 1973. *Gravitation*. W.H. Freeman and Co, San Francisco.
- Miyazaki, S., Komiyama, Y., Nakaya, H., Doi, Y., Furusawa, H., Gillingham, P., Kamata, Y., Takeshi, K., Nariai, K., 2006. HyperSuprime: Project Overview. In: *Society of Photo-Optical Instrumentation Engineers (SPIE) Conference Series*, vol. 6269.
- Mo, H.J., White, S.D.M., 1996. An analytic model for the spatial clustering of dark matter halos. *MNRAS* 282, 347.
- Mohayaee, R., Mathis, H., Colombi, S., Silk, J., 2006. Reconstruction of primordial density fields. *MNRAS* 365 (Jan.), 939–959.
- Monson, A.J., Freedman, W.L., Madore, B.F., Persson, S.E., Scowcroft, V., Seibert, M., Rigby, J.R., 2012. The Carnegie Hubble program: the leavitt law at 3.6 and 4.5 μm in the milky way. *ApJ* 759 (Nov.), 146.
- Morales, M.F., 2006. A technique for weak lensing with velocity maps: eliminating ellipticity noise in HI radio observations. *ApJ* 650, L21–L24.
- More, S., Kravtsov, A.V., Dalal, N., Gottlöber, S., 2011. The overdensity and masses of the friends-of-friends Halos and universality of Halo mass function. *ApJS* 195 (Jul.), 4.
- Moresco, M., Cimatti, A., Jimenez, R., Pozzetti, L., Zamorani, G., Bolzonella, M., et al., 2012. Improved constraints on the expansion rate of the Universe up to $z \sim 1.1$ from the spectroscopic evolution of cosmic chronometers. *JCAP* 8 (Aug.), 6.
- Moresco, M., Jimenez, R., Cimatti, A., Pozzetti, L., 2011. Constraining the expansion rate of the Universe using low-redshift ellipticals as cosmic chronometers. *JCAP* 3 (Mar), 45.
- Mortonson, M., Hu, W., Huterer, D., 2009a. Hiding dark energy transitions at low redshift. *Phys. Rev. D* 80, 067301.
- Mortonson, M.J., Hu, W., 2008. Model-independent constraints on reionization from large-scale cosmic microwave background polarization. *ApJ* 672 (Jan.), 737–751.
- Mortonson, M.J., Hu, W., Huterer, D., 2009b. Falsifying paradigms for cosmic acceleration. *Phys. Rev. D* 79, 023004.
- Mortonson, M.J., Huterer, D., Hu, W., 2010. Figures of merit for present and future dark energy probes. *Phys. Rev. D* 82, 063004.
- Mould, J., Blandford, R., Villumsen, J., Brainerd, T., Smail, I., Small, T., Kells, W., 1994. A search for weak distortion of distant galaxy images by large-scale structure. *MNRAS* 271 (Nov.), 31–38.
- Mould, J.R., Huchra, J.P., Freedman, W.L., Kennicutt Jr., R.C., Ferrarese, L., Ford, H.C., et al., 2000. The Hubble space telescope key project on the extragalactic distance scale. XXVIII. Combining the constraints on the Hubble constant. *ApJ* 529 (Feb.), 786–794.
- Mullis, C.R., Mcnamara, B.R., Quintana, H., Vikhlinin, A., Henry, J.P., Gioia, I.M., Hornstrup, A., Forman, W., Jones, C., 2003. The 160 square degree ROSAT survey: the revised catalog of 201 clusters with spectroscopic redshifts. *ApJ* 594 (Sep.), 154–171.
- Muzzin, A., Wilson, G., Yee, H.K.C., Hoekstra, H., Gilbank, D., Surace, J., et al., 2009. Spectroscopic Confirmation of Two Massive Red-Sequence-Selected Galaxy Clusters at $z \sim 1.2$ in the SpARCS-North Cluster Survey. *ApJ* 698 (Jun.), 1934–1942.
- Nagai, D., Vikhlinin, A., Kravtsov, A.V., 2007. Testing X-Ray Measurements of Galaxy Clusters with Cosmological Simulations. *ApJ* 655 (Jan.), 98–108.
- Nakamura, T., Chiba, T., 1999. Determining the equation of state of the expanding Universe: inverse problem in cosmology. *MNRAS* 306 (Jul.), 696–700.
- Narayanan, V.K., Berlind, A.A., Weinberg, D.H., 2000. Locally biased galaxy formation and large-scale structure. *ApJ* 528 (Jan.), 1–20.
- Narayanan, V.K., Weinberg, D.H., 1998. Reconstruction analysis of galaxy redshift surveys: a hybrid reconstruction method. *ApJ* 508 (Dec.), 440–471.
- Navarro, J.F., Frenk, C.S., White, S.D.M., 1996. The structure of cold dark matter halos. *ApJ* 462 (May), 563–+.
- Netterfield, C.B., Devlin, M.J., Jarosik, N., Page, L., Wollack, E.J., 1997. A measurement of the angular power spectrum of the anisotropy in the cosmic microwave background. *ApJ* 474, 47.
- Newman, J.A., 2008. Calibrating redshift distributions beyond spectroscopic limits with cross-correlations. *ApJ* 684 (Sep.), 88–101.
- Niemack, M.D., et al., 2010. ACTPol: A Polarization-Sensitive Receiver for the Atacama Cosmology Telescope. In: *Society of Photo-Optical Instrumentation Engineers (SPIE) Conference Series*, vol. 7741.
- Nissanke, S., Holz, D.E., Hughes, S.A., Dalal, N., Sievers, J.L., 2010. Exploring short gamma-ray bursts as gravitational-wave standard sirens. *ApJ* 725 (Dec.), 496–514.
- Nolta, M.R., Wright, E.L., Page, L., Bennett, C.L., Halpern, M., Hinshaw, G., et al., 2004. First year Wilkinson microwave anisotropy probe observations: dark energy induced correlation with radio sources. *ApJ* 608 (Jun.), 10–15.
- Norberg, P., Baugh, C.M., Hawkins, E., Maddox, S., Peacock, J.A., Cole, S., et al., 2001. The 2dF galaxy redshift survey: luminosity dependence of galaxy clustering. *MNRAS* 328 (Nov.), 64–70.
- Norman, M.L., Paschos, P., Harkness, R., 2009. Baryon acoustic oscillations in the Lyman alpha forest. *J. Phys. Conf. Ser.* 180 (1), 012021–+.
- Nugent, P., Kim, A., Perlmutter, S., 2002. K -corrections and extinction corrections for type Ia supernovae. *PASP* 114, 803–819.
- Nusser, A., Dekel, A., 1992. Tracing large-scale fluctuations back in time. *ApJ* 391 (Jun.), 443–452.
- Oguri, M., Hamana, T., 2011. Detailed cluster lensing profiles at large radii and the impact on cluster weak lensing studies. *MNRAS* 414 (Jul.), 1851–1861.
- Oguri, M., Inada, N., Strauss, M.A., Kochanek, C.S., Kayo, I., Shin, M.-S., et al., 2012. The sloan digital sky survey quasar lens search. VI. Constraints on dark energy and the evolution of massive galaxies. *AJ* 143 (May), 120.
- Oguri, M., Takada, M., 2011. Combining cluster observables and stacked weak lensing to probe dark energy: Self-calibration of systematic uncertainties. *Phys. Rev. D* 83 (2), 023008–+.
- Okumura, T., Matsubara, T., Eisenstein, D.J., Kayo, I., Hikage, C., Szalay, A.S., Schneider, D.P., 2008. Large-scale anisotropic correlation function of SDSS luminous red galaxies. *ApJ* 676 (Apr.), 889–898.
- Okumura, T., Seljak, U., McDonald, P., Desjacques, V., 2012. Distribution function approach to redshift space distortions. Part II: N -body simulations. *JCAP* 2 (Feb.), 10.
- Orban, C., Weinberg, D.H., 2011. Self-similar bumps and wiggles: Isolating the evolution of the BAO peak with power-law initial conditions. *Phys. Rev. D* 84 (6), 063501–+.
- Orsi, A., Baugh, C.M., Lacey, C.G., Cimatti, A., Wang, Y., Zamorani, G., 2010. Probing dark energy with future redshift surveys: a comparison of emission line and broad-band selection in the near-infrared. *MNRAS* 405 (Jun.), 1006–1024.
- Ostriker, J.P., Cen, R., 1996. Hydrodynamic simulations of the growth of cosmological structure: summary and comparisons among scenarios. *ApJ* 464 (Jun.), 27.
- Ostriker, J.P., Steinhardt, P.J., 1995. The observational case for a low density universe with a nonzero cosmological constant. *Nature* 377, 600–602.
- Overduin, J., Everitt, F., Mester, J., Worden, P., 2009. The science case for STEP. *Adv. Space Res.* 43, 1532–1537.
- Pacaud, F., Pierre, M., Adami, C., Altieri, B., Andreon, S., Chiappetti, L., et al., 2007. The XMM-LSS survey: the Class 1 cluster sample over the initial 5 deg² and its cosmological modelling. *MNRAS* 382 (Dec.), 1289–1308.
- Padmanabhan, N., Schlegel, D.J., Seljak, U., Makarov, A., Bahcall, N.A., Blanton, M.R., et al., 2007. The clustering of luminous red galaxies in the Sloan Digital Sky Survey imaging data. *MNRAS* 378 (Jul.), 852–872.
- Padmanabhan, N., White, M., 2009. Calibrating the baryon oscillation ruler for matter and halos. *Phys. Rev. D* 80 (6), 063508–+.
- Padmanabhan, N., White, M., Cohn, J.D., 2009. Reconstructing baryon oscillations: a Lagrangian theory perspective. *Phys. Rev. D* 79 (6), 063523–+.
- Padmanabhan, N., Xu, X., Eisenstein, D.J., Scalzo, R., Cuesta, A.J., Mehta, K.T., Kazin, E., 2012. A 2 per cent distance to $z = 0.35$ by reconstructing baryon acoustic oscillations - I. Methods and application to the Sloan Digital Sky Survey. *MNRAS* 427 (Dec.), 2132–2145.
- Paranjape, A., Gordon, C., Hotchkiss, S., 2011. Extreme tail of the non-Gaussian mass function. *Phys. Rev. D* 84 (2), 023517.
- Parkinson, D., Blake, C., Kunz, M., Bassett, B.A., Nichol, R.C., Glazebrook, K., 2007. Optimizing baryon acoustic oscillation surveys - I. Testing the concordance Λ CDM cosmology. *MNRAS* 377 (May), 185–197.
- Parkinson, D., Riemer-Sørensen, S., Blake, C., Poole, G.B., Davis, T.M., Brough, S., et al., 2012. The WiggleZ dark energy survey: final data release and cosmological results. *Phys. Rev. D* 86 (10), 103518.
- Peacock J.A., 2013. Slipher, galaxie, and cosmological velocity fields. arXiv:1301.7286.
- Peacock, J.A., Cole, S., Norberg, P., Baugh, C.M., Bland-Hawthorn, J., Bridges, T., et al., 2001. A measurement of the cosmological mass density from clustering in the 2dF Galaxy Redshift Survey. *Nature* 410 (Mar), 169–173.

- Peacock, J.A., Dodds, S.J., 1996. Nonlinear evolution of cosmological power spectra. *MNRAS* 280, L19.
- Peebles, P.J.E., 1973. Statistical analysis of catalogs of extragalactic objects. I. Theory. *ApJ* 185 (Oct.), 413–440.
- Peebles, P.J.E., 1980. *The Large-scale Structure of the Universe*. Princeton University Press, Princeton, NJ.
- Peebles, P.J.E., 1982. Large-scale background temperature and mass fluctuations due to scale-invariant primeval perturbations. *ApJ Lett.* 263 (Dec.), L1–L5.
- Peebles, P.J.E., 1989. Tracing galaxy orbits back in time. *ApJ Lett.* 344 (Sep.), L53–L56.
- Peebles, P.J.E., 2010. Phenomenology of the Invisible Universe. In: American Institute of Physics Conference Series, vol. 1241. pp. 175–182.
- Peebles, P.J.E., Daly, R.A., Juszakiewicz, R., 1989. Masses of rich clusters of galaxies as a test of the biased cold dark matter theory. *ApJ* 347 (Dec.), 563–574.
- Peebles, P.J.E., Ratra, B., 2003. The cosmological constant and dark energy. *Rev. Modern Phys.* 75, 559–606.
- Peebles, P.J.E., Yu, J.T., 1970. Primeval adiabatic perturbation in an expanding universe. *ApJ* 162 (Dec.), 815–+.
- Peeples, M.S., Weinberg, D.H., Dave, R., Fardal, M.A., Katz, N., 2010. Pressure support vs. Thermal broadening in the Lyman-alpha forest I: effects of the equation of state on longitudinal structure. *MNRAS* 404, 1281–1294.
- Pen, U.-L., Lee, J., Seljak, U., 2000. Tentative detection of galaxy spin correlations in the tully catalog. *ApJ Lett.* 543 (Nov.), L107–L110.
- Pen, U.-L., Zhang, T., van Waerbeke, L., Mellier, Y., Zhang, P., Dubinski, J., 2003. Detection of dark matter skewness in the VIRMOS-DESCART survey: implications for Ω_0 . *ApJ* 592 (Aug.), 664–673.
- Penzias, A.A., Wilson, R.W., 1965. A Measurement of excess antenna temperature at 4080-Mc/s. *ApJ* 142, 419–421.
- Percival, W.J., Baugh, C.M., Bland-Hawthorn, J., Bridges, T., Cannon, R., Cole, S., et al., 2001. The 2dF galaxy redshift survey: the power spectrum and the matter content of the Universe. *MNRAS* 327 (Nov.), 1297–1306.
- Percival, W.J., Cole, S., Eisenstein, D.J., Nichol, R.C., Peacock, J.A., Pope, A.C., Szalay, A.S., 2007. Measuring the Baryon acoustic oscillation scale using the sloan digital sky survey and 2dF galaxy redshift survey. *MNRAS* 381 (Nov.), 1053–1066.
- Percival, W.J., Reid, B.A., Eisenstein, D.J., Bahcall, N.A., Budavari, T., Frieman, J.A., et al., 2010. Baryon acoustic oscillations in the sloan digital sky survey data release 7 galaxy sample. *MNRAS* 401 (Feb.), 2148–2168.
- Percival, W.J., Sutherland, W., Peacock, J.A., Baugh, C.M., Bland-Hawthorn, J., Bridges, T., et al., 2002. Parameter constraints for flat cosmologies from cosmic microwave background and 2dFGRS power spectra. *MNRAS* 337 (Dec.), 1068–1080.
- Percival, W.J., White, M., 2009. Testing cosmological structure formation using redshift–space distortions. *MNRAS* 393 (Feb.), 297–308.
- Perlman, E.S., Horner, D.J., Jones, L.R., Scharf, C.A., Ebeling, H., Wegner, G., Malkan, M., 2002. The WARPS survey. VI. Galaxy cluster and source identifications from phase I. *ApJS* 140 (Jun.), 265–301.
- Perlmutter, S., Aldering, G., Goldhaber, G., Knop, R.A., Nugent, P., Castro, P.G., et al., 1999. Measurements of omega and lambda from 42 high-redshift supernovae. *ApJ* 517 (Jun.), 565–586.
- Perlmutter, S., Gabi, S., Goldhaber, G., Goobar, A., Groom, D.E., Hook, I.M., et al., 1997. Measurements of the cosmological parameters omega and lambda from the first seven supernovae at $z \geq 0.35$. *ApJ* 483 (Jul.), 565.
- Peterson J.B., Bandura K., Pen U.L., 2006. The Hubble sphere hydrogen survey. arXiv:astro-ph/0606104.
- Phillipps, S., 1994. A possible geometric measurement of the cosmological constant. *MNRAS* 269 (Aug.), 1077–+.
- Phillips, M.M., 1993. The absolute magnitudes of type IA supernovae. *ApJ* 413, L105–L108.
- Phillips, M.M., Lira, P., Suntzeff, N.B., Schommer, R.A., Hamuy, M., Maza, J., 1999. The reddening-free decline rate versus luminosity relationship for type IA supernovae. *AJ* 118 (Oct.), 1766–1776.
- Phinney E.S., et al. 2004. The big bang observer: direct detection of gravitational waves from the birth of the universe to the present. NASA Mission Concept Study.
- Pierce, M.J., Welch, D.L., McClure, R.D., van den Bergh, S., Racine, R., Stetson, P.B., 1994. The Hubble constant and Virgo cluster distance from observations of Cepheid variables. *Nature* 371 (Sep.), 385–389.
- Pierpaoli, E., Borgani, S., Scott, D., White, M., 2003. On determining the cluster abundance normalization. *MNRAS* 342 (Jun.), 163–175.
- Piffaretti, R., Arnaud, M., Pratt, G.W., Pointecouteau, E., Melin, J.-B., 2011. The MCXC: a meta-catalogue of x-ray detected clusters of galaxies. *A&A* 534 (Oct.), A109.
- Pillepich, A., Porciani, C., Reiprich, T.H., 2012. The X-ray cluster survey with eRosita: forecasts for cosmology, cluster physics and primordial non-Gaussianity. *MNRAS* 422 (May), 44–69.
- Planck Collaboration, 2006. Planck: The scientific programme. arXiv:astro-ph/0604069.
- Planck Collaboration, 2013. Planck intermediate results. III. The relation between galaxy cluster mass and Sunyaev–Zel’dovich signal. *A&A* 550, 129.
- Planck Collaboration, Ade, P.A.R., Aghanim, N., Arnaud, M., Ashdown, M., Aumont, J., Baccigalupi, C., Balbi, A., Banday, A.J., Barreiro, R.B., et al., 2011a. Planck early results. VIII. The all-sky early Sunyaev–Zel’dovich cluster sample. *A&A* 536 (Dec.), A8.
- Planck Collaboration, Aghanim, N., Arnaud, M., Ashdown, M., Aumont, J., Baccigalupi, C., Balbi, A., Banday, A.J., Barreiro, R.B., Bartelmann, M., et al., 2011b. Planck early results. XII. Cluster Sunyaev–Zel’dovich optical scaling relations. *A&A* 536 (Dec.), A12.
- Pober, J.C., Parsons, A.R., Deboer, D.R., McDonald, P., McQuinn, M., Aguirre, J.E., Ali, Z., Bradley, R.F., Chang, T.-C., Morales, M.F., 2013. The baryon acoustic oscillation broadband and broad-beam array: design overview and sensitivity forecasts. *AJ* 145 (Mar), 65.
- Popowski, P.A., Weinberg, D.H., Ryden, B.S., Osmer, P.S., 1998. Quasar clustering and spacetime geometry. *ApJ* 498 (May), 11.
- Press, W.H., Schechter, P., 1974. Formation of galaxies and clusters of galaxies by self-similar gravitational condensation. *ApJ* 187, 425–438.
- Quercellini, C., Amendola, L., Balbi, A., Cabella, P., Quartini, M., 2012. Real-time cosmology. *Phys. Rep.* 521 (Dec.), 95–134.
- Ratra, B., Peebles, P.J.E., 1988. Cosmological consequences of a rolling homogeneous scalar field. *Phys. Rev. D* 37, 3406.
- Rauch, M., Miralda-Escude, J., Sargent, W.L.W., Barlow, T.A., Weinberg, D.H., Hernquist, L., Katz, N., Cen, R., Ostriker, J.P., 1997. The opacity of the Ly alpha forest and implications for omega B and the ionizing background. *ApJ* 489 (Nov.), 7.
- Refregier, A., 2003. Shapelets: I. A method for image analysis. *MNRAS* 338, 35.
- Refregier, A., Bacon, D., 2003. Shapelets: II. A method for weak lensing measurements. *MNRAS* 338, 48.
- Refregier, A., Rhodes, J., Groth, E.J., 2002. Cosmic shear and power spectrum normalization with the Hubble space telescope. *ApJ* 572, L131–L134.
- Regös, E., Geller, M.J., 1989. Infall patterns around rich clusters of galaxies. *AJ* 98 (Sep.), 755–765.
- Reichardt, C.L., Stalder, B., Bleem, L.E., Montroy, T.E., Aird, K.A., Andersson, K., et al., 2013. Galaxy clusters discovered via the Sunyaev–Zel’dovich effect in the first 720 square degrees of the south pole telescope survey. *ApJ* 763 (Feb.), 127.
- Reid, B.A., Percival, W.J., Eisenstein, D.J., Verde, L., Spergel, D.N., Skibba, R.A., et al., 2010. Cosmological constraints from the clustering of the Sloan Digital Sky Survey DR7 luminous red galaxies. *MNRAS* 404 (May), 60–85.
- Reid, B.A., White, M., 2011. Towards an accurate model of the redshift–space clustering of haloes in the quasi-linear regime. *MNRAS* 417 (Nov.), 1913–1927.
- Reid, B.A., Samushia, L., White, M., Percival, W.J., Manera, M., Padmanabhan, N., et al., 2012. The clustering of galaxies in the SDSS-III Baryon oscillation spectroscopic survey: measurements of the growth of structure and expansion rate at $z = 0.57$ from anisotropic clustering. *MNRAS* 426 (Nov.), 2719–2737.
- Reid, M.J., Braatz, J.A., Condon, J.J., Lo, K.Y., Kuo, C.Y., Impellizzeri, C.M.V., Henkel, C., 2013. The megamaser cosmology project: IV. A direct measurement of the Hubble constant from UGC 3789. *ApJ* 767, 154.
- Reiprich, T.H., Böhringer, H., 2002. The mass function of an X-ray flux-limited sample of galaxy clusters. *ApJ* 567 (Mar.), 716–740.
- Reyes, R., Mandelbaum, R., Seljak, U., Baldauf, T., Gunn, J.E., Lombriser, L., Smith, R.E., 2010. Confirmation of general relativity on large scales from weak lensing and galaxy velocities. *Nature* 464 (Mar), 256–258.
- Rhodes, J., Leauthaud, A., Stoughton, C., Massey, R., Dawson, K., Kolbe, W., Roe, N., 2010. The effects of charge transfer inefficiency (CTI) on galaxy shape measurements. *PASP* 122 (Apr.), 439–450.
- Rhodes, J., Refregier, A., Collins, N.R., Gardner, J.P., Groth, E.J., Hill, R.S., 2004. Measurement of cosmic shear with the space telescope imaging spectrograph. *ApJ* 605 (Apr.), 29–36.
- Rhodes, J., Refregier, A., Groth, E.J., 2001. Detection of cosmic shear with the Hubble space telescope survey strip. *ApJ Lett.* 552 (May), L85–L88.

- Rhodes J.D., Massey R., Albert J., Taylor J.E., Koekemoer A.M., Leauthaud A., 2006. Modeling and correcting the time-dependent ACS PSF. In: Koekemoer, A.M., Goudfrooij, P., Dressel, L.L. (Eds.), *The 2005 HST Calibration Workshop: Hubble After the Transition to Two-Gyro Mode*. p. 21.
- Rhook, K.J., Geil, P.M., Wyithe, J.S.B., 2009. Measurement of the baryonic acoustic oscillation scale in 21cm intensity fluctuations during the reionization era. *MNRAS* 392 (Feb.), 1388–1396.
- Riess, A.G., 2012. An Independent Determination of WFC3-IR Zeropoints and Count Rate Non-Linearity from 2MASS Asterisms. *HST Instrument Science Report WFC3 2011-15*.
- Riess, A.G., Filippenko, A.V., Challis, P., Clocchiatti, A., Diercks, A., Garnavich, P.M., et al., 1998. Observational evidence from supernovae for an accelerating universe and a cosmological constant. *AJ* 116 (Sep.), 1009–1038.
- Riess, A.G., Fliri, J., Valls-Gabaud, D., 2012. Cepheid period-luminosity relations in the near-infrared and the distance to M31 from the Hubble space telescope wide field camera 3. *ApJ* 745 (Feb.), 156.
- Riess, A.G., Livio, M., 2006. The first type Ia supernovae: an empirical approach to taming evolutionary effects in dark energy surveys from SNe Ia at $z > 2$. *ApJ* 648, 884–889.
- Riess, A.G., Macri, L., Casertano, S., Lampeitl, H., Ferguson, H.C., Filippenko, A.V., Jha, S.W., Li, W., Chornock, R., 2011. A 3% solution: determination of the Hubble constant with the Hubble space telescope and wide field camera 3. *ApJ* 730 (Apr.), 119.
- Riess, A.G., Macri, L., Casertano, S., Sosey, M., Lampeitl, H., Ferguson, H.C., Filippenko, A.V., Jha, S.W., Li, W., Chornock, R., Sarkar, D., 2009. A redetermination of the Hubble constant with the Hubble space telescope from a differential distance ladder. *ApJ* 699 (Jul.), 539–563.
- Riess, A.G., Press, W.H., Kirshner, R.P., 1996. A precise distance indicator: type Ia supernova multicolor light curve shapes. *ApJ* 473, 88.
- Riess, A.G., Strolger, L.-G., Casertano, S., Ferguson, H.C., Mobasher, B., Gold, B., et al., 2007. New Hubble space telescope discoveries of type Ia supernovae at $z \geq 1$: narrowing constraints on the early behavior of dark energy. *ApJ* 659 (Apr.), 98–121.
- Riess, A.G., Strolger, L.-G., Tonry, J., Casertano, S., Ferguson, H.C., Mobasher, B., et al., 2004. Type Ia supernova discoveries at $z > 1$ from the Hubble space telescope: evidence for past deceleration and constraints on dark energy evolution. *ApJ* 607 (Jun.), 665–687.
- Rines, K., Geller, M.J., Kurtz, M.J., Diaferio, A., 2003. CAIRNS: the cluster and infall region nearby survey. I. Redshifts and mass profiles. *AJ* 126 (Nov.), 2152–2170.
- Rogstad, D.H., Shostak, G.S., 1972. Gross properties of five scd galaxies as determined from 21-centimeter observations. *ApJ* 176 (Sep.), 315–+.
- Ross, A.J., Ho, S., Cuesta, A.J., Tojeiro, R., Percival, W.J., Wake, D., et al., 2011. Ameliorating systematic uncertainties in the angular clustering of galaxies: a study using the SDSS-III. *MNRAS* 417 (Oct.), 1350–1373.
- Ross, A.J., Percival, W.J., Sánchez, A.G., Samushia, L., Ho, S., Kazin, E., et al., 2012. The clustering of galaxies in the SDSS-III Baryon Oscillation Spectroscopic Survey: analysis of potential systematics. *MNRAS* 424 (Jul.), 564–590.
- Rowe, B., 2010. Improving PSF modelling for weak gravitational lensing using new methods in model selection. *MNRAS* 404, 350–366.
- Rowe B., Bacon D., Massey R., Heymans C., Haeussler B., Taylor A., Rhodes J., Mellier Y., 2012. Flexion measurement in simulations of Hubble Space Telescope data. arXiv:1211.0966.
- Rowe, B., Hirata, C., Rhodes, J., 2011. Optimal linear image combination. *ApJ* 741 (Nov.), 46.
- Rozo E., Bartlett J.G., Evrard A.E., Rykoff E.S., 2012a. Closing the loop: a self-consistent model of optical, X-ray and SZ scaling relations for clusters of galaxies. arXiv:1204.6305.
- Rozo E., Evrard A.E., Rykoff E.S., Bartlett J.G., 2012b. A comparative study of local galaxy clusters: II: X-ray and SZ scaling relations. arXiv:1204.6292.
- Rozo, E., Rykoff, E., Koester, B., Nord, B., Wu, H.-Y., Evrard, A., Wechsler, R., 2011a. Extrinsic sources of scatter in the richness-mass relation of galaxy clusters. *ApJ* 740 (Oct.), 53.
- Rozo E., Rykoff E.S., Bartlett J.G., Evrard A.E., 2012c. A comparative study of local galaxy clusters: I. Derived X-ray observables. arXiv:1204.6301.
- Rozo, E., Rykoff, E.S., Koester, B.P., McKay, T., Hao, J., Evrard, A., et al., 2009. Improvement of the richness estimates of maxBCG clusters. *ApJ* 703 (Sep.), 601–613.
- Rozo, E., Vikhlinin, A., More, S., 2012d. The $Y_{SZ} - Y_X$ scaling relation as determined from Planck and Chandra. *ApJ* 760 (Nov.), 67.
- Rozo, E., Wechsler, R.H., Rykoff, E.S., Annis, J.T., Becker, M.R., Evrard, A.E., et al., 2010. Cosmological constraints from the sloan digital sky survey maxBCG cluster catalog. *ApJ* 708 (Jan.), 645–660.
- Rozo, E., Wu, H.-Y., Schmidt, F., 2011b. Stacked weak lensing mass calibration: estimators, systematics, and impact on cosmological parameter constraints. *ApJ* 735 (Jul.), 118–+.
- Rubin, V.C., Ford Jr., W.K., 1970. Rotation of the Andromeda Nebula from a spectroscopic survey of emission regions. *ApJ* 159 (Feb.), 379–+.
- Rudd, D.H., Nagai, D., 2009. Nonequilibrium electrons and the Sunyaev-Zel'dovich effect of galaxy clusters. *ApJ Lett.* 701 (Aug.), L16–L19.
- Rudd, D.H., Zentner, A.R., Kravtsov, A.V., 2008. Effects of baryons and dissipation on the matter power spectrum. *ApJ* 672, 19–32.
- Ryden, B.S., 1995. Measuring q_0 from the distortion of voids in redshift space. *ApJ* 452 (Oct.), 25.
- Ryden, B.S., Melott, A.L., 1996. Voids in real space and in redshift space. *ApJ* 470, 160–171.
- Rykoff, E.S., Koester, B.P., Rozo, E., Annis, J., Evrard, A.E., Hansen, S.M., Hao, J., Johnston, D.E., McKay, T.A., Wechsler, R.H., 2012. Robust optical richness estimation with reduced scatter. *ApJ* 746 (Feb.), 178.
- Sachs, R.K., Wolfe, A.M., 1967. Perturbations of a cosmological model and angular variations of the microwave background. *ApJ* 147, 73–90.
- Sahni, V., Shafieloo, A., Starobinsky, A.A., 2008. Two new diagnostics of dark energy. *Phys. Rev. D* 78 (10), 103502.
- Sakharov, A.D., 1966. The initial stage of an expanding universe and the appearance of a nonuniform distribution of matter. *Soviet J. Exp. Theoret. Phys.* 22 (Jan.), 241.
- Sako, M., Bassett, B., Becker, A., Cinabro, D., Dejongh, F., Depoy, D.L., et al., 2008. The sloan digital sky survey-II supernova survey: search algorithm and follow-up observations. *AJ* 135 (Jan.), 348–373.
- Salvaterra, R., Della Valle, M., Campana, S., Chincarini, G., Covino, S., D'Avanzo, P., et al., 2009. GRB090423 at a redshift of $z \approx 1$. *Nature* 461 (Oct.), 1258–1260.
- Samushia, L., Percival, W.J., Raccanelli, A., 2012. Interpreting large-scale redshift-space distortion measurements. *MNRAS* 420 (Mar), 2102–2119.
- Sandage, A., 1962. The change of redshift and apparent luminosity of galaxies due to the deceleration of selected expanding universes. *ApJ* 136 (Sep.), 319.
- Sarkar, D., Amblard, A., Cooray, A., Holz, D.E., 2008. Implications of two type Ia supernova populations for cosmological measurements. *ApJ* 684, L13–L16.
- Sarkar, D., Amblard, A., Holz, D.E., Cooray, A., 2008a. Lensing and supernovae: quantifying the bias on the dark energy equation of state. *ApJ* 678 (May), 1–5.
- Sarkar, D., Sullivan, S., Joudaki, S., Amblard, A., Holz, D.E., Cooray, A., 2008b. Beyond two dark energy parameters. *Phys. Rev. Lett.* 100 (24), 241302–+.
- Saro, A., Bazin G., Mohr J., Dolag K., 2012. Toward unbiased galaxy cluster masses from line of sight velocity dispersions. arXiv:1203.5708.
- Sawangwit, U., Shanks, T., Abdalla, F.B., Cannon, R.D., Croom, S.M., Edge, A.C., Ross, N.P., Wake, D.A., 2011. Angular correlation function of 1.5 million luminous red galaxies: clustering evolution and a search for baryon acoustic oscillations. *MNRAS* 416 (Oct.), 3033–3056.
- Sawangwit, U., Shanks, T., Croom, S.M., Drinkwater, M.J., Fine, S., Parkinson, D., Ross, N.P., 2012. Measuring BAO and non-Gaussianity via QSO clustering. *MNRAS* 420 (Mar), 1916–1925.
- Schaefer, B.E., 2007. The Hubble diagram to redshift > 6 from 69 Gamma-Ray Bursts. *ApJ* 660, 16–46.
- Schaye, J., 2001. Model-independent insights into the nature of the Lyman- α forest and the distribution of matter in the universe. *ApJ* 559, 507.
- Schechter, P., 1976. An analytic expression for the luminosity function for galaxies. *ApJ* 203, 297–306.
- Schlegel D., Abdalla F., Abraham T., Ahn C., Allende Prieto C., Annis J., et al. 2011. The BigBOSS experiment. arXiv:1106.1706.
- Schmidt, B.P., Suntzeff, N.B., Phillips, M.M., Schommer, R.A., Clocchiatti, A., Kirshner, R.P., et al., 1998. The high- Z supernova search: measuring cosmic deceleration and global curvature of the universe using type Ia supernovae. *ApJ* 507 (Nov.), 46–63.
- Schneider, P., Eifler, T., Krause, E., 2010. COSEBIs: extracting the full E - β -mode information from cosmic shear correlation functions. *A&A* 520 (Sep.), A116.
- Schneider, P., Er, X., 2008. Weak lensing goes bananas: what flexion really measures. *A&A* 485 (Jul.), 363–376.
- Schneider, P., Kilbinger, M., 2007. The ring statistics — how to separate E - and B -modes of cosmic shear correlation functions on a finite interval. *A&A* 462, 841–849.

- Schneider, P., Kilbinger, M., Lombardi, M., 2005. The three-point correlation function of cosmic shear. II. Relation to the bispectrum of the projected mass density and generalized third-order aperture measures. *A&A* 431 (Feb.), 9–25.
- Schneider, P., Lombardi, M., 2003. The three-point correlation function of cosmic shear. I. The natural components. *A&A* 397 (Jan.), 809–818.
- Schneider, P., van Waerbeke, L., Jain, B., Kruse, G., 1998. A new measure for cosmic shear. *MNRAS* 296, 873–892.
- Schrabback, T., Erben, T., Simon, P., Miralles, J.-M., Schneider, P., Heymans, C., et al., 2007. Cosmic shear analysis of archival HST/ACS data. I. Comparison of early ACS pure parallel data to the HST/GEMS survey. *A&A* 468 (Jun.), 823–847.
- Schrabback, T., Hartlap, J., Joachimi, B., Kilbinger, M., Simon, P., Benabed, K., et al., 2010. Evidence of the accelerated expansion of the Universe from weak lensing tomography with COSMOS. *A&A* 516 (Jun.), A63.
- Schuecker, P., Böhringer, H., Collins, C.A., Guzzo, L., 2003. The REFLEX galaxy cluster survey. VII. Ω_m and σ_8 from cluster abundance and large-scale clustering. *A&A* 398 (Feb.), 867–877.
- Schutz, B.F., 1986. Determining the Hubble Constant from Gravitational Wave Observations. *Nature* 323, 310–311.
- Schwab, J., Bolton, A.S., Rappaport, S.A., 2010. Galaxy-scale strong-lensing tests of gravity and geometric cosmology: constraints and systematic limitations. *ApJ* 708 (Jan.), 750–757.
- Scoccimarro, R., 2004. Redshift–space distortions, pairwise velocities and nonlinearities. *Phys. Rev. D* 70, 083007.
- Scoccimarro, R., Sheth, R.K., Hui, L., Jain, B., 2001. How many galaxies fit in a halo? constraints on galaxy formation efficiency from spatial clustering. *ApJ* 546, 20–34.
- Scolnic, D.M., Riess, A.G., Huber, M.E., Rest, A., Stubbs, C.W., Tonry, J.L., 2009. Optical cross-correlation filters: an economical approach for identifying SNe Ia and estimating their redshifts. *ApJ* 706 (Nov.), 94–107.
- Scowcroft, V., Freedman, W.L., Madore, B.F., Monson, A.J., Persson, S.E., Seibert, M., Rigby, J.R., Sturch, L., 2011. The Carnegie Hubble program: the leavitt law at 3.6 μm and 4.5 μm in the large magellanic cloud. *ApJ* 743 (Dec.), 76.
- Scranton, R., Connolly, A.J., Nichol, R.C., Stebbins, A., Szapudi, I., Eisenstein, D.J., et al., 2003. Physical evidence for dark energy. arXiv:astro-ph/0307335.
- Scranton, R., Ménard, B., Richards, G.T., Nichol, R.C., Myers, A.D., Jain, B., et al., 2005. Detection of cosmic magnification with the sloan digital sky survey. *ApJ* 633 (Nov.), 589–602.
- Sehgal, N., Trac, H., Acquaviva, V., Ade, P.A.R., Aguirre, P., Amiri, M., et al., 2011. The atacama cosmology telescope: cosmology from galaxy clusters detected via the Sunyaev–Zel’dovich effect. *ApJ* 732 (May), 44.
- Seljak, U., 2000. Analytic model for galaxy and dark matter clustering. *MNRAS* 318, 203.
- Seljak, U., Hamaus, N., Desjacques, V., 2009. How to suppress the shot noise in galaxy surveys. *Phys. Rev. Lett.* 103 (9), 091303.
- Seljak, U., Makarov, A., Mandelbaum, R., Hirata, C.M., Padmanabhan, N., McDonald, P., Blanton, M.R., Tegmark, M., Bahcall, N.A., Brinkmann, J., 2005. SDSS galaxy bias from halo mass-bias relation and its cosmological implications. *Phys. Rev. D* 71 (4), 043511.
- Seljak, U., McDonald, P., 2011. Distribution function approach to redshift space distortions. *JCAP* 11 (Nov.), 39.
- Seljak, U., Zaldarriaga, M., 1996. A line-of-sight integration approach to cosmic microwave background anisotropies. *ApJ* 469 (Oct.), 437–+.
- Semboloni, E., Hoekstra, H., Huang, Z., Cardone, V., Cropper, M., Joachimi, B., et al., 2013. On the shear estimation bias induced by the spatial variation of colour across galaxy profiles. *MNRAS* 432, 2385.
- Semboloni, E., Hoekstra, H., Schaye, J., van Daalen, M.P., McCarthy, I.G., 2011. Quantifying the effect of baryon physics on weak lensing tomography. *MNRAS* 417 (Nov.), 2020–2035.
- Semboloni, E., Mellier, Y., van Waerbeke, L., Hoekstra, H., Tereno, I., Benabed, K., Gwyn, S.D.J., Fu, L., Hudson, M.J., Maoli, R., Parker, L.C., 2006a. Cosmic shear analysis with CFHTLS deep data. *A&A* 452 (Jun.), 51–61.
- Semboloni, E., Mellier, Y., van Waerbeke, L., Hoekstra, H., Tereno, I., Benabed, K., Gwyn, S.D.J., Fu, L., Hudson, M.J., Maoli, R., Parker, L.C., 2006b. Cosmic shear analysis with CFHTLS deep data. *A&A* 452 (Jun.), 51–61.
- Seo, H.-J., Dodelson, S., Marriner, J., McGinnis, D., Stebbins, A., Stoughton, C., Vallinotto, A., 2010a. A Ground-based 21 cm Baryon acoustic oscillation survey. *ApJ* 721 (Sep.), 164–173.
- Seo, H.-J., Eckel, J., Eisenstein, D.J., Mehta, K., Metchnik, M., Padmanabhan, N., Pinto, P., Takahashi, R., White, M., Xu, X., 2010b. High-precision predictions for the acoustic scale in the nonlinear regime. *ApJ* 720 (Sep.), 1650–1667.
- Seo, H.-J., Eisenstein, D.J., 2003. Probing dark energy with baryonic acoustic oscillations from future large galaxy redshift surveys. *ApJ* 598 (Dec.), 720–740.
- Seo, H.-J., Eisenstein, D.J., 2005. Baryonic acoustic oscillations in simulated galaxy redshift surveys. *ApJ* 633 (Nov.), 575–588.
- Seo, H.-J., Eisenstein, D.J., 2007. Improved forecasts for the baryon acoustic oscillations and cosmological distance scale. *ApJ* 665, 14–24.
- Seo, H.-J., Siegel, E.R., Eisenstein, D.J., White, M., 2008. Nonlinear structure formation and the acoustic scale. *ApJ* 686 (Oct.), 13–24.
- Shandarin, S.F., Melott, A.L., 1990. Minimal spectrum of long-wave perturbations - Is linear growth correct only in the nonlinear regime? *ApJ* 364 (Dec.), 396–399.
- Shang, C., Haiman, Z., 2011. Cosmology with standard sirens: the importance of the shape of the lensing magnification distribution. *MNRAS* 411 (Feb.), 9–22.
- Shapiro, C., Dodelson, S., Hoyle, B., Samushia, L., Flaugher, B., 2010. Will multiple probes of dark energy find modified gravity? *Phys. Rev. D* 82, 043520.
- Shaw, L.D., Holder, G.P., Bode, P., 2008. The impact of Halo properties, energy feedback, and projection effects on the mass-SZ flux relation. *ApJ* 686 (Oct.), 206–218.
- Sheldon, E.S., Cunha, C.E., Mandelbaum, R., Brinkmann, J., Weaver, B.A., 2012. Photometric redshift probability distributions for galaxies in the SDSS DR8. *ApJS* 201 (Aug.), 32.
- Sheldon, E.S., Johnston, D.E., Frieman, J.A., Scranton, R., McKay, T.A., Connolly, A.J., Budavári, T., Zehavi, I., Bahcall, N.A., Brinkmann, J., Fukugita, M., 2004. The galaxy-mass correlation function measured from weak lensing in the sloan digital sky survey. *AJ* 127 (May), 2544–2564.
- Sheldon, E.S., Johnston, D.E., Scranton, R., Koester, B.P., McKay, T.A., Oyaizu, H., et al., 2009. Cross-correlation weak lensing of SDSS galaxy clusters. I. Measurements. *ApJ* 703 (Oct.), 2217–2231.
- Sherwin, B.D., et al., 2011. Evidence for dark energy from the cosmic microwave background alone using the Atacama Cosmology Telescope lensing measurements. *Phys. Rev. Lett.* 107, 021302.
- Sheth, R.K., Tormen, G., 1999. Large scale bias and the peak background split. *MNRAS* 308, 119.
- Shoji, M., Jeong, D., Komatsu, E., 2009. Extracting angular diameter distance and expansion rate of the universe from two-dimensional galaxy power spectrum at high redshifts: baryon acoustic oscillation fitting versus full modeling. *ApJ* 693 (Mar), 1404–1416.
- Silk, J., 1968. Cosmic black-body radiation and galaxy formation. *ApJ* 151 (Feb.), 459–+.
- Silverman, J.M., Ganeshalingam, M., Li, W., Filippenko, A.V., 2012. Berkeley supernova Ia program - III. Spectra near maximum brightness improve the accuracy of derived distances to type Ia supernovae. *MNRAS* 425 (Sep.), 1889–1916.
- Simpson, F., Bridle, S., 2006. The redshift sensitivities of dark energy surveys. *Phys. Rev. D* 73, 083001.
- Skordis, C., Albrecht, A., 2002. Planck-scale quintessence and the physics of structure formation. *Phys. Rev. D* 66, 043523.
- Slosar, A., Font-Ribera, A., Pieri, M.M., Rich, J., Le Goff, J.-M., Aubourg, É., et al., 2011. The Lyman- α forest in three dimensions: measurements of large scale flux correlations from BOSS 1st-year data. *JCAP* 9 (Sep.), 1.
- Slosar, A., Iršič, V., Kirkby, D., Bailey, S., Busca, N.G., Delubac, T., et al., 2013. Measurement of baryon acoustic oscillations in the Lyman-alpha forest fluctuations in BOSS data release 9. *JCAP* 04, 026.
- Smith, D.R., Bernstein, G.M., Fischer, P., Jarvis, M., 2001. Weak-lensing determination of the mass in galaxy Halos. *ApJ* 551 (Apr.), 643–650.
- Smith, K.M., Zahn, O., Dore, O., 2007. Detection of gravitational lensing in the cosmic microwave background. *Phys. Rev. D* 76, 043510.
- Smith, R.E., Peacock, J.A., Jenkins, A., White, S.D.M., Frenk, C.S., Pearce, F.R., Thomas, P.A., Efstathiou, G., Couchman, H.M.P., 2003. Stable clustering, the halo model and non-linear cosmological power spectra. *MNRAS* 341 (Jun.), 1311–1332.
- Smith, R.E., Scoccimarro, R., Sheth, R.K., 2008. Motion of the acoustic peak in the correlation function. *Phys. Rev. D* 77 (4), 043525–+.
- Smith, S., 1936. The mass of the virgo cluster. *ApJ* 83 (Jan.), 23.

- Smoot, G.F., Bennett, C.L., Kogut, A., Wright, E.L., Aymon, J., Boggess, N.W., et al., 1992. Structure in the COBE differential microwave radiometer first-year maps. *ApJ Lett.* 396 (Sep.), L1–L5.
- Sobral, D., Smail, I., Best, P.N., Geach, J.E., Matsuda, Y., Stott, J.P., Cirasuolo, M., Kurk, J., 2013. A large H α survey at $z = 2.23, 1.47, 0.84$ and 0.40 : the 11 Gyr evolution of star-forming galaxies from HiZELS. *MNRAS* 428 (Jan.), 1128–1146.
- Song, Y.-S., Hu, W., Sawicki, I., 2007. The large scale structure of f(R) gravity. *Phys. Rev. D* 75, 044004.
- Sorce, J.G., Tully, R.B., Courtois, H.M., 2012. The mid-infrared Tully–Fisher relation: calibration of the type Ia supernova scale and H_0 . *ApJ Lett.* 758 (Oct.), L12.
- Soucail, G., Kneib, J.-P., Golse, G., 2004. Multiple-images in the cluster lens Abell 2218: constraining the geometry of the Universe? *A&A* 417 (Apr.), L33–L37.
- Springel, V., White, S.D.M., Jenkins, A., Frenk, C.S., Yoshida, N., Gao, L., et al., 2005. Simulations of the formation, evolution and clustering of galaxies and quasars. *Nature* 435 (Jun.), 629–636.
- Stanek, R., Rasia, E., Evrard, A.E., Pearce, F., Gazzola, L., 2010. Massive Halos in millennium gas simulations: multivariate scaling relations. *ApJ* 715 (Jun.), 1508–1523.
- Stanek, R., Rudd, D., Evrard, A.E., 2009. The effect of gas physics on the halo mass function. *MNRAS* 394 (Mar), L11–L15.
- Stanford, S.A., Brodwin, M., Gonzalez, A.H., Zeimann, G., Stern, D., Dey, A., Eisenhardt, P.R., Snyder, G.F., Mancone, C., 2012. IDCS J1426.5+3508: discovery of a massive, infrared-selected galaxy cluster at $z = 1.75$. *ApJ* 753 (Jul.), 164.
- Stanford, S.A., Eisenhardt, P.R., Brodwin, M., Gonzalez, A.H., Stern, D., Jannuzi, B.T., Dey, A., Brown, M.J.I., Mckenzie, E., Elston, R., 2005. An IR-selected galaxy cluster at $z = 1.41$. *ApJ Lett.* 634 (Dec.), L129–L132.
- Starobinsky, A.A., 1998. How to determine an effective potential for a variable cosmological term. *Soviet J. Exp. Theoret. Phys. Letters* 68 (Nov.), 757–763.
- Steffen, A.T., Strateva, I., Brandt, W.N., Alexander, D.M., Koekemoer, A.M., Lehmer, B.D., Schneider, D.P., Vignali, C., 2006. The X-ray-to-optical properties of optically selected active galaxies over wide luminosity and redshift ranges. *AJ* 131 (Jun.), 2826–2842.
- Steigman, G., 2010. Primordial nucleosynthesis: the predicted and observed abundances and their consequences. arXiv:1008.4765.
- Steinhardt, P.J., Wang, L.-M., Zlatev, I., 1999. Cosmological tracking solutions. *Phys. Rev. D* 59, 123504.
- Stril, A., Cahn, R.N., Linder, E.V., 2010. Testing standard cosmology with large scale structure. *MNRAS* 404, 239.
- Stritzinger, M.D., Phillips, M.M., Boldt, L.N., Burns, C., Campillay, A., Contreras, C., et al., 2011. The carnegie supernova project: second photometry data release of low-redshift type Ia supernovae. *AJ* 142 (Nov.), 156.
- Stubbs, C.W., Tonry, J.L., 2006. Toward 1% photometry: end-to-end calibration of astronomical telescopes and detectors. *ApJ* 646, 1436–1444.
- Sullivan, M., Conley, A., Howell, D.A., Neill, J.D., Astier, P., et al., 2010. The dependence of type Ia supernovae luminosities on their host galaxies. *MNRAS* 406 (Aug.), 782–802.
- Sullivan, M., Guy, J., Conley, A., Regnault, N., Astier, P., Ballard, C., et al., 2011. SNLS3: constraints on dark energy combining the supernova legacy survey three-year data with other probes. *ApJ* 737 (Aug.), 102.
- Sun, M., Voit, G.M., Donahue, M., Jones, C., Forman, W., Vikhlinin, A., 2009. Chandra studies of the X-ray gas properties of galaxy groups. *ApJ* 693 (Mar), 1142–1172.
- Sunyaev, R.A., Zel'dovich, Y.B., 1970. Small-scale fluctuations of relic radiation. *Ap & SS* 7 (Apr.), 3–19.
- Susskind L., 2003. The anthropic landscape of string theory. arXiv:hep-th/0302219.
- Sutter, P.M., Lavaux, G., Wandelt, B.D., Weinberg, D.H., 2012. A first application of the Alcock–Paczynski test to stacked cosmic voids. *ApJ* 761 (Dec.), 187.
- Suyu S.H., Auger M.W., Hilbert S., Marshall P.J., Tewes M., Treu T., et al. 2012a. Two accurate time-delay distances from strong lensing: implications for cosmology. arXiv:1208.6010.
- Suyu, S.H., Hensel, S.W., Mckean, J.P., Fassnacht, C.D., Treu, T., Halkola, A., et al., 2012b. Disentangling baryons and dark matter in the spiral gravitational lens B1933+503. *ApJ* 750 (May), 10.
- Suyu, S.H., Marshall, P.J., Auger, M.W., Hilbert, S., Blandford, R.D., Koopmans, L.V.E., Fassnacht, C.D., Treu, T., 2010. Dissecting the gravitational lens B1608+656. II. Precision measurements of the Hubble constant, spatial curvature, and the dark energy equation of state. *ApJ* 711 (Mar), 201–221.
- Suzuki, N., Rubin, D., Lidman, C., Aldering, G., Amanullah, R., Barbary, K., et al., 2012. The Hubble space telescope cluster supernova survey. V. Improving the dark-energy constraints above $z = 1$ and building an early-type-hosted supernova sample. *ApJ* 746 (Feb.), 85.
- Szabo, T., Pierpaoli, E., Dong, F., Pipino, A., Gunn, J., 2011. An optical catalog of galaxy clusters obtained from an adaptive matched filter finder applied to sloan digital sky survey data release 6. *ApJ* 736 (Jul.), 21.
- Takada, M., Jain, B., 2003. The three-point correlation function for spin-2 fields. *ApJ Lett.* 583 (Jan.), L49–L52.
- Takada, M., Jain, B., 2004. Cosmological parameters from lensing power spectrum and bispectrum tomography. *MNRAS* 348 (Mar), 897–915.
- Tang, J., Abdalla, F.B., Weller, J., 2011. Complementarity of future dark energy probes. *MNRAS* 416 (Sep.), 2212–2232.
- Tanvir, N.R., Fox, D.B., Levan, A.J., Berger, E., Wiersema, K., Fynbo, J.P.U., et al., 2009. A γ -ray burst at a redshift of $z \approx 8.2$. *Nature* 461 (Oct.), 1254–1257.
- Taruya, A., Nishimichi, T., Saito, S., 2010. Baryon acoustic oscillations in 2D: Modeling redshift–space power spectrum from perturbation theory. *Phys. Rev. D* 82 (6), 063522–+.
- Tavio H., Cuesta A.J., Prada F., Klypin A.A., Sanchez-Conde M.A., 2008. The dark outside: the density profile of dark matter haloes beyond the virial radius. arXiv:0807.3027.
- Taylor, S.R., Gair, J.R., 2012. Cosmology with the lights off: Standard sirens in the Einstein Telescope era. *Phys. Rev. D* 86 (2), 023502.
- Tegmark, M., 1997. Measuring cosmological parameters with galaxy surveys. *Phys. Rev. Lett.* 79 (Nov.), 3806–3809.
- Tegmark, M., Blanton, M.R., Strauss, M.A., Hoyle, F., Schlegel, D., Scoccamarro, R., et al., 2004. The three-dimensional power spectrum of galaxies from the sloan digital sky survey. *ApJ* 606 (May), 702–740.
- Tegmark, M., Eisenstein, D.J., Strauss, M.A., Weinberg, D.H., Blanton, M.R., Frieman, J.A., et al., 2006. Cosmological constraints from the SDSS luminous red galaxies. *Phys. Rev. D* 74 (12), 123507–+.
- Tegmark, M., Hamilton, A.J.S., Strauss, M.A., Vogeley, M.S., Szalay, A.S., 1998. Measuring the galaxy power spectrum with future redshift surveys. *ApJ* 499 (May), 555–+.
- Tegmark, M., Rees, M.J., 1998. Why is the CMB fluctuation level 10^{-5} ? *ApJ* 499, 526–532.
- Tegmark, M., Zaldarriaga, M., 2010. Omniscope: large area telescope arrays with only NlogN computational cost. *Phys. Rev. D* 82 (10), 103501–+.
- Tinker, J., Kravtsov, A.V., Klypin, A., Abazajian, K., Warren, M., Yepes, G., Gottlöber, S., Holz, D.E., 2008. Toward a Halo mass function for precision cosmology: the limits of universality. *ApJ* 688 (Dec.), 709–728.
- Tinker, J.L., 2007. Redshift–space distortions with the Halo occupation distribution II: analytic model. *MNRAS* 374, 477–492.
- Tinker, J.L., Robertson, B.E., Kravtsov, A.V., Klypin, A., Warren, M.S., Yepes, G., Gottlöber, S., 2010. The large-scale bias of dark matter halos: numerical calibration and model tests. *ApJ* 724 (Dec.), 878–886.
- Tinker, J.L., Sheldon, E.S., Wechsler, R.H., Becker, M.R., Rozo, E., Zu, Y., et al., 2012. Cosmological constraints from galaxy clustering and the mass-to-number ratio of galaxy clusters. *ApJ* 745 (Jan.), 16.
- Tinker, J.L., Weinberg, D.H., Zheng, Z., 2006. Redshift–space distortions with the halo occupation distribution i: numerical simulations. *MNRAS* 368, 85–108.
- Tonry, J.L., Schmidt, B.P., Barris, B., Candia, P., Challis, P., Cocchiatti, A., et al., 2003. Cosmological results from high- z supernovae. *ApJ* 594 (Sep.), 1–24.
- Tripp, R., 1998. A two-parameter luminosity correction for Type IA supernovae. *A&A* 331 (Mar), 815–820.
- Trotta, R., Kunz, M., Liddle, A.R., 2011. Designing decisive detections. *MNRAS* 414 (Jul.), 2337–2344.
- Tselikhovich, D., Hirata, C., 2010. Relative velocity of dark matter and baryonic fluids and the formation of the first structures. *Phys. Rev. D* 82 (8), 083520.
- Tully, R.B., Fisher, J.R., 1977. A new method of determining distances to galaxies. *A&A* 54 (Feb.), 661–673.
- Tyson, J.A., Valdes, F., Jarvis, J.F., Mills Jr., A.P., 1984. Galaxy mass distribution from gravitational light deflection. *ApJ Lett.* 281 (Jun.), L59–L62.
- Valageas, P., Clerc, N., Pacaud, F., Pierre, M., 2011. Covariance matrices for halo number counts and correlation functions. *A&A* 536 (Dec.), A95.
- Valdes, F., Jarvis, J.F., Tyson, J.A., 1983. Alignment of faint galaxy images - Cosmological distortion and rotation. *ApJ* 271 (Aug.), 431–441.
- van Daalen, M.P., Schaye, J., Booth, C.M., Vecchia, C.D., 2011. The effects of galaxy formation on the matter power spectrum: a challenge for precision cosmology. *MNRAS* 415, 3649–3665.

- van den Bergh, S., 2011. The curious case of Lemaître's equation no. 24. *JRASC* 105 (Aug.), 151.
- van den Bosch, F.C., Weinmann, S.M., Yang, X., Mo, H.J., Li, C., Jing, Y.P., 2005. The phase-space parameters of the brightest halo galaxies. *MNRAS* 361 (Aug.), 1203–1215.
- van Engelen, A., Keisler, R., Zahn, O., Aird, K.A., Benson, B.A., Bleem, L.E., et al., 2012. A measurement of gravitational lensing of the microwave background using south pole telescope data. *ApJ* 756 (Sep.), 142.
- van Leeuwen, F., Feast, M.W., Whitelock, P.A., Laney, C.D., 2007. Cepheid parallaxes and the hubble constant. *MNRAS* 379, 723–737.
- Van Waerbeke, L., Mellier, Y., Erben, T., Cuillandre, J.C., Bernardeau, F., Maoli, R., et al., 2000. Detection of correlated galaxy ellipticities from CFHT data: first evidence for gravitational lensing by large-scale structures. *A&A* 358 (Jun.), 30–44.
- Van Waerbeke, L., Mellier, Y., Pelló, R., Pen, U.-L., McCracken, H.J., Jain, B., 2002. Likelihood analysis of cosmic shear on simulated and VIRMOS-DESCART data. *A&A* 393 (Oct.), 369–379.
- Van Waerbeke, L., Mellier, Y., Radovich, M., Bertin, E., Dantel-Fort, M., McCracken, H.J., et al., 2001. Cosmic shear statistics and cosmology. *A&A* 374 (Aug.), 757–769.
- Vanderlinde, K., Crawford, T.M., de Haan, T., Dudley, J.P., Shaw, L., Ade, P.A.R., et al., 2010. Galaxy clusters selected with the Sunyaev-Zel'dovich effect from 2008 south pole telescope observations. *ApJ* 722 (Oct.), 1180–1196.
- Velder, M., Kuijken, K., Schrabback, T., 2011. Probing galaxy dark matter haloes in COSMOS with weak lensing flexion. *MNRAS* 412 (Apr.), 2665–2677.
- Viel, M., Haehnelt, M.G., Springel, V., 2004. Inferring the dark matter power spectrum from the Lyman- α forest in high-resolution QSO absorption spectra. *MNRAS* 354, 684.
- Viel, M., Matarrese, S., Heavens, A., Haehnelt, M.G., Kim, T.-S., Springel, V., Hernquist, L., 2004. The bispectrum of the Lyman α forest at $z \sim 2 - 2.4$ from a large sample of UVES QSO absorption spectra (LUQAS). *MNRAS* 347 (Jan.), L26–L30.
- Vikhlinin, A., Kravtsov, A.V., Burenin, R.A., Ebeling, H., Forman, W.R., Hornstrup, A., Jones, C., Murray, S.S., Nagai, D., Quintana, H., Voevodkin, A., 2009. Chandra cluster cosmology project III: cosmological parameter constraints. *ApJ* 692 (Feb.), 1060–1074.
- Vogele, M.S., Szalay, A.S., 1996. Eigenmode analysis of galaxy redshift surveys. I. Theory and methods. *ApJ* 465 (Jul.), 34–+.
- Voges, W., Aschenbach, B., Boller, T., Bräuninger, H., Briel, U., Burkert, W., et al., 1999. The ROSAT all-sky survey bright source catalogue. *A&A* 349 (Sep.), 389–405.
- Voigt, L.M., Bridle, S.L., Amara, A., Cropper, M., Kitching, T.D., Massey, R., Rhodes, J., Schrabback, T., 2012. The impact of galaxy colour gradients on cosmic shear measurement. *MNRAS* 421 (Apr.), 1385–1398.
- Voit, G.M., 2005. Tracing cosmic evolution with clusters of galaxies. *Rev. Modern Phys.* 77 (Apr.), 207–258.
- von der Linden A., Allen M.T., Applegate D.E., Kelly P.L., Allen S.W., Ebeling H., et al. 2012. Weighing the giants I: weak lensing masses for 51 massive galaxy clusters - project overview, data analysis methods, and cluster images. arXiv:1208.0597.
- Wagner, C., Müller, V., Steinmetz, M., 2008. Constraining dark energy via baryon acoustic oscillations in the (an)isotropic light-cone power spectrum. *A&A* 487 (Aug.), 63–74.
- Walker, E.S., Hook, I.M., Sullivan, M., Howell, D.A., Astier, P., Ballard, C., et al., 2011. Supernova legacy survey: using spectral signatures to improve Type Ia supernovae as distance indicators. *MNRAS* 410 (Jan.), 1262–1282.
- Wang, L.-M., Steinhardt, P.J., 1998. Cluster abundance constraints on quintessence models. *ApJ* 508, 483–490.
- Wang, Y., 1999. Analytical modeling of the weak lensing of standard candles. *ApJ* 525, 651.
- Wang, Y., 2000. Flux-averaging analysis of type Ia supernova data. *ApJ* 536 (Jun.), 531–539.
- Wang, Y., 2008. Figure of merit for dark energy constraints from current observational data. *Phys. Rev. D* 77, 123525.
- Wang, Y., Chuang, C.-H., Mukherjee, P., 2012. Comparative study of dark energy constraints from current observational data. *Phys. Rev. D* 85 (2), 023517.
- Wang, Y., Chuang, C.-H., Hirata, C.M., 2013. Toward more realistic forecasting of dark energy constraints from galaxy redshift surveys. *MNRAS* 430, 2446.
- Wang, Y., Percival, W., Cimatti, A., Mukherjee, P., Guzzo, L., et al., 2010. Designing a space-based galaxy redshift survey to probe dark energy. *MNRAS* 409 (Dec.), 737–749.
- Wang, Y., Tegmark, M., 2005. Uncorrelated measurements of the cosmic expansion history and dark energy from supernovae. *Phys. Rev. D* 71, 103513.
- Watson, D., Denney, K.D., Vestergaard, M., Davis, T.M., 2011. A new cosmological distance measure using active galactic nuclei. *ApJ Lett.* 740 (Oct.), L49+.
- Wei, H., Zhang, S.N., 2008. How to distinguish dark energy and modified gravity? *Phys. Rev. D* 78 (2), 023011.
- Weinberg, D.H., 1992. Reconstructing primordial density fluctuations. I - Method. *MNRAS* 254 (Jan.), 315–342.
- Weinberg, D.H., 2005. Dark energy: the observational challenge. *New Astron. Rev.* 49, 337–345.
- Weinberg, D.H., Cole, S., 1992. Non-Gaussian fluctuations and the statistics of galaxy clustering. *MNRAS* 259 (Dec.), 652–694.
- Weinberg, D.H., Gunn, J.E., 1990. Large-scale structure and the adhesion approximation. *MNRAS* 247 (Nov.), 260.
- Weinberg, D.H., Katz, N., Hernquist, L., 1998. Simulating cosmic structure formation. In: Woodward, C.E., Shull, J.M., Thronson, Jr., H.A. (Eds.), *Origins*. In: *Astronomical Society of the Pacific Conference Series*, vol. 148, p. 21.
- Weinberg, S., 1989. The cosmological constant problem. *Rev. Modern Phys.* 61, 1–23.
- Weller, J., Lewis, A.M., 2003. Large-scale cosmic microwave background anisotropies and dark energy. *MNRAS* 346 (Dec.), 987–993.
- Wen, Z.L., Han, J.L., Liu, F.S., 2009. Galaxy clusters identified from the SDSS DR6 and their properties. *ApJ* 183 (Aug.), 197–213.
- Wen, Z.L., Han, J.L., Liu, F.S., 2010. Mass function of rich galaxy clusters and its constraint on σ_8 . *MNRAS* 407 (Sep.), 533–543.
- White M., 2003. The Ly- α forest. In: *The Davis Meeting on Cosmic Inflation*. arXiv:astro-ph/0305474.
- White, M., Cohn, J.D., Smit, R., 2010. Cluster galaxy dynamics and the effects of large-scale environment. *MNRAS* 408 (Nov.), 1818–1834.
- White, M., Song, Y.-S., Percival, W.J., 2009. Forecasting cosmological constraints from redshift surveys. *MNRAS* 397, 1348–1354.
- White, S.D.M., Efstathiou, G., Frenk, C.S., 1993. The Amplitude of mass fluctuations in the universe. *MNRAS* 262, 1023–1028.
- White, S.D.M., Navarro, J.F., Evrard, A.E., Frenk, C.S., 1993. The baryon content of galaxy clusters: a challenge to cosmological orthodoxy. *Nature* 366 (Dec.), 429–433.
- Williamson, R., Benson, B.A., High, F.W., Vanderlinde, K., Ade, P.A.R., Aird, K.A., et al., 2011. A Sunyaev-Zel'dovich-selected sample of the most massive galaxy clusters in the 2500 deg² South Pole Telescope Survey. *ApJ* 738 (Sep.), 139.
- Wilson G., Muzzin A., Lacy M., Yee H., Surace J., Lonsdale C., Hoekstra H., Majumdar S., Gilbank D., Gladders M., 2006. Clusters of galaxies at $1 < z < 2$: the Spitzer adaptation of the red-sequence cluster survey. arXiv:astro-ph/0604289.
- Wilson, G., Muzzin, A., Yee, H.K.C., Lacy, M., Surace, J., Gilbank, D., et al., 2009. Spectroscopic confirmation of a massive red-sequence-selected galaxy cluster at $z = 1.34$ in the SpARCS-south cluster survey. *ApJ* 698 (Jun.), 1943–1950.
- Wittman, D.M., Tyson, J.A., Kirkman, D., Dell'antonio, I., Bernstein, G., 2000. Detection of weak gravitational lensing distortions of distant galaxies by cosmic dark matter at large scales. *Nature* 405 (May), 143–148.
- Wood-Vasey, W.M., Friedman, A.S., Bloom, J.S., Hicken, M., Modjaz, M., Kirshner, R.P., et al., 2008. Type Ia supernovae are good standard candles in the near infrared: evidence from PAIRITEL. *ApJ* 689 (Dec.), 377–390.
- Wood-Vasey, W.M., Miknaitis, G., Stubbs, C.W., Jha, S., Riess, A.G., Garnavich, P.M., et al., 2007. Observational constraints on the nature of dark energy: first cosmological results from the ESSENCE supernova survey. *ApJ* 666 (Sep.), 694–715.
- Wu, H.-Y., Zentner, A.R., Wechsler, R.H., 2010. The impact of theoretical uncertainties in the Halo mass function and Halo bias on precision cosmology. *ApJ* 713 (Apr.), 856–864.
- Wyithe, J.S.B., Brown, M.J.I., 2010. The halo occupation distribution of HI from 21-cm intensity mapping at moderate redshifts. *MNRAS* 404 (May), 876–884.
- Wyithe, J.S.B., Dijkstra, M., 2011. Non-gravitational contributions to the clustering of Ly α selected galaxies: implications for cosmological surveys. *MNRAS* 415 (Aug.), 3929–3950.
- Wyithe, J.S.B., Loeb, A., Geil, P.M., 2008. Baryonic acoustic oscillations in 21-cm emission: a probe of dark energy out to high redshifts. *MNRAS* 383 (Jan.), 1195–1209.
- Xu, X., Cuesta, A.J., Padmanabhan, N., Eisenstein, D.J., McBride, C.K., 2013. Measuring D_A and H at $z = 0.35$ from the SDSS DR7 LRGs using baryon acoustic oscillations. *MNRAS* 431, 2834.

- Xu, X., Padmanabhan, N., Eisenstein, D.J., Mehta, K.T., Cuesta, A.J., 2012. A 2 per cent distance to $z = 0.35$ by reconstructing baryon acoustic oscillations - II. Fitting techniques. *MNRAS* 427 (Dec.), 2146–2167.
- Xu, X., White, M., Padmanabhan, N., Eisenstein, D.J., Eckel, J., Mehta, K., Metchnik, M., Pinto, P., Seo, H.-J., 2010. A new statistic for analyzing baryon acoustic oscillations. *ApJ* 718 (Aug.), 1224–1234.
- Yang, J.-M., Schramm, D.N., Steigman, G., Rood, R.T., 1979. Constraints on cosmology and neutrino physics from big bang nucleosynthesis. *ApJ* 227, 697–704.
- Yang, X., Mo, H.J., van den Bosch, F.C., Pasquali, A., Li, C., Barden, M., 2007. Galaxy groups in the SDSS DR4. I. The catalog and basic properties. *ApJ* 671 (Dec.), 153–170.
- Yoo, J., 2009. Complete treatment of galaxy two-point statistics: Gravitational lensing effects and redshift-space distortions. *Phys. Rev. D* 79 (2), 023517.
- Yoo, J., Dalal, N., Seljak, U., 2011. Supersonic relative velocity effect on the baryonic acoustic oscillation measurements. *JCAP* 7 (Jul.), 18.
- Yoo, J., Fitzpatrick, A.L., Zaldarriaga, M., 2009. New perspective on galaxy clustering as a cosmological probe: General relativistic effects. *Phys. Rev. D* 80 (8), 083514.
- Yoo, J., Seljak, U., 2012. Joint analysis of gravitational lensing, clustering, and abundance: Toward the unification of large-scale structure analysis. *Phys. Rev. D* 86 (8), 083504.
- Yoo, J., Tinker, J.L., Weinberg, D.H., Zheng, Z., Katz, N., Davé, R., 2006. From galaxy–galaxy lensing to cosmological parameters. *ApJ* 652 (Nov.), 26–42.
- Yoo, J., Weinberg, D.H., Tinker, J.L., Zheng, Z., Warren, M.S., 2009. Extending recovery of the primordial matter power spectrum. *ApJ* 698, 967–985.
- Young, O.E., Thomas, P.A., Short, C.J., Pearce, F., 2011. Baryon fractions in clusters of galaxies: evidence against a pre-heating model for entropy generation. *MNRAS* 413 (May), 691–704.
- Yu, H., Tozzi, P., Borgani, S., Rosati, P., Zhu, Z.-H., 2011. Measuring redshifts using X-ray spectroscopy of galaxy clusters: results from Chandra data and future prospects. *A&A* 529 (May), A65.
- Zaldarriaga, M., Scoccimarro, R., 2003. Higher order moments of the cosmic shear and other spin-2 fields. *ApJ* 584 (Feb.), 559–565.
- Zaldarriaga, M., Seljak, U., 1997. All-sky analysis of polarization in the microwave background. *Phys. Rev. D* 55 (Feb.), 1830–1840.
- Zaldarriaga, M., Seljak, U., 2000. CMBFAST for spatially closed universes. *ApJS* 129 (Aug.), 431–434.
- Zehavi, I., Zheng, Z., Weinberg, D.H., Blanton, M.R., Bahcall, N.A., Berlind, A.A., et al., 2011. Galaxy clustering in the completed SDSS redshift survey: the dependence on color and luminosity. *ApJ* 736 (Jul.), 59.
- Zehavi, I., Zheng, Z., Weinberg, D.H., Frieman, J.A., Berlind, A.A., Blanton, M.R., et al., 2005. The luminosity and color dependence of the galaxy correlation function. *ApJ* 630 (Sep.), 1–27.
- Zeimann, G.R., Stanford, S.A., Brodwin, M., Gonzalez, A.H., Snyder, G.F., Stern, D., Eisenhardt, P., Mancone, C., Dey, A., 2012. idcs j1433 2+3306: an Infrared-selected Galaxy Cluster at $z = 1.89$. *ApJ* 756 (Sep.), 115.
- Zel'dovich, Y.B., 1968. Special issue: the cosmological constant and the theory of elementary particles. *Soviet Phys. Usp.* 11 (Mar), 381–393.
- Zel'dovich, Y.B., 1970. Gravitational instability: an approximate theory for large density perturbations. *A&A* 5 (Mar), 84–89.
- Zentner, A.R., Rudd, D.H., Hu, W., 2008. Self calibration of tomographic weak lensing for the physics of baryons to constrain dark energy. *Phys. Rev. D* 77, 043507.
- Zentner, A.R., Semboloni, E., Dodelson, S., Eifler, T., Krause, E., Hearin, A.P., 2013. Accounting for baryons in cosmological constraints from cosmic shear. *Phys. Rev. D* 87, 3509.
- Zhang, P., Liguori, M., Bean, R., Dodelson, S., 2007. Probing gravity at cosmological scales by measurements which test the relationship between gravitational lensing and matter overdensity. *Phys. Rev. Lett.* 99, 141302.
- Zhang, P., Pen, U.-L., Bernstein, G., 2010. Self-calibration of photometric redshift scatter in weak-lensing surveys. *MNRAS* 405 (Jun.), 359–374.
- Zhao, G.-B., et al., 2010. Probing modifications of general relativity using current cosmological observations. *Phys. Rev. D* 81, 103510.
- Zheng, Z., Cen, R., Trac, H., Miralda-Escudé, J., 2011. Radiative transfer modeling of Ly α emitters. II. New effects on galaxy clustering. *ApJ* 726 (Jan.), 38–+.
- Zlatev, I., Wang, L., Steinhardt, P.J., 1999. Quintessence, cosmic coincidence, and the cosmological constant. *Phys. Rev. Lett.* 82 (Feb.), 896–899.
- Zu Y., Weinberg D.H., 2012. The Redshift–space cluster–galaxy cross-correlation function: I. Modeling galaxy infall onto millennium simulation clusters and SDSS groups. *arXiv:1211.1379*.
- Zu, Y., Weinberg, D.H., Rozo, E., Sheldon, E.S., Tinker, J.L., Becker, M.R., 2013. Cosmological constraints from the large scale weak lensing of SDSS MaxBCG clusters. *MNRAS* 431, 3319.
- Zunckel, C., Okouma, P., Muya Kasanda, S., Moodley, K., Bassett, B.A., 2011. Fundamental uncertainty in the BAO scale from isocurvature modes. *Phys. Lett. B* 696 (Feb.), 433–437.
- Zwicky, F., 1933. Die Rotverschiebung von extragalaktischen Nebeln. *Helv. Phys. Acta* 6, 110–127.
- Zwicky, F., 1937. On the masses of nebulae and of clusters of nebulae. *ApJ* 86 (Oct.), 217.